Lecture Notes in Physics

Springer
Berlin
Heidelberg
New York
Barcelona
Hong Kong
London
Milan
Paris
Singapore
Tokyo

The Editorial Policy for Proceedings

The series Lecture Notes in Physics reports new developments in physical research and teaching – quickly, informally, and at a high level. The proceedings to be considered for publication in this series should be limited to only a few areas of research, and these should be closely related to each other. The contributions should be of a high standard and should avoid lengthy redraftings of papers already published or about to be published elsewhere. As a whole, the proceedings should aim for a balanced presentation of the theme of the conference including a description of the techniques used and enough motivation for a broad readership. It should not be assumed that the published proceedings must reflect the conference in its entirety. (A listing or abstracts of papers presented at the meeting but not included in the proceedings could be added as an appendix.)

When applying for publication in the series Lecture Notes in Physics the volume's editor(s) should submit sufficient material to enable the series editors and their referees to make a fairly accurate evaluation (e.g. a complete list of speakers and titles of papers to be presented and abstracts). If, based on this information, the proceedings are (tentatively) accepted, the volume's editor(s), whose name(s) will appear on the title pages, should select the papers suitable for publication and have them refereed (as for a journal) when appropriate. As a rule discussions will not be accepted. The series editors and Springer-Verlag will normally not interfere with the detailed editing except in fairly obvious cases or on technical matters.

Final acceptance is expressed by the series editor in charge, in consultation with Springer-Verlag only after receiving the complete manuscript. It might help to send a copy of the authors' manuscripts in advance to the editor in charge to discuss possible revisions with him. As a general rule, the series editor will confirm his tentative acceptance if the final manuscript corresponds to the original concept discussed, if the quality of the contribution meets the requirements of the series, and if the final size of the manuscript does not greatly exceed the number of pages originally agreed upon. The manuscript should be forwarded to Springer-Verlag shortly after the meeting. In cases of extreme delay (more than six months after the conference) the series editors will check once more the timeliness of the papers. Therefore, the volume's editor(s) should establish strict deadlines, or collect the articles during the conference and have them revised on the spot. If a delay is unavoidable, one should encourage the authors to update their contributions if appropriate. The editors of proceedings are strongly advised to inform contributors about these points at an early stage.

The final manuscript should contain a table of contents and an informative introduction accessible also to readers not particularly familiar with the topic of the conference. The contributions should be in English. The volume's editor(s) should check the contributions for the correct use of language. At Springer-Verlag only the prefaces will be checked by a copy-editor for language and style. Grave linguistic or technical shortcomings may lead to the rejection of contributions by the series editors. A conference report should not exceed a total of 500 pages. Keeping the size within this bound should be achieved by a stricter selection of articles and not by imposing an upper limit to the length of the individual papers. Editors receive jointly 30 complimentary copies of their book. They are entitled to purchase further copies of their book at a reduced rate. As a rule no reprints of individual contributions can be supplied. No royalty is paid on Lecture Notes in Physics volumes. Commitment to publish is made by letter of interest rather than by signing a formal contract. Springer-Verlag secures the copyright for each volume.

The Production Process

The books are hardbound, and the publisher will select quality paper appropriate to the needs of the author(s). Publication time is about ten weeks. More than twenty years of experience guarantee authors the best possible service. To reach the goal of rapid publication at a low price the technique of photographic reproduction from a camera-ready manuscript was chosen. This process shifts the main responsibility for the technical quality considerably from the publisher to the authors. We therefore urge all authors and editors of proceedings to observe very carefully the essentials for the preparation of camera-ready manuscripts, which we will supply on request. This applies especially to the quality of figures and halftones submitted for publication. In addition, it might be useful to look at some of the volumes already published. As a special service, we offer free of charge LaTeX and TeX macro packages to format the text according to Springer-Verlag's quality requirements. We strongly recommend that you make use of this offer, since the result will be a book of considerably improved technical quality. To avoid mistakes and time-consuming correspondence during the production period the conference editors should request special instructions from the publisher well before the beginning of the conference. Manuscripts not meeting the technical standard of the series will have to be returned for improvement.

For further information please contact Springer-Verlag, Physics Editorial Department II, Tiergartenstrasse 17, D-69121 Heidelberg, Germany

Kolumban Hutter Yongqi Wang Hans Beer (Eds.)

Advances in Cold-Region Thermal Engineering and Sciences

Technological, Environmental, and Climatological Impact

Proceedings of the 6th International Symposium Held in Darmstadt, Germany, 22-25 August 1999

Springer

Editors

Kolumban Hutter
Yongqi Wang
Institut für Mechanik
TU Darmstadt
Hochschulstrasse 1
D-64289 Darmstadt, Germany

Hans Beer
Institut für Technische Thermodynamik
TU Darmstadt
Petersenstrasse 30
D-64287 Darmstadt, Germany

Cover picture:
Hoar frost formed in cold humid atmosphere (Photo: O. Buser, Davos)

Library of Congress Cataloging-in-Publication Data.
Die Deutsche Bibliothek - CIP-Einheitsaufnahme

Advances in cold region thermal engineering and sciences : technological, environmental, and climatological impact ; proceedings of the 6th international symposium held in Darmstadt, Germany, 22 - 25 August 1999 / Kulumban Hutter ... (ed.). - Berlin ; Heidelberg ; New York ; Barcelona ; Hong Kong ; London ; Milan ; Paris ; Singapore ; Tokyo : Springer, 1999
(Lecture notes in physics ; Vol. 533)
ISBN 3-540-66333-9
ISSN 0075-8450
ISBN 3-540-66333-9 Springer-Verlag Berlin Heidelberg New York

Typesetting: Camera-ready by the authors/editors
Cover design: *design & production*, Heidelberg

SPIN: 10720482 55/3144/du - 5 4 3 2 1 0 – Printed on acid-free paper

Foreword

This book on **Advances in Cold-Region Thermal Engineering and Sciences** consists of peer-reviewed articles and reviews presented as lectures at the *Sixth International Symposium on Thermal Engineering and Sciences for Cold Regions*, held at the campus of the *Darmstadt University of Technology*, Darmstadt, Germany, August 22 – 25, 1999, and is the sixth in a series of speciality meetings on the title topic: 1st, Edmonton, Canada, 1987; 2nd, Sapporo, Japan, 1989; 3rd, Fairbanks, USA, 1991; 4th, Hanover, USA, 1993; 5th, Ottawa, Canada, 1996. These symposia are not under the auspices of any particular society or organisation but, rather, are a gathering of independent investigators with a broad interest in thermal aspects in cold regions.

The exploration and development of natural resources in the Arctic regions face many unique engineering and environmental problems, including those related to the climate and global change. Arctic or cold environments provide many unique freezing or melting phenomena, both in technological applications and in the natural context, involving water, air, soil, entire ice sheets (such as Antarctica), biological systems and much more. Processes of heat and mass transfer involving phase transitions or phase change interfaces are of basic importance to cold regions engineering design, construction and operation, but also to geotechnicians, geologists, climatologists, cryologists (ice and snow scientists), etc. The approaches are multidisciplinary from descriptive to deductive, often involving simultaneous knowlege of natural scientists, engineers, physicists and mathematicians together.

The purpose of the symposium was to provide a forum for the review and dissemination of recent scientific and technical information related to all aspects of thermal engineering and sciences in cold regions. The topics that are particularly treated, may be headed as follows:

- Ice formation and decay
- Heat conduction with phase change
- Convection with freezing and melting
- Phase change in porous media
- Thermal properties at low temperature
- Frost heave and permafrost
- Climate impact in cold regions
- Icing on structures
- Ice as a structural material

- Thermal design of structures
- Solar energy and heat recovery
- Bio-engineering in cold climates
- Application of thermosyphons and heat pipes
- Latent heat storage, etc.

The symposium served both as a forum for the exchange of information and experience in cold region thermal science and engineering research, and as a means of encouraging cooperation and stimulation for future research.

We decided to perform thorough reviews of the contributing papers and to present the papers together as a formal book, because the content is of general interest to graduate students and researchers and engineers in universities and research institutions involved in cold regions science and technology. The book contains 50 articles, most, but not all, of the lectures that were presented at the symposium. The articles are grouped together according to six different topics:

- *Part I*: Phase Change Phenomena
- *Part II*: Ice Physics
- *Part III*: Large Ice Masses: Ice Sheets, Sea Ice
- *Part IV*: Snow Thermo-Mechanics, Avalanches
- *Part V*: Glaciers, Permafrost, Porous Media
- *Part VI*: Heat Storage, Heat Recovery.

Some could be grouped under different headings; all in all, they embrace equally the thermal engineering and the thermal sciences of cold regions.

We sincerely hope that this volume adequately adds to our current understanding of the thermal engineering and sciences in cold regions, and that it will also stimualte further research. If it helps us, moreover, in our concerted efforts to conserve or, if necessary, to restore the quality of our environment, both locally and globally, an important aspect of our objectives will have been met.

Darmstadt, June 1999

Kolumban Hutter
Yongqi Wang
Hans Beer

Acknowledgements

All articles in this book, including those summarizing a special topic, were peer reviewed by one to three referees and the texts printed in this book have profited from the work of these anonymous referees. We express to all of them our sincere thanks for the efforts they devoted to this work.

All the graphs contained in this book are mostly produced by the authors and if taken from other works, the copyrights to reproduce them in this book have been obtained by the authors themselves.

The Sixth International Symposium of Thermal Engineering and Sciences for Cold Regions was sponsored by the following institutions and/or organisations

- American Society of Mechanical Engineers (ASME)
- Canadian Society of Mechanical Engineers (CSME)
- Institute of Mechanics, Darmstadt University of Technology
- Institute of Technical Thermodynamics, Darmstadt University of Technology
- International Glaciological Society (IGS)
- Korean Society of Mechanical Engineers (KSME)
- Verein Deutscher Ingenieure (VDI-GVC)

and received financial support from

- Darmstadt University of Technology, Darmstadt, Germany
- Deutsche Forschungsgemeinschaft, Bonn, Germany
- US-Army Research and Standardization Group–UK, contract no. N68171-99-M-5360

The aid and support obtained from these institutions and organizations is gratefully acknowledged.

Any opinions, findings and conclusions or recommendations expressed in this book are those of the authors and do not necessarily reflect the views of the organizing institutions, editors and sponsors

- Darmstadt University of Technology, Darmstadt, Germany
- Deutsche Forschungsgemeinschaft, Bonn, Germany
- US-Army Research and Standardization Group–UK, contract no. N68171-99-M-5360

The Editors

Contents

Some Observations on the Historical Development of Conduction Heat Transfer
Kwo Chang Cheng 1

Part I. Phase Change Phenomena

Numerical and Experimental Investigation on Frosting of Energy-Recovery Ventilator
Stephane Bilodeau, Yves Mercadier, Patrick Brousseau 25

Melting of Unfixed Material Inside an Elliptical Capsule
Sergei Fomin, Alexander Wilchinsky, Takeo Saitoh 33

Experimental Study on the Critical Heat Flux of Ice Accretion Along a Fine Wire Immersed in a Cold Air Flow with Water Spray
Koji Fumoto, Hideaki Yamagishi, Shoichrou Fukusako 45

The Characteristics of Frost Growth on Parallel Plates
Heung Do Han, Sung Tack Ro 55

Effect of Ultrasonic Waves on Freezing of Supercooled Water
Tsutomu Hozumi, Akio Saito, Seiji Okawa 65

Numerical Modeling of Dendritic Ice Crystals
Masaaki Ishikawa, Patrick H. Oosthuizen, Tetsuo Hirata 73

Measurement of Temperature and Velocity Fields of Freezing Water Using Liquid Crystal Tracers
Tomasz A. Kowalewski 83

Heat Transfer Enhancement of a Direct Contact Melting Process by Oscillating Motion
Mineo Oka 91

Permeability of an Aqueous Solution in a State of Partial Solidification
Masashi Okada, Chaedong Kang, Haruhiko Okiyama 103

Lateral Freezing of a Porous Medium Saturated with an Aqueous Salt Solution
Muyngho Song, Raymond Viskanta 113

Spontaneous Melting of Ice in a $CaCl_2$ Solution
Masahiro Sugawara, Makoto Tago 131

An Analytic Solution Prescribing the Time-Dependent Formation of a Solid Crust Inside a Convectively Cooled Plane Channel
Bernhard Weigand, Michel Arnal, Zygmunt Lipnicki 147

Melting Heat-Transfer Characteristics of an Inclined Ice Plate Immersed in a Hydrophobic Liquid
Masahiko Yamada, Shoichiro Fukusako, Tsuyoshi Kawanami, Shigeki Hirano 159

Part II. Ice Physics

Plane Flow of an Ice Sheet Exhibiting Strain-Induced Anisotropy
Olivier Gagliardini, Jacques Meyssonnier 171

A Meso-Macro Model for the Description of Induced Anisotropy of Natural Ice, Including Grain Interaction
Günter Gödert 183

Classical Mixture Models for Polythermal Ice
Kolumban Hutter, Bob Svendsen 197

Modelling the Ice Single-Crystal Viscoplastic Behaviour
Philippe Mansuy, Jacques Meyssonnier, Armelle Philip 215

Remarks on Self-Consistent Modelling of Polycrystalline Ice
Jacques Meyssonnier, Armelle Philip 225

Anisotropic Isothermal Ice-Cap Flow with the Shallow Ice Approximation
Armelle Philip, Jacques Meyssonnier 237

Orthotropic Viscous Model for Ice
Ryszard Staroszczyk, Leslie W. Morland 249

Tertiary Flow Relations for Compression and Shear Components in Combined Stress Tests on Ice
Roland C. Warner, T.H. Jacka, Li Jun, W.F. Budd 259

Part III. Large Ice Masses: Ice Sheets, Sea Ice

An Iterative Solution Procedure for Shallow Stokes Flows. The Shallow Ice Approximation Revisited
Dambaru Raj Baral, Kolumban Hutter 273

Nested High-Resolution Modelling of the Greenland Summit Region
Ralf Greve, Bernd Mügge, Dambaru Baral, Olaf Albrecht, Alexey Savvin 285

Numerical Age Computation of the Antarctic Ice Sheet for Dating Deep Ice Cores
Bernd Mügge, Alexey Savvin, Reinhard Calov, Ralf Greve 307

Three-Dimensional Isothermal Boundary Layer Solutions of Slow Creeping Ice Flows Based on the Shallow Ice Approximation
Alexey A. Savvin, Kolumban Hutter, Alexander A. Dorfmann 319

A Comparison Study Between Two Visco-Plastic Sea-Ice Models
Louis-Bruno Tremblay 333

Influence of Ice Accumulation Distribution on Ice Sheet Stability
Alexander V. Wilchinsky 353

Part IV. Snow Thermo-Mechanics, Avalanches

A Computational Procedure for Instationary Temperature-Dependent Snow Creep
Perry Bartelt, Marc Christen 367

Transformation of the Snow Crystal to a Particle of Ice
Elena Guseva-Lozinski 387

Temperature and Temperature Gradient Dependence of Snow Recrystallization in Depth Hoar Snow
Yasushi Kamata, Sergey A. Sokratov, Atsushi Sato 395

On Creep Flow of Snow and Firn
Bernhard Meussen 403

Relation of Temperature Gradient to Heat Transfer in Snow
Sergey A. Sokratov, Yasushi Kamata, Atsushi Sato 409

Methods of Similitude in Granular Avalanche Flows
Yih-Chin Tai, Yongqi Wang, J.M.N.T. Gray, Kolumban Hutter 415

Part V. Glaciers, Permafrost, Porous Media

Experimental Study of Gas Hydrate Formation in Porous Media
Evgeny M. Chuvilin, Vladimir S. Yakushev, Elena V. Perlova 431

Electroacoustic Technique to Study Changes in the Liquid Phase State of Frozen Soils
Anatoly D. Frolov, Vadim B. Kravchenko, Andrei S. Pavlov 441

Permeability Effects on Winter-Time Natural Convection in Gravel Embankments
Douglas J. Goering, Pankaj Kumar 455

Barothermic Effect and Temperature Regime of Frozen Soil
Jacob B. Gorelik, Vladimir S. Kolunin, Aleksy K. Reshetnikov 465

Detecting Alpine Permafrost Using Electro-Magnetic Methods
Christian Hauck, Daniel Vonder Mühll 475

Climatic Warming and Permafrost
Virgil J. Lunardini 483

The Monitoring and Prediction of Permafrost Temperature, Distribution and Geocryological Processes Within Russia Under Global Climate Changes
Alexander Pavlov, Stanislav Grechishchev 503

Thermally Induced Temporal Strain Variations in Rock Walls Observed at Subzero Temperatures
Matthias Wegmann, G. Hilmar Gudmundsson 511

Soil Microstructure and the Thermodynamic Behaviour of Permafrost Affected Soils
Thomas Leslie White 519

Part VI. Heat Storage, Heat Recovery

Heat Transfer in Heat Storage Arrangements Under Melting
Vladimir A. Alexeev 535

Microscale Analysis of Ice Crystals Made from Aqueous Solutions by Scanning Tunneling Microscope
Takaaki Inada, Akira Yabe, Tsuyoshi Saito, Shu-Shen Lu, Xu Zhang, Kenji Yoshimura, Makoto Tanaka, Svein Grandum 545

Development Study of a Novel Tower-Style Tank for Simultaneous Storing Warm Water and Ice
Kunihiko Kitamura, Keiji Kurokawa, Yasutoshi Inatomi, Itsunari Fukushima, Osamu Miyatake 555

Latent Heat Storage in a Fixed-Bed Packed with Cross-Linked Polymer Particles
Hiroki Morita, Osamu Miyatake 563

Development of an Efficient Static-Type Ice Thermal Energy Storage Vessel Using a Low Concentration Aqueous Solution
Kengo Sasaguchi, Tomoaki Yoshiyama, Testushi Nozoe, Yoshiyuki Baba 575

Heat Storage for a Bus Petrol Internal-Combustion Engine
Leonard L. Vasiliev, Victor S. Burak, Andry G. Kulakov, Donatas A. Mishkinis, Pavel V. Bohan 585

Heat Pumps and Heat Pipes for Applications in Cold Regions
Leonard L. Vasiliev 595

Contributors

Olaf Albrecht Geographisches Institut, Eidgenössische Technische Hochschule Zürich, Winterthurerstrasse 190, CH-8057 Zürich, Switzerland
Vladimir A. Alexeev Scientific and Research Institute of Precision Instruments, Yurlovsky proezd.6.1, Moscow 127490, Russia
Michel Arnal ABB Power Generation Ltd, CH-5401 Baden, Switzerland
Yoshiyuki Baba Kyushu Electric Power Co., Inc. 2-1-82, Watanabe-Dori, Chuo-Ku, Fukuoka 810-8720, Japan
Dambaru Baral Institut für Mechanik, Technische Universität Darmstadt, Hochschulstraße 1, D-64289 Darmstadt, Germany
Perry Bartelt Head Avalanche Dynamics and Numerics, Swiss Federal Institute for Snow and Avalanche Research, CH-7260 Davos Dorf, Switzerland
Stephane Bilodeau Université de Sherbrooke , Département de génie mécanique, 2500, boul. Université, Sherbrooke, Québec J1K 2R1 Canada
Pavel V. Bohan Luikov Heat & Mass Transfer Institute, P.Brovka 15, 220072 Minsk, Belarus
Patrick Brousseau Université de Sherbrooke , Département de génie mécanique, 2500, boul. Université, Sherbrooke, Québec J1K 2R1 Canada
W. F. Budd Australian Antarctic Division, Box 252-80, Hobart, Tasmania 7001, Australia
Victor S. Burak Luikov Heat & Mass Transfer Institute, P.Brovka 15, 220072 Minsk, Belarus
Reinhard Calov Potsdam-Institut für Klimafolgenforschung, Postfach 601203, D-14412 Potsdam, Germany
Kwo Chang Cheng Department of Mechanical Engineering, University of Alberta, Edmonton, Alberta, Canada
Marc Christen Swiss Federal Institute for Snow and Avalanche Research, CH 7260 Davos Dorf, Switzerland
Evgeny M. Chuvilin Departament of Geocryology, Faculty of Geology, Vorobyevy Gory, Moscow State University, Moscow 119899, Russia
Alexander A. Dorfmann International Academy of Information, Harnackring 69, D-21031 Hamburg, Germany
Sergei Fomin Department of an Applied Mathematics, Kazan State University, Kazan, Russia
Anatoly D. Frolov Scientific Council on Earth Cryology, Russian Academy of Sciences, Fersman St 11, Moscow 117312, Russia

Shoichrou Fukusako Hokkaido University, Kita13, Nishi8, Kita-ku, Sapporo 060-8628, Japan

Itsunari Fukushima Environmental Engineering Division, Kyudenko Corporation, 1-23-35 Nanokawa, Minami-ku, Fukuoka 815-0081, Japan

Koji Fumoto Kushiro National College of Technology, Nishi2-32-1, Otanoshike, Kushiro 084-0915, Japan

Olivier Gagliardini Laboratoire de Glaciologie et Géophysique de l'Environnement, CNRS et Université Joseph Fourier (UJF - Grenoble I), BP96, 38402 Saint-Martin-d'Hères Cedex, France

Günter Gödert Institute of Materials Research, GKSS Research Center, Max-Planck-Strasse, D-21502 Geesthacht, Germany

Douglas J. Goering Department of Mechanical Engineering, University of Alaska, Fairbanks AK 99775, USA

Jacob B. Gorelik Earth's Cryosphere Institute SB RAS, 625000, Tyumen, P.b.1230, Russia

Svein Grandum Institute for Energy Technology, Kjeller, 2007, Norway

J.M.N.T. Gray Institut für Mechanik, Technische Universität Darmstadt, Hochschulstraße 1, D-64289 Darmstadt, Germany

Stanislav Grechishchev Earth Cryosphere Institute SB RAS, Moscow dept, Vavilova street, 30/6, room 85, Moscow 117982, Russia

Ralf Greve Institut für Mechanik, Technische Universität Darmstadt, Hochschulstraße 1, D-64289 Darmstadt, Germany

G. Hilmar Gudmundsson Laboratory of Hydraulics, Hydrology and Glaciology (VAW), ETH-Zentrum, CH-8092 Zürich, Switzerland

Elena Guseva-Lozinski Immenhoferstr. 38, D-70180 Stuttgart, Germany

Heung Do Han Department of Airconditioning and Refrigeration, Industrial Education Center, 219-5 Kasan-dong Kumchun-Gu Seoul, Korea 153-023

Christian Hauck Laboratory of Hydraulics, Hydrology and Glaciology (VAW), Federal Institute of Technology (ETH), CH-8092 Zürich, Switzerland

Shigeki Hirano Division of Mechanical Science, Graduate School of Engineering, Hokkaido University N13-W8, Sapporo 060-8628, Japan

Tetsuo Hirata Shinshu University, 500 Wakasato, Nagano 380-8553, Japan

Tsutomu Hozumi Department of Mechanical Engineering and Science, Faculty of Engineering, Tokyo Institute of Technology, Tokyo 152, Japan

Kolumban Hutter Institut für Mechanik, Technische Universität Darmstadt, Hochschulstraße 1, D-64289 Darmstadt, Germany

Takaaki Inada Mechanical Engineering Laboratory, Tsukuba, Ibaraki 305-8564, Japan

Yasutoshi Inatomi Environmental Engineering Division, Kyudenko Corporation, 1-23-35 Nanokawa, Minami-ku, Fukuoka 815-0081, Japan

Masaaki Ishikawa Shinshu University, 500 Wakasato, Nagano 380-8553, Japan

T. H. Jacka Antarctic CRC, Box 252-80, Hobart, Tasmania 7001, Australia

Yasushi Kamata National Research Institute for Earth Science and Disaster Prevention, Shinjo Branch of Snow and Ice Studies; Tokamachi 1400, Shinjo, Yamagata 996-0091, Japan

Chaedong Kang Aoyama Gakuin University, 6-16-1, Chitosedai, Setagaya-ku, Tokyo 157-8572, Japan

Tsuyoshi Kawanami Division of Mechanical Science, Graduate School of Engineering, Hokkaido University N13-W8, Sapporo 060-8628, Japan

Kunihiko Kitamura Department of Chemical Systems and Engineering, Faculty of Engineering, Kyushu University, 6-10-1 Hakozaki, Higashi-ku, Fukuoka 812-8581, Japan

Vladimir S. Kolunin Earth's Cryosphere Institute SB RAS, 625000, Tyumen, P.b.1230, Russia

Tomasz A. Kowalewski Polish Academy of Sciences, IPPT PAN, Center of Mechanics and Information Technology, Swietokrzyska 21, PL 00-049 Warszawa, Poland

Vadim B. Kravchenko Scientific Council on Earth Cryology, Russian Academy of Sciences, Fersman St 11, Moscow 117312, Russia

Andry G. Kulakov Luikov Heat & Mass Transfer Institute, P.Brovka 15, 220072 Minsk, Belarus

Pankaj Kumar Department of Mechanical Engineering, University of Alaska, Fairbanks AK 99775, USA

Keiji Kurokawa Thermal Storage Technical Department, West Japan Engineering Consultants Incorporation, 1-12-9 watanabe-dori, chuoku, Fukuoka 810-0004, Japan

Jun Li Antarctic CRC, Box 252-80, Hobart, Tasmania 7001, Australia

Zygmunt Lipnicki University of Zielona Gora, P-65-246 Zielona Gora, Poland

Shu-Shen Lu South China University of Technology, Guangzhou, 510641, China

Virgil J. Lunardini US-Army Cold Regions Reaearch and Engineering Laboratory, 72 Lyme Road, Hanover NH 03755, USA

Philippe Mansuy Laboratoire de Glaciologie et Géophysique de l'Environnement, CNRS et Université Joseph Fourier (UJF-Grenoble I), BP 96, F-38402 Saint-Martin d'Hères Cedex, France

Yves Mercadier Université de Sherbrooke , Département de génie mécanique, 2500, boul. Université, Sherbrooke, Québec J1K 2R1, Canada

Bernhard Meussen Vedior Engineering+Consulting GmbH, Wendenstrasse 23, D-20097 Hamburg, Germany

Jacques Meyssonnier Laboratoire de Glaciologie et Géophysique de l'Environnement, CNRS et Université Joseph Fourier (UJF-Grenoble I), BP 96, F-38402 Saint-Martin d'Hères Cedex, France

Donatas A. Mishkinis Luikov Heat & Mass Transfer Institute, P.Brovka 15, 220072 Minsk, Belarus

Osamu Miyatake Department of Chemical Systems and Engineering, Graduate School of Engineering, Kyushu University, 6-10-1 Hakozaki, Higashi-ku, Fukuoka 812-8581, Japan

Hiroki Morita HVAC & Plumbing Engineering Department, Kyudenko Corporation, 1-23-35 Nanokawa, Minami-ku, Fukuoka 815-0081, Japan
Leslie W. Morland School of Mathematics, University of East Anglia, Norwich NR4 7TJ, United Kingdom
Bernd Mügge Institut für Mechanik, Technische Universität Darmstadt, Hochschulstraße 1, D-64289 Darmstadt, Germany
Daniel Vonder Mühll Laboratory of Hydraulics, Hydrology and Glaciology (VAW), Federal Institute of Technology (ETH), CH-8092 Zürich, Switzerland
Testushi Nozoe Department of Mechanical Engineering and Materials Science, Kumamoto University 2-39-1, Kurokami, Kumamoto 860-8555, Japan
Mineo Oka PANDA Laboratory, 1642-406 Nagae, Hayama, Kanagawa, 240-0113 Japan
Masashi Okada Aoyama Gakuin University, 6-16-1, Chitosedai, Setagaya-ku, Tokyo 157-8572, Japan
Seiji Okawa Department of Mechanical Engineering and Science, Faculty of Engineering, Tokyo Institute of Technology, Tokyo 152, Japan
Haruhiko Okiyama Isuzu Motors Limited, 8 Tsuchidana, Fujisawa-si, Japan
Patrick H. Oosthuizen Queen's University, Kingston Ontario K7L3N6, Canada
Alexander Pavlov Earth Cryosphere Institute SB RAS, Moscow Dept, Vavilova Street, 30/6, room 85, Moscow 117982, Russia
Andrei S. Pavlov Scientific Council on Earth Cryology, Russian Academy of Sciences, Fersman St 11, Moscow 117312, Russia
Elena V. Perlova Departament of Geocryology, Faculty of Geology, Vorobyevy Gory, Moscow State University, Moscow 119899, Russia
Armelle Philip Laboratoire de Glaciologie et Géophysique de l'Environnement,, CNRS et Université Joseph Fourier (UJF-Grenoble I), BP 96, F-38402 Saint-Martin d'Hères Cedex, France
Aleksy K. Reshetnikov Earth's Cryosphere Institute SB RAS, 625000, Tyumen, P.b.1230, Russia
Sun Tack Ro Department of Mechanical Engineering, Seoul National University, Seoul Korea 151-742, Korea
Akio Saito Department of Mechanical Engineering and Science, Faculty of Engineering, Tokyo Institute of Technology, Tokyo 152, Japan
Tsuyoshi Saito University of Tsukuba, Tsukuba, Ibaraki 305-0004, Japan
Takeo Saitoh Department of Aeronautics and Space Engineering, Tohoku University, Sendai, Japan
Atsushi Sato National Research Institute for Earth Science and Disaster Prevention, Shinjo Branch of Snow and Ice Studies; Tokamachi 1400, Shinjo, Yamagata 996-0091, Japan
Alexey A. Savvin Institut für Mechanik, Technische Universität Darmstadt, Hochschulstraße 1, D-64289 Darmstadt, Germany

Kengo Sasaguchi Department of Mechanical Engineering and Materials Science, Kumamoto University 2-39-1, Kurokami, Kumamoto 860-8555, Japan

Sergey A. Sokratov National Research Institute for Earth Science and Disaster Prevention, Shinjo Branch of Snow and Ice Studies; Tokamachi 1400, Shinjo, Yamagata 996–0091, Japan
Institute of Geography, Russian Academy of Science; Staromonetnyi 29, Moscow 109017, Russia

Muyngho Song Department of Mechanical Engineering, Dongguk University, Seoul, Korea

Ryszard Staroszczyk School of Mathematics, University of East Anglia, Norwich NR4 7TJ, United Kingdom

Masahiro Sugawara Department of Mechanical Engineering, Faculty of Engineering and Resource Science, Akita University Akita 010-8502, Japan

Bob Svendsen Federal Institute for Materials Research, D-12000 Berlin, Germany

Makoto Tago Department of Mechanical Engineering, Faculty of Engineering and Resource Science, Akita University, Akita 010-8502, Japan

Yin-Chin Tai Institut für Mechanik, Technische Universität Darmstadt, Hochschulstraße 1, D-64289 Darmstadt, Germany

Makoto Tanaka Mechanical Engineering Laboratory, Tsukuba, Ibaraki 305-8564, Japan

Louis-Bruno Tremblay Lamont Doherty Earth Observatory of Columbia University, Rt 9W, Palisades, NY 10964, USA

Leonard L. Vasiliev Luikov Heat & Mass Transfer Institute, P.Brovka 15, 220072 Minsk, Belarus

Raymond Viskanta School of Mechanical Engineering, Purdue University, W. Lafayette, IN 47907-1288, USA

Yongqi Wang Institut für Mechanik, Technische Universität Darmstadt, Hochschulstraße 1, D-64289 Darmstadt, Germany

Roland C. Warner Antarctic CRC, Box 252-80, Hobart, Tasmania 7001, Australia

Matthias Wegmann Laboratory of Hydraulics, Hydrology and Glaciology (VAW), ETH-Zentrum, CH-8092 Zürich, Switzerland

Bernhard Weigand ITLR, University of Stuttgart, Pfaffenwaldring 31, D-70550 Stuttgart, Germany

Thomas Leslie White Geotechnical Science Laboratories, Carleton University 1125 Colonel By Drive, Ottawa, ON K1S 5B6, Canada

Alexander V. Wilchinsky Institute of Mathematics and Mechanics, Kazan State University, Kazan 420008, Russia

Akira Yabe Mechanical Engineering Laboratory, Tsukuba, Ibaraki, 305-8564, Japan

Vladimir S. Yakushev Russian Research Institute of Natural Gases and Gas Technologies, Moscow Region, p.Razvilka, 142717, Russia

Masahiko Yamada Division of Mechanical Science, Graduate School of Engineering, Hokkaido University N13-W8, Sapporo 060-8628, Japan
Hideaki Yamagishi Kushiro National College of Technology, Nishi2-32-1,Otanoshike, Kushiro 084-0915, Japan
Kenji Yoshimura Fukuoka Industrial Technology Center, Kitakyushu 807-0831, Japan
Tomoaki Yoshiyama Department of Mechanical Engineering and Materials Science, Kumamoto University 2-39-1, Kurokami, Kumamoto 860-8555, Japan
Xu Zhang Mechanical Engineering Laboratory, Tsukuba, Ibaraki 305-8564, Japan

Some Observations on the Historical Development of Conduction Heat Transfer

Kwo Chang Cheng

Department of Mechanical Engineering, University of Alberta, Edmonton, Alberta, Canada

Abstract. An attempt is made to obtain historical perspectives on the development of the mathematical theory of heat conduction considering Newton's law of cooling (1701) and its close connection with Fourier's work from 1807 to 1822 resulting in his epoch–making treatise on "The Analytical Theory of Heat". Fourier was the principal architect of the heat conduction theory. Fourier's work established a new methodology for the formulation and solution of physical problems, based on partial differential equations and marked a major turning point in the history of physics. The developments in the periods 1822 to 1900 and 1900 to 1950 are also briefly reviewed as are the classical (analytical) and numerical methods of solution for heat conduction problems. The analogy in heat, momentum, and mass transfer for transport phenomena is discussed. A list of recent conduction heat transfer books is presented to show the scope of recent developments. Some observations on conduction heat transfer are noted.

1 Introduction

L'étude approfondie de la nature est la source la plus féconde des découvertes mathématiques.

Profound study of nature is the most fertile source of mathematical discoveries. Joseph Fourier (1822)

It is almost 300 years since Newton's first enunciation of the law of cooling in his short paper (4 pages) published in the Philosophical Transactions, Abridged, Vol. II (1701). Newton's thermometer was graduated by the use of two fixed points and may have been the first one of the sort with which useful observations were made. In 1738 Daniel Bernoulli's "Hydrodynamica" was published. Joseph Fourier's "The Analytical Theory of Heat" appeared in 1822. Sadi Carnot's "Reflections on the Motive Power of Fire" (1824) started the beginnings of thermodynamics in physics. One notes that the three branches of thermal sciences consist of fluid mechanics (18th century), heat transfer (early 19th century) and classical thermodynamics (mid–19th century) in the chronological order of development as a branch of physics. The theory of heat in the 19th century physics includes thermometry, calorimetry, heat conduction, heat radiation, thermodynamics, kinetic theory of gases and statistical mechanics.

In modern heat transfer text books the three modes of heat transfer, namely, 1) conduction, 2) convection and 3) thermal radiation are usually

discussed separately following the classical synthesis of theoretical ideas concerning heat transfer established by physicists towards the end of the 19th century. The three modes of heat transfer are well discussed by Brush [1,2]. In 1915 Wilhelm Nusselt pointed out, however, that heat transfer has only two independent mechanisms, radiation and heat conduction, since heat could not be transferred by convection only without the action of thermal conduction [3]; the basic heat conduction equation of Fourier applies to both heat conduction and convection. Without thermal conductivity, the heat transfer from a solid body to the surrounding medium is zero, neither through conduction nor through forced or natural convection. If, however, the thermal conductivity of the fluid is not zero, then all the heat, except that transferred by radiation, will be transferred through conduction and transported by fluid motion [3].

It is known that heat is transported by fluid motion as a passive scalar quantity in forced convection. For natural convection, the buoyancy forces are the driving forces for the fluid motion. The close relationship between momentum and heat transport is well known. For laminar flow, the distinction is represented by the Prandtl number, but for turbulent flow, the turbulent Prandtl number, depending on flow condition and location, appears additionally. The amount of heat transfer may be increased by the fact that the fluid has a certain velocity, and this velocity affects the temperature gradient of fluid at the surface of the body. Thus heat transfer has only two mechanisms, conduction and radiation; convection indeed carries away what has been transferred by either one of the two mechanisms [3].

The purpose of this article is to review some aspects of the historical development of conduction heat transfer starting with Newton's law of cooling (1701) and Fourier's mathematical theory of heat conduction (1822). An attempt is made to point out the connections or relations between the works of the pioneers and the present-day research on conduction heat transfer. The historical perspectives on the development of the subject are of special interest here. The review is based on published historical expositions on the subject, review articles, textbooks by leaders and experts, book reviews and various other sources.

Experimentation (observation, measurement and experiment) and mathematization (analysis) as scientific methods started with Galileo and Newton. Newton's classical mechanics (Principia, 1687) was based on the study of motion of bodies during the phase of instantaneous rate of change. The same method was used by Fourier for temperature change of heated or cooled solids in his development of the mathematical theory of heat conduction. The major advances in scientific thoughts are usually based on previous theoretical or experimental works. Newton himself admitted having stood "on the shoulders of giants". The developments of fluid mechanics and heat transfer were based on well–planned experiments and their descriptions in the mathematical lan-

guage. The method still continues today. The experiments can also take the form of thought experiment such as that of the Carnot cycle.

2 Newton's Law of Cooling (1701)

Isaac Newton

Newton's (1642–1727) short paper describing his temperature scale and measurements to determine the high temperature such as red-hot iron contains also his law of cooling. The genesis of Newton's law of cooling was traced by Ruffner [4]. Grigull [5] presented a critical and definitive review on Newton's temperature scale and the law of cooling. Cheng and Fujii [6] discussed Isaac Newton and heat transfer. Newton's determination of high temperatures beyond the capability of the thermometer of his time was based on the law of cooling. His original paper is readily available [7,8]. The following two quotations from his 1701 paper "A Scale of the Degrees of Heat" identify the origins of the law of cooling:

> "For the heat which the hot iron communicates in a given time to cold bodies which are near it, that is, the heat which the iron loses in a given time, is proportional to the whole heat of the iron. And so, if the times of cooling are taken equal, the heats will be in a geometrical progression and consequently can easily be found with a table of logarithms."
>
> "For thus equal parts of the air are warmed in equal times and carry away a heat proportional to the heat of the iron."

One notes that in Newton's time the distinction between heat and temperature was not clear. In deducing the relationship between the temperature

excess of the hot iron over the temperature of uniformly flowing air and the cooling time, Newton did not show his analysis. Today Newton's law of cooling in physics states that the rate at which a hot body cools down should be in proportion to the body's excess temperature over its surroundings. Using equation, one obtains

$$-\frac{dT}{d\tau} \sim T \qquad \text{or} \qquad -\frac{dT}{T} \sim d\tau \ , \tag{1}$$

where T is the excess temperature and τ is the time. This yields

$$-\ln T \sim \tau \qquad \text{or} \qquad \tau \sim -\ln T + constant \ . \tag{2}$$

If one knows the time taken to cool from one measured temperature to another, one can, given the cooling time, find any required temperature [9]. Newton's method of measuring high temperature was based on the pyrometric method described. Cardwell [9] observes that Newton invoked his law of cooling, which seems to have been inspired analogously by his own demonstration that a moving body resisted in proportion to its velocity decelerates in proportion to that velocity. The analogy is of special interest here.

At this point the origin of the concept of heat transfer coefficient is of special interest. Using the concept of a wall heat flux q_w and introducing an empirical proportionality factor, Fourier [10] obtained his equation for external conductivity as

$$q_w = h\,(t_w - t_\infty) \tag{3}$$

where t_w is wall temperature, t_∞ is ambient temperature and $h = heat\ transfer\ coefficient = constant$. Equation (3) represents the first phenomenological heat transfer rate equation on record, now known generally as Newton's cooling law. Here one clearly recognizes Newton's legacy in convective mode of heat transfer. One also notes clearly the temperature difference as the driving force for convective heat transfer. The earliest heat rate equation laid down in 1701 by Isaac Newton represents an incidental by-product of his unsuccessful attempt to develop a high temperature thermometer [11]. Fourier's application of Newton's law of cooling in his mathematical theory of heat conduction takes the following form as the convective boundary condition

$$-k\left(\frac{\partial t}{\partial n}\right)_w = h\,(t_w - t_\infty) \tag{4}$$

where n is the external normal to the boundary surface.

Newton's law of cooling indeed marks a turning point in the history of science of heat. After the formal establishment of the first law of thermodynamics in 1850, Newton's heat transfer driving force also represents the first law temperature difference for heat transfer in contrast to the thermodynamic potential for the Carnot cycle.

In light of the present knowledge, one notes some implications for Newton's cooling problem. Using Clausius' definition of a differential entropy and Newton's law of cooling (see eq.(1)), one obtains

$$dS = - C_p \frac{dT}{T} = - C_p \, d(\ln T) \, , \tag{5}$$

where C_p = specific heat at constant pressure. Thus one sees that $dS \sim d\tau$ or $Entropy \sim Time$.
Integrating eq.(5) yields,

$$S_2 - S_1 \; = \; C_p \, (\ln T_1 \; - \; \ln T_2), \quad T_1 > T_2 \, . \tag{6}$$

Analogously, from the abstract concept of entropy based on the statistical mechanics concepts of Boltzmann and Gibbs near the end of the 19th century, one obtains [11]

$$S_2 - S_1 \; = \; k \, (\ln p_2 \; - \; \ln p_1) \tag{7}$$

where p = thermodynamic probability (the number of possible microstates for a given macroscopic state) and k = Boltzmann's constant. Here the historical connection (or interrelation) is of considerable interest.

In elementary (introductory) heat transfer textbooks, a simple theoretical analysis (a simplified heat balance equation for Newton's cooling problem) of first-order response for a temperature sensor, for example, is usually discussed. Expressed in terms of Newton's law of cooling and Black's heat capacity equation, one obtains

$$-\rho \, V \, C_p \, \frac{dt}{d\tau} \; = \; h \, A \, (t - t_\infty) \tag{8}$$

where t is the sensor temperature at time τ and $\rho \, V$ is (density times volume), C_p is the specific heat capacity and A is the surface area of the sensor. The present formulation using the first-order, first degree, linear differential equation is known as the lumped heat capacitance or parameter method representing Newton's cooling problem and has wide applications in design.

It is significant to point out that the concept of the conservation of heat is implicit in Newton's law of cooling or Newton's cooling problem. This aspect or interpretation of Newton's work is certainly of historical significance since without the concept of conservation of heat, Newton certainly could not have deduced the cooling law for his determination of high temperature (red-hot iron). Newton simply observed that heat removed from a hot object is carried away by the uniformly flowing wind. At this point it may be of interest to point out the role of $1/T$ in eq.(1) or (5). Consider a unit mass of gas of volume V. The first law of thermodynamics (the principle of energy balance)

becomes $dQ = dE + P\,dV$, where dQ is the heat introduced to the unit mass, E is its internal energy and P is the pressure. The expression for differential entropy dQ/T then becomes an exact differential and the expression $1/T$ plays the role of an integrating factor. The expression dT/T or $\Delta T/T$ occurs often in thermodynamics (see eq.(1), for example).

3 Fourier's Development of the Mathematical Theory of Heat Conduction in Solids (1807-1822)

3.1 Fourier's major publications

Joseph Fourier

The mathematical theory of heat conduction in solids was completed practically by Joseph Fourier (1768-1830) with the publication of his epoch-making manuscript on "The Analytical Theory of Heat" in 1822. A chronological account of Fourier's researches on heat is given by Herivel [12]. Fourier's important publications on heat are:

1) The 1807 Memoir on the Propagation of Heat, presented to the Institut de France. The full text (234 pages) is reproduced with illuminating commentary by Grattan–Guinness [13]. Fourier derived the basic heat conduction equation and the associated convective boundary condition, and solved various heat conduction problems (different geometrical shapes) using such mathematical techniques as separation of variables and Fourier series and other functions (eigenfunction and eigenvalue). Fourier's heat conduction problem itself lay outside the scope of rational and celestial mechanics which had been dominant in science since Newton's time. Hence Fourier's achievements constituted a major extension of mathematical physics [13]. Fourier

submitted the theoretical investigation of the propagation of heat including a few tables of experimental results to the mathematical and physical section of the Institut de France in Paris. Now Fourier, a man in his fortieth year had published only one paper in his life; a study of the Principle of Virtual Work, ten years previously [14].

2) The 1811 Prize Essay (Mémoire sur la propagation de la Chaleur) on a prize problem "Give the mathematical theory of heat and compare the result of this theory with exact experiments."

The adjudicators were Lagrange, Laplace, Legendre, Haüy and Malus. Fourier won the prize, but his work was severely criticized for its lack of rigour of analysis and methods, and the paper was not published at the time. Fourier always resented the treatment he had received. However, the importance of Fourier's work as a new approach and a powerful method in analysis was undeniable even from its beginning, and it sparked developments in pure mathematics [15]. It was only after Fourier became the perpetual secretary of the French Academy of Sciences in 1824 that his original paper was finally published in two parts in the Mémoires de l Académie Royale des Sciences (1819-20) and (1821-22) in the original form.

3) The Analytical Theory of Heat (1822) (466 pages) Fourier incorporated in his most famous 1822 treatise, practically without change, the first part of his 1811 memoir. After the publication of his treatise, it was recognized that the real advance had been made by him on the subject and the substantial accuracy of his reasoning was admitted. Fourier's treatise established on a firm mathematical basis the theory of heat conduction. The publication of Fourier's Analytical Theory of Heat in 1822 represents the most important landmark in the development of the basic theory for solving boundary value problems governed by linear partial differential equations. Fourier's approach (analysis) is one of the most important landmarks in the development of applied mathematics. The English translation with historical notes by A. Freeman first appeared in 1878 and the new Dover edition was first published in 1955.

4) Fourier's Collected Works (ed. G. Darboux, 2 Vols.) 1888–90.

Fourier's "Analytical Theory of Heat"(1822) and his 1811 paper without the first 79 articles can be found in his collected works. His original derivation of the energy equation for moving fluids (laminar flow) in 1820 as noted in his 1822 treatise can also be found in G. Darboux's edition of his collected works. Fourier derived the convective terms in the energy equation corresponding to the inertia terms in Euler's equations of motion for an ideal fluid; his conduction terms representing molecular action correspond to the viscous terms in the Navier–Stokes equations derived at a later date. Volume 2 (1890) of his collected works contains also his memoires on terrestrial and planetary space temperatures (1827) and on secular cooling of the terrestrial globe (1820).

3.2 The relationship between Fourier's heat conduction theory and newton's cooling problem

Newton's law of cooling apparently inspired the experimental works of Amontons (1703), Lambert (1779) and Biot (1804) dealing with the steady-state cooling of iron bar heated at one end. The related historical notes and the influence of Biot's work on Fourier are discussed in the historical monographs [13,16,17]. It is of interest to note that the first historical overview of the heat conduction theory was made by Mach [16] and the critical review was also made by Truesdell [17]. Biot [18] heated one end of a long thin iron bar in a furnace and measured the temperature of the bar at different distances with thermometers placed in holes filled with mercury and determined the temperature of the furnace by extrapolation. Biot distinguished between internal conduction and external radiation but failed to deduce the exponential drop in temperature by analysis using Newton's law of cooling; his work stimulated Fourier to study the problem of heat propagation in 1807; Fourier derived the correct diffusion equation predicting the exponential temperature drop in fin problem (extended surface). Fourier's indebtedness to Biot is discussed by Grattan-Guinness [13].

Fourier's one-dimensional heat conduction equation can be written as

$$\frac{\partial t}{\partial \tau} = \alpha \frac{\partial^2 t}{\partial x^2} , \tag{9}$$

where α is the thermal diffusivity and x is the spatial coordinate. The related convective boundary condition is given by eq.(4). The classical method of solution for eq.(9), using the separation of variables, $t = T(\tau)\, X(x)$, leads immediately to

$$\frac{dT}{T} = -\alpha p^2 \, d\tau \qquad \text{or} \qquad T(\tau) = A\, e^{-\alpha p^2 \tau} \tag{10}$$

and

$$\frac{d^2 X}{dx^2} + p^2 X = 0 \qquad \text{or} \qquad X(x) = B \sin px + C \cos px , \tag{11}$$

where p^2 is the separation constant. The general solution of eq.(9) consists of the product of the exponential function and the Fourier series. Equation (10) clearly corresponds to Newton's cooling problem. Also, by replacing the term $\partial^2 t / \partial x^2$ by a finite-difference form, one can readily see that the time rate of local temperature change is proportional to the existing average temperature difference; this is clearly analogous to Newton's law of cooling.

The substitution of Fourier series for $X(x)$ in eq.(9) also leads to [16]

$$\frac{dt}{d\tau} = -p^2 \alpha \, t . \tag{12}$$

It is seen that the rate of change of temperature is proportional to the temperature itself [16]. Thus the close relationship between Newton's cooling problem and Fourier's heat conduction problem is quite apparent. It is seen that the exponential term involving time in the analytical solution of the transient heat conduction problem represents Newton's legacy and the temperature distribution such as the Fourier series for $X(x)$ represents Fourier's basic contribution. The inter–relationship between the two problems noted is of historical interest. One further notes that the driving force for Newton's cooling problem is the finite temperature difference and Fourier law of heat conduction is caused by the infinitesimal temperature difference between two molecules. These temperature differences represent the first law temperature difference for heat transfer. This is in contrast to the thermodynamic temperature difference (potential) between the heat source and sink in the Carnot cycle for motive power of heat.

It is also of interest to observe that the ordinary differential equation in the form of eq.(10) is identical to that given in [19] for the linear flow of heat in an infinite medium by the Fourier transform method.

3.3 Some historical notes relating to Fourier's work

While Lambert, Biot, and others had developed more or less correct ideas on the heat conduction, it was Fourier who first brought order out of the confusion in which the experimental physicists had left the subject. Fourier's work represents the mathematization of the heat conduction phenomena in solids based directly on the laws for the conduction of heat derived from experiments and observations made by Fourier's predecessors and clarified and extended by Fourier himself. For Fourier these laws represent the fundamental axioms of the theory of heat just as Newton's laws of motion represented the fundamental axioms of his theory of dynamics [20]. For Fourier the laws of heat as formulated by him in mathematical terms represented a separate branch of physics which is independent of dynamics.

The basic principles applied by Fourier to continuous bodies are noted below by Grattan–Guinness [14].

1. *Calorimetry:* Heat lost/gained at a given period of time = (mass) × (specific heat) × (fall/rise in temperature of the point in that time)
2. *The Principle of Communication of Heat:* This is in fact Newton's law of cooling, improved from a proportionality statement to an exact relation: Heat diffused over an elemental area = (area of diffusion) × (coefficient of external conductivity) × (change in temperature)
3. *Temperature Gradient:* Heat diffused at an interior point of the body = (area of diffusion) × (coefficient of internal conductivity) × (temperature gradient at the point)

This principle would replace principle 2) (the generalized Newton's law of cooling) for internal heat diffusion; principle 2) would deal solely with external

heat diffusion (convection and radiation). At last Fourier had in his hands the tools with which to create his equations [14]. The foregoing discussion of Grattan–Guinness [14] indeed puts a clear perspective on Fourier's work. Fourier solved various heat conduction problems for bodies of different shapes (circular or rectangular infinite cylinders, cubes, spheres, rings and others) with convective boundary condition.

Fourier also studied the diurnal and annual variations of temperature underground and terrestrial temperatures. Fourier discussed the superficial temperatures of all the planets based on a radiation balance between the heat they receive from the sun and the cold of outer space. Fourier's application of his theory of heat to the following questions were discussed by Whewell [21]: a) The effect of solar heat upon the earth, and the laws of its distribution (motion) in the earth, b) the effect of the primitive central heat of the earth and the evidence of its existence (central heat), and c) the effect of the proper heat of the planetary spaces, and the evidence that such heat exists (cosmical heat). Fourier concluded that the temperature of the planetary spaces to be about 50°C below freezing without disclosing his reasoning.

Fourier, in his Preliminary Discourse of the 1822 treatise [10], sets up a new cosmology, the cosmology of heat, based on heat phenomena of the globe (terrestrial heat) and the absorption and radiation of heat by the atmosphere that determine the great movements of air like the trade winds and the climates of the continents. Fourier's heat cosmology is separate from the mechanical cosmology of the 17th and 18th centuries based on Newton's Principia. Fourier has a comprehensive understanding of the phenomena of heat and an insight into its cosmological significance. He succeeded in establishing the science of heat on a firm analytical or mathematical basis and thus systematized a wide range of phenomena in heat conduction problems [9] leading to the identification and clarification of the thermal conduction mode in modern heat transfer theory in engineering science.

The influence of Fourier's contributions to general mathematical physics is wide–ranging and is well covered in books dealing with the history of physics or mathematics. For the present purpose, one notes the article [14] and book [13] by Grattan–Guinness, and references [22–26]. The importance of Fourier's theory of dimensions was first brought prominently before the scientific world by Clark Maxwell [26].

The importance of Fourier's development of an arbitrary function in the trigonometrical series as relating to the works of D'Alembert, Euler, Bernoulli and Lagrange on the problem of vibration of strings is reviewed by Mach [16], Carslaw [27] and others. In the middle of the 18th century there was a prolonged controversy as to the possibility of the expansion of an arbitrary function of a real variable in a series of sines and cosines and multiples of the variable.

A detailed historical account of Fourier's work can be found in the monographs by Herivel [12] and Grattan–Guinness [13]. An account of Fourier's

life is given by Arago [22], Ravetz and Grattan–Guinness [23], and Herivel [12]. Fourier's contributions in science are also covered in numerous essays by historians in science.

With a strong recommendation from Legendre, Fourier applied for admission to the artillery school. He was refused with the statement, "Fourier, not being of noble birth, cannot enter the artillery, not even if he is a second Newton." Fourier was the son of a poor tailor.

In the preliminary Discourse of the 1822 treatise, Fourier provided a good exposition of his views, scientific approach, objectives, observations on scientific method and study of nature as the source of mathematical discoveries. His numerous famous statements (aphorisms) are quoted quite widely in monographs on heat conduction.

The concept of thermal conductivity required nearly three hundred years for its development since the time of Galileo. Burr [28] presented "Notes on the History of the Concept of Thermal Conductivity". Burr [29] also presented "Notes on the History of the Experimental Determination of the Thermal Conductivity of Gases" covering the period 1780 to 1930.

It is worth noting that Fourier's last burst of creative work came in 1817 and 1818, when he achieved an effective insight into the relation between integral–transform solutions (Fourier transforms) and operational calculus [23]. He conceived the integral transform method of Fourier transform formulas and the Fourier identity. His endeavor to relate the analytical solutions to precise measurements also led to his revolutionary conceptions of dimensions and physical constants.

In Chapter 5 of the 1822 treatise [10] dealing with the propagation of heat in a solid sphere, Fourier demonstrated his considerable physical insight into the physical meaning of his analytical solution. After carrying out an order of magnitude analysis for the terms in the exact series solution for the limiting case with very small Biot number, Fourier obtained an asymptotic solution with the product of Biot and Fourier numbers in the exponent of the exponential solution. The analysis can be regarded as the solution to Newton's cooling problem. This is considered to be a remarkable feat. The significance of the Biot number was clearly recognized by Fourier.

Fourier also applied his analysis on the cooling of a sphere of small dimension to the movement of heat in a thermometer surrounded by air or liquid. Apparently he noted the original concept of the time constant. He confirmed Newton's law of cooling experimentally and illustrated the method of determining the heat–transfer coefficient experimentally. Thus the genesis of determining heat–transfer coefficient in experimental heat transfer can be traced to Fourier's remarks in Section 2 of his Chapter 5 [10]. In light of the present state of knowledge in heat transfer, the content of Chapter 5 is indeed remarkable. He demonstrated his penetrating physical interpretation of his analysis. Indeed one may conclude that Fourier's scientific method of confirming theory with experiment is now a paradigm in heat transfer research.

It is quite puzzling that in spite of his faith in the importance of heat as a primary agent in the universe, Fourier seems to have shown no interest in the problem of the motive power of heat studied by Sadi Carnot (1824) [23].

4 Development in the 19th Century After Fourier (1822–1900)

Although Fourier treated a large number of cases for heat conduction problems using Fourier series and integrals, his work was extended and applied to more complicated problems by his contemporaries Laplace (nonsymetrical heat flow in a sphere, 1820) and Poisson (nonsymetrical heat flow in cylinder, 1821), later by many others, including Lamé (1837, 1861), Lord Kelvin, and Riemann [30]. G. Green's potential theory (1835) led to significant applications of Green's function to heat conduction problems in later years. The analytical solutions for ice formation problems were obtained by Franz Neumann (1860's) and J. Stefan (1891) assuming that there is no convection in the water, and the changes of volume on freezing or melting are neglected. This class of phase–change heat conduction problem is also known as the Stefan problem. The closely related problems are freezing or thawing of the soil, and natural or artificial refrigeration.

Duhamel obtained equations of thermoelasticity in 1837, studied conduction of heat in anisotropic solids (1832) and also obtained Duhamel's theorem for the case of surface condition prescribed as a function of time (1833) [31]. The mathematical theory of conduction of heat in crystals was studied by Duhamel (1832), Lamé (1861), Stokes (1851) and Boussinesq (1901) [31].

It was remarked by Fourier himself that the age of the Earth can be roughly estimated using the measured value of the geothermal temperature gradient. The classical work on the age of the Earth (about 94×10^6 years) is Kelvin's paper (1861). With the development of Fourier series, Fourier integrals, Fourier transforms, Laplace transforms, various operational methods, and special functions in applied mathematics by Bessel, Legendre, Green and others relating to the heat conduction problems in solids, the classical theory of heat conduction was completed by the end of the 19th century. One notes that heat conduction theory involving solids was developed in a relatively short period in time for applications to various cooling and heating problems encountered by the new technology in the early 20th century. The most authoritative treatise on the subject of heat conduction by Carslaw and Jaeger [31] contains much further information on historical notes relating to the works in the 19th century. The historical notes can also be found in Jakob [32].

5 Conduction Heat Transfer in the Period 1900–1950

In connection with a general review on the heat transmission across boiler heating surfaces, Dalby [33] presented a chronological summary of heat conductivity covering the period 1690-1909 listing over 500 papers relating to

heat transfer. Methods of measuring conductivity and the application of theory to practical problems were reviewed in [34]. Conduction heat transfer was reviewed by Jakob [35] and Knoblauch [36]. The exposition of heat transfer including heat conduction by early German heat transfer books by Gröber [37], ten Bosch [38], Merkel [39] and Schack [40] exerted considerable influence on subsequent heat transfer research worldwide and textbook writings in the first half of this century. The references quoted are of special interest. Lienhard [41] made observations on the German origins of American heat transfer pedagogy. The same observations appear to be valid also to Japanese heat transfer origins.

Carslaw's (1870–1954) [27,31,42–44] expositions on the mathematical theory of the conduction of heat in solids is considered to be the most authoritative in terms of its contents and bibliography. A list of his series of books is in order:

1. Fourier Series and Integrals and the Mathematical Theory of Heat Conduction, 1906 [42].
2. Introduction to the Mathematical Theory of the Conduction of Heat in Solids, 1921 [43].
3. Introduction to the Theory of Fourier's Series and Integrals, 1921 [43].
4. With Jaeger, Conduction of Heat in Solids. 1941, 1947, 1959 [31].
5. With Jaeger, Operational Methods in Applied Mathematics, 1941 [44].

The oldest book by Carslaw [42] dealt with the theory of heat conduction very much as Fourier did. New methods (Laplace transformation, use of Green's functions, integral transforms, and numerical methods) were added in subsequent revisions. The latest edition (1959) has been a standard reference work (over 700 references)for engineers and scientists and presents a great many exact solutions and results.

Max Jakob's important treatise [32] on "Heat Transfer" deals with the basic conduction equations, thermal properties of solids and fluids, and numerous solution methods including the classical, numerical, conformal mapping, sources and sinks, Heaviside operators, Laplace transforms, relaxation, finite differences and electrical analogy with a bibliography. The heat–conduction problems occupy about 360 pages in the book. McAdams' famous book [45] on "Heat Transmission" contains useful references to 1952. Numerous analytical solutions of heat conduction problems can also be found in the early Japanese monographs by Kodaira [46], Kawashimo [47] and Katto [48]. Kawashimo's book contains solutions for applied heat conduction problems (radiators, cooling fins, pistons) and high temperature heat conduction problems considering variable thermal properties. Early German books by Warburg [49], Hobson [50] and Bachmann [51] are also noted here. The applications of Fourier series to problems in applied mechanics can be found in S. Timoshenko's famous monographs on Theory of Elasticity (1951), Theory of Plates and Shells (1959), Theory of Elastic Stability (1936), Vibration Problems in En-

gineering (1928) and T. Von Kámán and M.A. Biot's Mathematical Methods in Engineering amoung others.

6 Methods of Solution for Conduction Heat Transfer Problems

Fourier's transient heat conduction problem is a parabolic problem which in steady state condition (Laplace equation) becomes elliptic. The solution methods can be classified into classical (analytical), approximate and numerical methods.

The exact solution methods include; 1) separation of variables using Fourier series, Fourier integrals, Bessel functions, Legendre functions etc., 2) Laplace transforms, 3) Fourier transforms, 4) Hankel transforms, 5) Green's function method, 6) Complex variables method (conformal transformations), and 7) methods of images and sources. For steady–state heat conduction, potential theory applies. One also notes that Fourier series solution converges slowly for small time and that Laplace transform solution is convenient for small time.

The approximate methods include: 1) Profile method, 2) Variational method, 3) Weighted residuals method (point-matching, least-squares, Galerkin procedure, integral method), and 3) Perturbation method.

The numerical methods include; 1) Finite-difference method, 2) Finite-element analysis/method, 3) Boundary element method, 4) Monte Carlo method, and 5) Finite analytic method. One also has various analogue methods. The evolution of solution methods for partial differential equations after the classical Fourier methods is of historical interest.

It is of interest to observe that many basic approaches for the mathematical methods in heat conduction theory can be carried over directly to the solution of laminar convection heat transfer problems for the corresponding geometrical shapes such as internal flows in parallel–plate channel, pipe, annular pipe etc. For these problems the coordinate in the main flow direction corresponds to time in transient heat conduction problems.

7 Analogy in Heat, Momentum, and Mass Transfer for Transport Phenomena

The following phenomenological laws are analogous:
1) Newton's law of viscous flow (1687), 2) Fourier's law of heat conduction (1822), and 3) Fick's law of mass diffusion (1855). The obvious analogy is due to random molecular motions for each process. One also notes that each physical quantity (momentum, heat and mass) can be transported by fluid motion. The idea of presenting a unified treatment of heat, mass, and momentum transfer as transport phenomena based on analogy evolved quite naturally in the mid–1950's. The outcome was the publication of two textbooks; one by Bird, Stewart and Lightfoot (1960) [52], and one by Rohsenow

and Choi (1961) [53]. It can be seen that the genesis of the analogy can be traced to the three basic laws of momentum, heat and mass transport noted above.

The analogy between a class of transient heat conduction problems and convective heat transfer problems with slug flow (uniform velocity) is quite well-known [54]. Thus the thermal entrance region problem for slug flow in a circular tube with constant wall temperature and uniform entry temperature (Graetz problem, 1883 [55]) is analogous to the transient heat conduction problem in an infinite cylinder with uniform initial temperature and constant surface temperature. Thus the analytical solution for the Graetz problem (1883) with slug flow can be deduced immediately from the analogous analytical solution obtained by Fourier (1822). One notes that Graetz number in convection corresponds to Fourier number in transient heat conduction. It should be pointed out that apparently Graetz (1883) [55] was not aware of the analogy. Similarly the analogy between the transient heat conduction problem in a semi–infinite solid and the convective heat transfer problem for slug flow on a flat plate with similar initial and boundary conditions is obvious. As a matter of fact the similarity variables for both problems are identical if one observes the analogy. In both cases noted above, one has the development of thermal boundary layers for slug flows in a tube and on a flat plate.

One also notes that the developments of hydrodynamic and thermal boundary layers for the Blasius flow (laminar flow) are identical when the the Prandtl number is unity. It is thus clear that the analytical solutions for a class of transient heat conduction problems involving infinite cylinders of various cross-sections (circular, rectangular and other noncircular forms) with convective boundary condition, for example, can be transformed directly into the corresponding solutions for convective heat transfer problems with slug flow. The close relationship between Fourier's transient heat conduction problem and convective heat transfer with slug flow is of special interest in the light of present laminar convective heat transfer theory.

In 1972 Schlünder [56] proposed that one can define the instantaneous heat transfer coefficient for Fourier's transient heat conduction problem in an infinite circular cylinder similar to that of the Graetz problem in a circular tube and obtain the time average heat transfer coefficient for Newton's cooling problem. The determination of the average temperature for Fourier's problem is then seen to be equivalent to Newton's cooling problem with infinite thermal conductivity. In determining the time average heat transfer coefficient, Schlünder [56] used the heat transfer coefficients for small time and large time. The implications for the Graetz problem (thermal entrance region problem) are quite obvious. Here one sees the close interrelationships between Newton's cooling problem (1701), Fourier's transient heat conduction problem (1822) and Graetz problem (1883) [52].

8 Recent Conduction Heat Transfer Books

Since the recent literature on conduction heat transfer is very extensive, one must consult at first, recent monographs and review articles for technical information. The following books contain recent information and the related references. The ice formation problems can occur in the atmosphere, in water bodies (rivers, lakes, seas) on earth surfaces and underground (permafrost) with heat conduction as a dominant heat transfer mechanism. Some aspects of freezing and melting heat transfer phenomena in cold regions are reviewed in [57]. An enormous amount of work has gone into measuring various phenomenological thermal properties like thermal conductivity [58] in the past. For convenience the books related to cold regions science and engineering or freezing and melting heat transfer phenomena are also listed here. The list is incomplete.

Table 1 Conduction Heat Transfer Books

- Schneider, P.J., *Conduction Heat Transfer*, Addison–Wesley, 1955
- Crank, J., *The Mathematics of Diffusion*, Oxford, 1956
- Carslaw, H.S. and Jaeger, J.C., *Conduction of Heat in Solids*, Oxford Univ. Press, 1959
- Eckert, E.R.G. and Drake, R.M., *Heat and Mass Transfer*, McGraw–Hill, 1959
- Parkus, H., *Instationäre Wärmespannungen*, Springer–Verlag, 1959
- Bird, R.B., Stewart, W.E. and Lightfoot, E.N., *Transport Phenomena*, John Wiley & Sons, 1960
- Boley, B.A. and Weiner, J.H., *Theory of Thermal Stresses*, John Wiley & Sons, 1960
- Ribaud, G., *Conduction de la Chaleur en Régime Variable*, Gauthier–Villars, 1960
- Gröber, H., Erk, S. and Grigull, U., *Fundamentals of Heat Transfer*, McGraw–Hill, 1961
- Datzeff, A., *Sur le Problème de la Propagation de la Chaleur dans les Corps Solids*, Gauthier–Villars, 1963
- Schewmon, P.G., *Diffusion in Solids*, McGraw–Hill, 1963
- Chalmers, B., *Principles of Solidification*, John Wiley & Sons, 1964
- Boelter, L.M.K., Cherry, V.H., Johnson, H.A. and Martinelli R.C., *Heat Transfer Notes*, McGraw–Hill, 1965
- Schuh, H., *Heat Transfer in Structures*, Pergamon Press, 1965
- Arpaci, V.S., *Conduction Heat Transfer*, Addison–Wesley, 1966
- Luikov, A.V., *Analytical Heat Diffusion Theory*, Academic Press, 1968
- Özisik, M.N., *Boundary Value Problems of Heat Conduction*, International Textbook, 1968
- Tye, R.P., (ed.), *Thermal Conductivity*, Vols. 1 and 2, Academic Press, 1969
- Datzeff, A., *Sur le Problème Linéaire de Stefan*, Gauthier–Villars, 1970

- Myers, G.E., *Analytical Methods in Conduction Heat Transfer*, McGraw–Hill, 1971
- Eckert, E.R.G. and Drake, R.M., *Analysis of Heat and Mass Transfer*, McGraw–Hill, 1972
- Kern, D.A. and Kraus, A.D., *Extended Surface Heat Transfer*, McGraw–Hill, 1972
- Pivovarov, A.A., *Thermal Conditions in Freezing Lakes and Rivers*, John Wiley & Sons, 1973
- Yamaguchi, M. and Nogi, T., *Stefan Problem*, Sangyo–Tosho, 1977 (in Japanese)
- Andersland, O.B. and Anderson, D.M., (eds.), *Geotechnical Engineering for Cold Regions*, McGraw–Hill, 1978
- Wilson, D.G., Solomon, A.D. and Boggs, P.T., *Moving Boundary Problems*, Academic Press, 1978
- Özisik, M.N., *Heat Conduction*, John Wiley & Sons, 1980
- Gray, D.M. and Male, D.H., (eds.), *Handbook of Snow*, Pergamon Press, 1981
- Higashi, A., *Fundamentals of Cold Regions Engineering Science*, Kokon–Shoin, 1981 (in Japanese)
- Johnston, G.H., (ed.), *Permafrost, Engineering Design and Construction*, John Wiley & Sons, 1981
- Lunardini,V.J., *Heat Transfer in Cold Climates*, Van Nostrand Reinhold, 1981
- Kinoshita, S., (ed.), *Physics of Frozen Ground*, Morikita, 1982 (in Japanese)
- Hutter, K., *Theoretical Glaciology*, Reidel, 1983
- Aziz, A. and Na, T.Y., *Perturbation Methods in Heat Transfer*, Hemisphere, 1984
- Crank, J., *Free and Moving Boundary Problems*, Oxford Univ. Press, 1984
- Grigull, U. and Sander, H., *Heat Conduction*, Hemisphere, 1984
- Kurz, W. and Fisher, D.J., *Fundamentals of Solidification*, Oxford Univ. Press, 1984
- Manzoor, M., *Heat Flow Through Extended Surface Heat Exchangers*, Springer–Verlag, 1984
- Mikhailov, M.D. and Özisik, M.N., *Unified Analysis and Solutions of Heat and Mass Diffusion*, John Wiley & Sons, 1984
- Beck, J.V., Blackwell, B. and St. Clair, C.R., *Inverse Heat Conduction: Ill–Posed Problems*, John Wiley & Sons, 1985
- Kakac, S. and Yener, Y., *Heat Conduction*, Hemisphere, 1985
- Rohsenow, W.M., Hartnett, J.P. and Ganic, E.N., (eds.), *Handbook of Heat Transfer*, Fundamentals (Vol. 1), Applications (Vol. 2), McGraw–Hill, 1985
- Ashton, G.D., (ed.), *River and Lake Ice Engineering*, Water Resources Publications, 1986

- Farouki, O.T., *Thermal Properties of Soils*, Trans. Tech. Publications, 1986
- Ho, C.Y., (ed.), *Specific Heat of Solids*, Hemisphere, 1988
- Lock, G.S.H., *The Growth and Decay of Ice*, Cambridge Univ. Press, 1990
- Cheng, K.C. and Seki, N., (eds.), *Freezing and Melting Heat Transfer in Engineering*, Hemisphere, 1991
- Lunardini, V.J., *Heat Transfer with Freezing and Thawing*, Elsevier, 1991
- Beck, J.V., et al., *Heat Conduction Using Green's Functions*, Hemisphere, 1992
- Alexiades, V. and Solomon, A.D., *Mathematical Modeling of Melting and Freezing Processes*, Hemisphere, 1993
- Gebhart, B., *Heat Conduction and Mass Diffusion*, McGraw–Hill, 1993
- Lock, G.S.H., *Latent Heat Transfer*, Oxford Univ. Press, 1994
- Poulikakos, D., *Conduction Heat Transfer*, Prentice–Hall, 1994
- Saitoh, T., *Moving Boundary Heat Transfer*, Yokendo, 1994 (in Japanese)
- Kaviany, M., *Principles of Heat Transfer in Porous Media*, Springer, 1995
- Fukusako, S. and Inaba, H., *Heat Transfer Phenomena Under Low Temperature Environments and their Applications*, Yokendo, 1996
- Rohsennow, W.M., Hartnett, J.P. and Cho, Y.I., (eds.), *Handbook of Heat Transfer*, 3rd. Ed., McGraw–Hill, 1998

9 Concluding Remarks and Some Observations

The history of heat transfer is now nearly 300 years old beginning with the enunciation of Newton's cooling law in 1701. The classical work of the conduction heat transfer belongs to applied mathematics. Fourier's work in 1822 marked the beginning of theoretical work in heat transfer and provided the basic methodologies for subsequent developments in convection heat transfer. Heat conduction is the basic mechanism in convection heat transfer and convection is closely related to fluid mechanics. Thermal radiation is related to electromagnetic theory and quantum mechanics and, represents the application of physics. Conduction heat transfer is the basic mode in heat transfer dealing with the heating or cooling of solids and the field of application is wide–ranging. Over the years many useful analytical solutions to a broad range of heat conduction problems have been found [31].

The problem of terrestrial temperatures led Fourier to develop his conduction theory. Fourier's exploitation of trigonometric series expansions greatly enhanced the power and scope for spectrum or harmonic analysis for the description of various physical processes in terms of frequencies (periodic wave–like motion). Brush's remark [59] in this connection is of interest:

> "Fourier's influence can be seen in both of the forms of quantum mechanics which were developed in 1925–26 : Schrödinger's wave mechanics based on a partial differential equation for the "wave function," and Heisenberg's matrix mechanics, based on the manipulation

of "Fourier coefficients" for transitions involving radiation of various frequencies."

This article deals only with some aspects of the historical development. Many topics closely related to conduction heat transfer were not considered. Within the scope of this article, recent contributions relating to the topics listed in Table 2 were not discussed.

Table 2 Examples of Topics Closely Related to Conduction Heat Transfer

1. Extended surfaces (fins)
2. Direct contact heat transfer
3. Temperature and heat flux measurements
4. Temperature control systems
5. Heat exchangers
6. Freezing, melting and solidification phenomena
7. Measurements and theoretical predictions of thermal conductivity (solid, liquid, gas)
8. Thermal stresses (thermoelasticity)
9. Hyperbolic heat conduction problems
10. Freezing or thawing of soils – its controls and applications (natural or artificial refrigeration)
11. Applications of molecular dynamics to heat conduction phenomena (microscale thermal phenomena)
12. Batch and unsteady processes in process heat transfer
13. Materials processing (crystal growth, casting, welding, heat treatment, semiconductor device fabrication, etc.) and high technology applications
14. Permafrost and frost heave phenomena
15. Physical and biological environments in cold regions (geophysical applications)
16. Food processing applications
17. Low temperature problems in biology
18. Aircraft icing

The list is incomplete and for reference only. For example, recent icing technology bibliography [60] lists 26 different topics and about 2000 references. A natural history of ice and snow is discussed in [61]. The phase–change heat transfer phenomena are also covered in geophysics (meteorology, oceanography, limnology), geology and glaciology.

With the development of new materials meeting the demands of high technology, it is increasingly important to understand the thermo–fluid phenomena at the atomic and molecular levels. Heat conduction is related to molecular action and the fundamental mechanism of molecular heat diffusion is of special interest. One notes that molecular heat transfer has received much attention in recent years [62]. Recent work includes molecular and microscale heat transfer in materials processing and other applications. The

concept of transmission of heat by waves was reviewed and interpreted by Joseph and Preziosi [63]. The field of conduction heat transfer is very broad and the literature is very extensive. With the new developments in manufacturing and materials processing involving high technology, the unsolved heat conduction problems remain and one expects further fundamental advances in this field in the future. The scope of this article is rather limited and the content remains to be improved.

Acknowledgement: The author wishes to thank Dr. K. Hutter for his valuable editorial comments leading to the improvement of the original manuscript.

References

1. Brush, S. G. (1976) The Kind of Motion We Call Heat, *A History of the Kinetic Theory of Gases in the 19th Century*, Books 1 and 2, North Holland Pub. Co., Amsterdam
2. Brush, S. G. (1988) *Gaseous Heat Conduction and Radiation in 19th Century Physics*, in: *History of heat Transfer*, eds. E. T. Layton and J. H. Lienhard, ASME, New York, 25–51
3. Schlünder, E. U. (1982) Wilhelm Nusselt's Opinion on Heat Transfer by Convection, *Chemical Engineering Fundamentals*, **1** / No. 2, 4
4. Ruffner, J. A. (1963) Reinterpretation of the Genesis of Newton's Law of Cooling, *Archive for History of Exact Sciences*, **2**, 138–153
5. Grigull, U. (1984) Newton's Temperature Scale and the Law of Cooling, *Wärme- und Stoffübertragung*, **18**, 195–199
6. Cheng, K. C., Fujii, T. (1998) Isaac Newton and Heat Transfer, *Heat Transfer Engineering*, **19**, 9–21
7. Newton, I. (1701) *A Scale of the Degrees of Heat*, in: Magie, W. F. (1935) *A Source Book in Physics*, McGraw-Hill, New York, 125–128
8. Newton, I. (1701) *A Scale of the Degrees of Heat*, in: Cohen, I. B. (1978) *Isaac Newton's Papers & Letters on Natural Philosophy and Related Documents*, 2nd edition, Harvard Univ. Press, Cambridge, 265-268
9. Cardwell, D. S. L. (1989) *From Watt to Clausius, The Rise of Thermodynamics in the Early Industrial Age*, Iowa State University, Ames
10. Fourier, J. (1822) *The Analytical Theory of Heat*, translated, with notes, by A. Freeman, Dover Publications (1955), New York
11. Soumerai, H. (1987) *Practical Thermodynamic Tools for Heat Exchanger Design Engineers*, John Wiley & Sons, New York
12. Herivel, J. (1975) *Joseph Fourier*, Clarendon Press, Oxford
13. Grattan-Guinness, I. (1972) *Joseph Fourier 1768–1830*, The MIT Press, Cambridge
14. Grattan-Guinness I. (1969) Joseph Fourier and the Revolution in Mathematical Physics, *J. Inst. Maths Applics.*, **5**, 230–253
15. Grattan-Guinness I. (1970) *The Development of the Foundations of Mathematical Analysis from Euler to Riemann*, Massachusetts Institute of Technology

16. Mach, E. (1986) Principles of the Theory of Heat, Historically and Critically Elucidated, D. Reidel Pub. Co., Boston; *Die Principien der Wärmelehre* (1st edition, 1886)
17. Truesdell, C. (1980) *The Tragicomical History of Thermodynamics*, 1822–1854, Springer–Verlag, New York
18. Biot, J. B. (1804) The Propagation of Heat and a New Way of Measuring High Temperatures Simply and Exactly, *Journal des Mines*, **17**, 203–244
19. Sneddon, I. N. (1951) *Fourier Transforms*, McGraw-Hill, New York, p.167
20. Herivel, J. W. (1966) Aspects of French Theoretical Physics in the Nineteenth Century, *The British J. for the History of Science*, **3**, 109–132
21. Whewell, W. (1836) Report on the Recent Progress and Present Condition of the Mathematical Theories of Electricity, Magnetism, and Heat, *Report of the British Association for the Advancement of Science*, John Murray, London, 1-34
22. Arago, F., (1833) *Joseph Fourier, Biographies of Distinguished Scientific Men*, Longman, Brown, Green, Longmans & Roberts : 242-286
23. Ravetz, J., Grattan–Guinness, I. (1972) Joseph Fourier, *Dictionary of Scientific Biography*, **5** : 93-99
24. Friedman, R. M. (1978) The Creation of a New Science : Joseph Fourier's Analytical Theory of Heat, *Historical Studies in the Physical Sciences* **4**, 73-99
25. Truesdell, C. (1984) *Rational Thermodynamics*, 2nd Edition, Springer–Verlag, New York
26. Merz, J. T. (1907) *A History of European Thought in the Nineteenth Century*, Vols. 1 and 2, William Blackwood and Sons, Edinburgh
27. Carslaw, H. S. (1921) *Introduction to the Theory of Fourier's Series and Integrals*, Macmillan and Co., London
28. Burr, A. C. (1933) Notes on the History of the Concept of Thermal Conductivity, *ISIS*, **20**, 246–259
29. Burr, A. C. (1934) Notes on the History of the Experimental Determination of the Thermal Conductivity of Gases, *ISIS*, **21**, 169–186
30. Ingersoll, L. R., Zobel, O. J., Ingersoll, A. C. (1948) *Heat Conduction, with Engineering and Geological Applications*, McGraw–Hill, New York
31. Carslaw, H. S., Jaeger, J. C. (1947, 1959) *Conduction of Heat in Solids*, Clarendon Press, London
32. Jakob, M., (1949) *Heat Transfer*, Vol. 1, John Wiley & Sons, New York
33. Dalby, W. E. (1909) Heat Transmission, *Proc. Inst. of Mechanical Engrs.*, 921–986
34. Glazebrook, R. (ed.), (1922) *A Dictionary of Applied Physics*, Vol. 1, Macmillan and Co., 429–470
35. Jakob, M. (1926) *Wärmeleitung*, in: Müller-Pouillets, Lehrbuch der Physik, II. Auflage, Druck und Verlag von Friedr. Vieweg & Sohn, Braunschweig, 871–937
36. Knoblauch, O. (1929) Wärmeleitung, *Handbuch der Experimental Physik*, Band **9**, Akademische Verlagsgesellschaft M.B.H., Leipzig, 191–267
37. Gröber, H. (1921) *Die Grundgesetze der Wärmeleitung und des Wärmeüberganges*, Verlag von Julius Springer, Berlin
38. ten Bosch, M. (1921) *Die Wärmeübertragung*, Verlag von Julius Springer, Berlin
39. Merkel, F. (1927) *Die Grundlagen der Wärmeübertragung*, Verlag von Theodor Steinkopff, Dresden
40. Schack, A. (1929) *Der industrielle Wärmeübergang*, Verlag Stahleisen m.b.H., Düsseldorf

41. Lienhard, J. (1979) Observations on the German Origins of American Heat Transfer Pedagogy, *Heat Transfer Engineering*, **1**, **7** and **64**
42. Carslaw, H. S. (1906) *Fourier's Series and Integrals and the Mathematical Theory of Heat Conduction*, Macmillian, New York
43. Carslaw, H. S. (1921) *Mathematical Theory of Heat, Macmillan*, New York; (1930) *Fourier Series and Integrals*, Macmillan, New York
44. Carslaw, H. S., Jaeger, J. C. (1941) *Operational Methods in Applied Mathematics*, Dover Publications, New York
45. McAdams, W. H. (1954) *Heat Transmissions*, McGraw–Hill, New York
46. Kodaira, Y. (1933) *Physical Mathematics*, Vols. 1 and 2, Iwanami–Shoten, Tokyo (in Japanese)
47. Kawashimo, K. (1941, 1971) *Heat Conduction Theory* 2nd ed., Ohmshia, Tokyo (in Japanese)
48. Katto, Y. (1956) *Heat Conduction Theory*, Kyoritsu Publications, Tokyo (in Japanese)
49. Warburg, E. (1924) *Über Wärmeleitung und andere ausgleichende Vorgäenge*, Julius Springer, Berlin
50. Hobson, E. W. (1903–1921) *Wärmeleitung, Mathematischer Teil*, in: *Encyklopaedie der mathematischen Wissenschaften*, **5**, (1), Article 4, I, B.G. Teubner, Leipzig and Berlin
51. Bachmann, H. (1938) *Tafeln über Abkühlungsvorgänge einfacher Körper*, Julius Springer, Berlin
52. Bird, R. B., Stewart, W. E., Lightfoot, E. N. (1960) *Transport Phenomena*, Wiley, New York
53. Rohsenow, W. M., Choi, H. (1961) *Heat, Mass, and Momentum Transfer*, Prentice–Hall, Englewood Cliffs, New Jersey
54. Cheng, K. C., Chen, C. K. (1992) Some Observations on the Relationship of Transient Heat Conduction to Convective Laminar Heat Transfer, General Papers, *HTD-Vol.* **212**, *ASME*, 19–29
55. Graetz, L. (1883) Über die Wärmeleitungsfähigkeit von Flüssigkeiten, *Ann. Phys.*, **18**, 79–94
56. Schlünder, E.U. (1972) Über die Brauchbarkeit des Newtonschen Abkühlungsgesetzes im Lichte der Fourierschen Wärmeleitungstheorie, *Wärme- und Stoffübertragung*, **5**, 9–14
57. Cheng, K.C., Seki, N., eds. (1991) *Freezing and Melting Heat Transfer in Engineering*, Hemisphere, New York
58. Powell, R.W., Touloukian, Y.S. (1973) *Thermal Conductivities of the Elements, Science*, **181**, 999–1008
59. Brush, S.G. (1976) Irreversibility and Indeterminism: Fourier to Heisenberg, *Journal of the History of Ideas*, **37**, 603–630
60. SAE Aircraft Icing Technology Subcommittee, (1987) Icing Technology Bibliography, *Society of Automotive Engineers*, Inc., Warrendale, PA
61. Tutton, A. E. H. (1927) *The High Alps, A Natural History of Ice and Snow*, Kegan Paul, Trench, Trubner & Co., London
62. Kotake, S. (1990) *Molecular Thermo–Fluid Dynamics*, Maruzen, Tokyo (in Japanese)
63. Joseph, D. D., Preziosi, L. (1989) Heat Waves, *Rev. Mod. Phys.*, **61**, 41-73

(Received 16 Feb. 1999, accepted 14 April 1999)

Numerical and Experimental Investigation on Frosting of Energy-Recovery Ventilator

Stephane Bilodeau, Yves Mercadier, and Patrick Brousseau

Université de Sherbrooke , Département de génie mécanique,
2500, boul. Université, Sherbrooke, (Québec) J1K 2R1 Canada

Abstract. Frosting of energy-recovery ventilators results in two major problems: increase of pressure losses and reduction of heat transfer rates. Frost formation of heat and mass exchangers used in these ventilation systems is investigated both experimentally and numerically. A numerical model for the prediction of the thermal behavior of the exchanger is presented. The model is validated with experimental data and is then employed to conduct a parametric study. Results indicate that the absolute humidity is the prevailing parameter for characterizing the frosting phenomenon. A frost-mass-fraction chart is established in terms of the absolute humidity of the warm exhaust stream and of the temperature of the cold supply stream. The effect of time and mass flowrate is also evaluated. The transient three-dimensional model shows that the absolute humidity and the temperature of both air flows vary nonlinearly in the frosted zone.

1 Introduction

Frosting of heat-recovery ventilators (HRV) and rotary heat and moisture exchangers (RHE) is frequently observed in cold climates. Frost builds up when the exhaust air stream from the exchanger is cooled below its dew point and moisture condenses on a cold surface below the freezing temperature. Frosting results in a reduction of the heat transfer rates and in an increase of the pressure losses through the heat exchanger.

Hygroscopic air-to-air rotary heat exchangers transfer energy in both sensible and latent heat forms in a periodic adsorption-regeneration cycle. In the adsorption part, the dew point decreases as the exhaust air stream flows through the microchannels and gives off water to the desiccant. In the regeneration part, the desiccant releases its humidity to the stream of dry air.

Holmberg [1] as well as Pfeiffer and Hbner [2] have conducted experimental studies on the frosting phenomenon during the operation of rotary regenerators. Frosting of such exchangers has also been investigated numerically by Attia and D'Silva [3] and by Stiesh et al. [4]. In both models, heat transfer was two-dimensional and the underlying mechanisms of frost formation were ignored. The present paper addresses this problem by developing a three-dimensional model which considers frosting. The model is validated with experimental data and is then used to examine the global performance of the RHE under frosting conditions. After the validation, the model will predict the impact of frost formation on the thermodynamic properties.

2 Mathematical Model

A mathematical model of a hygroscopic rotary regenerator under frosting conditions was developed. The transient three-dimensional multiphase flow equations were derived for a representative control volume (RCV) of the rotor [5,6]. The RCV as shown in Fig. 1 may contain three major constituents: a humid air flow (γ), a frost layer (with a solid phase *alpha* and the confined humid air *beta*), and a hygroscopic matrix (σ). These constituents are composed of additional components, notably dry air (a or af) and water vapor (v and vf).

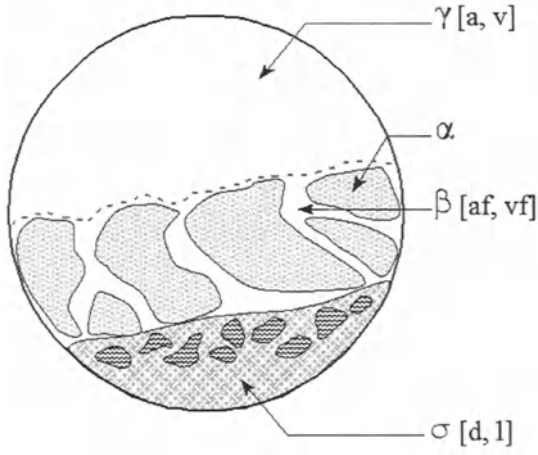

Fig. 1. Representative Control Volume (RCV)

In the RCV, it is assumed that the frost layer is a homogeneous porous medium with a uniform density. However, the frost properties are assumed to be time dependent. They are evaluated during the initial frost-layer-formation period and also during the full growth period. A previous paper has shown that neglecting the initial frost layer formation period leads to poor predictions of the frost density and conductivity [7]. The mass and energy conservation equations for the RCV have been presented in references [6,8] and need not be repeated here.

The computational methodology was thoroughly tested for heat and mass transfer in an RHE and the results were compared to those of Attia and D'Silva [3]. To further verify the accuracy of the model, experiments were conducted on rotary exchangers operating under total energy recovery conditions.

3 Experimental Investigation

The experimental setup is concerned with the frost formation in a rotary exchanger operating in conjunction with a total energy-recovery ventilation system. It consists of a hygroscopic thermal wheel installed in an enthalpy-recovery ventilator system. The test chamber controls the climatic conditions of the cold air supply whereas the exhaust-air-stream conditions are maintained by an independent furnace and humidifier (see Fig 2). Operating conditions range from $-30°C$ to $-40°C$ with dew point temperature ranging from $-30°C$ to $20°C$. The specific humidity of the inlet and outlet air streams are also recorded with the help of 4 dew point meters. The inlet and outlet temperatures of the air streams passing through the hygroscopic wheel are measured by an array of twenty uniformly distributed thermocouples connected to a data acquisition system [5].

Fig. 2. Validation of the model: Temperature and Humidity Data

Comparison between the experimentally determined and numerically predicted outlet temperature and absolute humidity for the warm supply (WS) is provided in Fig. 3. These figures reveal that the numerical predictions are in good agreement with the experimental results.

4 Results and Discussion

Series of numerical simulations were conducted to: (1) study the overall performance of RHE under frosting conditions, (2) predict the local thermodynamic properties, and (3) establish a frosting limit.

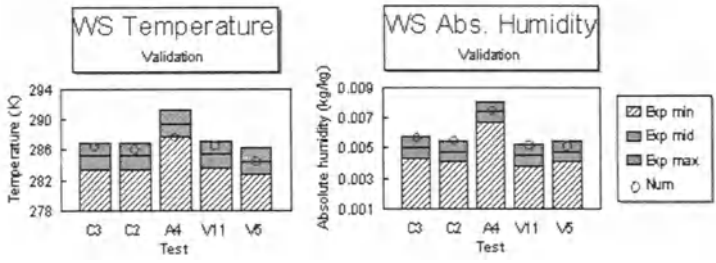

Fig. 3. Validation of the model: Temperature and Humidity Data

Fig. 4 exemplifies the effect of the mass flow rate of air on the predicted enthalpic effectiveness and on the frost formation. The effectiveness, ε, is defined here in terms of mass flow rates and enthalpies:

$$\varepsilon = \frac{\dot{m}_{cs}\,(H_{ws} - H_{cs})}{\dot{m}_{min}\,(H_{we} - H_{cs})} = \frac{\dot{m}_{we}\,(H_{we} - H_{cs})}{\dot{m}_{min}\,(H_{we} - H_{cs})}. \tag{1}$$

The subscripts CE, CS, WE,WS stand for the inlet and the outlet of the exhaust and the supply air flows, respectively: Cold Exhaust, Cold Supply, Warm Exhaust and Warm Supply. The frost mass fraction is defined as the ratio of the volume occupied by the frost layer to that of the control volume. Each dot on these figures is the result of a full simulation of the thermal behavior of the RHE.

Under normal operating conditions (without frosting), increasing the mass flow rate results in an increase of the thermal effectiveness. However, as depicted in Fig. 4 (for operating conditions maintained for 2 hours at $T_{cs} = -25°C$, $T_{we} = 22°C$ and $RH_{we} = 40\%$), when frosting occurs, increasing the mass-flow rate promotes frost formation, gradually reduces the flow passage and, as a result, the enthalpic effectiveness declines. Other results have shown that increasing the thickness of the wheel reduces frost formation and increases enthalpic effectiveness [6].

Fig. 5 illustrates typical axial temperature profiles for air and matrix both in the adsorption and in the regeneration zones (T_{cs} = -25degC, $RH_{cs} = 50\%$, T_{we} = 22degC, and $RH_{we} = 40\%$). It is observed, in the unfrosted portion of the wheel, that the temperature profile is quasi linear. Holmberg [1] suggests that the temperature profile may be approximated by a linear relation over the entire wheel using the inlet conditions. The present results show that this assumption is relevant in the unfrosted region of the wheel but may be off in the frosted region. Moreover, the bending of the temperature profiles is accentuated as the frost builds up. This figure also reveals that the frosting zone covers about one half of the width of the wheel. This zone is limited by an isotherm corresponding to a matrix temperature of 0°C (freezing set

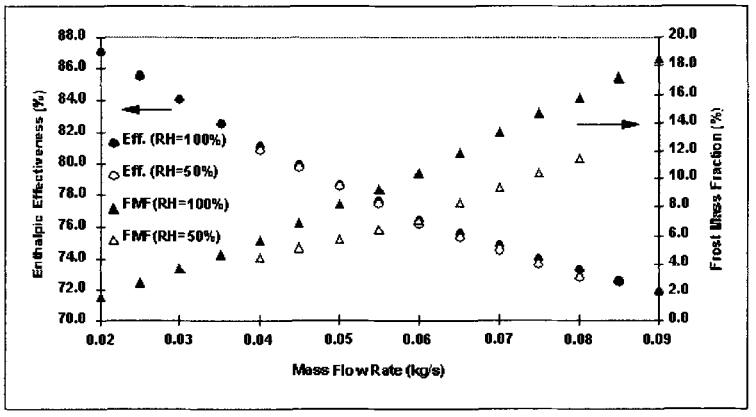

Fig. 4. Effect of the mass flowrate on the enthalpic effectiveness (Eff.) and on the frost mass fraction (FMF)

point). The frost threshold line reach this physical limit after only a few minutes (depending on operating conditions). Then, the frosted zone stops its axial growth and it grows only in thickness and density.

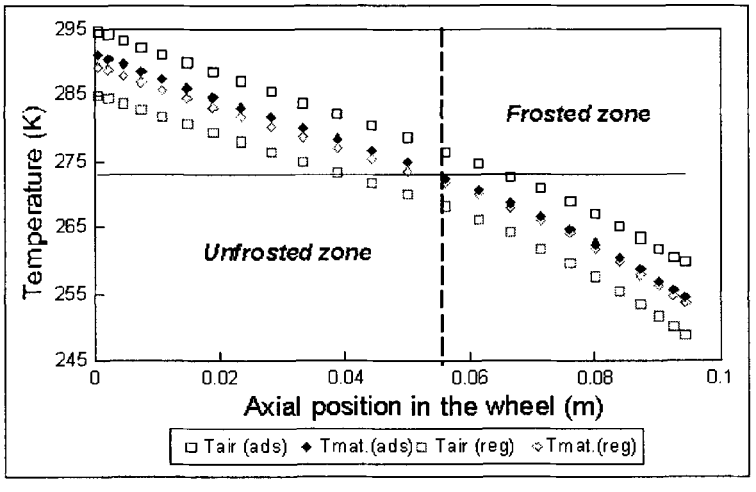

Fig. 5. Axial air and matrix temperature profiles in the wheel

The behavior of the interfacial humidity ratio between the airflow and the cold surface ressembles that of the corresponding temperature profiles exhibited in Fig. 5: the profiles are linear in the unfrosted zone and bend slightly in the frosted zone.

Fig. 6 exemplifies the evolution of the humidity ratio differential (between the surface of the matrix and the air flow) and of the frost mass fraction (FMF) across the wheel in both the adsorption and the regeneration zones. It is observed that the axial frost threshold is located near the center of the wheel (at about 58 mm) and that the driving force for the frost formation is maximum between the regeneration and the adsorption period (at 180°).

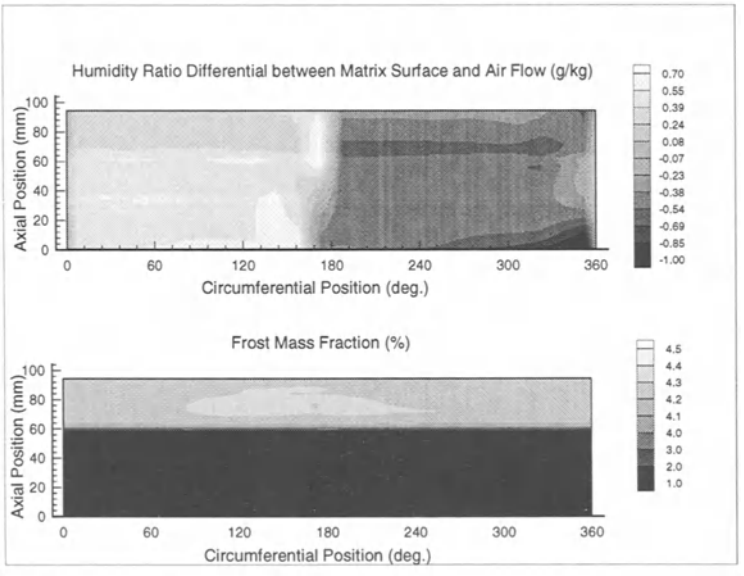

Fig. 6. Humidity gradient and frost mass fraction profiles in the wheel

The numerical simulations performed also indicate that, as the relative humidity of the warm exhaust (WE) increases, the matrix temperature in the cold supply (CS) region may augment up to 3°C in the range of the inlet conditions studied (−30°C to 25°C). The sorption phenomenon increases the enthalpic effectiveness and, at the same time, it reduces frost formation.

Fig. 7 illustrates the effect of temperature, humidity and time on the frosting limit. Examination of this figure reveals that after 30 minutes of operation, frosting may occur only under severe conditions (for T_{cs}under −20°C or W_{we} over 5 $g\,kg^{-1}$). As time passes however, the likelihood of frosting augments and stabilizes and an operating period of about 2 hours may be seen as the upper limit. This chart may prove very useful to establish control strategies for defrosting RHE. For instance, if $T_{cs} = -15°C$ and W_{we} =7 $g\,kg^{-1}$, one may envisage to preheat the cold supply air every 30 minutes to prevent frosting. On the other hand, if $T_{cs} = -20°C$ and W_{we}=4 $g\,kg^{-1}$, cyclic preheating would be necessary only at every 2 hours. This figure also

reveals that it will take more than a day of constant operation to reach complete frosting at T_{cs} over $-15°C$ and WWE under 2 g kg^{-1}.

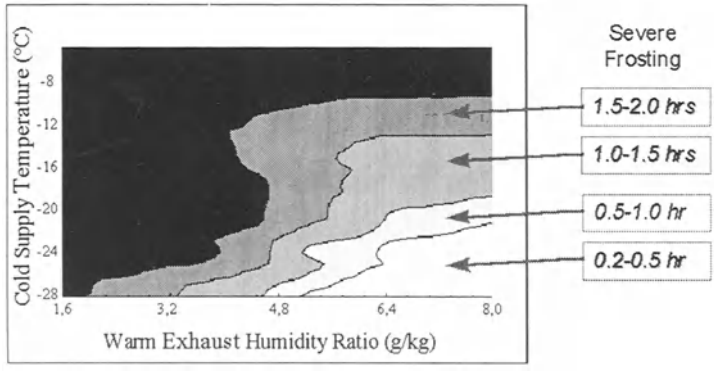

Fig. 7. Effect of temperature, humidity and time on frosting limit

As expected, frosting is strongly dependent of the exhaust air absolute humidity and on the cold supply temperature. The frosting limit is also influenced by the efficiency of the exchanger and by the geometry of the RHE. The results emphasize the importance of the operating conditions and of the thermodynamic properties of the humid air. Optimization is required to insure that proper control strategies are implemented for operating RHEs in cold climate.

5 Conclusion

Frost formation in rotary heat and mass exchangers was investigated both experimentally and numerically. A mathematical model, developed in [6] and [8], was used to predict the thermal behavior of the rotary exchanger. The transient three-dimensional model was validated with experimental data for temperature and humidity.

Results indicate that the absolute humidity is the prevailing parameter for characterizing the frosting phenomenon. A frost-mass-fraction chart was established in terms of the humidity ratio of the warm exhaust stream, of the temperature of the cold supply stream, and of the time. Unlike the widely retained assumption, it was shown that the absolute humidity and the temperature of both air flows vary non-linearly in the frosted zone.

Acknowledgements: The authors would like to thank the Natural Sciences and Engineering Reasearch Council of Canada and the Fonds pour la Formation de Chercheurs et l'Aide la Recherche du Quebec (FCAR) for their financial support. They also acknowledge the technical support from the Energy Diversification Research Laboratory of Natural Resources Canada.

References

1. Holmberg, R. B. (1993) Prediction of Condensation and Frosting Limits in Rotary Wheels for Heat Recovery in Buildings, *ASHRAE Transactions*, Atlanta, 64–69.
2. Pfeiffer, S. and Hbner, H. (1987) Untersuchungen zum Einfrieren von Regenerativ-Wrmebertragern, *Klima - Kälte - Heizung*, 449–452.
3. Attia, M. H. and D'Silva, N. S. (1983) On the Thermal Characteristics and Response Behavior of Residential Rotary Regenerative Heat Exchangers, *14th Sem. International Cent. Heat and Mass Transfer*, Hemisphere, 599–611.
4. Stiesh, G., S. A. Klein and J. W. Mitchell (1995) Performance of Rotary Heat and Mass Exchangers, *HVAC&R Research, ASHRAE*, Atlanta, **4**, 308–324.
5. Bilodeau, S. (1998) *Modelisation experimentale et numerique de la formation du givre dans le roues enthalpiques*, Ph.D. Thesis, Université de Sherbrooke, Canada.
6. Bilodeau, S., Brousseau, P., Lacroix, M., Mercadier, Y. (1998) Frost formation in rotary heat and mass exchangers, *International Journal of Heat and Mass Transfer*, Pergamon Press, Great Britain, accepted.
7. Tao, Y. X., Besant, R. W. , and Y. Mao (1993) Characteristics of frost growth on a flate plate during the early growth period, *ASHRAE Transaction: Symposia, CH-93-2-2, Atlanta*, 746–753.
8. Bilodeau, S., Brousseau, P., Lacroix, M., Mercadier, Y., (1996) Modelling of a Frost Formation in Rotary Heat Regenerator, *5th International Symposium on Thermal Engineering in Cold Regions, Ottawa*, 373–378.

(Received 05 March 1999, accepted 31 May 1999)

Melting of Unfixed Material Inside an Elliptical Capsule

Sergei Fomin[1], Alexander Wilchinsky[2], and Takeo Saitoh[3]

[1] Department of an Applied Mathematics, Kazan State University, Kazan, Russia
[2] Institute of Mathematics and Mechanics, Kazan State University, Kazan, Russia[†]
[3] Department of Aeronautics and Space Engineering, Tohoku University, Sendai, Japan

Abstract. An approximate mathematical model of contact melting of an unfixed material in an elliptical capsule is developed. The main characteristic scales and non-dimensional parameters which describe the principal features of the melting process are found. Choosing the special heat flux distribution on the wall of the capsule allows us to derive a closed-form evolution equation for the motion of the solid, which also determines the melting rate. It is shown that the melting rate depends on the shape of the capsule. The elliptical capsules show higher rate of melting than the circular ones. The vertically elongated capsules provide more effective melting than the horizontally elongated ones, even though they have the same aspect-ratios and vertical cross-sectional areas. The time required for complete melting can be achieved by the right choice of the shape of the capsule, which is specified by the value of the aspect ratio. This is especially important for the design of practical latent-heat-thermal-energy systems.

1 Introduction

Analysis of close-contact melting of a solid in a cavity is motivated by application in latent heat-of-fusion thermal-storage systems. Contact melting in a circular horizontal cylinder has been studied numerically by Saitoh and Hirose [1], analytically and experimentally by Bareiss and Beer [2]. Contact melting in a spherical capsule was investigated numerically by Moore and Bayazitoglu [3] and later, applying the technique proposed in [2], Bahrami and Wang [4] and Roy and Sengupta [5] reported analytical solutions. The general scheme for the scale analysis of the contact melting problem was proposed by Bejan [6]. Although the aforementioned investigations highlight the main characteristics of contact melting inside a capsule, the effect of the shape factor of its cross-section has not been analyzed. In 1998 Saitoh [7] pointed out that the shape of the capsule is an important factor which should be taken into consideration for optimal design and construction of the

[†] Present address: Institut für Mechanik, Hochschulstr. 1, Technische Universität Darmstadt, 64289 Darmstadt, Germany

latent-heat-thermal-storage systems. In the present paper the approximate approach developed by Bareiss and Beer [2] is applied with the higher order of accuracy for the mathematical modeling of contact melting in a horizontal elliptical cylinder and ellipsoidal capsule.

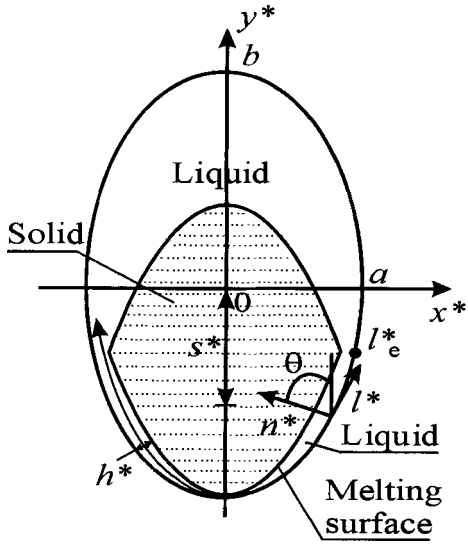

Fig. 1. Close-contact melting in an elliptical capsule

2 System Model and Analysis

The melting process within an elliptical capsule is illustrated in Fig.1. The equation $(x^*/a)^2 + (y^*/b)^2 = 1$ describes a generating curve of the surface of the capsule which can be an elliptical cylinder or an ellipsoid of revolution. In the first case (x, y) are Cartesian coordinates, and in the second case (x, y) are cylindrical coordinates, where x is a radial distance and y is the axis of symmetry. Initially, the elliptical capsule contains material in solid phase, which occupies the full space of the capsule. Then the wall temperature is raised to the value $T_w^* > T_m^*$ and is held at this value during the period necessary to melt the solid completely. The unfixed solid bulk sinks[1] because its density is higher than that of the molten liquid. The downward motion of the solid core is characterized by the time-dependent shift s of a material-fixed reference point, which is chosen to be the centre of the originally elliptical core. The motion of the solid bulk is accompanied by the generation of liquid

[1] We do not treat ice

at the melting surface. This liquid is squeezed up to the space above the solid through a narrow gap between the melting surface and the wall of the capsule. Conventionally, the solid-liquid interface can be divided into two parts by the time dependent value l_e of the tangential coordinate (Fig.1): a bottom interface ($l < l_e$), which represents the close-contact melting area, where most of the intensive melting occurs, and the upper interface, where much slower "latent" melting takes place. Experiments on melting in a circular horizontal tube conducted by Bareiss and Beer [2] showed that melting at the upper surface of the solid generated approximately 10-15 percent of the total melt. Moreover, in these experiments the upper surface of the solid core was very insignificantly changing its shape with time and, therefore, in the model the shape of this surface could be considered as approximately the same throughout the entire process. It was also found that the thickness of the molten layer in the close-contact area is considerably smaller than the characteristic size of the cavity. On the basis of these results, the primary assumptions made in the present study are the following:

(1) Melting at the upper surface of the solid core is negligibly small [2].
(2) The solid core is at the melting point.
(3) Thermophysical properties of the materials are constant.
(4) The pressure at the upper interface between the solid and liquid is hydrostatic.
(5) Since the thickness of the liquid layer in the close-contact area is very small in comparison with the dimension of the capsule, the lubrication-theory approach can be implemented for mathematical modeling of the heat and mass transfer processes in the molten layer. Therefore, the local two-dimensional curvilinear orthogonal coordinate system (l, n), which is often used in the boundary layer problem, is applied as shown in Fig.1.
(6) The motion of the liquid and the solid is non-inertial.

2.1 Governing equations

The transverse coordinate n^* is normalized by dividing lengths by the molten layer thickness so that $n = 0$ determines the capsule wall and $n = 1$ determines the solid-liquid interface. For the case under consideration we choose the scales as

$$s_0 = 2b, \quad l_0 = a, \quad n_0 = h_0, \quad T_0 = T_{w0} - T_m^*,$$

$$p_0 = bg(\rho_s - \rho_l), \quad u_0 = aw_0/h_0.$$

Here, T_{w0} is a characteristic temperature of the wall of the capsule. The characteristic excess pressure p_0 is taken as the typical difference between the gravitational and buoyancy forces acting on the solid per unit area of its surface. The other scales will be determined from investigation of the governing equations. On the basis of assumption (5), the conservation equations of mass, momentum and energy in dimensionless form can be written as

$$\frac{\partial w}{\partial n} + \frac{1}{x^\nu}\frac{\partial (x^\nu h u)}{\partial l} = 0, \qquad \nu = 0, 1, \tag{1}$$

$$\frac{\partial p}{\partial l} = \frac{\eta}{h^2}\frac{\partial^2 u}{\partial n^2}, \qquad \eta = \frac{\mu u_0 a}{p_0 h_0^2}, \tag{2}$$

$$\frac{\partial p}{\partial n} = 0, \tag{3}$$

$$Ste(u\frac{\partial T}{\partial l} + \frac{w}{h}\frac{\partial T}{\partial n}) = \frac{1}{h^2}\frac{\partial^2 T}{\partial n^2}, \tag{4}$$

where $\nu = 0$ corresponds to the elliptical cylinder and $\nu = 1$ corresponds to the ellipsoid of revolution. These are essentially the lubrication equations with an accuracy of $O(\varepsilon)$ expressed in curvilinear coordinates. Here the terms of $O(\varepsilon)$ are neglected since the parameter $\varepsilon = h_0/a$, which represents the ratio of the gap width scale to the characteristic dimension of the capsule, is very small and varies in the range $10^{-3} - 10^{-2}$ for different phase change materials used in the thermal storage systems. Equation (1) is the mass balance, (2) and (3) express the longitudinal and normal force balance, and (4) is the steady-state energy balance. The Stefan condition at the solid-liquid interface $n = 1$ yields

$$w = \left[\frac{\varphi}{h}\frac{\partial T}{\partial n}\right]_{n=1}, \qquad \varphi = \frac{k_l(T_{w0} - T_m^*)}{h_0 \rho_l L_m w_0}. \tag{5}$$

The transverse velocity at the solid-liquid interface $n = 1$ can also be found to order $O(\varepsilon)$ as

$$w = -\sigma\frac{\partial s}{\partial \tau}\cos\theta, \quad \sigma = \frac{2\rho_s b}{\rho_l w_0 \tau_0}. \tag{6}$$

From (3) it can be seen that p is a function of only one independent variable l. Equating $\eta = 1$ in (2), $\varphi = 1$ in the Stefan condition (5) and $\sigma = 1$ in (6) yields the scales for the molten layer thickness, the transverse velocity and the time as follows

$$h_0^4 = \frac{a^4 Ste\bar{b}^2}{Ar\ Pr}, \quad w_0 = \frac{k_l(T_{w0} - T_m^*)}{\rho_l h_0 L_m}, \quad \tau_0 = \frac{2b\rho_s}{w_0 \rho_l}. \tag{7}$$

Balancing the forces acting on the solid in the vertical direction, namely the gravitational force and the force exerted by the liquid, yields with an accuracy

of $O(\varepsilon)$

$$\int_0^{\sqrt{1-s^2}} px^\nu dx = F_\nu(s), \qquad \nu = 1, 0, \tag{8}$$

where

$$F_0 = (\arccos s - s\sqrt{1-s^2}), \quad F_1 = \frac{2}{3} - s + \frac{s^3}{3}. \tag{9}$$

The magnitude of the gravitational force in the right-hand side of equation (8) depends on the solid bulk volume which varies with time since s is a function of time. As it can be seen from equations (9) in the final stage of the melting process when s tends to 1, the volume of the solid bulk and, therefore, the magnitude of the gravitational force vanish to zero. In the left-hand side of equation (8) the force acting in the direction opposite to the gravitational force is represented by the force of pressure in the liquid layer. The other component of this force caused by the shear stresses is ignored since its magnitude is of $O(\varepsilon)$.

2.2 Evolution equation

Integrating equation (2) twice with respect to n and taking into account the no-slip conditions on both the capsule wall and the melting interface yields

$$u = \frac{h^2}{2}\frac{\partial p}{\partial l}(n^2 - n). \tag{10}$$

Substituting equation (10) into the continuity equation (1), integrating with respect to n and l, and taking into account (6) and the impermeability condition on the wall of the capsule, we derive the expressions for the pressure gradient and the transverse velocity

$$\frac{\partial p}{\partial l} = -\frac{12x(ds/d\tau)}{(\nu+1)h^3}, \tag{11}$$

$$w = (ds/d\tau)\cos\theta(2n^3 - 3n^2). \tag{12}$$

Using the expression for the pressure gradient (11) we can write the force balance equation (8) in the form

$$\frac{12(ds/d\tau)}{(\nu+1)^2}\int_0^{\sqrt{1-s^2}} \frac{x^{\nu+2}}{h^3\cos\theta}dx = F_\nu, \quad (\nu = 0, 1), \tag{13}$$

where F_0 and F_1 are determined by equations (9). Integrating the energy equation (4) with respect to n in the interval $(0,1)$ and using the mass conservation equation (1) and the Stefan condition (5), we derive the energy balance equation in the integral form

$$\frac{Ste}{hx^\nu}\frac{\partial}{\partial l}(hx^\nu \int_0^1 uTdn) = q_w - \frac{ds}{d\tau}\cos\theta, \tag{14}$$

where $q_w = q_w(l)$ is the transverse heat flux at the wall of the capsule.

2.3 Simplified model of close-contact melting

As it was already mentioned, the derivation of the mathematical model presented above is based on the fact that the parameter $\varepsilon = h_0/a \sim 10^{-3} - 10^{-2}$, therefore values of order $O(\varepsilon)$ are ignored. This model is governed by another small parameter - the Stefan number. For a number of situations and a variety of phase-change materials $Ste < 0.1$. The latter allows us to implement the perturbation methods and to neglect in the further analysis the terms of the order of $O(Ste^2)$. Within the bounds of the adopted accuracy the temperature profile which should be substituted into the left-hand side of equation (14) can be taken as follows

$$T = T_w(1-n) + O(Ste). \tag{15}$$

From the Stefan condition (5) and equation (15) it also follows that

$$T_w = h\cos\theta\frac{ds}{d\tau} + O(Ste). \tag{16}$$

Substituting into the left-hand side of the energy balance equation (14) the expression for the tangential velocity (10) and the linear temperature profile across the molten layer (15), where the pressure gradient $\partial p/\partial l$ and the wall temperature T_w are defined by equations (11) and (16) respectively, after integration over l, we derive with an accuracy of $O(Ste^2)$

$$h\cos\theta\frac{ds}{d\tau}Ste = 2\left(\frac{\nu+1}{(ds/d\tau)x^{\nu+1}}\int_0^l x^\nu q_w dl - 1\right). \tag{17}$$

If the heat flux distribution on the wall of the capsule $q_w = q_w(l)$ is given, then (17) together with the force balance equation (13) constitute the system of integro-differential equations, from which the shift of the solid core $s = s(\tau)$ and the thickness of the molten layer $h = h(l,\tau)$ can be determined. For the arbitrary q_w this system of equations can be solved numerically, however, the closed-form analytic solution can be readily obtained, provided that on

the wall of the capsule the special heat flux distribution is assumed as $q_w = \overline{q}\cos\theta$, where $\overline{q}$ is constant and $\cos\theta = dx/dl = \sqrt{1-x^2}/\sqrt{1+cx^2}$. In this case equation (17) converts to

$$\overline{h} = 2\left(\overline{q}/\frac{ds}{d\tau} - 1\right) \Big/ (Ste\frac{ds}{d\tau}), \tag{18}$$

from which it follows that the product $\overline{h} = h\cos\theta$ does not depend on x and can be a function of time only. As a result the force balance equation (13) reduces to

$$h^3 = \frac{12}{(\nu+1)^2 F_\nu}\frac{ds}{d\tau}\int_0^{\sqrt{1-s^2}} x^{\nu+2}\left(\frac{dx}{dl}\right)^2 dx. \tag{19}$$

For the further analysis we assume (and prove it below) that for the specified case the liquid temperature is a function of n only. Based on this assumption we reduce the energy equation (4) by ignoring the first term on the left-hand side. Then, substituting expression (12) for w into (4) yields

$$Ste\ \overline{h}(2n^3 - 3n^2)\frac{ds}{d\tau}\frac{\partial T}{\partial n} = \frac{\partial^2 T}{\partial n^2}. \tag{20}$$

For the case under consideration, the boundary conditions at the solid liquid interface (5) and $T = 0$ (sufficient to solve (20)) do not depend on l. Therefore, because (20) does not include coefficients depending on l, the temperature T will be a function of n only and the wall of the capsule is isothermal. The temperature distribution therefore can be readily found

$$T = \overline{h}\frac{ds}{d\tau}\exp\left(\frac{Ste\ \overline{h}}{2}\frac{ds}{d\tau}\right)\int_n^1 \exp\left(Ste\ \overline{h}\frac{ds}{d\tau}(n^2/2 - n^3)\right) dn. \tag{21}$$

If instead of the given heat flux as considered above the temperature on the wall of the capsule is given, $T|_{n=0} = T_w$, then after expansion of the exponential functions on Ste in (21) written for $n = 1$ and some simple manipulations we derive

$$\overline{h}(ds/d\tau) = T_w(1 - 7SteT_w/20). \tag{22}$$

Substituting equation (22) into the force balance equation (19) leads to the equation for the downward velocity of the solid bulk

$$ds/d\tau = [(\nu+1)^2 F_\nu T_w^3(1 - 7SteT_w/20)^3/12G_\nu]^{1/4}, \tag{23}$$

where for $\nu = 0$

$$G_0 = \begin{cases} (2+3s^2)(1-s^2)^{3/2}/15, & c = 0, \\ \dfrac{-(1-s^2)^{3/2}}{3c} + (\dfrac{1}{c} + \dfrac{1}{c^2})(\sqrt{1-s^2} - \dfrac{\arctan(\sqrt{c(1-s^2)})}{\sqrt{c}}), & c > 0, \\ \dfrac{-(1-s^2)^{3/2}}{3c} + (\dfrac{1}{c} + \dfrac{1}{c^2})(\sqrt{1-s^2} - \dfrac{\operatorname{arth}(\sqrt{-c(1-s^2)})}{\sqrt{-c}}), & c < 0 \end{cases}$$

and for $\nu = 1$

$$G_1 = \begin{cases} (1+2s^2)(1-s^2)^2/12, & c = 0, \\ -\dfrac{(1-s^2)^2}{4c} + \dfrac{(1+c)(1-s^2)}{2c^2} - \dfrac{1+c}{2c^3}\ln(\dfrac{1}{c} + 1 - s^2), & c \neq 0. \end{cases}$$

Equation (23) includes only two dimensionless parameters. Parameter $c = (b/a)^2 - 1$ depends on the aspect ratio b/a of the ellipse and the Stefan number characterizes the effect of the material properties and wall temperature. Since the wall temperature is constant (with regard to time also) and the functions F and G depend only on s and c, we can eliminate the factor at the right-hand side of (23) depending on T_w and Ste by rescaling the time τ

$$\tilde{\tau} = \tau[(\nu+1)^2 T_w^3 (1 - 7SteT_w/20)^3/12]^{1/4}$$

to derive in new variables

$$ds/d\tilde{\tau} = [F_\nu/G_\nu]^{1/4}. \tag{24}$$

Therefore, knowledge of the function $s(\tilde{\tau}, c)$ when b/a is fixed permits us to find the solution of the problem for all quantities of the cross-sectional area of the ellipse, wall temperature and material properties. On the other hand, if s^* and the time of complete melting τ_m^* are found from natural experiments on melting of any particular material in an elliptical capsule of fixed aspect ratio and arbitrary cross-sectional area, then s^* and τ_m^* can be readily obtained for any other material, wall temperature, cross-sectional area and the same elliptical aspect ratio by means of scale transformation.

Let us consider a different situation, when the ellipse cross-sectional area $r^2 = ab$ and the Stefans number are fixed, whereas the aspect ratio is changed. Considering two cases of melting of the same material induced by the same wall temperature inside the capsules with different ellipse aspect ratios, which are denoted by subscripts 1, 2, we have $\tau_{m1}^*/\tau_{m2}^* = (\bar{b}_1/\bar{b}_2)^{1/8}\tau_{m1}/\tau_{m2}$, where τ_m depends only on the aspect ratio of the ellipse. Hence, the ratio of dimensional times required for complete melting is affected only by the values of the aspect ratios and does not depend on the cross-sectional area of the capsule, material properties and wall temperature.

3 Results and Discussion

Among the different phase-change materials used in the thermal energy storage systems, n-octadecane is most frequently used. Physical properties of this material are well documented. Even though numerical computations provided below are for n-octadecane melting conditions, general conclusions can be drawn. In order to estimate the effect of the shape factor on the effectiveness of melting it is reasonable to consider capsules of the same cross-sectional area, which means that the quantity $r^2 = ab$ is fixed. Since the adopted scales depend on a and b, we present results of computations for an elliptic cylinder with $T_w = 1, Ste = 0.1$ and different a and b using the scales obtained above when $a = b = r$, which corresponds to a circular cylinder. Variables in these scales are denoted by bars.

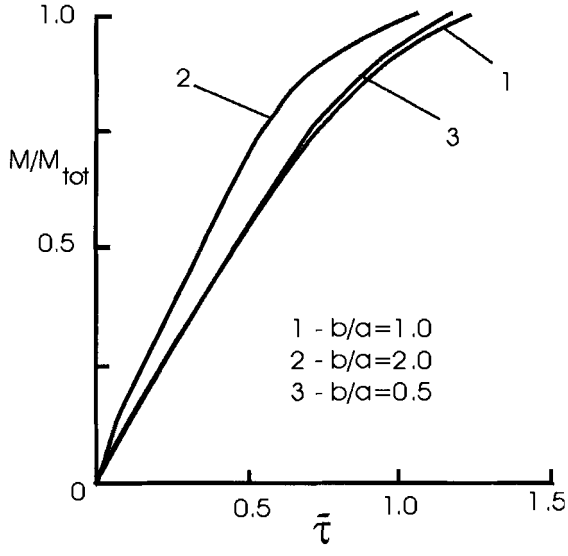

Fig. 2. Time variation of the fraction of the molten mass inside the elliptical capsules of the same cross-sectional area and different aspect ratios

Time variation of the molten mass fraction for the capsules of the same cross-sectional area and different aspect ratios is presented in Fig.2. As can be seen, for circular cylinders ($b/a = 1$) our results completely coincide with those obtained by previous authors. The elliptical capsules show higher rate of melting than the circular ones. Fig.3 shows how the complete time of melting varies with the aspect ratio $(b/a)^n$. For the vertically elongated capsules the exponent $n = 1$ and the aspect-ratio $b/a > 1$, for the horizontally elongated capsules $n = -1$ and, hence, the aspect-ratio $b/a < 1$. The results show that the parameter b/a can be used as a control parameter for the time of melting.

For instance the capsule with a circular cross-section requires longer time of melting since the curve in Fig.3 has the maximum in the point $b/a = 1$. The vertically elongated capsules ($b/a > 1, n = 1$) provide more effective melting than the horizontally elongated ones($b/a < 1, n = -1$), even though they have the same surface and cross-sectional areas. The time required for complete melting can be achieved by the right choice of the shape of the capsule, which is specified by the value of the aspect ratio.

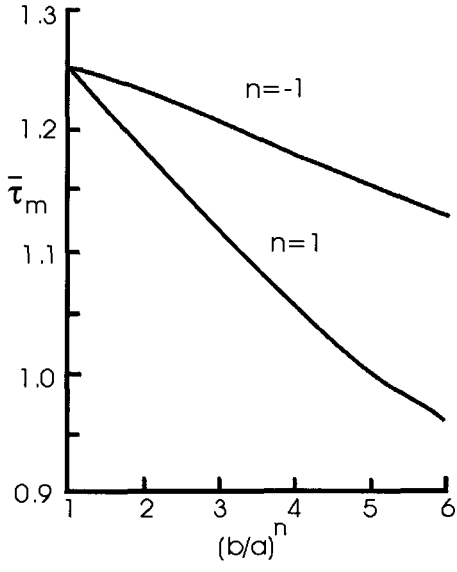

Fig. 3. Variation of the time of complete melting inside the elliptical capsules of the same cross-sectional area *vs* the ellipse aspect ratio

Nomenclature

Spatial characteristics:

l	tangential coordinate $= l^*/a$, as shown in Fig.1;
n	transverse coordinate $= n^*/h^*$, as shown in Fig.1;
x	dimensionless horizontal coordinate $= x^*/a$,
y	dimensionless vertical coordinate $= y^*/b$,
h	non-dimensional molten layer thickness,
$\overline{h}$	projection of h on the y-direction,
$\theta = (n, y)$	the angle, as shown in Fig.1;
a, b	horizontal and vertical semi axes of the ellipse,
c	parameter $= b^2/a^2 - 1$,

s shift of the reference point fixed in the solid core $= s^*/2b$,
$\bar{b}$ capsule aspect ratio $= b/a$ ($\bar{b} > 1$ for vertically elongated and $\bar{b} < 1$ for horizontally elongated capsules),
ε ratio of the molten layer thickness scale to the capsules radius $= h^*/a$,
$\nu = 0, 1$ parameter determining if an elliptical cylinder or an ellipsoid of revolution is considered.

Thermodynamic fields:

u, w dimensionless tangential and transverse velocities,
$\bar{p}$ liquid pressure,
p excess liquid pressure $= (\bar{p}^* - \rho_l g(b - y^*))/p_0$,
q_w transverse heat flux through the wall of the capsule,
$\bar{q}$ constant $= q_w/\cos\theta$,
T non-dimensional liquid temperature,
T_w non-dimensional wall temperature,
T_m^* dimensional melting temperature,
T_{w0} characteristic wall temperature,
τ non-dimensional time,
τ_m time required to complete melting of the solid core,
g gravitational acceleration.

Thermophysical material properties:

Ar Archimedus number $= \rho_l g b^3(\rho_s - \rho_l)/\mu^2$,
c_l liquid specific heat,
L_m melting latent heat,
k_l liquid heat conductivity,
Pr Prandtl number $= c_l\mu/k_l$,
Ste Stefan number $= c_l(T_{w0} - t_m)/L_m$,
μ liquid viscosity,
ρ_l density of the liquid,
ρ_s density of the solid.

Superscripts:

$*$ dimensional quantity.

Subscripts:

l liquid,
m melting,
s solid,
w wall of the capsule,
0 scales.

References

1. Saitoh T., Hirose K. (1982) High Raleigh numbers solutions to problems of latent heat thermal energy storage in a horizontal cylinder capsule. *ASME J. Heat Transfer.* **104**, 545-553
2. Bareiss M., Beer H. (1984) An analytical solution of the heat transfer process during melting of an unfixed solid phase change material inside a horizontal tube. *Int. J. Heat Mass Transfer* **27**, 739-746
3. Moore F., Bayazitoglu Y. (1982) Melting within a spherical enclosure. *ASME J. Heat Transfer* **104**, 19-23
4. Bahrami P. A., Wang T.G. (1987) Analysis of gravity and conduction driven melting in a sphere. *ASME J. Heat Transfer* **109**, 806-809
5. Roy S. K., Sengupta S. (1987) The melting process within spherical enclosure. *ASME J. Heat Transfer* **109**, 460-462
6. Bejan A. (1992) Single correlation for theoretical contact melting results in various geometries. *Int. Commun. Heat Mass Transfer* **19**, 473-483
7. Saitoh T. S. (1998) Latent Heat to be Utilized for the Latent Heat Thermal Energy Storage Capsule. *Japanese Patent* No.2755422

(Received 23 Feb. 1999, accepted 15 June 1999)

Experimental Study on the Critical Heat Flux of Ice Accretion Along a Fine Wire Immersed in a Cold Air Flow with Water Spray

Koji Fumoto[1], Hideaki Yamagishi[1], and Shoichrou Fukusako[2]

[1] Kushiro National College of Technology, Nishi2-32-1,Otanoshike, Kushiro 084-0915, Japan

[2] Hokkaido University, Kita13,Nishi8,Kita-ku, Sapporo 060-8628, Japan

Abstract. An experimental study was carried out on the critical heat flux of ice accretion along a horizontal wire immersed in a cold air stream with water spray. The critical heat flux was defined as the minimum heat flux, which could maintain de-icing along a wire. The air stream velocity and temperature range were from about 3 to 8 ms^{-1} and from -5 to -15 deg. C, respectively, and the average droplet diameter of the water-spray range was from 140 to 640 μm. In order to determine the effect of the wire diameter on the critical heat flux, three diameters, namely, 0.5, 0.8 and 1.0 mm were selected. The critical heat flux was determined from the profile of the variation of the wire temperature with the loading electric power on the wire. It was found for the conditions of the present experiments that the critical heat flux showed a linear increase with an increase in the air stream temperature and velocity. Moreover, the effects of the profile of droplet and wire diameter on the critical heat flux were examined.

1 Introduction

Ice accretion on structures occurs frequently in winter in cold regions, and causes various accidents. Recently, a number of problems concerning both anti-icing and de-icing of structures have been investigated. In order to economically establish practical counter-measures, quantitative study of heat transfer on icing or de-icing on the surface of a structure is needed.

There have been many reports on the characteristics of ice accretion on the surfaces of structures. For example, L.Makkonen [1], G.S.Lock and I.B.Foster [2], P.Personne and J.F.Gayet [3] studied the mass and profile of ice accretion on a cylindrical surface. L.Makkonen [4] analyzed numerically the heat balance along a wire in a cold air stream. P.Personne and J.F.Gayet [3] and N.Seki et al. [5] reported data for anti-icing on a cylindrical surface. E.M.Gates et al. [6] investigated numerically the characteristics of the velocity and temperature of droplets in a cold air stream. The present authors [7] on the other hand proposed a formula based on experiments which is conecerned with the critical heat flux for a single distribution of the droplet diameter and three wire diameters.

In the present study, we examined the adequateness of this experimentally based formula for three cases of the distribution of the droplets. The effect of the diameter of the droplet on the critical heat flux was also investigated.

2 Experimental Apparatus and Procedures

2.1 Experimental apparatus

A diagram of the experimental test facility is shown in Fig. 1. The main components of the experimental apparatus are a wind tunnel, test section, spray-generation system, and associated measurement instruments. The wind tunnel was set up in a refrigeration room (2.8m wide × 1.8m long × 2.2m high), the temperature of which was controlled in the range from 20 to -30 deg. C, by an evaporator and defrosting heater. The air stream in the wind tunnel was generated by suction of a fan. The air stream flowed to the test section through a guide vane and an area of fine grids. Droplets were injected from a water spray nozzle at the end of the contraction section.

A fine platinum wire is horizontally fixed in the test section located 750mm downward from the nozzle. The cross section of the test section was 60 × 60 mm. The test section was made of a transparent plastic plate. Wires of three different diameters (0.5, 0.8 and 1.0mm) were tested. The supply rate of the droplets was adjusted by operating a valve. The air stream and droplet temperatures were measured by thermocouples (d=0.3mm, Cu-C) and the temperature of the water in the nozzle was controlled by a heater.

Fig. 2 shows the measurement circuit of the wire. The circuit consists of a platinum wire, a standard resistor and a constant current power source. The wire has a compensation section at each end. The length of each section is 5mm. It is assumed that the temperature distribution in the direction along the wire is uniform and that the influence of the axial temperature distribution is negligible.

2.2 Experimental procedures

The water spray was injected at a constant flow rate for given values of temperature and velocity of the airflow. A video camera was used to confirm the beginning of refrigeration along the wire. Potentials at both ends of the wire were recorded simultaneously and continuously using a digital multi meter. Measurements were stopped when ice had formed along the whole length of the wire. An electrical current that had sufficient power for anti-icing along the wire was passed through the wire at the beginning of each run, and the power was then gradually and linearly decreased with time. A computer program was used to control the electric power.

Experiments were conducted under the following conditions: range of air temperature, -8 to -20 deg. C; air velocity, 3 to 15 ms^{-1}; mass-flow rate, 5 to 15 $kgm^{-2}h^{-1}$; and diameter of droplets, 140 to 640μm.

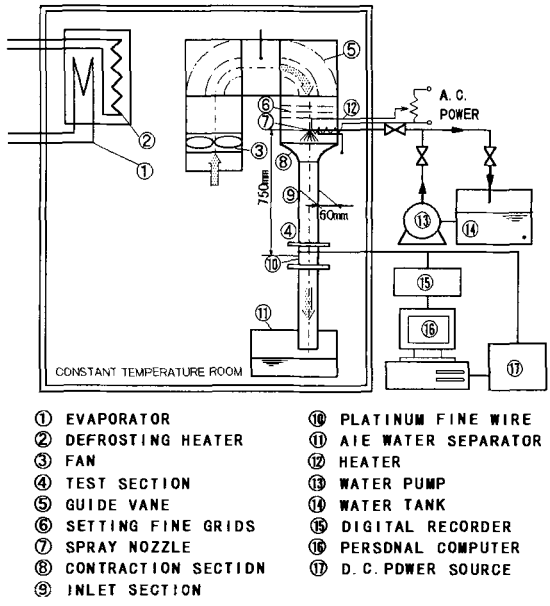

Fig. 1. Schematic diagram of experimental apparatus

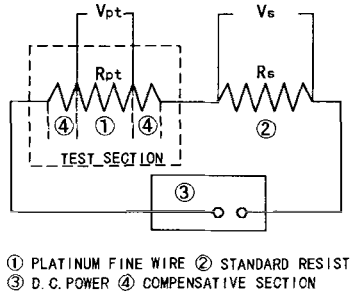

Fig. 2. Electric circuit for the measurements

The accuracies of the measured values were within ±0.05% for the potential at both ends of the wire, ±0.2% for the heat flux along the wire and ±0.3% for the temperature of the wire surface. The accuracy of the temperature difference of the wire surface and airflow was within ±0.3%; the accuracies of the airflow velocity and droplet diameter were not clear.

2.3 Distribution of air flow velocity in the wind tunnel

Fig. 3 shows three profiles of airflow velocity in the test section of the wind tunnel. These profiles were measured using a Pitot tube with an outer diameter of 1.2 mm. Each profile was obtained from data on 90 grid points in the

cross section. Perhaps the entrance effect does not entirely disappear, however every distribution of the velocity is nearly uniform in the test section except for the area near the wall. The influence of the transitional velocity profile on the present problem is not discussed.

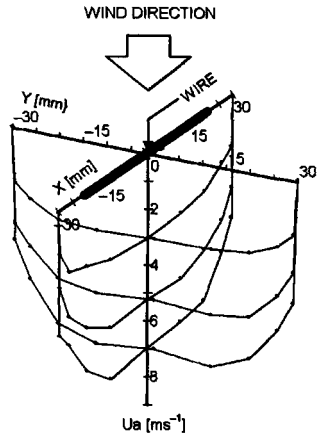

Fig. 3. Velocity profiles of air flow at a horizontal cross section of test section ($U_a = 2.8, 5.2, 6.4 ms^{-1}$)

2.4 Profile of droplet diameter

Three kinds of spray nozzle were used, and the three average droplet diameters were 140, 220 and 640μm. Here, the average diameter is defined at the Sauta mean diameter (see the table of nomenclature). These three average diameters of the droplets were estimated from the distribution shown in Fig. 4. These profiles were obtained by analysis, using an image-processing program, photographs taken of spray that was trapped by an oil pan set at the end of the wind tunnel. The profiles shown in Fig. 4 are based on an analysis of thousand droplets.

2.5 Method for estimating the critical heat flux

The critical heat flux on the surface of the wire can be determined by measuring the variation of the temperature of the wire with the reduction in the electric power supplied to the wire. Fig. 5 shows an example of the transitional wire temperature as a function of the electric power. An electrical current powerful enough for anti-icing along the wire was passed through the wire at the beginning of the run, and then the power was gradually linearly decreased with time. Consequently, the wire and the water layer along the wire were slowly cooled, and the temperature of the water film dropped to below the freezing point. When this process was continued, the water film began to freeze while radiating latent heat along the wire. As a result, the

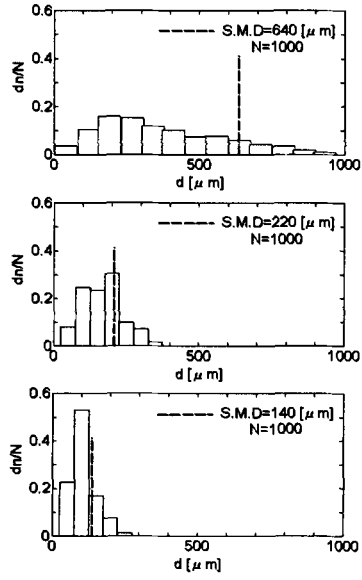

Fig. 4. Profile of droplet diameter

temperature of the wire rose again and reached the freezing point. The heat flux of the wire surface at this moment was easily determined from the electric power, as shown in Fig. 5. This procedure can not be accomplished without electronically monitoring it.

3 Results and Discussion

3.1 Effects of airflow temperature and velocity

Fig. 6 shows that the critical heat flux obtained from these experiments (the average droplet diameter was 140μm) correlates with the airflow temperature. The experimental parameter was the mean velocity of the airflow in the wind tunnel. Although the sample is small, it can be seen that the critical heat flux increased rapidly as the temperature of the airflow decreased and its velocity increased. These results indicate that the airflow temperature and velocity play an important role in determining the critical heat flux. It is obvious that the volume of the electric power supplied to the wire must be increased in order to compensate for increased icing as the super-cooling of the droplets entering the test section is intensified by the reduction of the airflow temperature. On the other hand, the effect of the airflow velocity on the critical heat flux is more difficult to explain, because the velocity of the droplet affects both the super-cooling of the droplets and the heat transfer on the surface of the wire. The results shown in Fig. 6 indicate that, when the velocity of the airflow is increased, the increment of heat radiation by

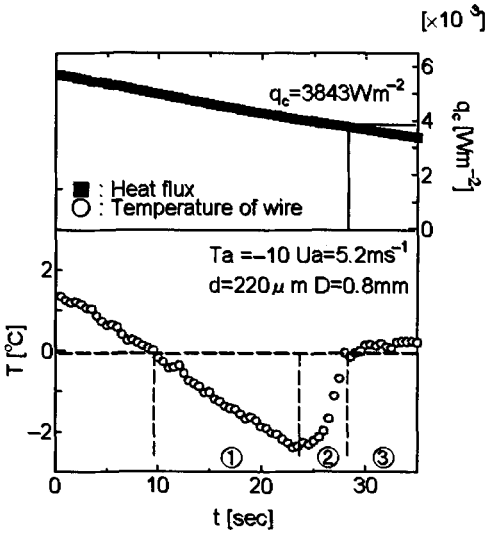

Fig. 5. Method for estimating the critical heat flux

enhancement of the heat transfer along the wire becomes more predominant than the electric power supplied to the wire to be decreased by weakening the super-cooling of the droplet. This weakening of the super-cooling of the droplet is caused by the fact that the time, which the droplet is exposed in the cool airflow becomes short with increment of the airflow velocity.

The data obtained by Horibe et al. [8] are shown in Fig. 6 for comparison. Their data were obtained under the following experimental condition; cylinder diameter = 30mm, airflow velocity = 6ms^{-1}, and average droplet diameter = 200μm. As shows in Fig. 6, the results of their experiments are not inconsistent with the present data.

3.2 Effects of droplet diameter profile and wire diameter

In order to examine the influence of the droplet diameter on the critical heat flux, we performed experiments using droplets of three different average diameters. Fig. 7 shows that the data obtained from these experiments correlate with the velocity of the airflow in the wind tunnel. That the critical heat flux increases with the velocity of the airflow in each case is thought to be caused by the heat transfer coefficient along the wire surface which increases as the airflow velocity increases.

The results shown in Fig. 7 also indicate that the droplet diameter has a remarkable effect on the critical heat flux. A possible reason for this is that the heat capacity of the droplets increases as they increase in size; consequently, large droplets are not as super-cooled by the air stream as are smaller droplets by the time they come in contact with the wire. Therefore, larger droplets

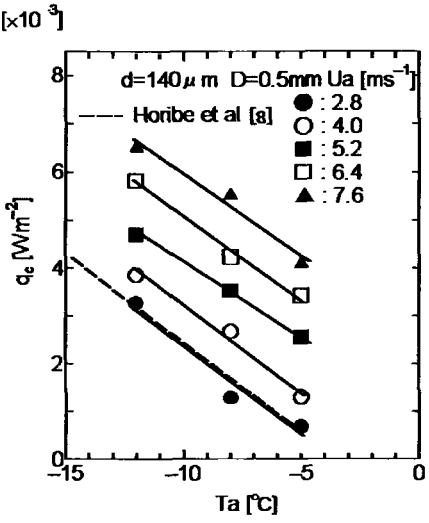

Fig. 6. Effects of airflow temperature and velocity on the critical heat flux

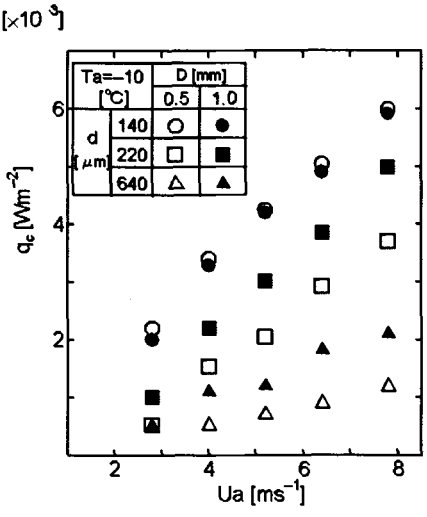

Fig. 7. Effects of the droplet-diameter profile and the wire diameter on the critical heat flux

transfer greater amounts of heat energy to the wire. It is thought, therefore, that the heat input into the wire necessary to compensate for the loss of latent heat through refrigeration is lower when large droplets are used. Further, Fig. 7 also indicates that the effect of the wire diameter on the critical heat flux becomes more significant when the diameter is larger. However, this relation is presently not clearly understood.

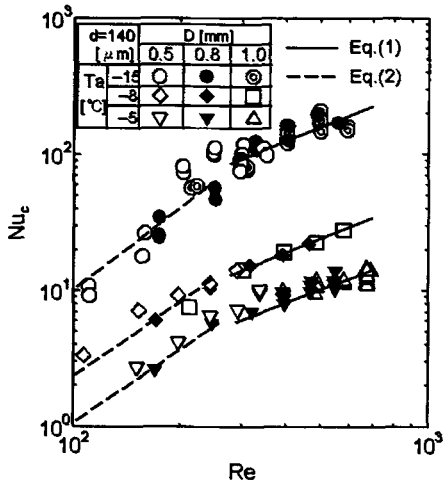

Fig. 8. Reduction by non dimensional parameters for critical heat flux

3.3 Arrangement by non-dimensional parameters

The authors [5] proposed two empirical equations by which the non-dimensional critical heat transfer coefficient, that is, the critical Nusselt number, can be correlated to the Reynolds number by introducing the Stefan number as a mediating parameter. For definitions of these see the table of nomenclature. These experimental formulae are based on the data obtained from experiments in which the average droplet diameter was 140μm. The two empirical equations are

$$Nu_c = 1.34 \times 10^{-4} \cdot e^{-18St} \cdot Re^{1.72}, 100 \leq Re \leq 250\,, \tag{1}$$

$$Nu_c = 4.82 \times 10^{-3} \cdot e^{-22St} \cdot Re^{1.02}, 250 \leq Re \leq 700\,. \tag{2}$$

The values of the constants and exponents in these equations are obtained by the least squares method. These equations and experimental data are shown in Fig. 8. When the average droplet diameter was 140μm, it was found that the diameter of the wire had little influence on the value of the critical Nusselt number. However, as these equations were not determined under wide conditions, this validity must be verified for different situations.

Fig. 9 shows the results obtained by entering the data collected by the above experiments into these two equations. The uppermost lines are plotted using Eqs. (1) and (2). The values derived from these equations vary according to the average droplet diameter. This suggests that the average droplet diameter must be considered for the formulation of the data.

However, the formula expressed as $Nu_c = A \cdot exp(-B \cdot St)Re^n$ appears to be valid. Before this formula can be applied more generally, it is necessary that it is modified so that the constants A includes the average diameter. As

shown in Fig. 9, the slope of the fitted line is nearly the same in every case of the droplet, therefore, the constant B does probably not contain the average diameter of the droplet.

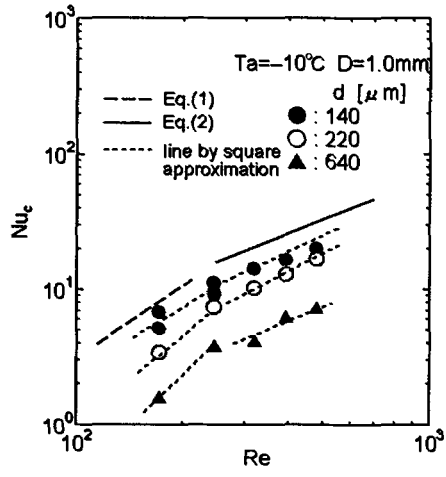

Fig. 9. Reduction by non dimensional parameters for critical heat flux

4 Conclusions

Our investigation of the critical heat flux along a fine platinum wire leads us to the following conclusions:

- The critical heat flux along a fine wire decreases linearly with the temperature of the airflow, and it increases as the average diameter of droplets in the spray increases.
- The effect of wire diameter on the critical heat flux becomes more significant as the droplet diameter is increased.
- The dependence of the critical heat flux on the temperature and velocity of the air stream can be expressed as a non-dimensional relation expressing the Nusselt number as a foundation of the Reynolds and the Stefan numbers.
- A more general formula that includes the distribution of the diameters of the droplets in the spray is needed in order to more accurately estimate critical heat flux.

Acknowledgement: We wish to thank Associate Professor, Masahiko Yamada of the Hokkaido University and Associate Professor, Akihiko Horibe of the Okayama University for important suggestions.

Nomenclature

C_p : specific heat at constant pressure
D : diameter of wire
d : droplet diameter (Sauta mean diameter (S.M.D) = $\Sigma \Delta n d_i^3 / \Sigma \Delta n d_i^2$)
L : latent heat of freezing
N : total number of droplets
n : number of droplets
Nu : Nusselt number ($= q_c \cdot D / [\lambda_a \cdot (T_{pt} - T_a)]$)
q : heat flux
R : resistor
Re : Reynolds number ($= U_a \cdot D / \nu_a$)
St : Stefan number ($= (T_a - T_f) \cdot C_p / L$)
T : temperature
t : time
U : average velocity
V : voltage
λ : thermal conductivity
ν : kinematic viscosity

Subscripts:

a : air flow
c : critical
f : freezing
pt : platinum wire
s : standard resistor

References

1. L.Makkonen (1987),"Salinity and Growth Rate of Ice Formed by Sea Spray", *Cold Reg. Sci. Tech.*, **14**,163-171.
2. G.S.H.Lock, I.B. Foster (1989),"Observations on the Formation of Spongy Ice from Fresh Water", *Proc. 2nd Int. Symp. Cold Reg. Heat Transf. Conf.*,129-133.
3. P.Personne, J.F.Gayet (1988),"Ice accretion on wires and anti-icing included by the Jule effect", *J. Appl. Meteor.*, **27**,101-114.
4. L.Makkonen (1984),"Modeling of ice accretion on wire", *J. Clim. Appl. Meteror.* , **23**,929-939.
5. N.Seki et al.(1982),"Heat Transfer from a Horizontal Circular Cylinder Immersed in a Cold Air Stream with Water Spray", *Trans. JSME*, **48**(428), 749-757. In Japanese
6. E.M.Gates et al. (1987),"Spray evolution in icing wind tunnels", *Cold Regions Sci. Technol.*, **15**, 65-74.
7. K.Fumoto et al.(1997),"Characteristics and Critical Heat Flux of Ice Accretion along a Fine Wire Immersed in a Cold Air Stream with Water Spray (Effects of Temperature and Velocity of Air Stream)", *Trans. JSME*, **63**(615), 171-178. In Japanese
8. A.Horibe et al.(1991),"De-icing Heat Transfer along a Horizontal Cylinder Immersed in a Cold Air Flow with Spraying Seawater", *Trans. JSME*, **57** (544), 4209-4215. In Japanese

(Received 16 Feb. 1999, accepted 1. June 1999)

The Characteristics of Frost Growth on Parallel Plates

Heung Do Han[1] **and Sung Tack Ro**[2]

[1] Kyonggi Institute of Technology, Shihwa Industrial Complex 3-102, Shiheung City, Kyonggi-Do, Korea
[2] Seoul National University, Seoul 151-742, Korea

Abstract. An experimental investigation was undertaken to characterize the effect of environmental conditions on frost growth on a vertical plate in a parallel flow geometry. Humid air was conditioned to have a dew point below $0°C$ and laminar flow prevailed. The test section was fabricated by using three cooling plates with individual insulators to minimize longitudinal conduction. It is known that frost formation on the heat exchanger surfaces seriously affects the performance of the system. The frost is dominantly formed in the inlet region of a heat exchanger. In order to understand the characteristics of frost growth in the entrance region, several experiments were carried out. The experimental parameters were plate temperature, air humidity, air temperature, air Reynolds number, location, and uncooled inlet length. The frosting conditions were limited to air temperatures from 5 to $15°C$, air Reynolds numbers from 1600 to 2270, air humidity ratios from 0.00275 to 0.0037 kg_w/kg_a, and plate temperatures from -10 to $-20°C$. Frost growth toward the front of the plate was thicker and denser than toward the rear. In the low humidity conditions below $0°C$ dew point frost growth increased with decreasing plate temperature and increasing humidity . For laminar flow, the dew point below $0°C$ and non-cyclic frosting period, the frost thickness increased with increasing air temperature. This behavior can be explained by an increase of the transfer rate and a non-cyclic frosting without melting in a sublimation-ablimation process. The average growth thickness at three locations showed little dependence on the Reynolds numbers. However, there were only small differences in the front and rear plates. Frost thickness decreased with increasing uncooled inlet length. This result could be used to suppress frost growth in the plate finned tube heat exchanger.

1 Introduction

When a humid air stream is brought into contact with a cooled surface below the dew and freezing temperatures, frost will form on the surface. As the frost thickens, it decreases the air flow area and acts as a thermal insulator. These are well-known facts in processes where heat is transferred to a refrigerated surface as in air-to-air heat pumps and refrigeration equipment. Frost formation over cold surfaces may impair the thermal performance and eventually lead to serious operational problems in the compressor. In those circumstances, the systems using air-to-air evaporator must also have a defrosting process. To facilitate the design tasks and the selection of the defrost

cycles of such cooling equipment, it is necessary to throughly understand the frost formation process both theoretically and experimentally as well as under realistic operational conditions.

The frost formation process accompanied with simultaneous heat and mass transfer is complex because of the continuous changes of the frost properties and the frost structures, which are also affected by many environmental conditions. Important environmental conditions are air temperature, air humidity ratio, Reynolds number and cooling plate temperature. In spite of more than several decades of research by a large number of researchers, many important characteristics of frost growth can not yet be accurately predicted. As for the effect of the air temperature on frost growth, Trammell [1] remarked that air temperature had a lesser effect on the rate of increase of frost thickness than the other parameters. Brian [2] showed in experiments that the frost thickness decreased with increasing air temperature. However, there was no coincidence of the Reynolds numbers. O'Neal and Tree [3] report data for which there was no difference in height, during the first three hours; at the end of six hours, the difference in frost height was less than 7%. They concluded that air temperature had almost no effect on frost growth for air temperatures in the range from 5 to 12 $^{\circ}C$. Tao [4] numerically calculated that for air temperatures below freezing frost thickness increased with increasing air temperature. They explained the increase of the frost thickness with increasing air temperature by sublimation and ablimation processes. As for the effect of the air velocity on frost growth, many experimental studies were done. Studies pertaining to flat plate geometry are those of Yonko [5], Trammell [1], Biguria [6] and Tokura [7]. Studies on parallel plates include those of Brian [8], Yamakawa [9], O'Neal [3] and Lee [10]. Despite the relatively large number of experimental articles dealing with the effect of the air velocity on frost growth, there exist still gaps and inconsistencies.

The present experimental investigation attempts to understand the influence of environmental conditions on frost growth, especially low humidity and laminar flow. The tested geometries were parallel plates because more than 90% of the heat transfer area is combined to the flat plate finned coil. Also, in order to investigate the entrance effect on the frost growth, the test section was fabricated with three cooling parts with individual insulators. The experimental parameters are: plate temperature, air humidity, air temperature, air Reynolds number, location, and uncooled length of the inlet.

2 Experimental Apparatus

The experiments were performed by using a closed circuit of wind tunnel as shown in Fig. 1. The experimental system was largely composed of three sections: climate chamber, test section and blower chamber. The temperature and the humidity of the air was controlled in the climate chamber. The frost was formed and investigated in the test section. The air stream was forced

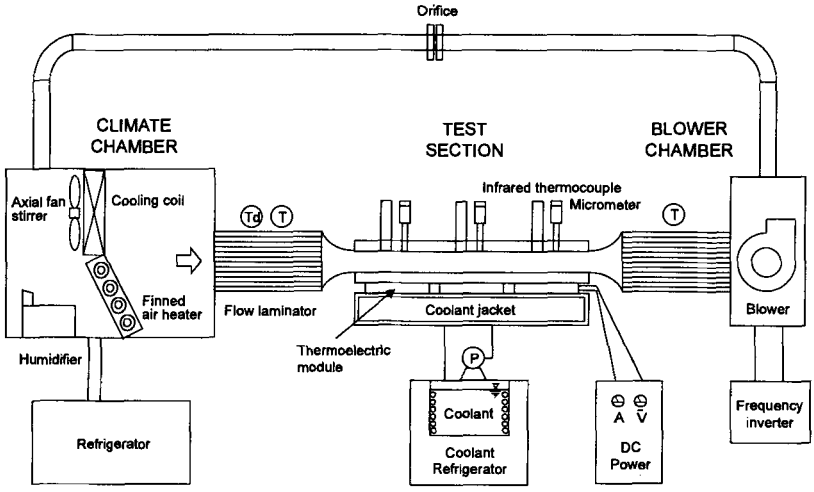

Fig. 1. Experimental apparatus

to circulate and regulated in the blower chamber. The conditioned air from the climate chamber was brought into the test section. Following the test section, the air was drawn into the blower chamber and then returned to the climate chamber through the acrylic pipe. The wind tunnel had a test section 10mm wide by 164mm high and 306mm long. The main component of the test section was a parallel-plate-heat exchanger. One of the heat-exchanger plates was constructed of stainless steel while the other was acrylic plastic. The stainless steel side was composed of three cooling modules as shown in Fig. 2. In the fabrication of the test section, cork insulator with 5mm thickness was

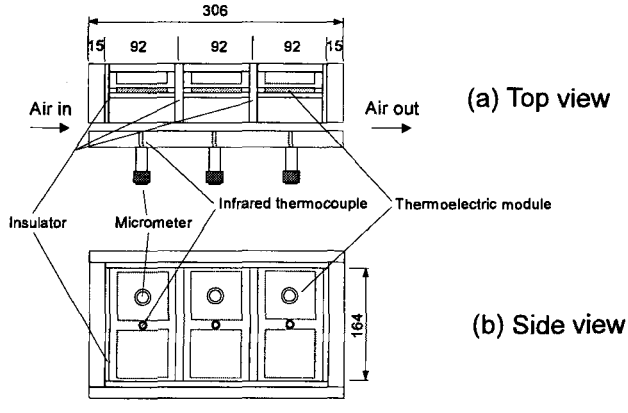

Fig. 2. Test section

used between cooling modules to minimize the longitudinal heat conduction. Each cooling module had a cooling area 82mm wide by 164mm high and was made by using a thermoelectric device to refrigerate the stainless steel side. Its detailed structure is shown in Fig. 3. The thermoelectric device

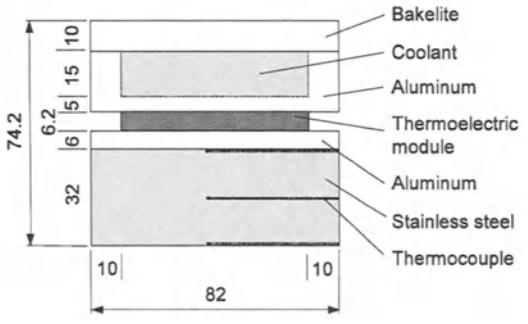

Fig. 3. Cooling module

(MELCOR model CP-2-127-06L) is capable of imposing temperature in the range from -40 to 100°C and deliver up to 120W. A chilled ethylene glycol solution from a refrigerating system cooled the aluminum jacket of the cooling module. The hot side of the thermoelectric device is attached to the surface of the aluminum jacket by using a high thermal conductivity thermal paste. Depending on the voltage of the DC power supply to the thermoelectric device and ethylene glycol solution temperature, the plate can be cooled and maintained at temperatures ranging from -30 to -5°C. A PID controller controls the DC power and can set the plate temperature with an accuracy of 0.5°C. In order to measure the temperature distribution in the stainless steel plate, three holes with 0.8mm diameter perpendicular to the thickness were drilled 41mm deep at the center position of the plate. T type thermocouples with 0.2mm diameter were inserted in each hole.

The frost thickness was measured by a micrometer with a resolution of 0.001mm. A reading was taken when the shaft of the micrometer touched the frost surface. To ensure the accuracy of the measurement, the end of the micrometer shaft was observed visually using an infrared ray with illumination from the bottom side. The criterion for reading was when there was no light between the end of the shaft and the frost surface. The error in the measurement was estimated as 0.1mm. A thickness value was determined by taking the average of three measurements.

Once all environmental conditions reached steady state, each experiment was conducted over 3 hours. The frost thickness was measured every 10 minutes at the front, middle and rear plates. The distances were 61, 153

and 245mm from the leading edge. The other measurements were recorded every 1 minute to the PC by GPIB communication.

3 Results and Discussion

Fig. 4 and Fig. 5 show the variation of the frost thickness with time for the locations along the plates. As seen in the figures, frost growth toward the front plate is much larger than toward the rear. This is attributed to the

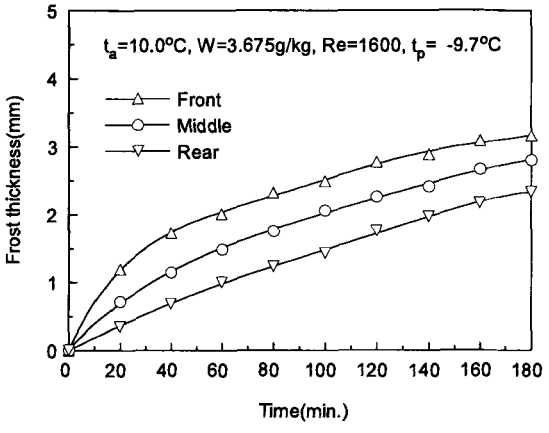

Fig. 4. Variation of frost thickness with time for the locations along the plate

fact that the heat and mass-transfer coefficients are higher toward the front in the developing region. Since the flow will be restricted most where the frost growth is highest, this point is disadvantageous to the plate finned tube heat exchanger. A uniform growth over the cooling surface is needed. This concept is important in the design of plate-finned-tube-heat-exchanger operating under frosted condition. In the entrance region of the parallel plates, the heat and mass-transfer coefficients change rapidly. The length of the plate-finned-tube evaporator to the air stream is short, and the front of the plate may be positioned in the developing region. Therefore, it is necessary to investigate the effect of the flow pattern in the entrance on the frost growth. The flow pattern is changed by inserting insulated flow guide plates ahead of the test plate. Fig. 6 represents the variation of the frost thickness with the dimensionless length of the flow guide, x_0/D_h. x_0 is the length of the flow-guide plate and D_h is the hydraulic diameter based on the parallel plates. An interesting result occurred in determining the effect of the flow guide on the frost growth. Frost growth decreased with increasing length of the flow guide. It should be mentioned that the heat and mass-transfer coefficients decrease by

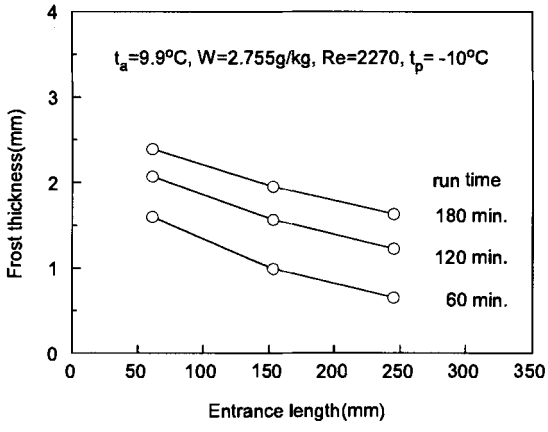

Fig. 5. Variation of frost thickness with the locations along the plate and parameterized for time

the effect of the development of the velocity profile. Its result may be useful in suppressing the frost growth toward the front plate.

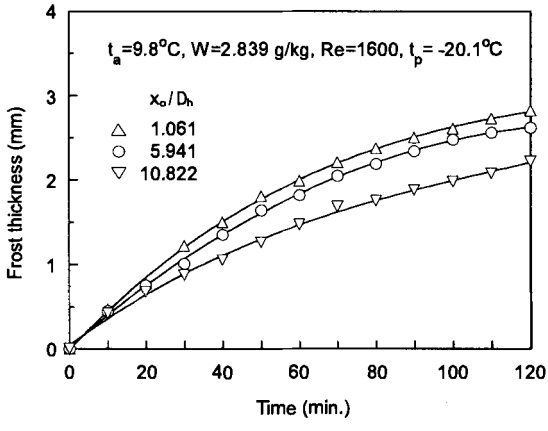

Fig. 6. Variation of frost thickness with time and dimensionless uncooled inlet length, x_0/D_h

Fig. 7 shows the effect of the plate-surface temperature on the frost thickness. The plate-surface temperatures were -20°C and -10°C. The higher growth rates occurred at the lower surface temperature. Similarly to the result displayed in Fig. 4, frost growth in the front of the cooling plate is much larger than in the rear. In Fig. 8, the dependence of the frost thickness on the

humidity is shown. The frost thickness increases with increasing humidity as a result of the increased water content at large humidity.

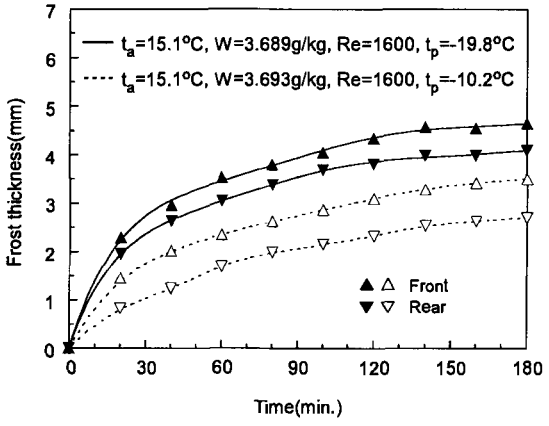

Fig. 7. Variation of frost thickness with time for two different plate temperatures

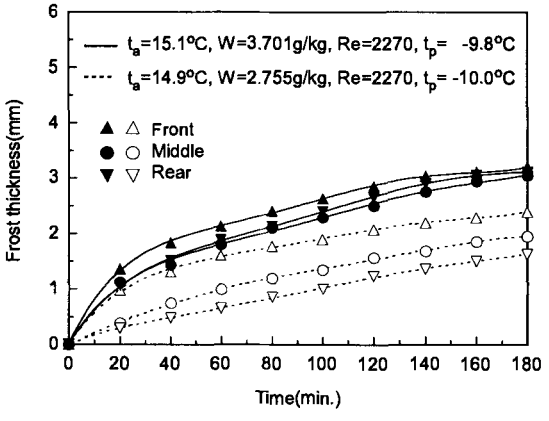

Fig. 8. Variation of frost thickness with time for two different humidity ratios

Fig. 9 indicates the variation of the frost thickness with the Reynolds number. The values of the Reynolds number considered in the present work are limited to laminar flow. The frost thickness is slightly different in the front and the rear, however the average values on the three locations are approximately the same. In the front plate, the frost thickness for the small Reynolds number was thicker than that for the high Reynolds number, by

contrast, this was opposite in the rear plate. As known from previous research, it would appear that with regard to the effect of the air velocity or Reynolds number the frost growth results are not always in agreement. For

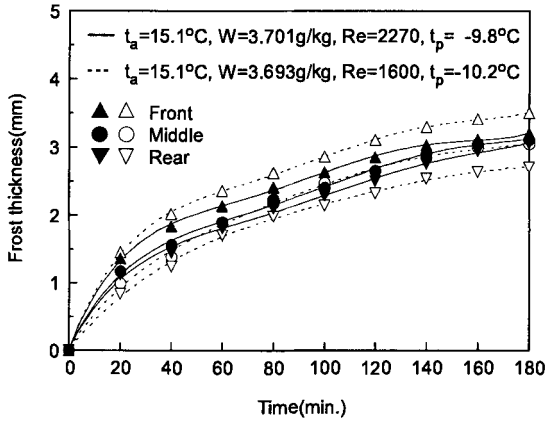

Fig. 9. Variation of frost thickness with time for two different Reynolds numbers

a flat plate, Yonko [5] found that frost growth was increased with increasing air velocity, instead, data taken by Biguria [6] showed that frost growth decreased. Tokura [7] concluded that frost growth was independent of the air velocity. For parallel plates, data taken by Yamakawa [9] and O'Neal and Tree [3] showed increased frost thickness with increasing Reynolds number. However, those of Brian [8] showed a decrease. Surveying the above results, there are many factors affecting the frost growth: transfer coefficients, driving potentials in the heat and mass transfer, melting on the frost surface, frictional drag and location. These factors are complexly coupled with each other. In general, frost thickness tends to increase for increased transfer coefficients and driving potential. Factors for decreasing frost thickness are the melting phenomena and the increased frictional drag on the frost surface. In Fig. 9, the decrease of the frost thickness in the front with increasing Reynolds number may be due to frictional effects on the frost growth. More research is needed on the effects of frictional drag and transfer rate, before definite inferences can be made.

Finally, Fig. 10 shows the effect of the air temperature on the frost growth. The frost thicknesses for an air temperature of $15°C$ are larger than those for an air temperature $10°C$. This is different from results of O'Neal an Tree [3] who showed data for which the frost thickness decreased by 7% with increasing air temperature. Previous investigators explained this result as the melting process with increasing air temperature. However, we experimented with conditions for which the dew point was below freezing. Even though we

do not show the data for the frost-surface temperature in this paper, they were below $0°C$ during the three hours run. Therefore, melting cannot have caused a decrease of thickness. Tao [4] reported simulations according to which the frost thickness increased with increasing air temperature under conditions of the air temperature below freezing. They explained this observation as sublimation and ablimation process, but, they commented that experimental validation was needed. The present result is attributed to the above reason. In conclusion, frost thickness increases with increasing air temperature under which the dew point is below $0°C$.

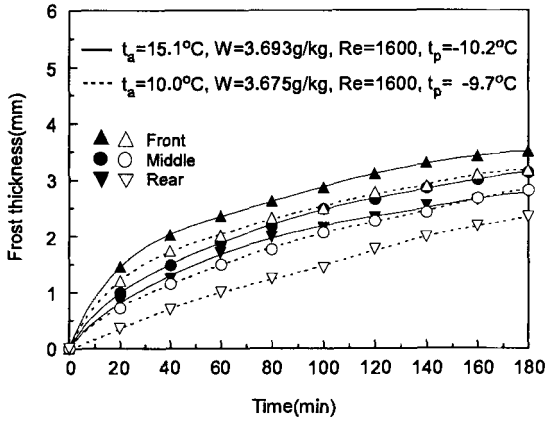

Fig. 10. Variation of frost thickness with time for two different air temperatures

4 Conclusions

We investigated the characteristics of frost growth in the developing region of parallel plates. In particular, the effect of environmental conditions, such as low humidity with dew point below $0°C$ and laminar flow conditions, on the frost growth were experimented. The following results were obtained:

- The location is a important factor on the frost growth in the developing region. The frost thickness is more thick near to the leading edge.
- The frost growth decreases by inserting an inlet flow guide. Therefore, this guide could be used to suppress frost growth on the front side of the evaporator.
- The effect of the air humidity and plate temperature on the frost growth is in agreement with the previous results even under low humidity with dew point below $0°C$.

- By varying the Reynolds number in the laminar region, there were small differences in the front and rear plates. However, the average frost thickness was almost independent of the Reynolds number.
- The frost thickness increases with increasing air temperature when the dew point is below $0°C$. This result supports Tao's simulation and means that the air dew point is an important factor on the frost growth.

Acknowledgement: This work was supported by Turbo and Power Research Center at Seoul National University. We express special thanks to the staff of the Center.

References

1. Trammel, G.J., Little, D.C. and Killgore, E.M. (1968) A study of frost formed on a flat plate held at sub-freezing temperatures. *ASHRAE J.* **10**, 42–47
2. Brian, P.L.T., Reid, R.C. and Shah, Y.T. (1970) Frost deposition on cold surfaces. *I&EC Fundamentals* **9**, No.3, 375–380
3. O'Neal, D.L. and Tree D.R. (1984) Measurement of frost growth and density in a parallel plate geometry. *ASHRAE Trans.* **91**, Pt.2, 278–290
4. Tao, Y.-X, Mao, Y. and Besant, R.W. (1994) Frost growth characteristics on heat exchanger surfaces: measurement and simulation studies. *J. of ASME, HTD-Vol.* **286**, 29–38
5. Yonko, J.D. and Sepsy, C.F. (1967) An investigation of the thermal conductivity of frost while forming on a flat horizontal plate. *ASHRAE Trans.* **73**, Pt.2, 1.1.1–1.1.10
6. Biguria, G. and Wenzel, L.A. (1970) Measurement correlation of water frost thermal conductivity and density. *I&EC Fundamentals* **9**, No.1, 129–138
7. Tokura, I., Saito, M. and Kishinami, K. (1988) Prediction of growth rate and density of frost layer developing under forced convection. *Warme- und Stoffübertragung* **22**, 285–290
8. Brian, P.L.T., Reid, R.C. and Brazinsky, I. (1969) Cryogenic frost properties. *Cryogenic technology* **5**, No.5, 205–212
9. Yamakaya, N., Takahashi, N. and Ohtani, S. (1972) Forced convection heat and mass transfer under frost conditions. *Heat transfer-japanese research* **1**, No.2, 1–10
10. Lee, K.S., Kim, W.S. and Lee, T.H. (1997) A one-dimensional model for frost formation on a cold flat surface, *Int. J. Heat Mass Transfer* **40**, No.18, 4359–4365

(Received 17 Feb. 1999, accepted 06 April 1999)

Effect of Ultrasonic Waves on Freezing of Supercooled Water

Tsutomu Hozumi, Akio Saito, and Seiji Okawa

Department of Mechanical Engineering and Science, Faculty of Engineering, Tokyo Institute of Technology, Tokyo 152, Japan

Abstract. In order to confirm the effect of ultrasonic waves on freezing of supercooled water, various levels of ultrasonic waves were applied to supercooled water. The frequencies of the waves applied were 28 kHz, 40 kHz, 45 kHz, 50 kHz, and 1 MHz. In order to clarify the mechanism of the effect of the ultrasonic waves, several experimental conditions were selected and the results were compared. Each test section was cooled at a constant cooling rate, and the ultrasonic waves were continuously applied to all test sections, varying the frequency and the intensity. It was found that the existence of a free surface touching a metal bar with an addition of ultrasonic waves has an effect on freezing of supercooled water.

1 Introduction

The existence of supercooled states is one of the most frequent problems in the development of ice storage devices. Hence, the study of the mechanism of the supercooling phenomenon is indispensable. There are a few reports which point out the effect of ultrasonic waves on freezing of supercooled water. Smith-Johannsen [1] applied to supercooled water ultrasonic waves whose frequency was 1 MHz. He reported that the ultrasonic wave is effective to maintain the supercooled state. On the other hand, Inada et al. [2, 3] applied ultrasonic waves of 28 kHz and 45 kHz to supercooled water. They said that these waves are effective for freezing supercooled water. Taking such a background into consideration, the investigations of applying ultrasonic waves to ultra pure water under several conditions were carried out. The effect of ultrasonic waves on freezing of supercooled water is discussed.

2 Experiment

In order to confirm the effect of ultrasonic waves to freezing of supercooled water, various levels of ultrasonic waves were applied to supercooled water. The applied frequencies of the waves were 28 kHz, 40 kHz, 45 kHz, 50 kHz, and 1 MHz. In order to clarify the mechanism of the effect of ultrasonic waves, eight experiments, i.e. tests A to H, were selected as shown in Table 1.

They were separated according to the conditions as follows: (i) existence of a free surface or oil-water interface, (ii) volume of water, (iii) purity of water,

Table 1. Test conditions

Test No.	f [kHz]	I [W cm^{-2}]	Volume [cm^3]	Surface	Metal bar	Type
A	28	0.03	0.8	oil	insertion	Vibrating bar
	28	0.10	0.8	oil	insertion	
			0.8	oil	insertion	
B	40	0.04	0.2	oil		Vibrating from
	40	0.12	0.2	oil		underneath
			0.2	oil		
C	45	0.13	1.0	air		Vibrating from
			1.0	air		underneath
D	45	0.13	1.0	oil		Vibrating from
			1.0	oil		underneath
E	45	0.13	1.0	air	insertion	Vibrating from
			1.0	air	insertion	underneath
F	45	0.13	1.0	oil	insertion	Vibrating from
			1.0	oil	insertion	underneath
G	50	0.10	0.8	oil	insertion	Vibrating bar
	50		0.8	oil	insertion	
H	1 MHz	0.06	0.2	oil		Vibrating from
			0.2	oil		underneath

(iv) existence of a dipped metal bar, (v) variation of the frequency and (vi) intensity of the ultrasonic waves. In Table 1, f and I are the frequency and the intensity of the ultrasonic wave, and "Volume" is the volume of the water sample. "Surface" is that material interface which touches the surface of the water sample. "Metal bar" indicates the existence of the dipped metal bar into the water sample, and "Type" shows the kind of ultrasonic vibrator, i.e. vibrating from underneath the sample or vibrating the dipped bar. The samples of tests A to H are arranged into four different ways as shown in Fig. 1.

1. The water surface is exposed to the atmosphere,
2. The water surface is covered with silicone oil,
3. The water surface is exposed to the atmosphere and a stainless bar is dipped into the water,

4. The water surface is covered with silicone oil and a stainless bar is dipped into the water.

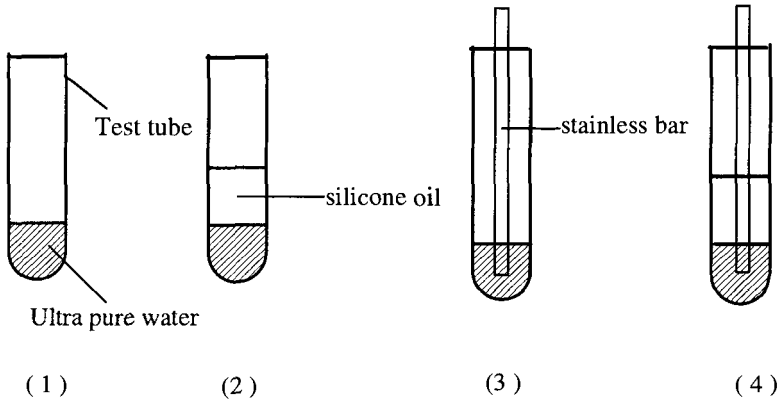

Fig. 1. Samples of tests A to H

The sample vessel is a test tube which is made of polypropylene. The size of this vessel is 12 mm in outer diameter, 11 mm in inner diameter and 120 mm in height. The size of the stainless bar is 4 mm in diameter and 130 mm in length. The tip of this bar is grinded.

The experimental system is depicted in Fig. 2. The ultra pure water which has passed through an ultra filter, an ion exchanger and a distiller, is put into the sample vessel. Impurities larger than 1.0×10^{-9} m were removed, and the specific resistance was kept larger than 18.3 MΩcm. The sample vessel is put in a cooling bath and a constant cooling rate of 0.1 K min^{-1} is applied. The water sample eventually becomes supercooled. When the measured temperature reaches 0^0C, ultrasound is applied to the water sample. The experiment is carried out until the water in the vessel solidifies. The degree of supercooling at freezing is determined by measuring the temperature just before a rapid increment of temperature due to freezing. During the experiment, the process of freezing is recorded by a VTR camera which enables to take 30 photographs per second. Then, the instance of freezing and its location in the water are observed. Each sample vessel is cooled at a constant cooling rate and the ultrasonic wave is continuously applied to each sample vessel. In order to confirm that the results do not depend upon the configuration of the apparatus, many samples are used in the experiment under the same conditions. Likewise, to avoid the influence of preceding experiments, each water sample and vessel was used only once.

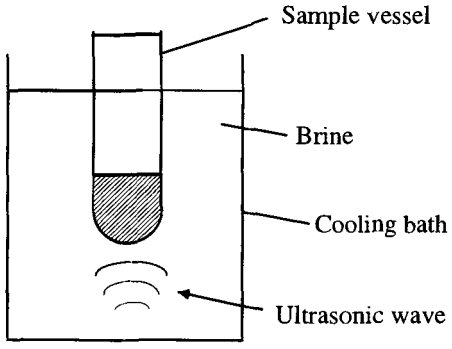

Fig. 2. Outline of the tests

3 Experimental Results

A typical example of temperature measurements is shown in Fig. 3. When the water sample freezes, the measured temperature increases rapidly. The temperature just before solidification is called the temperature of supercooling at freezing, T. The absolute value of T is called the degree of supercooling at freezing, ΔT.

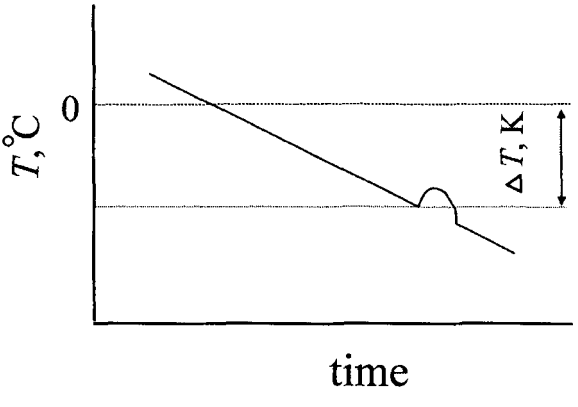

Fig. 3. Relation between temperature and time at supercooling

The average values, ΔT_{ave}, for the tests A to H are compared in Table 2: N is the frequency of distribution for freezing. No cavitation was observed in

Table 2. Test conditions

Test No. No.	Total of N of N	ΔT_{ave}, K [K]	f, kHz [kHz]	I, W/cm^2 [W cm^{-2}]	Surface	Stainless bar
A	40	14.6	28	0.03	oil	insertion
	30	15.2	28	0.10	oil	insertion
	50	14.5			oil	insertion
B	70	17.2	40	0.04	oil	
	31	17.2	40	0.12	oil	
	161	16.9			oil	
C	27	17.1	45	0.13	air	
	27	18.3			air	
D	27	16.0	45	0.13	oil	
	27	17.1			oil	
E	33	8.6	45	0.13	air	insertion
	31	12.4			air	insertion
F	22	15.0	45	0.13	oil	insertion
	31	14.4			oil	insertion
G	31	15.0	50	0.10	oil	insertion
	50	14.5			oil	insertion
H	16	17.0	1 MHz	0.06	oil	
	161	16.9			oil	

any test. It was found that a distinct difference in ΔT_{ave} between the case in which the ultrasonic wave was applied and the case without it appeared only in test E.

Fig. 4 shows the result of test E. The probability P_i is defined as the probability of freezing at temperature T_i when the water is cooled from 0^0C at a constant cooling rate. When the ultrasonic wave was applied, $\Delta T_{ave} = 8.6$ K was obtained, which was distinctly different from the value for the case without ultrasound, i.e., 12.4 K. When the ultrasonic wave was applied, the distribution spread out widely from $\Delta T = 1$ to 22 K. Therefore, although $\Delta T_{ave} = 8.6$ K is rather high, it is found that most samples froze at $\Delta T = 2$ K. A small peak in the distribution was found at $\Delta T = 20$ K, but this occured with only three samples. Hence, if the total frequency of the distribution is considered, ΔT_{ave} should be closer to $\Delta T = 2$ K. On the other hand, freezing

was most frequent in the ΔT = 8 to 12 K range when no ultrasound was applied.

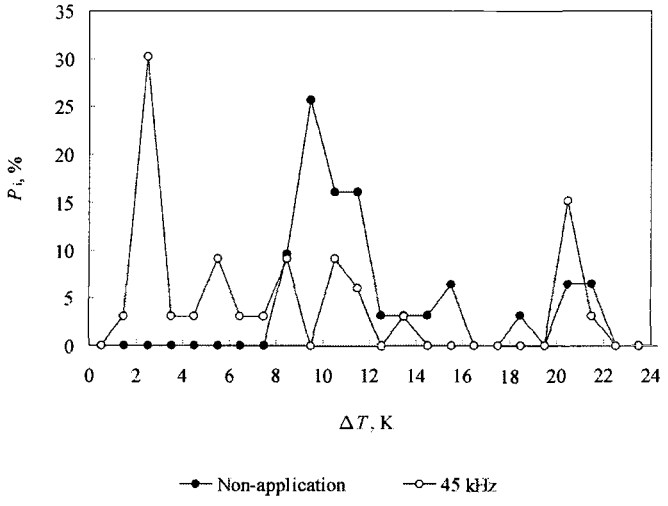

Fig. 4. Relation between P_i and ΔT of test E

The locations of nucleation were observed as follows: It could not be specified in the case of tests B, D and H. These are the groups of samples which have oil-water interfaces and no bar was inserted. It is confirmed that most locations of nucleation in tests A, F and G are at the tip of the dipped stainless bar. The most frequent locations of nucleation in the case of test C are at the free surface. The most frequent locations of nucleation in the case of test E with the application of the ultrasonic wave are at the touching point of the free surface and the dipped stainless bar, and are at the tip of the bar when no ultrasound was applied.

4 Discussion

The effect of ultrasonic waves on freezing of supercooled water can be considered from the experimental point of view as follows:

(1) In the case of the water samples exposed to the atmosphere, the ultrasonic waves had no effect on freezing of supercooled water.
(2) In the case when the water samples were covered with silicone oil, the ultrasonic waves had no effect on freezing of supercooled water, even when the frequency and the intensity of the waves were varied.

(3) In the case when the water samples were exposed to the atmosphere and a metal bar was dipped into the water, the ultrasonic waves were effective to freezing of supercooled water.
(4) In the case when the water samples were covered with silicone oil and a metal bar was dipped into the water, the ultrasonic wave had no effect on the freezing of supercooled water, even when the frequency and the intensity of the waves were varied.

The purpose of condition (2) was to isolate the water sample from the outside and no other factor than the ultrasonic waves should be of influence. From the results of tests B, D and H it was found that the ultrasonic waves have no effect on the freezing of supercooled water. In the case of condition (1), there is possibly some influence, different from that of ultrasound, i.e. existence of a free surface. However, from the results of test C, it was found that the ultrasonic waves have no effect on freezing of supercooled water with only a free surface. In the case of condition (4), there is also a possible influence on freezing other than the ultrasonic waves, i.e. a dipped metal bar into the water sample. From the results of tests A, F and G, it was found that the ultrasonic waves have no effect on freezing of supercooled water with only a dipped metal bar. On the other hand, in the case of condition (3), there are two possible influences on freezing other than the ultrasonic waves, i.e. the existence of a free surface and a dipped metal bar. The results of test E indicate that the existence of a free surface and a dipped metal bar with ultrasonic waves has an effect on freezing of supercooled water. In most cases of test E, the location of the nucleation was observed at the touching point of the free surface and the dipped metal bar.

5 Conclusions

The experiments and considerations reveal that the combination of a free surface touching a metal bar dipped into the water with the addition of ultrasonic waves has an effect on the freezing of supercooled water. On the other hand, if the water surface is covered with another substance or no metal bar is dipped into the water, there is no influence of the ultrasonic waves on the freezing of supercooled water even when the frequency and the intensity were varied.

Acknowledgements: We thank A. Ota, K. Kikuhara, T. Matsui and A. Yoshii for valuable assistance. We are indebted to Research for the Future of the Japan Society for the Promotion of Science.

References

1. Smith-Johannsen, R.(1948) *Science* **108**, 652–654

2. Inada, T., Kamio, N., Yabe, A., Tanaka, M., Kozawa, Y. (1997) *34th National Heat Transfer Symp. of Japan*, 703–704
3. Inada, T., Zhang, X., Yabe, A., Tanaka, M., Kozawa, Y. (1998) *35th National Heat Transfer Symp. of Japan*, 895–896.

(Received 16 Feb. 1999, accepted 16 April 1999)

Numerical Modeling of Dendritic Ice Crystals

Masaaki Ishikawa[1], Patrick H. Oosthuizen[2], and Tetsuo Hirata[1]

[1] Shinshu University, 500 Wakasato, Nagano 380-8553, Japan
[2] Queen's University, Kingston Ontario K7L3N6, Canada

Abstract. It is useful to be able to predict the growth of a mushy region accurately for designing a harvest-type ice storage system. The discussion here is focused on non-isotropic thermal conductivity and the effects of non-equilibrium conditions, which are not considered in conventional models. Because the non-isotropic structure depends on subcooled conditions, it is important to consider these effects on the growth of a mushy region. In this study, some ideas are proposed for considering the non-isotropic conductivity which reflects the inner structure. When the subcooling degree when nucleation starts is given, it is possible to consider the effects of subcooling on growth of a mushy region by applying the Universal Law and Fourier's Law to changing the crystal growth mode.

1 Introduction

Small fragments of ice in chilled water are useful in thermal energy storage techniques because of liquidity. An aqueous solution is a useful material for making ice with liquidity (liquid ice). When the solution whose concentration is lower than its eutectic concentration is cooled, the layer called the "mushy zone" can be observed. This mushy layer consists of small dendrites of pure ice and unsolidified solution. In a harvest-type ice storage system [1], for example, we can get liquid ice by collecting the mushy layer mechanically. In this system, it is important to have available reasonable mathematical models for the prediction of mush generation. In this study, the discussion is focused on non-isotropic thermal conductivity and on the parameters which are needed for making proper numerical models. Then the effects of non-equilibrium are discussed because the non-isotropic structures depend on subcooled conditions. An ethyleneglycol-water solution is assumed in numerical results.

In traditional numerical methods, only an enthalpy balance of each control volume is used to determine the local solid fraction. In most cases [4,7,9], thermal conductivities are also given by the arithmetic average according to the local solid fraction. The assumption of local equilibrium then gives the relation between local temperature and local concentration according to the equilibrium diagram. Thus the local solid fraction can be determined from the diagram. However, such relations are reasonable only when the structure is isotropic. Actually, the structure of a mushy region depends not only on a simple enthalpy balance but also on the surrounding structures and the local conditions.

The two current problems are

- Thermal conductivity and other physical properties depend on the inner structure of a mushy region because of non-isotropicity.
- There is a limit to the assumption of local thermal equilibrium.

2 Non-isotropic Structures

2.1 Universal law

The shapes of each ice crystal plate in subcooled pure water are described by the following equations, these being shown in Fig. 1 [2].

$$\log V = 0.2546(\log \Delta T)^2 + 3.4201 \log \Delta T - 1.3959 \tag{1}$$

$$R_x/d_0 = 425\Delta T^{-0.58} \tag{2}$$

$$R_y/d_0 = 4532\Delta T^{-0.86} \tag{3}$$

$$0.001 \leq \Delta T \leq 0.07$$

These equations are based on the Universal Law [3,5] of ice crystal growth. Some examples are shown in Fig. 2. Even if the supercooling degree is changed, or even if the local subcooling is completely disappeared, the structure is still assumed to keep the characteristic shape. Thus applying these equations to each crystal growth is a reasonable model to start with. When subcooling is small (0.1°C), the shape of ice crystal is round and thick. While subcooling becomes large (2.0°C), crystals become thin. The time scale is also different in each case.

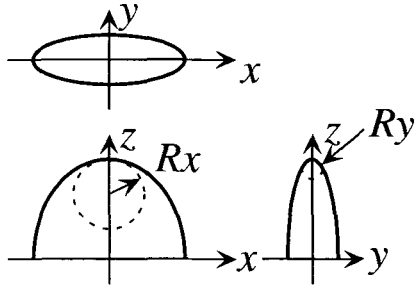

Fig. 1. Tip shape of each crystal

2.2 Conductivity

Consider one single numerical control volume as shown in Fig. 3. Each control volume here is taken to be a cube of 2mm. It is divided into three dimensional subgrids, each of which has sides of 50μm. Positions of primary arms are set

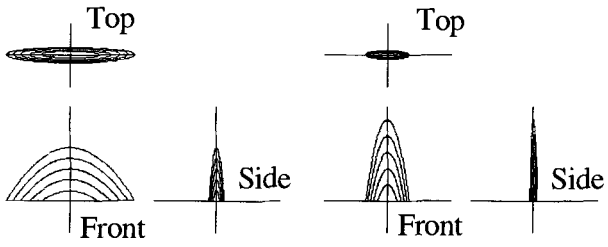

Fig. 2. Shape of each crystal: Left: $T_{sub} = 0.1°C$, $dt = 180sec$, Right: $T_{sub} = 2.0°C$, $dt = 0.3sec$

to have suitable intervals on a bottom plane. The ice crystals grow normal to the bottom surface. Secondary branches are not considered. The shapes of each crystal are expressed by the Universal Law. The positions of starting primary arms are related to the mean distance between them. In this study, the positions and the flat directions are determined by random numbers as is shown in Fig. 4. The minimum distance between those points is chosen as $100\mu m$ and $200\mu m$ respectively. Bianchi et.al. [6] chose the mean distance as $100\mu m$. The inner structure is described as solid-liquid flags in each subgrid. Some structures which are used for calculating non-isotropic conductivity are shown in Fig. 5.

The conductivity for each direction is calculated numerically as shown in Fig. 6. The parallel model means that the solid parts are located parallel to the direction of the heat flux, while the series model means that the solid parts are normal to the heat flux direction. In the case that the minimum distance is $100\mu m$, when the subcooling is 0.1°C, the structure in the z-direction is close to the series model, and the structures in the x and y directions are close to the parallel model. While in the case that the subcooling comes to 2.0°C, the results are opposite, i.e. the structure in the x and y-direction is close to the series model, while that in the z direction is close to the parallel model.

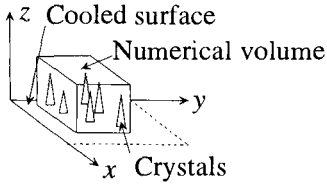

Fig. 3. Overview of a numerical grid

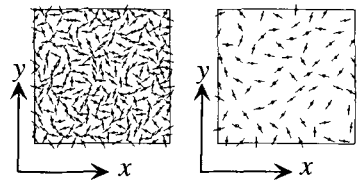

Fig. 4. Initial positions and directions of crystals: Left: $100\mu m$, Right: $200\mu m$

2.3 Other possible parameters

According to the above models, the average conductivity in a control volume depends on the structure of dendritic ice crystals. However, in practical calculations, it is impossible to calculate this type of numerical simulation in each control volume. Then the average conductivity models that reflect this fact are needed as described before. The possible parameters that should be contained in representative values of a control volume are as follows:

- subcooling degree
- local concentration
- dimensions of control volume
- position and distance of each crystal
- directions of primary arms
- effects of secondary branches[6,8]

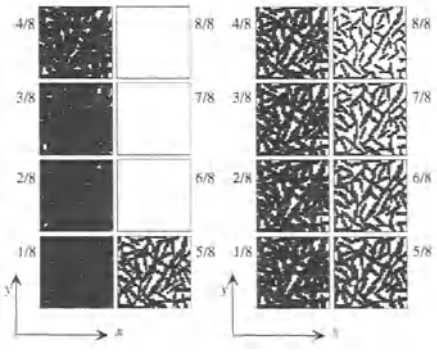

Fig. 5. Inner structure: Black part means solid, Left: $T_{sub} = 0.1°C$, Right: $T_{sub} = 2.0°C$, All planes are normal to z-axis and the distances from the bottom are 1/8, 2/8 ... and 8/8

3 Non-equilibrium Conditions

3.1 Problems

Fig. 7 shows the coordinate system of a sample problem. A mushy region grows from the bottom towards the top. In a traditional enthalpy method, the phase change is based on the local equilibrium condition. The local condition changes along A, B and C in Fig. 8 (left), and the local solid fraction is DC/EC. However, the actual process proceeds along A, B and C in Fig. 8 (right) because subcooling A'B occurs. In this case, the local solid fraction and the local conductivity change along A'B, which affects the growth of a mushy region. In this section, the discussion is focused on how to take the effect of subcooling into account for a macroscopic numerical simulation.

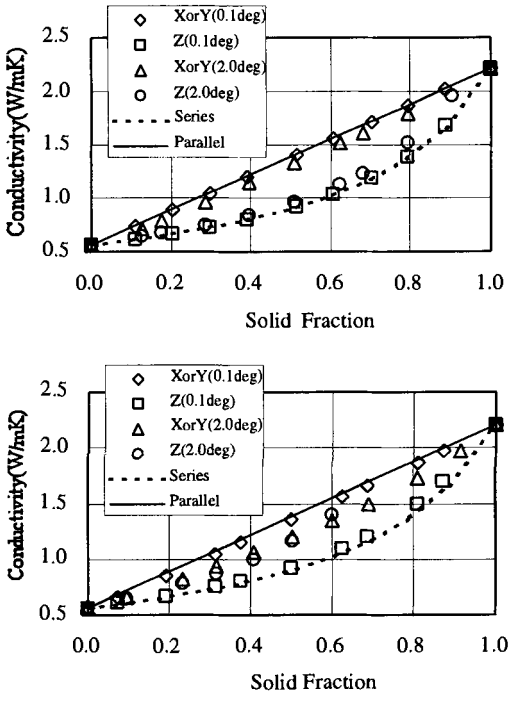

Fig. 6. Conductivity of each direction: Upper: 100μm, Lower: 200μm

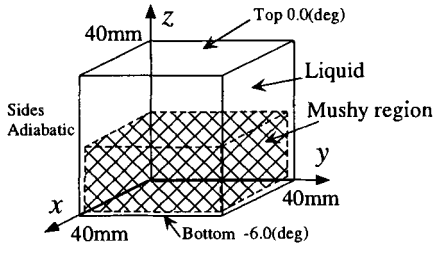

Fig. 7. Coordinate systems of a sample problem

3.2 Basic equations

The structure of each numerical volume is shown in Fig. 9. In an equilibrium model, the temperature in a volume in which phase change is occuring is regarded as uniform and is T_f. However in the process from B to C in Fig. 8 (right), temperatures in the solid and liquid parts are different. Thus by treating the temperature in each phase separately, non-equilibrium conditions can be taken into account. Furthermore in this idea, no special treatment is

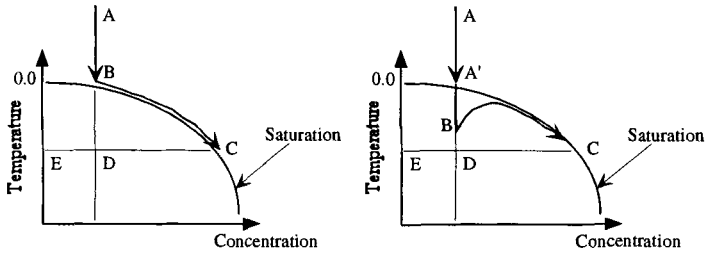

Fig. 8. Equilibrium chart: Left: Equilibrium solidification, Right: Subcooled solidification

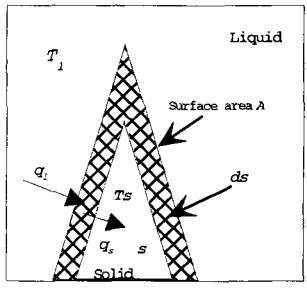

Fig. 9. Control volume

needed for a solid-liquid interface because ds/dt is the only parameter that gives the solid-liquid boundary condition in the basic equations. The total latent heat released is $\rho_s L dv_s$, which is transferred to both the solid and liquid parts. The energy equations for the solid and liquid parts are

$$\frac{\partial \rho_s C p_s T_s}{\partial t} + \frac{\partial}{\partial x_j}(-\lambda_j^s \frac{\partial T_s}{\partial x_j}) = \alpha \rho_s L \frac{ds}{dt} \tag{4}$$

$$\frac{\partial \rho_l C p_l T_l}{\partial t} + \frac{\partial}{\partial x_j}(\rho_l C p_l T_l u_j - \lambda_j^l \frac{\partial T_l}{\partial x_j}) = (1-\alpha)\rho_s L \frac{ds}{dt}. \tag{5}$$

The effects of density change also appear in the mass conservation equation i.e.,

$$\frac{\partial \rho_l u_j}{\partial x_j} = (\rho_s - \rho_l)\frac{ds}{dt}. \tag{6}$$

When solidification takes place, the solute is discharged from the solid part. The concentration in a control volume becomes high during the solidification process. The effect appears as a source term in the concentration transport equation i.e.,

$$\frac{\partial \rho_l C}{\partial t} + \frac{\partial}{\partial x_j}(\rho_l C u_j - D\frac{\partial C}{\partial x_j}) = \frac{\rho_s C}{1-C}\frac{ds}{dt}. \tag{7}$$

The Navier-Stokes equation is

$$\frac{\partial u_j}{\partial t} + \frac{\partial}{\partial x_j}(u_i u_j - \nu \frac{\partial u_i}{\partial x_j}) = -\frac{1}{\rho_l}\frac{\partial p}{\partial x_i} + G_i. \tag{8}$$

A volume integral region for the liquid is $(1-s)V$, which is applied to (5), (6), (7) and (8), while for the solid part the region is sV, which is applied to (4).

3.3 Crystal growth velocity

The most important point is how to determine ds/dt, which appears in (4), (5), (6) and (7). When a liquid part in a control volume is under subcooled condition, crystals grow according to the Universal Law. The tip velocity is given by (1) according to the local subcooling rate. The crystal growth rate is then expressed as a product of the tip velocity and the area of the solid-liquid interface in a control volume. The actual crystal growth rate is then given as

$$\frac{ds}{dt} = v_{tip} A \times C_1. \tag{9}$$

The constant value in (9) needs to be tuned. When subcooling disappears, crystals grow according to the Fourier Law

$$\frac{ds}{dt} = (\lambda_s \frac{T_f - T_s}{\Delta s} - \lambda_l \frac{T_l - T_f}{\Delta l}) \frac{A}{\rho_s L V} \times C_2 \tag{10}$$

$$\Delta s = \frac{sV}{A} \quad , \quad \Delta l = \frac{(1-s)V}{A}.$$

The relation between surface area and solid fraction in a control volume is then needed. For a successful numerical simulation, Fig. 10 should be expressed by a proper function. For example, if it is expressed as a 4th order polynomial function,

$$A = \{2 \log T_{sub} + 0.86\}\{-16(s-0.5)^4 + 1\}. \tag{11}$$

4 Numerical Procedures and Calculations

4.1 Numerical procedures

When a nucleation occurs a subcooling degree is chosen. Then the first mesh begins to solidify. When the first mesh comes to a certain condition, the second mesh begins to solidify. In this study the criteria is expressed in a simple manner because it is difficult to be described. The second mesh is here assumed to start solidifying when the solid fraction of the first mesh is above 30%. If solidification starts in a control volume, the solid growth speed, local solid fraction and surface area can be calculated by (9) - (11). Then the macroscopic field which is given by (4) - (8) is calculated.

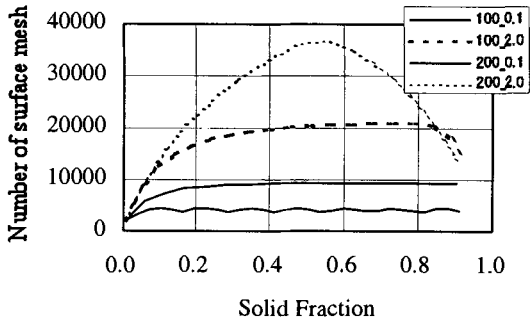

Fig. 10. Surface area in a control volume

4.2 Numerical results

In this calculation, the phase change material is ethyleneglycol aqueous solution of 10wt%. In Fig. 7, the temperatures of the bottom and the top plane are $-6°C$ and $0°C$, respectively. The subcooling degree is $2°C$ and the minimum distance of each crystal is $100\mu m$. Fig. 11 shows the change of total solid volume. Ice crystals grow rapidly within about an hour. Fig. 12 shows the distribution of local solid fraction and local surface area while Fig. 13 shows the distribution of temperature and concentration. Although Fig. 12 shows that the tip of ice crystals reaches 9mm, the concentration is almost uniform between 7mm and 9mm as shown in Fig. 13. Furthermore, there is little temperature difference between the solid and the liquid. The difference is important however small it is because the non-equilibrium term ds/dt is a function of the difference as is described in (9) and (10).

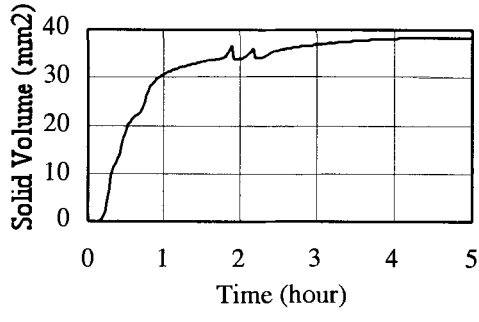

Fig. 11. Solid volume change: $T_{sub} = 2.0°C$

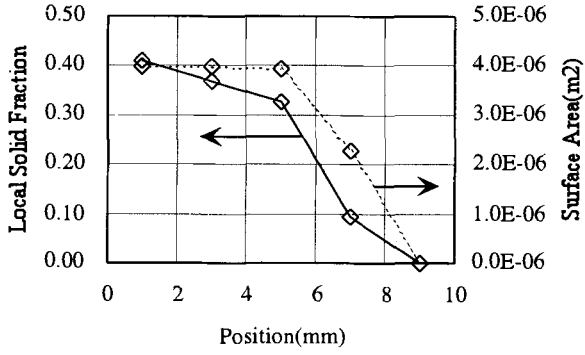

Fig. 12. Local solid fraction and surface area

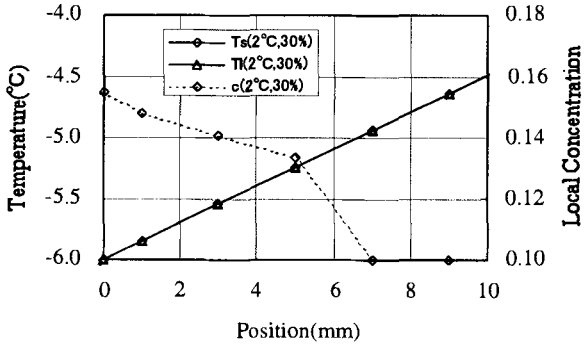

Fig. 13. Local temperature and concentration: Solid lines show the temperature distribution and the broken line shows concentration

5 Conclusions

In this study, the importance of non-isotropic conductivity is discussed. Then a new method of considering the non-equilibrium state is proposed. Some numerical results are also shown. Although the present model is not well tuned in a quantitative manner, it provides a useful method for considering non-isotropic conductivity and non-equilibrium state in macroscopic numerical models.

This work was financially supported by the Japan Society of the Promotion of Science (JSPS-RFTF97P01003).

Nomenclatures

A: surface area (mm^2)
C: concentration
C_1,C_2: constants
Cp: specific heat
dv_s: change of solid volume in a numerical control volume
s: local solid volume fraction in a numerical control volume
ΔT: dimensionless subcooling degree $= CpT_{sub}/L$
L: latent heat
T_{sub}: subcooling degree
V: dimensionless tip velocity $= v_{tip}d_0/2\alpha$, control volume
d_0: capillary length
α: surface tension, energy distribution rate

References

1. Fukusako, S., Yamada, M. (1989) Thermal Conductivity of a Frozen Layer of Ethylene Glycol Solution, *Bulletin of the Faculty of Engineering, Hokkaido University*, **146** (in Japanese)
2. Ramagopal, A., William N. G. (1989) Dendritic Growth of an Elliptical Paraboloid with Forced Convection in the Melt, *Journal of Fluid Mechanics*, **208**, 575–593
3. Gonda, T., Nakahara, S., Seki, T. (1990) The Formation of Side Branches of Dendritic Ice Crystals Growing from Vapor and Solution, *Journal of Crystal Growth*, **99**, 183–187
4. Burns, A. S., Stickler, L. A., Stewart, W. E. Jr. (1992) Solidification of an Aqueous Salt Solution in a Circular Cylinder, *Transactions of the ASME Journal of Heat Trasfer*, **114**, 30–33
5. Furukawa, Y., Shimada, W. (1993) Three dimensional Pattern Formation during Growth of Ice Dendrites (its relation to universal law of dendritic growth), *Journal of Crystal Growth*, **128**, 234–239
6. Bianchi, M., Viskanta, R. (1995) Thermal Conductivity of the Mushy Zone and the Completely Solidified Region During the Solidification of a Binary Alloy, IMECE HTD, *Proceedings of the ASME Heat Transfer Division*, **317**, 2, 323–331
7. Lu, J. W., Chen, F. (1995) Onset of Double-diffusive Convection of Unidirectionally Solidifying Binary Solution with Variable Viscosity, *Journal of Crystal Growth*, **149**, 131–140
8. Billia, B., Jamgotchian, H., Thi, H. N. (1996) Influence of Sample Thickness on Cellular Branches and Cell-dendrite Transition in Directional Solidification of Binary Alloys, *Journal of Crystal Growth*, **167**, 265–276
9. Lu, J. W., and Chen, F. (1996) Stability of Double-Diffusive Convection in a Freckle-free Solidification System, *Journal of Crystal Growth*, **165**, 137–146

(Received 14 Feb. 1999, accepted 1 June 1999)

Measurement of Temperature and Velocity Fields of Freezing Water Using Liquid Crystal Tracers

Tomasz A. Kowalewski

Polish Academy of Sciences, IPPT PAN,
Center of Mechanics and Information Technology,
Swietokrzyska 21, PL 00-049 Warszawa, Poland

Abstract. A new experimental technique based on a computational analysis of the colour and displacement of thermochromic liquid crystal tracers was applied to determine both the temperature and velocity fields of freezing water. The technique combines Digital Particle Image Thermometry and Digital Particle Image Velocimetry. Full 2-D temperature and velocity fields are determined from a pair or a longer sequence, of colour images taken for the selected cross-section of the flow.

1 Introduction

Application of numerical methods for freezing problems necessitates the solution of non-linear partial differential equations of fluid variable properties coupled with moving solid/liquid interfaces. Due to the complexity of the problem, it is not a trivial task to determine precisely an error in the numerical results. The limited accuracy of different numerical methodologies and inevitable simplifications introduced in the models are usually difficult to predict a priori [1]. Hence, the experimental verification of numerical models has special importance for phase change problems. For the same reason, full field measurements of velocity and temperature become crucial for flow problems accompanied by phase changes. With this objective in view, a new experimental technique based on a computational analysis of the colour and displacement of thermochromic liquid crystal tracers (TLCs) was applied to determine both the temperature and velocity fields of the flow. The method combines Digital Particle Image Thermometry and Digital Particle Image Velocimetry. Full 2-D temperature and velocity fields are determined from a pair or a longer sequence of colour images taken for the selected cross-section of the flow.

2 Particle Image Thermometry and Velocimetry

Liquid crystals are highly anisotropic fluids that exist between the boundaries of the solid phase and the conventional isotropic liquid phase. Thermochromic liquid crystals are temperature indicators that modify incident white light.

The displayed colour is proportional to temperature: red at the low temperature margin of the colour-play interval and blue at the high end. The colour change is reversible and is the basis of numerous applications of TLCs in heat transfer studies. Several types of TLC foils or paints are available for the measurement of the surface temperature. The application of TLCs as tracers opens a new possibility of instantaneous full field measurements of temperature and velocity in thermally driven flow. Liquid crystals dispersed into the liquid become small thermometers monitoring the local fluid temperature [2].

For flow visualization the classical "light sheet" technique is used. The collimated source of white light illuminates the selected cross-section of the flow and colour images are acquired in the perpendicular direction. Illuminated TLC-tracers appear on images as clouds of coloured spots conveyed by the fluid. Digital acquisition of the images allows quantitative measurement of both the temperature and displacement of the tracers. The temperature measurements are based on a digital colour analysis of RGB[1] images. The RGB representation of the colour can be transformed to other *trichromic decomposition*. The choice of the colour space is not unique, several standards have been developed, especially for the colour television or printing applications. For evaluating the temperature so called HSI[2] representation of the RGB colour space is the most favourable. The hue (chromaticity) represents the dominant wavelength of the colour and its value which depends directly on the TLCs temperature. The light intensity (or brightness) is defined simply as a sum of its three primary components: $I = \sqrt{(R^2 + G^2 + B^2)/3}$. For the 8-bit representation the maximum intensity is equal 255. Saturation represents colour purity. It can be easily found as a remainder after subtraction of white background from the light intensity: $S = 255 \cdot (1 - min(R, G, B)/I)$. Pure colours have saturation equal to 255. The hue value is calculated as a normalized value of the dominating colour. To make use of the 8-bit signal dynamics and limiting ourselves to the spectral colours, the following formula is used to calculate the hue value:

$$H = \begin{cases} 63 + ((G' - R') \cdot 63)/(G' + R') \text{ for } B' = 0 \\ 189 + ((B' - G') \cdot 63)/(B' + G') \text{ for } R' = 0 \end{cases} \quad (1)$$

where, $R' = R - min(R, G, B)$, similar for G' and B'.

The incoming RGB signals from the video camera are transformed pixel by pixel into hue, saturation and intensity. The red, green and blue colours correspond to the hue values of 0, 126 and 252, respectively. The temperature is determined by relating the hue to a temperature calibration function. Our 8-bit representation of the hue value ensures resolution better than 1%. However, the colour-temperature relationship is strongly non-linear (Fig. 1). Hence, the accuracy of the measured temperature depends on the colour

[1] Red, Green and Blue intensities produced by a video camera

[2] Hue, Saturation and Intensity

(hue) value. The relative error, based on the temperature range defined by the TLCs colour-play limits, varies from 3% to 10%. For the TLCs used (TM from Merck) there results an absolute accuracy of 0.15°C for lower temperatures (red-green colour range) and 0.5°C for higher temperatures (blue colour range). The most sensitive region is the colour transition from red to green which takes place over a temperature variation of less than one degree Celsius. To improve the accuracy of temperature measurements, some experiments were repeated using four different types of TLCs, so that their combined colour-play range covered temperatures from -5°C to 14°C.

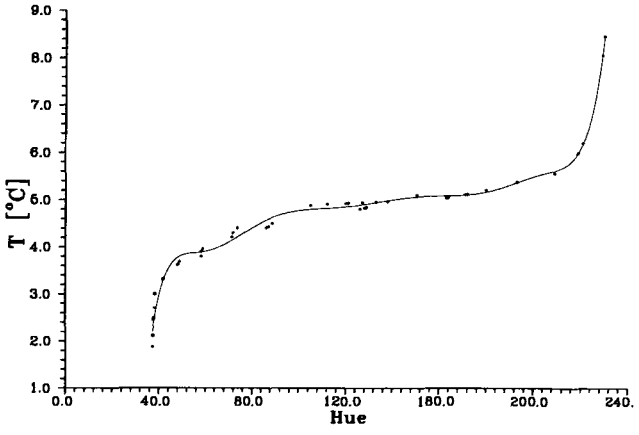

Fig. 1. Temperature vs. Hue for TLCs used. Calibration curve is obtained by 8th order polynomial fitted to the experimental points

The 2-D velocity vector field was measured by Digital Particle Image Velocimetry (DPIV). By this method, the motion of the TLC tracers observed in the plane of the illuminating light sheet, is analysed. To improve contrast and amplify intensity of the particle images a special filtering technique is applied. It is based on a local analysis of the average intensity within small (3x3 pixel) windows. Pixels with intensity well above the average are treated as particles and their intensity is amplified. In such a way bright images of the tracers with preserved intensity variation, well suited for DPIV, are obtained. In the classical DPIV analysis the magnitude and direction of the velocity vectors are determined by using an FFT-based cross-correlation between small sections (interrogation windows) of one pair of images taken at the given time interval. The spatial resolution of the method is limited by the minimum number of tracers present in the interrogation window. Further improvement in the evaluation accuracy allows the recently developed ODP-PIV[3] method of image analysis [3]. Due to an iterative search algorithm used, a dense velocity field is obtained, with displacement value calculated at each

[3] Orthogonal Dynamic Programming - Particle Image Velocimetry

image pixel. The accuracy of the FFT-based DPIV and that of the ODP-PIV method is 0.6 pixels and 0.15 pixels, respectively. This means that for a typical displacement vector of 10 pixels the relative accuracy of the velocity measurement (for a single point) is better than 6%.

3 Problem Formulation and Experimental Procedure

We consider convective flow of freezing water in a simple geometry, a cube shaped cavity of 38mm internal size. One of its walls is held at a temperature of -10°C. As it is below the freezing temperature of the water, hence ice forms there. Two configurations are investigated. In the first, flow develops in the cavity with a horizontal temperature gradient between two opposite isothermal walls (Fig. 2a). One of the isothermal walls has a temperature of 10°C, the other one -10°C. The cavity is surrounded by air at room temperature (25°C). The remaining four walls, made of 6mm thick Plexiglas, are nominally insulators. The thermal conductivity of Plexiglas is three times smaller than that of water. However, it appears that even that small thermal conductivity of the side walls has an apparent effect on the development of fine flow structures and must be considered in numerical simulations.

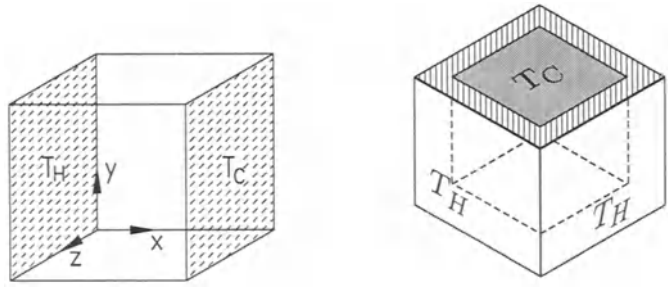

Fig. 2. Differentially heated Plexiglas cavity with the two metal walls kept at temperatures T_H and T_C *(left)*. Lid cooled cavity with the metal lid kept at temperature T_C, and five Plexiglas walls surrounded by external fluid at temperature T_H *(right)*

In the second configuration (Fig. 2b), the top wall of the cavity is isothermal and kept at the low temperature T_c=-10°C. The other five walls are non-adiabatic, made of 8mm thick Plexiglas. The cavity is immersed in an external water bath kept at temperature T_h=20°C. Due to forced convection in the bath it can be assumed that the temperature at the external surfaces of the box is close to the bath temperature. Because of the final conductivity of Plexiglas the temperature field at the inner surfaces of the walls adjusts itself, depending on both the flow inside the box and the heat flux through and along the walls.

The experimental apparatus used consists of a convection box, a halogen tube lamp, a 3-chip colour CCD camera (Sony XC003) and a 32-bit PCI-bus

frame grabber (AM-STD ITI). The flow field is illuminated with a 2mm thick sheet of white light from a specially constructed halogen lamp, and observed in the perpendicular direction. The temperature of the isothermal walls and that of the water in the bath (eventually surrounding the cavity) are controlled by thermostats. The computer controlled system of three stepping motors allows the acquisition of images of several cross-sections, both for horizontal and vertical planes, fully automatically within several seconds. This allows a three-dimensional analysis of the whole flow domain. The computer also controls switching of the halogen lamp and records readings from four control thermocouples and the thermostats. A fine dispersion of raw liquid crystal material was used as tracers. Their mean diameter is about 50μm. To get a general view of the flow pattern, several images recording periodically within a given time have been added in the computer memory.

4 Selected Results

4.1 Differentially heated cavity

The two opposite metal walls of the cube are assumed to be isothermal. Due to temperature gradients existing between the walls the recirculating flow is generated in the cavity. This flow configuration resembles a popular "bench mark" case, natural convection in a cubical cavity with differentially heated end walls. However, the behaviour of natural convection of water in the vicinity of the freezing point creates interesting and also difficult features for numerical modelling of flow structures. It is mainly due to the strongly nonlinear temperature dependence of the density function with the extremum at 4°C. The competing effects of positive and negative buoyancy force result in a flow with two distinct circulations (Figs. 3,4). There is "normal" clockwise circulation, where the water density decreases with temperature (upper-left cavity region) and "abnormal" convection with the opposite density variation and counter-clockwise rotation (lower-right region). At the upper part of the cold wall the two circulations collide with each other, intensifying the heat transfer and effectively decreasing the interface growth. Below, the convective heat transfer from the hot wall is limited by the abnormal circulation, separating it from the freezing front. Hence, the phase front is only initially flat. As time passes it deforms strongly, getting a characteristic "belly" at its lower part. This type of flow structure appeared to be very sensitive to thermal boundary conditions at the side walls. Despite improvements in the numerical model we used, the computational results differ in detail from their experimental counterparts [4]. An eventual source of observed discrepancies could be the supercooling of water, which delays creation of the first ice layer and deforms the flow pattern at the top of the cavity (comp. Fig. 3a). It is well known that pure water may supercool as far as -40°C, before freezing occurs. Seeding of the flow with thermochromic liquid crystals allowed us to visualize that in fact initial water temperature reaches about -7°C before freezing starts.

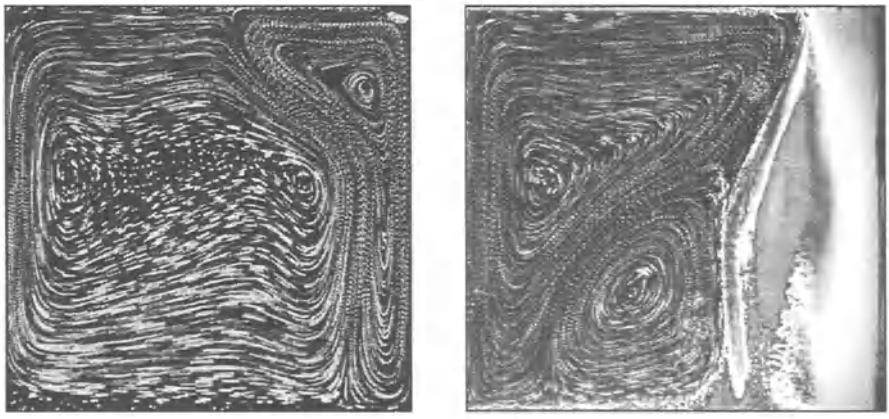

Fig. 3. Flow structure observed for the centre plane (z=0.5) in the differentially heated cavity at 60s *(left)* and 2600s *(right)* after cooling started

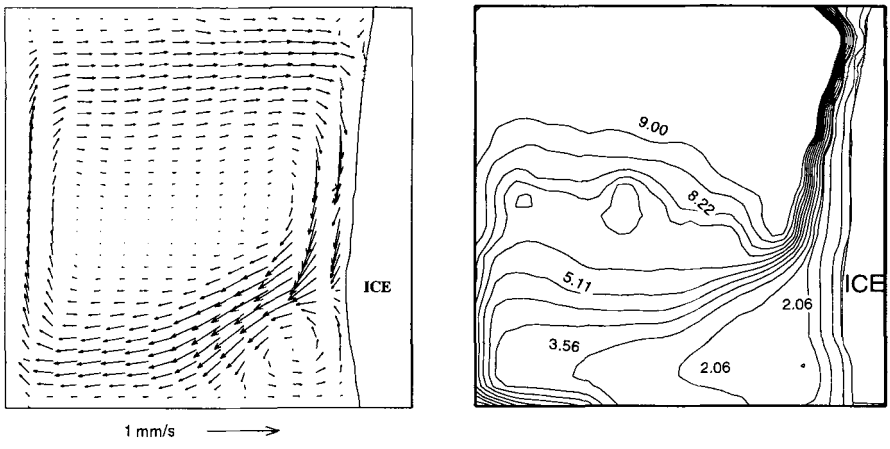

Fig. 4. Velocity *(left)* and temperature isotherms *(right)* field evaluated for water freezing in the differentially heated cube at 500s, T_H=10°C, T_C=-10°C

4.2 Lid cooled cavity

The problem of melt-flow in a lid-cooled cavity has a practical application in a number of manufacturing processes and physical situations. A large scale example is the freezing of water reservoirs, where at night, cooling from above initiates freezing and generates convective flow beneath the ice. On a smaller scale, it has been recognized in crystal growth problems that the flow pattern beneath the solidifying surface is of critical importance to crystal quality. The occurrence of convective flow in the presence of vertical temperature gradients is known to be stable only within a relatively narrow range of Rayleigh numbers. In our experiments on a lid-cooled cavity there was heat

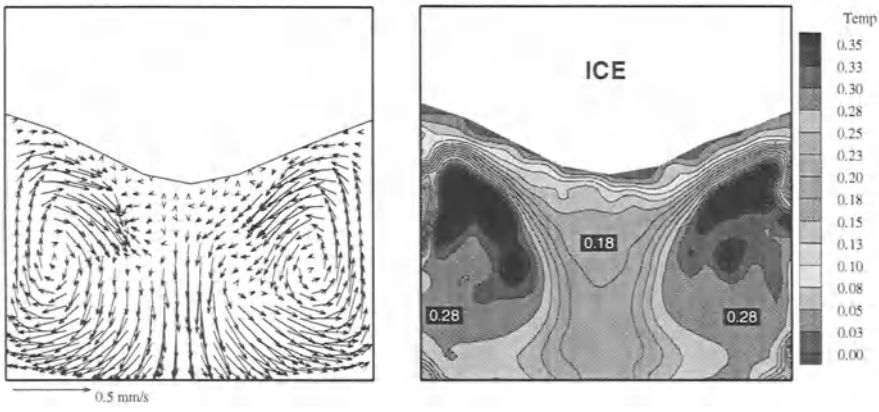

Fig. 5. Velocity *(left)* and non-dimensional temperature *(right)* field evaluated for water freezing in the lid cooled cavity after 5 hours, T_H=20°C, T_C=-10°C

flux into the liquid through the sides and bottom walls. It has been found that these boundary conditions have a stabilising effect on the overall flow, and stable flow structures are possible at $Ra > 10^6$, well above the second critical number for the Rayleigh-Bénard instability. However, various modes of instabilities are observed during the onset of convection. Before a stable final flow structure is achieved, several oscillatory changes in its pattern are observed [5]. The initial flow instabilities, clearly visible in the TLCs visualized temperature field, are also reproduced in the numerical simulations [6]. When a phase change takes place, in our case freezing on a lid surface, strongly non-linear coupling of the flow and interface is responsible for the interface geometry. Despite the fact that freezing starts at a planar surface, the ice surface does not remain planar. Its distortion in turn affects the convection in the whole cavity. A complex interaction between the flow, the moving boundary and the latent heat removed at the solid/liquid interface determines the flow pattern which is established. Fig. 5 shows the temperature and velocity field evaluated for the quasi-steady state, i.e. 5 hours after the experiment was started. The flow visualisation performed in the lid cooled cavity shows the existence of a complex spiralling structure transporting fluid up along the side walls and down in a central cold jet along the cavity axis. A colour play of TLCs seeded flow images taken directly under the lid shows this flow structure in the temperature pattern. Both the particle tracks and temperature distribution measured underneath the lid indicate the existence of eight symmetric cells created by the flow (comp. Fig. 6). This is also manifested in the complex structure of the ice surface. In both the computed and observed ice surface, a star-like grooving reflects eight-fold symmetry of the flow [6]. It was found that heat flux through, as well as along the walls has to be incorporated in the numerical model to obtain observed flow pattern. It was only as a result of the use of both the experimental and numerical methods that the fine structures of the thermal flow were fully understood.

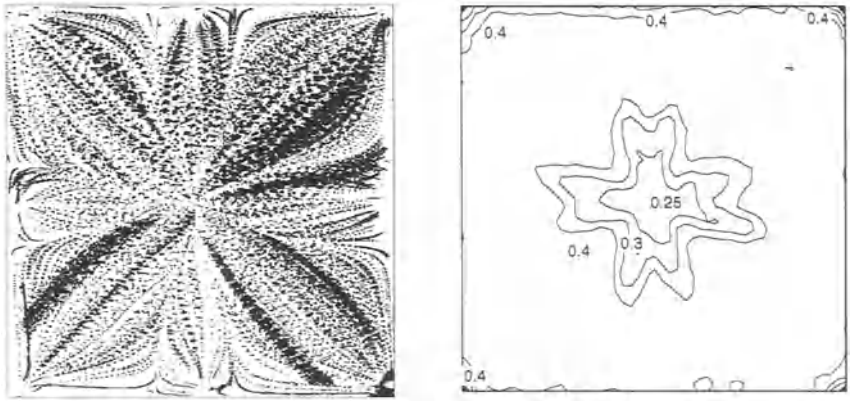

Fig. 6. Flow structure observed for the horizontal plane (y=0.9) beneath the cooled lid; particle tracks *(left)* and non-dimensional temperature isotherms evaluated from the colour of TLC tracers *(right)*

5 Conclusions

The present study has demonstrated the applicability of cholesteric liquid crystals to the quantitative measurements of full field instantaneous temperature distribution in freezing water. The simultaneous measurement of the velocity and temperature fields using TLC tracers, allows a detailed experimental description of the complex flow structures appearing in the convective flow associated with phase change, and their direct comparison with the numerical counterparts. Several discrepancies found between predicted and observed flow indicates the necessity of careful experimental verification of the numerical codes used for simulating phase change problems. It seems that the presented experimental technique offers a valuable tool for the code validation procedure.

References

1. Kowalewski T. A. (1998) Experimental validation of numerical codes in thermally driven flows. *Adv. in Comput. Heat Transfer* CHT-97, 1–15, Begel House Inc., New York.
2. Hiller W., Kowalewski T. A. (1987) Simultaneous measurement of the temperature and velocity fields in thermal convective flows. *Flow Visualization IV*, 617–622, Hemisphere.
3. Quénot G., Pakleza J., Kowalewski T. A. (1998) Particle Image Velocimetry with Optical Flow. *Exp. in Fluids* **25**, 177–189.
4. Kowalewski T. A., Rebow M. (1999) Freezing of water in the differentially heated cubic cavity. *Int. J. of Comp. Fluid Dyn.* **11**, no. 3-4, 193–210.
5. Kowalewski T. A., Cybulski A. (1996) Experimental and numerical investigations of natural convection in freezing water. *Int. Conf. on Heat Transfer with Change of Phase*, Kielce, Mechanics **61**/2, 7–16.
6. Kowalewski T. A., Cybulski A. (1997) Natural convection with phase change (in polish). *IPPT Reports* **8**/97, IPPT PAN, Warszawa.

(Received 14 Feb. 1999, accepted 15 March 1999)

Heat Transfer Enhancement of a Direct Contact Melting Process by Oscillating Motion

Mineo Oka

PANDA Laboratory, 1642-406 Nagae, Hayama, KANAGAWA, 240-0113 Japan

Abstract. Direct contact melting takes place in many natural and technological processes. Important applications of this process are thermal storage systems. In these systems, phase change material (PCM) is stored in a small capsule that is melted by heating peripherally. In this melting process, the melting rate is an important factor for the efficiency of the system. In this paper, we propose to use vibration of the heating wall to enhance the melting rate. The effect of this vibrating motion of the heating wall is studied. Unlike in earlier steady analyses we present here a theoretical study of the non-steady heat transfer of the direct contact. It is made clear that the vibrating motion of the heating wall enhances the heat transfer and melting rate.

1 Introduction

Direct contact melting processes take place in a number of natural and technological processes. Recently, this process was investigated as a basic mechanism of a thermal energy storage system. In this system, Phase Change Material (PCM) is packed in a capsule. In the melting processes, capsules are heated peripherally. Solid PCM is pushed toward the heating wall by its weight. A thin liquid layer is formed between the contact surface of the heating wall and the solid PCM. The melted liquid PCM flows out through this gap. Almost all melting occurs in this thin liquid layer.

Many basic research studies were performed about this process not only experimentally, but also numerically and analytically. They are summarized by Bejan [1]. The melting rate is an important factor for the efficiency of the thermal storage system. Several researches were performed to enhance this melting rate. Oka and Hasegawa [2], and Taghavi [3] suggested utilization of the rotating motion. Saito, et al. proposed to employ heating walls with grooves [4] [5] [6] [7]. In order to enhance the melting rate, it is important to reduce the pressure in the gap and to bring the melting surface close to the heating wall. Oka and Hasegawa advocated for the use of porous material as a heating wall [9] [10] [11].

In this paper, we demonstrate that vibrating motion is an effective the heating wall to enhance the melting rate and heat transfer between the solid and the heating wall. Our study will be a theoretical analysis of this vibrating problem.

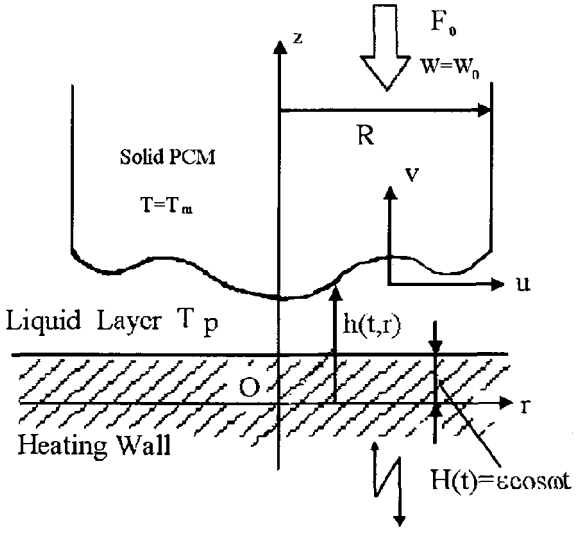

Fig. 1. Geometry and Co-ordinate System

2 Full Governing Equations

To grasp the main purpose of this paper, namely the investigation of the effect of the vibration motion, it is best to use a simple geometry so that analytical methods can be employed. In this paper, a two dimensional flat heating wall is considered (Fig. 1). Cylindrical coordinates, r, z are used. In the course of melting, the whole solid PCM is assumed to be at the melting temperature, T_m.

There are several limiting conditions under which the melting process can be analysed, e. g. (1) external force is given, (2) melting Rate is given, (3) gap height is given. In former researches, case (1) is used, because this condition is closely related to the practical cases. Oka, et al. [8] investigated and compared these three conditions and found that from a mathematical point of view these three cases are essentially the same. In this paper, case (2) is studied to build up the governing equations, because of the simplicity of the reduction. The horizontal heating wall is vertically vibrated with a harmonic excitation of given amplitude and frequency. That is, the heating-wall position is given by $H(t) = \varepsilon \cos \omega t$. When the PCM melts close to the heating wall, a thin liquid layer is formed between the melting surface and the heating wall. Let the position of the melting surface be $h(r,t)$; then the gap thickness is $h(r,t) - H(t)$. The melted liquid flows through this layer with horizonal velocity component, u and vertical one, v. Denote the temperature

of the liquid by T, the wall temperature by T_w which is given and constant. The PCM is pushed to the heating wall by the force F_0. This force is resultant force of weight of the PCM and other external foreces.

The temperature difference between the heating wall and the melting temperature is relatively small. So, all physical quantities such as viscosity and conductivity are assumed to be constant. The governing equations in dimensional form are as follows:

$$\frac{1}{r}(ru)_r + v_z = 0, \tag{1}$$

$$u_t + uu_r + vu_z = -\frac{1}{\rho}p_r + \nu\left(\left\{\frac{1}{r}(ru)_r\right\}_r + u_{zz}\right), \tag{2}$$

$$v_t + uv_r + vv_z = -\frac{1}{\rho}p_z + \nu\left(\frac{1}{r}(rv_r)_r + v_{zz}\right), \tag{3}$$

$$T_t + uT_r + vT_z = \chi\left(\frac{1}{r}(rT_r)_r + T_{zz}\right), \tag{4}$$

$$z = h(r,t): \quad u = 0, \quad v = -W, \quad T = T_m, \quad -\rho c\chi T_z = \rho_s LW, \tag{5}$$

$$z = H(t) = \varepsilon\cos\omega t: \quad u = 0, \quad v = H_t, \quad T = T_w. \tag{6}$$

(1) is the balance of mass, (2) and (3) are the horizontal and vertical component of the balance of linear momentum and (4) is the energy balance, all for an incompressible Navier-Stokes-Fourier fluid in cylindrical co-ordinates. (5) and (6) describe the no-slip and thermal boundary conditions at the moving wall and moving PCM boundary (melting surface), respectively.

3 Non-Dimensionalized Equations

To non-dimensionalize the above equations, typical scales will now be introduced; they define in turn dimensionless quantities which provide information about the significance of the viscous terms arising in the equations describing the problem. Let F_0, h_0, W_0 be scales for the external force, gap thickness and vertical velocity of the fluid at the melting wall. Then

$$St = \frac{h_0 W_0}{\chi} \tag{7}$$

is a measure for the ratio of vertical heat convection (due to melting) to conduction. Furthermore, balancing the horizontal pressure gradient with the corresponding viscous term, we obtain the estimate,

$$\frac{1}{\rho}\frac{F_0}{\pi R^2}\frac{1}{R} = \frac{\nu W_0 R}{h_0}\frac{1}{h_0^2} \quad \Rightarrow \quad F_0 = \frac{\pi\rho\nu W_0 R^4}{h_0^3}, \tag{8}$$

where R is the radius of the cylindrical PCM. If W_0 is given, h_0 and F_0 are,

$$h_0 = \frac{\chi St}{W_0}, \quad F_0 = \frac{\pi\rho\nu R^4}{\chi^3 St^3} W_0^4. \tag{9}$$

On the other hand, there are several time scales in this problem, viz.,

1. time scale of oscillation (non-steadiness): $1/\omega$,
2. time scale of fluid flow: h_0/W_0,
3. heat transfer (Fourier number): h_0^2/χ ,
4. time scale of melting: $(PCMVolume)/\left(\pi W_0 R^2\right)$.

Since the melting rate changes in accordance with the weight of the PCM by melting, the time scale of this change (4.) is small compared with others e.g., the time scale of fluid flow rate (2.) and can be neglected. Using relation (9), the ratio of 3. to 2. is equal to St. The ratio 2. to 1. measures the importance of the non-steady-term to the convection terms in the Navier-Stokes equation, defined here as $\gamma \equiv h_0\omega/W_0$. Then the ratio of 3. to 1. is expressed as γSt, i.e., the ratio of the heat transfer to the non-steadiness. Negligibility of 4. is tantamount to the assumption that the process can be regarded as periodic. Using these parameters, non-dimensionalized governing equations take the following form:

$$\frac{1}{r}(ru)_r + v_z = 0, \tag{10}$$

$$u_{zz} = p_r + \Re\left(u_t + uu_r + vu_z\right) - \alpha^2\left\{\frac{1}{r}(ru)_r\right\}_r, \tag{11}$$

$$p_z = \alpha^2 v_{zz} - \alpha^2\Re\left(v_t + uv_r + vv_z\right) + \alpha^4\left(\frac{1}{r}(rv_r)_r\right), \tag{12}$$

$$T_{zz} = St\left(\gamma T_t + uT_r + vT_z\right) + \alpha^2\frac{1}{r}(rT_r)_r, \tag{13}$$

$$z = h(r,t) : u = 0, v = -W, T = 0, -T_z = W + \gamma h_t, \tag{14}$$

$$z = \varepsilon\cos t : u = 0, v = -\varepsilon\sin t, T = 1, \tag{15}$$

where

$$\alpha := \frac{h_0}{R} \qquad \text{(aspect ratio)} \qquad \sim 10^{-4} - 10^{-3}, \tag{16}$$

$$St := \frac{c\Delta T}{L} \qquad \text{(Stefan number)} \qquad \sim 10^{-3} - 10^{-2}, \tag{17}$$

$$\Re := \frac{h_0 W_0}{\nu} = \frac{St}{Pr} \qquad \text{(Reynolds number)} \qquad \sim 10^{-4} - 10^{-3}, \tag{18}$$

$$\gamma := \frac{h_0 \omega}{W_0} \qquad \text{(Strouhal number)} \qquad \sim 1 - 10, \tag{19}$$

$$\mathrm{Pr} := \frac{\nu}{\chi} \qquad \text{(Prandtl number)} \qquad \sim 10, \tag{20}$$

and all quantities are now dimensionless. With ΔT 1-10 $^\circ C$, R 5-10 cm and the external force 10-100N, which are values used in the experiments by Saito, et al [4] and material parameters, specific heat: c, latent heat: L, heat conductivity: k, viscosity: ν, density: ρ, thermal conductivity: χ, etc., typical values of which are $c = 4k\,\mathrm{Jkg^{-1}K^{-1}}$, $L = 334k\,\mathrm{Jkg^{-1}}$, $k = 0.55\mathrm{Wm^{-1}K^{-1}}$, $\nu = 1.79m\,\mathrm{Pas}$ (water), order of magnitudes of the non-dimensional parameters are as given in (16) - (20). As for water, the Prandtl number is $\mathrm{Pr} \approx 13$ so that the Reynolds number is 10 times smaller than the Stefan number. Terms that include $\Re$ can be neglected, while those involving the Prandtl number may be negligible in many practical cases.

Invoking these assumptions, the approximate governing equations are obtained as follows:

$$\frac{1}{r}(ru)_r + v_z = 0, \tag{21}$$

$$u_{zz} = p_r, \tag{22}$$

$$p_z = 0, \tag{23}$$

$$T_{zz} = St\,(\gamma T_t + uT_r + vT_z)\,, \tag{24}$$

$$z = h(r,t): \quad u = 0, \quad v = -1, \quad T = 0, \quad -T_z = 1 + \gamma h_t, \tag{25}$$

$$z = \varepsilon \cos t: \quad u = 0, \quad v = -\varepsilon\gamma \sin t, \quad T = 1. \tag{26}$$

The force F is obtained by integrating pressure (if inertia should be taken into account, this contribution should be added in the integrand).

$$F = 2\pi \int_0^1 p \cdot r dr \tag{27}$$

4 Similarity Solutions

We can see that the system consisting of (21) - (27) admits a similarity solution of the form

$$u = r\phi_z(z,t), \quad v = -2\phi(z,t), \quad p = 3A(t)\left(1-r^2\right). \tag{28}$$

Substituting this into the governing equations yields the single equation

$$\phi_{zzz}(z,t) = -6A(t); \tag{29}$$

integrating this twice and invoking the boundary conditions, this equation can be solved

$$\phi(z,t) = -\tfrac{1}{2}A\left[(h-z)^2\left\{2(z-\varepsilon\cos t)+h-\varepsilon\cos t\right\}\right]+\tfrac{1}{2}, \tag{30}$$

where

$$A = \frac{1-\varepsilon\gamma\sin t}{(h-\varepsilon\cos t)^3} \tag{31}$$

The gap h being the only remaining unknown quantity is determined by solving the energy equation (24). The force is given by integrating (27), that is

$$F = 6\pi A(t)\int_0^1 \left(1-r^2\right)\cdot r dr = \frac{3}{2}\pi A(t). \tag{32}$$

5 Temperature for the Non-Convective Case ($St = 0$)

As h, in this case, is a function of time only, the boundary conditions for temperature in (25) and (26) are

$$z = h(t): \quad T = 0, \quad T_z = -(1+\gamma h_t), \tag{33}$$

$$z = \varepsilon\cos t: \quad T = 1. \tag{34}$$

When the convection terms in the energy equation (24) can be neglected, this equation reduces to

$$T_{zz} = 0 \tag{35}$$

with the solution

$$T = \frac{h-z}{h-\varepsilon\cos t} \tag{36}$$

satisfying two thermal boundary conditions, (25) and (26). Substituting this into the second boundary condition in (25), we obtain the final equation that determines the gap h; this first order ODE is

$$\gamma h_t = -1 + \frac{1}{h - \varepsilon \cos t}. \tag{37}$$

As a first step to solving it, assume that the amplitude of the vibration, ε is small. Then the gap h can be expanded in a power series of ε,

$$h = 1 + \varepsilon h_1 + \varepsilon^2 h_2 + \cdots \tag{38}$$

(the zeroth order solution is obviously 1). Substituting this into (37), expanding the second term on the right-hand side using Taylor series expansion and equating coefficients of equal powers of ε, we obtain

$$\gamma h_{1t} + h_1 = \cos t, \tag{39}$$

$$\gamma h_{2t} + h_2 = h_1^2 + \cos^2 t - 2h_1 \cos t, \tag{40}$$

$$\gamma h_{3t} + h_3 = 2h_1 h_2 - h_1^3 + \left(-2h_2 + 3h_1^2\right) \cos t - 3h_1 \cos^2 t + \cos^3 t, \tag{41}$$

$$\begin{aligned} \gamma h_{4t} + h_4 = {} & 2h_1 h_3 + h_2^2 - 3h_1^2 h_2 + h_1^4 + 2\left(-h_3 + 3h_1 h_2 - 2h_1^3\right) \cos t \\ & -3\left(-h_2 + 2h_1^2\right) \cos^2 t - 4h_1 \cos^3 t + \cos^4 t, \end{aligned} \tag{42}$$

etc. We are looking for periodic solutions; homogeneous solutions that converge to zero can be omitted. Periodic solutions are as follows:

$$h_1 = \frac{1}{1 + \gamma^2} \left(\cos t + \gamma \sin t\right), \tag{43}$$

$$\begin{aligned} h_2 = {} & \frac{\gamma^2}{2\left(1 + \gamma^2\right)} \\ & - \frac{\gamma^2}{2\left(1 + \gamma^2\right)^2 \left(1 + 4\gamma^2\right)} \times \left[2\gamma\left(2 - \gamma\right) \sin 2t + \left(1 - 5\gamma^2\right) \cos 2t\right], \end{aligned} \tag{44}$$

$$\begin{aligned} h_3 = {} & \frac{\gamma^3}{4\left(1 + \gamma^2\right)^3 \left(1 + 4\gamma^2\right)} \times \left[-2\gamma\left(5 + 2\gamma^2\right) \cos t + \left(3 - 7\gamma^2 - 4\gamma^4\right) \sin t\right] \\ & + \frac{\gamma^3}{4\left(1 + \gamma^2\right)^3 \left(1 + 4\gamma^2\right)\left(1 + 9\gamma^2\right)} \times \\ & \times \left[2\gamma\left(5 - 41\gamma^2 + 26\gamma^4\right) \cos 3t - \left(1 - 40\gamma^2 + 91\gamma^4 - 12\gamma^6\right) \sin 3t\right], \end{aligned} \tag{45}$$

$$h_4 = \frac{\gamma^4\left(3-7\gamma^2-4\gamma^4\right)}{8\left(1+\gamma^2\right)^3\left(1+4\gamma^2\right)} + [\text{terms including } cos2t, \sin 2t, \cdots]. \quad (46)$$

We are interested in the average gap height rather than the periodic motion. It is calculated from the constant terms in (44) and (46) i.e.,

$$\bar{h} = 1 + \frac{\gamma^2}{2\left(1+\gamma^2\right)^2}\varepsilon^2 + \frac{\gamma^4\left(3-7\gamma^2-4\gamma^4\right)}{8\left(1+\gamma^2\right)^3\left(1+4\gamma^2\right)}\varepsilon^4 + \cdots \quad (47)$$

(Odd order terms do not affect the average gap height).

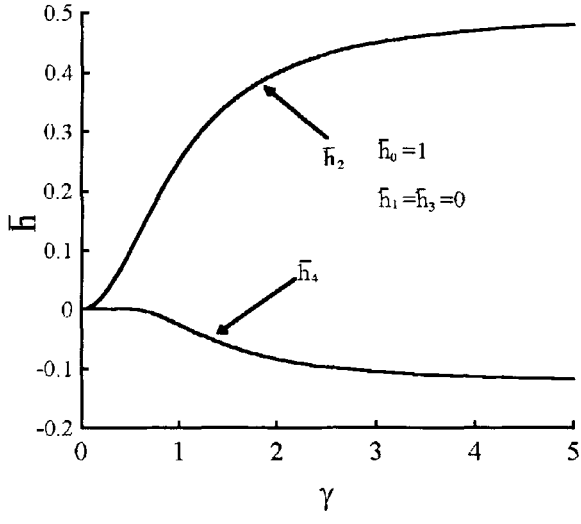

Fig. 2. Solutions of the Avarage Gap Height

Fig. 2 displays how $\bar{h}_2$ and $\bar{h}_4$ arising in (47) vary as functions of the Strouhal number. Evidently, the first correcting term, $\bar{h}_2$ takes positive values. This means that the vibrating motion always enhances the gap height. In this paper, the melting rate is fixed; thus, as the gap height becomes larger, the total force is reduced. However, this result can also be interpreted for the situation when the total force is given and helds fixed: in this case, the vibrating motion should reduce the gap height. On the other hand, the second correcting term, $\bar{h}_4$ takes negative values, thus reducing the gap height again somewhat. This term should be small in comparison to $\bar{h}_2$ in order not to change the sign of the combination and indeed $|\bar{h}_4|$ is smaller than $|\bar{h}_2|$. From Fig. 2 it is seen that this is the case for $\gamma \in (1, 10)$ which corresponds to $1/\omega \approx 10^3 - 10^4$, valid under many practical situations. Fig. 3 displays the gap height as a function of γ for various values of ε. It is seen that the gap height can be increased by approximately 10 % by the vibrating motion of the heating wall.

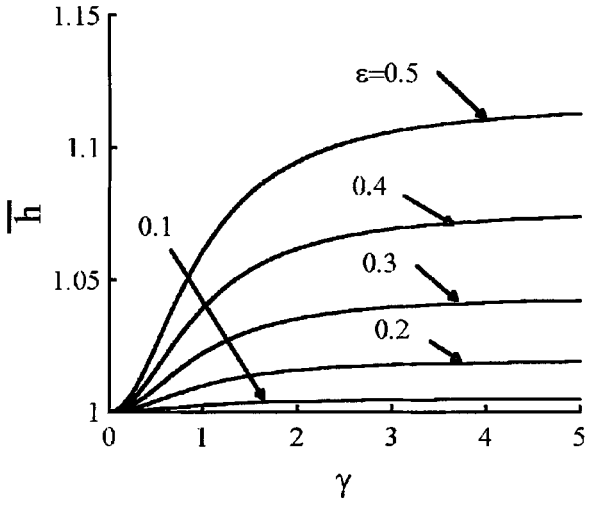

Fig. 3. Avarage Gap Height Change

6 Effect of Convection: Infuence of the Stefan Number

In many practical applications, the Stefan number, St is small so that it can be neglected; however in some cases, it is becoming large. In these cases, convection effects are no longer negligible. Here, we consider the convection effect in the energy equation. If the Stefan number is small compared to unity, the first order perturbation correction can be considered. More specifically, let the temperature be expanded in a power series of the Stefan number as follows,

$$T = T_0 + St \cdot T_1 + \cdots . \tag{48}$$

The zeroth order term, T_0 is given by (36). Letting h be an unknown function, the first order term, T_1 is obtained by solving the equation

$$T_{1zz} = St\,(\gamma T_{0t} + u_0 T_{0r} + v_0 T_{0z})\,, \tag{49}$$

subject to the boundary conditions

$$z = h(t): \quad T_1 = 0, \tag{50}$$

$$z = \varepsilon \cos t: \quad T_1 = 0, \tag{51}$$

in which

$$T_0 = \frac{h - z}{h - \varepsilon \cos t}, \tag{52}$$

$$u_0 = 3A\,(h-z)\,(z-\varepsilon\cos t)\,r, \tag{53}$$

$$v_0 = A\,(h-z)\,(z-\varepsilon\cos t)\,[h-z-(z-\varepsilon\cos t)] - \frac{z-\varepsilon\cos t}{h-\varepsilon\cos t} - \varepsilon\gamma\sin t\frac{h-z}{h-\varepsilon\cos t}. \tag{54}$$

As (52)-(54) are polynomials of z, T_{1zz} is also given by a polynomial of z. Thus it can be integrated in z subject to the boundary conditions (50)-(51). The calculation is straightforward, but the result is too long to print out. On the other hand, the unknown function, h, and its derivative, h_t, are included in the expression of T_1 that are determined by the boundary condition,

$$T_z\,(z=h) = -\,(1+\gamma h_t)\,. \tag{55}$$

To solve this equation, h, h_t and T are expanded in a power series of both ε and St. Here, solutions up to the first order are considered, i.e.,

$$h = h_{00} + \varepsilon h_{01} + \cdots + St\,(h_{10} + \varepsilon h_{11} + \cdots) + \cdots\,. \tag{56}$$

Coresponding to this, T is also expanded in power series of ε and St,

$$T = T_{00} + \varepsilon T_{01} + \cdots + St\,(T_{10} + \varepsilon T_{11} + \cdots) + \cdots\,. \tag{57}$$

$T_{00z}, \cdots, T_{11z}$ are calculated from T_0 and T_1 and the results are as follows:

$$T_{00z} = -1, \tag{58}$$
$$T_{10z} = h_{10} + \tfrac{7}{20}, \tag{59}$$
$$T_{01z} = h_{01} - \cos t, \tag{60}$$
$$T_{11z} = \tfrac{1}{3}h_{01t} - 2h_{01}h_{10} + h_{11} + 2h_{10}\cos t - \tfrac{1}{6}\sin t + \tfrac{3}{20}\gamma\sin t. \tag{61}$$

Substituting these into (55), the equations that determine h are given by

$$h_{00} = 1,$$
$$\gamma h_{10t} + h_{10} = -\tfrac{7}{20} \quad \Rightarrow \quad h_{10} = -\tfrac{7}{20}, \tag{62}$$
$$\gamma h_{01t} + h_{01} = \cos t, \quad \Rightarrow \text{ Solution is (43)}, \tag{63}$$
$$\gamma h_{11t} + h_{11} = \tfrac{1}{3}h_{01t} - 2h_{01}h_{10} + 2h_{10}\cos t - \tfrac{1}{6}\sin t + \tfrac{3}{20}\gamma\sin t. \tag{64}$$

h_{00} and h_{10} are given explicitly and h_{01} and h_{11} are given by ordinary differential equations that are solved successively. Indeed, h_{01} is the same equation as for the case $St = 0$, (39), whose solution is given by (43). Substituting the solutions of h_{01} and h_{10} into (64), the differential equation that determines h_{11} is

$$\gamma h_{11t} + h_{11} = \frac{1}{60}\{42\cos t + (10-9\gamma)\sin t\} + \frac{1}{30\,(1+\gamma^2)}\{-21\,(\cos t + \gamma\sin t) + 10\,(\sin t - \gamma\cos t)\} \tag{65}$$

Its zeroth order solution becomes,

$$h_0 = 1 - \frac{7}{20}St. \tag{66}$$

This means that the gap height h is getting smaller by the convective effect. This effect appears in the non-vibration case since $h_0 \neq 1$. As for the first order solution of ε, $h_{01t} + Sth_{11t}$, the non-homogeneous terms of (63) and (65) are proportional to $\sin t$ and $\cos t$ so that $h_1 = h_{01} + Sth_{11}$ do not effect the average gap height. The effect of convection will appear only in higher order terms.

7 Conclusions

Direct contact melting processes that take place in a capsule for a thermal storage system are investigated theoretically. To enhance the melting rate and heat transfer, a vibrating motion of the heating wall is proposed, The process at a flat heating wall is investigated analytically using the perturbation method. An axi-symmetric cylindrical coordinate system is used, and the equations describing the complicated boundary value problem are non-dimensionalized by introducing problem oriented scales. As a result, small parameters enter the problem, suggesting approximations. When convection is ignored or small and constant melting rate is assumed, analytical perturbation solutions are possible. It is found that by vibrating the heating wall, the average gap height is enlarged. This means that heat transfer is enhanced. It is concluded that the average gap height is reduced, and the melting rate is enlarged when the total force is given. This effect appears in 1000 to 10000Hz frequency band in many practical applications. The gap height is enlarged by 10% by the vibrating motion of the heating wall.

References

1. Bejan, A.(1992) Single Correlation for Theoretical Contact Melting Results in Various Geometries, *Int. Comm. Heat and Mass Transfer*, **19**, p. 473.
2. Oka, M. and Hasegawa (1990) Contact Melting of Rotating Phase-Change Material on a Heated Wall *Trans. JSME*, Vol. B. **56-524**, p. 1131, (Japanese).
3. Taghavi, K., (1990) Analysis of Direct-Contact Melting under Rotation *ASME, Jour. Heat Transfer*, **112**, p. 137.
4. Saito, A., et al. (1991-3) Heat Transfer Enhancement in Direct Contact Melting Process, *Trans. 68th JSME Annual Meeting*, Vol. B, p. 242 (Japanese).
5. Saito, A., et al. (1991-5) Analytical Study on Heat transfer Enhancement in Direct Contact Melting Process, *Trans. the 28th Japan Heat Transfer Symposium*, p. 29 (Japanese).
6. Saito, A., et al. (1991-7) Heat transfer Enhancement in Direct Contact Melting Process, *Trans. Japanese Assoc. of Refrigeration*, **8-2**, p. 141 (Japanese).
7. Saito, A., et al. (1991-9) Heat Transfer Enhancement in Direct Contact Melting Process, *Trans. JSME B*, Vol. 57, p. 3141 (Japanese).

8. Oka, M. and Hasegawa (1989) On the Steady Melting of a Phase-Change Material Placed on a hot Wall, *Trans. JSME B* Vol. 55, **55**, p. 1653, (Japanese).
9. Oka, M. and Hasegawa (1995) Direct Contact Melting Process on a Porous Heating Wall, *IMECE HTD*, **321**, p. 733.
10. Oka, M. and Hasegawa (1996-5) Direct Contact Melting Process on a Curved wall Coated with a Porous layer, *5th Int. Sym. Thermal Eng. and Sc. for Cold Regions*, p. 207.
11. Oka, M. and Hasegawa (1996-8) Contact Melting Process on an Arbitrary shape wall Coated by Porous layer, *31st IECEC*, p. 2084.
12. Moallemi, M. K. et al.(1986) An Experimental and Analytical Study of Close Contact Melting, *trans. ASME, Jour. Heat Transfer*, **108**, p. 894.

(Received 12 April 1999, accepted 25 May 1999)

Permeability of an Aqueous Solution in a State of Partial Solidification

Masashi Okada[1], Chaedong Kang[1], and Haruhiko Okiyama[2]

[1] Aoyama Gakuin University, 6-16-1, Chitosedai, Setagaya-ku, Tokyo, 157-8572 JAPAN
[2] Isuzu Motors Limited, 8 Tsuchidana, Fujisawa-si, JAPAN

Abstract. A mushy zone was formed by solidifying a NaCl aqueous solution in a rectangular tube. The permeability was measured under various volume fractions of the liquid in the mushy zone and the dendritic ice in the solidification process was observed with a CCD microscope. The following results were obtained: The permeability increases with the volume fraction of the liquid phase; it decreases by increasing the supercooling degree of the solution or increasing the initial concentration of the solution, and is constant after the mushy zone was formed. The arm space of the dendrites becomes narrower as the supercooling degree of the solution increases. A relation between the permeability and the arm space of the dendrites was obtained.

1 Introduction

Solidification phenomena of aqueous solutions are found e.g. in thermal ice storage systems [1] or in dilution treatments of waste solutions by freeze [2]. To clarify the phenomenon is an important subject in order to operate the systems with higher performance. This phenomenon is different from the behavior of a single component, as it represents a complicated double diffusive convection problem that is governed by concentration differences caused by freezing and temperature differences by cooling. The phenomenon is further complicated because a mushy zone arises that is mixed with a solid phase of a three-dimensional dendrite and a liquid phase. Permeability is one of the main characteristics governing the flow mechanisms in the mushy zones [3]. It is necessary to measure it in order to understand the solidification phenomenon. Up to today, the permeability of a mushy zone was not adequately measured. Murakami et al. obtained experimentally the permeability of a cylindrical dendritic structure using borneol-paraffin [4]. This study clarified the fact that the permeability depended on the flow direction relative to the dendritic arm structure, and they deduced a relation among the permeability, the dendritic arm space and the volume fraction of the liquid phase. Streat and Weinberg showed a relation between the permeability of a Pb-20% Sn alloy and the first dendritic arm [5]. The permeability in the mushy zone is determined by the geometry of the flow path, which changes by the freezing process of the aqueous solution. Kunimine and others [6] experimented with

the solidification of a sodium chloride aqueous solution. Yoshioka et al. [7] used a succinonitryl-acetone solution and clarified that (i) the cooling velocity after solidification affects the dendritic arm growth, and (ii) the appearance of a secondary arm is influenced by the velocity of the crystal growth and the initial concentration. However, the effect on the permeability of several conditions such as initial concentration, supercooling degree, cooling time after the formation of the mushy zone and the dendritic shape was not found.

In this study, the permeability of the mushy zone was measured. In order to form it, the sodium chloride aqueous solution was filled into a horizontal tube and solidified by cooling. Through measurement, the effects on the permeability of parameters such as the liquid-phase-volume fraction, initial concentration, supercooling degree and cooling time were clarified. A transient measuring method to determine the permeability was used; it was designed by the authors [8]. Furthermore, the shape of the dendrite was observed with a microscope, and a relation between the permeability and the arm space of the dendrites was obtained.

2 Method of Measurement

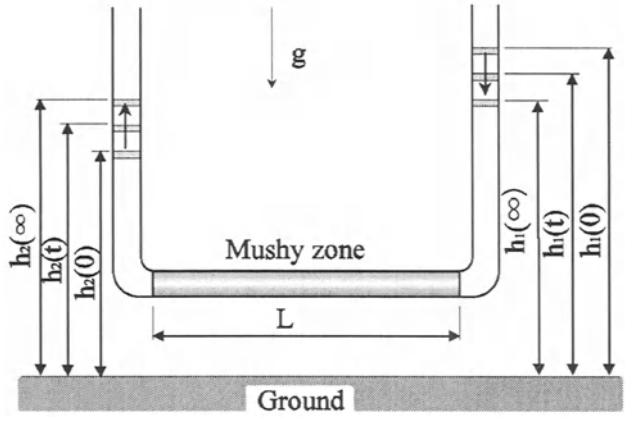

Fig.1. Principle of transient measurement method

Fig.1 shows the transient measuring method for permeability. A mushy zone is formed at a horizontal tube region (length of L) of an U-shaped tube. Then, an aqueous solution is poured into the tube, an initial potential head difference of $(h_1(0) - h_2(0))$ is made by closing the end of the tube, and finally the end is instantaneously opened. Because in the limit of Darcy's law the flow velocity in the tube is proportional to the pressure gradient, the equations

$$v = -\frac{k}{\mu}\frac{\partial P}{\partial x} = \frac{k}{\mu}\frac{\rho g}{L}\{h_1(t) - h_2(t)\}, \tag{1}$$

$$v = -\frac{dh_1(t)}{dt} = \frac{dh_2(t)}{dt} \tag{2}$$

are valid for a constant cross sectional area of tube. Also, we assumed that the pressure drop only happens within the mushy zone of length L, since inertia force and pressure loss by wall friction and elbow are negligible. The solution of (1) and (2) is,

$$\ln \frac{h_1(t) - h_1(\infty)}{h_1(0) - h_1(\infty)} = -2Kt, \tag{3}$$

$$K = \frac{k}{\mu} \frac{\rho g}{L}, \tag{4}$$

where $h_1(\infty)$ is the height of the potential head when the head difference $h_1(\infty) - h_2(\infty)$ is practically zero. By measuring the height of the potential head $h_1(t)$ with time t, the line slope K, using a least square approximation, is obtained from equation (3); finally, the permeability k is obtained from equation (4).

3 Experiments

Permeability was measured by using the experimental apparatus of Fig.2. The cooling part is a rectangle of dimension $20 \times 8 \times 200mm^3$ as shown in Fig.3. The material of tubes A and B is polycarbonate. In tube A, for the purpose of forming the mushy zone from the cooling surface, two parallel copper plates were cooled by brine. A smooth fitting was given at the connection from the circular to the rectangular tube so that the flow resistance due to tube geometry should not affect the measurement of the permeability.

In the solidification process, as the dendrites are formed at the inside wall in tube A, the concentration of the solution increases with the separation of the solute. The temperature and concentration of the solution flowing in tube A should be equal to the corresponding values in the mushy zone to be measured. In the experiment, at first, the aqueous solution in tube A was cooled until it reached a fixed supercooling degree and then solidified to overgrown dendritic mushy zone. After that, the solution was kept at a temperature where a fixed liquid phase volume fraction (χ) was obtained. The temperature was obtained from the phase diagram. The temperature in tube A fixes the concentration of the solution. An aqueous solution with equal temperature and concentration as in tube A prepared in tube B, is now let to flow into tube A. With this arrangement, ice which has been formed in tube A neither melts nor grows, and the permeability is measurable. The experimental parts A, B and the cooling part of the tube were covered with an insulator. For two initial concentrations of 3 $wt\%$ and $5wt\%$ of aqueous solution, the permeability was measured with a liquid-phase-volume fraction of 0.3, 0.4, 0.5 and 0.6. The supercooling degree was from 0 to 5 deg.C.

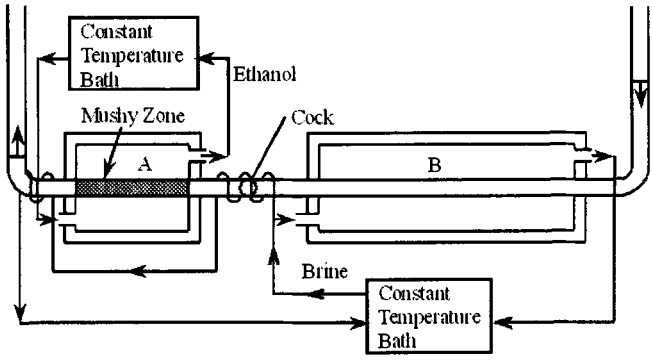

Fig.2. Schematic diagram of experimental apparatus

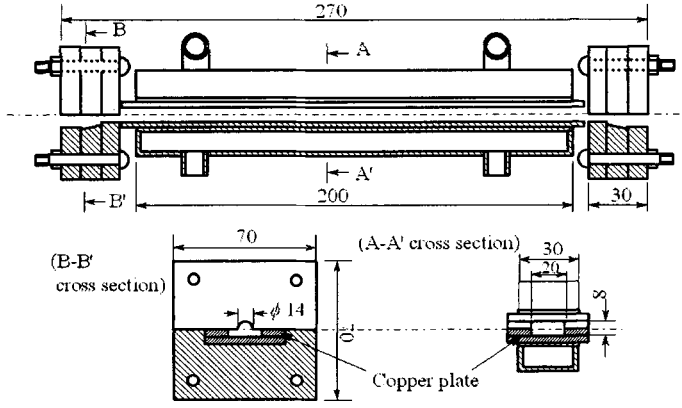

Fig.3. Experimental apparatus of part A (rectangular tube)

Another apparatus (Fig.4) was used for visualizing the dendritic growth. The hatched test section of $10 \times 1 \times 80mm^3$ was cooled one-dimensionally, in order to make the first dendritic arm grow as one-dimensionally as possible. The growth was observed by a CCD microscope.

4 Experimental Results

4.1 Pressure loss

In order to estimate the measurement errors, (1) was altered to include curvature and wall friction effects as follows:

$$v = \frac{k}{\mu}\frac{\rho g}{L}\{h_1(t) - h_2(t) - R_1 - R_2\}, \quad R_1 = \frac{\zeta}{g}v^2, \quad R_2 = \frac{32\mu\ell}{\rho g d^2}v. \tag{5}$$

In the Darcy flow region the elbow effect is negligible. R_2, desribing the friction loss in the tube at the maximum flow velocity is also negligible, because it is less than 1%, compared to the term involving $h_1(t) - h_2(t)$.

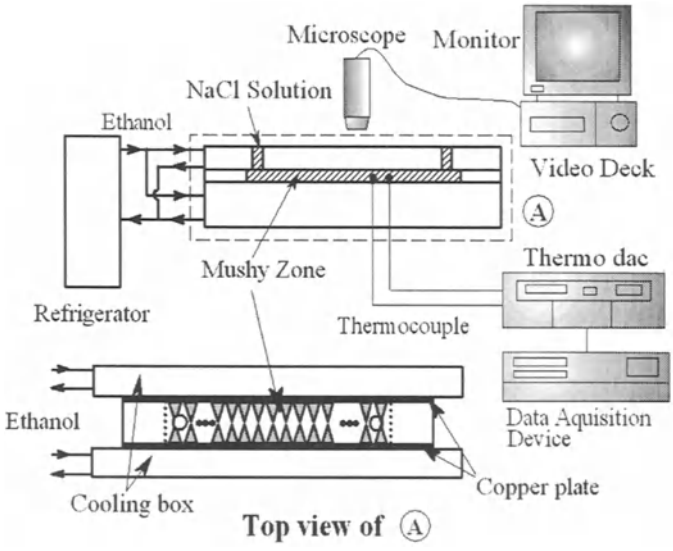

Fig.4. Apparatus for visualization

4.2 Permeability in rectangular tube

Fig.5 shows result of the time variation of the temperature in the test part A. T-type thermocouples were set up at positions 1 and 2, 20 and 180mm from the left elbow. This figure shows an example of zero supercooling degree ($5wt\%$ of initial concentration, 0.3 of liquid-phase-volume fraction), i.e. solidification without supercooling. Temperature, T_1 was nearly equal to T_2. Fig.6 shows the time variation of the potential-head displacement with $3wt\%$ of the initial concentration and 0.3 of the liquid-phase-volume fraction. The line, which was fitted by the least square method, agreed well with the measured data. This result shows that the measuring method based on Eq.(3) is successful.

The influence of the degree of supercooling on the permeability was also investigated. Fig.7 shows a time variation of the temperature during cooling with $3wt\%$ of initial concentration and 0.3 of liquid-phase-volume fraction. The supercooled aqueous solution was solidified by putting DC voltage to an electrode inserted in the solution. Dendrites were formed with a temperature rise near the freezing point. After that, cooling was continued to -6.4 deg.C in order to obtain a given liquid-phase-volume fraction, and then the permeability was measured. Fig.8 shows that as the supercooling degree increases, the permeability decreases. The line in Fig.8 was obtained by least square approximation.

Once the mushy zone was formed, it was kept at a constant temperature for a large time period. Then the permeability was measured. Fig.9 shows that the temperature was kept up at -6.4deg.C during 6 hrs with $3wt\%$ of initial concentration and 0.3 of liquid phase volume fraction. The permeabil-

ity was measured after a holding time as indicated in Fig.9. By repeating the measuring procedure with various holding times, the results shown in Fig.10 were obtained. From this figure, it is found that there is nearly no change of permeabilities within 12 hours, i.e., diffusion of solute in the solution, secondary arm and third arm formation of dendrites and recrystalization of dendrites within 12 hours did not influence the permeability. Fig.11 shows

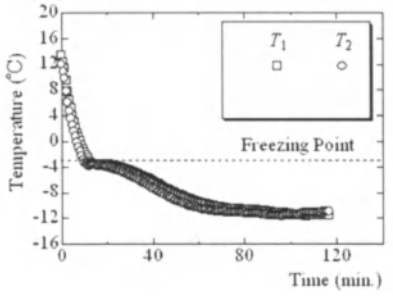

Fig.5. Time variation of temperatures during the dissolution

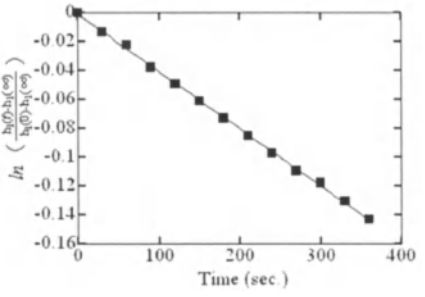

Fig.6. Time variation of potential head displacement

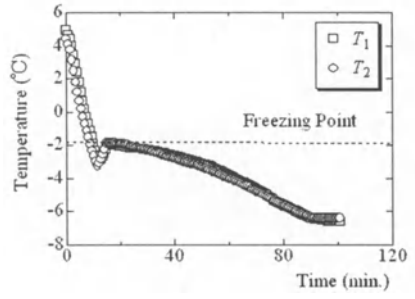

Fig.7. Time variation of temperatures during the dissolution (supercooling degree 2 deg.C)

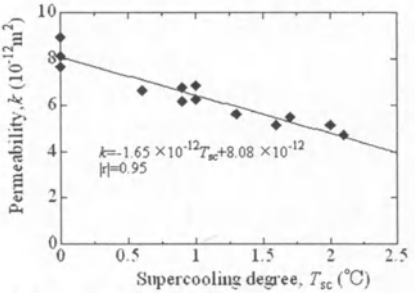

Fig.8. Relation between k and supercooling degree of solution

the relations between the liquid-phase-volume fraction and permeability at 0 supercooling degree. In a log-log scale the permeability increased linearly with the liquid-phase-volume fraction. Furthermore, the permeability for an initial concentration of $5wt\%$ had the tendency to be lower than that for an initial concentration of $3wt\%$ under the same liquid-phase-volume fraction. Since dendrites grow from the cooling surfaces, the liquid-phase-volume fraction near the cooling surface might be larger than that near the center of the rectangular tube and, therefore, the size of the rectangular tube might

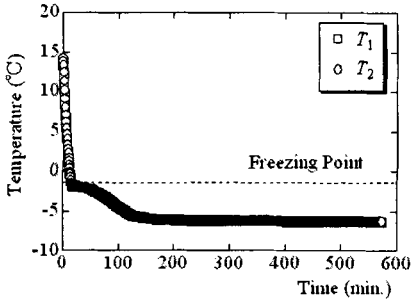

Fig.9. Time variation of temperatures during the dissolution (kept to the temperature in 6 hrs)

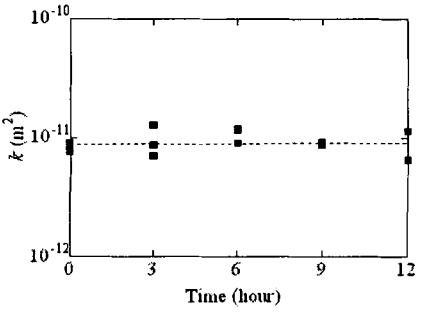

Fig.10. Relation between k and time after the mushy zone was formed

affect the measured permeability. Thus, in order to observe the effect of the aspect ratio of the cross section to the local liquid fraction, the permeability was measured again by using a new rectangular tube with a different aspect ratio ($32 \times 5mm^2$). The results are showed in Fig.11 with diamond symbols. A difference of the permeabilities on the two aspect ratios could not be found. This fact shows that the mushy zone in the tube may be assumed to be uniform. The measured permeability was compared with a well known Kozeny-Carman relationship for porous media,

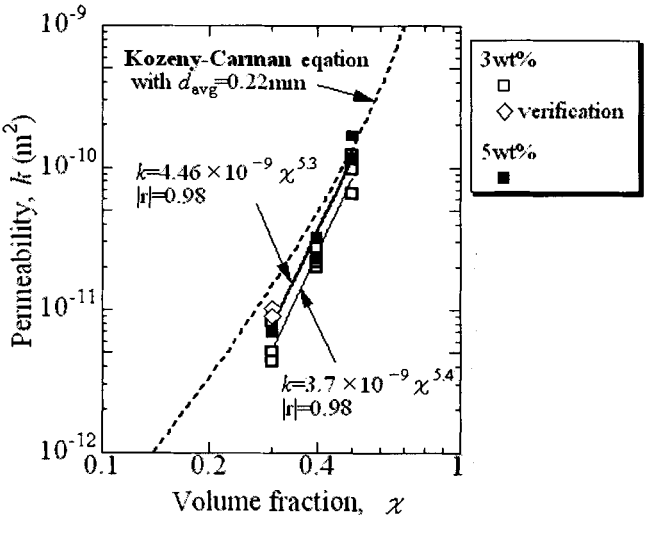

Fig.11. Relation between permeability and liquid-volume-fraction (T_{sc}=0 deg.C)

$$k_{KC} = \frac{\overline{D_p}^2}{180} \frac{\chi^3}{(1-\chi)^2}, \tag{6}$$

where $\overline{D_p}$ is the characteristic length, and for a packed bed of particles the mean diameter of the particles is used as the $\overline{D_p}$. In Fig.11, the dendritic arm spacing which will be mentioned later is substituted for $\overline{D_p}$ with value 0.22mm. The measured permeability agreed well with the Kozeny-Carman relationship (6). Furthermore, the 5.3 or 5.4 power obtained by the least square method agreed well with the 5.5 power in the relationship found by Rumpf and Gupte [9]

$$k = \frac{\overline{D_p}^2}{5.6K} \chi^{5.5}. \tag{7}$$

The observation of the formation and growth of dendrites in an aqueous solution was performed under various supercooling degrees and an initial concentration of $3wt\%$ and a liquid-phase-volume fraction of 0.3. Fig.12a shows the dendritic ice at the initial formation and Fig.12b shows that for a liquid-phase-volume fraction of 0.3. It was found that the first arm of the dendritic ice showed nearly one directional growth. The interval between the arms was obtained from the measurements. Fig.13 shows the relation between the first arm spacing and the supercooling degree. As the supercooling degree increases, the first arm spacing decreases. In order to obtain a relation between the permeability and the dendritic ice structure, the relation between the first dendritic arm space and the supercooling degree shown in Fig.13 were substituted into the approximate equation obtained from the relation between the supercooling degree and the permeability (Fig.8). The result, a relation between the first arm space and the permeability, is presented in Fig.14. The approximate line obtained by the least square method agrees well with the results. It is found that the permeability is proportional to the power 2.6 of the first arm spacing.

5 Conclusion

Our experiments give rise to the following conclusions:

- Permeability is proportional to the volume fraction of the liquid phase with the power and can be expressed by the equations (6) or (7).
- Permeability decreases with increasing supercooling degree of the solution or increasing initial concentration of the solution.
- Permeability is constant once the mushy zone is formed and a constant temperature is maintained.
- The first arm space of dendrites becomes narrower as the supercooling degree of the solution increases.

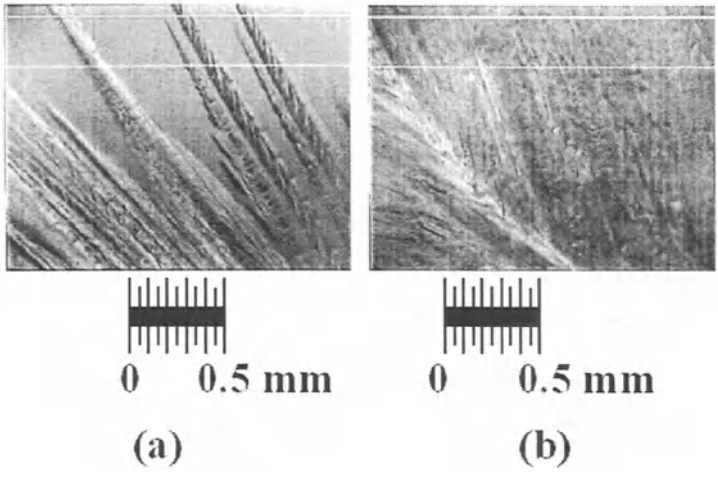

Fig.12. Arms of dendritic ice (Supercooling degree 3 deg.C, microscopic view with ×150) (a) Initial formation (b) $\nu = 0.3$

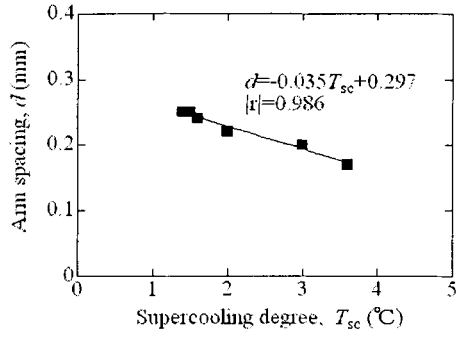

Fig.13. Relation between dendrite arm space and supercooling degree

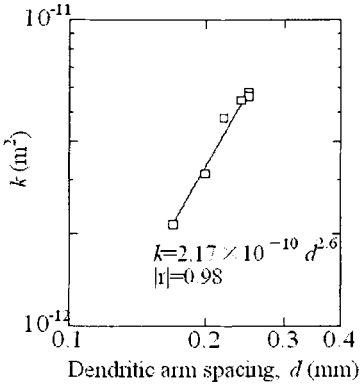

Fig.14. Relation between permeability and dendritic arm spacing

Nomenclature

d	dendritic arm spacing [mm]
h	potential head of solution [m]
k	permeability of mushy zone [m^2]
K	slope relative to change in time of dimensionless head [s^{-1}]
ℓ	length of U-shaped tube [m]
R_1	curvature loss in tube
R_2	friction loss in tube
t	time [sec]
μ	viscosity of aqueous solution [$kgm^{-1}s^{-1}$]

ρ density of aqueous solution [kgm^{-3}]
χ liquid phase volume fraction (porosity)

Acknowledgements: We thank Lecturer M.Tateno, Kougakuin Univ., Mr. T.Sanda, Y.Tsuda, K.Hanatani, H.Kikuchi and T.Nagataki undergraduate students of Aoyama Gakuin university for valuable assistance. The present study is supported by the Research for the Future Program of the Japan Society for the Promotion of Science, 97P01003.

References

1. Ishikawa T., Hirata T. et al. (1997) Freezing of solution around Horizontal cylinders. *34th National Heat Transfer Symp.* Japan, 713-714.
2. Teduka M., Sirato, H. et al. (1997) Dilution treatment of wastewater by freeze method. *The 75th JSME Spring Annual Meeting,* **3**(98-1), 373-374.
3. Matsumoto K., Okada M. et al. (1993) Solidification of porous medium saturated with aqueous solution in a rectangular cell-II. *Int. J. Heat Mass Transfer,* **38**(16) 2935-2943.
4. Murakami M., Shiraishi A. et al. (1983) Inter-dendritic fluid flow normal to primary dendrite arms in cubic alloys. *Acta. Metall.*, **31** 1417-1424.
5. Streat N., Weinberg F. (1976) Interdendritic fluid flow in a Lead-Tin alloy. *Metall. Trans.*, **7B**, 417-428.
6. Kunimine K., Hayashi Y. et al. (1993) Micro-Macro solidification of supercooled mixtures. *Thermal Sci. and Eng.*, **1**(4) 9-17.
7. Yoshioka H., Furuichi T. et al. (1997) Formation of mushy-zone and it's growth model. *34th National Heat Transfer Symp.* Japan, 463-464.
8. Okada M., Matsumoto K. et al. (1996) Influence of initial concentration and supercooling degree on the permeability of a porous medium saturated with partially solidified aqueous solution. *Int. J. Heat Mass Transfer.* **39**(18), 3845-3853.
9. Dullien F.A.L. (1979) *Porous media - Fluid transport and pore structure.* Academic Press. New York, 159-163.

(Received 17 Feb. 1999, accepted 29 April 1999)

Lateral Freezing of a Porous Medium Saturated with an Aqueous Salt Solution

Muyngho Song[1] and Raymond Viskanta[2]

[1] Department of Mechanical Engineering, Dongguk University, Seoul, Korea
[2] School of Mechanical Engineering, Purdue University, W. Lafayette, Indiana, U.S.A.

Abstract. Lateral freezing of a porous medium saturated with an aqueous salt solution was investigated experimentally and theoretically to obtain the improved understanding of the solute redistribution during solid/liquid phase change. The emphasis was on the interaction between hydrodynamics and transport of energy and species in the solidifying and unsolidified regions and on the effect of the flow characteristics of the porous matrix and dendrite arrays. Freezing experiments were performed in a square cross-section enclosure chilled and heated from the side by imposing uniform but different temperatures, and filled with the artificial porous structure. The latticed structure of the porous matrix phase and the shadowgraph enabled the flow visualization and the observation of the solidus and liquidus positions. Simultaneous measurements of local temperature and liquid composition at selected locations were also made. An analytical model based on the mass, momentum, heat, and species conservation and relations from the phase diagram is used, and the predictions are compared with experimental data.

1 Introduction

Solidification of a liquid saturated porous medium occurs in a wide variety of situations in geophysics and engineering. Examples include seasonal freezing of soil, artificial freezing of ground as a construction technique for supporting poor soils, insulation of underground buildings, latent heat of fusion energy storage in porous media and production and storage of frozen foods [9]. Metallurgical applications include manufacturing of composite materials and purification of metals, and medical applications include cryopreservation and banking of biological cells and tissues [11].

While the solidification of a mixture without the porous matrix phase has received considerable research attention, a very small number of studies have been reported on the subject of the alloy solidification in the presence of a porous matrix phase. The literature dealing with the freezing of a pure liquid saturated porous medium is abundant and extensive review is available [9]. There has been only a handfull of studies devoted to phase change in porous media saturated by solutions [4,5], and reference is made to the literature for more complete citation of earlier publications. For example, Okada et al. [4] conducted an experimental and theoretical study of the downward and lateral freezing of a packed bed of glass beads saturated with an aqueous sodium

chloride solution, which was initially undercooled. The convective motion of interdendritic liquid significantly influenced the growth velocity of the solid phase under the conditions tested. Studies on the solidification of an alloy in the presence of a porous matrix phase dealing with the opposing thermal and solutal buoyancy forces or dealing with the anisotropic flow characteristics of the porous matrix phase could not be identified in the published literature.

The present paper reports on an experimental and theoretical investigation of the lateral freezing of a porous medium saturated with an aqueous salt solution. Major attention was directed to the influence of the porous matrix phase on the interaction of hydrodynamics and advective heat and species transfer and on the solute redistribution during phase change. The difficulty in the flow structure visualization which is common in the experiments involving a porous medium is resolved by the latticed structure of the porous matrix, and the monitoring of the liquid composition at multiple locations were performed by utilizing the experimental diagnostics based on the electrochemical principles.

2 Experiments

2.1 Test cell and porous matrix

Solidification of a porous medium saturated with an aqueous salt solution was made to occur within the square cross-section test cavity having the dimensions of 148 mm in height and width and of 74 mm in depth. The sketch of the test cell assembly is shown in Fig. 1.

The vertical end walls were 6 mm thick copper plates of heat exchangers and served as the hot and cold walls. Ethyl alcohol (200 proof) was circulated from the constant temperature bath through the channels formed by the outer surface of the copper plates and the passages milled in the 33 mm thick carbon plastic (Lexan) blocks. Each heat exchanger, which is an assembly of a copper plate and a machined carbon plastic block, had three coolant passages which extended over the upper, middle and lower thirds of the copper plates. The vertical front and back walls and the horizontal top and bottom walls were made of 25 mm thick acrylic plates. All the acrylic walls were covered with 25 mm thick Styrofoam insulation during the test run except for the brief moments of visualization. When the insulation was removed for the visual access, the convective air motion at the outer surfaces of the front and back walls needs to be minimized to prevent condensation of the moisture in the ambient air and to maintain the thermal insulation. A pair of 3 mm thick glass plates was placed outside the Styrofoam layers which covered the front and back walls. During the visual access, only the central square portion of the insulation (148 mm $\times$148 mm large) was removed so that the gaps between the glass and acrylic plates were kept sealed with the remaining Styrofoam. The glass plate at the back wall was translucent to serve as the diffusing screen for the shadowgraph images. Liquid tight holes to allow for

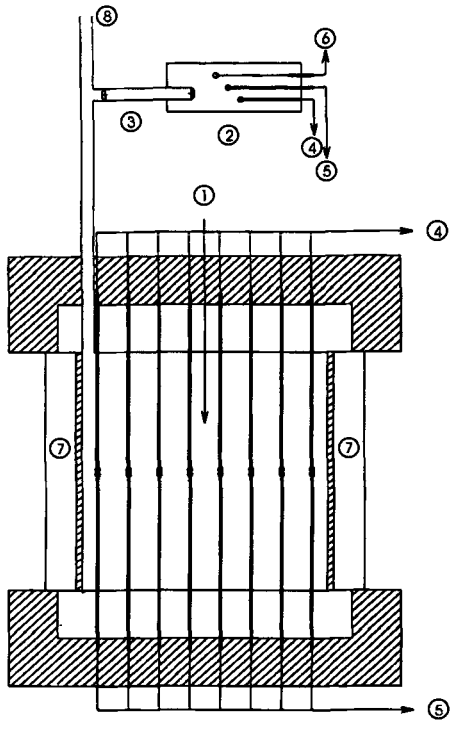

Fig. 1. Schematic diagram of experimental apparatus: 1 - test cavity; 2 - reference cavity; 3 - salt bridge; 4 - data logger (thermocouples); 5 - data logger (concentration probes); 6 - data logger (chloriding electrode); 7 - heat exchanger; 8 - overflow port.

the insertion of thermocouples, concentration probes and filling/draining lines were placed in the top and bottom walls. The entire test assembly, including the test cell, heat exchangers and the insulation, was placed on an aluminum frame with leveling screws.

The porous matrix, which occupied the test cavity, was a rectangular latticed framework of evenly spanned permeable plates which were either perpendicular or parallel to the heat exchanging end walls (Fig. 2). The permeable plates were 3.18 mm thick perforated Polypropylene plates chosen among the few commercially available materials (distributed by McMaster-Carr Supply Co.). The perforated holes which provided about 25 open areas were staggered-centered, 2.38 mm in diameter, 4.76 mm in spacing, and were aligned to allow for the insertion of probes. The macroscopic characteristics of the porous media such as the porosities and permeabilities depended on the spacings of the permeable plates and are given in Table 1. The detailed

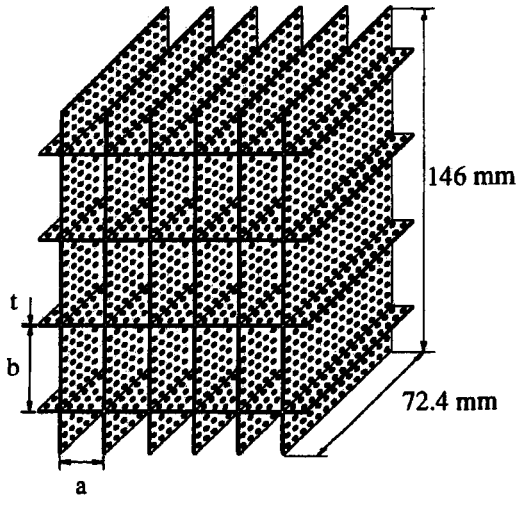

Fig. 2. Configuration of the porous matrix (see Table 1 for the values of a, b, and t).

explanation about the porous matrix configurations and the measurements of the macroscopic flow characteristic are given by Song and Viskanta [6].

Table 1. Charateristics of porous structures ($K_o = 8.37 \times 10^{-9}$ m^2). K_x and K_y are permeabilities in the $x-$ and $y-$directions, respectively, and a and b are the spacings shown in Fig. 2

Porous structure	a (mm)	b (mm)	ε_m	K_o/K_x	K_o/K_y
I	No porous structure		0	0	0
II	36.4	18.2	0.256	0.116	0.208
III	18.2	18.2	0.199	0.232	0.232

2.2 Phase change material

The void of the porous matrix phase within the test cavity was filled with 27 [wt.%] ammonium chloride aqueous (H_2O-NH_4Cl) solution, which has been

used as a phase change material in numerous previous solidification studies owing to the well established property-data base and the manageable range of phase-change temperature [10]. The phase-change process of aqueous ammonium chloride solution is well established in the published literature [12] and need not be repeated here. Suffice it to say that solidification of an off-eutectic composition aqueous ammonium chloride solution differs significantly from that of pure substances or that of an eutectic composition liquid and is characterized by the dependence of the solidification temperature on the liquid concentration and by the solubility difference between the liquid and solid phases. When the aqueous ammonium chloride solution of concentration greater than the eutectic (hypereutectic) composition solidifies, solid NH_4Cl forms and water is rejected into the liquid phase at the solid/liquid interface. In the immediate vicinity of the solid/liquid interface, the rejected species build up to change the interfacial liquid concentration closer to the eutectic composition. The liquid in the front of the moving interface is undercooled and the resulting morphological instability leads to a pattern formation. Among the most common modes of crystal growth are the dendritic patterns in which tree like microscopic structures develop over a volume having much larger spatial extents than the length scales of the array of the dendrites [3]. This region is called the mushy region and is usually treated as a porous medium in the macroscopic solidification models. The temperature of the liquid in the mushy region can be significantly lower than what is depicted by the liquidus of the equilibrium phase diagram due to the presence of undercooling.

During the solidification of the porous medium initially saturated with an off-eutectic liquid alloy, three distinct regions are found; the already solidified, the unsolidified, and the solidifying regions. Throughout the discussion, these three regions will be referred to as the solid, liquid and mushy regions according to the entities occupying the void of the porous matrix phase. Therefore, the solid region is composed of the porous matrix, primary solid and eutectic composition solid phases, and the mushy region is composed of the porous matrix, primary solid and liquid phases, while the liquid region has only the porous matrix and liquid phases. The thermophysical properties of all phases are presented in Table 2. The boundaries between the liquid and mushy regions and between the mushy and solid regions will be referred to as liquidus and solidus interfaces, as these boundaries confine the regions where no solid phase or liquid phase exist.

2.3 Test procedure

The preparation of each experiment included: 1) the assembly of the test cell with the porous structure inside, 2) saturation of the porous matrix with the aqueous NH_4Cl solution of the predetermined concentration, and 3) establishment of the uniform initial temperature condition.

Table 2. Thermophysical properties of each phase.

Phase	Liquid	Solid NH_4Cl	Ice	Eutectic solid	Porous matrix
ρ [kgm^{-3}]	1082	1530	920	998	910
c_P [Jkg^{-1}K^{-1}]	3324	1496	1950	1861	1520
k [Wm^{-1}K^{-1}]	0.408	2.5	2.0	2.1	0.22
L, M, N [kJkg^{-1}]	333.7	68.7	0	13.5	0
μ [Nsm^{-2}]	1.43×10^{-3}				
D [m^{2}s^{-1}]	1.0×10^{-9}	0	0	0	
β_T [K^{-1}]	3.23×10^{-4}				
β_C [K^{-1}]	-0.279				

The solution of the predetermined concentrations (27 $\pm$0.02 wt.% NH_4Cl) was obtained by mixing deionized water of a resistivity larger than 15 Mohm-cm with a requisite amount of research grade ammonium chloride grains (manufactured by J.T.Baker Inc.). In order to avoid entrapment of air bubbles in the small pores of the porous structure and blocking the flow passages, the solution was degassed and slowly (0.6 cm^{3}s^{-1}) siphoned into the test cavity. The initial uniform temperature condition was reached by controlling the temperatures of both end walls. The desired uniformity (initial temperature $\pm$1 °C) was reached within about 10 hours.

The heat exchangers were connected to two constant temperature baths (NESLAB ULT-80DD for the cold coolant and HAAKE A82 for the hot coolant) through a valve system. The cold wall temperature reached the desired value in less than 4 minutes with the cold bath temperature 10 °C below the desired cold wall temperature. With the help of a booster pump the center temperature of the cold heat transfer surface was maintained within $\pm$1 °C of the desired temperature. The uniformity of temperature on the heat transfer surface was insured with the five thermocouples, placed close to the test cavity along the centerline of each copper plate. As the heat transfer rates between the phase-change medium and copper plates were noticeably nonuniform along the height. With the adjustments of the flow rate made manually and intermittently, it was possible to maintain the temperature distribution along the height of the hot and cold walls within $\pm$0.5 °C of the wall-center temperature during the first 30 minutes of solidification and within $\pm$0.2 °C afterwards.

Measurements of the temperatures inside the test cavity were made with type-T thermocouples, calibrated within an accuracy of $\pm$0.1 °C. Due to the

highly corrosive nature of the aqueous NH_4Cl solution, the copper and constantan lead wires were sheathed by a 1.65 mm O.D. stainless steel tube, and the thermocouple bead was grounded inside the closed end of the sheathing tube (Omega TMQSS-62). Measurements of the local liquid concentrations in the liquid and mushy regions were made with the concentration probes which has an uncertainty of $\pm 2.5\%$ of the solute concentration reading. A probe to measure the local liquid concentration was a 0.8 mm O.D. silver wire electrically insulated from the solution by a 0.3 mm thick Kynar layer, except at the plain cut tip cross-section. As the electrochemical potential of the chloride ion in the solution is mainly determined by the local temperature and chemical composition, the local liquid concentration could be determined from the relative electric potential of the working electrode and the local temperature data measured with thermocouples. The simultaneous measurement of the temperature and liquid concentration is also preferred for the more accurate estimation of the local undercoolings. For each measuring position, a pair of temperature and liquid concentration probes was inserted from the opposite directions through the liquid tight holes placed in the top and bottom walls, and the sensing tips were separated from each other with a gap less than 1 mm. A detailed discussion concerning the theory, fabrication, calibration and uncertainties of the concentration probe are found in Song and Viskanta [8].

The qualitative observations of the flow structures in the liquid region were made possible by the latticed arrangement of the porous structure and the shadowgraph technique utilizing the mercury arc lamp as a light source. The shadowgraph images of the test cavity were visualized on the translucent glass plate, which is the last component of the test cell assembly in the light path. The images were photographed at about 15, 30, 60, 120, 120, and 480 minutes after the initiation of cooling.

3 Results and Discussion

3.1 Experimental conditions

Solidification experiments were conducted for three different porous matrix configurations as well as for different combinations of hot and cold wall temperatures. Table 3 summarizes the experimental conditions which are discussed. During the lateral solidification of a 27 wt.% ammonium chloride aqueous solution, the thermal and solutal buoyancy forces oppose each other in the mushy region as the interdendritic liquid is colder and richer in water compared to the initial solution. Even though the change of the liquid density along the liquidus of equilibrium phase diagram is dominated by the solutal expansion, the flow in the mushy region is not unidirectionally upward, since it interacts with the flow in the liquid region (which is generally downward near the liquidus interface). The interaction of the momentum, energy and species transport with the separation, migration and growth of the equiaxed crystal also presents another and different aspect to the phenomenon from the

lateral solidification of the hypoeutectic solution. The experimental studies on the lateral solidification of a hypereutectic aqueous ammonium chloride solution in the absence of a porous structure have been made and revealed the nature of the double-diffusive transport process [1,2]. New results and discussion of the transport features revealed by the novel concentration measurement diagnostics technique and the effect of the porous structure under different temperature conditions as well as additional results on solidification of solutions in porous structures are given by Song [7].

Table 3. Experimental conditions

Experiment	Porous structure	T_h (^{0}C)	T_c (^{0}C)
1	I	20	-30
2	II	20	-40
3	II	40	-40
4	III	20	-40

3.2 Experiment 1 - Absence of porous matrix

The temperature and liquid concentration data measured at $\eta = 0.07$ during Experiment 1 indicated that significant undercooling existed both in the liquid and mushy regions near the bottom of the test cell [Fig. 3a]. The extent of the undercooling in the liquid region was fairly uniform and almost unchanged, as both the temperature and liquid concentration were uniform and decreased continuously. The extent of the undercooling in the mushy region was close to that in the liquid region but tended to increase as the solidus interface was approached. At $\eta = 0.5$ [Fig. 3b], the temperature and liquid concentration in the liquid region differed little from those at $\eta = 0.07$, when the measuring positions belonged to the lower fluid layer. This indicated that both the temperature and concentration distribution in the lower fluid layer were rather uniform. When the lowest DDI (double diffusive interface) passed the measuring positions at $\eta = 0.5$, both the temperature and the concentration in the liquid region decreased drastically. Since the liquid in the middle fluid layer was not undercooled, the equilibrium liquidus temperatures dropped by a larger extent compared to the temperature drop. The temperature and concentration distributions in the middle and upper fluid layers were also fairly uniform and the transient changes were much smaller

than those in the lower fluid layer [Fig. 3b]. The difference between the medium temperature and the equilibrium liquidus temperature at $\xi = 0.07$ and $\eta = 0.93$ (not shown) reversed at t $\approx$ 95 min, as the growth of the primary solid phase ceased and remelting started to occur.

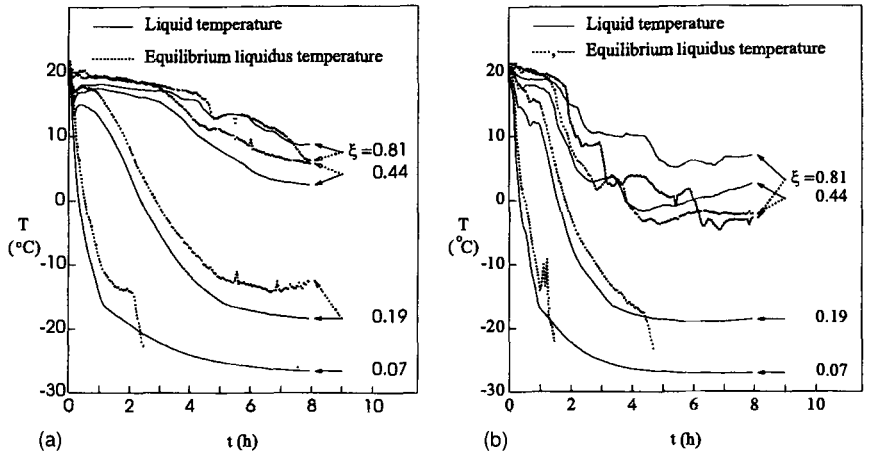

Fig. 3. Transient temperature and liquid concentration readings (Experiment 2): (a) $\eta = 0.07$ and (b) $\eta = 0.5$

3.3 Experiments 2, 3 and 4 - Presence of porous matrix

The porous structure obstructed the migration of the separated crystals as well as the fluid motion during Experiment 2. Initially, the NH_4Cl crystals separated from the mushy region near the cold wall could not descend to the bottom but were captured by the porous plates surrounding the voids adjacent to the cold wall [Fig. 4a]. Unlike the single layer of mushy region grown from the separated crystals encountered in Experiment 1, which extended along the bottom, the buildup and growth of separated crystals occurred along the horizontal porous plates near the cold wall. The shapes of the rising water-rich plumes suggested that the cell-type flows developed within the voids near the cold wall. At t = 30 min [Fig. 4b], a couple of DDIs appeared below the top wall. As the primary solid phase growing around the second vertical porous plate from the cold wall linked the primary solid phase around the horizontal porous plates, the mushy and liquid regions were not simply connected. The growth of the primary phase within the voids between the second and third vertical porous plates from the cold wall was not active until the major portion of the voids next to the cold wall were filled with the mush. For the remaining duration of the experiment, the formation, motion

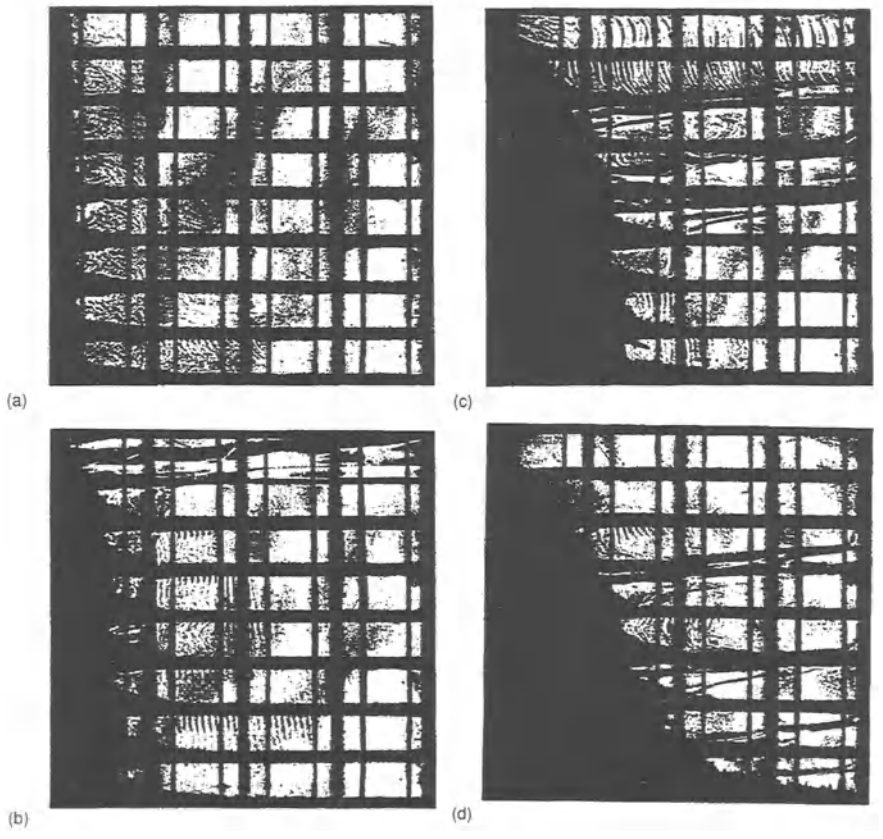

Fig. 4. Shadowgraph images taken during Experiment 2: (a) $t = 5$ *min*, (b) $t = 30$ *min*, (c) $t = 120$ *min*, and (d) $t = 240$ *min*.

and merging of DDIs were qualitatively the same as those observed in Experiment 1, where the porous structure was absent. However, the number of DDIs was larger in the presence of the porous matrix phase due to the reduced intensity of thermally driven flow, and the velocity of descending DDIs were greater due to the lower cold wall temperature and enhanced formation of the solid phases [Fig. 4d]. After the liquid concentration in the top fluid layer reached about 21 wt.% NH_4Cl ($t \approx 100$ min), no additional DDI (or fluid layer) formed, and the vertical extent of the fluid layers above the lowest DDI kept on increasing. The images of streak arrays, branched out from the horizontal porous plates found near the top wall in Fig. 4c, were made when the DDI passed the horizontal porous plates and indicated that the mixing between the bulk fluid and remaining solution trapped by the porous matrix phase was not complete. The same type of images could be also made when

the water-rich fluid was swept through the horizontal porous plates by the thermally driven flow and were found in the vicinity of the porous plate near the mushy region.

The transient variation of the temperature and liquid concentration measured during Experiment 2 showed similar qualitative trends as those during Experiment 1. The horizontal distribution of the temperature and liquid concentration in the liquid region was less uniform compared to that in Experiment 1, since the advective transport of energy and species was reduced by the flow resistance offered by the porous structure. Similar to the data of Experiment 1, the temperatures measured in the liquid region were lower than the equilibrium liquidus temperatures (the medium was undercooled) below the lowest DDI, and were either higher than or almost equal to the equilibrium liquidus temperatures in the fluid layers above the lowest DDI. The undercooling of the interdendritic liquid also existed, but the extent was no larger than the ones in Experiment 1, despite the larger cooling rate caused by the lower cold wall temperature. Due to the different cold wall temperatures, a direct comparison of the measured concentrations was not made.

In Experiment 3, the solution in the test cavity was solidified under the same conditions as Experiment 2, except that the hot wall temperature was higher (40 ^{0}C). Due to the intense thermal flow, the overall volume fractions of the solid phases were smaller and the formation of DDI was retarded, compared to Experiment 2. The streak-type images found below the lowest DDI [Figs. 5a and 5b], suggest that a considerable amount of water-rich fluid discharged into the liquid region was swept away from the liquidus interface and was mixing with the bulk liquid over the liquid region. Only

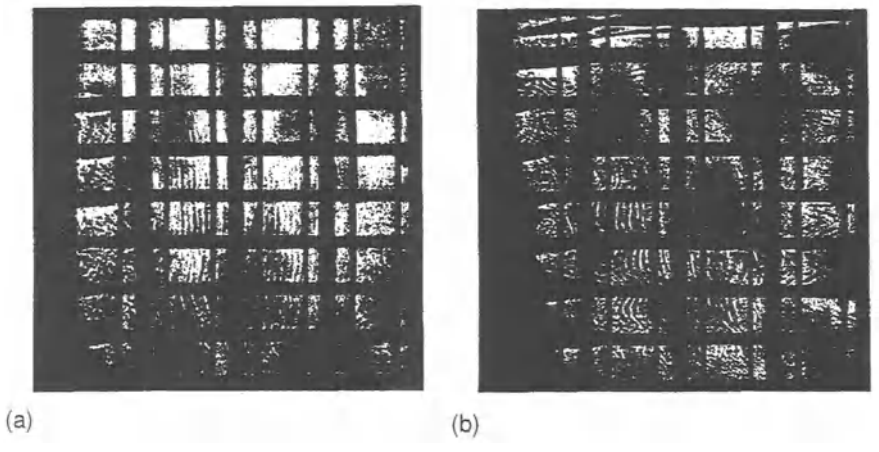

Fig. 5. Shadowgraph images taken during Experiment 3: (a) $t = 30$ *min* and (b) $t = 60$ *min*.

one DDI persisted to the end of the run (not shown), and the liquid region was divided into two fluid layers having similar vertical extent at t = 480 min. The temperature of the medium in the mushy region closely matched the local equilibrium liquidus temperature during Experiment 3, indicating that the undercooling of the interdendritic liquid was substantially reduced. The undercooling of the bulk liquid in the liquid region did not occur.

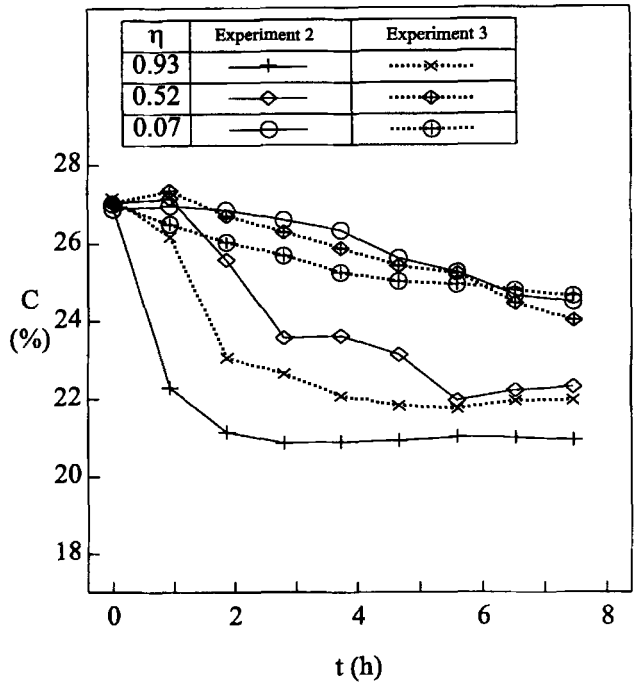

Fig. 6. Comparison of the measured concentrations for Experiments 2 and 3 at $\xi = 0.68$.

The trends in the liquid concentration measured with time at three different heights along $\xi = 0.68$ are compared in Fig. 6. The time rate of the liquid concentration change below the lowest DDI was almost constant for both cases but was larger when the thermal flow was relatively intense (Experiment 3). The decrease of the liquid concentration near the top wall ($\eta = 0.93$) was initially fast, but gradually decelerated with time as the new DDIs ceased to form and the vertical extent of the fluid layer just below the top wall started to increase. The overall decrease in the liquid concentration at $\eta = 0.93$ was smaller in Experiment 3 due to the less amount of solid phases formed. During Experiment 2, the liquid concentration at η =0.52 and 0.07 rapidly

approached the values at η =0.93 whenever the DDI passed the measuring position. The amount of these decreases was larger at the higher measuring position (η = 0.52) for the same DDI and smaller for the higher DDI at the same measuring position. During Experiment 3, the measured liquid concentrations at η =0.52 were slightly higher than those at η =0.07 until the DDI passed the measuring position at η =0.52.

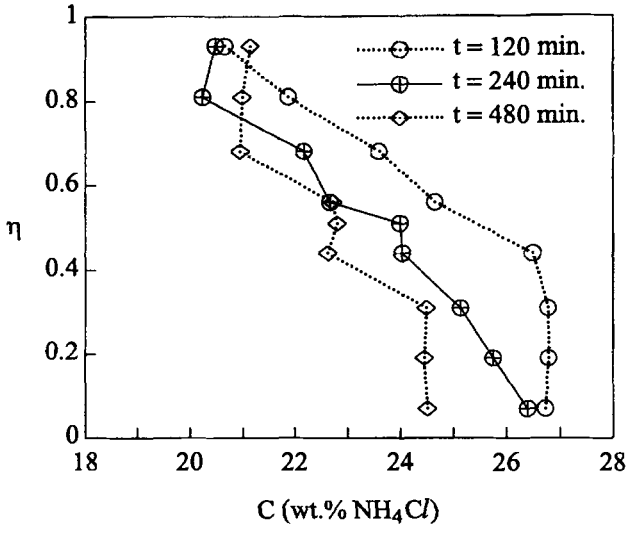

Fig. 7. Measured concentration distributions for Experiment 4 at ξ = 0.68.

The experimental conditions for Experiment 4 were the same as those of Experiment 2, except that a different porous structure was employed. The permeability of the porous structure occupying the cavity in Experiment 4 was isotropic and about 50% smaller compared to the x-directional permeability (or about 90% of the y-directional permeability) of the porous structure employed in Experiment 4. The number of DDIs and the advance rate of the liquidus interface were greater in Experiment 4 due to the reduced thermal flow in the liquid region [7], but the slope of the DDI increased as the horizontal permeability decreased by larger extent. Since the trends in the temperature and liquid concentration during Experiment 2 and 4 differed little from each other, only a comparison of the measured liquid concentration at t = 120 min is presented in Fig. 7. At all locations, the liquid concentrations measured in Experiment 4 were closer to the eutectic composition as compared to those in Experiment 2, probably due to the larger amount of solid phases associated with the less intense thermal flow in the liquid region.

However, the differences between the measured liquid concentrations, for the given change in the porous structure permeability, were generally smaller than the measurement uncertainty (5% of the reading).

The liquid concentration data (not shown) for Experiment 4 indicated that the difference between the concentrations at ξ =0.68 of the adjacent fluid layers was about the same at t = 120 min. The piecewise uniform profiles at later times (t = 240 and 480 min) confirmed that the vertical distributions of the liquid concentration were fairly uniform within a fluid layer, but the discrete changes in the liquid concentration existed across the DDIs. The magnitude of the discrete change in the liquid concentration across the DDI increased from the bottom toward the top wall at later times, and the average liquid concentration of a given fluid layer slowly increased with time.

3.4 Comparison of model predictions and experimental data

A theoretical, two-dimensional model has been developed [7] to simulate solidification of an aqeous solution in a porous matrix discussed in the experiments. The model solved transient, two-dimensional conservation equations for mass, momentum, species and energy for the liquid, primary solid and eutectic. Use was also made of the equilibrium phase diagram for the aqueous ammonium chloride solution. The theoretical and computational details are lengthy and cannot be included here because of space limitations, but they can be found elsewhere [7].

In order to validate the mathematical models, the conditions for Experiment 4 were numerically simulated and the predicted results compared with the experimental data. The thermophysical properties for the model input were the same as those in Table 2, except that all the phase densities are assumed to be the same and fixed at the value of 1082 kgm^{-3}.

The predicted temperature profiles are compared with the experimental data in Fig. 8 for t=1 h. A good agreement was obtained except near the top wall (η = 0.93), where the temperature of the medium was underpredicted owing to the overprediction of discharge of cold interdendritic liquid into the liquid region across the top portion of the liquidus interface. It is believed that the permeability of the mushy region in the direction normal to the primary arms was overestimated. The strong solutal stratification resulted from vigorous discharge of interdendritic liquid into the liquid region may have suppressed the division of the liquid region into multiple double-diffusive layers which occurred in the experiment. Further research is needed to better understand the flow structure resulting from the double-diffusive instability during solidification of a mixture.

A comparison of the predicted concentration distribution with experimental data along the vertical line at ξ =0.68 also indicated that the discharge of interdendritic liquid into the liquid region was overpredicted (Fig. 9). The measured concentration profile at t=2 h revealed the gradual variation between the initial concentration and the eutectic composition in the upper

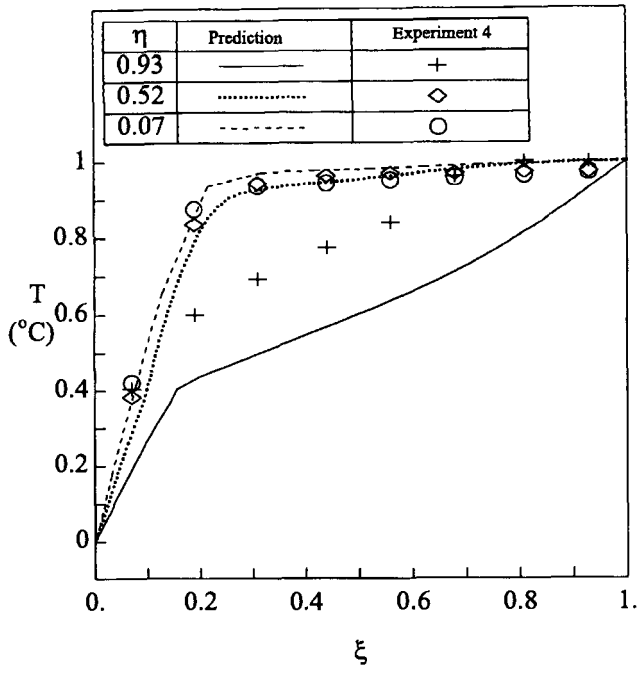

Fig. 8. Comparison between the predicted and measured temperature profiles for Experiment 4 at $t = 60$ *min*.

half of the liquid region, whereas the predicted profile had the uniform portion near the top wall for which the calculated concentration was within 2 wt.% from the eutectic composition. At t=8 h, the predicted concentration profile is uniform for the height of the liquid region, while the measured values varied between 20 and 25%, due to the difference in the calculated and actual flow structure.

The discrepancy between the predictions and experimental data are partly due to the uncertainties in determining the flow characteristics of the dendrite array and partly due to the difference in the flow structure in the liquid region which has comparable temperature and concentration gradients in terms of equivalent buoyancy forces. For accurate prediction of mixture solidification, a reliable mathematical model which determines the dendritic permeability from the local solidification parameters within an acceptable uncertainty needs to be developed.

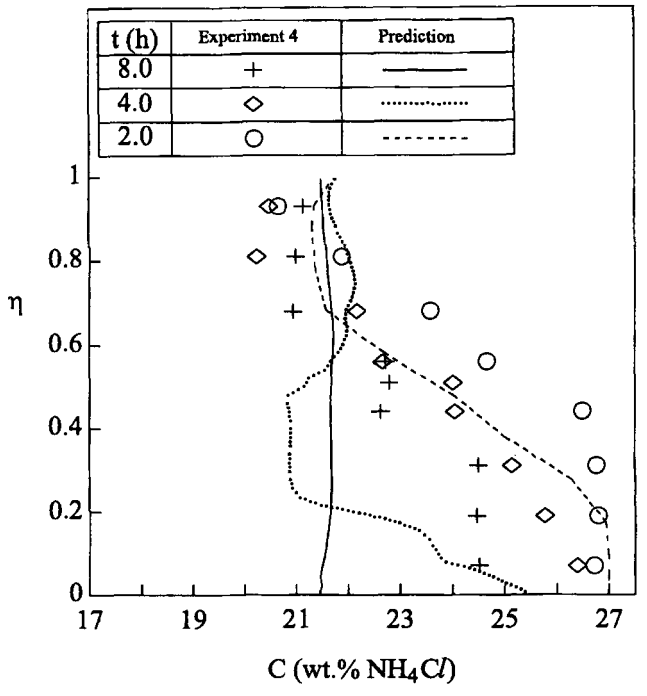

Fig. 9. Comparison of liquid concentration distributions along the vertical line for Experiment 4.

4 Conclusions

An experimental and analytical study on the lateral freezing of a porous medium saturated with an aqueous salt solution has been performed to obtain the improved understanding of the solute redistribution during phase change. Major focus of the research was directed to the influence of the porous matrix phase on the interaction of hydrodynamics and advective heat and species transfer.

Solidification of an aqueous ammonium chloride solution was studied within a square cross-section test enclosure, which was cooled and heated at a pair of vertical end walls by imposing uniform but different temperatures. Artificial structures compatible with the flow visualization were constructed and served as the solid matrix of the porous medium. The flow structure in the liquid region was characterized by the double-diffusive interfaces and multiple fluid layers even in the presence of porous structure. In the absence of the porous structure, a considerable portion of the primary solid phase initially formed on the vertical cold wall separated and stranded on the bot-

tom wall. The porous structure obstructed the migration of the crystals and offered an additional resistance to the motion of the fluid both in the liquid and mushy regions. The presence of the porous structure noticeably altered the distribution and the growth kinetics of the primary solid phase. When the hot wall temperature was lower and/or the permeability of the porous structure was smaller, the advance of the liquidus interface and the number of double-diffusive interfaces increased due to the reduced flow intensity in the liquid region.

Mathematical models based on heat and species conservation and relations from the phase diagram were suggested, and the predicted results for the representative conditions are compared with the experimental data. The discrepancy between the predictions and experimental data are partly due to the uncertainties in determining the flow characteristics of the dendrite array and partly due to the difference in the flow structure in the liquid region.

Nomenclature

C concentration of solute, [wt.%],
T temperature, [°C],
t time, [s],
x horizontal coordinate, [m],
y vertical coordinate, [m],
η dimensionless vertical coordinate, [y/H],
ξ dimensionless horizontal coordinate, [x/H].

References

1. Beckermann C. (1987) *Melting and Solidification of Binary Mixtures with Double Diffusive Convection in the Melt.* Ph.D. Thesis, Purdue University, West Lafayette, Indiana
2. Christenson M.S., Incropera F.P. (1989) Solidification of an Aqueous Ammonium Chloride Solution in a Rectangular Cavity - I. Experimental Study. *Int. J. Heat Mass Transfer* **32**, 47-68
3. Kurz W., Fisher D.J. (1989) *Fundamentals of solidification*, Trans Tech Publication Ltd., Switzerland
4. Okada M., Ochi M., Tateno M. (1998) Solidification of a Supercooled Aqueous Solution in a Porous Medium. In: Lee J.S. (Ed.) Heat Transfer, *11th International Heat Transfer Conf., Kyongju, Korea*, Aug. 23-28, 1998. KSME, Korea, Vol. 7, pp. 169-174
5. Song M., Choi J., Viskanta R. (1993) Upward Solidifiation of a Binary Solution Saturated Porous Medium. *Int. J. Heat Mass Transfer* **15**, 3687-3695
6. Song M., Viskanta R. (1994) Flow Charateristics of Anisotropic Structures Constructed with Porous Layers. *Transport in Porous Media* **15**, 151-174
7. Song, M. (1995) *Solidification of an Anisotropic Porous Medium Saturated with a Binary Alloy.* Ph.D. Thesis, Purdue University, W. Lafayette, IN.

8. Song M., Viskanta R. (1995) Electrochemical Method to Measure the Composition of the Liquid Phase During the Solidification of $NH_4Cl - H_2O$ System. *Review of Scientific Instruments* **66**, 4336-4340
9. Viskanta R. (1991) Phase Change Heat Transfer in Porous Media. In: Zarling, Z.P. (Ed.) *3rd International Symposium on Cold Regions Heat Transfer*, 1991, University of Alaska, Fairbanks, 1-24
10. Viskanta R. (1992) Transport Phenomena During Solidification of Bianry Systems. In: Azevedo, L.F.A. et al. (Eds) *4th Brazilian Thermal Science Meeting, Rio de Janeiro, Brazil, 1992. Brazilian Society of Mechanical Engineers, Rio de Janeiro*, pp. P-39 to P-50
11. Viskanta R., Bianchi M.V.A., Critser J.K., Gao D. (1997) Solidification Process of Solutions. *Cryobiology* **34**, 348-362
12. Zemanski M.W., Dittman R.H. (1981) *Heat and Thermodynamics*, Mc-Graw Hill Co, New York

(Received 22 Feb. 1999, accepted 18 May 1999)

Spontaneous Melting of Ice in a $CaCl_2$ Solution

Masahiro Sugawara and Makoto Tago

Department of Mechanical Engineering, Faculty of Engineering and Resource Science, Akita University Akita 010-8502, Japan

Abstract. This paper is concerned with the melting of a vertical ice plate into a calcium chloride aqueous solution inside a square cavity. The initial temperatures of the ice and the liquid are -5°C and 0°C respectively, and the initial solute (i.e. $CaCl_2$) concentration of the liquid is 20wt% at the beginning of melting. The ice melts spontaneously with decreasing temperature in the melting system. This typical melting behavior is mainly attributed to the combined effects of the driving forces of diffusion of solute($CaCl_2$)/solvent(H_2O), and also heat transfer near the melting front. A complicated double diffusive convection in the liquid layer affects the melting rate of the ice. It is seen that the numerical results, including some assumptions in the melting-front-control volume of the continuum model [15, 16], predict well the melting rate and abrupt temperature decrease in the melting system.

1 Introduction

The melting of ice in mixtures began as a problem for the melting of glaciers in sea water motivated by oceanographers. The melting of glaciers in sea water has become more important recently because of the increasing temperature in the earth's environment. Therefore it is important to correctly analyze the melting rate of ice in mixtures. Some studies on melting have been previously reported. Griffin [1] analyzed the heat, mass, and momentum transfer during the melting of glacial ice in sea water. Marschall [2] presented a similarity solution for free convection on glacial ice in saline water, and computed interfacial temperatures and concentrations as functions of environmental temperatures. Huppert and Turner [3] presented experimental results for melting of an ice block in an initial saline gradient or in initial uniform salinity; they measured a series of horizontal layers with double diffusive convection. Josberger and Martin [4] investigated experimentally and analytically the melting of a vertical ice wall in salt water, and reported three different flow regimes. Carey and Gebhart [5],[6] considered the melting of a vertical ice plate in saline water analytically and experimentally, and predicted the interfacial temperatures and concentrations and the velocity profiles near the melting front. Sammakia and Gebhart [7] measured the interfacial temperatures and concentrations, and velocity profiles near a vertical ice surface, and also presented visual observations of complicated flows

in the salt water. Johnson and Mollendorf [8] investigated transport processes from a vertical ice surface melting in saline water, and proposed a new concept of "saline gradient dominates temperature gradient". Sugawara et al. [9] investigated the melting of a horizontal ice layer from above in sodium, calcium, magnesium chloride and urea aqueous solutions with radiative heating. Beckermann and Viskanta [10] presented numerical and experimental investigations for double-diffusive convection due to melting of a vertical ice layer in an ammonium chloride-water solution and predicted stratified upper and uncontaminated lower regions and also predicted vertical variations of interfacial temperature and concentration. Schutz and Beer [11] investigated experimentally and analytically the melting of ice in pure and saline water inside a square cavity, they mainly considered the effect of the maximum density on the natural convection in the liquid for the case of low liquid concentrations. Fukusako et al. [12] reported an experimental study of the melting of a horizontal ice cylinder in saline water. Sugawara and Sasaki [13] investigated experimentally and analytically the abrupt temperature decrease in a melting system of snow. However, no quantitative predictions for the melting rate have been reported in the above studies even though it is important to correctly predict the melting amount for glacial ice in sea water or in some application of cold heat storage systems with change of phase.

Recently, Sugawara and Fujita [14] studied the melting of a vertical ice layer subject to a double field of temperature and concentration; they presented a quantitative prediction of the melting rate and temperature depression under the restricted condition that the temperature between the ice and the liquid was initially the same. This paper is concerned with the melting of a vertical ice plate into a calcium chloride aqueous solution inside a square cavity, which is considered as an extension of a previous work [14] because of a higher liquid temperature than that of the ice plate at the beginning of melting process. A two-dimensional numerical calculation including some assumptions in the melting-front-control volume of the continuum model [15, 16] is presented to quantitatively predict the melting rate and temperature decrease in the melting system.

2 Analytical Procedure

Fig. 1 shows a two-dimensional physical model and the coordinate system considered in the present study. H and L are the height and length of the cavity including an ice plate and the liquid, respectively. As external boundaries we assume that the region is thermally insulated and non-permeable for species. It is assumed that the flow in the liquid is two-dimensional and laminar, and the Boussinesq approximation is considered to avoid complex calculations. The volumetric change of the solid and liquid due to phase change is equally ignored in this procedure (i.e. $\rho_s = \rho_\ell$, $f = g$). The continuum equations governing the conservation of mass, momentum, energy and species

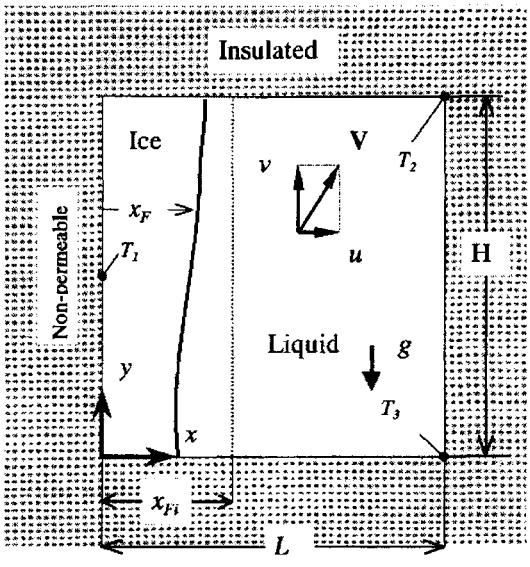

Fig. 1. Schematic presentation of the physical model and coordinate system

in the melting system which were derived by Bennon and Incropera [15,16] may be expressed briefly as follows,

continuity

$$\frac{\partial}{\partial t}(\rho) + \nabla \cdot (\rho \boldsymbol{V}) = 0, \tag{1}$$

momentum

$$\frac{\partial}{\partial t}(\rho u) + \nabla \cdot (\rho \boldsymbol{V} u) = \nabla \cdot (\mu_\ell \frac{\rho}{\rho_\ell} \nabla u) - \frac{\mu_\ell}{K} \frac{\rho}{\rho_\ell} u - \frac{\partial p}{\partial x}, \tag{2}$$

$$\frac{\partial}{\partial t}(\rho v) + \nabla \cdot (\rho \boldsymbol{V} v) = \nabla \cdot (\mu_\ell \frac{\rho}{\rho_\ell} \nabla v) - \frac{\mu_\ell}{K} \frac{\rho}{\rho_\ell} v - \frac{\partial p}{\partial y}$$
$$+\rho g[\beta_T (T - T_r) + \beta_m (m_\ell - m_{\ell r})], \tag{3}$$

energy

$$\frac{\partial}{\partial t}(\rho T) + \nabla \cdot (\rho \boldsymbol{V} T) = \frac{1}{c} \nabla \cdot (k \nabla T) - \frac{L}{c} \dot{M} - \frac{\rho T}{c} \frac{\partial c}{\partial t} - \frac{\rho \boldsymbol{V} T}{c} \cdot \nabla c$$
$$-\frac{1}{c} \nabla \cdot [\rho \boldsymbol{V} \{L + f_s (c_\ell - c_s) T\}], \tag{4}$$

species

$$\frac{\partial}{\partial t}(\rho m) + \nabla \cdot (\rho \boldsymbol{V} m) = \nabla \cdot (\rho D \nabla m) + \nabla \cdot [\rho D \nabla (m_\ell - m)] - \nabla \cdot [\rho (m_\ell - m) \boldsymbol{V}]. \tag{5}$$

The dependent variables and physical properties are defined as follows:

$$\begin{aligned} &\boldsymbol{V} = f_\ell \boldsymbol{V}_\ell, \quad m = f_s m_s + f_\ell m_\ell, \quad \rho = g_{si}\rho_s + g_{\ell i}\rho_\ell \\ &k = g_s k_s + g_\ell k_\ell, \quad c = f_s c_s + f_\ell c_\ell, \quad L = (c_s - c_\ell)T_e + h_f. \end{aligned} \tag{6}$$

In the present model, the density is assumed to be constant and has the initial expressed in (6).

Solid and liquid mass fraction in the melting front control volume: Thermodynamic equilibrium is assumed in the melting-front-control volume including ice and liquid regions, and mass fraction of solid (ice) and liquid in it will be defined as (see Fig. 2)

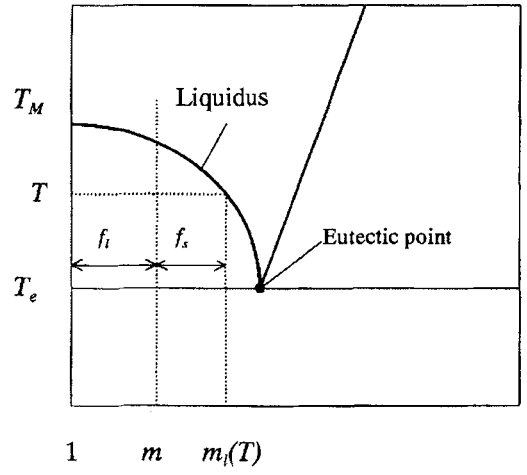

Fig. 2. Concept of solid and mass fraction in the melting-front-control volume in an equilibrium phase diagram (i.e. concept to evaluate the melting rate in the modified continuum model)

$$f_s = \frac{m - m_\ell(T)}{1 - m_\ell(T)}, \quad f_\ell = 1 - f_s, \tag{7}$$

where $m_\ell(T)$ is the thermodynamic equilibrium-water concentration given by following equation [17]

$$\begin{aligned} m_\ell(T) = 1 - (&3.0441 \times 10^{-3} - 2.4679T - 0.17063T^2 - 8.4228 \times 10^{-3}T^3 \\ &-2.1251 \times 10^{-4}T^4 - 2.0672 \times 10^{-6}T^5)/100. \end{aligned} \tag{8}$$

The melting-front-control volumes are also assumed to be porous media, and for their permeability the Kozeny-Carman equation [16] is employed.

$$K = K_0 \left[\frac{g_\ell^3}{(1 - g_\ell)^2} \right]. \tag{9}$$

It should be noticed that in the energy equation (4) the enthalpy is replaced by the temperature to avoid an abrupt change of the enthalpy near the melting front, although the energy equation is originally expressed in terms of the enthalpy.

initial conditions (t=0):

$$T = T_{si},\ m = m_{si} = 1,\ u = v = 0,\ \text{at}\ 0 < x < x_{Fi},\ 0 \le y \le H, \tag{10}$$

$$T = T_{\ell i},\ m = m_{\ell i} = 0.8,\ u = v = 0,\ \text{at}\ x_{Fi} < x < L,\ 0 \le y \le H, \tag{11}$$

boundary conditions:

$$\frac{\partial T}{\partial x} = 0,\ \frac{\partial m}{\partial x} = 0,\ u = v = 0,\ \text{at}\ x = 0,\ x = L,\ 0 \le y \le H, \tag{12}$$

$$\frac{\partial T}{\partial y} = 0,\ \frac{\partial m}{\partial y} = 0,\ u = v = 0,\ \text{at}\ y = 0,\ y = H,\ 0 \le x \le L. \tag{13}$$

3 Numerical Procedure

Each above mentioned governing equation has been cast in the form

$$\frac{\partial}{\partial t}(\rho\phi) + \nabla \cdot (\rho \boldsymbol{V} \phi) = \nabla \cdot (\Gamma_\phi \nabla \phi) + S_\phi, \tag{14}$$

where ϕ, Γ_ϕ, and S_ϕ represent a general continuum-dependent variable, diffusion coefficient, and source term, respectively. The **SIMPLER** algorithm [18] for solving coupled elliptic partial differential equations can be used, with slight modifications for different source terms S_ϕ. Since each of the continuum equations is valid throughout the entire domain including solid and liquid and thus eliminates the need to track the melting front, consideration needs only be given to external boundary conditions, i.e., zero velocities, insulated and non-permeable (see Fig. 1).

Some assumptions to evaluate the melting rate: The species equation in the continuum model [15, 16] does not include the effect of a semi-permeable plane between ice and liquid regions, that is a very important relation to estimate the melting rate. Generally the melting rate is determined by the relation

$$\dot{m}_n = \frac{j}{1 - m_{\ell F}} = -\frac{\rho D}{1 - m_{\ell F}} \frac{\partial m_\ell}{\partial n}, \tag{15}$$

valid for a semi-permeable plane [19]. Since a sharp interface (melting front) does not appear in the continuum model, the melting rate can be calculated from $\partial f_\ell/\partial t$ based on the concentration m as the solution of the species equation (see (7)). However $\partial f_\ell/\partial t$ does not include the effect of a semi-permeable plane indicated by (15) due to the proper nature of the continuum model. Therefore, it is necessary to include the semi-permeable effect into the continuum model. In the present study the following treatment is able to overcome the problem. Mass transfer in the melting-front-control volume including ice and liquid regions (x_F) should be dominated by diffusion (Fickian) due to the proper nature of the melting front as illustrated in Fig. 3. Therefore the melting mass per unit time and volume,$\rho(\partial f_\ell/\partial t)$, is assumed to relate approximately to the semi-permeable plane of (15) as follows

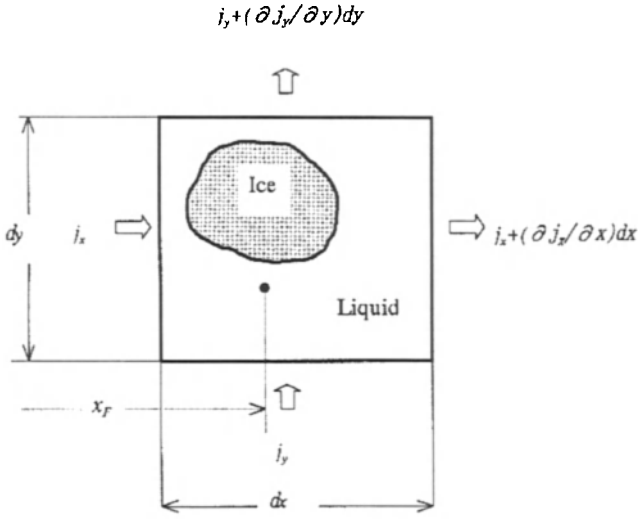

Fig. 3. Illustration of the melting-front-control volume for the calculation of the melting mass per unit volume and time

$$\rho\frac{\partial f_\ell}{\partial t} \cong -\frac{\partial j_x}{\partial x} - \frac{\partial j_y}{\partial y} \cong -(1 - m_{\ell F})\nabla\dot{m}. \tag{16}$$

The melting mass per unit time and volume appeared in the second term on the right hand side of the energy (4) is defined as

$$\dot{M} = -\nabla\dot{m} \cong \frac{\rho}{1 - m_{\ell F}}\frac{\partial f_\ell}{\partial t}. \tag{17}$$

Since the above relation means that the melting mass will jump in the melting-front-control volume, the liquid fraction f_ℓ should be replaced by

a new value during the iteration process. This procedure may be expressed as

$$\dot{M}^i \cong \frac{\rho}{1 - m^i_{\ell F}} \frac{f^i_\ell - f^0_\ell}{\Delta t}, \quad f^{i+1}_\ell = f^0_\ell + \frac{\dot{M}^i}{\rho} \nabla t. \tag{18}$$

Treatment of physical properties: Harmonic means of physical properties are adopted in this numerical calculation due to their abrupt change near the melting front; this has been recommended by Patankar [18] to obtain physically correct solutions. However diffusion in the solid (ice) region has been neglected in the continuum model [15, 16]. Since this signifies that the mass diffusion coefficient of ice is also zero (i.e.$D_s = 0$), the harmonic mean of the mass diffusion coefficient at the interface of the control volumes becomes zero, when the liquid mass fraction of the control volume becomes unity (i.e. $f_{\ell F} \Rightarrow 1$). Under such a situation the melting stops and no longer continues, which is physically improbable. To overcome this difficulty, the mass diffusion coefficient in the continuum model is assumed as

$$D = D_F + f_\ell D_\ell, \tag{19}$$

where D_F is assumed to have a very small value of $D_F = 0.00001 D_\ell$, that might be seen as a surface diffusion on the solid material. This assumption does not affect the calculation of the concentration in the solid and liquid domains due to the very small value of D_F.

Table 1. Physical properties of $CaCl_2$-H_2O mixture

(T= - 5°C, $1 - m_\ell = 20$ wt%)

$c_\ell = 3.044$	kJ(kgK)$^{-1}$	$\rho_s = 920$	kgm^{-3}
$c_s = 2.39$	kJ(kgK)$^{-1}$	$\beta_T = 0.00033$	K^{-1}
$\lambda_\ell = 0.535 \times 10^{-3}$	kJ(msK)$^{-1}$	$\beta_m = -0.916$	(kg/kg)$^{-1}$
$\lambda_s = 2.21 \times 10^{-3}$	kJ(msk)$^{-1}$	$D_\ell = 0.335 \times 10^{-9}$	m^{2}s
$\mu_\ell = 0.00386$	kg(ms)$^{-1}$	$h_f = 279$	kJkg^{-1}
$\rho_\ell = 1193.9$	kgm^{-3}	$K_0 = 5.56 \times 10^{-11}$	m^2

Table 1 shows the physical properties used in the present numerical predictions which were taken from the references [17, 20]. The thermal volumetric expansion coefficient β_T and the concentration volumetric expansion coefficient β_m were calculated from their definition by a least square approximation of the relation of density, temperature and concentration. Since it is

difficult to find the mass diffusion coefficient D_ℓ of a $CaCl_2$ aqueous solution for high concentrations and low temperatures which appears in the present study, $D_\ell = 0.335 \times 10^{-9} \mathrm{m^2 s^{-1}}$ was adopted as a mean value for mixtures by the same treatment as in the former report [14]. The temperature dependence of the latent heat for melting will be expressed as follows [21]

$$h_f = h_{fM} - T^2(c_\ell^\alpha - c_s^\alpha)\left(\frac{T_M}{T^2} - \frac{1}{T}\right). \tag{20}$$

The following criterion for the iteration convergence was adopted.

$$\frac{\left|\phi^{i+1} - \phi^i\right|_{max}}{\left|\phi^{i+1}\right|_{max}} < \varepsilon_\phi. \tag{21}$$

Since the numerical solution will be largely dependent on the mesh size Δx in the x-direction due to the very complicated flow in the melt liquid and the very thin diffusion boundary layer adjacent to the melting front, it is necessary to set very small mesh sizes to obtain precise and physically reasonable numerical solutions. In these calculations, variable mesh sizes were adopted in the x-direction, which increase gradually with a rate of 1.5 times till $i = 4$ (i.e. $\Delta x_{i+1} = 1.5\Delta x_i$) as an initial set-up in the liquid domain. The most desirable mesh size Δx_F in the control volume of the melting front is 0.1 mm [14], and accordingly, it is necessary to have the same mesh size in solid (ice) domain, initially $\Delta x = 0.1$ mm.

Definition of mean melting mass M and physical properties: The mean melting mass per unit area ($H \times 1$) is defined as

$$M = \left[\int_0^t \int_0^H \int_0^L \dot{M} dx dy dt\right] \Big/ H; \tag{22}$$

it allows comparison with the experiments.

4 Experiment

Instrumentation: All ice melting experiments were performed in a temperature controlled room. The initial temperatures of the ice plate and liquid were arranged by adjusting the room temperature, and the room temperature was maintained slightly below the initial temperature of the ice plate during the melting process. Fig. 4 shows a schematic view of an ice plate and a test cavity employed in this experiment. The cavity was made of lucite and styrofoam plates. The height of the ice plate and cavity is H, also corresponding to the depth of the liquid. A square cross sectional gap, having dimension of $2x_{Fi}$ was manufactured in a center position in the cavity to slide down the ice plate at the beginning of the experiment. The length L of the cavity was adjusted by setting the desired thick styrofoam plates in the cavity, as shown

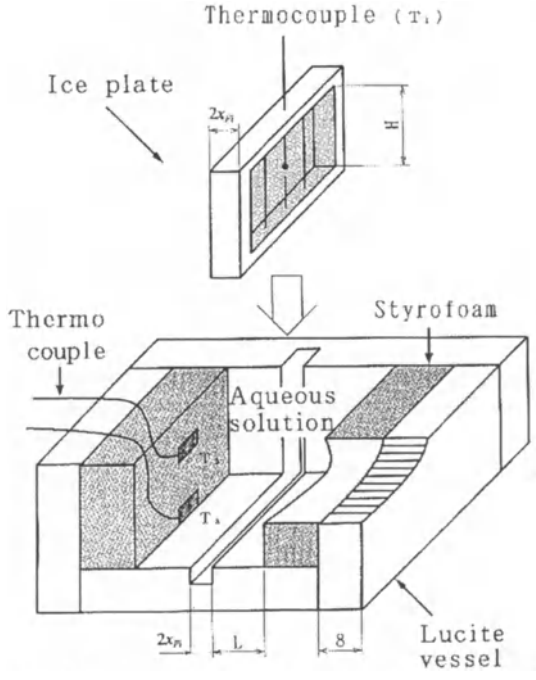

Fig. 4. View of the experimental apparatus for the melting of an ice plate

in Fig. 4. The side wall of the styrofoam had two thermocouple sensors with copper foil for the measurement of the temperatures T_2 and T_3. The ice plate was formed inside a lucite made frame to prevent crush and corner melting of it. The greatest difficulty in this experiment was to measure the temperature at the melting front T_F. It is difficult to measure T_F directly because of the steep temperature gradient near the melting front.To overcome this difficulty the local temperature inside the ice plate T_1 (see Fig. 1) was measured. Except at an early stage of melting, T_1 was assumed to equal T_F due to the larger thermal conductivity of the ice compared to that of the liquid. The transient temperature depression in the ice plate, T_1, was measured with a thermocouple placed in a thin stainless tube located in the center of the ice plate ($y = H/2$). These thermocouples were connected to a digital mulchmeter (YOKOGAWA, MODEL-7561), a programmable scanner (YOKOGAWA, MODEL-7501), and a personal computer (NEC, PC9801).

The accuracy of the temperature measurement was about $\pm 0.2°C$. The determination of the initial concentration of the mixture was performed by measuring the masses of $CaCl_2$ and distilled water with an accuracy of $\pm$ 0.2wt%. The experimental uncertainty of the mean melting mass M is about $\pm$ 5%.

Procedures and materials: The cavity was filled with a calcium chloride aqueous solution of a prescribed initial solute concentration $1 - m_{\ell i}$=0.2 (20wt%), and the liquid was adjusted to the initial temperature $T_{\ell i}$. On the other hand, the temperature of the ice plate, produced outside the cavity, was adjusted to the initial temperature T_{si}. Next, the ice plate was gently immersed into the liquid to prevent disturbing the liquid. After a pre-selected time interval, the ice plate was quickly pulled out and the nominal liquid stuck to the ice surfaces was wiped off with a blotting paper. Then the mass of the ice plate was measured to obtain the mean melting mass M.

Two techniques for flow visualization were employed using powder milk tracers to catch the stream lines and black ink solution to investigate the direction of the flow, which revealed a very complicated double diffusive convection in the melt liquid. Before the melting experiment, a small amount of powder milk was suspended in the liquid. A slit light beam of halogen lamps was illuminated from above during 15 seconds, just after the desired melting time had passed, and photographs were taken at the same time. The liquid used in this experiment is a solution of a calcium chloride ($CaCl_2$) in water (H_2O). The equilibrium phase diagram of the liquid is of an eutectic type as illustrated in Fig. 2, and the liquidus line indicating thermodynamic equilibrium of temperature and concentration is expressed by (8). The air bubble free ice plate used in this experiment was made of distilled and degasified water because air bubbles rejected from the melting front would disturb the flow in the liquid. The ice plate was flattened by melting the surface of it with a weakly heated copper plate.

5 Results and Discussion

Flow, isotherms and concentration isopleths in the melting system: Fig. 5 shows (a) velocity vectors, (b) isotherms, and (c) isopleths of solute concentration in the melting system during the melting process. The liquid temperature near the melting front will decrease due to the absorption of latent heat for spontaneous ice melting controlled by temperature and concentration, which causes the liquid density to increase. This would cause the liquid to flow downward (negative buoyancy). On the other hand, the concentration near the melting front will decrease due to the release of melt water, which causes the liquid density to decrease. This will destabilize the liquid (positive buoyancy). However the predominance of the positive buoyancy due to density/concentration decrease (i.e.$|\beta_m| \gg |\beta_T|$) causes the liquid to move upward as shown in Fig. 5a. Therefore there appears a very thin concentration-boundary layer adjacent to the melting front. On the other hand, outside the concentration-boundary layer appears a downward thermal convection like a counter clock-wise circulation. Eventually low density and low temperature melt liquid rises up along the melting front and accumulates in an upper part of the liquid, which can be recognized as a stratified layer

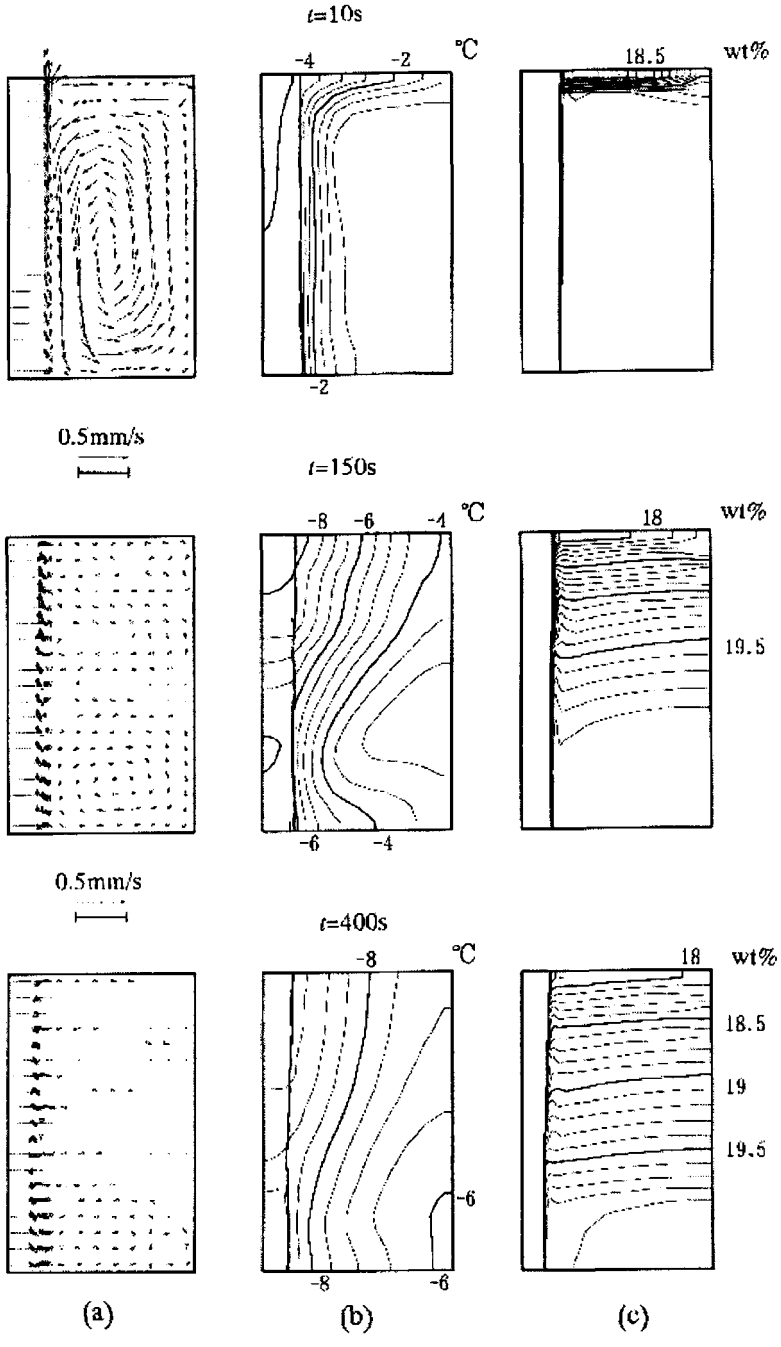

Fig. 5. Time history of (a)velocity vectors, (b) isotherms [°C](equal increments), and (c) solute concentration isopleths of $1 - m_\ell$ [wt%] (equal increments) (H=20 mm, L=12.5 mm, x_{Fi}=2,5 mm)

as shown in Fig. 5c. This diluted stratified layer is almost quiescent as can be seen by the velocity vectors. The diluted layer thickness increases gradually during the melting process. In the thermal convection layer under the diluted layer the concentration of the liquid remains almost at the initial concentration ($1 - m_{\ell i}$=0.2 (20wt%)), while the temperature of it decreases gradually. However, the flow velocity in the undiluted layer becomes gradually weak as time passes. The liquid domain in the cavity is almost totally contaminated by the melt water after t=400s, and a small circulation of thermal convection is seen near the bottom of the cavity. The ice plate will continue to melt until the melting system reaches entirely the thermodynamic equilibrium of both, uniform temperature and concentration.

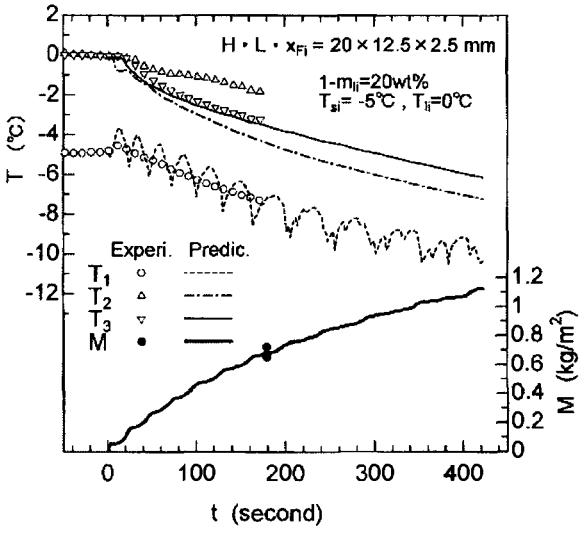

Fig. 6. Comparison of predictions and experiments for the temperature decrease of T_1, T_2, T_3 and the mean melting mass M

Transient temperature decrease in the melting system and mean melting mass: Fig. 6 shows the comparisons of predictions and experiments for the transient temperature decrease in the melting systems and for the transient mean melting mass. As already explained above, the initial temperature of the ice plate T_{si} is -5 °C and the initial liquid temperature $T_{\ell i}$ is 0°C. Since the initial thickness of the ice plate x_{Fi} is very thin (2.5 mm), the temperature in the ice T_1 is considered to be approximately equal to the melting front temperature T_F, except during an early stage of melting. The experimentally obtained temperature of the ice T_1 slightly increases after the melting starts to a maximum of about -4.5°C. Then the temperature decreases monotonically during the melting process. This typical behavior

of the temperature T_1 transience is considered to correspond approximately to the behavior of the melting front temperature T_F as mentioned above. This typical behavior of the temperature decrease seems curious, however it is reasonable if attributed to the spontaneous melting of ice in mixtures induced by the driving force of mass diffusion. Moreover, Fig. 6 visualizes that the numerically obtained temperature T_1 decreases with a wavy fluctuation. This physically improbable behavior is ascrived to a proper nature of the continuum model employed in the present study, which is one of the weak points of the model. Generally it is said that the continuum model are considered unsuitable for addressing a discrete phase change having a sharp melting front like in the present study, and also are frequently criticized for "smearing" discrete phenomena. However it is seen that the present numerical results predict quantitatively well the experimental results. Therefore it is noteworthy that the presented numerical treatment related to the melting-front-control volume makes it possible to apply the continuum model to the discrete phase-change problem.

The concentration gradient which appears near the melting front induces the melting of ice. At this time it is necessary to absorb the heat for melting from ice and liquid regions, and therefore a temperature gradient will appear at the melting front as outlined by the concept of Johnson and Mollendorf [8] and as mentioned in the Introduction. For this reason the temperature of the melting system will decrease spontaneously as shown in Fig. 6. The Lewis number Le is very large and amounts to 400 in this problem. This means that the rate of mass diffusion is very slow as compared to the rate of heat conduction. Therefore, the melting of ice will be dominated by mass diffusion. The temperatures T_2 and T_3 on opposite points of the vertical insulated wall (see Fig. 1) will begin to decrease monotonically from the initial temperature of the liquid at 0°C. This is attributed to the flow circulation in the liquid as shown in Fig. 5. The numerically obtained mean melting mass M increases monotonically during the melting process, and as time passes the melting rate decreases as in a classical Stefan problem. However M indicates a slightly wavy fluctuation. This is also ascribed to the proper nature of the continuum model as mentioned above for the temperature decrease of T_1. It is noteworthy that M takes a comparatively large value of about 0.7 kgm^{-2} at t=180s. In case of equal initial temperatures of the liquid and the ice plate ($T_{\ell i} = T_{si}$=-5°C), M decreases to about 0.4 kgm^{-2} at t=180s [14]. Therefore the initial liquid temperature will largely affect the melting rate of ice in the mixtures.

6 Concluding Remarks

The melting of a vertical ice plate immersed into a calcium chloride aqueous solution was considered numerically and by experiments. Summing up the results, the following can be concluded:

- The ice plate melted spontaneously under a double diffusive effect of temperature and concentration.
- The present two-dimensional numerical model, complemented by some assumptions for the melting-front-control volume of the continuum model [15, 16], was able to predict approximately the melting rate and the abrupt temperature decrease in the melting system, which had not been previously reported.
- It was found that the mesh size Δx_F of the control volume near the melting front should employ a small size of about 0.1 mm to predict correctly the melting mass and the complicated double diffusive natural convection in the liquid phase due to the very thin concentration boundary layer adjacent to the melting front.

Acknowledgements: The authors wish to acknowledge support for this study by the technical official T. Fujita and the under graduate student T. Oshima.

Nomenclature

a : thermal diffusivity of the liquid, m^2s^{-1}
c : specific heat, $kJ(kgK)^{-1}$
D : mass diffusion coefficient, m^2s^{-1}
f : mass fraction (see Fig. 2)
g : gravitational acceleration, ms^{-2} or volume fraction
h_f : latent heat of melting at the eutectic temperature T_e, $kJkg^{-1}$
H : height of the cavity (=height of an ice plate and liquid layer), mm
j : net mass diffusion (Fickian), $kgm^{-2}s^{-1}$
K : permeability, m^2
K_0 : permeability coefficient, m^2
L : length of the cavity, mm, or (6)
Le : Lewis number
m : concentration, kg/kg
m_ℓ : water (solvent) concentration kg/kg
$1 - m_\ell$: $CaCl_2$ (solute) concentration kg/kg
$\dot{m}$: melting mass per unit area and time (=melting rate), $kgm^{-2}s$
M : mean melting mass per unit area, kgm^{-2}
$\dot{M}$: melting mass per unit volume and time, (17), $kgm^{-3}s^{-1}$
p : pressure, Nm^{-2}
S_ϕ: source term
t : time, s
T : temperature, °C in (8) or K in (20)
T_1 : temperature in the middle ($x = 0$, $y = H/2$) of an ice plate (see Fig. 1), °C or K

T_2 : temperature at the upper right side corner ($x = L$, $y = H$) (see Fig. 1 and Fig. 4), °C or K
T_3 : temperature at the lower right side corner ($x = L$, $y = 0$) (see Fig. 1 and Fig. 4), °C or K
T_e : eutectic temperature of a $CaCl_2$ aqueous solution, °C or K
T_F : temperature at the melting front, °C or K
T_M : 0 °C (273.15 K)
u : x-component velocity, ms^{-1}
v : y-component velocity, ms^{-1}
$\mathbf{V}$: velocity vector, ms^{-1}
x : horizontal coordinate
x_F : thickness of ice plate
Δx_F : x-direction mesh size of the melting front and solid region control volume (0.1 mm)
y : vertical coordinate
β_m : concentration expansion coefficient, $(kg/kg)^{-1}$
β_T : temperature expansion coefficient, K^{-1}
Γ_ϕ : general diffusion coefficient
ε_ϕ : convergence criterion ($=10^{-5}$), (21)
λ : thermal conductivity, $kJ(msK)^{-1}$
μ : viscosity, $kg(ms)^{-1}$
ρ : density, kgm^{-3}
ϕ : general dependent variables (u, v, T, m)

Subscrits:
F : melting front
i : initial
ℓ : liquid
m : concentration
M : evaluated at T_M
r : reference value
s : solid (ice)
T : temperature

Superscripts:
α : water (H_2O)
0 : old value at time t of the variable
i : iteration number, equations (18) and (21)
n : nominal to surface

References

1. O. M. Griffin, Heat, mass, and momentum transfer during the melting of glacial ice in sea water, *ASME Journal of Heat Transfer* **95**, 317-323 (1973).
2. E. Marschall, Free convection melting on glacial ice in saline water, *Lett. Heat Mass Transfer* **4**, 381-384 (1977).

3. H. E. Huppert and J. S. Turner, Ice blocks melting into a salinity gradient, *J. Fluid Mech.* **100** (part2), 367-384 (1980).
4. E. G. Josberger and S. Martin, A laboratory and theoretical study of the boundary layer adjacent to a vertical melting ice wall in salt water, *J. Fluid Mech.* **111**, 439-473 (1981).
5. V. P. Carey and B. Gebhart, Transport near a vertical ice surface melting in saline water, some numerical calculations, *J. Fluid Mech.* **117**, 379-402 (1982a).
6. V. P. Carey and B. Gebhart, Transport near a vertical ice surface melting in saline water, experiments at low salinities, *J. Fluid Mech.* **117**, 403-423 (1982b).
7. B. Sammakia and B. Gebhart, Transport near a vertical ice surface melting in water of various salinity levels, *Int. J. Heat Mass Transfer* **26**, 1439-1452 (1983).
8. R. S. Johnson and J. C. Mollendorf, Transport from a vertical ice surface melting in saline water, *Int. J Heat Mass Transfer* **27**, 1928-1932 (1984).
9. M. Sugawara, H. Inaba, H. Nishimura and M. Mizuno, Melting of horizontal ice layer from above by combined effect of temperature and concentration of aqua-solvent, *Wärme- und Stoffübertragung* **21**, 227-232 (1987).
10. C. Beckermann and R. Viskanta, Double-diffusive convection due to melting, *Int. J. Heat Mass Transfer* **31**, 2077-2089 (1988).
11. W. Schutz and H. Beer, Melting of ice in pure and saline water inside a square cavity, *Chemical Engineering and Processing* **31**, 311-319, (1992).
12. S. Fukusako, M. Tago, M. Yamada, K. Kitayama and C. Watanabe, Melting heat transfer from a horizontal ice cylinder immersed in quiescent saline water, *ASME Journal of Heat Transfer* **114**, 34-4 (1992).
13. M. Sugawara and S. Sasaki, Melting of snow with double effect of temperature and concentration, *ASME Journal of Heat Transfer* **115**, 771-775 (1993).
14. M. Sugawara and T. Fujita, Melting of an ice layer with double effect of temperature and concentration (2nd report, Development of numerical prediction with flow visualization), *Trans. of JSME (Ser. B)* **63**, 2784-2792 (1997).
15. W. D. Bennon and F. P. Incropera, A continuum model for momentum, heat and species transport in binary solid-liquid phase change systems-I. Model formulation, *Int. J. Heat Mass Transfer* **30**, 2161-2170 (1987).
16. W. D. Bennon and F. P. Incropera, A continuum model for momentum, heat and species transport in binary solid-liquid phase change systems-II. Application to solidification in a rectangular cavity, *Int. J. Heat Mass Transfer* **30**, 2171-2187 (1987).
17. Japan Society of Mechanical Engineering, JSME Data Book: *Thermo-physical Properties of Fluid* (in Japanese), 461-467 (1983).
18. S. V. Patankar, *Numerical Heat Transfer and Fluid Flow*, Hemisphere Pub. Co, (1980)
19. E. R. G. Eckert and R. M. Drake, Analysis of Heat and Mass Transfer, McGraw-Hill Book Company, 718-719 (1972).
20. *Hand Book of Air Conditioning System Design* (part 4), McGraw-Hill Book Company, 32-35 (1965).
21. O. M. Silvares, E. G. Cravalho, W. M. Toscano, and C. E. Huggins, The Thermodynamics of Water Transport From Biological Cells During Freezing, *Transactions of the ASME*, Series C, **97**, 582-588 (1975).

(Received 12 Feb. 1999, accepted 28 May 1999)

An Analytic Solution Prescribing the Time-Dependent Formation of a Solid Crust Inside a Convectively Cooled Plane Channel

Bernhard Weigand[1], Michel Arnal[2], and Zygmunt Lipnicki[3]

[1] ITLR, University of Stuttgart, Pfaffenwaldring 31, D-70550 Stuttgart, Germany
[2] ABB Power Generation Ltd, CH-5401 Baden, Switzerland
[3] University of Zielona Gora, P-65-246 Zielona Gora, Poland

Abstract. A simple, analytical, approximate solution is given for calculating the time-dependent development of the ice-layer thickness inside a parallel-plate channel with forced-convection, laminar flow. The upper and the lower walls of the channel are cooled by uniform external convection. By ignoring the effect of acceleration on the shape of the velocity profile, which is due to the converging ice-layers in the axial direction, an analytical solution for the variation of the ice-layer thickness with time and axial position could be obtained.

The approximate solution was compared with numerical calculations and good agreement was found. The resulting closed-form solution for the ice-layer thickness shows that several solutions can exist. An analysis of the results shows which of the possible solutions is the physically relevant one.

1 Introduction

The freezing of liquids in forced-convection internal flows is of technical importance. This type of solidification process arises for example, in the flow of liquid metals in parallel-plate heat exchangers. Furthermore, it is also observed in casting operations, where molten material is poured through channels and nozzles, the walls of which are initially below the freezing temperature of the flowing metal.

Many theoretical and experimental studies have been performed which examine the fluid flow and heat transfer in circular tubes and parallel-plate channels with a constant wall temperature. Early investigations were reported by Zerkle and Sunderland [11] and Lee and Zerkle [3] for the steady-state freezing of laminar flow inside a horizontal tube. Under the assumption of a parabolic, axial-velocity distribution along the entire length of the tube and with an appropriate coordinate transform, they were able to reduce the problem to the classical Graetz problem without solidification. Özisik and Mulligan [5] used a slug-flow approximation for the liquid core to analyze transient freezing in isothermal circular tubes. Weigand and Beer [8] studied the transient development of the frozen crust in a plane channel with a constant wall temperature. For laminar flow, they obtained an approximate,

analytical solution for the distribution of the ice-layer thickness assuming a parabolic axial velocity distribution along the length of the channel.

All the above-mentioned studies focused on the case of a uniform temperature for the cooled walls. When the pipe or duct is exposed to a meteorological environment or is buried in permafrost with thermal insulation, then a convective boundary condition outside the channel is more realistic. Zerkle [10] studied the case of convective-cooling boundary conditions for a laminar pipe flow. Cheng and Wong [1] examined the equivalent case for laminar flow inside a plane channel. They obtained the freezing front for steady-state conditions by making the simplifying assumption of Zerkle and Sunderland [11]. By using several integral transforms Sadeghipour et al. [6] obtained the analytical temperature distribution inside a convectively cooled pipe. However, the distribution of the frozen crust had to be calculated numerically by the authors.

Sampson and Gibson [7], Weigand and Ruß [9] and Lipnicki and Weigand [4] studied the occurrence of solid blockage due to freezing in a pipe and a parallel plate channel. In contrast to all the above-mentioned papers, these studies were based on the assumption of a constant pressure drop along the pipe or channel length for all times. This made it possible to simulate the complete blockage due to freezing, because the volume flow tends to zero with increasing ice-layer thickness.

The object of the present paper is to develop a simple approximate solution for the time-dependent growth of the ice-layers in a convectively-cooled, parallel-plate channel with laminar flow. The flow rate in the channel is assumed to be constant, so that complete blockage due to freezing in the channel can never occur. Because the analysis results in a closed-form solution for the thickness of the frozen crust as a function of time and axial coordinate, the existence of multiple solutions for the ice-layer thickness at a particular time can be easily examined.

2 Analysis

Fig. 1 shows the geometry and coordinate system of the symmetric plane channel. The laminar flow enters the cooled test section at $x = 0$ with a fully-developed velocity profile and constant temperature T_0. At time t = 0, the ambient temperature is suddenly lowered from T_0 to the temperature T_∞ for the region $x > 0$. The external temperature T_∞ is lower than the freezing temperature T_F of the fluid.

Heat transfer takes place by conduction through the channel walls and by convection to the surroundings. Therefore, the liquid is cooled as it flows through the channel and eventually the freezing temperature T_F of the fluid is reached at the walls for $x = L_S$. Thus, the thermal entrance region consists of an ice-free zone and a freezing zone, where the solid layer increases monotonically with the axial coordinate.

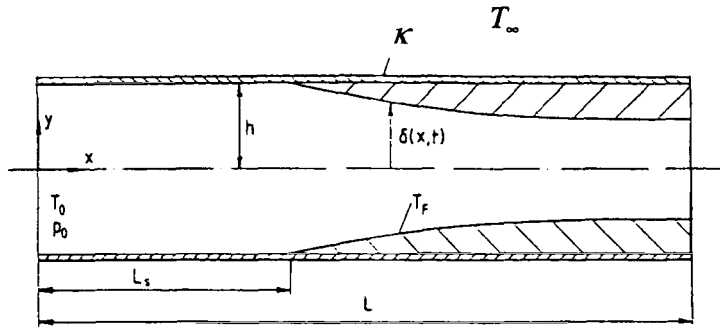

Fig. 1. Physical model and coordinate system

In the following analysis it is assumed that the flow is laminar, the physical properties are constant and axial heat conduction, viscous energy dissipation and free convection are negligible. Furthermore, quasi steady-state conditions are assumed. This is justified because typical time scales in the fluid flow are $O(\delta^2/\nu_L)$ and much smaller than the typical time scale of the freezing process, which is $O(r_S\delta^2\rho_S/k_F/(T_0 - T_F))$. All variables are summarized and defined in the Nomenclature at the end of the text.

2.1 The energy equation

The energy equation for the liquid region can be simplified by invoking the assumptions mentioned above. One obtains:

$$u\frac{\partial T}{\partial x} + v\frac{\partial T}{\partial y} = a_L\frac{\partial^2 T}{\partial y^2}. \tag{1}$$

(1) can be solved separately for the ice-free zone ($x < L_S$) and the freezing zone ($x \geq L_S$).

The solidification - free zone ($0 \leq x < L_S$). In this region Poiseuille flow occurs and no ice-layers are present at the channel walls. The energy equation for the hydrodynamically fully-developed flow in the thermal entrance region of the parallel plate channel is given in dimensionless form as

$$\frac{3}{2}(1-\bar{y}^2)\frac{\partial\bar{\theta}}{\partial\bar{x}} = \frac{\partial^2\bar{\theta}}{\partial\bar{y}^2}, \tag{2}$$

with the boundary conditions

$$\bar{x}=0: \quad \bar{\theta}=1, \qquad \bar{y}=0: \quad \frac{\partial\bar{\theta}}{\partial\bar{y}}=0, \qquad \bar{y}=1: \quad \frac{\partial\bar{\theta}}{\partial\bar{y}}=-\gamma\bar{\theta} \tag{3}$$

and the following dimensionless quantities

$$Re_h=\frac{\bar{u}_0 h}{\nu_L}, \qquad Pr=\frac{\nu}{a}, \qquad \bar{x}=\frac{x}{h}\frac{1}{Re_h Pr}, \qquad \bar{y}=\frac{y}{h},$$

$$\tilde{l}=\frac{l}{h}, \qquad \bar{\theta}=\frac{T-T_\infty}{T_0-T_\infty}, \qquad \gamma=\frac{\kappa h}{k_L}, \qquad \tilde{u}=\frac{u}{\bar{u}_0}. \tag{4}$$

The parameter γ, which appears in (3), represents the effect of external convective cooling. For $\gamma \to 0$, an adiabatic channel is represented, while for $\gamma \to \infty$ a uniform wall-temperature T_∞ is given.

The energy equation (2) together with the boundary conditions according to (3) can be solved by the method of separation of variables. One obtains:

$$\bar{\theta}=\sum_{n=1}^{\infty} A_n F_n(\bar{y}) exp(-\frac{\alpha_n^2}{4}\bar{x}). \tag{5}$$

The constants A_n and the Eigenvalues α_n for various values of γ can be found in the literature, see Hsu [2]. The Eigenfunctions $F_n(\bar{y})$ that appear in (5) are the solutions of the associated Sturm-Liouville problem, see Hsu [2].

The location at which the ice-layer starts to grow on the cooled walls ($x = L_S$) can be found from (5) by setting $T = T_F$ and $\bar{y} = 1$. This results in the following implicit equation for x_S:

$$\frac{T_F-T_\infty}{T_0-T_\infty}=\sum_{n=1}^{\infty} A_n F_n(1) exp(-\frac{\alpha_n^2}{4}\bar{x}_S)=\frac{1}{1+\theta_\infty}, \quad \theta_\infty=\frac{T_0-T_F}{T_F-T_\infty}. \tag{6}$$

The calculated value for the origin of the frozen crust x_S in a laminar flow is identical to that given by Cheng and Wong [1] for steady-state conditions.

The freezing zone ($L_S < x < L$). In the freezing zone, the velocity profile is assumed to be similar to that in the solidification - free zone. This assumption results in:

$$u=\frac{3}{2}\bar{u}\left[1-\left(\frac{y}{\delta(x,t)}\right)^2\right], \quad \bar{u}=\bar{u}_0\frac{h}{\delta(x,t)}, \quad v=\frac{y}{\delta(x,t)}\frac{\partial\delta}{\partial x}u, \tag{7}$$

where the velocity component v is obtained from the continuity equation. Note that in (7) it has been assumed that the freezing rate at the wall does not affect mass conservation in the longitudinal direction. The energy equation (1) in the freezing zone is given in dimensionless form by:

$$\frac{3}{2}\left(1-\eta^2\right)\frac{\partial\theta}{\partial\xi}=\frac{\partial^2\theta}{\partial\eta^2}, \tag{8}$$

with the dimensionless quantities:

$$\eta=\frac{y}{\delta},\quad \xi=\int_{\bar{x}_S}^{\bar{x}}\frac{d\alpha}{\bar{\delta}(\tau,\alpha)},\quad \tilde{\delta}=\frac{\delta}{h},\quad \theta=\frac{T-T_F}{T_0-T_F}. \tag{9}$$

(7) has to be solved in accordance with the following boundary conditions:

$$\begin{aligned}&\xi=0:\ \theta=\frac{1+\theta_\infty}{\theta_\infty}\bar{\theta}\left(\bar{x}_S\right)-\frac{1}{\theta_\infty},\\ &\eta=0:\ \frac{\partial\theta}{\partial\eta}=0,\quad \eta=1:\ \theta=0.\end{aligned} \tag{10}$$

Using the method of separation of variables, the solution of (8) can be found to be:

$$\theta=\sum_{m=1}^{\infty}B_m G_m(\eta)exp(-\frac{\beta_m^2}{4}\xi) \tag{11}$$

The Eigenfunctions $G_m(\eta)$ are solutions of the associated Sturm-Liouville problem. The Eigenvalues β_m can be found from the literature, Hsu [2].

2.2 Temperature distribution in the solid region

Assuming constant properties in the solid region and neglecting axial heat conduction, the energy equation in the solid phase for quasi-steady conditions can be easily integrated. The resulting temperature distribution in the solid is:

$$\frac{T_S-T_F}{T_F-T_\infty}=\frac{\tilde{y}-\tilde{\delta}}{\tilde{\delta}-1-k_S/(k_L\gamma)} \tag{12}$$

2.3 Growth of the solidified crust

The time-dependent development of the ice-layer at the channel walls is calculated from the interface energy equation, which takes the following form if terms proportional to $(\partial\delta/\partial x)^2$ are neglected:

$$k_S \left.\frac{\partial T_S}{\partial y}\right|_{y=\delta} - k_L \left.\frac{\partial T}{\partial y}\right|_{y=\delta} = \rho_S r_S \left(\frac{\partial \delta}{\partial t}\right)_x \tag{13}$$

(13) states the fact that the heat conducted into the solid plus that arising from the phase change equals the heat transported from the liquid to the interface. Introducing (12) into (13) yields:

$$\tilde{\delta}\left(\frac{\partial \tilde{\delta}}{\partial \tau}\right)_{\bar{x}} = \frac{\tilde{\delta}}{\tilde{\delta} - 1 - k_S/(k_L\gamma)} - \frac{1}{B} f(\xi, Pr) \tag{14}$$

where the following abbreviations have been used

$$\tau = FoSte, \quad Fo = \frac{ta_S}{h^2}, \quad Ste = \frac{c_S(T_F - T_\infty)}{r_S},$$

$$B = \frac{k_S}{k_L}\frac{1}{\theta_\infty}, \quad f(\xi, Pr) = \left.\frac{\partial \theta}{\partial \eta}\right|_{\eta=1}. \tag{15}$$

The function $f(\xi, Pr)$ in (14) represents the heat flux from the water to the ice-layer and must be calculated from (11). (14) has to be solved with the boundary condition:

$$\tilde{\delta}\,(\tau = 0, \xi) = 1. \tag{16}$$

(14) is a strongly nonlinear, integro-differential equation for δ. Because the heat flux from the flow to the ice-layer $f(\xi, Pr)$ is a known function, the equation can be solved by numerical integration. However, an approximate solution of (14) can also be derived as follows. By transforming the axial coordinate in (14) one gets:

$$\left(\frac{\partial \tilde{\delta}}{\partial \tau}\right)_{\bar{x}} = \left(\frac{\partial \tilde{\delta}}{\partial \tau}\right)_{\xi} + \left(\frac{\partial \tilde{\delta}}{\partial \xi}\right)_{\tau}\left(\frac{\partial \xi}{\partial \tau}\right)_{\bar{x}}. \tag{17}$$

In the preceding analysis, terms proportional to $(1/\tilde{\delta})(\partial\tilde{\delta}/\partial\xi)$ are assumed to be negligible. By employing this assumption in (14), the equation can

be integrated analytically, using (17). After some algebra one obtains the following closed-form solution for the development of the ice-layer thickness as a function of time and space:

$$\tau\left(\frac{\gamma_1}{\gamma_1-\tilde{\delta}_S}\right)-\tilde{\delta}_S\left(\tilde{\delta}_S-\gamma_1\right)ln\left(\frac{\tilde{\delta}-\tilde{\delta}_S}{1-\tilde{\delta}_S}\right) -\frac{1}{2}\left(\tilde{\delta}^2-1\right)-\left(\tilde{\delta}_S-\gamma_1\right)\left(\tilde{\delta}-1\right)=0 \tag{18}$$

with the following dimensionless quantities:

$$\tilde{\delta}_S=\frac{f(\xi,Pr)\gamma_1}{f(\xi,Pr)-B},\quad \gamma_1=1+\frac{k_S}{k_L}\frac{1}{\gamma}. \tag{19}$$

Upon inspection, it is clear that (18) satisfies the boundary condition given in (16). Consider the limiting case of a constant wall temperature, which means that $\gamma\to\infty$ and therefore that $\gamma_1\to 1$ in (18). For this case, (18) reduces to the equation given by Weigand and Beer [8].

Although the analysis given here has focused on internal laminar flow, (18) is also valid for turbulent internal flows if the appropriate heat flux $f(\xi,Pr)$ from the water to the ice-layer is used in (19). Expansions similar to those given in (5) also exist for turbulent flows. However, the expansions for the so-called turbulent Graetz problem are not given in Hsu [2].

3 Results and Discussion

Fig. 2 shows the transient development of the frozen crust for $\gamma=10$ and $B=10$. It can be seen that the thickness of the frozen crust increases monotonically with time. In the figure, the validity of the approximate solution obtained (18) is demonstrated by comparing it to the numerical integration of (14). One can see that the numerical solution, which was obtained with a four-stage Runge-Kutta method, agrees very well with the approximate analytical solution.

For smaller values of the convective parameter γ, the rate of heat transfer to the surroundings decreases. This can be seen by comparing Fig. 3(a) and Fig. 3(b), where the transient growth of the ice-layer is shown for two different values of γ. It can be seen that the thickness of the ice-layers is nearly independent of the axial coordinate for large values of x and small values of γ.

Excluding small values of the axial coordinate in (14) and neglecting the convective heat transferred from the fluid to the solid-liquid interface one obtains:

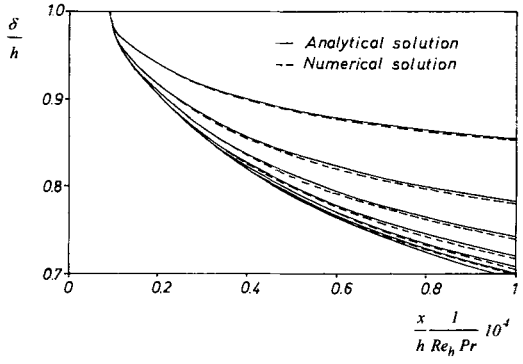

Fig. 2. Transient development of the frozen crust as a function of the dimensionless position with time-steps, $\Delta\tau = 0.15$. Parameters are $B = 10$, and $\gamma = 10$. Approximate analytical solutions are compared with the exact numerical results

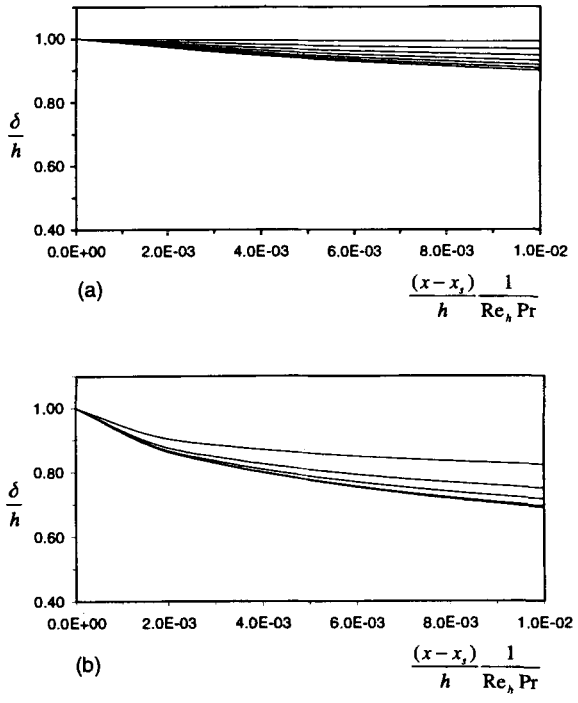

Fig. 3. Transient development of the frozen crust as a function of the dimensionless position. (**a**) $B = 2$, $\gamma = 0.15$, $\Delta\tau = 6$. (**b**) $B = 2$, $\gamma = 10$, $\Delta\tau = 0.4$

$$\left(\frac{\partial\tilde{\delta}}{\partial\tau}\right)_{\bar{x}} = \frac{1}{\tilde{\delta} - 1 - k_S/(k_L\gamma)}, \tilde{\delta}(0,\xi) = 1, \tag{20}$$

and integration leads to:

$$\tilde{\delta} = -\sqrt{2\tau + (\gamma_1 - 1)^2} + \gamma_1. \tag{21}$$

(21) reveals the above-mentioned constant thickness of the frozen crust for larger values of x. The same result is obtained from (14) if one assumes that the dimensionless freezing parameter B is very large. For such situations $\tilde{\delta}_S$ will attain very small values. Under this assumption and by assuming $\tilde{\delta} \gg \tilde{\delta}_S$ and $\tilde{\delta}_S \ll 1$ (21) can also be derived from (18) if one neglects the logarithmic term in (18).

3.1 Multiple solutions of the interface energy equation

As mentioned previously, (14) is a strongly non-linear, integro-differential equation. Therefore it is possible that the equation reveals multiple solutions for the thickness of the frozen crust. Because an approximate, closed-form solution has been derived, it is easy to check which of the possible solutions is the physically correct one. Fig. 4 shows a plot of the function $f(\tilde{\delta})$ derived from (18) and defined as:

$$f(\tilde{\delta}) = \frac{\tilde{\delta} - \tilde{\delta}_S}{1 - \tilde{\delta}_S} exp\left[\frac{\tilde{\delta}^2 - 1}{2\tilde{\delta}_S(\tilde{\delta}_S - \gamma_1)} + \frac{\tilde{\delta} - 1}{\tilde{\delta}_S}\right] - exp\left[\frac{\tau\gamma_1}{\tilde{\delta}_S(\tilde{\delta}_S - \gamma_1)^2}\right]. \tag{22}$$

The particular case illustrated shows the function at two different times with a single zero point which is the solution for the ice-layer thickness. The steady-state ice-layer thickness is also shown for comparison. As expected, as time increases the time-dependent ice layer thickness approaches the steady-state solution.

Because the ice-layer will always grow in thickness with time and position, $\partial\delta/\partial\tau$ must always be smaller or equal to zero. If this fact is used together with (14), it is possible to derive the following equation:

$$\tilde{\delta} \geq \frac{f(\xi, Pr)\gamma_1}{f(\xi, Pr) - B} = \tilde{\delta}_S \tag{23}$$

which states simply the fact that the developing ice-layer thickness must always be smaller than the steady-state thickness. It is also interesting to note that a developing ice-layer thickness which is larger than the stationary thickness ($\tilde{\delta} < \tilde{\delta}_S$) is automatically excluded due to the logarithmic term in (18). This means that the physically unrealistic solution cannot occur, due to the form of the equation.

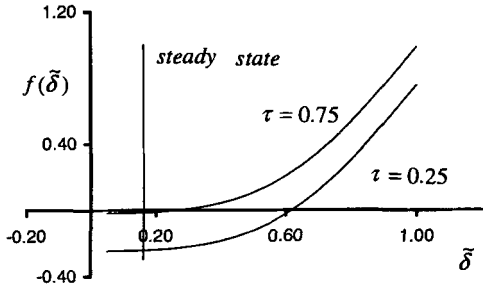

Fig. 4. Representative solutions of the interface energy equation given at different times, τ and compared with the steady-state solution. Parameters are $B = 10$, and $\gamma = 10$

4 Conclusions

A simple, analytical, approximate solution has been derived for calculating the transient development of the ice-layers on the cooled walls inside a convectively-cooled, parallel plate channel. The approximate solution has been compared with a numerical calculation and good agreement was found. The model given in the paper can easily be applied to turbulent internal flows by replacing the function representing the heat flux from the ice-layer into the internal flow in (18) and (19). The closed-form approximate solution for the ice-layer thickness shows that several solutions can exist. An analysis of the solution shows which of the possible solutions is the physically relevant one.

Nomenclature

a	thermal diffusivity	B	dimensionless freezing parameter $= k_S/(k_L\theta_\infty)$
A_n	Eigenfunction	F_n	Eigenfunction
Fo	Fourier number $= ta_s/h^2$	k	thermal conductivity
h	distance from centerline to the wall		
L	channel length	L_S	start of the ice layer
Pr	Prandtl number	r_S	heat of fusion
Re_{4h}	Reynolds number $= \bar{u}_0 4h/\nu_L$	Ste	Stefan number $= c_S(T_F - T_\infty)/r_S$
T	temperature	T_F	liquid freezing temperature
T_0	liquid inlet temperature	T_∞	coolant inlet temperature

$\bar{u}_0$ axial mean velocity at the entrance of the test section
θ Dimensionless temperature
θ_∞ Superheat ratio $= (T_0 - T_F)/(T_F - T_\infty$
τ dimensionless time $= FoSte$
κ overall external heat transfer coefficient $= [1/h_\infty + \delta_{wall}/k_{wall}]^{-1}$
γ convective parameter $= \kappa h/k_L$
α_n, β_n Eigenvalues
x, y coordinates
ν kinematic viscosity
δ free channel height

Subscripts

S solid
∞ coolant
L liquid
F freezing

Appendix A. Turbulent Internal Flow

For turbulent internal flow in the parallel plate channel the model given in the present paper can easily be applied by replacing the heat flux from the flow to the ice-layer in (18) and (19). For turbulent internal flow one may assume that

$$u/\bar{u} = g\,(y/\delta(x,t))\,, \tag{A.1}$$

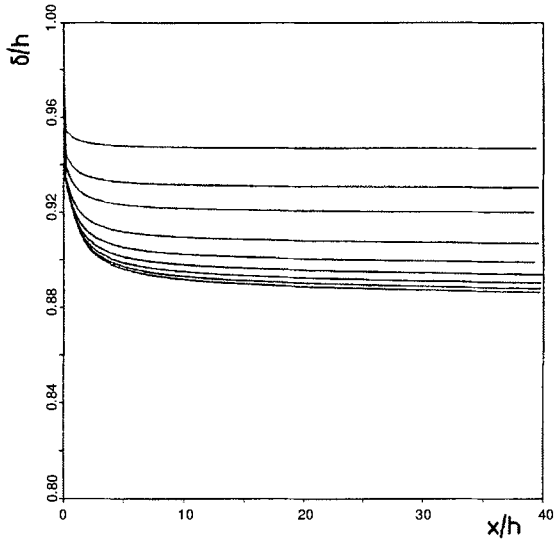

Fig. 5. Transient development of the frozen crust for turbulent flow. Parameters are $B = 5$, $\gamma \to \infty$, $\Delta\tau = 0.002$

where g is the velocity profile for a hydrodynamically fully developed flow between parallel plates. The solution of the energy equation leads then to a turbulent Graetz problem. The reader is referred to [12]. Fig. 5 shows the transient development of the frozen crust for turbulent internal flow in a parallel plate channel for $\gamma \to \infty$ for $Re_h = 5000$ and $Pr = 10$. It can be seen that the steady-state thickness of the crust is much thinner than for laminar flow because of the higher heat flux from the flow to the crust. The relative error between the numerical solution of (14) and the analytical approximate solution is smaller than 1% for turbulent flow and $\gamma \to \infty$ for $B < 20$.

References

1. Cheng, K. C., Wong, S.-L. (1977) Asymmetric solidification of flowing liquid in a convectively cooled parallel plate channel. *Appl. Sci. Res.* **33**, 309–335
2. Hsu, C. J. (1971) Laminar flow heat transfer in circular or parallel–plate channels with internal heat generation and the boundary conditions of the third kind. *J. of the Chin. Inst. of Chem. Eng.* **2**, 85–100
3. Lee, D. G., Zerkle, R. D. (1969) The effect of liquid solidification in a parallel–plate channel upon laminar-flow heat transfer and pressure drop. *J. Heat Transfer* **91**, 583–585
4. Lipnicki, Z., Weigand, B. (1996) An experimental investigation of the freeze shut of a convectively cooled parallel plate channel. *Proc. Fifth Int. Symp. Thermal Eng. and Sci. for Cold Regions*, Ottawa, Canada, 270–275
5. Özisik, M. N., Mulligan, J. C. (1969) Transient freezing of liquids in forced flow inside circular tubes. *J. Heat Transfer* **91**, 385–390
6. Sadeghipour, M. S., Özisik, M. N., Mulligan, J. C. (1982) Transient freezing of a liquid in a convectively cooled tube. *J. Heat Transfer* **104**, 316–322
7. Sampson, P., Gibson, R. D. (1981) A mathematical model of nozzle blockage by freezing. *Int. J. Heat Mass Transfer* **24**, 231–241
8. Weigand, B., Beer, H. (1992) Transient freezing of liquids in forced laminar liquid flow in a cooled parallel plate channel. *Wärme- und Stoffübertragung* **27**, 77–84
9. Weigand, B., Ruß, G. (1993) The freeze–shut of a convectively cooled parallel plate channel subjected to laminar internal liquid flow. *Wärme- und Stoffübertragung* **28**, 17–25
10. Zerkle, R. D. (1970) The effect of external thermal insulation on liquid solidification in a tube. *Proc. of the Southeastern Sem. of Thermal Sci.*, 1–19
11. Zerkle, R. D., Sunderland, J. E. (1968) The effect of liquid solidification in a tube upon laminar–flow heat transfer and pressure drop. *J. Heat Transfer* **90**, 183–190
12. Sakakibara, M., Endoh, K. (1977), Analysis of heat transfer in the entrance region with fully developed turbulent flow between parallel plates. *Heat Transfer / Japanese Research*, **6**, 54-61.

(Received 18 Feb. 1999, accepted 2 June 1999)

Melting Heat-Transfer Characteristics of an Inclined Ice Plate Immersed in a Hydrophobic Liquid

Masahiko Yamada, Shoichiro Fukusako, Tsuyoshi Kawanami, and Shigeki Hirano

Division of Mechanical Science, Graduate School of Engineering,
Hokkaido University N13-W8, Sapporo 060-8628, Japan

Abstract. An experimental study was conducted to investigate the melting heat-transfer characteristics of an inclined ice plate within a hydrophobic liquid. Recently, both melting of an ice layer and freezing of water within a hydrophobic liquid received increasing attention because of their close relation and their use in Science and Engineering. For example, the freezing of an aqueous solution within a hydrophobic liquid gives a basic model for the freezing of biomaterials. Furthermore, the melting of an ice layer has close relations to cold thermal storage using ice. In the present study, both perfluolocarbon (PFC) and silicon oil were adopted as the testing liquids. The ambient liquid temperatures ranged from 5 to 40°C. The inclination angle of the ice plate was varied from 0 to 180° at 30° steps. The experimental results revealed that the inclination angle of the ice layer has a vital effect on the melting heat-transfer characteristics of the ice.

1 Introduction

It is well known that materials such as oil, high-grade alcohol, some proteins and materials with a hydrophobic basis in the molecular structure do not solve with water in the liquid phase. Metals in some combination, such as aluminum and lead or lead and silicon do not diffuse into each other not even in their liquid phase. In freezing and melting of biomaterials containing proteins with hydrophobic properties, the phase change problem is that of an immiscible system. In these phase change problems of such an immiscible system, considerable effects of liquid films and droplets are formed by the melt material along the interface between the solid and ambient liquid, and these affect the melting characteristics. Melting phenomena are different from those of conventional melting because the melt liquid does not diffuse into the ambient liquid.

Melting of single component systems such as ice, pure metal, ordinary PCM as well as miscible multi-component systems with concentration diffusion, such as melting of ice in an aqueous solution, have extensively been studied. On the other hand, for melting problems without concentration diffusion, as e. g. melting of ice in a hydrophobic liquid such as oil and the

melting of benzene in hot water, very little research work has been reported so far.

Melting heat-transfer characteristics of an ice layer within a hydrophobic liquid has been reported for both a horizontal and for a vertical ice plate and horizontal ice cylinder [1-4]. The behavior of the melt-water layer formed on the ice plate exerts considerable effects on the melting of the ice layer, thus determinig the configuration of ice layer itself. We know of no investigation for the case of an inclined ice plate for which the effect of the behavior of the melt water will be accentuated.

In the present study, the effects of a variety of factors are studied such as temperature, inclination angle of the ice layer and the kind of ambient liquid. These have been investigated experimentally to determine the characteristic behavior of the melt-water film and the melt-water droplets, and to correlate them with the melting rate of ice layer.

2 Experimental Apparatus and Procedure

2.1 Experimental apparatus

Fig. 1 shows a schematic diagram of the experimental apparatus in the present study. It consists of a test vessel, a hydrophobic liquid reservoir, a supporting device of the ice plate (a cooling device), and cooling systems.

Fig. 2 shows a detail of the ice support (cooling device). It is made of both the cooling room, through which temperature controlled brine is circulated, and the insulation part which is filled with polystyrene foam to avoid heat loss. By spraying the cooling brine directly to the backside of the cooled plate, uniformity of the temperature of the cooled plate is achieved. The temperature of the cooled surface is measured by C-A thermocouples situated on the back-side of the cooled plate. The inclination angle of the ice support can be set in the range from 0 (upward horizontal) to 180° (downward horizontal) in steps of 30°.

The test vessel is made of an acrylic plate with interior dimensions of 280x260x130 mm. Double-glazing was utilized as a front window. The test vessel was covered with a thermal insulation of 50 mm thickness to keep the heat loss at a minimum. A thermostat was set above the test vessel to keep the temperature of the testing liquid constant by using both heater and stirrer. For the visualization of the flow pattern of the ambient fluid, aluminum powder and He-Ne laser was employed as a tracer and light source, respectively.

2.2 Procedure

In the present study, silicon oil and perfluorocarbon (PFC) were adopted as testing hydrophobic liquids. After reaching constant initial temperature of

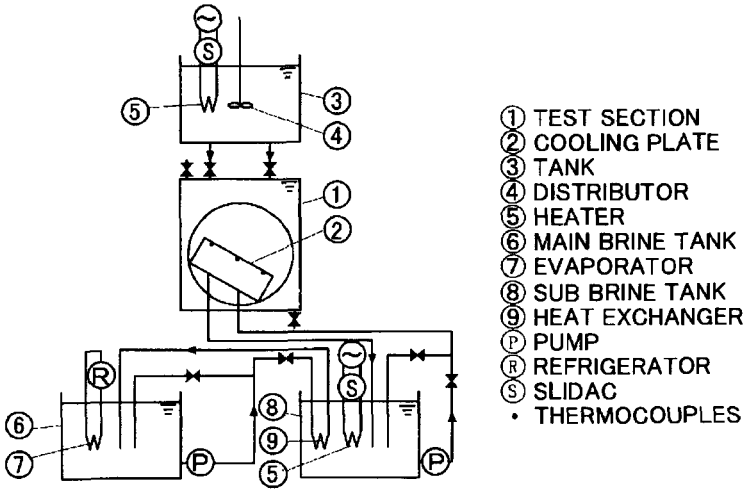

Fig. 1. Schematic diagram of the experimental apparatus

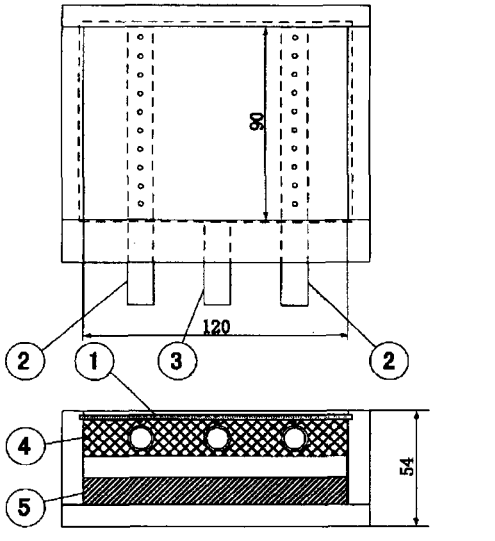

Fig. 2. Details of the ice support (cooling device)

the testing liquids within the reservoir, a transparent ice plate, 25mm high, 120mm wide, and 90mm long, was set on the cooled plate. By keeping the temperature of the cooled plate at about -2°C, the ice support was installed in the test vessel with prescribed inclination angle. Then the testing liquid was introduced into the test vessel from the reservoir above. After calming the turbulence by the introducing the test liquid, (about after a couple of minutes) the experiment was started.

With a prescribed interval from the start of the experimental run, the ice plate was photographed. The flow pattern of ambient liquid was also photographed with the exposure time of 30 sec. to 3min.

2.3 Heat transfer coefficient

By assuming that heat conduction within the ice layer can be neglected, the energy balance at the ice surface may be described as,

$$\rho_i L \frac{dy}{dt} = h_x (T_\infty - T_0)\,, \tag{1}$$

where T_0 and T_∞ are the temperatures far away from the interface in the liquid and the ice, respectively. Thus, the local heat transfer coefficient can be calculated by the equation

$$h_x = \frac{\rho_i L}{T_\infty - T_0} \frac{dy}{dt}\,, \tag{2}$$

where dy/dt is the melting rate which was assessed by the photographed ice configuration in prescribed time interval.

3 Results and Discussion

3.1 Melting characteristics

Figs. 3 and 4 show the melt-ice-layer configuration at three different times in silicon oil and PFC, respectively. The melting rate is more prononnced at the upper portion of the ice plate for silicon oil, and the ice configuration is wedge-shaped as shown in Fig. 3. On the other hand, for PFC shown in Fig. 4, the ice layer is more uniformly melting except at the lower portions of ice layer as manifested by the uniform thickness of the ice layer. At the bottom part of the ice layer the melting proceeds at the upper ice surface, not on the side surface. The reasons why we have there considerable differences in the melting behavior between silicon oil and PFC lies in the difference of the density between the ambient liquid and the melt water.

Fig. 5 shows the flow pattern along with brief sketches to explain the behavior of the melt layer and the temperature distribution of the ambient fluid

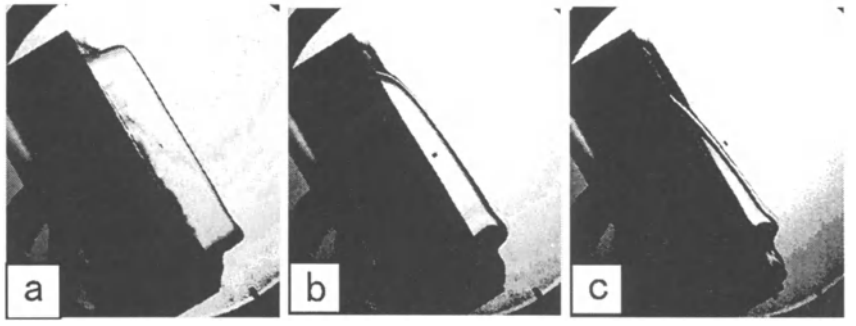

Fig. 3. Melting characteristics of the ice layer in silicon oil, a:0min. b:20min. c:40min.

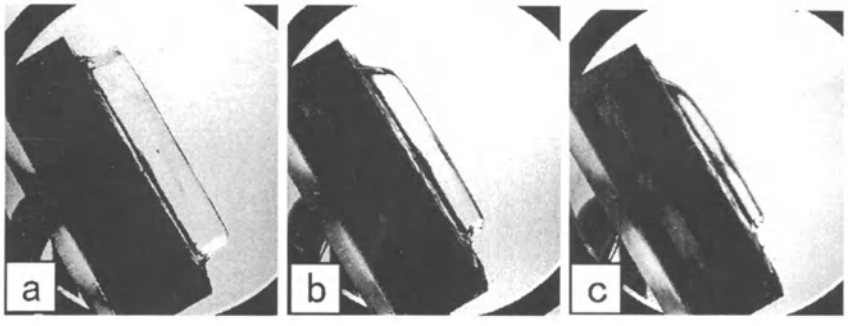

Fig. 4. Melting characteristics of the ice layer in PFC, a:0min. b:20min. c:40min.

around the ice layer for silicon oil and PFC, respectively. It can be observed in Fig. 5a that the ambient liquid flows towards the horizontal direction and then, reaches the ice layer to be cooled on the ice surface. The melt water flows downward along the ice surface because its density is larger than that of the ambient fluid. In other words, the flow direction of the melt water coincides with that of the ambient fluid flow. The movement of the ambient fluid on the ice surface is very smooth, the melt water flows downward so that the thickness of the melt-water layer grows along its downward path. The temperature distributions of the melt water and the ambient fluid at the interface are also sketched in Fig. 5a. The ambient fluid with high temperature gets in contact with the melt water film with lower temperature. As they move downslope they adjust their temperature as indicated in panel 3 of Fig. 5a. Thus, the temperature difference between the ambient fluid (silicon oil) and the melt water film decreases as one moves down to the lower portion of the ice layer. Consequently, melting of ice layer is larger in the upper portion of the ice layer where the temperature difference is greater than in the lower portion.

On the other hand, for the case of PFC shown in Fig. 5b, since the density of PFC is greater than that of melt water, the melt-water layer flows upward along the surface of the ice layer. Due to the bi-directional flow of the ambient fluid and the melt water on the ice surface, some small turbulence in the melt water flow is observed. Moreover, the thickness of the melt-water layer is not monotone along the downslope direction; it is larger in the upper part of the ice layer. Furthermore, the temperature distribution of ambient liquid and the melt water may be estimated as shown in panel 3 of Fig. 5b. Quite contrary to the case of silicon oil, the temperature of the melt-water layer is higher in the upper part; as a result, the temperature difference between the ambient liquid and the melt-water layer is almost constant as shown in Fig. 5b. Consequently, the ice layer in the PFC case is melting almost uniformly.

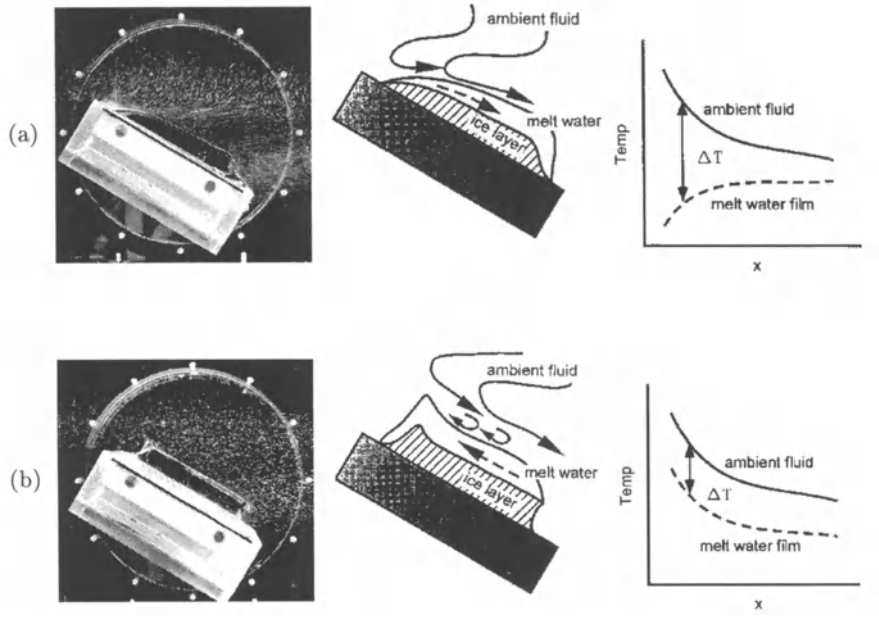

Fig. 5. Schematic sketch of the flow pattern and temperature distribution of the ambient liquid for silicon oil (a) and PFC (b)

3.2 Heat transfer characteristics

Figs. 6 and 7 show the melting heat-transfer coefficient of the ice layer for silicon oil and PFC, respectively. In silicon oil (Fig. 6) it shows a tendency

to be larger for the upper portion of the ice layer than that for the lower potion, and it decreased with time. On the other hand, in the PFC-case shown in Fig. 7, the melting heat-transfer coefficient is spatially almost constant. Furthermore, it does not so much decrease with time as for silicon oil.

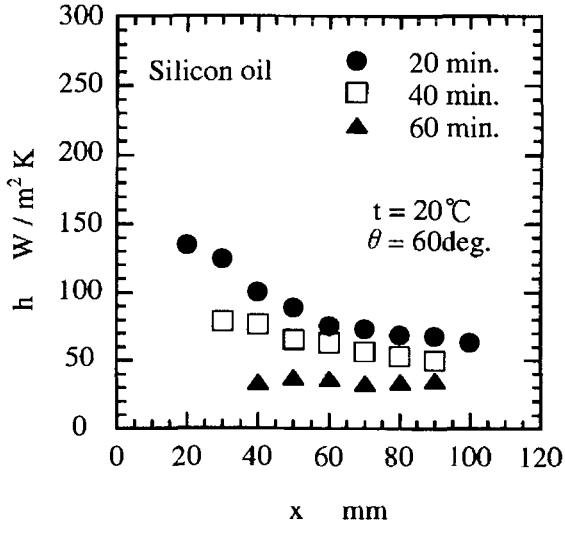

Fig. 6. Heat transfer coefficient for silicon oil

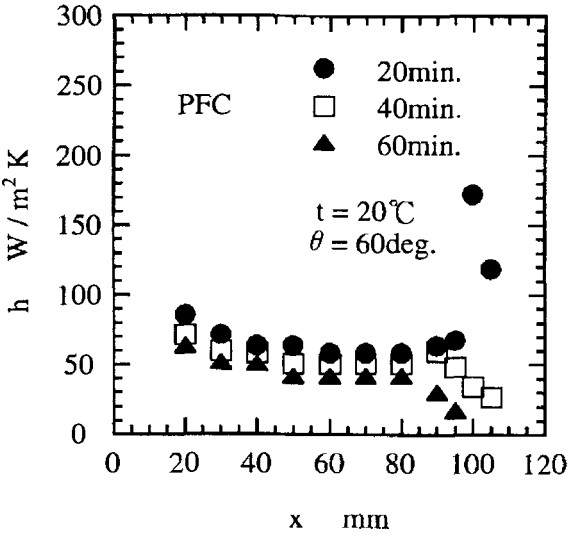

Fig. 7. Heat transfer coefficient for PFC

3.3 Effects of inclination angle of ice layer

Figs. 8 and 9 show the effect of the inclination angle of the ice layer on the melting heat-transfer coefficient. In these figures, the ordinate denotes the average heat transfer coefficient, while the abscissa shows the inclination angle from the horizontal orientation of the ice layer. Each symbol in these figures represents the different combinations of ambient liquid temperature and elapsed time from the start of melting as listed in the frames. For the case of silicon oil shown in Fig. 8, the average heat transfer coefficient shows a tendency to decrease as the inclination angle increases. This seems to be so except for the horizontal ice plate.

As shown in Fig. 5b, the ambient fluid touches the ice layer from the horizontal direction and then changes its flow direction. As the inclination angle of the ice layer increase, the change of the flow direction becomes small and the enhancement effect of melting by the ambient liquid flow decreases. As the inclination angle increases further to the vertical and downward direction, the melt water flow on the ice surface shows an increased tendency to separate from the ice surface, a fact which decreases the melting effect on the ice surface. Thus, the behavior of the melt-water layer (temperature and flow) changes the melting heat-transfer coefficient

For the case of silicon oil, as the inclination angle increases to be almost (downward) horizontal, the separation of the melt water increases its effects. As a result, the ice configuration becomes more complicated, and

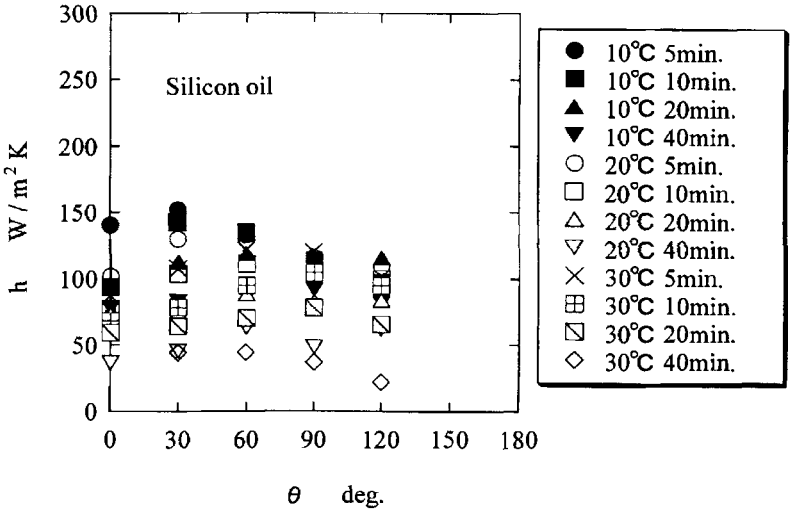

Fig. 8. Effect of the inclination angle on the heat transfer coefficient

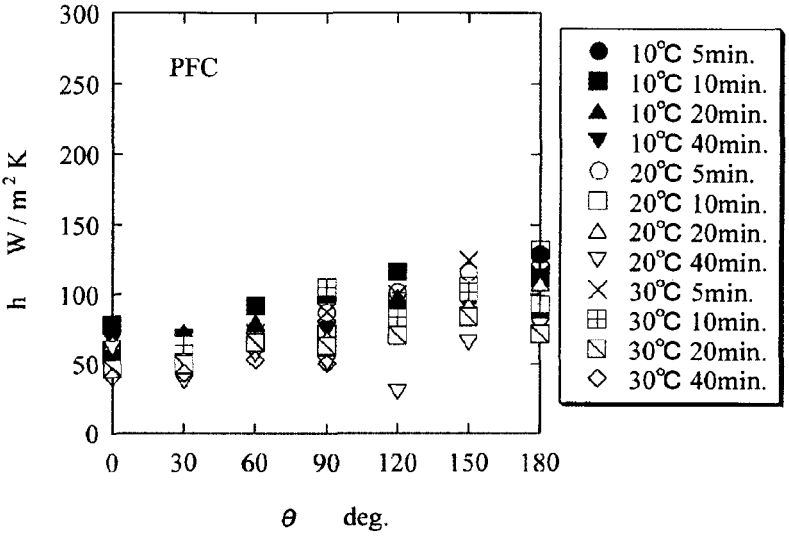

Fig. 9. Effect of the inclination angle on the heat transfer coefficient

it is impossible to assess the melting heat-transfer coefficient from the ice configuration. On the other hand, for the case of PFC shown in Fig. 9, the melting heat transfer coefficient showed a tendency to increase with the inclination angle of the ice layer. As shown in Fig. 5b, for the flow direction of the ambient fluid is opposite to that of the melt water flow, the effects of the ambient-fluid convection is small compared to the case of silicon oil.

From the horizontal to the vertical, as the separation of melt water is increased, the melting heat-transfer coefficient increases. On the other hand, from the vertical to the downward horizontal, the convective motion of the ambient fluid is promoted by the cooling effect of the downward ice layer and so the average heat transfer coefficient increases.

4 Conclusions

In this paper the melting characteristics of the inclined ice plate within the hydrophobic liquid were experimentally investigated. The following conclusions may be drawn within the parameter range covered in the present study:

(1) For the case of silicon oil, the melting rate is greater at the upper part of ice layer which is thus wedge shaped, while for the case of PFC the melting rate is uniform at almost all parts of ice layer.
(2) As the inclination angle of the ice layer increases, the average melting heat transfer coefficient decreases for the case of silicon oil. This is due

to the fact that with an increase of the inclination angle of the ice plate, the effect of the ambient liquid, and the tendency of the melt water-layer to separate from the ice layer decrease. For the case of PFC, with an increase of the inclination angle the average heat transfer coefficient increases. This is due to the effect of the separation of the melt-water layer and the promotion effect of the ambient flow.

(3) The melting characteristics of the inclined ice layer within the hydrophobic liquid are strongly influenced by the density difference of the melt water and the ambient fluid. The melting rate for silicon oil is greater than that for PFC, while the density difference between the melt water is smaller for silicon oil.

References

1. Ishikawa, M., Hirata, T., and Tamaki, H.(1991) Melting and Solidification Phenomena of Two Insoluble Phase Change Materials in a Cylindrical Capsule, *Trans. Jpn. Soc. Mech. Eng.* **57**, 4174–4181.
2. Yamada M., Fukusako S., and Emman-Bellah M.(1996) Free convection heat transfer around a horizontal ice cylinder formed through melting within an immiscible liquid, *Heat and Mass Transfer* **31**, 419–426
3. Yamada M., Fukusako S., and Emman-Bellah M.(1997) Experiments on melting of a vertical ice layer immersed in immiscible liquid, *Heat and Mass Transfer* **32**, 447–454
4. Yamada M., Fukusako S. et al. (1998) Melting Heat Transfer Characteristics of a Horizontal Ice Cylinder Immersed in an Immiscibel Liquid, *Heat Transfer Japanese Research* **27**(5), 336–352

(Received 19 May 1999, accepted 1. June 1999)

Plane Flow of an Ice Sheet Exhibiting Strain-Induced Anisotropy

Olivier Gagliardini and Jacques Meyssonnier

Laboratoire de Glaciologie et Géophysique de l'Environnement,
CNRS et Université Joseph Fourier (UJF - Grenoble I),
BP96, 38402 Saint-Martin-d'Hères Cedex, France

Abstract. A model for the anisotropic behaviour of polar ice and the evolution of its strain-induced anisotropy is presented. At the scale of the ice polycrystal, the ice fabric is described by a continuous Orientation Distribution Function (ODF), and the stress in each grain is assumed to be the same as the bulk stress (static model). Assuming a linear transversely isotropic behaviour of the ice single crystal, the constitutive law for an orthotropic polycrystal is obtained, as well as the analytical expression for the ODF which depends on three independent parameters only. Applications to the large-scale flow of an ideal ice-sheet are presented. Assuming a fixed geometry of the ice-sheet, the velocities and the fabrics corresponding to stationary plane-strain flow are obtained by solving a coupled problem.

1 Introduction

Observations on ice cores drilled in Antarctica and Greenland have shown that polycrystalline ice develops a fabric (*i.e.* a lattice preferred orientation of its constituent grains), which is induced by the strain undergone by the ice as it descends from the free surface to the depth of an ice-sheet.

Since it is not possible to reproduce experimentally the conditions which occur in an ice-sheet, the results from models for the anisotropic behaviour of ice must be compared with field data, as has been done, for example, in [2]. The difficulty is that these models require, as input, the knowledge of the strain history undergone by the ice. Results from anisotropic ice flow models which use the ice fabric as an input (*e.g.*[3]) can be useful, but, since fabrics can be measured only at a very few drilling sites, additional assumptions must be made to extrapolate these fabrics to the whole ice-sheet flow domain. This shows that in order to properly account for the anisotropy of ice we have to consider the ice fabric as an unknown of the ice-sheet flow problem.

On the other hand, a common feature of ice-sheet models is the very large amount of data which are processed. Even by discretizing the flow domain with a coarse mesh (*e.g.* $30km$ in the horizontal plane, $30m$ along the vertical, without a detailed description of the bed-rock topography) some 10^5 to 10^6 nodes are required to solve the isotropic ice flow problem. In order to make an ice-sheet model usable when extending it to the flow of anisotropic ice, the models for the behaviour of anisotropic ice and fabric evolution must be as efficient as possible and not too much time consuming.

In this paper, a complete solution (*i.e.*velocity and fabric fields) for the stationary flow of a two-dimensional ice-sheet is presented. This solution was obtained by incorporating a micro-macro model ([4,5]) for the behaviour of anisotropic ice into a finite-element code for the ice flow simulation. The micro-macro model considers a polycrystal of ice as a representative elementary volume of ice which stands as a material point of the continuum at the scale of the ice-sheet. Some of the assumptions of this model, presented in the following, seem to be rather crude but their aim is to fulfil the main objective of minimization of the amount of data storage and computation time.

2 Rheological Model for Orthotropic Polycrystalline Ice

2.1 Notation and main assumptions

In the following three Cartesian reference frames are used (see Fig. 1):

- $\{\mathsf{R}\}$ is a global fixed reference frame, whose plane (x_1, x_2) is the plane of the ice-sheet flow.
- $\{^o\mathsf{R}\}$ is the material reference frame of an orthotropic polycrystal of ice, whose axes $^o x_i$ are perpendicular to the planes of orthotropic symmetry. Furthermore it is assumed that the plane of symmetry $(^o x_1, ^o x_2)$ of the polycrystal coincides with the plane (x_1, x_2) of the ice-sheet flow (*i.e.* $^o x_3 = x_3$).
- $\{^g\mathsf{R}\}$ is a local frame attached to an individual grain, whose $^g x_3-$axis is the hexagonal symmetry axis of the grain ($c-$axis).

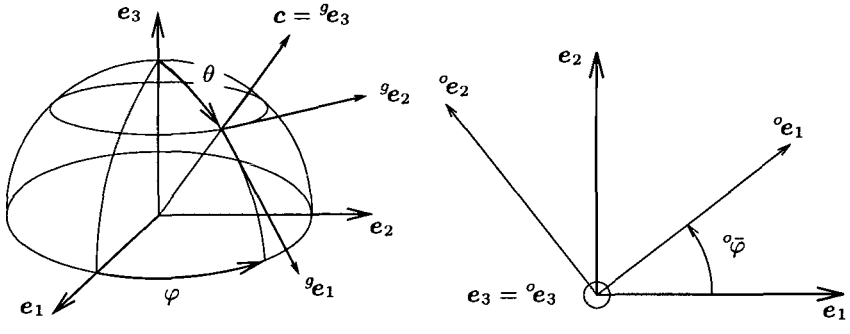

Fig. 1. Definition of the grain local frame $\{^g\mathsf{R}\}$ and the material frame $\{^o\mathsf{R}\}$ with respect to the global fixed reference frame $\{\mathsf{R}\}$

Macroscopic quantities, associated with a representative polycrystal or the ice-sheet, are overlined. The superscripts 'g' and 'o' denote any non-scalar

quantity expressed in the local $\{^g\mathsf{R}\}$ and the material $\{^o\mathsf{R}\}$ frames respectively. Otherwise, (*i.e.* if no superscript is applied) the quantity is expressed in the global frame $\{\mathsf{R}\}$.
Following [4,5], the main assumptions made are as follows:

(1) The representative polycrystal experiences a uniform state of stress, *i.e.* the stress in each grain equals the bulk stress applied on the boundary of the polycrystal (Reuss assumption leading to the so-called static or uniform-stress model). Since the ice is incompressible, the following relation holds

$$\boldsymbol{S} = \bar{\boldsymbol{S}}, \tag{1}$$

where $\boldsymbol{S}$ and $\bar{\boldsymbol{S}}$ are the microscopic and macroscopic deviatoric stresses, defined as functions of the stresses $\boldsymbol{\sigma}$ and $\bar{\boldsymbol{\sigma}}$ and the isotropic pressures p and $\bar{p}$ by $S_{ij} = \sigma_{ij} - p\delta_{ij}$, $\bar{S}_{ij} = \bar{\sigma}_{ij} - \bar{p}\delta_{ij}$, respectively.
(2) Each grain exhibits a linear behaviour and is considered as a transversely isotropic continuous medium, whose symmetry axis is the crystal $c-$axis. As a consequence, the orientation of a grain relative to the global frame $\{\mathsf{R}\}$ is determined solely by the direction of its $c-$axis and is defined by two angles, the co-latitude θ and the latitude φ (see Fig. 1).
(3) Each grain in the polycrystal occupies the same volume.
(4) The total number of grains does not change during the deformation, *i.e.* recrystallization processes, such as grain growth or polygonization, are not taken into account.

2.2 Grain behaviour

Following [6] and [4], the ice crystal is assumed to behave as a linear transversely isotropic medium. The simplest relation between the strain-rate $\boldsymbol{D}$ and the deviatoric stress $\boldsymbol{S}$ is then expressed by

$$\boldsymbol{D} = \frac{\psi}{2}\left(\beta\boldsymbol{S} + (1-\beta)(\boldsymbol{M}_3\boldsymbol{S} + \boldsymbol{S}\boldsymbol{M}_3 - 2\,\mathrm{tr}(\boldsymbol{M}_3\boldsymbol{S})\boldsymbol{M}_3)\right). \tag{2}$$

where $\boldsymbol{M}_3$ is the structure tensor defined by $\boldsymbol{M}_3 = \boldsymbol{c}\otimes\boldsymbol{c}$ ($\boldsymbol{c}$ is the grain $c-$axis unit vector : ${}^g\boldsymbol{c} = (0,0,1)$ in the local frame). The parameter ψ is the fluidity, inverse of viscosity, for shear parallel to the basal plane of the grain, and β is the ratio of the shear fluidity in the basal plane to that parallel to the basal plane. β is a measure of the grain anisotropy: when $\beta = 0$ the grain can deform only by basal glide, as assumed in many models [7,8,3,9], while $\beta = 1$ corresponds to an isotropic grain. Since the ice single crystal deforms mainly by shear parallel to its basal plane [1], the value of β should be significantly less than 1.

2.3 Fabric evolution

Following [6], the fabric of the ice polycrystal is described by an Orientation Distribution Function (ODF), which gives the relative density of grains whose $c-$axes have the orientation (θ, φ) in the global frame $\{\mathsf{R}\}$. By definition,

$$\frac{1}{2\pi}\int_0^{2\pi}\int_0^{\pi/2} f(\theta,\varphi)\sin\theta\,\mathrm{d}\theta\,\mathrm{d}\varphi = 1. \tag{3}$$

The expressions of the rate of rotation (or spin) of a grain, $\boldsymbol{W}$ in the global reference frame $\{\mathsf{R}\}$, and ${}^{g}\boldsymbol{W}$ in the local frame $\{{}^{g}\mathsf{R}\}$, are related by

$$(\boldsymbol{R}^T\dot{\boldsymbol{R}} + {}^{g}\boldsymbol{W} - \boldsymbol{R}^T\boldsymbol{W}\boldsymbol{R})\,{}^{g}\boldsymbol{c} = 0, \tag{4}$$

where $\boldsymbol{R}$ is the rotation matrix to pass from $\{{}^{g}\mathsf{R}\}$ to $\{\mathsf{R}\}$, and ${}^{g}\boldsymbol{c}$ is the $c-$axis unit vector expressed in $\{{}^{g}\mathsf{R}\}$ ([6]). Since the basal planes of a grain remain parallel to each other during the deformation, the component of the velocity along the ${}^{g}x_3$ axis ($c-$axis), when expressed in the rotating frame of the grain $\{{}^{g}\mathsf{R}\}$, is a function of ${}^{g}x_3$ only. This leads to the kinematic relations

$${}^{g}W_{13} = {}^{g}D_{13} \quad {}^{g}W_{23} = {}^{g}D_{23}. \tag{5}$$

To obtain the rate of rotation of the grain reference frame (*i.e.* the lattice spin) from (4), it is necessary to make an additional assumption that the spin of the grain $\boldsymbol{W}$, expressed in the global reference frame $\{\mathsf{R}\}$, is equal to the macroscopic spin of the polycrystal (Taylor-type assumption),

$$\boldsymbol{W} = \bar{\boldsymbol{W}}. \tag{6}$$

With relations (5) and (6), equation (4) provides two relations for the change in grain orientation

$$\dot{\theta} = -{}^{g}D_{13} + \bar{W}_{13}\cos\varphi + \bar{W}_{23}\sin\varphi, \tag{7a}$$

$$\dot{\varphi}\sin\theta = -{}^{g}D_{23} - \bar{W}_{12}\sin\theta + (\bar{W}_{23}\cos\varphi - \bar{W}_{13}\sin\varphi)\cos\theta. \tag{7b}$$

Since recrystallization is not taken into account, the change in the relative number of grains in an interval $(d\theta, d\varphi)$ around (θ, φ) is solely due to grains entering or leaving this interval (there is no spontaneous nucleation or disappearance of grains). As a consequence, at each material point $\boldsymbol{x}$ in the ice-sheet, the polycrystal fabric is described by the ODF which varies according to

$$\frac{\partial f\sin\theta}{\partial t} + \frac{\partial f\sin\theta}{\partial x_i}\bar{u}_i + \frac{\partial \dot{\theta} f\sin\theta}{\partial\theta} + \frac{\partial \dot{\varphi} f\sin\theta}{\partial\varphi} = 0, \tag{8}$$

where $\bar{u}_i$ are the velocity components at $\boldsymbol{x}$. Fabric evolution is described by equations (7a), (7b) and (8).

Following [6,5], we adopt a parameterized form of the ODF derived from analytical results obtained in [4] for the case of an orthotropic polycrystal with fixed principal directions of loading. This ODF depends on four parameters

$$f(\theta,\varphi,\ \bar{k}_1,\bar{k}_2,\bar{k}_3,{}^o\bar{\varphi}) = \left[\sin^2\theta\left(\bar{k}_1^2\cos^2(\varphi-{}^o\bar{\varphi})+\bar{k}_2^2\sin^2(\varphi-{}^o\bar{\varphi})\right)+\bar{k}_3^2\cos^2\theta\right]^{-3/2}. \tag{9}$$

This function describes an orthotropic fabric, with planes of symmetry $({}^ox_1, {}^ox_2)$, $({}^ox_2, {}^ox_3)$ and $({}^ox_3, {}^ox_1)$. In the following, the plane $({}^ox_1, {}^o x_2)$ coincides with the flow plane (x_1, x_2) of the ice-sheet. Since the conservation equation (3) implies that $\bar{k}_1\bar{k}_2\bar{k}_3 = 1$, only three parameters in (9) are independent. Each parameter $\bar{k}_i$ gives the strength of concentration of $c-$axes in the direction ${}^ox_i$ of the material frame $\{{}^o\mathsf{R}\}$ (a small value of $\bar{k}_i$ corresponds to $c-$axes gathered along direction ${}^ox_i$; when $\bar{k}_i = \bar{k}_j$ the plane $({}^ox_i, {}^o x_j)$ is a plane of isotropy). ${}^o\bar{\varphi}$ is the angle which defines the rotation of $\{{}^o\mathsf{R}\}$ with respect to the global frame $\{\mathsf{R}\}$ in plane (x_1, x_2) (see Fig. 1).

2.4 Viscous law

The macroscopic strain-rate $\bar{\boldsymbol{D}}$ of the polycrystal, in response to the prescribed deviatoric stress $\bar{\boldsymbol{S}}$, is defined as the weighted average of the strain-rates $\boldsymbol{D}$ of its constituent grains as

$$\bar{D}_{ij} =< D_{ij} >= \frac{1}{2\pi}\int_0^{2\pi}\int_0^{\pi/2} D_{ij}(\theta,\varphi) f(\theta,\varphi)\sin\theta\,\mathrm{d}\theta\,\mathrm{d}\varphi. \tag{10}$$

By substituting (2) into (10), and using expression (9) for the ODF, the linear orthotropic viscous law giving the macroscopic strain-rate as a function of the deviatoric stress is obtained as

$$\bar{\boldsymbol{D}} = \sum_{r=1}^{3}\left[\bar{\alpha}_r\,\mathrm{tr}({}^o\bar{\boldsymbol{M}}_r\,\bar{\boldsymbol{S}})\,{}^o\bar{\boldsymbol{M}}_r^D + \bar{\alpha}_{r+3}(\bar{\boldsymbol{S}}\,{}^o\bar{\boldsymbol{M}}_r + {}^o\bar{\boldsymbol{M}}_r\,\bar{\boldsymbol{S}})^D\right], \tag{11}$$

where ${}^o\bar{\boldsymbol{M}}_r = {}^o\boldsymbol{e}_r \otimes {}^o\boldsymbol{e}_r$ are three structure tensors defined by the unit vectors ${}^o\boldsymbol{e}_r$ of the material frame $\{{}^o\mathsf{R}\}$ and $(.)^D$ denotes the deviatoric part of $(.)$. The six response coefficients $\bar{\alpha}_i$, functions of the grain rheological parameters ψ and β, are obtained as follows:

$$\begin{bmatrix}\bar{\alpha}_1\\ \bar{\alpha}_2\\ \bar{\alpha}_3\\ \bar{\alpha}_4\\ \bar{\alpha}_5\\ \bar{\alpha}_6\end{bmatrix} = \frac{\psi(\beta-1)}{2}\begin{bmatrix} 0 & -6 & 12 & 8 & -22 & 8\\ 0 & 6 & -12 & -6 & 6 & 8\\ 2 & -10 & 0 & 8 & 6 & -6\\ \beta/(2(\beta-1)) & 1 & -3 & -2 & 6 & -2\\ \beta/(2(\beta-1)) & -2 & 3 & 2 & -2 & -2\\ (2-\beta)/(2(\beta-1)) & 3 & 0 & -2 & -2 & 2\end{bmatrix}\begin{bmatrix}1\\ J_{30}\\ J_{32}\\ J_{50}\\ J_{52}\\ J_{54}\end{bmatrix}, \tag{12}$$

where J_{30}, J_{32}, J_{50}, J_{52} and J_{54} are five moments given by

$$J_{pq} = \frac{2}{\pi} \int_0^{\pi/2} \int_0^{\pi/2} f(\theta, \varphi +^o \bar{\varphi}) \sin^p\theta \sin^q\varphi \, \mathrm{d}\theta \, \mathrm{d}\varphi. \tag{13}$$

For isotropic ice, $f(\theta, \varphi) = 1$, $\bar{k}_1 = \bar{k}_2 = \bar{k}_3 = 1$, the J_{pq} values are $J_{30} = 2/3$, $J_{32} = 1/3$, $J_{50} = 8/15$, $J_{52} = 4/15$ and $J_{54} = 1/5$. Then, the macroscopic orthotropic law (11) reduces to a linearly isotropic viscous law (*i.e.* Glen's law with $n = 1$)

$$\bar{\boldsymbol{D}} = \frac{\bar{B}_1}{2} \bar{\boldsymbol{S}}, \tag{14}$$

where the fluidity $\bar{B}_1$ is related to the grain rheological parameters by [4,5]

$$\bar{B}_1 = \frac{\psi}{5}(3\beta + 2). \tag{15}$$

It follows from (15) that the ratio of the fluidity ψ for shear parallel to the grain basal plane to the fluidity $\bar{B}_1$ of isotropic ice reaches its maximum value of 2.5 when the grain behaviour is the most anisotropic one (*i.e.* when $\beta = 0$). This value is lower than the experimental value of 10 obtained by [10]. Therefore the influence of anisotopy on ice-sheet flow, as given by the present model, is under-estimated.

3 Ice-Sheet Flow Model

The stationary flow of an ice-sheet with a fixed geometry (the vertical at the dome is a symmetry axis) is solved for given boundary conditions (no stress and isotropic fabric at the free surface, no-sliding on the bed-rock).

3.1 Velocity field

Following [11], the solution in terms of the velocity $\bar{u}_i$ and isotropic pressure $\bar{p}$ is obtained, for a given fabric field, by minimizing, among the admissible velocity fields, the functional

$$J(\bar{u}_i, \bar{p}) = \int_{\mathcal{D}} \left(\bar{\phi}_D + \bar{p}\bar{D}_{ii} - \rho g_i \bar{u}_i \right) \mathrm{d}\mathcal{D} - \int_E \bar{\sigma}^0 \bar{u}_i n_i \, \mathrm{d}s, \tag{16}$$

where $\bar{\sigma}^0$ is the atmospheric pressure applied on the free surface E and $\bar{\phi}_D$ is the dissipation potential of the orthotropic polycrystal which gives the deviatoric stress as a function of the strain-rate as $\bar{\boldsymbol{S}} = \partial\bar{\phi}_D / \partial\bar{\boldsymbol{D}}$. This relation can be put into the same form as (11) by interchanging $\bar{\boldsymbol{D}}$ and $\bar{\boldsymbol{S}}$, and replacing the fluidities $\bar{\alpha}_i$ with six viscosities $\bar{\eta}_i$ whose expressions are obtained by identification (see [12] for these relations).

The functional equation (16) is solved by the finite-element method, using six- node triangular elements with a quadratic interpolation of the velocities and a linear interpolation of the pressure. The ODF (9) is obtained by a quadratic interpolation of the parameters $\bar{k}_1$, $\bar{k}_2$ and ${}^o\bar{\varphi}$ given at each node of the mesh.

3.2 Fabric field

Following [13], the ODF parameters corresponding to stationary flow are obtained by solving equation (8) along the flow streamlines computed from the finite-element solution for the velocities and assuming that the ice is isotropic at the ice-sheet surface. Denoting by s the curvilinear co-ordinate along a streamline and $\bar{u}_s$ the velocity tangent to this streamline, under the assumption of stationarity $\partial(f \sin\theta)/\partial t = 0$, equation (8) transforms into

$$\frac{\partial f \sin\theta}{\partial s}\bar{u}_s + \frac{\partial \dot{\theta} f \sin\theta}{\partial \theta} + \frac{\partial \dot{\varphi} f \sin\theta}{\partial \varphi} = 0. \tag{17}$$

The ODF parameters at each node M of the finite-element mesh are computed in two stages as follows:

- the streamline passing through M is computed from M to the ice-sheet surface by solving the set of equations $\mathrm{d}x_i/\mathrm{d}t = -\bar{u}_i$ (upstream procedure). During this phase, $\bar{S}_{11}$, $\bar{S}_{22}$, $\bar{S}_{12}$ and the rotation rate $\bar{W}_{12}$ are calculated at each time step by using the finite-element solution for the velocity and the constitutive law (11), then stored.
- the evolution of the ODF parameters along the stream-line is calculated from the surface where ice is assumed to be isotropic. By assuming that the directions of the principal stresses do not change significantly during the time step, the ODF given by (9) satisfies (17) and the parameters $\bar{k}_i$ are shown (see [12]) to be the solution of

$$d\bar{k}_1/\bar{k}_1 = (\psi/4)(\bar{S}_{11} + \bar{S}_{22} + \bar{S})dt, \quad d\bar{k}_2/\bar{k}_2 = (\psi/4)(\bar{S}_{11} + \bar{S}_{22} - \bar{S})dt, \tag{18}$$

where $\bar{S}^2 = (\bar{S}_{11} - \bar{S}_{22})^2 + 4\bar{S}_{12}^2$. During a time step $\mathrm{d}t$, the orientation change of the orthotropic frame $\{{}^o\mathrm{R}\}$, *i.e.* $\mathrm{d}{}^o\bar{\varphi}$, is taken as the weighted average of the rotation $\dot{\varphi}dt$ of the grains given by (7b). These equations are solved by using the Runge-Kutta method (with initial condition at the surface $\bar{k}_1 = \bar{k}_2 = 1$).

3.3 Coupled problem

The velocity and fabric fields corresponding to stationary flow are calculated by solving iteratively the velocity problem (equation (16) for a given fabric

field, then the fabric problem (equations (18)) for a given velocity field, until convergence is achieved (*i.e.*when the norm of the relative deviation of each variable $\bar{u}_i, \bar{k}_i, {}^o\bar{\varphi}$ for two consecutive iterations is less than 10^{-3}). It has been verified that the choice of the initial fabric field (respecting the condition of isotropy at the surface) does not affect the results.

4 Applications

4.1 Conditions of the numerical simulations

All the variables are made dimensionless by using the depth at the dome H_0, the gravity forces ρg and the fluidity of isotropic ice $\bar{B}_1$ at $-10°C$ as scaling values (stresses are scaled by $\rho g H_0$, and velocities by $\bar{B}_1 \rho g H_0^2$). Dimensionless variables are denoted by a tilde.

We adopt a simplified ice-sheet geometry, with a flat bed-rock and a fixed surface elevation given by Vialov's profile [14] $\tilde{H}^4 = 1 - (\epsilon \tilde{x}_1)^2$, where $\epsilon = H_0/L$ is the aspect ratio of the ice-sheet, fixed to the value 0.018 in the following. With this fixed geometry, the accumulation-rate corresponding to stationary flow must be considered as a variable determined by the solution of the flow problem.

Since the fluidities $\bar{B}_1$ and ψ verify relation (15), the dimensionless variables of the model, including the ODF parameters, depend only on the grain anisotropy parameter β and the temperature. In the following the results of three simulations, whose conditions are summarized in Table 1, are compared. The non-isothermal temperature field named "GRIP" is deduced from the profile shown on Fig. 2a measured in the GRIP borehole, [15], by assuming that the temperature is a function of the reduced elevation $\hat{x}_2 = x_2/H$ only. Note that since the viscosity of ice exhibits an exponential dependence on the temperature, changing the reference temperature would affect the velocities by a scaling factor (as a change in the value of $\bar{B}_1$ would do) but not the ODF as can be inferred from (17).

Table 1. Conditions of the tests.

	Grain anisotropy β	Temperature profile
Test 1	$\beta = 0.25$	"GRIP"
Test 2	$\beta = 0.25$	isothermal
Test 3	$\beta = 0.1$	"GRIP"

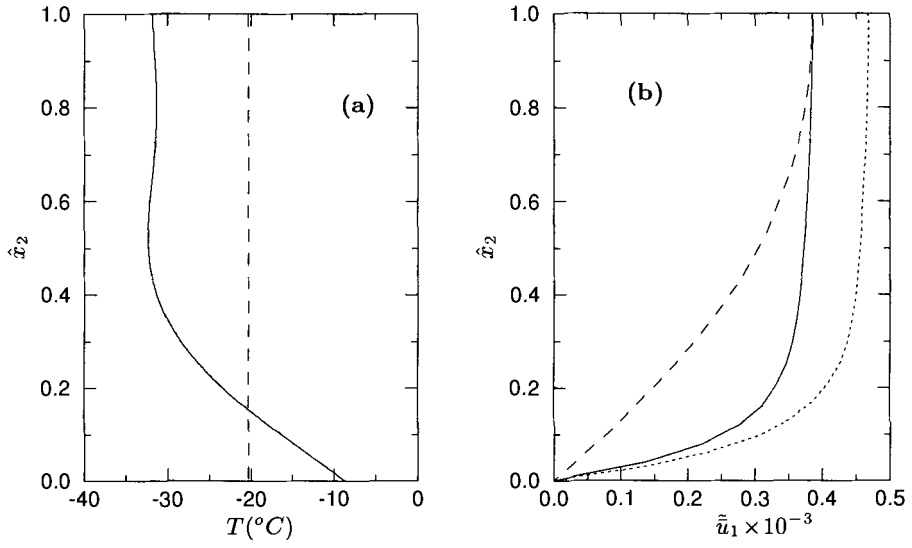

Fig. 2. **(a)** Evolution of the temperature as a function of the reduced elevation $\hat{x}_2$ as measured by [15] in the GRIP ice core (*solid line*) and the isothermal profile (*dashed line*). **(b)** horizontal velocity as a function of the reduced elevation $\hat{x}_2$ at $\tilde{x}_1 = 10$ for Test 1 (*solid line*), Test 2 (*dashed line*) and Test 3 (*dotted line*)

4.2 Influence of the temperature

The influence of the temperature is assessed by comparing Test 1 and Test 2. The constant temperature in Test 2 was chosen so that Test 1 and Test 2 give the same surface horizontal velocity at $\tilde{x}_1 = 10$.

Owing to the increase in the temperature at GRIP by $23.3°C$ from the surface to the bedrock, the fluidities $\bar{B}_1(T)$ and ψ are increased by a factor of approximately 30 from the top to the bottom. On the other hand, due to the development of anisotropy from the surface to the bedrock, the shear fluidity (in the flow plane) can be increased by a maximum factor of about 1.8 (obtained by assuming that all the $c-$axes are aligned along the vertical, so that the macroscopic shear fluidity equals the grain fluidity for shear parallel to the basal plane ψ given by (15) with $\beta = 0.25$). However Fig. 3 shows that the "GRIP" temperature field (Test 1) significantly slows down the concentration of the fabric (given by the smallest parameter $\bar{k}_2$) as a function of depth, compared to the isothermal flow: the difference in $\bar{k}_2$ between Test 1 and Test 2 increases with depth until it reaches the threshold value of $\bar{k}_{2c} = 10^{-3}$ for which it is assumed that all the grains have the same orientation and the fabric cannot concentrate any further ($\bar{k}_{2c}$ is reached at $\hat{x}_2 = 0.4$ in Test 2 and at $\hat{x}_2 = 0.2$ in Test 1). The two other parameters $\bar{k}_1$ and $\bar{k}_3$ satisfy $\bar{k}_1/\bar{k}_{2c} > 10^6$ and $\bar{k}_3/\bar{k}_{2c} > 100$ when the threshold value $\bar{k}_{2c}$ is reached.

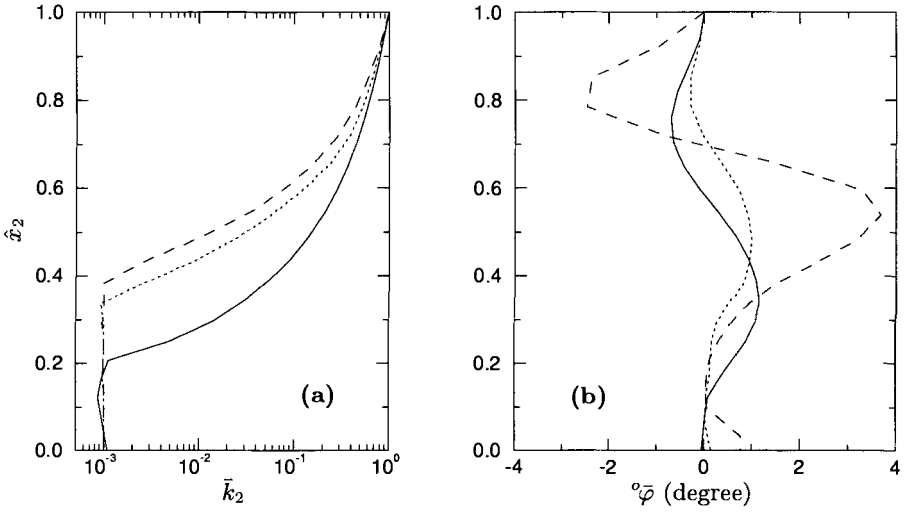

Fig. 3. Evolution of fabric parameters $\bar{k}_2$ **(a)** and $^{o}\bar{\varphi}$ **(b)** as a function of the reduced elevation $\hat{x}_2$ at $\tilde{x}_1 = 10$ for Test 1 (*solid line*), Test 2 (*dashed line*) and Test 3 (*dotted line*)

Even if the flows are very similar (owing to the adjustment of the temperature in Test 2), horizontal velocity profiles (see Fig. 2b) show that for Test 2 the deformation is relatively homogeneous while the effect of the GRIP temperature field is to concentrate the deformation in a basal layer (about 20% of the total thickness). Ice being less deformed near the surface, fabric concentration is slower than for isothermal conditions. An additional consequence is that the direction of the preferred orientation of the grains is closer to the vertical for Test 1 than for Test 2 (see $^{o}\bar{\varphi}$ in Fig. 3b). Also, owing to the shape of the velocity profiles, the accumulation rate for the "GRIP" flow is 1.2 to 1.4 greater than for the isothermal.

4.3 Influence of grain anisotropy

The influence of the grain anisotropy, described by β, is shown by comparing Test 1 and Test 3 (see Table 1). At the scale of the polycrystal, the rate of fabric concentration increases as the anisotropy of the grain increases (*i.e.* β decreases) [6,4,5]. This holds at the scale of the ice-sheet since the decrease of $\bar{k}_2$ with depth is faster for Test 3 ($\beta = 0.1$) than for Test 1 ($\beta = 0.25$) as shown in Fig. 3.

Since for a given fabric the macroscopic fluidity increases with the grain anisotropy (see relations (11) , (12) , (15) and [12]), the effect of the rate of fabric concentration on the velocities is enhanced. Accordingly, the accumulation rate for Test 3 is about 1.3 times larger than that of Test 1.

5 Conclusion

A model for the flow of an ice-sheet exhibiting strain-induced anisotropy has been presented. The fabric of an orthotropic ice polycrystal is described by using an ODF which depends on three independent parameters only. Assuming a linear transversely isotropic behaviour of the grain and a uniform state of stress, the constitutive law of the polycrystalline ice is obtained by homogenization. As a consequence of the assumed linear behaviour of the grain, the polycrystal behaviour is also linear. This assumption seems to be well adapted to describe polar ice rheology from the surface to the two-thirds of the ice sheet thickness [10]. Deeper, as the temperature and the stress increase, the value $n = 3$ would be more suitable.

The model has been applied to the simulation of the stationary flow of a two dimensional ice-sheet with a fixed geometry. The finite-element flow computation was carried out by assigning the values of the ODF parameters at each node of the mesh, then the evolution of the fabric was calculated along the flow streamlines derived from the velocity field, and the process was repeated until convergence was achieved. For a given aspect ratio of the ice-sheet, the influence of both temperature and grain anisotropy on the velocity and fabric fields has been shown. A field of temperature derived from GRIP field measurements slows down the rate of fabric evolution with depth (compared to that obtained for an isothermal flow) and an increase of the grain anisotropy leads to an increase of both the velocity and the rate of fabric evolution.

This study demonstrates the efficiency of our model to simulate the flow of ice-sheets exhibiting strain-induced anisotropy and shows that it could be used to determine the velocities and the ice fabrics for more complex bedrock and surface topographies, for instance in the vicinity of the drilling sites in Antarctica and Greenland.

Acknowledgements: This work was supported by the Commission of European Communities under contract ENV4-CT95-0125 "Fabric Development and Rheology of Polar Anisotropic Ice for Ice Sheet Flow Modelling". O. Gagliardini was granted a BDI-scholarship by the french Centre National de la Recherche Scientifique (Département SPI): this financial support is greatly acknowledged. LGGE-CNRS is associated to Université Joseph Fourier-Grenoble I.

References

1. P. Duval, M.F. Ashby, and I. Anderman. (1983) Rate-controlling processes in the creep of polycrystalline ice. *J. Phys. Chem.*, **87**, 4066–4074.
2. O. Castelnau, Th. Thorsteinsson, J. Kipfstuhl, P. Duval, and G.R. Canova. (1996) Modelling fabric development along the GRIP ice core, central Greenland. *Ann. Glaciol.*, **23**, 194–201.

3. A. Mangeney, F. Califano, and K. Hutter. (1997) A numerical study of anisotropic, low Reynolds number, free surface flow of ice-sheet modeling. *J. Geophys. Res.*, **102**(B10), 22,749–22,764.
4. O. Gagliardini and J. Meyssonnier. (1999) Analytical derivations for the behaviour and fabric evolution of a linear orthotropic ice polycrystal. *J. Geophys. Res.* In Press.
5. R. Staroszczyk and O. Gagliardini (1999) Two orthotropic models for strain-induced anisotropy of polar ice. *J. Glaciol.* In press.
6. J. Meyssonnier and A. Philip. (1996) A model for the tangent viscous behaviour of anisotropic polar ice. *Ann. Glaciol.*, **23**, 253–261.
7. L. Lliboutry. (1993) Anisotropic, transversely isotropic non linear viscosity of rock ice and rheological parameters inferred by homogenization. *Int. J. Plast.*, **9**, 619–632.
8. C. J. Van der Veen and I. M. Whillans. (1994) Development of fabric in ice. *Cold Reg. Sci. Technol.*, **22**(2), 171–195.
9. G. Gödert and K. Hutter. (1998) Induced anisotropy in large ice shields: Theory and its homogenization. *Continuum Mech. Thermodyn.*, **10**, 293–318.
10. P. Pimienta, P. Duval, and V.Y. Lipenkov. (1987) Mechanical behaviour of anisotropic polar ice. *In International Association of Hydrological Sciences, Publication 170 (Symposium on The Physical Basis of Ice Sheet Modelling, Vancouvert)*, pages 57–66.
11. J. Meyssonnier. (1989) Ice flow over a bump : experiment and numerical simulations. *J. Glaciol.*, **35**(119), 85–88.
12. O. Gagliardini. (1999) Simulation numérique d'un écoulement bidimensionnel de glace polaire présentant une anisotropie induite évolutive. *Thèse de Doctorat de l'Université Joseph Fourier-Grenoble I.*
13. O. Gagliardini and J. Meyssonnier. (1997) Flow simulation of a firn-covered cold glacier. *Ann. Glaciol.*, **24**, 242–247.
14. S. S. Vialov. (1958) Regularities of glacial shields movements and the theory of plastic viscous flow. *Physics of the movements of ice IAHS*, **47**, 266–275.
15. N. S. Gundestrup, D. Dahl-Jensen, S. J. Johnsen, and A. Rossi. (1993) Borehole survey at dome GRIP 1991. *Cold Reg. Sci. Technol.*, **21**, 399–402.

(Received 19 Feb. 1999, accepted 22 Feb. 1999)

A Meso-Macro Model for the Description of Induced Anisotropy of Natural Ice, Including Grain Interaction

Günter Gödert

Institute of Materials Research, GKSS Research Center,
Max-Planck-Strasse, D-21502 Geesthacht, Germany

Abstract. Since the temperature of the polar environment is close to the melting temperature deformation of natural ice is mainly due to creep, and the fabric evolution takes place under relatively low stress levels. Therefore, a linear viscous relation between stress and strain rate is supposed. A macroscopic flow law for natural ice is derived, which takes into account the effect of load-induced anisotropy due to the hexagonal single-crystal symmetry. Attention is focused on the main effect of crystal lattice rotation. Grain interaction is taken into account by two parameters. Existence of a continuous so-called orientation distribution function, ODF, is assumed. A coupled Finite Element-Finite Volume approach is proposed to account for coarse-scale orientational flux. For different consistency conditions, Voigt/Taylor and Sachs/Reuss, an orientation update is derived for planar flow, which results in just three additional degrees of freedom at each (FE-)integration point to account for orthotropic material symmetry.

1 Introduction

The aim of this work is to propose a model which is capable of describing the evolution of the mechanical properties of natural ice due to load induced fabric development. Similar to [4] we extend the classical continuum description, which in the following is referred to as the macro- or coarse-scale continuum by the so-called meso- or fine-scale continuum, which contains the c-axes orientations of a polycrystalline aggregate. To achieve the transition from the mesoscopic level to macroscopic entities, we adopt the concept of a *region of influence* around each material point of the continuum. The grain may be identified uniquely by its **c**-axis unit vector if its *position*, *size* and *shape* are neglected. Then each macro-material point possesses all possible orientations, which are describable by means of a continuous (and differentiable) ODF, $f(\mathbf{x},\mathbf{n},t) : I\!R^3 \times S^2 \times I\!R \longrightarrow I\!R$, where $\mathbf{x}$ is the position of each point, $\mathbf{n}$ denotes a point on the unit sphere S^2 associated to the **c**-axis orientation, and t is the time. Obviously $f(\cdot,\mathbf{n},\cdot) = f(\cdot,-\mathbf{n},\cdot)$, and to pass from an arbitrary mesoscopic quantity, χ_n, to its macroscopic counterpart, χ, a volume averaging procedure is applied as in $(1)_2$ below.

Let $\mathbf{x}$ and $\mathbf{X}$ be the positions of a material point of the macro-continuum in its present and reference configuration, respectively. Then, the motion of

the macro-continuum is obtained as the homogenized fine-scale motion,

$$\mathbf{x} = \chi(\mathbf{X}, t), \quad \text{where} \quad \chi(\mathbf{X}, t) := \int_{S^2} f \chi_n(\mathbf{X}, \mathbf{n}, t) d^2n \,, \tag{1}$$

where $d^2n := \sin\Theta d\Theta d\Phi$ and $S^2 := (\Theta \in [0, \pi]) \times (\Phi \in [0, 2\pi])$. The decomposition of the fine-scale deformation gradient $\mathbf{F}_n$ is given by

$$\mathbf{F}_n = \mathbf{R}_n \mathbf{F}_n^I, \quad \text{with} \quad \mathbf{F}_n^I := \mathbf{I} + \gamma_n \otimes \overline{\mathbf{n}} \quad \text{and} \quad \mathbf{R}_n \mathbf{R}_n^T = \mathbf{I}, \tag{2}$$

in which $\mathbf{F}_n^I$, $\mathbf{R}_n$, γ_n and $\overline{\mathbf{n}}$ denote the inelastic deformation gradient, elastic rotation, basal sliding vector and the **c**-axis unit-vector in the reference configuration, respectively. Material time differentiation then yields the fine scale actual velocity gradient, which may be decomposed into its symmetric, $\mathbf{D}_n = \mathbf{D}_n^I$, and skew-symmetric, $\mathbf{W}_n = \mathbf{W}_n^e + \mathbf{W}_n^I$, part, respectively. As in [5], $\mathbf{W}_n^e := \dot{\mathbf{R}}_n \mathbf{R}_n^T$ describes the motion of the individual orientation; if $\mathbf{W}_n = \mathbf{W}$ is assumed, then

$$\dot{\mathbf{n}} = \mathbf{W}\mathbf{n} - \mathbf{D}_n\mathbf{n} + (\mathbf{n} \cdot \mathbf{D}_n\mathbf{n})\mathbf{n}, \quad \mathbf{n}(t = t_0) = \mathbf{n}_0. \tag{3}$$

2 Balance Laws, Constitutive Equations and Motion

In addition to the classical mechanical balance laws for *mass*, *linear* and *angular momentum*, balance of crystal orientation must be considered. However, to assure the balance of dissipated energy during the meso-macro transition, the energy consistency condition (CC), $\epsilon = \int_{S^2} f \epsilon_n d^2n$ with $\epsilon_n := \mathbf{S}_n \cdot \mathbf{D}_n$, must be fulfilled. Depending on the underlying coarse scale formulation, the localised orientational balances take the forms

$$\partial_t \tilde{f} + \mathrm{div}_{\mathbf{x}}(\mathbf{v}\tilde{f}) = -\mathrm{div}_{\mathbf{n}}(\dot{\mathbf{n}}\tilde{f}), \qquad \dot{f} = -\mathrm{div}_{\mathbf{n}}(\dot{\mathbf{n}} f), \tag{4}$$

with respect to *Eulerian*, $\tilde{f}$, and *Lagrangian*, f, coordinates, respectiveley. The divergence operators $\mathrm{div}_{\mathbf{x}}$ and $\mathrm{div}_{\mathbf{n}}$ are referred to the coarse and the fine scales, respectively, and production (recrystalisation) as well as non-convective fine-scale flux of orientation is neglected. The material under consideration is characterized by constitutive assumptions for the fine-scale state variables, which are generally given by

$$\mathbf{Z}_n = \hat{\mathbf{Z}}_n(\mathbf{L}, \mathbf{T}, \overset{<2k>}{\mathbf{M}}, \overset{<k>}{\mathbf{N}}), \quad k = 1, 2, \ldots \quad \text{with} \quad \overset{<k>}{\mathbf{M}} := \int_{S^2} \overset{<k>}{\mathbf{N}} \, d^2n \,, \tag{5}$$

$\overset{<k>}{\mathbf{N}} := \mathbf{n} \otimes \overset{<k-1>}{\mathbf{N}}$ and $\overset{<0>}{\mathbf{N}} := 1$. If no tensor order is explicitly given, the tensor is assumed to be of second order. In this work $\mathbf{Z}_n$ may be identified with the stress $\mathbf{T}_n$, the stretching $\mathbf{D}_n$, or it takes the place of the fine-scale evolution equation, $\dot{\mathbf{n}}$. Only the simple cases will be considered, where either stretching

(Voigt/Taylor, VT) or stress (Sachs/Reuss, SR) is assumed to be uniform within the region of influence.

It is well known, [1], that the contribution of the pyramidal and prismatic slip-planes is quite small in comparison to sliding along the basal plane, which represents the most active glide plane. This suggests to reduce the single crystal deformation to basal slip only. Furthermore, the stress level in the upper parts of an ice-sheet, where the single-crystals arrange themselves towards a distinct fabric is quite low, so that we may reduce the constitutive relation between the resolved stress and the basal gliding to a linear relationship, $\dot{\gamma}_n = \mu \tau_n$. Rewriting the resolved quantities, $\dot{\gamma}_n$ and τ_n, generally by $\mathbf{z}_n := \mathbf{Z}_n \mathbf{n} - \overset{<3>}{\mathbf{N}} \cdot \cdot \mathbf{Z}_n$, where the double dot denotes twofold contraction, one may deduce the fine scale constitutive equation for the VT and the SR assumption according to

$$\mathbf{T}_n = \mu^{-1} \overset{<4>}{\mathbf{C}}_n \cdot \cdot \mathbf{D} \qquad \text{and} \qquad \mathbf{D}_n = \mu \overset{<4>}{\mathbf{C}}_n \cdot \cdot \mathbf{T}, \tag{6}$$

respectively, where $\overset{<4>}{\mathbf{C}}_n$ denotes the projection of a coarse scale quantity to the basal plane,

$$\overset{<4>}{\mathbf{C}}_n := \overset{<4>}{\mathbf{I}} \mathbf{N} \cdot \cdot \overset{<4>}{\mathbf{I}} - \overset{<4>}{\mathbf{N}} \quad \text{with} \quad \overset{<4>}{\mathbf{I}} \cdot \cdot \mathbf{X} = \tfrac{1}{2}(\mathbf{X} + \mathbf{X}^T) \,. \tag{7}$$

From (6), the coarse scale constitutive equations are simply obtained if the fine-scale orientation tensors are replaced by their associated coarse scale structure tensors,

$$\overset{<4>}{\mathbf{C}} = \overset{<4>}{\mathbf{I}} \mathbf{M} \cdot \cdot \overset{<4>}{\mathbf{I}} - \overset{<4>}{\mathbf{M}} \,. \tag{8}$$

Because of the underlying incompressibility of the fine-scale deformation, $\overset{<4>}{\mathbf{C}}$ is semi-definite in the sense that it maps only the deviatoric part of a tensor uniquely. Note, that due to different orientation evolution equations (3) for the SR and VT assumption, in general the resulting structure tensors will not be the same in the two cases. To turn the evolution equation (3) from a purely kinematical relation to a constitutive equation, $\mathbf{D}_n$ has to be replaced by $(6)_2$ or by $\mathbf{D}$, which is consistent with the SR or the VT assumption, respectively. However, there is still no influence of the grain environment taken into account. One possibility to account for the grain interaction is to assume, in contrast to (3), a general relation between the total fine-scale spin $\mathbf{W}_n$ and the macro spin $\mathbf{W}$. Since this kind of generalization excludes the VT-based approach, it will not be further considered, and we will focus attention on two principal mechanisms which the grain may experience from its environment; it will be called global and local grain interaction, respectively.

The first one makes use of the idea that if all grains are similarly oriented their mean velocity is changed due to the fact that the mesoscopic velocity

field becomes more homogeneous. This global interaction effect will be taken into account by uniformly modifying the orientational velocity field,

$$\dot{\tilde{\mathbf{n}}} := \nu_1 \dot{\mathbf{n}}, \tag{9}$$

where ν_1 is supposed to be a function of the orientational state variables of the polycrystal and $\nu_1 = 1$ if the classical VT assumption is applied.

Furthermore, there is also an interaction between individual grains, which affects the orientational flow. Recently interacting grains were modeled by using a self-consistent approach [1], which considers each grain as an inclusion within a homogeneous medium, reflecting the mean material properties [7]. Inspired by these ideas and recalling that the grains are smeared over the region of influence one may suppose that there exists a single inner grain of orientation $\mathbf{n}_i$ embedded within an arbitrarily oriented exterior region, with orientation $\mathbf{n}_o$. It is obvious from (3), that if $\mathbf{n}_i \neq \mathbf{n}_o$ the velocities will also differ, and one may intuitively expect that the inner-grain-velocity is affected by the relative velocity, $\dot{\tilde{\mathbf{n}}}_{i_{rel}} := \dot{\tilde{\mathbf{n}}}_o - \dot{\tilde{\mathbf{n}}}_i$ in the sense of a viscous friction law, which yields the modified inner-grain-velocity

$$\dot{\tilde{\tilde{\mathbf{n}}}}_i = \dot{\tilde{\mathbf{n}}}_i + \nu_2 \dot{\tilde{\mathbf{n}}}_{i_{rel}} \ , \tag{10}$$

where $\nu_2 \in [0,1]$ is also assumed to be a function of the orientational state of the polycrystal only. It reflects that if the polycrystal is completely oriented, $\nu_2 = 1$, the inner-grain is rigidly coupled to the exterior region, $\dot{\tilde{\tilde{\mathbf{n}}}}_i = \dot{\tilde{\mathbf{n}}}_o$, whereas, if there is a random distribution of **c**-axes, the effect of local grain interaction is supposed to be neutralized; therefore, macroscopically, there should be no coupling visible at all, $\nu_2 = 0$. Superimposing the effect of all exterior orientations weighted by their actual occurence then leads us to the effective elastic spin on the fine scale,

$$\overset{e}{\tilde{\tilde{\mathbf{W}}}}_n = \nu_1(\mathbf{W} - \nu_2 \mathbf{W}_{\mathrm{M}}^I - (1-\nu_2)\mathbf{W}_n^I) \ , \quad \text{with} \quad \mathbf{W}_{\mathrm{M}}^I = \mu(\mathbf{TM} - \mathbf{MT}). \tag{11}$$

In general the coefficients ν_i are given by an expression similar to (5). Here we assume that grain interaction is sufficiently considered if the ν_i depend on $\mathbf{M}$ only.

To demonstrate how ν_2 acts on the fine-scale flow the most simple choice for ν_2, the Heavyside function $H(M_{max} - M_{th})$ will be considered. It switches ν_2 from 0 to 1 if a threshold value of alignment M_{th} is exceeded by the maximum principal value of $\mathbf{M}$, M_{max} [1]. If the **c**-axes reflect strong alignment, the key requirement of the theory that every macro-point possesses all orientations is violated. Then $\mathbf{M}$ degenerates to $\mathbf{m} \otimes \mathbf{m}$, where $\mathbf{m}$ denotes the

[1] It is more convenient to measure alignment by $M_a := \frac{3}{2}(M_{max} - \frac{1}{3}) \in [0,1]$ or $M_a := 2(M_{max} - \frac{1}{2}) \in [0,1]$ if the underlying mesoscopic flow is 3D or 2D, respectively.

axis of alignment. Accordingly, the coarse scale constitutive equations reduce to $\mathbf{D} = \mu(\tau_m \otimes \mathbf{m} + \mathbf{m} \otimes \tau_m)$, and the polycrystalline material approximately behaves like a single crystal; The meso-scale appears to be rigidly connected to the coarse scale. Consequently, the global interaction should vanish, i.e. $\nu_1 = 1$. If now one replaces the stresses τ_m again by the sliding $\dot{\gamma}_m$, the exterior inelastic spin takes the form $\mathbf{W}^I_{\mathbf{M}} = (\mathbf{DM} - \mathbf{MD})$, which corresponds to the plastic spin of Dafalias (1984), however may have been directly deduced from (11) if the VT assumption would have been applied for the exterior inelastic spin instead of SR. This can be justified if we look at a strongly aligned polycrystalline aggregate, where, due to the smoothness of the fine-scale flow, all orientations (grains) will suffer more or less the same incremental motion. Therefore, the resulting structure will not be essentially affected if $\mathbf{M}$ is replaced by $\mathbf{N}$, so that $\mathbf{W}^I_{\mathbf{M}}$ will be approximately given by $(\mathbf{DN} - \mathbf{ND})$.

Summarizing the above considerations the resulting SR-fine-scale-evolution-equation is finally chosen as

$$\dot{\tilde{\tilde{\mathbf{n}}}} = \tilde{\tilde{\mathbf{W}}}^e_n \mathbf{n}\,, \qquad \text{with} \quad \tilde{\tilde{\mathbf{W}}}^e_n = \begin{cases} \nu_1(\mathbf{W} - \mu(\mathbf{TN} - \mathbf{NT})) & : \quad M_a \leq M_{th}\,, \\ \nu_1(\mathbf{W} - (\mathbf{DN} - \mathbf{ND})) & : \quad M_a > M_{th}\,, \end{cases} \tag{12}$$

where ν_1 must be fitted by experimental data, however for convenience will be neglected in what follows, i.e. $\nu_1 = 1$ according to VT.

Now the fine scale quantities are all describable by means of macroscopic quantities which are supposed to be stepwise constant. This enables us to integrate $\dot{\tilde{\tilde{\mathbf{n}}}}$, which yields a functional relation for the motion of the fine scale material point

$$\mathbf{n} = \Upsilon(\mathbf{n}_0, \mathbf{x}_0, t - t_0), \tag{13}$$

in which the orientation at the present time t is related to its value, $\mathbf{n}_0$, at the initial time t_0, and position $\mathbf{x}_0$. Assuming further the existence of the inverse mapping Υ^{-1}, the conservation of orientation yields

$$f(\mathbf{n}, \mathbf{x}, t) = \frac{\partial \Upsilon^{-1}}{\partial \mathbf{n}} f(\mathbf{n}_0, \mathbf{x}_0, t_0) \tag{14}$$

for the actual ODF, which is now in principle constructable from its initial state if the fine-scale motion is known.

3 Planar Flow

To hold the theory considerably simple so as to obtain analytical results as far as possible we will restrict ourselves to planar deformation, $\mathbf{v} \in I\!R^2$, but fully three-dimensional mesoscopic flow, $\dot{\mathbf{n}} \in T_{S^2}$, as one would expect in

the vicinity of an ice divide. Furthermore, decoupling was applied to obtain the results below, where the macroscopic state was assumed to be constant during the incremental solution of the mesoscopic evolution equation. If we identify $\mathbf{e}_3$ with the anti-plane direction, the orientation can be written as $\mathbf{n} = \sin\Theta\mathbf{e}_R + \cos\Theta\mathbf{e}_3$, with $\mathbf{e}_R := \cos\Phi\mathbf{e}_1 + \sin\Phi\mathbf{e}_2$. Following the calculations outlined above, one obtains a general expression for the ODF,

$$f = f_{S^2}(\mathbf{x}, \mathbf{n}, t) = \frac{\lambda}{4\pi}[f_{S^1}^{-1}\lambda\sin^2\Theta + \cos^2\Theta]^{-\frac{3}{2}} f_{S^2}(\mathbf{x}_0, \mathbf{n}_0, t_0), \tag{15}$$

which shows that it depends completely on the in-plane orientational distribution f_{S^1} and one additional parameter $\lambda := e^{-3\sum\triangle t(d_{n33})}$, with $d_{n_{ij}} := \mathbf{e}_i \cdot \mathbf{D}_n\mathbf{e}_j$, so that the integration along Θ may be carried out analytically. f_{S^1} describes the distribution of the **c**-axes along the circle $S^1 = S^2 \cap I\!R^2$ and is given as the mean value of f_{S^2} with respect to Θ. Therefore, to obtain the general ODF for this case it is sufficient to know the in-plane ODF which may be derived if one applies the procedure outlined above to the in-plane motion of the **c**-axes,

$$f_{S^1}(\cdot, t) = \frac{d\Phi_0}{d\Phi} f_{S^1}(\cdot, t_0) = \int_0^\pi f_{S^2}(\cdot, t)\sin\Theta d\Theta. \tag{16}$$

It can be shown that

$$f_{S^1}(\cdot, t) = \frac{1}{a + b\sin(2\Phi) + c\cos(2\Phi)} \tag{17}$$

represents the general form of the in-plane ODF, no matter what the underlying loading conditions may be and which CC was chosen [6]. Hence, the evolution of the ODF is reduced to the evolution of the parameters $\mathbf{a}^T := (a, b, c)$, which are functions of the actual state variables acting during the time increment. The evolution of the ODF-parameters is given by

$$\mathbf{a}^k = \mathbf{G}_{k-1}^k \cdot \mathbf{a}^{k-1}\ , \tag{18}$$

where the transition matrix, $\mathbf{G}_{k-1}^k$ represents the loading conditions acting during the time step $\triangle t := t_k - t_{k-1}$ as well as information about the initial ODF, *cf.* [6]. Summarizing: the actual ODF is given if the actual coefficients of the in-plane ODF are known. Therefore, the evolution of the ODF is reduced to the evolution of **a**. A further reduction of the set of parameters to just two independent parameters is possible if the probabilistic nature of the ODF, the constraint condition $\int_{S^1} f_{S^1} d\Phi = 1$ is taken into account.

To justify the incremental computation of the polycrystalline structure, it should be mentioned that, in general, the evolution of the macroscopic motion of the body and the mesoscopic evolution of its internal structure are coupled. If these processes are associated with different time scales decoupling is justified and the underlying meso-structure is assumed to be constant during the computation of the macro-motion, which should be the case for very slow flow of polar ice.

4 Numerics

The finite element (FE) approximation, to which the results below are referred, is based on the elasto/visco-elasto analogy using rectangular four-node-quasi-incompressible elements. Usually the ice-flow is described by the Stokes equations referred to Eulerian coordinates. Note, that although f_{S^1} was originally defined with respect to Lagrangian coordinates, the Eulerian description of the ODF must reflect the same structure as (17), however, in addition to the Lagrangian update (18), the convective coarse-scale flux of orientation must be considered. If flux across the element boundaries is taken into account, reformulation of f_{S^1} in terms of coarse-scale-Eulerian-coordinates (indicated by a tilde) becomes necessary.

This will finally be done by adopting an explicit time-integration scheme based on a finite volume (FV) approximation using (4), where the FV-mesh is chosen to coincide with the FE-mesh. This enables us to use the velocity field, obtained from the FE-analysis, for the computation of the orientational flux.

In view of an explicit time-integration scheme, based on a FV approximation, the orientational balance (4) will be rewritten in its conservative form with respect to a certain volume-element V_{ij}

$$\int_{V_{ij}} \partial_t \tilde{f}_{ij} dV + \int_{\partial V_{ij}} \mathbf{u} \cdot \mathbf{v} \tilde{f}_{ij} ds = \int_{V_{ij}} \dot{f}_{ij} dV, \tag{19}$$

where the superposed dot denotes the material and $\partial_t()$ the local time derivative, respectively. Furthermore, ∂V_{ij} represents the element boundary and $\mathbf{u}$ its outward unit normal vector. Recalling that the initial 'values' of $\tilde{f}$ and f are the same for each time step, $\tilde{f}_{ij}^{k-1} = f_{ij}^{k-1}$, the application of the mean-value-theorem yields

$$\tilde{f}_{ij}^{k} = f_{ij}^{k} - \frac{\triangle t}{V_{ij}} \int_{\partial V_{ij}} f_{ij}^{k-\beta}(\cdot, s) \mathbf{u} \cdot \mathbf{v} ds \,, \qquad \beta \in [0,1] \,, \tag{20}$$

where the explicit integration scheme is obtained, if $\beta = 1$. The ODF at the element boundary, $f_{ij}^{k-1}(\cdot, s)$ is given by a linear interpolation between the ODF's of two adjacent elements, that is the mean value of the adjacent ODF's.

Note that $\tilde{f}_{ij}^{k}$ still represents a function of Φ, which is uniquely defined by three parameters, $\mathbf{a}_{ij}^{k}$ for each element. So, these coefficients may be calculated in general from the three independent values of the actual ODF. For example: If we choose $(\Phi_1, \Phi_2, \Phi_3) = (0, \pi/6, \pi/3)$ the coefficient matrix $\mathbf{a}_{ij}^{k}$ for each element is determined by

$$\mathbf{g}_{ij}^{k} = \mathbf{C} \cdot \mathbf{a}_{ij}^{k}, \quad \text{with} \quad \mathbf{g}_{ij}^{k} := \begin{bmatrix} f_{(\Phi_1)}^{-1} \\ f_{(\Phi_2)}^{-1} \\ f_{(\Phi_3)}^{-1} \end{bmatrix}_{ij}^{n} \quad \mathbf{C} := \begin{bmatrix} 1 & 0 & 1 \\ 1 & \frac{\sqrt{3}}{2} & \frac{1}{2} \\ 1 & \frac{\sqrt{3}}{2} & -\frac{1}{2} \end{bmatrix}. \tag{21}$$

In summary, the calculation of the orientational flux is reduced to the solution of three additional equations for each element; by them we embrace the whole range of anisotropy with respect to the framework given above, i.e. the ODF is capable of representing orthotropic symmetry only. Again, if the conservation of orientation is taken into account, the set of additional equations experiences a further reduction by 1 and is then within agreement with the classical theory of planar orthotropy, which is uniquely determined by two parameters, one direction and one additional material parameter.

By definition, the ODF is not defined on the element boundaries, except approximately due to the above mentioned linear interpolation. Therefore, the original domain will be surrounded by additional finite volumes, so-called boundary-volumes, where the boundary conditions are prescribed by a certain coefficient vector **a** for each of them. In principle, we distinguish three different types of boundary-volumes, see Fig. 1: *Free boundary*, across which material as well as fabric transport takes place; *Stationary boundary*, across which ODF is assumed to be stationary, however material transport may occur; *Fixed boundary*, where neither material nor orientation may cross the boundary line and consequently no boundary condition has to be applied. In our problem the free surface of a glacier is partly identified with a free boundary, where, because of the randomness of the snow-crystal-orientation, $\mathbf{a}^T = (1, 0, 0)$ will be prescribed, whereas, if the streamlines are directed outward, the state of orientation within the domain will not be influenced, therefore this part should be modelled as a stationary boundary. Due to the symmetry, the velocity field at the ice-divide is restricted to the vertical direction, so no material and hence no horizontal flux of orientation has to be considered. Therefore, similar to the bottom-line, it possesses all the properties of a fixed boundary.

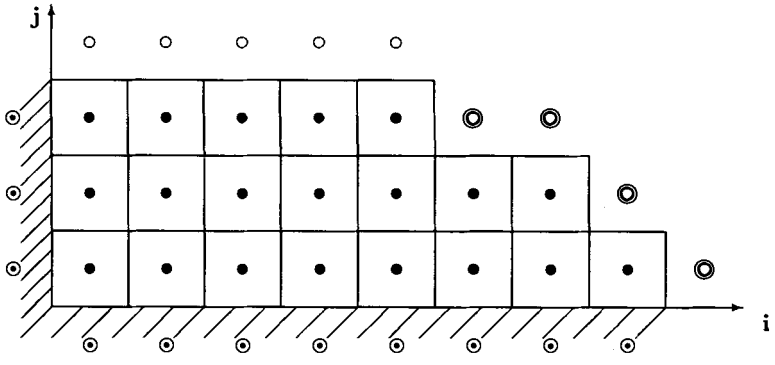

Fig. 1. Schematic ice-sheet discretization by a coupled finite-element-finite-volume approach. (◎ stationary, ⊙ fixed and ○ free boundary)

5 Application

In this section some results for stationary planar and axi-symmetric flow under SR conditions will be presented. The results of the latter are employed to identify the grain interaction parameter ν_2, which will then be used in the planar flow computations.

Identification of ν_2 is done by accommodation of the theoretical results to measurement data of the GRIP-core as well as to those obtained in [1] by using a so-called Visco-Plastic-Self-Consistent approach (VPSC). The deformation as well as the underlying loading conditions are assumed to be axi-symmetric,

$$\mathbf{F} = \gamma \mathbf{e}_1 \otimes \mathbf{e}_1 + \gamma \mathbf{e}_2 \otimes \mathbf{e}_2 + \gamma^{-2} \mathbf{e}_3 \otimes \mathbf{e}_3 \ , \qquad \mathbf{T} = \sigma_{33} \mathbf{e}_3 \otimes \mathbf{e}_3 . \tag{22}$$

To this end the ODF is needed for axi-symmetric loading conditions, which is also covered by (15) if we consider that $f_{S^1} = 1$; The anisotropy is then completely given through the parameter λ. Since $\mathbf{W} = \mathbf{0}$ for this case, the principal axes of the deformation as well as those of the structure tensor $\mathbf{M}$ coincide, so that additionally $\mathbf{W}_\mathbf{M} = \mathbf{0}$. Considering grain interaction the modified evolution equation is obtained if

$$\mathbf{D}_n = \frac{\mu}{2} \nu_1 (1 - \nu_2) \mathbf{S}, \qquad \mathbf{S} = \mathbf{T} - \tfrac{1}{3} \mathrm{tr}(\mathbf{T}) \tag{23}$$

is introduced into (3) and from which λ may be identified as

$$\lambda = \mathrm{e}^{[} -3 \int_{(t)} d_{n_{33}} dt] \approx \mathrm{e}^{[} \mu \sigma \Delta t \sum_{(i)} [\nu_1 (1 - \nu_2)]_i] \ . \tag{24}$$

Neglecting the evolution of the interaction parameters within the time step Δt, λ is approximately given by the right-hand term of (24), if the product $(\mu \sigma \Delta t)$ is taken to be constant during the computation. In contrast to λ, the anisotropy of the GRIP-core-data, displayed in Fig. 2, is related to $R_o := 2 \| \int_{H^2} f \mathbf{n} d^2 n \| - 1$, where $\| \cdot \|$ denotes the Euclidean norm. R_o gives the intensity of the actual fabric restricted to rotational symmetry [8]. It is vanishing if the **c**-axes are distributed randomly and $R_o = 1$ if all grains are oriented along the axes of revolution.[2] Accomplishing the integration over the hemisphere H^2 one obtains

$$R_o = 2 \frac{\sqrt{\lambda}}{1 + \sqrt{\lambda}} - 1 \ , \tag{25}$$

[2] However, due to the fact that the computation of R_o implies the a priori knowledge of the fabric-symmetry axes, which may in general also evolve, but are often assumed to be fixed, it does not represent the appropriate alignment measure for continuum-mechanics modelling. Furthermore, R_o can not distinguish between single-maximum and girdle fabrics

which gives the correspondence between both parameters.

We already mentioned that ν_1 and ν_2 are supposed to depend on the actual orientational state, given by M_a, which is obviously also expressable in terms of λ. For convenience and for reasons of consistency of the theory we prefer M_a as an alignment measure, however will give results with respect to R_o to make them comparable to other theories [1]. Accordingly, with $2\mathrm{sym}(\mathbf{F}) := \mathbf{F} + \mathbf{F}^T$ the cumulated strain,

$$\epsilon_c = |\mathbf{e}_3 \cdot (\mathrm{sym}(\mathbf{F}) - \mathbf{I})\mathbf{e}_3| = 1 - \frac{1}{\gamma^2}, \tag{26}$$

is given as a function of λ if the stresses (22) are introduced into the macroscopic constitutive equation, (6),(8), which yields $d_{33} = -2\dot{\gamma}/\gamma = \mu\sigma(M_{33} - M_{3333})$. Integration then leads to

$$\gamma^2 = \gamma_0^2 \exp[\mu\sigma\triangle t \sum_{(i)} [M_{33} - M_{3333}]_i] \tag{27}$$

where M_{33} and M_{3333} are λ-dependent components of the second and fourth order structure tensor, respectively.

Due to the homogeneous fine-scale flow toward an alignment of the **c**-axes along the principal loading axis, the single maximum does preserve its position. Therefore, ν_1 seems not to be affected, i.e. $\nu_1 = 1$. In contrast to this, $\nu_2 \neq 0$ because of the increasing alignment. Recalling that $\nu_2 = 0$ if the crystallites are distributed randomly, ν_2 can be generally approximated in terms of M_a by an homogeneous polynomial,

$$\nu_2 := \sum_{i=1}^{N} \alpha_i M_a^i \approx \alpha M_a \ , \tag{28}$$

where only the first order approximation is assumed to be relevant. As it was done by the authors of [1] and [3] we apply this model to the GRIP-ice-core-data given in Fig. 2. It is obvious from Fig. 2 that the curve obtained by an interaction given by $\alpha = 1.1$ represents the best fit to the data. On the other hand the VPSC-model [1], based on a non-linear stress-strain-rate-relation, can be reproduced in a wide range if $\alpha = 0.6$.

If the plane case, i.e. $f = f_{S^1}$ is considered, the material structure is completely determined by just one element of the fourth order structure tensor, $M_{1122} = 1/4 \int \sin^2 2\Phi f_{S^1} d\Phi$. As a result of the vanishing spin under biaxial load, the principal axes and values of the structure tensor coincide with those of the stresses, respectively, no matter which CC is chosen. However, examining simple shear, the material response depends on the underlying CC. First, homogeneous macro-deformation is applied to the material under pure SR-conditions. Fig. 3 shows the evolution of the shear viscosity μ_{12} due to initially ($t < 3$) biaxial compression along $\mathbf{e}_2$ and subsequent simple shear deformation. During shearing the deformation due to compression is frozen. Although

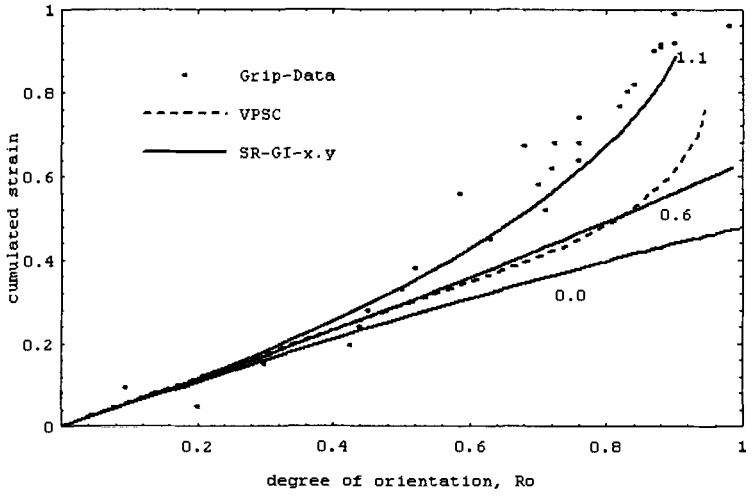

Fig. 2. Evolution of the cumulated linear strain under uniaxial compression as a function of the degree of orientation R_o for three ingeraction parameters, $x.y = \{0.0,\ 0.6,\ 1.1\}$, in comparison to GRIP-data and VPSC; SR-GI-1.1 $\Longleftrightarrow$ Sachs/Reuss, with $\alpha = 1.1$.

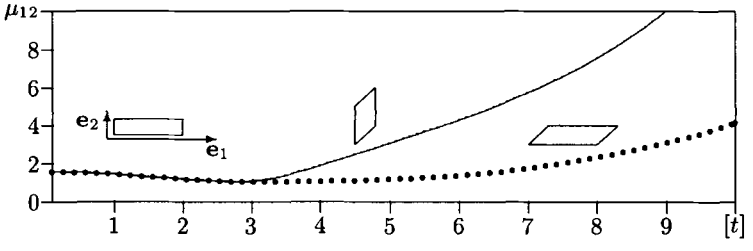

Fig. 3. The shear viscosity is decreasing under compression and increasing if shearing takes place and vice versa; However the increase is much larger if the material is sheared along $\mathbf{e}_2$ than along $\mathbf{e}_1$. Ice shows hardening behaviour if the pure SR condition is applied.

the fabric reflects a so called easy-glide-configuration with respect to simple shear along $\mathbf{e}_1$ it turns out to be unstable if the pure (SR) conditions are applied. The increase of μ_{12} as a result of shearing differs, depending on the slip direction $\mathbf{e}_1$ and $\mathbf{e}_2$. Fig. 4a displays the influence of different values of the linear interaction coeffiecient $\alpha > 1$. It can be seen from Fig. 4 that, if instead of the pure SR-model-grain interaction $\nu_2 \neq 0$ is taken into account, the shear viscosity after an initial growth decreases until it reaches in general half of its initial value. Qualitatively this behaviour is justified by

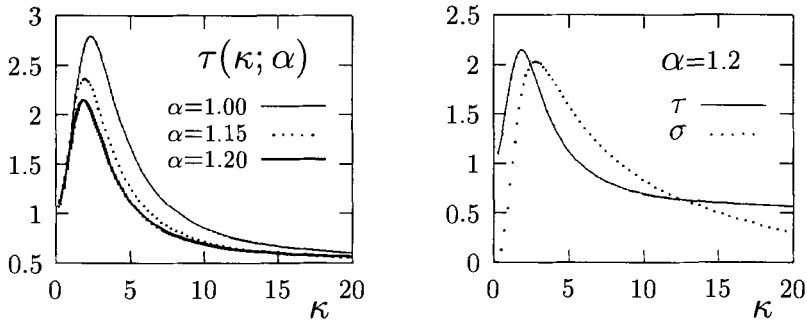

Fig. 4. Variation of the normalized: a) shear stress τ for different values of the grain interaction coefficient α, b) shear stress τ and normal stress σ for simple shear deformation and $\alpha = 1.2$ with the shearing κ

experiments, *cf.* [8]. Quantitatively it may be interpreted by the fact that in the two dimensional case the relative number of well oriented glide planes varies from 0.5 for randomly distributed crystals to 1 if total alignement is achieved. Further accomodation to real or labratory measurement is possibel by making an appropriate choice to the fine-scale accelerating factor ν_1 and by treating the constant viscosity μ also as a function of the orientational state, the applied stress and temperature.

Finally, a rectangular domain 10 times longer than high was considered as a simple model for stationary, plane, nearby-ice-divide flow, driven by gravity, Fig. 5. The plots a), b), c) show a sequence of the evolving anisotropy represented by the normalized fourth order moment $\tilde{M}_{1122} \in [0, 2]$, where if $\tilde{M}_{1122} \longrightarrow 0$ the material prefarably deforms by shearing, whereas if $\tilde{M}_{1122} \longrightarrow 2$ the resistance against biaxial deformation with respect to the underlying global coordinate system becomes small. The plots represent the data obtained after 1/2, 3/4 and 1/1 of the computation time, which was divided into 600 steps. The computation starts from an initally over-all isotropic configuration, for which $\tilde{M}_{1122} = 1$. The top line, $y = 1$, of the pictures represents a free surface, where $\tilde{M}_{1122} = 1$ was prescribed as a boundary condition. At the bottom line, $y = 0$, no slip was assumed, whereas at the right edge, $x = 10$, the horizontal velocity is supposed to vanish (symmetry condition). At $x = 0$ stationary boundary conditions are applied with respect to $\tilde{M}_{1122}$.

By means of the $\tilde{M}_{1122}$-isolines one may distinguish three principal regions. First, the upper region, where $\tilde{M}_{1122}$ is decreasing, with distinct layers, which are slightly inclined and hence reflect the variation of the vertical fabric-transport due to the varying horizontal velocity along x. This most regular part develops monotonically, however reaches a limit after half of the iterations. Second, the intermediate layer where $\tilde{M}_{1122}$ achieves its minimum values, and finally the nearby ice-divide region close to the bottom, where $\tilde{M}_{1122}$ retains its initial value caused by the boundary as well as the

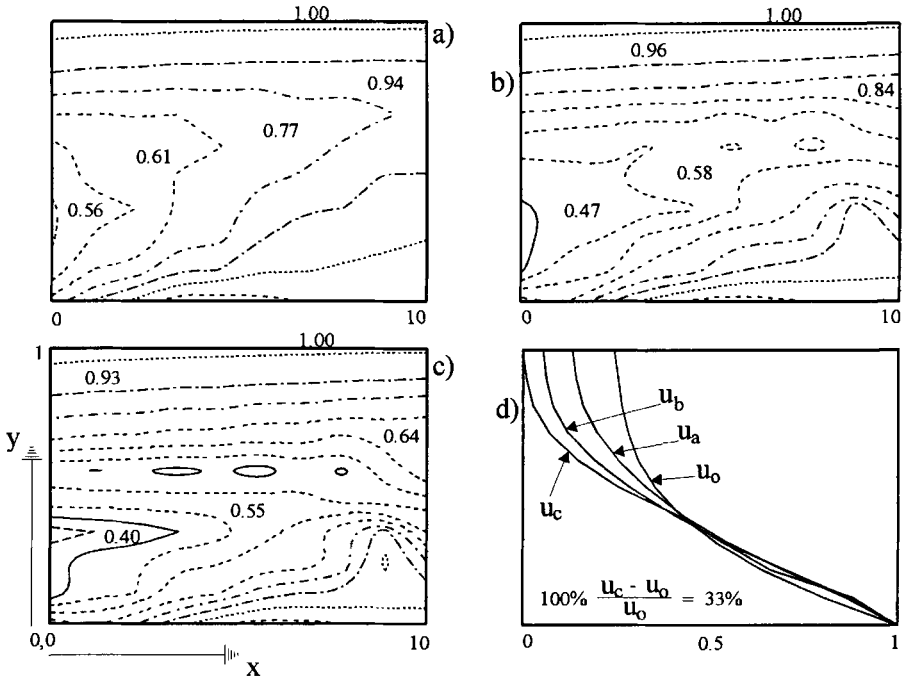

Fig. 5. a), b), c): Evolution of the anisotropy of a rectangular domain $(x, y) \in [0, 10] \times [0, 1]$ under gravitational loading by means of the normalized fourth order moment $\tilde{M}_{1122} := 8M_{1122}$. The numbers are representing the mean values of $\tilde{M}_{1122}$ within the region bounded by the $\tilde{M}_{1122}$-isolines. d): Evolution of the horizontal velocity field $u(y)$ at $x = 2$ with respect to the state of anisotropy plotted in a), b), c).

symmetry conditions, which prevent sufficient deformation. This can be indirectly deduced from Fig. 5b and Fig. 5c where a stable "isotropic bump" has developed. The evolution of the vertical velocity field of the cross-section located at $x = 1$ is given in Fig. 5d. Comparision of the free-surface velocities, $v_x(x = 1, y = 1)$, at the beginning and the end of the computation reveals an acceleration of the surface-flow of $\approx 30\%$.

6 Conclusion

We proposed an decoupled two-scale description of the load induced evolution of the orthotropic anisotropy of natural ice. The underlying evolution equation accounts for the change of the orientation of the **c**-axes of the polycrystal. To obtain the actual orientational state we proposed an exact-solution-based method, which was generalized to Eulerian coordinates and results in three additional material parameters at each integration point to account for the

evolving orthotropy. It could be shown by comparison with measurement data, that it is crucial to take grain interaction into account. The uniform-stress assumption in conjunction with one phenomenological grain interaction parameter was capable of reproducing the orientational data of polar ice-core-data. Strong influence of the grain interaction parameter on the material response was observed, which could not be considered in detail in this paper. However, it should be mentioned that in contrast to the supposition, $0 \leq \nu_2 \leq 1$, taken from physical arguments related to classical friction laws, a good fit of the GRIP-data was achieved for $\nu_2 = 1.1$. This is not necessarily a contraction, and neither is it unphysical, rather it reveals that beside the strain-induced grain rotation the influence of other mechanisms (polygonization) become dominant if the polycrystal becomes strongly aligned. On the structural level we showed, Fig. 5, that reasonable results were obtainable by applying this approach to modelling ice-sheet flow. To concentrate on the proper material response, not affected by a varying free-surface as well as by a wavy bedrock, a rectangular domain was chosen as the most simple case of two-dimensional near-by-ice-divide flow. A more elaborate discussion of the influence of different initial and boundary conditions as well as the extension of the mesoscopic mechanisms will be published elsewhere.

Acknowledgements: This work was funded in parts by the European Community within the Program: Environment and Climate, Contract No. ENV4-CT95-0125.

References

1. Castelnau O., Thorsteinsson T., Kipfstuhl J., Duval P. and Canova G. (1996) Modelling fabric development along the GRIP ice core, central Greenland. *Ann. Glaciol.*, **23**, 194-201
2. Dafalias Y.F. (1984) The plastic spin concept and a simple illustration of its role in finite plastic transformations. *Mech. Mat.*, **3**, 223
3. Gagliardini O. (1999) *Simulation numérique d'un écoulement bidimensionnel de glace polaire présentant une anisotropie induite évolutive.* Thèse de Doctorat de l'Université Joseph Fourier-Grenoble I
4. Gagliardini O. and Meyssonnier J. (1999) Analytical derivations for the behaviour and fabric evolution of a linear orthotropic ice polycrystal, *J. Geophys. Res.*, In press.
5. Gödert G. & Hutter K. (1998) Induced anisotropy in large ice shields: theory and its homogenisation,*Continuum Mech. Thermodyn.*, **10**: 293-318
6. Gödert G. & Hutter K. (1998) Material update procedure for planar flow of ice with evolving anisotropy, *Ann. Glaciol.*, **30**, In press
7. Meyssonnier & Philip (1996) A model for a tangent viscous behaviour of anisotropic polar ice. *Ann. Glaciol.*, **23**, 253-261
8. Thorsteinsson T. (1997) *Textures and fabrics in the GRIP ice core, in relation to climate history and ice deformation*, Berichte zur Polarforschung No.205 AWI-Bremerhaven

(Received 06 April 1999, accepted 14 June 1999)

Classical Mixture Models for Polythermal Ice

Kolumban Hutter[1] and Bob Svendsen[2]

[1] Institute of Mechanics, Darmstadt University of Technology, Hochschulstr. 1, 64289 Darmstadt, Germany
[2] Federal Institute for Materials Research, 12000 Berlin, Germany

Abstract. In this work, cold ice is treated as a heat conducting, viscous fluid, and temperate ice as a saturated mixture of a nearly density preserving, viscous heat conducting fluid (ice) and a nearly incompressible, ideal heat-conducting fluid (water) which exchange mass via phase change. Cold and temperate ice are separated by a singular surface, i.e., the cold-temperate transition surface (CTS), across which Stefan-type energy transfer occurs.

With the help of a general thermodynamic theory for binary mixtures, we derive an approximate formulation for polythermal ice accurate to linear orders in the volume fraction of the water. We show that the standard polythermal ice models are straightforward reductions of this formulation and we derive explicit expressions for the volumetric and surfacial melting rates using approximate energy balances.

1 Introduction

Since the late seventies, a number of continuum-mechanical models of polythermal ice sheets, i. e., ice sheets containing cold and temperate regions have been proposed [1,8,10–12]. They dealt with the derivation of the field equations and the Stefan-type transition condition at the phase boundary separating the cold and temperate ice. [12] summarizes and discusses earlier work and [1] corrects an inadequate expression for the heat flux, among other things. The theory is now routinely applied in climate modelling of large ice sheets, [2], and glaciers, [5,6,9,4] and others, but has never been formulated from a rigorous thermodynamic point of view. This is accomplished in the current work under the assumption that the pore space in which water in the ice collects is small. A binary mixture concept derived from first thermodynamic principles, [3,17], is used and equations are consistently linearized in the water volume fraction. The two possible models that emerge from this approach delineate the approximations of the earlier formulations and put them on more solid ground. The simplier of these two models describes temperate ice as a mixture involving the balance laws of mass for ice and water, as well as momentum and energy balances for the mixture as a whole to derive a phenomenological relationship for the dissipative moisture production. This model is in agreement with the earlier models of Hutter [10–12], Greve [1] and (in a restrictive sense) Fowler and Larson [8]. The more sophisticated model works with mass and momentum balances for both ice and water, thus accounting better for seepage processes via Darcy interaction between ice and

water. As in the first model, the moisture production is determined here via the mixture energy balance. Models of this complexity have been proposed by Fowler [7] and Hutter [12], albeit with simpler constitutive relations than obtained in the current approach.

One *proviso* to the present formulation should perhaps be made. The mixture concept supposes that each constituent is present in each material point of the mixture. This assuption may in fact in reality not be borne out and may overemphasize the role of the formal derivation. While this argument must be accepted, we may counterargue from an *a posteriori* point of view. The consistently linearized[1] formulation generates equations which are very close to those of the previously and less rigorously derived theories which is encouraging. In this regard the most critical assumption of previous work is the identification of the growth rate of the internal energy of the mixture with the latent heat gain due to melting of ice, a relation representing a derived result here. Via the mixture approach, then, we are able to unify and generalize a number of previous disparate formulations in the common framework of classical mixture theory. Hopefully, the reader will gain in this way a means to understand the differences and similarities of these previous formulations.

2 General Local Balance & Sum Relations

Consider a mixture containing N constituents. The general local balance relation for the field density $\underset{a}{\psi}$ associated with a constituent with spatial velocity $\underset{a}{\boldsymbol{v}}$ can be written in the form

$$\partial \bar{\underset{a}{\psi}} = \bar{\underset{a}{\pi}}^{\psi}_{\mathrm{V}} + \operatorname{div}\left(\bar{\underset{a}{\boldsymbol{\phi}}}^{\psi} - \bar{\underset{a}{\psi}}\, \underset{a}{\boldsymbol{v}} \right) + \bar{\underset{a}{\sigma}}^{\psi}_{\mathrm{V}} + \bar{\underset{a}{\gamma}}^{\psi}_{\mathrm{V}}, \tag{1}$$

where ∂ represents the partial time derivative operator. Here $\bar{\underset{a}{\pi}}^{\psi}_{\mathrm{V}}$, $\bar{\underset{a}{\sigma}}^{\psi}_{\mathrm{V}}$ and $\bar{\underset{a}{\gamma}}^{\psi}_{\mathrm{V}}$ represent the internal production, external supply, and interaction supply, rate densities per unit mixture volume, respectively, of a quantity whose density per unit mixture volume is represented by $\bar{\underset{a}{\psi}}$. Likewise, $\bar{\underset{a}{\boldsymbol{\phi}}}^{\psi}$ represents the constituent flux density per unit mixture area of this quantity. These constituent fields per unit mixture volume, or in the case of $\bar{\underset{a}{\boldsymbol{\phi}}}^{\psi}$, per unit mixture area, are related to the corresponding fields per unit constituent volume or area using the constituent volume fraction $\underset{a}{\nu}$, i.e.,

$$\bar{\underset{a}{f}} = \underset{a}{\nu}\, \underset{a}{f}. \tag{2}$$

[1] Linearized in the volume fraction of the water.

Table 1 lists the thermomechanical cases of the fields appearing in (1). Notation is standard, however, $\underset{a}{E} := (\underset{a}{\epsilon} + \frac{1}{2}\underset{a}{\boldsymbol{v}} \cdot \underset{a}{\boldsymbol{v}})$. Moment of momentum balance

Table 1. Constituent Densities

Balance	$\underset{a}{\psi}$	$\underset{a}{\pi}^{\psi}_{\mathrm{V}}$	$\underset{a}{\bar{\boldsymbol{\phi}}}^{\psi}$	$\underset{a}{\sigma}^{\psi}_{\mathrm{V}}$	$\underset{a}{\gamma}^{\psi}_{\mathrm{V}}$
mass	$\underset{a}{\varrho}$	0	0	0	$\underset{a}{c}$
momentum	$\underset{a}{\varrho}\,\underset{a}{\boldsymbol{v}}$	0	$\underset{a}{\boldsymbol{T}}$	$\underset{a}{\boldsymbol{b}}$	$\underset{a}{\boldsymbol{m}}$
total energy	$\underset{a}{\varrho}\,\underset{a}{E}$	0	$\underset{a}{\boldsymbol{T}}^{T}\,\underset{a}{\boldsymbol{v}} - \underset{a}{\boldsymbol{q}}$	$\underset{a}{r} + \underset{a}{\boldsymbol{b}} \cdot \underset{a}{\boldsymbol{v}}$	$\underset{a}{e}$
entropy	$\underset{a}{\varrho}\,\underset{a}{\eta}$	$\underset{a}{\pi}^{\varrho\eta}_{v}$	$-\underset{a}{\theta}^{-1}\,\underset{a}{\boldsymbol{q}}$	$\underset{a}{\theta}^{-1}\,\underset{a}{r}$	$\underset{a}{\gamma}^{\varrho\eta}_{\mathrm{V}}$

is satisfied automatically by requesting that $\underset{a}{\boldsymbol{T}} = \underset{a}{\boldsymbol{T}}^{T}$ for each constituent, which we assume in what follows.

The mixture general local balance relation is of the same form as (1), i.e.,

$$\partial\psi = \pi^{\psi}_{\mathrm{V}} + \operatorname{div}\left(\boldsymbol{\phi}^{\psi} - \psi\boldsymbol{v}\right) + \sigma^{\psi}_{\mathrm{V}}, \tag{3}$$

where the mixture fields have the same interpretation as their counterparts in the constituent balance relation (1). Interpretations are as in Table 1, but without subscripts for mixture quantities, and the entropy flux is given by $\boldsymbol{\phi}^{\varrho\eta}$ and its interaction rate density by $\sigma^{\varrho\eta}_{\mathrm{V}}$. Obviously also $\boldsymbol{T} = \boldsymbol{T}^{T}$. The balance relations (1) and (3) are related to each other by the sum relations

$$(\psi, \pi^{\psi}_{\mathrm{V}}, \sigma^{\psi}_{\mathrm{V}}) = \sum_{a=1}^{N} (\underset{a}{\bar{\psi}}, \underset{a}{\bar{\pi}}^{\psi}_{\mathrm{V}}, \underset{a}{\bar{\sigma}}^{\psi}_{\mathrm{V}}), \qquad \boldsymbol{\phi}^{\psi} - \psi\boldsymbol{v} = \sum_{a=1}^{N} \left[\underset{a}{\bar{\boldsymbol{\phi}}}^{\psi} - \underset{a}{\bar{\psi}}\,\underset{a}{\boldsymbol{v}}\right]. \tag{4}$$

(e.g., [16]), which hold, iff the sum of the constituent interaction supply rate densitites vanishes, i.e.,

$$\sum \underset{a}{\bar{\gamma}}^{\psi}_{\mathrm{V}} = 0. \tag{5}$$

It is often convenient to define the specific thermodynamic fields per unit mass, denoted by φ_a and φ. Then $\underset{a}{\psi} = \underset{a}{\varrho}\,\underset{a}{\varphi}$ and $\psi = \varrho\varphi$, respectively, and the sum relation $(4)_1$ takes the form

$$\varphi = \sum \underset{a}{\bar{\xi}}\,\underset{a}{\varphi}, \tag{6}$$

where

$$\bar{\xi}_a := \varrho^{-1}\,\bar{\varrho}_a \qquad \Rightarrow \qquad \bar{\varrho}_a = \bar{\xi}_a\,\varrho, \tag{7}$$

represents the constituent mass fraction in the mixture. Obviously then

$$\rho = \sum \bar{\varrho}_a \qquad \Rightarrow \qquad 1 = \sum \bar{\xi}_a, \tag{8}$$

$$\rho \boldsymbol{v} = \sum \bar{\varrho}_a\,\boldsymbol{v}_a \qquad \Rightarrow \qquad \sum \boldsymbol{J}_a = \sum \bar{\varrho}_a\,\boldsymbol{u}_a = \boldsymbol{0}, \tag{9}$$

where

$$\boldsymbol{J}_a := \bar{\varrho}_a\,\boldsymbol{u}_a, \quad \boldsymbol{u}_a := \boldsymbol{v}_a - \boldsymbol{v}. \tag{10}$$

The quantity $\boldsymbol{v}$ is called the barycentric velocity, and $\boldsymbol{u}_a$ the constituent diffusion velocity. Lastly, the sum relation for the specific internal energy yields

$$\varepsilon = \sum \bar{\xi}_a(\epsilon_a + \tfrac{1}{2}\,\boldsymbol{u}_a.\boldsymbol{u}_a). \tag{11}$$

The flux sum relation $(4)_2$ can be expressed in the alternative form

$$\boldsymbol{\phi}^{\psi} = \sum \left[\bar{\boldsymbol{\phi}}^{\psi}_a - \bar{\psi}_a\,\boldsymbol{v}_a\right] + \psi\boldsymbol{v} = \sum \left[\bar{\boldsymbol{\phi}}^{\psi}_a - \bar{\psi}_a\,\boldsymbol{u}_a\right] \tag{12}$$

using $(4)_1$ and the constituent diffusion velocity $(10)_2$. In particular,

$$\boldsymbol{T} = \sum \left[\bar{\boldsymbol{T}}_a - \bar{\varrho}_a\,\boldsymbol{u}_a \otimes \boldsymbol{u}_a\right] = \sum \left[\bar{\boldsymbol{T}}_a - \bar{\boldsymbol{J}}_a \otimes \boldsymbol{u}_a\right], \tag{13}$$

$$\begin{aligned}\boldsymbol{q} &= \sum\{\boldsymbol{q}_a + \left[\bar{\varrho}_a(\epsilon_a + \tfrac{1}{2}\,\boldsymbol{u}_a.\boldsymbol{u}_a)\boldsymbol{1} - \bar{\boldsymbol{T}}_a\right]\boldsymbol{u}_a\} \\ &= \sum\{\boldsymbol{q}_a + \left[(\epsilon_a + \tfrac{1}{2}\,\boldsymbol{u}_a.\boldsymbol{u}_a)\boldsymbol{1} - \boldsymbol{T}_a/\varrho_a\right]\bar{\boldsymbol{J}}_a\},\end{aligned} \tag{14}$$

$$-\boldsymbol{\phi}^{\varrho\eta} = \sum \left[-\theta_a^{-1}\,\bar{\boldsymbol{q}}_a + \bar{\varrho}_a\,\eta_a\,\boldsymbol{u}_a\right] = \sum \left[-\theta_a^{-1}\,\bar{\boldsymbol{q}}_a + \eta_a\,\bar{\boldsymbol{J}}_a\right] \tag{15}$$

for the mixture Cauchy stress, heat flux and entropy flux, respectively. In the derivation of these we also used the symmetric relations $\bar{\boldsymbol{J}}_a \otimes \boldsymbol{u}_a = \boldsymbol{u}_a \otimes \bar{\boldsymbol{J}}_a$.

Let S be a non-material singular surface; across such a surface with spatial velocity $\boldsymbol{w}_s$ and unit normal $\boldsymbol{n}_s$ pointing in the positive direction such that $w_s = \boldsymbol{w}_s \cdot \boldsymbol{n}_s \geq 0$, we have the "jump" balance relations

$$\left[\!\left[\bar{\psi}_a\right]\!\right] w_s + \left[\!\left[\bar{\boldsymbol{\phi}}^{\psi}_a - \bar{\psi}_a\,\boldsymbol{v}_a\right]\!\right] = \pi^{\psi}_{as} + \sigma^{\psi}_{as} + \gamma^{\psi}_{as}, \tag{16}$$

$$[\![\psi]\!]\, w_s + [\![\boldsymbol{\phi}^{\psi} - \psi\boldsymbol{v}]\!] = \pi^{\psi}_s + \sigma^{\psi}_s \tag{17}$$

(see, e.g., [17]) for the constituent and mixture fields, respectively, where $[\![f]\!] := f^- - f^+$, as usual and $z := \boldsymbol{z} \cdot \boldsymbol{n}_s$ for any vector $\boldsymbol{z}$. Note that the surface fields appearing on the right-hand side of (16) and (17) have the same interpretation with respect to S as their "volume" counterparts appearing in (1) and (3) do with respect to the "bulk" material. Consistency of (16) and (17) requires that the sum relations

$$\pi_s^\psi = \sum_a \pi_s^\psi, \qquad \sigma_s^\psi = \sum_a \sigma_s^\psi \tag{18}$$

hold together with

$$\sum_a \gamma_s^\psi = 0. \tag{19}$$

These fields account for the effects of possible surface processes on the thermodynamic quantity in question.

A moving surface can also be represented geometrically or kinematically in the form $F_s(\boldsymbol{x}, t) = 0$; its time derivative following the surface yields

$$\partial F_s + (\operatorname{grad} F_s) \cdot \boldsymbol{w}_s = 0 \quad \Rightarrow \quad \partial F_s + (\operatorname{grad} F_s) \cdot \boldsymbol{v}^\pm = -\|\operatorname{grad}\| a_s^\pm, \tag{20}$$

where we have introduced the mixture specific volume flux on the nonmaterial surface S relative to the $(+)$ or $(-)$ sides, i.e.,

$$a_s^\pm := (w_s - v^\pm), \tag{21}$$

and used the relation $\operatorname{grad} F_s = \|\operatorname{grad} F_s\| \boldsymbol{n}_s$. In terms of $a_s^\pm$, the mixture mass jump balance on S takes the form

$$\varrho^- a_s^- = \varrho^+ a_s^+ =: -\mathcal{M} \tag{22}$$

via (17) with $\pi_s^\varrho = 0 = \sigma_s^\varrho$. $\mathcal{M}$ is called the *diffusive mass flux through the singular surface*. Using $\psi = \varrho \varphi$, (7), (10) and (22), the constituent jump balance relations (16) can also be expressed in the forms

$$-\mathcal{M} \left[\!\!\left[\bar{\xi}_a \varphi_a \right]\!\!\right] + \left[\!\!\left[\bar{\phi}_a^\psi - \varphi_a \bar{\boldsymbol{J}}_a \right]\!\!\right] = \left[\!\!\left[\bar{\phi}_a^\psi - \varphi_a \bar{\boldsymbol{J}}_s \right]\!\!\right] = \pi_s^\psi + \sigma_s^\psi + \gamma_s^\psi, \tag{23}$$

where

$$\boldsymbol{J}_s := \varrho_a (\boldsymbol{v}_a - \boldsymbol{w}_s) = \boldsymbol{J}_a - \varrho \xi_a (\boldsymbol{w}_s - \boldsymbol{v}) \tag{24}$$

represents the constituent mass flux density relative to S. On the basis of (22) and $\psi = \varrho\varphi$, (17) takes the form

$$-\mathcal{M} [\![\varphi]\!] + [\![\phi^\psi]\!] = \pi_s^\psi + \sigma_s^\psi. \tag{25}$$

Again, we emphasize that (23) and (25) are based on $\pi_s^\varrho = 0 = \sigma_s^\varrho$. In particular, the second of these conditions implies that no external mass is supplied to S beyond the jump contributions.

3 Temperate Ice Thermodynamic Fields

In this work, we are interested in so-called polythermal ice, which consists of "cold" and "temperate" regions. Cold ice consists of ice alone, while temperate ice represents ice containing a "small" amount of water. i.e., the water $(a = w)$ volume fraction $\underset{w}{\nu}$ in temperate ice is typically 10^{-2} [12], and in any case $\underset{w}{\nu} \lesssim 10^{-1}$. We will use this fact in what follows to obtain the approximate relations for various temperate ice thermodynamic fields and balance relations in terms of those of the water and ice constituents (see also [7]).

Following the standard model (e.g., [12]), ice is assumed to be a Fourier heat conducting, constant density, non-Newtonian fluid; similarly, water is modelled as a heat conducting density preserving, ideal fluid. This concept must be altered in a full mixture theory to justify the temperate ice equations as derived and motivated by Hutter [12] and amended by Greve [1]. Accordingly, we suppose the volume fraction of the fluid, $\underset{w}{\nu}$, or the porosity to be an independent constitutive quantity. A mixture theory involving this has been derived by Svendsen and Hutter [3]. In its specialization here we restrict this variable to enter the dissipative (ice) stress, but not the thermodynamic potentials which determine the stresses in thermodynamic equilibrium. In fact it is supposed that the caloric equations of state of a constituent depend solely on the temperature and density of that constituent. With this *proviso* the following assumptions are made[2]

$$
\begin{aligned}
&\underset{i}{\varrho} \cong \text{const.}, && \underset{w}{\varrho} \cong \text{const.},\\
&\underset{i}{\boldsymbol{S}} := \underset{i}{\boldsymbol{T}} + \underset{i}{\pi}\,\mathbf{1}, && \underset{w}{\boldsymbol{S}} := \underset{w}{\boldsymbol{T}} + \underset{w}{\pi}\,\mathbf{1} = \mathbf{0},\\
&\underset{i}{\boldsymbol{D}} = \hat{A}(\underset{i}{\theta}, \underset{w}{\nu})\hat{f}(II_{\underset{i}{\boldsymbol{S}}})\,\underset{i}{\boldsymbol{S}}, && \qquad (26)\\
&\underset{i}{\varepsilon} = \hat{\underset{i}{\varepsilon}}(\underset{i}{\theta}, \underset{i}{\varrho}) && \underset{w}{\varepsilon} = \hat{\underset{w}{\varepsilon}}(\underset{w}{\theta}, \underset{i}{\varrho})\\
&\underset{i}{\boldsymbol{q}} = -\underset{i}{\kappa}\,\operatorname{grad}\underset{i}{\theta}, && \underset{w}{\boldsymbol{q}} = -\underset{w}{\kappa}\,\operatorname{grad}\underset{w}{\theta},
\end{aligned}
$$

where $\underset{a}{\boldsymbol{S}}$ is the constituent stress deviator, $\underset{a}{\pi}$ are the constituent pressures, and $II_{\boldsymbol{S}} = \frac{1}{2}\underset{i}{\boldsymbol{S}} \cdot \underset{i}{\boldsymbol{S}}$. Furthermore, the densitites of ice and water are assumed

---

[2] The function A should depend on $\underset{i}{\theta}$ and $\underset{i}{\nu}$; however, we will use also the saturation condition $\nu_i + \nu_w = 1$, so $\hat{A}(\theta_i, \nu_w)$ is equally meaningful.

to be so close to being constant that their variation is only taken into account in the caloric equations of state, but nowhere else. So the constituent thermodynamic pressure is $\underset{a}{p}$ and given by the free energy $\underset{a}{\psi}(\underset{a}{\theta}, \underset{a}{\varrho})$ by the relation

$$\underset{a}{p} = \varrho\, \underset{a}{\varrho}\, (\partial \underset{a}{\psi} / \partial \underset{a}{\varrho}), \tag{27}$$

which differs from $\underset{a}{\pi}$ by the saturation pressure. When evaluating $\underset{a}{\dot{\varepsilon}}$ for instance we ignore the density dependence and write

$$\dot{\underset{i}{\varepsilon}} = (\partial \hat{\underset{i}{\varepsilon}} / \partial \underset{i}{\theta})\, \dot{\underset{i}{\theta}} = \underset{i}{\varrho}\, \dot{\underset{i}{\theta}}. \tag{28}$$

In so doing we tacitly assume that the term $(\partial \hat{\underset{i}{\varepsilon}} / \partial \underset{i}{\varrho})\, \dot{\underset{i}{\varrho}}$ is negligible in comparison to the term in (28). Because of saturation and mass balance,

$$\underset{w}{\nu} + \underset{i}{\nu} = 1 \qquad \text{and} \qquad \bar{\underset{w}{\xi}} + \bar{\underset{i}{\xi}} = 1 \tag{29}$$

in a binary mixture of water and ice. In what follows we shall assume that $\underset{w}{\nu} \ll 1$ so that any dependence on $\underset{w}{\nu}$ or its derivatives of higher than first order can be ignored. From (8) and $\bar{\underset{a}{\varrho}} = \underset{a}{\varrho}\, \underset{a}{\nu}$ we have, respectively[3],

$$\varrho = \bar{\underset{w}{\varrho}} + \bar{\underset{i}{\varrho}} = \underset{i}{\varrho} + \underset{wi}{\varrho}\, \underset{w}{\nu}, \quad \underset{w}{\xi} = \frac{\bar{\underset{w}{\varrho}}}{\varrho} = \frac{\underset{w}{\varrho}\, \underset{w}{\nu}}{\underset{i}{\varrho} + \underset{wi}{\varrho}\, \underset{w}{\nu}} = r\, \underset{w}{\nu} + O(2), \quad r := \frac{\underset{w}{\varrho}}{\underset{i}{\varrho}}, \tag{30}$$

where $O(2)$ designates terms quadratic in $\underset{w}{\nu}$, or derivatives of it or quadratic combinations of these. We shall write $O(\nu_m^2)$ if the error is exactly of order ν_m^2. Furthermore, $\underset{wi}{f} := \underset{w}{f} - \underset{i}{f}$ for any field f; the first of (30) is exact, the second has an error[4] of order 2 in $\underset{w}{\nu}$. In much the same we may then deduce

[3] The density ratio is denoted here by r, the same symbol as the energy supply. Since the latter is always zero in this application there is no danger of confusion.

[4] We use the following numbers for estimations [15]; $\underset{i}{\varrho} = 9.18 \times 10^2 \mathrm{kgm}^{-3}$, $\underset{w}{\varrho} = 1. \times 10^3 \mathrm{kgm}^{-3}$, $\underset{i}{\kappa} = 2.2 \times 10^0 \mathrm{Jm}^{-1}\mathrm{K}^{-1}\mathrm{s}$, $C\underset{i}{\varrho} = 2.01 \times 10^3 \mathrm{Jkg}^{-1}\mathrm{K}^{-1}$, $\underset{wi}{h} = 3.35 \times 10^5 \mathrm{Jkg}^{-1}$. This gives $\underset{wi}{\varrho} = 82\,\mathrm{kg\,m}^{-3}$, $\varrho \leq 926\,\mathrm{kg\,m}^{-3}$, $\underset{w}{\xi} < 1.1$, etc .

the following relations:

$$
\begin{aligned}
\boldsymbol{v} &= \underset{w}{\bar{\xi}}\,\underset{w}{\boldsymbol{v}} + \underset{i}{\bar{\xi}}\,\underset{i}{\boldsymbol{v}} = \underset{i}{\boldsymbol{v}} + \underset{wi}{\boldsymbol{v}}\,\underset{w}{\bar{\xi}} = \underset{i}{\boldsymbol{v}} + r\,\underset{wi}{\boldsymbol{v}}\,\underset{w}{\nu} + O(\underset{w}{\nu}^2),\\
\boldsymbol{D} &= \underset{i}{\boldsymbol{D}} + \underset{w}{\bar{\xi}}\,\underset{wi}{\boldsymbol{D}} + \mathrm{sym}\{\underset{wi}{\boldsymbol{v}} \otimes (\mathrm{grad}\,\underset{w}{\bar{\xi}})\}\\
&= \underset{i}{\boldsymbol{D}} + r\,\underset{wi}{\boldsymbol{D}}\,\underset{w}{\nu} + r\mathrm{sym}\{\underset{wi}{\boldsymbol{v}} \otimes (\mathrm{grad}\,\underset{w}{\nu})\} + O(2),\\
\underset{w}{\boldsymbol{u}} &= (1 - \underset{w}{\bar{\xi}})\,\underset{wi}{\boldsymbol{v}} = \underset{wi}{\boldsymbol{v}} - r\,\underset{wi}{\boldsymbol{v}}\,\underset{w}{\nu} + O(\underset{w}{\nu}^2),\\
\underset{i}{\boldsymbol{u}} &= -\underset{w}{\bar{\xi}}\,\underset{wi}{\boldsymbol{v}} = -r\,\underset{wi}{\boldsymbol{v}}\,\underset{w}{\nu} + O(\underset{w}{\nu}^2),\\
\underset{w}{\bar{\boldsymbol{J}}} &= \underset{w}{\bar{\varrho}}(1 - \underset{w}{\bar{\xi}})\,\underset{wi}{\boldsymbol{v}} = \underset{w}{\varrho}\,\underset{wi}{\boldsymbol{v}}\,\underset{w}{\nu} + O(\underset{w}{\nu}^2),\\
\underset{i}{\bar{\boldsymbol{J}}} &= -\underset{wi}{\varrho}(1 - \underset{w}{\bar{\xi}})\,\underset{wi}{\boldsymbol{v}} = -\underset{w}{\varrho}\,\underset{wi}{\boldsymbol{v}}\,\underset{wi}{\nu} + O(\underset{w}{\nu}^2).
\end{aligned}
\tag{31}
$$

Note that $\underset{wi}{\boldsymbol{v}}$ is analogous to the *seepage velocity* in soil mechanics. Equations (31) concern the independent fields. As for the dependent ones the water mass flux $\underset{w}{\bar{\boldsymbol{J}}}$ relative to temperate ice is assumed to obey the Fickian relation

$$
\underset{a}{\bar{\boldsymbol{J}}} = -\underset{w}{\mu}(\mathrm{grad}\,\underset{a}{\bar{\xi}}) = -r\,\underset{w}{\mu}(\mathrm{grad}\,\underset{w}{\nu}) + O(2), \tag{32}
$$

where $\underset{w}{\mu}$ represents the water mass diffusivity. It is thought to lie in the range $10^{-2} - 10^{-6}$ kg m^{-1}s^{-1} (e.g., [14]) but is not well quantified. For the temperate ice specific internal energy ε, we obtain

$$
\begin{aligned}
\varepsilon &= \underset{w}{\bar{\xi}}(\underset{w}{\varepsilon} + \tfrac{1}{2}\,\underset{w}{\boldsymbol{u}} \cdot \underset{w}{\boldsymbol{u}}) + \underset{i}{\bar{\xi}}(\underset{i}{\varepsilon} + \tfrac{1}{2}\,\underset{i}{\boldsymbol{u}} \cdot \underset{i}{\boldsymbol{u}})\\
&= \underset{i}{\varepsilon} + (\underset{wi}{\varepsilon} + \tfrac{1}{2}\,\underset{wi}{\boldsymbol{v}} \cdot \underset{wi}{\boldsymbol{v}})\,\underset{w}{\bar{\xi}} - \tfrac{1}{2}(\underset{wi}{\boldsymbol{v}} \cdot \underset{wi}{\boldsymbol{v}})\,\underset{w}{\bar{\xi}}^2\\
&= \underset{i}{\varepsilon} + r(\underset{wi}{\varepsilon} + \tfrac{1}{2}\,\underset{wi}{\boldsymbol{v}} \cdot \underset{wi}{\boldsymbol{v}})\,\underset{w}{\nu} + O(\underset{w}{\nu}^2).
\end{aligned}
\tag{33}
$$

Introducing the constituent specific enthalpy $\underset{a}{h} := \underset{a}{\varepsilon} + \underset{a}{\varrho}^{-1}\,\underset{a}{p}$, where $\underset{a}{p}$ represents the constituent thermodynamic pressure, we obtain the expression

$$
\underset{wi}{\varepsilon} = \underset{wi}{h} - (\underset{w}{\varrho}^{-1}\,\underset{w}{p} - \underset{i}{\varrho}^{-1}\,\underset{i}{p}) \tag{34}
$$

for the difference in specific internal energy $\underset{wi}{\varepsilon}$ between water and ice, where $\underset{wi}{h}$ represents the ice latent heat of melting (usually denoted by L). Since

the ice and water constituents of temperate ice are assumed to remain on the ice-water phase boundary (PB) during their motion/deformation, we have $p_w = p_{PB} = p_i$, implying

$$\varepsilon_{wi} = h_{wi} - (\varrho_w^{-1} - \varrho_i^{-1}) p_{PB} = h_{wi} + \varrho_{wi}\, p_{PB} / \varrho_w\, \varrho_i \tag{35}$$

from (34). With $p_{PB} \lesssim 10^6$ Pa, we have $\varrho_{wi}\, p_{PB} / \varrho_w\, \varrho_i \lesssim 100$ J/kg and so $\varepsilon_{wi} \approx h_{wi}$. Under the assumption $\varepsilon_{wi} \gg \frac{1}{2}\, \boldsymbol{v}_{wi} \cdot \boldsymbol{v}_{wi}$, $(33)_2$ yields the expressions

$$\varepsilon = \varepsilon_i + \varepsilon_{wi}\, \bar{\xi}_w = \varepsilon_i + r\, \varepsilon_{wi}\, \nu_a + O(\nu_w^2) \tag{36}$$

for the temperate ice specific internal energy ε to first order in $\bar{\xi}_a$ and ν_w. Since estimates of $\|\boldsymbol{v}_w\|$ and so $\|\boldsymbol{v}_{wi}\|$ are problematic, we simply note that $\frac{1}{2}\, \boldsymbol{v}_{wi} \cdot \boldsymbol{v}_{wi}$ will be less than $\varepsilon_{wi} \approx h_{wi}$ if $\|\boldsymbol{v}_w\| \lesssim 26\text{ms}^{-1}$; for comparison, note that $\|\boldsymbol{v}_i\| \lesssim 10^{-6}$ ms^{-1}, so omitting $\frac{1}{2}\, \boldsymbol{v}_{wi}^2$ is physically reasonable. Turning now to the temperate ice specific entropy η, we obtain

$$\eta = \bar{\xi}_w\, \eta_w + \bar{\xi}_i\, \eta_i = \eta_i + \eta_{wi}\, \bar{\xi}_w = \eta_i + r\, \eta_{wi}\, \nu_{wi} + O(\nu_w^2) \tag{37}$$

from (6) and Table 1. In terms of the constituent specific free enthalpy (chemical potential)

$$g_a := \varepsilon_a + \varrho_a^{-1}\, p_a - \theta_a\, \eta_a = h_a - \theta_a\, \eta_a, \tag{38}$$

η_{wi} takes the form

$$\eta_{wi} = \theta_w^{-1}\, (h_w - g_a) - \theta_i^{-1}\, (h_i - g_i). \tag{39}$$

Again, since ice and water are assumed to remain on the phase boundary during their motion or deformation, we necessarily have

$$g_w = g_i, \quad \theta_w = \theta_{PB} = \theta = \theta_i, \tag{40}$$

where θ represents the mixture temperature. Thus, from (39) we deduce $\eta_{wi} = \theta_{PB}\, h_{wi}$, and consequently from (37) we obtain

$$\eta = \eta_i + \theta_{PB}^{-1}\, r\, h_{wi}\, \nu_w + O(\nu_w^2) \tag{41}$$

for the temperate ice specific entropy η. From (13), using $\underset{i}{\boldsymbol{J}} = -\underset{w}{\boldsymbol{J}}$ and employing $(31)_5$ we find that

$$\begin{aligned}\boldsymbol{T} &= \bar{\underset{w}{\boldsymbol{T}}} + \bar{\underset{i}{\boldsymbol{T}}} - \bar{\underset{w}{\boldsymbol{J}}} \otimes \underset{w}{\boldsymbol{u}} - \bar{\underset{i}{\boldsymbol{J}}} \otimes \underset{i}{\boldsymbol{u}} \\ &= \underset{i}{\boldsymbol{T}} - (\underset{wi}{\pi}\mathbf{1} + \underset{i}{\boldsymbol{S}} + \underset{w}{\boldsymbol{J}} \otimes \underset{wi}{\boldsymbol{v}})\,\underset{w}{\nu} \\ &= \underset{i}{\boldsymbol{T}} - (\underset{wi}{\pi}\mathbf{1} + \underset{i}{\boldsymbol{S}} + \underset{w}{\varepsilon}\,\underset{wi}{\boldsymbol{v}} \otimes \underset{wi}{\boldsymbol{v}})\,\underset{w}{\nu} + O(\underset{w}{\nu}^2).\end{aligned} \tag{42}$$

Similarly, the temperate ice heat-flux density takes the form

$$\begin{aligned}\boldsymbol{q} &= \bar{\underset{w}{\boldsymbol{q}}} + \bar{\underset{i}{\boldsymbol{q}}} + [(\underset{w}{\varepsilon} + \tfrac{1}{2}\,\bar{\underset{w}{\boldsymbol{u}}} \cdot \bar{\underset{w}{\boldsymbol{u}}})\mathbf{1} - \underset{w}{\boldsymbol{T}}/\underset{w}{\varrho}]\,\bar{\underset{w}{\boldsymbol{J}}} + [(\underset{i}{\varepsilon} + \tfrac{1}{2}\,\bar{\underset{i}{\boldsymbol{u}}} \cdot \bar{\underset{i}{\boldsymbol{u}}})\mathbf{1} - \underset{i}{\boldsymbol{T}}/\underset{i}{\varrho}]\,\bar{\underset{i}{\boldsymbol{J}}} \\ &= \underset{i}{\boldsymbol{q}} + \underset{wi}{\boldsymbol{q}}\,\underset{w}{\nu} + \{[\underset{wi}{\varepsilon} + (\tfrac{1}{2} - \bar{\underset{w}{\xi}})(\underset{wi}{\boldsymbol{v}} \cdot \underset{wi}{\boldsymbol{v}}) + \underset{w}{\pi}/\underset{w}{\varrho}]\mathbf{1} + \underset{i}{\boldsymbol{T}}/\underset{i}{\varrho}\}\,\bar{\underset{w}{\boldsymbol{J}}} \\ &= \underset{i}{\boldsymbol{q}} + \{\underset{wi}{\boldsymbol{q}} + \underset{w}{\varrho}[(\underset{wi}{\varepsilon} + \underset{w}{\pi}/\underset{w}{\varrho})\mathbf{1} + \underset{i}{\boldsymbol{T}}/\underset{i}{\varrho}\} + \tfrac{1}{2}(\underset{wi}{\boldsymbol{v}} \otimes \underset{wi}{\boldsymbol{v}})]\,\underset{wi}{\boldsymbol{v}}\}\,\underset{w}{\nu} + O(\underset{w}{\nu}^2)\end{aligned} \tag{43}$$

from (14), again using (9), $(26)_2$,$(26)_3$ and $(31)_5$. Now, using Fourier's heat law

$$\underset{a}{\boldsymbol{q}} = -\underset{a}{\kappa}\,(\operatorname{grad}\underset{a}{\theta}) = -\underset{a}{\kappa}\,\underset{PB}{\delta}\,(\operatorname{grad} p_{PB}), \quad \underset{PB}{\delta} := -\frac{\underset{wi}{\varrho}\,\underset{PB}{\theta}}{\underset{w}{\varrho}\,\underset{i}{\varrho}\,\underset{wi}{h}}, \tag{44}$$

where $\underset{PB}{\delta}$ is the Clausius-Clapeyron relation, and introducing the assumption that

$$\underset{wi}{\varepsilon} \gg \tfrac{1}{2}\,\underset{wi}{\boldsymbol{v}} \cdot \underset{wi}{\boldsymbol{v}} + \frac{1}{\underset{w}{\varrho}}\,\underset{w}{\pi} + \frac{1}{\sqrt{3}\,\underset{i}{\varrho}}\,\|\underset{i}{\boldsymbol{T}}\|, \tag{45}$$

(43) takes the form

$$\begin{aligned}\boldsymbol{q} &= -(\underset{i}{\kappa} + \underset{wi}{\kappa}\,\underset{w}{\nu})\,\underset{PB}{\delta}\,(\operatorname{grad} p_{PB}) + \underset{wi}{\varepsilon}\,\bar{\underset{w}{\boldsymbol{J}}} \\ &= -\underset{i}{\kappa}\,\underset{PB}{\delta}\,(\operatorname{grad} p_{PB}) + [\underset{w}{\varrho}\,\underset{wi}{\varepsilon}\,\underset{wi}{\boldsymbol{v}} - \underset{i}{\kappa}\,\underset{PB}{\delta}\,(\operatorname{grad} p_{PB})]\,\underset{w}{\nu} + O(\underset{w}{\nu}^2).\end{aligned} \tag{46}$$

Note that, with $\|\underset{i}{\boldsymbol{T}}\| \lesssim 10^6$ Pa, the third term on the right-hand side of (45) is $\lesssim 500\ \mathrm{J\,kg^{-1}}$. Lastly,

$$
\begin{aligned}
-\phi^{\varrho\eta} &= \underset{w}{\theta}^{-1}\,\underset{w}{\boldsymbol{q}} + \underset{w}{\theta}^{-1}\,\underset{i}{\boldsymbol{q}} + \underset{w}{\eta}\,\underset{w}{\bar{\boldsymbol{J}}} + \underset{i}{\eta}\,\underset{i}{\bar{\boldsymbol{J}}} \\
&= -\underset{PB}{\theta}^{-1}\,(\underset{i}{\kappa} + \underset{wi}{\kappa}\,\underset{w}{\nu})\,\delta_{PB}\,(\operatorname{grad} p_{PB}) + \underset{PB}{\theta}^{-1}\,\underset{wi}{h}\,\underset{w}{\bar{\boldsymbol{J}}} \qquad (47)\\
&= -\underset{PB}{\theta}^{-1}\,\underset{i}{\kappa}\,\delta_{PB}\,(\operatorname{grad} p_{PB}) \\
&\quad + \underset{PB}{\theta}^{-1}\left[\underset{w}{\varrho}\,\underset{wi}{h}\,\underset{wi}{\bar{\boldsymbol{v}}} - \underset{wi}{\kappa}\,\delta_{PB}\,(\operatorname{grad} p_{PB})\right]\underset{i}{\nu} + O(\underset{w}{\nu}^2)
\end{aligned}
$$

follows from Table 1 and (15) for the temperate ice entropy-flux density $-\phi^{\varrho\eta}$. Using (35), $(43)_2$,(44) and $(47)_2$ yields the expression

$$
\begin{aligned}
\phi^{\varrho\eta} = -(1/\theta_{PB})\boldsymbol{q} + (1/\theta_{PB})\Big\{\Big[&(\underset{wi}{\varrho}\,p_{PB}/\underset{w}{\varrho}\,\underset{i}{\varrho}) \\
&+(\tfrac{1}{2} - \underset{w}{\bar{\xi}})(\underset{wi}{\boldsymbol{v}}\cdot\underset{wi}{\boldsymbol{v}}) + \underset{w}{\pi}/\underset{w}{\varrho}\Big]\mathbf{1} + \underset{i}{\boldsymbol{T}}/\underset{i}{\varrho}\Big\}\,\underset{w}{\bar{\boldsymbol{J}}} \qquad (48)
\end{aligned}
$$

for the temperate ice entropy flux $\phi^{\varrho\eta}$ in terms of its heat flux $\boldsymbol{q}$ and the water mass flux $\underset{w}{\bar{\boldsymbol{J}}}$. In general, then, $\phi^{\varrho\eta}$ and $\boldsymbol{q}$ are not collinear, although the coefficient of $\underset{w}{\bar{\boldsymbol{J}}}$ in (48) is probably quite small.

4 Temperate Ice Balance Relations

The *mass balances* can be stated either as

$$
\begin{aligned}
&\partial\,\underset{w}{\bar{\varrho}} + \operatorname{div}(\underset{w}{\bar{\varrho}}\,\underset{a}{\boldsymbol{v}}) = \underset{w}{\bar{c}}, && \partial\varrho + \operatorname{div}(\varrho\boldsymbol{v}) = 0,\\
&\qquad\qquad \text{or} \qquad\qquad && \\
&\partial\,\underset{i}{\bar{\varrho}} + \operatorname{div}(\underset{i}{\bar{\varrho}}\,\underset{i}{\boldsymbol{v}}) = \underset{i}{\bar{c}}, && \varrho\,\dot{\underset{w}{\xi}} + \operatorname{div}\underset{w}{\bar{\boldsymbol{J}}} = \bar{c}. \qquad (49)
\end{aligned}
$$

The equations on the left are the mass balances for the constituents water and ice, those on the right are for the mixture as a whole (using $\underset{i}{\bar{c}} = -\underset{w}{\bar{c}}$) and the water mass. In either case a closure condition for $\underset{w}{\bar{c}}$ must be written down. We will determine it below by the energy balance. In what follows we regard $\underset{w}{\nu}$ as a basic field and not $\underset{w}{\bar{\xi}}$.Transformation from $\underset{w}{\bar{\xi}}$ to $\underset{w}{\nu}$ are always possible to order $O(2)$ by use of $(30)_2$. With $\dot{\varrho}/\varrho = \underset{wi}{\bar{\varrho}}\,\dot{\underset{w}{\nu}}/\varrho = \underset{wi}{\xi}\,\dot{\underset{w}{\nu}} = (r-1)\,\dot{\underset{w}{\nu}} + O(2)$, we see that $\dot{\varrho}/\varrho$ is $O(\dot{\underset{w}{\nu}})$; however the pre-factor $(r-1)$ is small as well and

will here also be considered of $O(\underset{w}{\nu})$. Then $\dot{\varrho}/\varrho$ is $O(2)$ and the mixture mass balance $(49)_3$ reduces to $\operatorname{div} \boldsymbol{v} = 0$. Thus with the above deductions and (32) we have for $(49)_{3,4}$ to $O(2)$

$$\operatorname{div} \boldsymbol{v} = 0, \qquad \varrho(r \underset{w}{\nu})^{\cdot} = \operatorname{div}(\underset{w}{r} \operatorname{grad}(r \underset{w}{\nu})) + \underset{w}{c}, \tag{50}$$

with the possible replacements of $r \underset{w}{\nu}$ by $\bar{\underset{w}{\xi}}$.

The momentum balance laws take the forms

$$\begin{aligned} \bar{\underset{w}{\varrho}} \underset{w}{\boldsymbol{v}}' + \bar{\underset{w}{c}} \underset{w}{\boldsymbol{v}} &= -\operatorname{grad} \bar{\underset{w}{\pi}} + \bar{\underset{w}{\varrho}} \boldsymbol{g} + \bar{\underset{w}{\boldsymbol{m}}}, \\ \bar{\underset{i}{\varrho}} \underset{i}{\boldsymbol{v}}' + \bar{\underset{i}{c}} \underset{i}{\boldsymbol{v}} &= -\operatorname{grad} \bar{\underset{i}{\pi}} + \operatorname{div} \bar{\underset{i}{\boldsymbol{S}}} + \bar{\underset{w}{\varrho}} \boldsymbol{g} + \bar{\underset{i}{\boldsymbol{m}}} \end{aligned} \tag{51}$$

for water and ice, respectively, from (1) and Table 1, $(49)_{1,2}$, assuming $\underset{a}{\boldsymbol{b}} = \bar{\underset{a}{\varrho}} \boldsymbol{g}$, and defining $\underset{a}{\boldsymbol{v}}' := \partial \underset{a}{\boldsymbol{v}} + (\operatorname{grad} \underset{a}{\boldsymbol{v}}) \underset{a}{\boldsymbol{v}}$ as usual. For the temperate ice (i.e., mixture) linear momentum balance, we obtain

$$\varrho \dot{\boldsymbol{v}} = \operatorname{div} \boldsymbol{T} + \varrho \boldsymbol{g} \tag{52}$$

from (3), Table 1, $(49)_3$ with $\boldsymbol{b} = \varrho \boldsymbol{g}$. It is customary to work with the mixture momentum balance only. This frees us from postulating a constitutive equation for the interaction force $\underset{i}{\boldsymbol{m}} = -\underset{w}{\boldsymbol{m}}$. One is then left with (42) as expression of the stress.

The specific internal energy balance for the mixture is given by

$$\varrho \dot{\varepsilon} = \boldsymbol{T} \cdot \boldsymbol{D} - \operatorname{div} \boldsymbol{q} + \varrho r. \tag{53}$$

Since the temperature in temperate ice (and its constituents) is in essence by definition fixed at the ice melting point, this last balance plays no "active" role here; we can, however, use it as follows. Substituting (36) and $(46)_1$ into (53), and rearranging, we obtain

$$\begin{aligned} \boldsymbol{T} \cdot \boldsymbol{D} + \varrho r = \varrho \dot{\varepsilon} + \operatorname{div} \boldsymbol{q} &= \varrho[\dot{\underset{i}{\varepsilon}} + \dot{\underset{wi}{\varepsilon}} \bar{\underset{w}{\xi}}] + \varrho \underset{wi}{\varepsilon} \dot{\bar{\underset{w}{\xi}}} \\ &\quad + \operatorname{div}(\underset{wi}{\varepsilon} \bar{\underset{w}{\boldsymbol{J}}}) - \operatorname{div}[(\underset{i}{\kappa} + \underset{wi}{\kappa} \underset{i}{\nu}) \delta_{PB} (\operatorname{grad} p_{PB})] \\ &= \varrho[\dot{\underset{i}{\varepsilon}} + \dot{\underset{wi}{\varepsilon}} \bar{\underset{w}{\xi}}] - \operatorname{div}[(\underset{i}{\kappa} + \underset{wi}{\kappa} \underset{i}{\nu}) \delta_{PB} (\operatorname{grad} p_{PB})] \\ &\quad + (\operatorname{grad} \underset{wi}{\varepsilon}) \cdot \bar{\underset{w}{\boldsymbol{J}}} + \underset{wi}{\varepsilon} \bar{\underset{w}{c}}, \end{aligned} \tag{54}$$

where we have used the water mass balance in the form $(49)_4$ to write $(54)_3$. From $(54)_3$, we then deduce the expression

$$\underset{wi}{\varepsilon}\,\bar{\underset{w}{c}} = \boldsymbol{T}\cdot\boldsymbol{D} + \varrho r + [\operatorname{grad}(\underset{i}{\kappa} + \underset{wi}{\kappa}\,\underset{w}{\nu}) - \underset{wi}{c_\varrho}\,\bar{\underset{a}{\xi}}]\cdot\delta_{PB}(\operatorname{grad} p_{PB}) - \varrho[\underset{i}{c_\varrho} + \underset{wi}{c_\varrho}\,\bar{\underset{w}{\xi}}]\delta_{PB}\,\dot{p}_{PB} \tag{55}$$

for the water mass interaction supply rate density $\bar{\underset{w}{c}}$ in temperate ice with $\dot{\underset{a}{\varepsilon}} = \underset{a}{c_\varrho}\,\delta_{PB}\,\dot{p}_{PB}$ and $(\operatorname{grad}\underset{a}{\varepsilon}) = \underset{a}{c_\varrho}\,\delta_{PB}(\operatorname{grad} p_{PB})$. Clearly, (55) unifies the water mass and temperate ice internal energy balances. If we neglect the non-mechanical energy supply rate density ϱr, as well as the $(\operatorname{grad} p_{PB})$ and $\dot{p}_{PB}$ terms in this last result, it simplifies to $\bar{\underset{w}{c}} = \boldsymbol{T}\cdot\boldsymbol{D}/\underset{wi}{\varepsilon}$; with $\underset{wi}{\varepsilon} \approx \underset{wi}{h}$ as discussed above, this corresponds to the usual constitutive assumption (e.g., [10,12]). From $(31)_2$ and (42), we also have

$$\boldsymbol{T}\cdot\boldsymbol{D} = \underset{i}{\boldsymbol{T}}\cdot\underset{i}{\boldsymbol{D}} + [r(\underset{i}{\boldsymbol{T}}\cdot\underset{wi}{\boldsymbol{D}}) - (\underset{wi}{\pi}\,\mathbf{1} + \underset{i}{\boldsymbol{S}} + \underset{w}{\varepsilon}\,\underset{wi}{\boldsymbol{v}}\otimes\underset{wi}{\boldsymbol{v}})\cdot\underset{i}{\boldsymbol{D}}]\,\underset{w}{\nu} + r(\underset{i}{\boldsymbol{T}}\,\underset{wi}{\boldsymbol{v}})\cdot(\operatorname{grad}\underset{w}{\nu}) + O(2) \tag{56}$$

for the mechanical dissipation in temperate ice.

At this stage two possible theories of polythermal ice become apparent: The simpler of the two uses (50) and (54) as the balance laws of mass for the mixture and the constituent water as well as the mixture momentum and regards these as five field equations for $\boldsymbol{v}$, $\underset{w}{\nu}$ (or $\bar{\underset{w}{\xi}}$) and a pressure π with closure condition (55) for the water mass supply rate density $\underset{wi}{\boldsymbol{v}}$ and constitutive relations for p_{PB} (via the free energy $\underset{a}{\psi}$), $\underset{i}{\kappa}, \underset{w}{\kappa}, \underset{i}{C\varrho}, \underset{w}{C\varrho}$. Note, these are all known as material parameters of ice and water, respectively. $\boldsymbol{T}$ and $\boldsymbol{T}\cdot\boldsymbol{D}$ can not be evaluated from (42) and (56), respectively, in this case, because these expressions involve the peculiar velocities $\underset{a}{\boldsymbol{v}}\,(a = i, w)$, which one does not regard as independent fields. Instead,

$$\boldsymbol{D} = \hat{A}(\theta_{PB}, \underset{w}{\nu})f(II_{\boldsymbol{S}})\boldsymbol{S},$$

where

$$\boldsymbol{T} = \boldsymbol{S} - \pi\mathbf{1}, \qquad II_{\boldsymbol{S}} := \tfrac{1}{2}\boldsymbol{S}\cdot\boldsymbol{S}, \qquad \pi = p_{PB} \tag{57}$$

are postulated, which formally closes the theory. This essentially is the formulation of Hutter, [10], [11] [12] and Greve [1].

Alternatively, and more accurately one uses (50) and (51) as field equations for the eight fields $\underset{i}{\boldsymbol{v}}$, $\underset{w}{\boldsymbol{v}}$, $\underset{w}{\nu}$ (or $\underset{\bar{w}}{\bar{\xi}}$) and a pressure π again with closure relation (55) for $\underset{w}{\bar{c}}$ and constitutive relations for p_{PB}, $\underset{i}{\kappa}$, $\underset{w}{\kappa}$, $C\underset{i}{\varrho}$, $C\underset{w}{\varrho}$, as before, but now (56) is meaningful (to linear order in $\underset{w}{\nu}$) and $\underset{i}{\boldsymbol{T}}$ may be evaluated with the aid of (42) and a stress-stretching relation for the ice as prescribed in (26). Two further closure conditions are those for $\underset{i}{\pi}$, $\underset{w}{\pi}$ and $\underset{w}{\boldsymbol{m}}$; they are (see [4])

$$\underset{w}{\pi} = \underset{w}{\nu}\pi, \qquad \underset{i}{\pi} = (1 - \underset{w}{\nu})\pi, \qquad \underset{w}{\boldsymbol{m}} = -\pi \operatorname{grad} \underset{w}{\nu} + O(2). \tag{58}$$

A theory of this complexity was given by Fowler [7], Greve [1] and Hutter, [9], [10], [11], but neither is as detailed as this one.

5 Jump Balance Relations at the CTS

Let the (+)-side of the CTS represent cold ice, and the (−)-side temperate ice. Assuming that no external mass is supplied to the CTS beyond jump contributions, i.e., $\sigma^{\varrho}_{\mathrm{CTS}} = 0$, we have

$$[\![\varrho]\!]\, \boldsymbol{w}_{\mathrm{CTS}} - [\![\varrho \boldsymbol{v}]\!] = 0 \quad \text{or} \quad \mathcal{M}_{\mathrm{CTS}} = -\varrho^{\pm} a^{\pm}_{\mathrm{CTS}}, \tag{59}$$

for the mixture mass jump balance from Table 1, (17) and (22) with $\pi^{\varrho}_{\mathrm{CTS}} = 0$. The condition $\underset{w}{\nu}^{+} = 0$ and (31) imply that $[\![\varrho]\!] = \varrho^{-} - \varrho^{+} = \underset{wi}{\varrho}^{-}\, \underset{w}{\nu}^{-}$ for the mass density jump across the CTS. With $\underset{w}{\nu}^{-} \lesssim 10^{-1}$, we have $[\![\varrho]\!] \lesssim 8.2$ kg m^{-3}, or about 1% of ϱ^{-}; consequently, we neglect the density difference between cold and temperate ice, i.e., we set

$$[\![\varrho]\!] = 0 \qquad \Rightarrow \qquad [\![\boldsymbol{v}]\!] = \boldsymbol{0}. \tag{60}$$

Thus, with a very small error the velocity field is continuous across the CTS. Assuming $\underset{w}{\pi}^{\varrho}_{\mathrm{CTS}} = 0$, the water mass jump balance is given by

$$\gamma^{\varrho}_{w\,\mathrm{CTS}} = \underset{a}{\bar{\varrho}}^{-}\, a^{-}_{w\,\mathrm{CTS}} = -\mathcal{M}_{\mathrm{CTS}}\, \underset{a}{\bar{\xi}}^{-} - \underset{a}{\bar{\boldsymbol{J}}}^{-} = -\underset{w}{\bar{\boldsymbol{J}}}^{-}_{\mathrm{CTS}} = -\gamma^{\varrho}_{i\,\mathrm{CTS}} \tag{61}$$

from Table 1, (19),(23), and $\underset{a}{\nu}^{+} = 0$.

Turning now to momentum, assuming $\pi^{\varrho \mathrm{V}}_{w\,\mathrm{CTS}} = 0$ the water momentum jump balance is given by

$$\gamma^{\varrho \mathrm{V}}_{w\,\mathrm{CTS}} = \bar{\varrho}^{-}_{a}\; a^{-}_{w\,\mathrm{CTS}}\; \boldsymbol{v}^{-}_{a} + \bar{\boldsymbol{T}}^{-}_{a}\, \boldsymbol{n}_{\mathrm{CTS}} = \gamma^{\varrho}_{w\,\mathrm{CTS}}\; \boldsymbol{v}^{-}_{a} - \bar{\pi}^{-}_{a}\, \boldsymbol{n}_{\mathrm{CTS}} \tag{62}$$

from Table 1, (19),(23), $(26)_2, (61)_1$, and $\nu^{+}_{w} = 0$. This last relation yields the expression

$$\bar{\pi}^{-}_{a} = (\,\gamma^{\varrho}_{w\,\mathrm{CTS}}\; \boldsymbol{v}^{-}_{a} - \gamma^{\varrho \nu}_{w\,\mathrm{CTS}}\,) \cdot \boldsymbol{n}_{\mathrm{CTS}}$$

for the volume-fraction-weighted water constraint pressure on the CTS. As for the mixture, we have

$$-\mathcal{M}_{\mathrm{CTS}}\, [\![\boldsymbol{v}]\!] + [\![\boldsymbol{T}]\!]\, \boldsymbol{n}_{\mathrm{CTS}} = \boldsymbol{0} \quad \overset{(60)}{\Rightarrow} \quad [\![\boldsymbol{T}]\!]\, \boldsymbol{n}_{\mathrm{CTS}} = \boldsymbol{0}, \tag{63}$$

i.e., the traction is continuous across the CTS. Substituting (42) in $(63)_2$ and taking the trace and the deviator, respectively, yields

$$\left[\!\left[\, \pi_{i} \,\right]\!\right] = [\, \pi_{wi} + \tfrac{1}{3}\, \varrho^{-}_{w}\; (\, \boldsymbol{v}^{-}_{wi} \cdot \boldsymbol{v}_{wi})]\; \nu^{-}_{w}\,, \quad \left[\!\left[\, \boldsymbol{S}_{i}\, \boldsymbol{n}_{\mathrm{CTS}} \,\right]\!\right] = \boldsymbol{S}^{-}_{i}\, \boldsymbol{n}_{\mathrm{CTS}}\; \nu^{-}_{w} \tag{64}$$

for the jump of the ice stress across the CTS.

¿From Table 1 and (25), with $\pi^{\varrho E}_{w\,\mathrm{CTS}} = 0 = \sigma^{\varrho E}_{w\,\mathrm{CTS}}$, the total energy-jump balance becomes $-\mathcal{M}_{\mathrm{CTS}}\, [\![\varepsilon + \tfrac{1}{2}\boldsymbol{v}\cdot\boldsymbol{v}]\!] + [\![\boldsymbol{T}^{T}\boldsymbol{v} - \boldsymbol{q}]\!] \cdot \boldsymbol{n}_{\mathrm{CTS}} = 0$, or, since $[\![\boldsymbol{v}]\!] = \boldsymbol{0}$ and $[\![\boldsymbol{T}\boldsymbol{n}_{\mathrm{CTS}}]\!] = \boldsymbol{0}$,

$$-\mathcal{M}_{\mathrm{CTS}}\; \underbrace{[\![\varepsilon]\!]}_{\bar{\xi}^{-}_{w}\; \bar{\varepsilon}^{-}_{wi}} \; - \underbrace{[\![\boldsymbol{q}\cdot\boldsymbol{n}_{\mathrm{CTS}}]\!]}_{q^{-} - \bar{q}^{+}_{i}} = 0. \tag{65}$$

Substituting the result (46) for the temperate ice heat flux in (65) and rearranging yields

$$\begin{aligned} \bar{q}^{+}_{i} &= \varepsilon^{-}_{wi}\; (\, \bar{J}^{-}_{a} + \mathcal{M}_{\mathrm{CTS}}\, \bar{\xi}^{-}_{a}\,) - \delta_{PB}\, [(\operatorname{grad} p_{PB}) \cdot \boldsymbol{n}_{\mathrm{CTS}}]\, (\, \kappa^{-}_{i} + \kappa^{-}_{wi}\; \nu^{-}_{w}\,) \\ &= \varepsilon^{-}_{wi}\; \bar{J}^{-}_{w\,\mathrm{CTS}} - \delta_{PB}\, [(\operatorname{grad} p_{PB}) \cdot \boldsymbol{n}_{\mathrm{CTS}}]\, (\, \kappa^{-}_{i} + \kappa^{-}_{wi}\; \nu^{-}_{w}\,) \\ &= h^{-}_{wi}\; \bar{J}^{-}_{w\,\mathrm{CTS}} - \delta_{PB}\, [(\operatorname{grad} p_{PB}) \cdot \boldsymbol{n}_{\mathrm{CTS}}]\; \kappa^{-}_{wi}\; \nu^{-}_{w} + (\, \varrho^{-}_{wi}\; p_{PB} / \varrho^{-}_{w}\; \varrho^{-}_{i}\,)\; \bar{J}^{-}_{w\,\mathrm{CTS}} \\ &\quad - \delta_{PB}\, [(\operatorname{grad} p_{PB}) \cdot \boldsymbol{n}_{\mathrm{CTS}}]\, \kappa^{-}_{i}\,. \end{aligned} \tag{66}$$

Lastly, we consider the mixture entropy jump balance. In this case, we have

$$-\mathcal{M}_{\mathrm{CTS}}\,[\![\eta]\!] + [\![\phi^{\varrho\eta}]\!] = \pi^{\varrho\eta}_{\mathrm{CTS}} \geq 0 \tag{67}$$

from Table 1 and (25) with $\sigma^{\varrho\eta}_{\mathrm{CTS}} = 0$. Using the result (41), the first term on the left-hand side of (67) takes the form

$$\mathcal{M}_{\mathrm{CTS}}\,[\![\eta]\!] = \theta^{-1}_{PB}\,\mathcal{M}_{\mathrm{CTS}}\,\underset{wi}{h}\,\underset{a}{\bar{\xi}^{-}}\,. \tag{68}$$

For the entropy flux density jump $[\![\phi^{\varrho\eta}]\!]$, we obtain

$$[\![\phi^{\varrho\eta}]\!] = -\theta^{-1}_{PB}\,\underset{wi}{h^{-}}\,\bar{J}^{-}_{w} + \theta^{-1}_{PB}\,\delta_{PB}\,[(\mathrm{grad}\,p_{PB})\cdot\boldsymbol{n}_{\mathrm{CTS}}]\,\underset{wi}{\kappa^{-}}\,\nu^{-}_{w} + \theta^{-1}_{PB}\,q^{+}_{i} \tag{69}$$

with $\phi^{\varrho\eta} = -q^{+}_{i}\,/\,\theta^{+}_{i}$ from Table 1 and $(47)_3$. Substituting (68) and (69) into (67) yields the reduced form

$$\theta_{PB}\,\pi^{\varrho\eta}_{\mathrm{CTS}} = q^{+}_{i} - \underset{wi}{h^{-}}\,\bar{J}^{-}_{w\mathrm{CTS}} + \delta_{PB}\,[(\mathrm{grad}\,p_{PB})\cdot\boldsymbol{n}_{\mathrm{CTS}}]\,\underset{wi}{\kappa^{-}}\,\nu^{-}_{w} \geq 0 \tag{70}$$

of the mixture entropy jump balance at the CTS. A comparison of $(66)_3$ and $(70)_1$ implies

$$\theta_{PB}\,\pi^{\varrho\eta}_{\mathrm{CTS}} = (\,\underset{wi}{\varrho^{-}}\,p_{PB}\,/\,\underset{wi}{\varrho}\,\varrho^{-}_{i}\,)\,\bar{J}^{-}_{w\mathrm{CTS}} - \delta_{PB}\,[(\mathrm{grad}\,p_{PB})\cdot\boldsymbol{n}_{\mathrm{CTS}}]\,\kappa^{-}_{i} \geq 0. \tag{71}$$

This completes the formulation of condition at the CTS.

The significant statements are $(60)_2$ expressing continuity of the barycentric velocity field across the CTS; (61) (62), (63) and (64) defining the mass flux and the traction transition conditions across the CTS, and (65) or (66) defining the Stefan type boundary condition which essentially determines the melting/ freezing rate $\mathcal{M}_{\mathrm{CTS}}$ at the CTS.

The complete treatment is given elsewhere.

6 Summary and Conclusions

In this work, we formulated a detailed model for polythermal ice based on classical continuum mixture theory. Using the fact that the water or mixture volume fraction in polythermal ice is generally on the order of a few percent, we obtained approximate expressions for the field quantities linear in the moisture volume fraction. Using these results mass and linear momentum balance laws for the ice and the water were derived. Formulating the balance relation of energy for the temperate ice led to an explicit formula for the volumetric melting rate that determines the moisture mass balance. Depending on whether the balance law of linear momentum for the mixture as a whole

or for the ice and the water were formulated resulted in temperate ice theories as deduced in [1,6,10–12] or in [7,12], respectively. While some details of the results are somewhat different from earlier formulations, the derivation essentially proves earlier theories correct.

Applying the formulation proposed in [17] to the thermomechanical balances we were also able to corroborate the Stefan-type boundary conditions that must hold at the phase interface between cold and temperate ice.

In summary the results corroborate earlier formulations with sufficient satisfaction, making them now also trustworthy to the critical glaciologist.

Acknowledgements: We thank D. Baral for TEXing the manuscript. We thank also Prof. L. W. Morland for his critical review of this paper.

References

1. Greve, R. (1997) A continuum-mechanical formulation for shallow polythermal ice sheets. *Philosophical transactions of the Royal Society London* A**355**, 921-974.
2. Greve, R., Weis, M. & Hutter, K. (1998) Paleoclimatic evolution and present conditions of the Greenland Ice Sheet in the vicinity of Summit: an approach by large-scale modelling. *Paleoclimates* **2**, 133-161.
3. Svendsen, B. & Hutter, K. (1995) On the thermodynamics of a mixture of isotropic materials with constraints. *Int. J. Engng. Sci.* **33**, 2021-2054
4. Hutter, K., Lalovi, L. & Vulliet, L. (1998) Thermodynamically based mixture models of saturated and unsaturated soils. *Mechanics of Frictional Material* **3**, 1-44
5. Blatter, H. (1991) Effect of climate on the cryosphere. *Zürcher Geogr. Schr.* **41**, 98pp
6. Blatter, H. & Hutter, K. (1991) Polythermal conditions in arctic glaciers. *Journal of Glaciology* **37**, 261-269
7. Fowler, A. C. (1984) On the transport of moisture in polythermal glaciers. *Geophys. Astrophys. Fluid Dynamics* **28**, 99-140
8. Fowler, A. C. & Larson., D. A. (1978) On the flow of polythermal glaciers. I. Model and preliminary analysis. *Proc. R. Soc. Lond.* A**363**, 217-242
9. Funk, M., Echelmeyer, K. & Iken, A. (1994) Mechanisms of fast flow in Jacobshavns Isbrae, West Greenland: Part II. Modeling of englacial temperatures. *Journal of Glaciology* **40**(136), 569-585.
10. Hutter, K. (1982) A mathematical model of polythermal glaciers and ice sheets. *J. Geophys. Astrophys. Fluid Dyn.* **21**, 201-224
11. Hutter, K. (1983) *Theoretical glaciology; material science of ice and the mechanics of glaciers and ice sheets.* D. Reidel Publishing Company, Dordrecht, Holland, 510pp.
12. Hutter, K. (1993) Thermo-mechanically coupled ice sheet response. Cold, polythermal, temperate. *J. Glaciol.* **39**(131), 65-86
13. Hutter, K. & Engelhardt, H. (1988) The use of continuum thermodynamics in the formulation of ice sheet dynamics. *Ann. Glaciol.* **11**, 46-51

14. Hutter, K., Blatter, H. & Funk, M. (1988) A model computation of moisture content in polythermal glaciers. *Journal of Geophysical Research* **93**(B10), 12205-12214.
15. Paterson, W. S. B. (1981) *The physics of Glaciers.* Pergamon Press.
16. Truesdell, C. (1984) *Rational Thermodynamics.* Springer-Verlag
17. Svendsen, B & Gray, J.N.T.M. (1996) On balance relations for a classical mixture containing a moving, non-material surface, *Cont. Mech. Thermodyn.* **8**, 171-187.

(Received 19. April 1999, accepted 15. May 1999)

Modelling the Ice Single-Crystal Viscoplastic Behaviour

Philippe Mansuy, Jacques Meyssonnier, and Armelle Philip

Laboratoire de Glaciologie et Géophysique de l'Environnement,
CNRS et Université Joseph Fourier (UJF-Grenoble I),
BP 96, F-38402 Saint-Martin d'Hères Cedex, France.

Abstract. Modelling the viscoplastic behaviour of an ice polycrystal by using "micro-macro" approaches requires an appropriate modelling of the mechanical behaviour of its constituent grains. To this aim compressive creep tests have been carried out on thick sections of fine-grained isotropic ice containing a circular inclusion made of a single-crystal of ice. The experimental results, notably the evolution of the crystallographic orientation of the inclusion during the tests, are compared with finite-element simulations based on a simple model for the description of the grain behaviour. It is shown that under the conditions of the tests (*i.e.*large diameter of the inclusion compared to the matrix grain size) a set of parameters for this model derived from single-crystal experimental data is more appropriate than a set obtained by the analysis of results from mechanical tests on anisotropic polycrystals.

1 Introduction

Owing to its strong viscoplastic anisotropy the ice single-crystal is generally considered as deforming essentially by slip on the basal planes, normal to the hexagonal symmetry axis ($c-$axis). Under the same effective strain-rate non-basal deformation requires a stress at least 60 times larger than deformation by basal glide [4]. In order to take into account this essential feature of the ice single crystal behaviour, the present model considers ice as a transversely isotropic medium with a weak resistance to shear parallel to the basal plane. The interest of this homogenous continuous formulation is that it allows analytical calculations for linear behaviour, and that it is easier to handle in finite-element computations than a model based on dislocation glide on distinct crystallographic planes as used in [2]. The aim of this paper is to assess the validity of this model of the grain by comparing experimental data with numerical simulations of the experiments. These experiments were carried out in the laboratory on artificial ice samples specially designed to reproduce Eshelby's inclusion problem [5].

2 Experiments

2.1 Specimen preparation and experimental device

Each specimen of laboratory-made ice consisted of a monocrystalline circular inclusion embedded in a fine-grained isotropic ice matrix.

The circular inclusion, $30\,mm$ in diameter, was cut from a single-crystal so that the crystal $c-$axis lies in its plane . The disc obtained was stuck on a metallic plate, surrounded by calibrated grains of ice ($0.64\,mm < \phi < 1.6\,mm$) which were saturated with water and put to freeze on a cold table. Then each sample was machined with a milling machine to obtain a plate 210 mm high, 140 mm wide and 8 mm thick. Doing so, the $c-$axis of the inclusion was in the plane of the specimen. The size of the grains in the matrix, compared to the diameter of the inclusion and to the thickness of the sample, allows to consider the matrix as a macroscopically isotropic medium.

The thick plates obtained were tested under compresive creep by using a testing machine located in a cold room at $-10 \pm 0.1\,°C$. The testing machine looked like a "guillotine". The specimen was in a vertical plane, with one edge resting on a lower fixed beam, and an upper moving blade exerting the compressive loading (Fig. 1). To avoid buckling, the specimen was placed between two glass plates. Loading was applied directly by means of a hanging tray loaded with lead bricks. To avoid crack formation during the tests the creep compressive stress was set to 0.5 MPa (up to now, this value has been kept the same for all the tests). The displacement of the upper blade was measured with respect to the fixed lower blade, with an accuracy within $1\,\mu m$ to $5\,\mu m$ depending on the LVDT (the presence of the glass plates impeded a direct measurement of deformation on the specimen itself). Since the glass plates

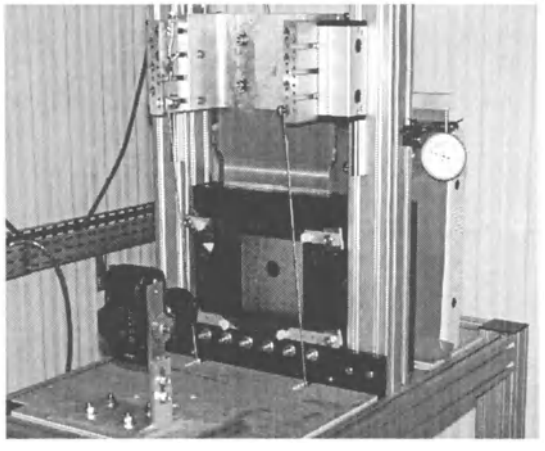

Fig. 1. Testing machine used for creep experiments

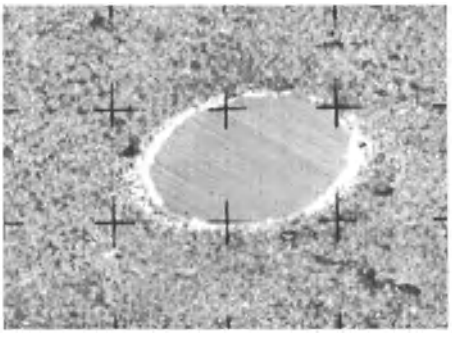

Fig. 2. Inclusion initially circular and oriented at 45° after a deformation of 8.6 % of the specimen. The rotation of the basal plane is about 16.5°.

prevented any displacement perpendicular to the plane of the specimens, the conditions of the tests were those of plane strain.

2.2 Measurements

Visualization of the deformation of the specimen was made possible by an appropriate lighting of the ice: a lamp was placed at the back of the testing machine and two polarizers were placed on each side of the specimen. A survey of the deformation was obtained by taking photographs at regular time intervals. As shown in Fig. 2 these photographs allowed to follow the evolution of the shape of the inclusion deforming into an ellipso"i d and of its crystallographic orientation. The direction of the basal plane was visible during the whole duration of the tests owing to the macrohomogeneity of the deformation which seemed to involve only basal glide. The activation of basal glide gave rise to localized shear bands which appear as dark parallel lines in Fig. 2. The results from the analysis of the photographs were the rotation of the basal plane and the geometry of the inclusion versus time (or strain).

Because of the long duration of the tests (from 15 to 45 days), only a few tests were performed until now. The present paper presents the results obtained for inclusions whith basal plane at 45° from the direction of compression, that is in the well oriented or easy glide configuration.

3 Models for the Inclusion and Matrix Behaviours

3.1 Model for the matrix

The viscoplastic behaviour of isotropic ice is usually described by a Norton-Hoff type power law, known as Glen's law in glaciology. This relation which

holds for an incompressible medium expresses the strain-rate $\dot{\epsilon}$ as a function of the deviatoric stress s as

$$\dot{\epsilon}_{ij} = \frac{1}{2} B_n(T) \tau^{n-1} s_{ij}. \tag{1}$$

τ is the effective shear stress (second invariant of s) defined by $\tau^2 = s_{ij}s_{ij}/2$, and $B_n(T)$ is a fluidity which depends on the temperature T (according to Arrhenius'law). For testing conditions such that $\tau > 0.1MPa$ the exponent n is equal to 3 [4]. In the following temperature variations are not taken into account (all the tests were performed at the same temperature of $-10°C$) and the coefficient $B_n(T)$ will be denoted simply by B_n. In view of numerical computations, it is convenient to write relation (1) as a viscous-type law, under the form $s_{ij} = 2\eta^\star \dot{\epsilon}_{ij}$, where $\eta^\star$ is an apparent viscosity given by

$$\eta^\star = {B_n}^{-1/n} \dot{\gamma}^{1/n-1}, \tag{2}$$

where $\dot{\gamma}$ is the effective shear strain-rate defined as

$$\dot{\gamma}^2 = 2\dot{\epsilon}_{ij}\dot{\epsilon}_{ij}. \tag{3}$$

3.2 Model for the inclusion

Following [10] the ice grain is considered as an incompressible transversely isotropic medium whose rotational symmetry axis is the crystal $c-$axis (the plane of isotropy corresponds to the grain basal plane). In a reference frame with the x_3 axis along the $c-$axis direction, and for linear behaviour, the anisotropic constitutive viscous law is written as

$$\begin{aligned} &s_{11} = 2\eta_{12}(\dot{\epsilon}_{11} - \frac{2}{3}(\alpha-1)\dot{\epsilon}_{33}), \quad s_{22} = 2\eta_{12}(\dot{\epsilon}_{22} - \frac{2}{3}(\alpha-1)\dot{\epsilon}_{33}), \\ &s_{12} = 2\eta_{12}\dot{\epsilon}_{12}, \\ &s_{33} = 2\eta_{12}(1 + \frac{4}{3}(\alpha-1))\dot{\epsilon}_{33}, \quad s_{23} = 2\eta_{12}\beta\dot{\epsilon}_{23}, \quad s_{31} = 2\eta_{12}\beta\dot{\epsilon}_{31}, \end{aligned} \tag{4}$$

where η_{12} is the viscosity for shear in the basal plane, $\beta\eta_{12}$ is the viscosity for shear parallel to the basal plane, and α is the ratio of the axial viscosity along the x_3- axis to the axial viscosity in the plane of isotropy (x_1, x_2) (the axial viscosity in a given direction being defined as the apparent viscosity for an uniaxial compression along that direction).

Following [11], the non-linear behaviour of the grain is described in the simplest way by assuming that the dissipation potential ϕ is given by

$$\phi = \frac{n}{n+1} {A_n}^{-1/n} \dot{\gamma}_\circ^{1+1/n}, \tag{5}$$

where

$$\dot{\gamma}_\circ^2 = (4\alpha - 1)\dot{\epsilon}_{33}^2 + (\dot{\epsilon}_{11} - \dot{\epsilon}_{22})^2 + 4\dot{\epsilon}_{12}^2 + 4\beta(\dot{\epsilon}_{23}^2 + \dot{\epsilon}_{31}^2), \tag{6}$$

is the sum of the invariants by rotation around the $x_3 - axis$ defined in the reference frame of the inclusion.

Relation (4) derives from (5) when $n = 1$ and $A_1^{-1} = \eta_{12}$. When $\alpha = \beta = 1$, (5) reduces to the dissipation potentiel for the isotropic Glen law ($\dot{\gamma}_\diamond = \dot{\gamma}$ given by (3)) with $A_n = B_n$. The apparent viscosity $\eta_{12}^\star$ which corresponds to (5) is

$$\eta_{12}^\star = {A_n}^{-1/n} {\dot{\gamma}_\diamond}^{1/n-1}. \tag{7}$$

3.3 Model parameters

So far, the parameters involved in the description of the matrix and inclusion behaviours are B_n and n for the matrix (equation (1)), A_n, n, α and β for the inclusion (equations (5) and (6)).

Since in the present study the applied stress was $0.5MPa$, the exponent n of Glen's law (1) can be taken as $n = 3$ [4,7]. Although the value of n seems close to 2 for an isolated single crystal [4], the same value of n was taken for the matrix and the inclusion in a first approach to simplify the presription of the boundary conditions (see section 4.1). Taking into account the values of the fluidity B_3 at $-10°C$ obtained by different authors [4,6,7,1,9], the mean value $B_3 = 18.6MPa^{-3}yr^{-1}$ for isotropic ice at $-\ 10°C$ was adopted.

The parameters A_n, α and β of the inclusion are much less documented and only rough estimates can be deduced from the very few data available on non-basal glide.

Denoting by $\mu_{\|iso}$ the ratio of the strain-rate observed when the grain is sheared parallel to its basal plane to that observed on isotropic ice under the same effective shear stress, the apparent visosities $\eta^\star$ and $\eta_{12}^\star$ given by (2) and (7) are linked by $\eta^\star = \mu_{\|iso}\beta\eta_{12}^\star$ and the invariants $\dot{\gamma}$ and $\dot{\gamma}_\diamond$ by $\dot{\gamma}_\diamond = \mu_{\|iso}\beta^{1/2}\dot{\gamma}$. The following relation beetween A_n and B_n is obtained

$$A_n/B_n = \mu_{\|iso}\beta^{(n+1)/2}. \tag{8}$$

Denoting by $\mu_{\|\perp}$ the ratio of the strain-rate observed when the grain is sheared parallel to its basal plane to that observed under compression along the $c-$axis direction, under the same effective shear stress τ ($\tau^2 = 3s_{33}^2/4$ in uniaxial compression, $\tau^2 = s_{23}^2$ in simple shear) and writing equation (5) in these two loading cases leads to

$$\beta = 3^{-3/4}(2\mu_{\|\perp})^{-1/2}(4\alpha - 1) \approx 0.31{\mu_{\|\perp}}^{-1/2}(4\alpha - 1). \tag{9}$$

If the inclusion is considered as an isolated single-crystal, according to [4] $\mu_{\|iso}$ would be in the order of 10^3, $\mu_{\|\perp}$ in the order of 10^4, and α should be between 1 and 4. Then from (9) and (8), for $\alpha = 1$, β is about 10^{-2} if $n = 3$ and A_n/B_n is about 0.1.

Otherwise, if the inclusion is seen as a grain in a polycrystal (*i.e.*its mean behaviour taking into account the effect of grain boundaries), according to

data on polar ice exhibiting a strong fabric with the $c-$axes aligned along the same direction [3,12], much smaller values of $\mu_{\|iso} = 10$ and $\mu_{\|\perp} = 50$ are to be considered. With $n = 3$ and for $\alpha = 1$, β is about 10^{-1} , and A_n/B_n is about 0.2.

4 Numerical Simulation

4.1 Finite-element model

The numerical simulations were performed by using the finite-element method with a velocity-pressure formulation [8] and neglecting gravity forces. The condition of plane strain was assumed and the two-dimensional problem was solved in a fixed global frame (e_X, e_Y), the material symmetry reference frame of the inclusion being denoted by (e_x, e_y) with its $y-$axis parallel to the $c-$axis of the grain and its $x-$axis (basal plane) being at angle φ with respect to the $X-$axis. For the inclusion, care was taken to compute the viscosity matrix (4) and the apparent viscosity $\eta_{12}^{\star}$ given by (7) in the local frame (e_x, e_y) of the inclusion before expressing this matrix in the global frame (e_X, e_Y). The finite-element mesh, consisting of six-nodes triangular elements, was refined in the vicinity of the inclusion-boundary interface where stress concentrations take place. The nodes at the very interface were doubled to allow the discontinuity of the pressure between the inclusion and the matrix, while the continuity of the velocity was constrained as an external condition.

The deformation of the specimen versus time was simulated by updating the position of the nodes at each time step (forward procedure). The change in the orientation of the basal plane of the inclusion was obtained by decomposing the spin $\boldsymbol{W}$ of the inclusion as the sum of the plastic spin $\boldsymbol{W}_i$ due to its viscoplastic deformation and expressed in the local frame, and of the lattice rotation rate $\dot{\boldsymbol{R}}$, $\boldsymbol{R}$ being the rotation matrix to pass from the local to the global frame (see [10]) as

$$\boldsymbol{W}\boldsymbol{c} = (\boldsymbol{R}\boldsymbol{W}_i\boldsymbol{R}^T)\boldsymbol{c} + \dot{\boldsymbol{R}}\boldsymbol{c}_i, \tag{10}$$

where $\boldsymbol{c}_i = (0, 1)$ is the $c-$axis unit vector expressed in the local frame of the inclusion and $\boldsymbol{c} = \boldsymbol{R}\boldsymbol{c}_i$. With the expression

$$\boldsymbol{R} = \begin{bmatrix} \cos\varphi & -\sin\varphi \\ \sin\varphi & \cos\varphi \end{bmatrix}, \tag{11}$$

equation (10) reduces to

$$w_{XY} = w_{xy} - \dot{\varphi}. \tag{12}$$

Since the basal planes remain parallel to each other, the component of the velocity v along the $y-$ axis ($c-$axis) must be a function of y only when

expressed in the rotating frame of the grain, so that $w_{xy} = \dot{\epsilon}_{xy}$. It follows that

$$\dot{\varphi} = w_{XY} - \dot{\epsilon}_{xy} = \partial v / \partial x, \tag{13}$$

where v is expressed in the local frame of the inclusion. This equation was used to calculate the rotation of each triangular element forming the inclusion during the time-step, so that in principle the orientations of these elements can evolve differently during a numerical simulation.

The boundary conditions were prescribed as follows: constant velocity on the upper side of the specimen ; zero velocity on the lower boundary ; free-surface on the vertical sides of the specimen. The prescribed velocity was adjusted at each time step so that the total force F acting on the upper edge of the specimen was equal to the applied constant load. This was done by computing the power $\mathcal{P}$ dissipated for a prescribed velocity of 1, then by scaling this velocity by the factor U such that $U^{1/n}\mathcal{P} = F$. The computation was continued until a total strain of 10% corresponding to the end of the experimental tests was achived. The finite-element solution was checked for the first step (*i.e.* circular inclusion) in the linear case, against the analytical solution given by [11].

4.2 Results

The finite-element simulations were carried out for an inclusion initially oriented at 45° from the direction of compression. The runs were performed with the fixed values $n = 3$ and $B_3 = 18.6 MPa^{-3} yr^{-1}$, and for an applied constant load of $0.5 MPa$. Different sets of parameters A_3/B_3, α and β were tried. The corresponding runs are listed in Table 1. Test1 conditions correspond to a single-crystal whose properties are derived from [4] (*i.e.* $\mu_{\|iso} = 10^3$, $\mu_{\|\perp} = 10^4$), assuming $\alpha = 1$. Test2 parameters are derived from the results for anisotropic polar ice with vertical c–axes from [3,12] which give $\mu_{\|iso} = 10$ and $\mu_{\|\perp} = 50$, assuming also $\alpha = 1$.

For all numerical tests, the orientations of the elements constituting the inclusion remained always very close to each other (deviation less than 1%).

Table 1. Values of the inclusion parameters A_3/B_3, α and β used in numerical simulations ($n = 3$, $B_3 = 18.6 MPa^{-3} yr^{-1}$)

Name	A_3/B_3	α	β	Name	A_3/B_3	α	β
Test1	0.1	1.	0.01	Test4	10^{-4}	1.	0.01
Test2	0.17	1.	0.13	Test5	10^{-4}	1.	0.1
Test3	10^{-4}	1.	10^{-4}	Test6	10^{-4}	1.	0.5

Fig 3 compares the observed evolution of the orientation φ of the inclusion versus total strain with the simulations. Note that the measurements made during two experiments (with two different specimens) are very similar. Test1-2-3-4 results shown in this figure fall inside the range of accuracy of the observations ($\pm 2°$). Since all simulations were done for the same total duration, the premature ending of the Test2 curve indicates a too slow evolution of the inclusion orientation versus time. The comparison of Test3-4-5-6 shows the influence of β for a very low fluidity parameter A_3: the highest value of β (Test6) results in a hard inclusion, while the smallest (Test3) corresponds to a grain deforming practically only by basal glide.

Fig. 4 shows the evolution versus strain of the shape of the inclusion, defined by the aspect ratio b/a of an ellipse which fits the inclusion-matrix interface (on the photographs for experimental data and on the deformed meshes for the simulations). Test1 results are the closest to observations. The trends observed for the evolution of the orientation of the inclusion are the same: for a given total strain, Test3 shows the most flattened shape, while the hard inclusion of Test6 exhibits a very small amount of deformation.

No significant influence of the parameter α (in the range 0.5 - 10) was observed for numerical tests performed with reasonable values of A_3 and β (corresponding to Test1 and Test4).

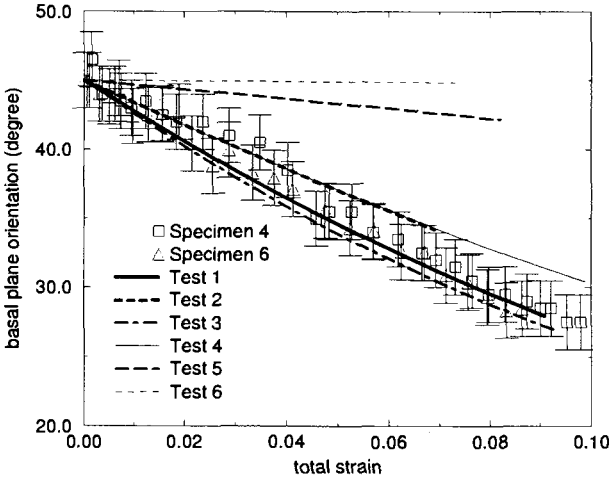

Fig. 3. Evolution of the cristallographic orientation of the inclusion as a function of the total strain for different values of α, β and λ.

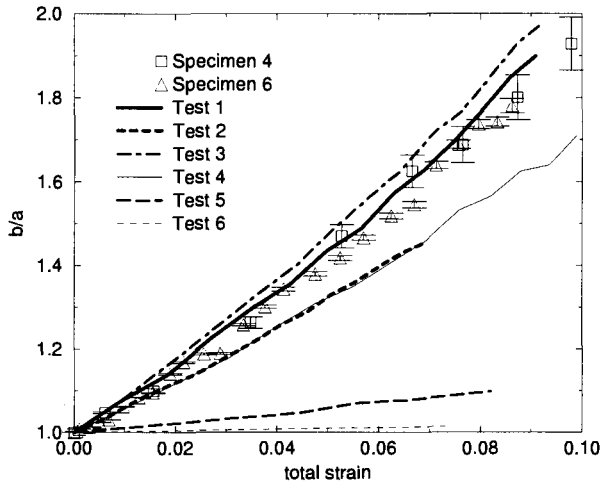

Fig. 4. Evolution of the shape of the inclusion as a function of the total strain for different values of α, β and λ.

5 Conclusion

Compressive creep tests carried out on thick sections of fine-grained isotropic ice containing a circular inclusion made of an ice single crystal were described. By making the grain size of the matrix much smaller than the inclusion diameter, it was possible to obtain a macrohomogeneous strain in the inclusion, as predicted by Eshelby's solution [5]. Finite-element simulations of the tests were performed by assuming a transversely isotropic behaviour of the ice single-crystal. A comparison with observations of the evolution of an inclusion initially oriented at 45° from the direction of loading was presented. This comparison was made on the evolution of the orientation of the inclusion basal planes, visible during the tests, and on the elliptic shape of the inclusion. The numerical computations showed that the model is essentially influenced by the viscosity for shear parallel to the basal plane (parameters A_3 and β), and that the best set of parameters to characterize the transversely isotropic behaviour of the inclusion seems closer to that derived from [4] for the isolated single-crystal than that derived from the results on anisotropic polar ice [3,12] when considering the inclusion as a grain in a polycrystal.

A future development of this preliminary work will be to increase the amount of experimental data (testing different initial orientations of the inclusion, different levels of compressive stress). As regards modelling of the ice polycrystal evolving anisotropy by "micro-macro" approaches, this work shows that additional experimental work should be done to account for grain-

grain interactions. Conditions under which the macrohomogeneity of the deformation is destroyed could be obtained by using the same kind of test but inserting a small number of intermediate-size grains at the inclusion-matrix interface to induce stress-concentrations, or by replacing the inclusion by a cluster of large-sized grains with controlled orientations.

Acknowledgements: The financial supports of the Commission of European Communities (contract ENV4-CT95-0125 "Fabric Development and Rheology of Polar Anisotropic Ice for Ice Sheet Flow Modelling"), of the Centre National de la Recherche Scientifique (Programme INSU-Géomatériaux) and of the Université Joseph Fourier Grenoble-I are greatly acknowledged.

References

1. Budd, W. F. and Jacka, T. H. (1989) A review of ice rheology for ice sheet modelling. *Cold Reg. Sci. Technol.* **16**, 107–144.
2. Castelnau, O., Duval, P., Lebensohn, R. A. and Canova, G. (1996) Viscoplastic modeling of texture development in polycristalline ice with a self-consistent approach : Comparison with bound estimates. *J. Geophys. Res.*, **101**(6), 13,851–13,868.
3. Duval, P. and Le Gac, H. (1983) Mechanical behaviour of antartic ice. *Ann. Glaciol.*, **3**, 92–95.
4. Duval, P., Ashby, M. F. and Anderman, I. (1983) Rate-controlling processesin the creep of polycristalline ice. *J. Phys. Chem.*, **87**(21), 4066–4074.
5. Eshelby, J.D. (1957) The determination of the elastic field of an ellipsoidal inclusion, and related problems. *Proc. Roy. Soc.* A, **241**, 376–396.
6. Jacka, T. H. (1984) The time and strain required for development of minimum strain rates in ice. *Cold Reg. Sci. Technol.*, **8**(3), 261–262.
7. Lliboutry, L. and Duval, P. (1985) Various isotropic and anisotropic ices found in glacier and polar ice caps and their corresponding rheologies. *Annales Geophysicæ*, **3**(2), 207–224.
8. Meyssonnier, J. (1989) Ice flow over a bump: experiment and numerical simulations. *J. Glaciol.*, **35**(119), 85–97.
9. Meyssonnier, J. and Goubert, A. (1994) Transient creep of polycristalline ice under uniaxial compression : an assessment of internal state variable models. *Ann. Glaciol.*, **19**, 55–62.
10. Meyssonnier, J. and Philip, A. (1996) A model for the tangent viscous behaviour of anisotropic polar ice. *Ann. Glaciol.*, **23**, 253–261.
11. Meyssonnier, J. and Philip, A. (1999) Remarks on self-consistent modelling of anisotropic polar ice for ice-sheet flow simulations. (*this symposium*).
12. Pimienta, P., Duval, P. and Lipenkov, V. Y. (1987) Mechanical behaviour of anisotropic polar ice. *International Association of Hydrological Sciences Publication*, **170**(Symposium at Vancouver 1987—*Physical Basis of Ice Sheet Modelling*), 57–66.

(Received 22 Feb. 1999, accepted 23 Feb. 1999)

Remarks on Self-Consistent Modelling of Polycrystalline Ice

Jacques Meyssonnier and Armelle Philip

Laboratoire de Glaciologie et Géophysique de l'Environnement,
CNRS et Université Joseph Fourier (UJF-Grenoble I),
BP 96, F-38402 Saint-Martin d'Hères Cedex, France.

Abstract. The ability of the one-site self-consistent scheme to model the behaviour of polycrystalline ice is assessed by studying the particular case of a two-dimensional polycrystal which represents natural S2-columnar ice. The self-consistent analysis is carried out analytically and its results are compared with finite-element computations. Despite a weak representation of the interaction between a grain and its surroundings, due to the strong anisotropy of the ice crystal, the resulting macroscopic behaviour is found to be acceptable.

1 Introduction

The problem of fabric development in polar ice has been addressed recently and many models have been developed to account for the anisotropic behaviour of ice, the evolution of its strain induced anisotropy, and to simulate the flow of anisotropic ice. Apart from phenomenogical models [14,15] which could prove to be very efficient to solve large scale flow of ice-sheets, most of them are based on the uniform-stress assumption [3,5,9,10,16] or on a self-consistent scheme [1,12] to model the anisotropic behaviour of ice. The uniform-stress model considers each grain as an isolated crystal subjected to the state of stress applied on the polycrystal boundary and provides a lower bound for the mean viscosity of the aggregate [8]. On the other hand, the simplest one-site version of the self-consistent model takes the interaction between grains into account to some extent, by considering each grain as an inclusion embedded in a homogeneous medium which has the mean properties of the aggregate. As a consequence it can give some information on what happens at the grain scale in addition to the macroscopic properties. The aim of the present paper is to assess the validity of this scheme when applied to ice whose single crystal exhibits a very strong anisotropy [2]. The analysis is made simple by considering S2-columnar ice which forms on lakes and rivers. Since this kind of ice consists of long columnar grains aligned along the same direction and whose $c-$axes are oriented randomly in the plane perpendicular to their long direction, S2 ice is transversely isotropic. Owing to the strong anisotropy of the single crystal, the viscoplastic deformation of a grain loaded in a plane which contains its $c-$axis can be considered as two-dimensional, and this plane strain assumption can be extended to model the flow of S2 ice

loaded in its plane of isotropy. As a consequence the inclusion problem can be treated as that of a two-dimensional circular anisotropic inclusion embedded in a two-dimensional isotropic equivalent medium.

2 Models for the Grain and for the S2-Ice Polycrystal

Each grain is modelled as a transversely isotropic incompressible continuous medium whose symmetry axis is the $c-$axis of the crystal. In the linear case this is exactly equivalent to the classical approach used in polycrystal plasticity which involves the basal prismatic and pyramidal slip systems [13]. In the non-linear case this simplification of the actual behaviour of the ice crystal is justified by Kamb [7] as far as basal glide is the dominant mechanism. As concerns S2-columnar ice, since the $c-$axes of the grains are randomly distributed in the plane perpendicular to their long direction, the polycrystal can also be considered as a macroscopically transversely isotropic incompressible continuous medium.

The general constitutive relation for a linear transversely isotropic incompressible medium, expressed in the material-symmetry-reference frame with rotational symmetry axis along the x_3- direction, links the deviatoric stress tensor $\boldsymbol{s}$ and the strain-rate tensor $\boldsymbol{d}$ by

$$\begin{aligned} s_{11} &= 2\eta_{12}(d_{11} - \tfrac{2}{3}(\alpha-1)d_{33}), & s_{23} &= 2\eta_{12}\beta d_{23}, \\ s_{22} &= 2\eta_{12}(d_{22} - \tfrac{2}{3}(\alpha-1)d_{33}), & s_{31} &= 2\eta_{12}\beta d_{31}, \\ s_{33} &= 2\eta_{12}(1 + \tfrac{4}{3}(\alpha-1))d_{33}, & s_{12} &= 2\eta_{12}d_{12}, \end{aligned} \tag{1}$$

where η_{12} is the viscosity for shear in the plane of isotropy (x_1, x_2), α is the ratio of the axial viscosity along the x_3-axis to the axial viscosity in the plane of isotropy (x_1, x_2) (*i.e.* viscosities corresponding to uniaxial compression along these axes), and β is the ratio of the viscosity for shear parallel to the plane of isotropy to η_{12}. When $\alpha = \beta = 1$ the medium is isotropic and (1) reduces to the Newtonian viscous law with $\eta_{12} = \eta$, *i.e.* $s_{ij} = 2\eta d_{ij}$. Relation (1) is valid for the grain, the x_3-axis corresponding to the grain $c-$axis, and for the S2 polycrystal, the x_3-axis corresponding then to the long direction of the columns.

A generalisation of (1) to non-linear behaviour (see Appendix A) is obtained by replacing the viscosity η_{12} in (1) by an apparent viscosity defined as

$$\eta_{12}^{\star} = A^{-1/n}\dot{\gamma}_{\diamond}^{(1-n)/n}, \tag{2}$$

where

$$\dot{\gamma}_{\diamond}^2 = (4\alpha - 1)d_{33}^2 + (d_{11} - d_{22})^2 + 4d_{12}^2 + 4\beta(d_{23}^2 + d_{31}^2). \tag{3}$$

3 Inclusion-Problem Solution for Linear Behaviour

Two reference frames are used to solve the problem under the assumption of plane strain: a local reference frame $\mathcal{R}(x,y,z)$ attached to the inclusion and a fixed global reference frame $\overline{\mathcal{R}}(X,Y,Z)$ attached to the homogeneous matrix which represents the S2-ice polycrystal. The long direction of the columns is along the $z-$axis of $\mathcal{R}$, which coincides with the $Z-$axis of $\overline{\mathcal{R}}$. The $c-$axis of the inclusion is along the $y-$axis and the basal planes are parallel to the $x-$axis, at angle φ from the $X-$axis of $\overline{\mathcal{R}}$. Loading is exerted in the $(X,Y)=(x,y)$ plane. To avoid complicated notation, the components of vectors and tensors are written with lowercase indices when expressed in the inclusion-reference frame $\mathcal{R}$ and with uppercase indices when expressed in the global reference frame $\overline{\mathcal{R}}$, and quantities related to the homogeneous matrix are overlined : as an example the viscosity in the basal plane of the inclusion is denoted by $\eta_{zx}=\eta$, whereas the viscosity of the matrix in its plane of isotropy (X,Y) is denoted by $\overline{\eta}_{XY}=\overline{\eta}$.

The detailed solution of the inclusion problem is given in Appendix B. In the following we need only the solution for the interior of the inclusion *i.e.*

$$d_{xx}=\frac{2}{1+\lambda\alpha}\overline{d}_{xx}\ ,\qquad d_{xy}=\frac{2}{1+\lambda\beta}\overline{d}_{xy}\ , \tag{4}$$

where $\lambda=\eta/\overline{\eta}=\overline{A}/A$ and $\overline{\boldsymbol{d}}$ denotes the strain-rate applied to the matrix at infinity [1]. Equation (4) takes into account the plane strain assumption and the incompressibility condition for both inclusion and matrix, that is

$$\begin{aligned} &d_{xx}+d_{yy}=0\ ,\quad d_{zz}=d_{xz}=d_{yz}=0\ ,\\ &\overline{d}_{xx}+\overline{d}_{yy}=0\ ,\quad \overline{d}_{zz}=\overline{d}_{xz}=\overline{d}_{yz}=0\ . \end{aligned} \tag{5}$$

An intermediate relation which will be useful gives the strain-rate in the inclusion expressed in $\mathcal{R}$ as a function of the macroscopic strain-rate expressed in $\overline{\mathcal{R}}$ as

$$\begin{aligned} d_{xx}&=\frac{2}{1+\lambda\alpha}(\overline{d}_{XX}\cos 2\varphi+\overline{d}_{XY}\sin 2\varphi)\ ,\\ d_{xy}&=\frac{2}{1+\lambda\beta}(-\overline{d}_{XX}\sin 2\varphi+\overline{d}_{XY}\cos 2\varphi)\ . \end{aligned} \tag{6}$$

Finally, the expression of (4) in the global reference frame is obtained as

$$\begin{aligned} d_{XX}&=2(\frac{\cos^2 2\varphi}{1+\lambda\alpha}+\frac{\sin^2 2\varphi}{1+\lambda\beta})\overline{d}_{XX}+(\frac{1}{1+\lambda\alpha}-\frac{1}{1+\lambda\beta})\sin 4\varphi\,\overline{d}_{XY}\ ,\\ d_{XY}&=(\frac{1}{1+\lambda\alpha}-\frac{1}{1+\lambda\beta})\sin 4\varphi\,\overline{d}_{XX}+2(\frac{\sin^2 2\varphi}{1+\lambda\alpha}+\frac{\cos^2 2\varphi}{1+\lambda\beta})\overline{d}_{XY}\ . \end{aligned} \tag{7}$$

[1] The typical length of the polycrystal (macroscale) is assumed to be much larger than the grain diameter (microscale), so that on the microscale the boundaries of the polycrystal are at infinity. This loose terminology will be used throughout.

4 Self-consistent Macroscopic Linear Behaviour

Within the framework of the classical one-site self-consistent method such as used by [1,12,4], macroscopic quantities are defined as the mean values of their local correspondents derived from the solution of the inclusion problem. By assuming that all the grains have the same cylindrical shape and are oriented at random, the mean value of a quantity G is defined as

$$< G >= \frac{1}{\pi} \int_0^{\pi} G(\varphi) d\varphi \ . \tag{8}$$

Self-consistency is obtained by expressing the macroscopic strain-rate $\overline{\boldsymbol{d}}$ prescribed at infinity on the boundary of the matrix as the mean value of $\boldsymbol{d}$ given by (7) in which $\overline{\eta}$ is taken as the macroscopic viscosity to be determined. Applying (8) to the two members of (7) leads to the single equation

$$\frac{1}{1+\lambda\alpha} + \frac{1}{1+\lambda\beta} = 1, \tag{9}$$

whose solution is

$$\lambda = \frac{\eta}{\overline{\eta}} = \frac{\overline{A}}{A} = \frac{1}{\sqrt{\alpha\beta}}. \tag{10}$$

Note that for linear behaviour and for inclusions having the same shape, expressing self-consistency on the stresses leads to the same equation.

5 Dissipation

5.1 Linear behaviour

For linear behaviour the power dissipated per unit volume in the inclusion is

$$\mathcal{P} = s_{ij} d_{ij} = \eta \dot{\gamma}_\diamond^2 \ . \tag{11}$$

Under the conditions of plane strain and incompressibility (5), and with the indices $1,2,3$ in (1) and (3) related to z,x,y respectively, expression (3) for $\dot{\gamma}_\diamond$ becomes

$$\dot{\gamma}_\diamond^2 = 4(\alpha d_{xx}^2 + \beta d_{xy}^2) \ , \tag{12}$$

and using (6)

$$\dot{\gamma}_\diamond^2 = 16 \Big(\frac{\alpha}{(1+\lambda\alpha)^2} (\overline{d}_{XX} \cos 2\varphi + \overline{d}_{XY} \sin 2\varphi)^2 + \frac{\beta}{(1+\lambda\beta)^2} (\overline{d}_{XX} \sin 2\varphi - \overline{d}_{XY} \cos 2\varphi)^2 \Big) \ . \tag{13}$$

From (8), (11) and (13) the mean value of the power dissipated by all the inclusions is obtained as

$$< \mathcal{P} >= \eta < \dot{\gamma}_\diamond^2 >= 2\eta\left(\frac{\alpha}{(1+\lambda\alpha)^2} + \frac{\beta}{(1+\lambda\beta)^2}\right)\overline{\dot{\gamma}}^2 , \tag{14}$$

where

$$\overline{\dot{\gamma}}^2 = 4(\overline{d}_{XX}^2 + \overline{d}_{XY}^2) . \tag{15}$$

Denoting by $\overline{\mathcal{P}} = \overline{\eta}\,\overline{\dot{\gamma}}^2$ the power dissipated per unit volume of the equivalent polycrystal, equation (14) becomes

$$< \mathcal{P} >= 2\lambda\left(\frac{\alpha}{(1+\lambda\alpha)^2} + \frac{\beta}{(1+\lambda\beta)^2}\right)\overline{\mathcal{P}} . \tag{16}$$

With the self-consistent solution (10) the following relation between the grain parameters α, β and the viscosity ratio λ holds

$$\frac{\alpha}{(1+\lambda\alpha)^2} = \frac{\beta}{(1+\lambda\beta)^2} = \frac{\alpha\beta}{(\sqrt{\alpha}+\sqrt{\beta})^2} , \tag{17}$$

so that, using (13) and (15),

$$\dot{\gamma}_\diamond^2 = 4\frac{\alpha\beta}{(\sqrt{\alpha}+\sqrt{\beta})^2}\overline{\dot{\gamma}}^2 . \tag{18}$$

This shows that the classical one-site self-consistent model applied to the linear behaviour of S2-columnar ice leads to a solution for which the power dissipated in a grain $\mathcal{P} = \eta\,\dot{\gamma}_\diamond^2$ does not depend on its orientation, which is quite a disconcerting and questioning result. From (16) and (17) the mean value of the power dissipated by all the inclusions is

$$< \mathcal{P} >= 4\frac{\sqrt{\alpha\beta}}{(\sqrt{\alpha}+\sqrt{\beta})^2}\overline{\mathcal{P}} . \tag{19}$$

The ratio $< \mathcal{P} > /\overline{\mathcal{P}}$ is less than unity for any value of β/α different from 1, and tends towards zero with β. For a particular material (which is not ice) such that $\alpha = \beta$ (but not necessarily isotropic *i.e.* with $\alpha = \beta = 1$) the mean power dissipated by the grains equals the power dissipated at the macroscopic level. This is understandable since in this particular case the self-consistent solution (10) implies $\lambda\alpha = \lambda\beta = 1$, and equation (7) degenerates to $d_{XX} = \overline{d}_{XX}$ and $d_{XY} = \overline{d}_{XY}$ which corresponds precisely to the Taylor assumption. For ice the value of α can be taken in the order of 1 whereas β is in the range 0.001 to 0.05 [2,11]; then $< \mathcal{P} > /\overline{\mathcal{P}}$ is rather low and cannot be greater than 0.6.

Another way of tackling the problem is to express the self-consistency on the dissipated power rather than on the strain-rates. Then the self-consistency equation inferred from (16) is

$$2\lambda\left(\frac{\alpha}{(1+\lambda\alpha)^2}+\frac{\beta}{(1+\lambda\beta)^2}\right)=1\ . \tag{20}$$

Equation (20) can be written in the more explicit form

$$(\lambda^2\alpha\beta-1)^2+\lambda^2(\alpha-\beta)^2=0\ , \tag{21}$$

which shows that the unique solution corresponds to that obtained by expressing self-consistency on the strain-rates (10) but is only possible if the inclusion material is such that $\alpha=\beta$ (apart from the trivial solution obtained for an isotropic inclusion, in which case $\lambda=1$).

5.2 Non-linear behaviour

An estimate of the non-linear macroscopic behaviour can be obtained by assuming a uniform strain-rate in the inclusion and in the matrix [4,8]. Since for linear behaviour self-consistency on the strain-rates leads to a solution (10) such that $\dot{\gamma}_\diamond$ is a constant independent of the grain orientation, it is straightforward to show that this solution also applies for non-linear behaviour (however without any guarantee of uniqueness): assuming $\dot{\gamma}_\diamond = Constant$ the self-consistency condition on the strain-rates expressed by using (8) and (7) is (9), then (10) and (17) hold, and expression (13) for $\dot{\gamma}_\diamond$ reduces to (18) that is $\dot{\gamma}_\diamond = Constant$. Using expression (2) for the apparent viscosities of the inclusion and the matrix, the self-consistent solution (10) becomes

$$\lambda=\frac{\eta^\star}{\overline{\eta}^\star}=\frac{A^{-1/n}\dot{\gamma}_\diamond^{(1-n)/n}}{\overline{A}^{-1/n}\overline{\dot{\gamma}}^{(1-n)/n}}=\frac{1}{\sqrt{\alpha\beta}}, \tag{22}$$

and using (18) the macroscopic fluidity parameter $\overline{A}$ is obtained as

$$\frac{\overline{A}}{A}=\left(\frac{2}{\sqrt{\alpha}+\sqrt{\beta}}\right)^{n-1}\frac{1}{\sqrt{\alpha\beta}}. \tag{23}$$

6 Discussion and Conclusion

The validity of the one-site self-consistent solution (23) was assessed by comparison with two-dimensional finite-element computations. The S2-ice polycrystal was modelled by a rectangular array of $32 \times 32 = 1024$ identical hexagonal grains with coplanar $c-$axes. Each grain was formed by six six-node triangular elements, and its behaviour was modelled by (1) and (2). The computations were made under the assumption of plane strain and by

prescribing a uniaxial state of stress on the boundary. The value of α was fixed to 1, and for each chosen value of β several computations were made with different random distributions of the grains orientations. The results are shown in Fig. 1 under the form of log-log diagrams, together with the upper and lower bounds given by the Taylor (uniform strain-rate) and Reuss (uniform stress) assumptions. Considering the large gap between the upper and lower bounds which increases as β decreases (for $\beta = 10^{-3}$ the ratio of the two bounds is about 250 for $n = 1$ and about 7.5×10^4 for $n = 3$) the self-consistent solution (23) appears to be acceptable in the range of β relevant for ice. The ratio of the macroscopic fluidity parameters $\overline{A}$ and A obtained by using finite-elements and relation (23) is between 1 and 3.

The one-site self-consistent model is based on the assumption that the neighbourhood of a grain can be considered as a homogeneous medium. For S2-ice, and under the condition of plane strain, this leads to a non-negligible difference between the power dissipated by the macroscopic medium and the mean power dissipated by the grains, increasing with the grain anisotropy. As a consequence if the macroscopic behaviour derived from this scheme as a mean property remains acceptable, one should be careful when using the solution of the inclusion problem to derive local properties at the grain scale. The surprising result obtained in this study ($\dot{\gamma}_\circ$ independent of the grain orientation) may be a consequence of the plane strain assumption but also of the weak representation of the grain-grain interaction by the one-site model.

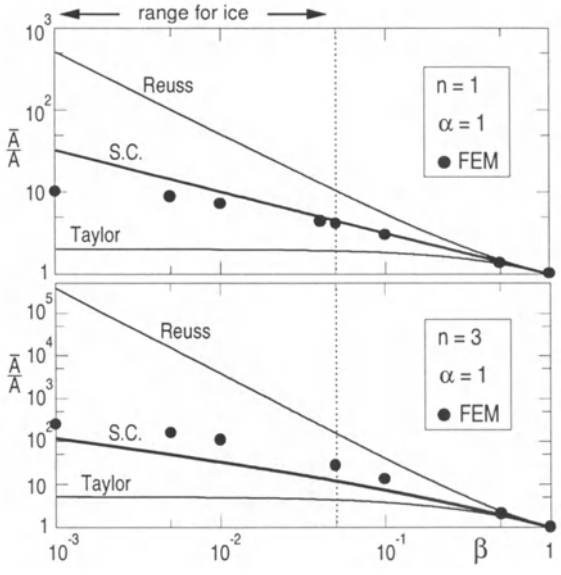

Fig. 1. Evolution of the macroscopic fluidity as a function of β given by the self-consistent model (S.C.) compared to finite-element results

Appendix A

A more convenient expression equivalent to (1) which accounts for incompressibility by involving independent components only, is obtained by using a vector notation $\boldsymbol{S}$ and $\boldsymbol{D}$ for $\boldsymbol{s}$ and $\boldsymbol{d}$, respectively (see [8]), defined as

$$\boldsymbol{S} = \{S_1, S_2, S_3, S_4, S_5\} = \{\frac{s_{11} - s_{22}}{\sqrt{2}}, \sqrt{\frac{3}{2}}s_{33}, \sqrt{2}s_{23}, \sqrt{2}s_{31}, \sqrt{2}s_{12}\},$$
$$\boldsymbol{D} = \{D_1, D_2, D_3, D_4, D_5\} = \{\frac{d_{11} - d_{22}}{\sqrt{2}}, \sqrt{\frac{3}{2}}d_{33}, \sqrt{2}d_{23}, \sqrt{2}d_{31}, \sqrt{2}d_{12}\}. \tag{A.1}$$

With this notation relation (1) for linear behaviour becomes

$$S_1 = 2\eta D_1,\ S_2 = 2\eta\frac{4\alpha - 1}{3}D_2,\ S_3 = 2\eta\beta D_3,\ S_4 = 2\eta\beta D_4,\ S_5 = 2\eta D_5. \tag{A.2}$$

Since notation (A.1) is chosen so that $s_{ij}d_{ij} = S_iD_i$ the following expressions for the dissipation potentials Ψ_D and Ψ_S which by definition obey $\boldsymbol{S} = \partial\Psi_D/\partial\boldsymbol{D}$ and $\boldsymbol{D} = \partial\Psi_S/\partial\boldsymbol{S}$ are readily derived:

$$\begin{aligned}\Psi_D &= \eta\big(D_1^2 + \frac{4\alpha - 1}{3}D_2^2 + \beta(D_3^2 + D_4^2) + D_5^2\big),\\ \Psi_S &= \frac{1}{4\eta}\big(S_1^2 + \frac{3}{4\alpha - 1}S_2^2 + \frac{1}{\beta}(S_3^2 + S_4^2) + S_5^2\big).\end{aligned} \tag{A.3}$$

Using Lliboutry's notation [9] for the invariants by rotation about the x_3-axis

$$\begin{aligned}\dot\gamma_{ax}^2 &= 2D_2^2, \quad & \dot\gamma_\perp^2 &= 2(D_1^2 + D_5^2), \quad & \dot\gamma_\parallel^2 &= 2(D_3^2 + D_4^2),\\ \tau_{ax}^2 &= S_2^2/2, \quad & \tau_\perp^2 &= (S_1^2 + S_5^2)/2, \quad & \tau_\parallel^2 &= (S_3^2 + S_4^2)/2,\end{aligned} \tag{A.4}$$

and with the notation

$$\dot\gamma_\diamond^2 = \frac{4\alpha - 1}{3}\dot\gamma_{ax}^2 + \dot\gamma_\perp^2 + \beta\dot\gamma_\parallel^2, \qquad \tau_\diamond^2 = \frac{3}{4\alpha - 1}\tau_{ax}^2 + \tau_\perp^2 + \frac{1}{\beta}\tau_\parallel^2, \tag{A.5}$$

the dissipation potentials for linear behaviour can be written as

$$\Psi_D = \frac{1}{2}\eta\dot\gamma_\diamond^2 \quad \text{and} \quad \Psi_S = \frac{1}{2\eta}\tau_\diamond^2. \tag{A.6}$$

A simple generalisation of these relations to non-linear behaviour, similar to that proposed by [6], is taken as

$$\Psi_D = \frac{n}{n+1}A^{-1/n}\dot\gamma_\diamond^{(n+1)/n} \quad \text{and} \quad \Psi_S = \frac{A}{n+1}\tau_\diamond^{n+1}. \tag{A.7}$$

The two invariants $\dot{\gamma}_\diamond$ and $\tau_\diamond$ are then linked by

$$\dot{\gamma}_\diamond = A\tau_\diamond^n, \tag{A.8}$$

and an apparent viscosity can be defined as

$$\eta^\star = A^{-1/n}\dot{\gamma}_\diamond^{(1-n)/n} = A^{-1}\tau_\diamond^{1-n}. \tag{A.9}$$

When the medium is isotropic $\alpha = \beta = 1$, $\dot{\gamma}_\diamond^2 = 2d_{ij}d_{ij}$, $\tau_\diamond^2 = s_{ij}s_{ij}/2$, then (A.8) and (A.7) reduce to the usual Glen's relation and expressions of the dissipation potentials for isotropic ice.

Appendix B

In this section all the quantities related to the homogeneous matrix are overlined. The solution of the inclusion problem is achieved by using polar co-ordinates (r, θ), θ being measured from the $x-$axis of the local reference frame $\mathcal{R}$ attached to the inclusion (the $x-$axis is at angle φ from the $X-$axis of the global reference frame $\overline{\mathcal{R}}$).

According to Eshelby's result (see [8]), the strain-rate inside the circular inclusion must be a constant, so that the velocity $\boldsymbol{u}$ in the inclusion is sought as a linear function of x and y in the form

$$u_x = ax + (b+c)y, \quad u_y = (b-c)x - ay, \quad u_z = 0, \tag{B.1}$$

which satisfies the incompressibility and plane strain conditions, and where a, b and c are constants. With (B.1), relation (1) for the inclusion (*i.e.* with indices $1, 2, 3$ corresponding to z, x, y respectively) written under the condition of plane strain ($d_{zz} = d_{11} = 0$), gives the deviatoric stresses in the inclusion as

$$\begin{aligned} &s_{xx} = 2\eta\frac{2\alpha+1}{3}a, \quad s_{yy} = -2\eta\frac{4\alpha-1}{3}a, \quad s_{zz} = 2\eta\frac{2\alpha-2}{3}a, \\ &s_{xy} = 2\eta\beta b, \quad s_{xz} = s_{yz} = 0. \end{aligned} \tag{B.2}$$

The expression for $\boldsymbol{u}$ in polar co-ordinates is

$$u_r = r(a\cos 2\theta + b\sin 2\theta), \quad u_\theta = -r(a\sin 2\theta - b\cos 2\theta + c), \quad u_z = 0. \tag{B.3}$$

With the notation $\xi = r/r_0$, where r_0 is the radius of the inclusion, the components of the velocity $\overline{u}$ and the isotropic pressure $\overline{p}$ in the matrix are

sought in the form

$$\begin{aligned}
\overline{u}_r &= r_0 \sum_{k=-1,0,1} \xi^{2k-1} \left[\left(\tfrac{2k}{2k+1}\overline{a}_k \xi^2 + \overline{b}_k\right) \sin 2k\theta + \left(\tfrac{2k}{2k+1}\overline{c}_k \xi^2 + \overline{d}_k\right) \cos 2k\theta \right], \\
\overline{u}_\theta &= r_0 \sum_{k=-1,0,1} \xi^{2k-1} \left[\left(\tfrac{2k+2}{2k+1}\overline{a}_k \xi^2 + \overline{b}_k\right) \cos 2k\theta - \left(\tfrac{2k+2}{2k+1}\overline{c}_k \xi^2 + \overline{d}_k\right) \sin 2k\theta \right], \\
\overline{u}_z &= 0 \ , \\
\overline{p} &= -4\overline{\eta} \sum_{k=-1,0,1} \xi^{2k} \left[\overline{a}_k \sin 2k\theta + \overline{c}_k \cos 2k\theta \right],
\end{aligned} \tag{B.4}$$

where a_k, b_k, c_k and d_k are constants, and which leads to

$$\begin{aligned}
\overline{d}_{rr} &= \sum_{k=-1,0,1} (2k-1)\xi^{2k-2} \left[\left(\tfrac{2k}{2k-1}\overline{a}_k \xi^2 + \overline{b}_k\right) \sin 2k\theta + \left(\tfrac{2k}{2k-1}\overline{c}_k \xi^2 + \overline{d}_k\right) \cos 2k\theta \right], \\
\overline{d}_{r\theta} &= \sum_{k=-1,0,1} (2k-1)\xi^{2k-2} \left[\left(\tfrac{2k}{2k-1}\overline{a}_k \xi^2 + \overline{b}_k\right) \cos 2k\theta - \left(\tfrac{2k}{2k-1}\overline{c}_k \xi^2 + \overline{d}_k\right) \sin 2k\theta \right], \\
\overline{d}_{\theta\theta} + \overline{d}_{rr} &= 0, \quad \overline{d}_{rz} = \overline{d}_{\theta z} = \overline{d}_{zz} = 0.
\end{aligned} \tag{B.5}$$

Under the condition of plane strain, relation (1) for the matrix (*i.e.* with indices $1, 2, 3$ corresponding to x, y, z respectively) gives $\overline{s}_{xx} = -\overline{s}_{yy} = 2\,\overline{\eta}\ \overline{d}_{xx}$, $\overline{s}_{xy} = 2\,\overline{\eta}\ \overline{d}_{xy}$, $\overline{s}_{zz} = \overline{s}_{xz} = \overline{s}_{yz} = 0$, and the stress components in the matrix, derived from (B.4) and (B.5), satisfy formally the equilibrium equations.

Denoting by $\overline{d}_{xx}^{\infty}$, $\overline{d}_{xy}^{\infty}$ the strain-rate at infinity expressed in the local reference frame of the inclusion and by $\overline{\Omega}^{\infty}$ and $\overline{p}^{\infty}$ the rigid-body rotation rate and the pressure applied at infinity, the boundary conditions at infinity ($\xi \to +\infty$) are satisfied if

$$\overline{a}_1 = \overline{c}_1 = 0, \quad \overline{b}_1 = \overline{d}_{xy}^{\infty}, \quad \overline{d}_1 = \overline{d}_{xx}^{\infty}, \quad \overline{c}_0 = -\overline{p}^{\infty}/(4\overline{\eta}), \quad \overline{a}_0 = \overline{\Omega}^{\infty}/2. \tag{B.6}$$

The remaining coefficients $\overline{b}_0$, $\overline{d}_0$, $\overline{a}_{-1}$, $\overline{b}_{-1}$, $\overline{c}_{-1}$, $\overline{d}_{-1}$ for the matrix, a, b, c for the inclusion, and the pressure p inside the inclusion, are found by expressing the continuity of the velocity and the continuity of the stress vector at the inclusion-matrix interface ($\xi = 1$). Using (B.6), the conditions $\overline{u}_r = u_r$, $\overline{u}_\theta = u_\theta$, and $\overline{s}_{r\theta} = s_{r\theta}$ on $\xi = 1$, lead after a simple calculation to

$$\begin{aligned}
&\overline{b}_0 = \overline{d}_0 = 0, \quad \overline{b}_{-1} = -\overline{a}_{-1} = K_\beta\, \overline{d}_{xy}^{\infty}, \quad \overline{c}_{-1} = -\overline{d}_{-1} = K_\alpha\, \overline{d}_{xx}^{\infty}, \\
&a = (1 + K_\alpha)\overline{d}_{xx}^{\infty}, \quad b = (1 + K_\beta)\overline{d}_{xy}^{\infty}, \quad c = -\overline{\Omega}^{\infty},
\end{aligned} \tag{B.7}$$

where $K_\alpha = (1 - \lambda\alpha)/(1 + \lambda\alpha)$, $K_\beta = (1 - \lambda\beta)/(1 + \lambda\beta)$ and $\lambda = \eta/\overline{\eta}$. The condition of continuity of the radial component of the stress vector at the inclusion-matrix interface, *i.e.* $\overline{p} + \overline{s}_{rr} = p + s_{rr}$ on $\xi = 1$, determines the

pressure inside the inclusion as $p = \overline{p}^{\infty} + 2\eta(\alpha - 1)a/3$. From this equation and relations (B.1) and (B.7), the solution for the points inside the inclusion, expressed in the inclusion-reference frame, is obtained as

$$\begin{aligned} u_x &= (1 + K_\alpha)\overline{d}_{xx}^{\infty} x + ((1 + K_\beta)\overline{d}_{xy}^{\infty} - \overline{\Omega}^{\infty})y, \\ u_y &= ((1 + K_\beta)\overline{d}_{xy}^{\infty} + \overline{\Omega}^{\infty})x - (1 + K_\alpha)\overline{d}_{xx}^{\infty} y, \\ p &= \overline{p}^{\infty} + 2\eta(\alpha - 1)(1 + K_\alpha)\overline{d}_{xx}^{\infty}/3, \\ d_{xx} &= (1 + K_\alpha)\overline{d}_{xx}^{\infty} = -d_{yy}, \\ d_{xy} &= (1 + K_\beta)\overline{d}_{xy}^{\infty}. \end{aligned} \tag{B.8}$$

Note that in the main text (sections 3 to 5) $\overline{d}_{xx}^{\infty}$ and $\overline{d}_{xy}^{\infty}$ have been replaced by $\overline{d}_{xx}$ and $\overline{d}_{xy}$ respectively, for the sake of simplicity.

Using (B.4),(B.6) and (B.7), the solution for the points in the matrix is obtained as

$$\begin{aligned} &\overline{u}_r = r_0\xi\big[(1 + K_\alpha\xi^{-2}(2 - \xi^{-2}))\cos 2\theta\,\overline{d}_{xx}^{\infty} + (1 + K_\beta\xi^{-2}(2 - \xi^{-2}))\sin 2\theta\,\overline{d}_{xy}^{\infty}\big], \\ &\overline{u}_\theta = r_0\xi\big[\overline{\Omega}^{\infty} - (1 + K_\alpha\xi^{-4})\sin 2\theta\,\overline{d}_{xx}^{\infty} + (1 + K_\beta\xi^{-4})\cos 2\theta\,\overline{d}_{xy}^{\infty}\big], \\ &\overline{p} = \overline{p}^{\infty} - 4\overline{\eta}\xi^{-2}(K_\alpha\cos 2\theta\,\overline{d}_{xx}^{\infty} + K_\beta\sin 2\theta\,\overline{d}_{xy}^{\infty}), \\ &\overline{d}_{rr} = \big[1 - K_\alpha\xi^{-2}(2 - 3\xi^{-2})\big]\cos 2\theta\overline{d}_{xx}^{\infty} + \big[1 - K_\beta\xi^{-2}(2 - 3\xi^{-2})\big]\sin 2\theta\overline{d}_{xy}^{\infty}, \\ &\overline{d}_{r\theta} = -\big[1 + K_\alpha\xi^{-2}(2 - 3\xi^{-2})\big]\sin 2\theta\overline{d}_{xx}^{\infty} + \big[1 + K_\beta\xi^{-2}(2 - 3\xi^{-2})\big]\cos 2\theta\overline{d}_{xy}^{\infty}, \\ &\overline{d}_{\theta\theta} + \overline{d}_{rr} = 0, \quad \overline{d}_{rz} = \overline{d}_{\theta z} = \overline{d}_{zz} = 0. \end{aligned} \tag{B.9}$$

The strain-rate components in the matrix, expressed in the reference frame of the inclusion, are given by

$$\begin{aligned} \overline{d}_{xx} &= \overline{d}_{rr}\cos 2\theta - \overline{d}_{r\theta}\sin 2\theta, \\ \overline{d}_{xy} &= \overline{d}_{rr}\sin 2\theta + \overline{d}_{r\theta}\cos 2\theta, \\ \overline{d}_{xx} + \overline{d}_{yy} &= 0, \quad \overline{d}_{xz} = \overline{d}_{yz} = \overline{d}_{zz} = 0. \end{aligned} \tag{B.10}$$

Acknowledgements: The financial support of the Commission of European Communities (contract ENV4-CT95-0125 "Fabric Development and Rheology of Polar Anisotropic Ice for Ice Sheet Flow Modelling" is greatly acknowledged.

References

1. Castelnau, O., Duval, P., Lebensohn, R. A. and Canova, G. (1996) Viscoplastic modeling of texture development in polycristalline ice with a self-consistent approach : Comparison with bound estimates. *J. Geophys. Res.*, **101**(6), 13 851–13 868.

2. Duval, P., Ashby, M. F. and Anderman, I. (1983) Rate-controlling processes in the creep of polycristalline ice. *J. Phys. Chem.*, **87**(21), 4 066–4 074.
3. Gagliardini, O. and Meyssonnier, J. (1999) Analytical derivations for the behavior and fabric evolution of a linear orthotropic ice polycrystal. *J. Geophys. Res.*, In Press.
4. Gilormini, P. (1996) A critical evaluation for various non-linear extensions of the self-consistent model. *IUTAM Symposium on Micromechanics of Plasticity and Damage of Multiphase Materials, A. Pineau and A. Zaoui (eds.), Kluwer Academic Publishers, The Netherlands*, 67-74.
5. Gödert, G. and Hutter, K. (1998) Induced anisotropy in large ice shields: Theory and its homogenization. *Continuum Mech. Thermodyn.*, **10**, 293–318.
6. Johnson, A.F. (1982) Creep characterization of eutectic composites. *Mechanical behaviour of anisotropic solids, Proceedings of the Euromech Colloquium 115, J.P. Boehler Ed., Martinus Nijhoff Publishers and Editions du CNRS, 1982*, 927 pp.
7. Kamb, W.B. (1961) The glide direction in ice. *J. Glaciol.*, **3** (30), 1 097–1 106.
8. Kocks, U.F., Tomé, C.N. and Wenk, H.R. (1998) Texture and Anisotropy, Preferred Orientations in Polycrystals and their Effect on Materials Properties. *Cambridge University Press, 1998*, 676 pp.
9. Lliboutry, L. (1993) Anisotropic, transversely isotropic non linear viscosity of rock ice and rheological parameters inferred by homogenization. *Int. J. Plast.*, **9**, 619–632.
10. Mangeney, A., Califano, F. and Hutter, K. (1997) A numerical study of anisotropic, low Reynolds number, free surface flow of ice-sheet modeling. *J. Geophys. Res.*, **102**(B10), 22 749–22 764.
11. Mansuy, P., Meyssonnier, J. and Philip, A. (1999) Modelling viscoplasticity of the ice single crystal *This Symposium.*
12. Meyssonnier, J. and Philip, A. (1996) A model for the tangent viscous behaviour of anisotropic polar ice. *Ann. Glaciol.*, **23**, 253–261.
13. Meyssonnier, J. and Philip, A. (1999) Comparison of Finite-Element and homogenization methods for modelling the viscoplastic behaviour of a S2-columnar ice polycrystal. *Ann. Glaciol.*, **30**, In Press.
14. Morland, L. W. and Staroszczyk, R. (1998) Viscous response of Polar ice with evolving fabric. *Continuum Mech. Thermodyn.*, **10**(3), 135–152.
15. Staroszczyk, R. and Morland, L. W. (1999) Orthotropic viscous response of polar ice. *Journal of Engineering Mathematics*, In Press.
16. Van der Veen, C. J. and Whillans, I. M. (1994) Development of fabric in ice. *Cold Reg. Sci. Technol.*, **22**(2), 171–195.

(Received 24 March 1999, accepted 24 May 1999)

Anisotropic Isothermal Ice-Cap Flow with the Shallow Ice Approximation

Armelle Philip and Jacques Meyssonnier

Laboratoire de Glaciologie et Géophysique de l'Environnement,
CNRS et Université Joseph Fourier (UJF - Grenoble I),
BP96, 38402 Saint-Martin-d'Hères Cedex, France.

Abstract. The influence of polar ice anisotropy on the two-dimensional plane strain and steady-state flow of an isothermal ice-sheet is analysed by using the Shallow Ice Approximation (SIA). The SIA solution is obtained up to the second order in the aspect-ratio ϵ of the ice-sheet for the flow of orthotropic ice when one of the planes of orthotropy is the plane of the ice-sheet flow. The solution is discussed for the special case of transverse isotropy when the rotational symmetry axis is in the plane of the flow, but not necessarily vertical. It is shown that in general non-negligible additional terms appear in the solution at order $\mathcal{O}(\epsilon^0)$ by comparison to the solution for isotropic ice.

1 Introduction

During the gravity driven flow of an ice-sheet, preferential distributions of crystallographic orientations of ice develop. Deep ice-cores from Greenland and Antarctica exhibit different types of structural anisotropy, depending on the strain history undergone by ice: at Vostok (Antarctica) the $c-$axes are randomly distributed in a vertical plane [7], whereas at GRIP (Greenland) the $c-$axes are almost aligned along the vertical [12]. Since ice can deform more easily by dislocation glide on the basal plane than on any other crystallographic plane [7], the viscoplastic behaviour of textured polycrystalline ice is anisotropic. However ice-cap flow simulations usually consider isotropic ice, and in order to simplify the solution of the mechanical equations the Shallow Ice Approximation (SIA) [3,11] is often used. The SIA is based on the difference in the order of magnitude of the gradients along the vertical and horizontal directions expected from the small aspect ratio ϵ of the ice-sheet, defined as the ratio of the ice thickness to the ice-sheet length, and of the slow variations of the ice-sheet surface and of the bedrock topographies with respect to the horizontal co-ordinates. These conditions are rather well satisfied for Antarctica ($\epsilon \approx 10^{-3}$) and Greenland ($\epsilon \approx 5 \times 10^{-3}$) which exhibit very low surface slopes in the order of 2×10^{-3} [1]. With the SIA the solution of the flow can be achieved by power series expansion of the small parameter ϵ up to the desired order.

Mangeney et al. [8,9] have shown the influence of anisotropy on a two-dimensional ice-sheet flow of transversely isotropic ice, in the special case of

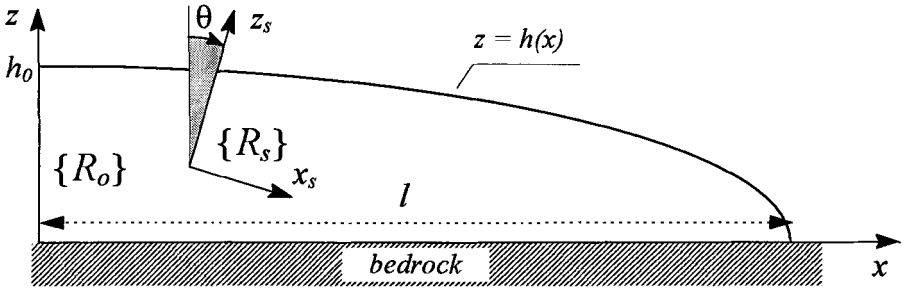

Fig. 1. Ice-sheet domain and definition of the material symmetry and global reference frames.

a rotational symmetry axis which remains vertical everywhere. Two different types of simulations were done by using either a finite difference method or the SIA up to the second order in ϵ. However, the type of anisotropy which was accounted for corresponds to the fabric observed in the GRIP ice-core and may be too restrictive. The present paper aims to analyse the influence of a type of anisotropy which can approximate in a better way that expected from the different observations made on ice-cores. As a first approach and for the sake of simplicity, two-dimensional plane strain and steady-state conditions are assumed. The solutions of the SIA are obtained up to the second order in ϵ for isothermal flow of ice exhibiting a fixed orthotropy, one of the planes of orthotropy being the plane of the ice flow. Linear rheology and constant accumulation rate are also presumed.

2 Plane Strain Flow of Orthotropic Ice

2.1 Basic equations

A steady isothermal ice-sheet flow is considered in a fixed Cartesian frame $R_0\ \{x, y, z\}$ with the $z-$ axis directed vertically upward. Ice is assumed to flow in the (x, z) plane (see Fig.1). The equations to be solved are the mass conservation and the balance of momentum expressed as

$$div(\boldsymbol{u}) = 0\ , \qquad div(\boldsymbol{\sigma}) = \rho g \boldsymbol{e}_z\ , \tag{1}$$

where $\boldsymbol{u}$ is the ice velocity of components u_x and u_z, g is the gravity constant, $\boldsymbol{e}_z$ is the unit vector in the $z-$direction, ρ is the density of ice and $\boldsymbol{\sigma}$ is the stress tensor. The deviatoric stresses, denoted by $\boldsymbol{s}$, are such that $\sigma_{ij} = s_{ij} + p\delta_{ij}$, where p is the pressure. The general constitutive relation for anisotropic ice is written as

$$s_{ij} = m_{ijkl}\, d_{kl}\ , \tag{2}$$

where $\boldsymbol{d}$ and $\boldsymbol{m}$ are the strain-rate tensor and the fourth-order viscosity tensor, respectively. The material-symmetry-reference frame whose axes are x_s, y_s and z_s, is denoted by R_s (see Fig.1). In the orthotropic case, the non-zero components of $\boldsymbol{m}$ expressed in R_s are m_{iijj}, m_{ijij}, m_{ijji} (no sum). Transverse isotropy is a particular type of orthotropy when one of the R_s axes, say z_s, is an axis of rotational symmetry. Then the constitutive relation for a linearly transversely isotropic viscoplastic medium [10] can be written in R_s as

$$\begin{aligned} &s^s_{xx} = 2\eta(d^s_{xx} - \tfrac{2}{3}(\alpha-1)\,d^s_{zz}) \ , \quad s^s_{yy} = 2\eta(d^s_{yy} - \tfrac{2}{3}(\alpha-1)\,d^s_{zz}) \ , \\ &s^s_{zz} = 2\eta(1 + \tfrac{4}{3}(\alpha-1))\,d^s_{zz} \ , \\ &s^s_{yz} = 2\eta\beta\,d^s_{yz} \ , \quad s^s_{xz} = 2\eta\beta\,d^s_{xz} \ , \quad s^s_{xy} = 2\eta\,d^s_{xy} \ , \end{aligned} \tag{3}$$

where η is the viscosity for shear in the plane of isotropy (x_s, y_s), and α and β define the degree of anisotropy. α is the ratio of the axial viscosity along the z_s-axis to the axial viscosity in the isotropic plane and β is the ratio to η of the viscosity for shear parallel to the plane (x_s, y_s). When $\alpha = \beta = 1$ the medium is isotropic and (3) reduces to a Newtonian viscous law.

In the present study the (x_s, z_s) plane of symmetry of the material-symmetry-reference frame R_s coincides with the (x, z) plane of the global reference frame R_0, however R_s and R_0 are assumed to have only the y_s and y axes in common. As a consequence, the condition of plane flow in the (x, z) plane implies

$$\begin{aligned} &d_{yy} = d^s_{yy} = 0 \ , \qquad d_{xy} = d_{yz} = d^s_{xy} = d^s_{yz} = 0 \ , \\ &s_{yy} = s^s_{yy} \ , \quad \text{and} \quad s_{xy} = s_{yz} = s^s_{xy} = s^s_{yz} = 0 \ , \end{aligned} \tag{4}$$

and, in general, the viscosity components m_{xxxz}, m_{yyxz}, m_{zzxz} and m_{xyyz} (and the symmetric components $m_{ijkl} = m_{jikl} = m_{klij}$ etc.) have non-zero values when expressed in the fixed frame R_0. This is also true for transverse isotropy. Then the principal directions of the strain-rates are in general different from those of the deviatoric stresses: for a given shear strain-rate d_{xz}, s_{xz}, but also the diagonal components s_{xx}, s_{yy} and s_{zz}, are non-zero in R_0, and for a given d_{xx} or d_{zz}, s_{xz} is non-zero as well.

2.2 Boundary conditions

The ice-sheet surface is defined by its elevation $h(x)$ and the ice-sheet dome is located at $x = 0$. The $z-$axis is a symmetry axis for the 2D flow problem. The bedrock is assumed to be flat (equation $z = 0$), so that the surface elevation coincides with the ice thickness. The boundary conditions are as follows :
- p being defined with respect to the atmospheric pressure, the condition at the free surface with outward normal unit vector $\boldsymbol{n}$ is

$$\sigma_{ij} n_j = 0 \ , \qquad \text{on} \quad z = h(x) \ , \tag{5}$$

- ω being the vertical accumulation rate, assumed to be the same everywhere[1][3], an additional condition on $z = h(x)$, required to satisfy steady-state, is $\boldsymbol{u} \cdot \boldsymbol{n} = \boldsymbol{\omega} \cdot \boldsymbol{n}$, with $\boldsymbol{\omega} = (0, -\omega)$ and $\omega > 0$, that is

$$u_x \frac{dh(x)}{dx} - u_z = \omega \ , \qquad \text{on} \quad z = h(x) \ , \tag{6}$$

- adherence of the ice at the bedrock contact is assumed, *i.e.*

$$\boldsymbol{u} = 0 \ , \qquad \text{on} \quad z = 0 \ . \tag{7}$$

2.3 The Shallow Ice Approximation (SIA)

Following [9], a first set of dimensionless variables denoted by a tilde symbol is defined by using the ice thickness at the dome $\mathcal{L} = h(0) = h_0$ as a length scale, the maximum hydrostatic stress $\mathcal{S} = \rho g h_0$ as a stress scale, and the accumulation rate $\mathcal{U} = \omega$ as velocity unit. Consequently the other scaling values are $\mathcal{T} = (h_0/\omega)$ for time, $\mathcal{D} = \omega/h_0$ for strain-rates and $\mathcal{M} = (\rho g h_0^2/\omega)$ for viscosities. With this notation, the scaled ice thickness at the dome is $\tilde{h}(0) = \tilde{h}_0 = 1$ and the ice-sheet length is $\tilde{l} = l/h_0 >> 1$. The equations to be solved with the tilde variables are formally the same as (1), (2), (5), (6) and (7) in which ρg and ω are replaced by 1.

In the framework of the SIA, a second change of variables is made so that the reduced ice-sheet length L is 1. These new dimensionless variables are denoted by their corresponding capital letters in the following. The actual co-ordinates x and z, and the surface elevation h transform respectively into X, Z and H such that

$$X = \epsilon \tilde{x} = \epsilon x/\mathcal{L} \ , \quad Z = \tilde{z} = z/\mathcal{L} \ , \quad H = \tilde{h} = h/\mathcal{L} \ . \tag{8}$$

Since the vertical velocity is much smaller than the horizontal, the stretched velocities are defined as

$$U_x = \epsilon \tilde{u}_x = \epsilon u_x/\mathcal{U} \ , \quad U_z = \tilde{u}_z = u_z/\mathcal{U} \ . \tag{9}$$

Then the definitions of X, Z, U_x and U_z constrain the change in the strain-rate components as

$$D_{xx} = \tilde{d}_{xx} = \frac{\partial U_x}{\partial X} \ , \quad D_{zz} = \tilde{d}_{zz} = \frac{\partial U_z}{\partial Z} \ , \quad 2D_{xz} = \frac{1}{\epsilon}\frac{\partial U_x}{\partial Z} + \epsilon \frac{\partial U_z}{\partial X} \ . \tag{10}$$

In the same way, since the flow is driven by gravity and the surface slope is very small, the deviatoric stresses are small compared to the isotropic pressure p so that the stretched stresses are defined as

$$P = \tilde{p} = p/\mathcal{S} \ , \quad S_{ij} = \tilde{s}_{ij}/\epsilon = s_{ij}/(\epsilon \mathcal{S}) \ . \tag{11}$$

[1] This is Vialov's assumption; for steady-state it requires a Dirac type calving rate at the snout.

Following [9], with expressions (10) and (11) for the stretched strain-rates and deviatoric stresses a coherent stretching of the viscosities is chosen as

$$M_{ijkl} = \frac{m_{ijkl}}{\mathcal{M}\epsilon^2} = \frac{\tilde{m}_{ijkl}}{\epsilon^2} \ . \tag{12}$$

By using relations (8) - (12), the equations and the boundary conditions of the problem (1) - (7) are then expressed in terms of the stretched variables X, Z, H, $\boldsymbol{U}$, $\boldsymbol{D}$, $\boldsymbol{S}$, P, $\boldsymbol{M}$ and ϵ. Note that the condition of plane flow (4) implies $S_{xy} = S_{yz} = 0$. The reduced equations of the problem (mass conservation, balance of momentum, constitutive law, free-surface condition, surface accumulation rate and bedrock contact conditions) are

$$\begin{aligned}
&D_{xx} + D_{zz} = 0 \ , \\
&\epsilon\frac{\partial S_{xx}}{\partial X} + \frac{\partial S_{xz}}{\partial Z} + \frac{\partial P}{\partial X} = 0 \ , \quad \epsilon^2\frac{\partial S_{xz}}{\partial X} + \epsilon\frac{\partial S_{zz}}{\partial Z} + \frac{\partial P}{\partial Z} = 1 \ , \\
&S_{ij} = \epsilon M_{ijkl} Dkl \ , \\
&(P + \epsilon S_{xx})\frac{\partial H}{\partial X} - S_{xz} = 0 \ , \quad P + \epsilon S_{zz} - \epsilon^2\frac{\partial H}{\partial X}S_{xz} = 0 \ , \text{ on } Z = H, \\
&U_x\frac{\partial H}{\partial X} - U_z = 1 \ , \text{ on } Z = H, \\
&U_x = U_z = 0 \ , \text{ on } Z = 0.
\end{aligned} \tag{13}$$

By expressing $\boldsymbol{U}$, P, and $\boldsymbol{S}$ as power series of ϵ, this set of equations can be solved for each order $\mathcal{O}(\epsilon^n)$ (see the Appendix). The solution at order ϵ^0 for general orthotropy, but fixed directions of the material-symmetry-reference frame, is found as

$$\begin{aligned}
&H = H^{(0)} = (1 - 6M_{xzxz}X^2)^{1/4} \ , \\
&U_x^{(0)} = 3\frac{X}{H}\Big[\frac{Z}{H} - \frac{1}{2}\Big(\frac{Z}{H}\Big)^2\Big] \ , \quad U_z^{(0)} = -\frac{3}{2}\Big(\frac{Z}{H}\Big)^2\Big[\frac{Z}{6H} + \frac{1}{H^4}\Big(1 - \frac{Z}{2H}\Big)\Big] \ , \\
&P^{(0)} = Z - H \ , \quad S_{xz}^{(0)} = 3M_{xzxz}X\frac{H - Z}{H^3} \ , \\
&S_{xx}^{(0)} = 3M_{xxxz}X\frac{H - Z}{H^3} \ , \quad S_{yy}^{(0)} = 3M_{yyxz}X\frac{H - Z}{H^3} \ , \\
&S_{zz}^{(0)} = 3M_{zzxz}X\frac{H - Z}{H^3} \ , \quad S_{xy}^{(0)} = S_{yz}^{(0)} = 0 \ .
\end{aligned} \tag{14}$$

The detailed analytical expressions for the solutions at first and second orders for the flow of orthotropic ice and their derivations are given in the Appendix. Note also that the margin position is not at $X = 1$ but at $X = [6M_{xzxz}]^{-1/2}$, in the neighbourhood of which the SIA is not valid; so the solution there is considered only to be formal.

2.4 Results and discussion

The general solution (14), (A.8) and (A.9) does not require that the material-symmetry-reference frame R_s and the fixed global frame R_0 are the same. As

an application, the flow of transversely isotropic ice such that R_s is deduced from R_0 by a rotation θ from z to z_s around the $y-$axis (see Fig.1), is examined. Using θ as a parameter allows to describe different situations from GRIP where ice exhibits a vertical rotational symmetry axis ($\theta = 0°$), to Vostok where the $c-$axes are randomly distributed in a vertical plane assumed to be perpendicular to the horizontal $x-$axis ($\theta = 90°$). By varying θ it is also possible to describe transversely isotropic ice whose rotational symmetry axis passes from the vertical to the horizontal direction, as observed in a core from Law-Dome (Antarctica) [5]. Moreover, during a bore-hole drilling the drill may not be perfectly vertical, the process of making thin sections of ice cut perpendicular to the long direction of the ice-core is not error free, and at the end it is difficult to obtain the orientation of the rotational symmetry axis of a transversely isotropic observed fabric with an accuracy less than a few degrees. In [2] fabric evolution along the GRIP core was obtained from a numerical simulation coupling a model for the behaviour of anisotropic ice and a finite element simulation of the flow. The calculated fabric was shown to exhibit transverse isotropy with a rotational symmetry axis being at a small angle from the vertical, between 0° and 4°.

In the following, the influence of the strength of transverse isotropy, characterised by α and β in (3), and of θ (for the extreme cases $\theta = 0$ and $\theta = \pi/2$, as well as for a small disorientation from the vertical) is discussed. In order to obtain the general trends while simplifying the analysis, fixed values of θ and of the anisotropy parameters are taken for the whole ice-sheet. From (12) the stretched value M of η in (3) is $M = \tilde{\eta}/\epsilon^2 = \eta/(\epsilon^2 \mathcal{M})$, and the components of the viscosity tensor involved at order ϵ^0, expressed in R_0, are

$$
\begin{aligned}
M_{xzxz} &= M[\,\beta \cos^2 2\theta + \alpha \sin^2 2\theta\,], \\
M_{xxxz} &= 2M[\,\frac{\alpha}{3}(3\sin^2\theta - 1) + \frac{\beta}{2}\cos 2\theta - \frac{1}{6}\,]\sin 2\theta\ , \\
M_{yyxz} &= -\frac{2}{3}M(\alpha - 1)\sin 2\theta\ , \\
M_{zzxz} &= 2M[\,\frac{\alpha}{3}(3\cos^2\theta - 1) - \frac{\beta}{2}\cos 2\theta - \frac{1}{6}\,]\sin 2\theta\ .
\end{aligned}
\tag{15}
$$

In the following the comparisons are made by fixing the value of M relative to that corresponding to the flow of isotropic ice ($\alpha = \beta = 1$), that is $M = 1/6$ (obtained for $H = 0$, $X = L = 1$, and $M_{xzxz} = M$, in the expression for H in (14)). Doing so, we allow L to be different from 1 (then, keeping $H(0) = 1$, ϵ is no longer the ice-sheet aspect ratio l/h_0 but a small parameter in the order of l/h_0).

The surface elevation, the velocities and the shear stress given by (14) depend on M_{xzxz}. Moreover, expressions (15) imply that the deviatoric stresses $S^{(0)}_{xx}$, $S^{(0)}_{zz}$ and $S^{(0)}_{yy}$ are not zero in general when θ is different from 0 and $\pi/2$ as pointed out in section 2.1, and they depend on the anisotropy parameters α and β. Thus the solution does not correspond merely to that obtained by

Table 1. Solutions at order $\mathcal{O}(\epsilon^0)$ for different kinds of transverse isotropy and different orientations of the rotational symmetry axis with respect to the vertical (U_x at $(L/2, H(L/2))$, S_{xz}, S_{xx}, S_{zz}, S_{yy} at $(L/2, 0)$)

	iso	$\alpha = 1$, $\beta = 0.04$				$\alpha = 0.8$, $\beta = 0.5$			
θ		0°	5°	10°	45°	0°	5°	10°	45°
M_{xzxz}	0.167	0.0066	0.0115	0.025	0.167	0.083	0.085	0.089	0.133
L	1	5	3.8	2.56	1	1.414	1.402	1.367	1.118
U_x	0.806	4.029	3.069	2.065	0.806	1.14	1.13	1.102	0.901
S_{xz}	0.289	0.058	0.075	0.113	0.289	0.20	0.20	0.21	0.258
S_{xx}	0	0	-0.18	-0.228	0	0	-0.025	-0.047	-0.022
S_{zz}	0	0	0.18	0.228	0	0	0.016	0.029	-0.021
S_{yy}	0	0	0	0	0	0	0.009	0.018	0.043

using an enhancement factor [6,4]. However the enhancement factor, equal to M_{xzxz}/M, is correct for H, $S_{xz}^{(0)}$, $U_x^{(0)}$ and $U_z^{(0)}$. The shape of the ice-sheet is the same as that given by Vialov [13] with the isotropic viscosity M replaced by M_{xzxz}. Table 1 shows a few examples of the effect of anisotropy on the reduced components M_{xzxz}, L, and $U_x(L/2, H(L/2))$, $S_{xz}(L/2, 0)$, $S_{xx}(L/2, 0)$, $S_{zz}(L/2, 0)$, $S_{yy}(L/2, 0)$, for two types of transverse isotropy and four values of θ, compared to the isotropic case. The first set of anisotropy parameters ($\alpha = 1$, $\beta = 0.04$) corresponds to the extreme case when all the $c-$axes are aligned along the same direction and ice is assumed to behave as an isolated grain [10]. The second set ($\alpha = 0.8$, $\beta = 0.5$) corresponds to a smaller strength of anisotropy. Since H, U_x, U_z, S_{xz} and S_{yy} take the same values for θ and $\pi/2 - \theta$, and S_{zz} and S_{xx} are exchanged when θ is changed in $\pi/2 - \theta$, Table 1 shows the results for $0 < \theta < \pi/4$.

For a fixed accumulation rate the main influence of anisotropy is on the ice-sheet length which can reach five times that of the isotropic ice-sheet. Accordingly, for a given elevation (from (14) $H(L/2) = const.$) the horizontal surface velocity U_x depends strongly on the strength of the anisotropy and on θ, whereas for a fixed accumulation rate the vertical surface velocity U_z does not depend on M_{xzxz}. An important result is that a small disorientation of the rotational symmetry axis with respect to the vertical leads to diagonal deviatoric stresses of the same order of magnitude as the shear stress (see Table 1).

Finally the results given in the Appendix show that, for a flat bedrock, the solution at order $\mathcal{O}(\epsilon^1)$ is not zero in general when θ is different from 0 and $\pi/2$: it depends on the anisotropy but remains negligible (*i.e.* the solution at order $\mathcal{O}(\epsilon^1)$ is actually about 10^3 times smaller than the solution at order ϵ^0). The solution at order $\mathcal{O}(\epsilon^2)$ is found to be negligible as well. Note that these results were obtained for linear rheology and a flat base, and would be certainly different in a more complex situation (nonlinear rheology and/or perturbed bedrock topography).

3 Conclusion

The SIA solution for the two-dimensional plane strain and steady flow of an isothermal ice-sheet over a flat bedrock, assuming a linearly orthotropic behaviour of ice, has been calculated up to the second order in the aspect ratio ϵ. In the general case when the material symmetry axes do not coincide with the horizontal and vertical axes of the global frame, the SIA solution at order zero involves all the variables and especially all the deviatoric stresses. This solution has been analysed in the special case of transversely isotropic ice whose rotational symmetry axis lies in the plane of the ice-sheet flow. It has been found that the diagonal components S_{xx}, S_{yy}, S_{zz} can be of the same order as the shear stress when the rotational symmetry axis is not vertical (whereas these components are zero for isotropic ice). However, the solutions at orders greater than $\mathcal{O}(\epsilon^0)$ remain negligible, even when the orthotropy symmetry axes do not coincide with the fixed reference-frame axes. For a given accumulation rate the degree of development of anisotropy has a strong influence on the ice-sheet length and on the horizontal velocity.

Further development should take into account the evolution of anisotropy with the ice strain-history and a more realistic bedrock topography, which will enhance the influence of anisotropy by involving much more complex states of stress in the ice-sheet.

Appendix A

Equations at orders $\mathcal{O}(\epsilon^0)$, $\mathcal{O}(\epsilon^1)$ and $\mathcal{O}(\epsilon^2)$

The variables $\boldsymbol{U}$, P and $\boldsymbol{S}$ are expanded in power series of ϵ up to the second order, as for example $U_x = U_x^{(0)} + \epsilon U_x^{(1)} + \epsilon^2 U_x^{(2)} + \mathcal{O}(\epsilon^3)$. Then the reduced equations of the problem (13) are split in parts corresponding to each order $\mathcal{O}(\epsilon^n)$, which gives

- mass conservation

$$\mathcal{O}(\epsilon^n)\text{:}\ \frac{\partial U_x^{(n)}}{\partial X} + \frac{\partial U_z^{(n)}}{\partial Z} = 0\ , \qquad \text{for } n = 0, 1, 2\ , \tag{A.1}$$

- balance of momentum

$$\begin{aligned}
&\mathcal{O}(\epsilon^0)\text{:}\ \frac{\partial P^{(0)}}{\partial X} + \frac{\partial S_{xz}^{(0)}}{\partial Z} = 0\ , && \frac{\partial P^{(0)}}{\partial Z} = 1\ , \\
&\mathcal{O}(\epsilon^1)\text{:}\ \frac{\partial P^{(1)}}{\partial X} + \frac{\partial S_{xz}^{(1)}}{\partial Z} + \frac{\partial S_{xx}^{(0)}}{\partial X} = 0\ , && \frac{\partial P^{(1)}}{\partial Z} + \frac{\partial S_{zz}^{(0)}}{\partial Z} = 0\ , \\
&\mathcal{O}(\epsilon^2)\text{:}\ \frac{\partial P^{(2)}}{\partial X} + \frac{\partial S_{xz}^{(2)}}{\partial Z} + \frac{\partial S_{xx}^{(1)}}{\partial X} = 0\ , && \frac{\partial P^{(2)}}{\partial Z} + \frac{\partial S_{zz}^{(1)}}{\partial Z} + \frac{\partial S_{xz}^{(0)}}{\partial X} = 0\ ,
\end{aligned} \tag{A.2}$$

- constitutive law

$$\begin{aligned}
&\mathcal{O}(\epsilon^0)\text{: } S_{ij}^{(0)} = M_{ijxz}\frac{\partial U_x^{(0)}}{\partial Z}\ ,\\
&\mathcal{O}(\epsilon^1)\text{: } S_{ij}^{(1)} = M_{ijxx}\frac{\partial U_x^{(0)}}{\partial X} + M_{ijzz}\frac{\partial U_z^{(0)}}{\partial Z} + M_{ijxz}\frac{\partial U_x^{(1)}}{\partial Z}\ ,\\
&\mathcal{O}(\epsilon^2)\text{: } S_{ij}^{(2)} = M_{ijxx}\frac{\partial U_x^{(1)}}{\partial X} + M_{ijzz}\frac{\partial U_z^{(1)}}{\partial Z} + M_{ijxz}\Big(\frac{\partial U_z^{(0)}}{\partial X} + \frac{\partial U_x^{(2)}}{\partial Z}\Big)\ ,\\
&(ij = xx, yy, zz, xz)
\end{aligned} \tag{A.3}$$

In principle, in order to express the boundary conditions on the surface, the elevation H should be expanded as the other variables, and any variable $Q(Z)$ should be developed on $Z = H$ as a Taylor expansion around $Z = H^{(0)}$, that is

$$\begin{aligned}
Q(H) = Q^{(0)} &+ \epsilon\Big(H^{(1)}\frac{\partial Q^{(0)}}{\partial Z} + Q^{(1)}\Big)\\
&+ \epsilon^2\Big(\frac{1}{2}{H^{(1)}}^2\frac{\partial^2 Q^{(0)}}{\partial Z^2} + H^{(2)}\frac{\partial Q^{(0)}}{\partial Z} + H^{(1)}\frac{\partial Q^{(1)}}{\partial Z} + Q^{(2)}\Big) + \mathcal{O}(\epsilon^3)\ ,
\end{aligned} \tag{A.4}$$

where $Q^{(0)}, Q^{(1)}, Q^{(2)}$ and their partial derivative are taken at $Z = H^{(0)}$. This would lead to very complicated calculations in the case of general orthotropy. Since the aim of the present calculation is to show that the solutions at orders $\mathcal{O}(\epsilon)$ and $\mathcal{O}(\epsilon^2)$ are actually negligible, we simplify the problem by assuming that the surface elevation is fixed as $H = H^{(0)}$, and by letting the reduced surface accumulation Ω vary according to $\Omega = 1 + \epsilon\Omega^{(1)} + \epsilon^2\Omega^{(2)} + \mathcal{O}(\epsilon^3)$. This simplification is relevant if $\epsilon\Omega^{(1)}$ and $\epsilon^2\Omega^{(2)}$ are negligible compared to 1, that is far from the ice-sheet margin. The reduced boundary conditions of the problem (13), with surface boundary conditions applied on $Z = H^{(0)}$, are

- free-surface boundary condition, on $Z = H = H^{(0)}$

$$\begin{aligned}
&\mathcal{O}(\epsilon^0)\text{: } \frac{\partial H}{\partial X}P^{(0)} - S_{xz}^{(0)} = 0\ , && P^{(0)} = 0\ ,\\
&\mathcal{O}(\epsilon^1)\text{: } \frac{\partial H}{\partial X}(P^{(1)} + S_{xx}^{(0)}) - S_{xz}^{(1)} = 0\ , && P^{(1)} + S_{zz}^{(0)} = 0\ ,\\
&\mathcal{O}(\epsilon^2)\text{: } \frac{\partial H}{\partial X}(P^{(2)} + S_{xx}^{(1)}) - S_{xz}^{(2)} = 0\ , && P^{(2)} + S_{zz}^{(1)} - \frac{\partial H}{\partial X}S_{xz}^{(0)} = 0\ ,
\end{aligned} \tag{A.5}$$

- surface accumulation rate, on $Z = H = H^{(0)}$

$$\begin{aligned}
&\mathcal{O}(\epsilon^0)\text{: } \frac{\partial H}{\partial X}U_x^{(0)} - U_z^{(0)} = 1\ ,\\
&\mathcal{O}(\epsilon^n)\text{: } \frac{\partial H}{\partial X}U_x^{(n)} - U_z^{(n)} = \Omega^{(n)}\ , \qquad \text{for } n = 1, 2\ ,
\end{aligned} \tag{A.6}$$

- bedrock contact, on $Z = 0$

$$\mathcal{O}(\epsilon^n)\text{: } U_x^{(n)} = U_z^{(n)} = 0\ , \qquad \text{for } n = 0, 1, 2\ . \tag{A.7}$$

Solutions at orders $\mathcal{O}(\epsilon^0)$, $\mathcal{O}(\epsilon^1)$ and $\mathcal{O}(\epsilon^2)$

The SIA solution at order $\mathcal{O}(\epsilon^0)$ is obtained by integration of equations (A.1),(A.2),(A.3), with boundary conditions (A.5), (A.6) and (A.7) at order $\mathcal{O}(\epsilon^0)$, as follows: $P^{(0)}$ is obtained by integration of the second equation (A.2), with boundary condition (A.5), then $S_{xz}^{(0)}$ is derived from the first equation (A.2), with boundary condition (A.5), knowing $P^{(0)}$. $U_x^{(0)}$ is then deduced from (A.3), with boundary condition (A.7), and the integration of the mass conservation equation (A.1), with boundary condition (A.7), gives the expression of $U_z^{(0)}$. The other non-zero components $S_{xx}^{(0)}$, $S_{yy}^{(0)}$ and $S_{zz}^{(0)}$ of $\boldsymbol{S}$ are given by (A.3). The ice-sheet geometry is obtained by integration of (A.6), with the condition $H^{(0)}(0) = H(0) = 1$. The SIA solution at order $\mathcal{O}(\epsilon^0)$ is given by relations (14).

In the following H' denotes the first derivative of $H(X) = H^{(0)}(X)$, H'' the second derivative, etc.

The solution at order $\mathcal{O}(\epsilon^1)$ is obtained by following the same steps than for the solution at order $\mathcal{O}(\epsilon^0)$ (*i.e.* calculation of $P^{(1)}$, then $S_{xz}^{(1)}$, $U_x^{(1)}$ and $U_z^{(1)}$), by integration of equations (A.1),(A.2),(A.3), with boundary conditions (A.5) and (A.7) at order $\mathcal{O}(\epsilon^1)$, with the knowledge of the solution at order $\mathcal{O}(\epsilon^0)$. This solution is as follows:

$$
\begin{aligned}
U_x^{(1)} &= \frac{M_{zzxz} - M_{xxxz}}{M_{xzxz}^2} Z\big[H''(\frac{Z^2}{3} - HZ + \frac{H^2}{2}) - H'^2(Z - H)\big], \\
U_z^{(1)} &= \frac{M_{xxxz} - M_{zzxz}}{M_{xzxz}^2} Z^2\big[H'''(\frac{Z^2}{12} - \frac{HZ}{3} + \frac{H^2}{4}) - 3H'H''(\frac{Z}{3} - \frac{H}{2}) + \frac{H'^3}{2}\big], \\
P^{(1)} &= -\frac{M_{zzxz}}{M_{xzxz}} H'(Z - H), \\
S_{xz}^{(1)} &= \frac{M_{zzxz} - M_{xxxz}}{M_{xzxz}} (Z - H)\big[H''\frac{Z - H}{2} - H'^2\big].
\end{aligned}
\tag{A.8}
$$

The other non-zero components $S_{xx}^{(1)}$, $S_{yy}^{(1)}$ and $S_{zz}^{(1)}$ are obtained from (A.3). The SIA solution at order $\mathcal{O}(\epsilon^2)$ is obtained as

$$
\begin{aligned}
U_x^{(2)} = {} & \frac{(M_{xxxz} - M_{zzxz})^2}{M_{xzxz}^3} Z\big[H'''(Z^3 - 4HZ^2 + 3ZH^2 + H^3)/6 \\
& \qquad - H'H''(4Z^2 - 6HZ - H^2)/2 + H'^3 Z\big] \\
& - \frac{M_{xxxx} + M_{zzzz} - 2M_{xxzz}}{M_{xzxz}^2} Z\big[H'''(Z^3 - 4HZ^2 - 8H^3)/24 \\
& \qquad + H'H''(-Z^2 + 4H^2)/2 + HH'^3\big] \\
& + \frac{1}{M_{xzxz}} Z\big[H'''(Z^3 - 4HZ^2 + 3H^2Z - 2H^3)/12 \\
& \qquad + H'H''(-2Z^2 + 3HZ - 3H^2)/2 + H'^3(Z - 2H)/2\big],
\end{aligned}
$$

$$
\begin{aligned}
U_z^{(2)} = &- \frac{(M_{xxxz} - M_{zzxz})^2}{M_{xzxz}^3} Z^2 \big[H''''(2Z^3 - 10HZ^2 + 10ZH^2 + 5H^3)/60 \\
&\quad + H'H'''(-4Z^2 + 8HZ + 3H^2)/6 \\
&\quad + H''^2(-2Z^2 + 4HZ + H^2)/4 + H'^2H''(4Z + H)/2\big] \\
&+ \frac{M_{xxxx} + M_{zzzz} - 2M_{xxzz}}{M_{xzxz}^2} Z^2 \big[H''''(Z^3 - 5HZ^2 - 20H^3)/120 \\
&\quad + H'H'''(-Z^2 + 3H^2)/6 + H''^2(-Z^2 + 8H^2)/8 \\
&\quad + 7H''H'^2H/2 + H'^4/2\big] \\
&- \frac{1}{M_{xzxz}} Z^2 \big[H''''(Z^3 - 5HZ^2 + 5H^2Z - 5H^3)/60 \\
&\quad + H'H'''(-Z^2 + 2HZ - 3H^2)/3 + H'^2H''(Z - 3H) \\
&\quad - H'^4/2 + H''^2(-Z^2 + 2HZ - 3H^2)/4\big],
\end{aligned}
$$

$$
\begin{aligned}
P^{(2)} = &(Z - H)\big[H'^2 - H''(Z - H)/2\big] - S_{zz}^{(1)}, \\
S_{xz}^{(2)} = &\frac{(M_{xxxz} - M_{zzxz})^2}{M_{xzxz}^2} \big[H'''(2Z^3 - 6HZ^2 + 3ZH^2 + H^3)/6 \\
&\quad - H'H''(6Z^2 - 6HZ - H^2)/2 + H'^3Z\big] \\
&- \frac{M_{xxxx} + M_{zzzz} - 2M_{xxzz}}{M_{xzxz}} \big[H'''(Z^3 - 3HZ^2 + 2H^3)/6 \\
&\quad + H'H''(-3Z^2 + 4H^2)/2 + HH'^3\big] \\
&+ (Z - H)\big[H'''(Z - H)^2/6 - 3H'H''(Z - H)/2 + H'^3\big].
\end{aligned}
\tag{A.9}
$$

The other non-zero components $S_{xx}^{(2)}$, $S_{yy}^{(2)}$ and $S_{zz}^{(2)}$ are obtained from (A.3). This solution at order $\mathcal{O}(\epsilon^2)$ is obtained by following the same steps than for the solutions at orders $\mathcal{O}(\epsilon^0)$ and $\mathcal{O}(\epsilon^1)$ (*i.e.* calculation of $P^{(2)}$,then $S_{xz}^{(2)}$, $U_x^{(2)}$ and $U_z^{(2)}$), by integration of equations (A.1),(A.2),(A.3), with boundary conditions (A.5) and (A.7) at order $\mathcal{O}(\epsilon^2)$, with the knowledge of the solutions at orders $\mathcal{O}(\epsilon^0)$ and $\mathcal{O}(\epsilon^1)$.

Acknowledgement: This work was supported by the Commission of European Communities under contract ENV4-CT95-0125 "Fabric Development and Rheology of Polar Anisotropic Ice for Ice-Sheet Flow Modelling". LGGE-CNRS is associated to Université Joseph Fourier-Grenoble I.

References

1. Brisset, L. and Remy, F. (1996) Antarctic topography and kilometer-scale roughness derived from ERS-1 altimetry. *Ann. Glaciol.*, **23**, 374–381.

2. Gagliardini, O. (1999) *Simulation numérique d'un écoulement bidimensionnel de glace polaire présentant une anisotropie induite évolutive.* Thèse de Doctorat de l'Université Joseph Fourier-Grenoble I.
3. Hutter, K. (1983) *Theoretical Glaciology.* Reidel Pub. Compagny, Dordrecht and Terra Scientific Pub. Company Tokyo.
4. Schott Hvidberg, C., Dahl-Jensen, D. and Waddington, E.D. (1997) Ice flow between the Greenland ice-core project and Greenland ice-sheet project 2 boreholes in central Greenland . *J. Geophys. Res.*, **102**(B10), 26851–26859.
5. Jacka, T.H. and Budd, W.F. (1989) Isotropic and anisotropic flow relations for ice dynamics. *Ann. Glaciol.*, **12**, 81–84.
6. Lile, R.C. (1978) The effect of anisotropy on the creep of polycrystalline ice. *J. Glaciol.*, **21**, 475–483.
7. Lipenkov, V.Ya., Barkov, N.I., Duval, P. and Pimenta, P. (1989) Crystalline texture of the 2083m ice-core at Vostok station, Antarctica. *J. Glaciol.*, **35**, No. 121, 392–398.
8. Mangeney, A., Califano, F., and Hutter, K. (1997) A numerical study of anisotropic, low Reynolds number, free surface flow of ice-sheet modeling. *J. Geophys. Res.*, **102**(B10), 22749–22764.
9. Mangeney, A. and Califano, F. (1998) The shallow ice approximation for anisotropic ice: formulation and limits *J. Geophys. Res.*, **103**(B1), 691–705.
10. Meyssonnier, J. and Philip, A. (1996) A model for the tangent viscous behaviour of anisotropic polar ice. *Ann. Glaciol.*, **23**, 253–261.
11. Morland, L.W. (1984) Thermomechanical balances of ice-sheet flows. *Geophys. Astrophys. Fluid Dyn.*, **29**, 237–266.
12. Thorsteinsson, T., Kipfstuhl, J. and Miller, H. (1997) Textures and fabrics in the GRIP ice core. *J. Geophys. Res.*, **102** (C12), 26583–26599.
13. Vialov, S.S. (1958) Regularities of glacial shields movements and the theory of plastic viscous flow. *Physics of the movements of ice IAHS*, **47**, 266–275.

(Received 02 March 1999, accepted 1 June 1999)

Orthotropic Viscous Model for Ice

Ryszard Staroszczyk and Leslie W. Morland

School of Mathematics, University of East Anglia, Norwich NR4 7TJ,
United Kingdom

Abstract. An orthotropic constitutive model for the strain-induced anisotropy of polar ice is considered. The ice is modelled as a viscous and incompressible fluid with evolving fabric that depends on local deformations, and the viscous law expresses the stress in terms of the strain-rate, strain and three structure tensors based on the principal stretch axes. The model is first adopted to illustrate the evolution of the ice viscosities during continued uni-axial compression and simple shearing, and then it is applied to the simulations of a steady ice sheet flow. For a fixed free surface elevation, the accumulation rates required to maintain the prescribed geometry, as well as the velocity depth-profiles, are calculated and compared with those obtained for the isotropic ice.

1 Introduction

The evolution of fabric, and the consequent induced anisotropy of the viscous response, due to the re-alignment of crystal axes as ice is sheared during its descent from the surface of an ice sheet, requires a macroscopic constitutive law which captures the main effects and is suitable for numerical simulations of ice sheet flows. One approach has been the introduction of an evolving orientation distribution function (ODF) which gives a weighting to each possible crystal c-axis orientation, and is used to derive the macroscopic response by applying the homogenization method; see, for example, Svendsen and Hutter [1], Meyssonnier and Philip [2] and Gagliardini and Meyssonnier [3]. An alternative approach is to assume directly a macroscopic viscous law with dependencies and symmetries that could approximate such fabric evolution. Morland and Staroszczyk [4] and Staroszczyk and Morland [5] have developed an orthotropic viscous response model in which the planes of reflexional symmetry are defined by the current principal stretch axes. Although this implies that the fabric evolution, and underlying microprocesses at the grain level, are independent of the deformation path, which may be an oversimplification, we adopt this form of response again in order to modify the previous example models to satisfy different correlations with observation.

Staroszczyk and Morland [5] derived directional viscosity equalities and inequalities which a valid model must satisfy, and showed how a restricted form of the general orthotropic law, with simple forms of the response functions, could meet these requirements in addition to satisfying limit behaviours in uni-axial compression and simple shearing. It was subsequently pointed out by associates that the experimental data for the uni-axial compression limit

adopted were not appropriate to cold polar ice, being high strain-rate response of warm ice, and in particular, the adopted limit factor below unity should be replaced by one much greater than unity. New response functions are now constructed which satisfy the required viscosity relations and the new limit behaviour, and for example functions the illustrations of continued uni-axial compression and simple shearing are presented. The viscous model has been used in numerical simulations of a plane ice sheet flow, for which the velocities at the free surface and their depth profiles are shown to illustrate the influence of ice anisotropy on the ice sheet flow.

2 Orthotropic Viscous Model

Let Ox_i $(i = 1,2,3)$ be spatial rectangular Cartesian co-ordinates with OX_i $(i = 1,2,3)$ particle reference co-ordinates, and v_i the velocity components, then the deformation gradient $\mathbf{F}$ and strain-rate $\mathbf{D}$ have components

$$F_{ij} = \frac{\partial x_i}{\partial X_j}, \quad D_{ij} = \frac{1}{2}\Big(\frac{\partial v_i}{\partial x_j} + \frac{\partial v_j}{\partial x_i}\Big). \tag{1}$$

The Cauchy-Green strain $\mathbf{B}$, its principal stretch axes given by unit vectors $\mathbf{e}^{(r)}$ $(r = 1,2,3)$, and the squares of the principal stretches b_r are defined by

$$\mathbf{B} = \mathbf{F}\mathbf{F}^T, \quad \mathbf{B}\mathbf{e}^{(r)} = b_r\mathbf{e}^{(r)}, \quad \det(\mathbf{B} - b_r\mathbf{I}) = 0, \quad b_r = \lambda_r^2, \tag{2}$$

where λ_r are principal stretches along the vectors $\mathbf{e}^{(r)}$. The latter relation is a cubic with positive roots, and we adopt the ordering $b_1 \geq b_2 \geq b_3 > 0$, with strict inequalities except when the ice is in an undeformed isotropic state $\mathbf{B} = \mathbf{I}$, $b_1 = b_2 = b_3 = 1$; that is, we assume that the maximum compression is in the $\mathbf{e}^{(3)}$ direction. By incompressibility,

$$\operatorname{div}\mathbf{v} = 0, \quad b_1b_2b_3 = 1, \quad b_1 > 1, \quad b_3 < 1\,. \tag{3}$$

The orthotropic structure tensors describing reflexional symmetries in the principal stretch planes normal to the axes $\mathbf{e}^{(r)}$ are defined by

$$\mathbf{M}^{(r)} = \mathbf{e}^{(r)} \otimes \mathbf{e}^{(r)}, \quad (r = 1,2,3). \tag{4}$$

The deviatoric stress is defined in terms of the Cauchy stress $\boldsymbol{\sigma}$ and mean pressure p by

$$\hat{\boldsymbol{\sigma}} = \boldsymbol{\sigma} + p\mathbf{I}, \quad p = -\frac{1}{3}\operatorname{tr}\boldsymbol{\sigma}, \quad \operatorname{tr}\hat{\boldsymbol{\sigma}} = 0, \tag{5}$$

where p is a workless constraint not given by a constitutive law, but determined by momentum balance and boundary conditions. In order to include the commonly adopted viscous rate factor $a(T)$, where T denotes temperature, we introduce a modified strain-rate $\tilde{\mathbf{D}} = \mathbf{D}/a(T)$.

We now re-examine the orthotropic viscous law proposed by Staroszczyk and Morland [5], which is restricted to two sets of tensor generators, each with a coefficient given by one response function of a single deformation invariant argument which define the strength of the anisotropy, and a common strain-rate dependent factor to determine the isotropic response:

$$\hat{\boldsymbol{\sigma}} = \mu_0\,(\operatorname{tr}\tilde{\mathbf{D}}^2)\Big\{\sum_{r=1}^{3} f(b_r)\Big[\mathbf{M}^{(r)}\tilde{\mathbf{D}} + \tilde{\mathbf{D}}\mathbf{M}^{(r)} - \frac{2}{3}\operatorname{tr}(\mathbf{M}^{(r)}\tilde{\mathbf{D}})\mathbf{I}\Big]$$

$$+\, g(K)\Big[\tilde{\mathbf{D}}\mathbf{B} + \mathbf{B}\tilde{\mathbf{D}} - \frac{2}{3}\operatorname{tr}(\tilde{\mathbf{D}}\mathbf{B})\mathbf{I}\Big]\Big\}, \quad K = \operatorname{tr}\mathbf{B}, \quad f(1) + g(3) = 1\,, \qquad (6)$$

where $\mu_0\,(\operatorname{tr}\tilde{\mathbf{D}}^2)$ defines the isotropic viscosity at temperature T when $\mathbf{B} = \mathbf{I}$. It was shown in [4] and [5] that the other terms in a general orthotropic law (Boehler [6]) do not contribute to the instantaneous viscosities which can be detected by simple shear experiments. Furthermore, present experimental configurations cannot distinguish dependence of coefficients on more than one invariant. The form (6) was shown to be sufficiently flexible to describe known responses.

3 Viscosity Relations and Limits

Instantaneous directional viscosities μ_{ij} are defined by the initial ratio of the deviatoric stress to strain-rate in simple shear in the x_i direction on a plane normal to the x_j direction starting from a frozen fabric at zero stress. Here, and in the subsequent response analyses, we consider applied isochoric deformations and determine the deviatoric stress response given by the law (6). For a fabric deformation defined by principal stretches along the co-ordinate axes, (6) gives

$$\mu_{ij} = \frac{\hat{\sigma}_{ij}}{2\tilde{D}_{ij}} = \frac{1}{2}\,\mu_0(\operatorname{tr}\tilde{\mathbf{D}}^2)\Big[f(b_i) + f(b_j) + (b_i + b_j)\,g(K)\Big], \quad (i \neq j)\,, \qquad (7)$$

and since this must remain bounded as any axial stretch increases indefinitely, we rewrite g and the normalisation $(6)_3$ as

$$g(K) = K^{-1}G(K), \quad K = b_1 + b_2 + b_3, \quad f(1) + \frac{1}{3}G(3) = 1, \qquad (8)$$

where $G(K)$ is bounded. The inequalities required for a valid response [5] are

$$b_1 = b_2 = b_3 = 1: \quad \mu_{ij} = \mu \quad (i,j = 1,2,3)\,, \qquad (9)$$

$$b_1 = b_2 > 1 > b_3: \quad 0 < \mu_{13} = \mu_{23} < \mu_{12}\,, \qquad (10)$$

$$b_1 > b_2 > 1 > b_3: \quad 0 < \mu_{13} < \mu_{23} < \mu_{12}\,, \qquad (11)$$

$$b_1 > b_2 = 1 > b_3: \quad 0 < \mu_{13} < \mu_{23} = \mu_{12}\,, \qquad (12)$$

$$b_1 > 1 > b_2 > b_3: \quad 0 < \mu_{13} < \mu_{12} < \mu_{23}\,, \qquad (13)$$

$$b_1 > 1 > b_2 = b_3: \quad 0 < \mu_{13} = \mu_{12} < \mu_{23}\,, \qquad (14)$$

The equalities (9), (10)and (14) are automatically satisfied. The equality (12) provides a relation for $G(K)$ in terms of $f(b)$, namely

$$G(K) = -\frac{K\, b_1}{b_1^2 - 1}\left[f(b_1) - f(b_1^{-1})\right], \quad 2\, b_1 = K - 1 + \sqrt{(K-1)^2 - 4} \geq 2; \tag{15}$$

that is, the model is defined by prescribing a single response function $f(b_r)$. The limits of (15) as $b_1 \to 1$, $K \to 3$, and as $b_1 \to \infty$, $K \sim b_1$, combined with the normalisation $(6)_3$, show that

$$f(1) - f'(1) = 1, \quad G(\infty) = f(0) - f(\infty); \tag{16}$$

the first relation is a restriction on $f(b_r)$ $(r = 1, 2, 3)$ at $b_r = 1$.

Application of the model (6) to uni-axial compression in the x_3 direction, with equal lateral stretches $\lambda_1 = \lambda_2$, shows that as $b_1 \to \infty$, with $K \sim 2b_1$,

$$\frac{\hat{\sigma}_{11}}{2\mu_0 \tilde{D}_{11}} = \frac{\hat{\sigma}_{33}}{2\mu_0 \tilde{D}_{33}} \to \frac{1}{3} f(\infty) + \frac{2}{3} f(0) + \frac{1}{6} G(\infty) = A, \tag{17}$$

where A is the ratio of the anisotropic to isotropic viscosity, or reciprocal of an axial enhancement factor. Similarly, for an indefinite simple shear at constant rate $D_{13} = \frac{1}{2}\dot{\gamma}$ in the Ox_1x_3 plane, following any initial frozen plane deformation,

$$\frac{\hat{\sigma}_{13}}{\mu_0 \dot{\gamma}} \to \frac{1}{2} f(\infty) + \frac{1}{2} f(0) + \frac{1}{2} G(\infty) = S, \tag{18}$$

where S is the ratio of the anisotropic to isotropic viscosity, or reciprocal of the shear enhancement factor. The three relations $(16)_2$, (17) and (18) define the limit values

$$f(0) = S, \quad f(\infty) = 6A - 5S, \quad G(\infty) = 6(S - A). \tag{19}$$

The previous model examples were based on the factors measured by Budd and Jacka [7], giving

$$S = 1/8\,, \quad A = 1/3\,, \quad f(0) = 1/8\,, \quad f(\infty) = 11/8\,, \quad G(\infty) = -5/4\,. \tag{20}$$

It has been noted (P. Duval and J. Meyssonnier, private communication) that the above axial factor A less than unity was measured for warm ice under relatively high stresses, and for cold polar ice at low deviatoric stresses (less than 0.2 MPa, which is a typical magnitude for ice sheets) this viscosity factor would be much greater than unity. According to Pimienta *et al.* [8], the factor A for ice with a single maximum fabric can be as high as 10, although recently Mangeney *et al.* [9] give the value of about 3 for the ice near the bottom of the GRIP ice core, deduced from the data provided by Thorsteinsson *et al.* [10].

The limit value of the shear viscosity factor for the GRIP ice, as estimated by Mangeney *et al.* [9], is equal to about 0.4. However, this limit behaviour is still at relatively small shear in a central part of the ice sheet, and it is expected that the limit for larger shear will be significantly smaller. Hence. for our illustrations we choose the value $S = 0.2$.

4 Illustrations

We now show that simple forms of the function $f(b)$ can meet the limits (19) with values of A greater than unity and satisfy the viscosity relations (9)–(14). For illustration purposes, we adopt the following simple monotonic increasing functions:

$$f(b_r) = f(\infty) - [f(\infty) - f(0)]\,\mathrm{e}^{(}-\alpha b_r^m), \quad \alpha > 0, \quad m > 0, \tag{21}$$

$$f(b_r) = f(0) \; + [f(\infty) - f(0)]\tanh(\alpha b_r^m), \quad \alpha > 0, \quad m > 0, \tag{22}$$

where α is determined by the restriction $(16)_1$ m is a free parameter, and $r = 1, 2, 3$. For the adopted values $A = 3$ and $S = 0.2$, the limits (19) are

$$f(0) = 0.2\,, \quad f(\infty) = 17\,, \quad G(\infty) = -16.8\,. \tag{23}$$

First we consider an axial compression in the x_3 direction, defined by the axial stretch $\lambda_3 < 1$, with equal lateral stretches λ_1 and λ_2 along the x_1 and x_2 co-ordinate axes, for which the deformation is defined by

$$x_1 = \lambda_1 X_1, \quad x_2 = \lambda_2 X_2, \quad x_3 = \lambda_3 X_3, \quad \lambda_1 = \lambda_2 > 1, \quad \lambda_3 = \lambda_1^{-2} < 1. \tag{24}$$

For this deformation field, the constitutive law (6) yields the following relation describing the evolution of the normalised axial viscosity with increasing stretch:

$$\frac{\hat{\sigma}_{33}}{2\mu_0 \tilde{D}_{33}} = \frac{1}{3}\left[f(b_1) + 2f(b_1^{-2}) + g(K)(b_1 + 2b_1^{-2})\right], \tag{25}$$

where $K = 2b_1 + b_1^{-2}$. Figure 1 illustrates the variation of the ratio $\hat{\sigma}_{33}/(2\mu_0 \tilde{D}_{33})$ with the stretch λ_1 for different response functions (21) and (22). The curves labelled (1) and (2) correspond to the function (21) with $m = 1.5$ and 2 respectively, and the labels (3) and (4) refer to the function (22) with $m = 1$ and 1.5 respectively. These particular values of m in (21) and (22) have been chosen as they provide good correlation with the micro-macroscopic model [3], see Staroszczyk and Gagliardini [11].

Next we consider a simple shear at constant strain-rate $D_{13} = \frac{1}{2}\dot{\gamma}$, following an initial plane compression and stretch that has been frozen at constant $\lambda_3 = \lambda_1^{-1} \leq 1$ by the removal of the stress and strain-rate. The deformation is now described by

$$x_1 = \lambda_1 X_1 + \kappa X_3, \quad x_2 = X_2, \quad x_3 = \lambda_1^{-1} X_3, \tag{26}$$

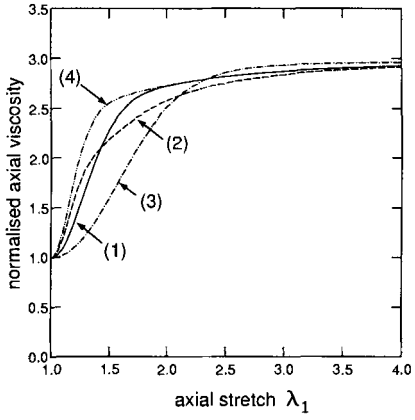

Fig. 1. Evolution of the normalised viscosity $\hat{\sigma}_{33}/(2\mu_0 D_{33})$ with increasing stretch λ_1 in uni-axial compression for different fabric response functions $f(b_r)$.

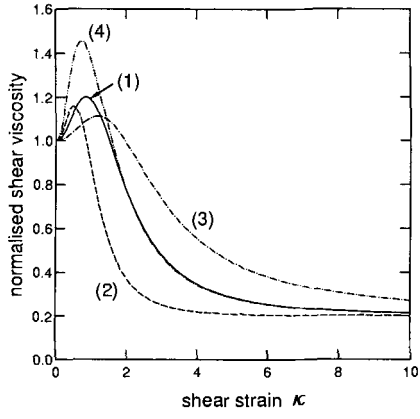

Fig. 2. Evolution of the normalised viscosity $\hat{\sigma}_{13}/(\mu_0\dot{\gamma})$ with increasing strain κ in simple shear started from an isotropic state ($\lambda_3 = 1$) for different fabric response functions $f(b_r)$.

for which the evolution of the normalised shear viscosity is described by

$$\frac{\hat{\sigma}_{13}}{\mu_0\dot{\gamma}} = \frac{1}{2}\left[f(b_1) + f(b_1^{-1}) + g(K)(\lambda_1^2 + \lambda_1^{-2} + \kappa^2)\right], \tag{27}$$

where now $K = b_1 + 1 + b_1^{-1}$. Figure 2 shows, for different model functions (21) and (22), the variation of the ratio $\hat{\sigma}_{13}/(\mu_0\dot{\gamma})$ with increasing shear κ started from the isotropic state ($\lambda_1 = \lambda_3 = 1$); the same labelling as in the previous figure applies. In Figure 3 we illustrate, for the function (21) with $m = 1.5$, the evolution of the normalised shear viscosity for shearing in the Ox_1x_3 plane, started from different anisotropic states induced by the initial plane pre-compression along the x_3 axis defined by the stretch $\lambda_3 \leq 1$. Corresponding to the previous plot is Figure 4, in which the evolution of the current maximum compression axis, being the preferred crystal $c-$axis direction, against the initial (prior to shearing) compression axis is shown for different axial stretches λ_3.

In Figure 5 we illustrate the development of fabric due to simple shear in the Ox_1x_3 plane following different plane compression along the x_3 axis defined by the stretch $\lambda_3 \leq 1$. The diagrams of the $c-$axis orientation distribution have been obtained by using a formula relating the ODF in the micro-macroscopic model [3] to the principal stretches λ_r ($r = 1, 2, 3$) in the present model (O. Gagliardini, private communication).

The orthotropic viscous law (6) with the two response functions $f(b_r)$ and $G(K)$ has been applied to the numerical simulations of a plane, gravity driven, steady-state flow of an isothermal ice sheet on a rigid horizontal bedrock in order to investigate the influence of the ice anisotropy on the flow. The flow

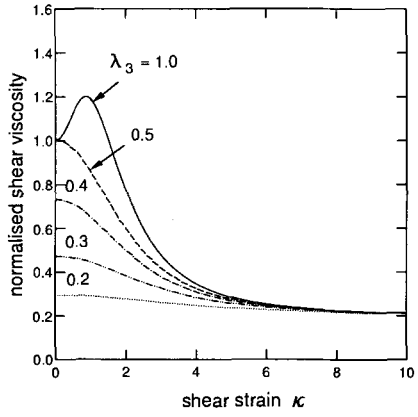

Fig. 3. Evolution of the normalised viscosity $\hat{\sigma}_{13}/(\mu_0\dot{\gamma})$ with the strain κ in simple shear started from different anisotropic states defined by λ_3.

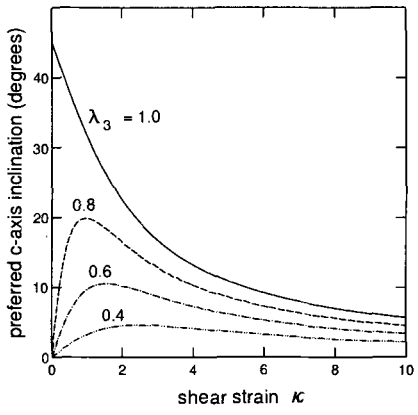

Fig. 4. Evolution of the preferred $c-$axis inclination with the strain κ in simple shear started from different anisotropic states defined by λ_3.

of an idealised symmetric ice sheet, sketched in Figure 6, is considered, and a fixed free surface elevation is assumed, for which the accumulation rates necessary to maintain the prescribed geometry are calculated.

For the plane flow, the momentum balance equations in the Cartesian co-ordinates x and z as indicated in Figure 6 are

$$\frac{\partial \hat{\sigma}_{xx}}{\partial x} + \frac{\partial \hat{\sigma}_{xz}}{\partial z} - \frac{\partial p}{\partial x} = 0, \quad \frac{\partial \hat{\sigma}_{xz}}{\partial x} + \frac{\partial \hat{\sigma}_{zz}}{\partial z} - \frac{\partial p}{\partial z} = \rho g, \tag{28}$$

where ρg is the ice density times gravitational acceleration and is assumed constant. The mass balance is here the incompressibility condition

$$\frac{\partial u}{\partial x} + \frac{\partial w}{\partial z} = 0, \tag{29}$$

where u and w are the velocity components in the x and z directions respectively. A kinematic condition at the free surface $h = h(x)$ is expressed, for a steady-state flow, by

$$u_s \frac{\partial h}{\partial x} - w_s = q, \tag{30}$$

where u_s and w_s are the free surface horizontal and vertical velocities, and $q = q(x)$ is the accumulation rate. The free surface is assumed to be traction-free; that is at $z = h(x)$ we have

$$\boldsymbol{\sigma}\, \mathbf{n}_s = \mathbf{0}, \tag{31}$$

where $\mathbf{n}_s$ is a unit outward normal to the free surface. At the flat base $z = 0$ no-slip conditions are adopted, hence $u = w = 0$ there, and at the ice divide $x = 0$, in view of the symmetry of the problem, $u = 0$ and $\hat{\sigma}_{xz} = 0$.

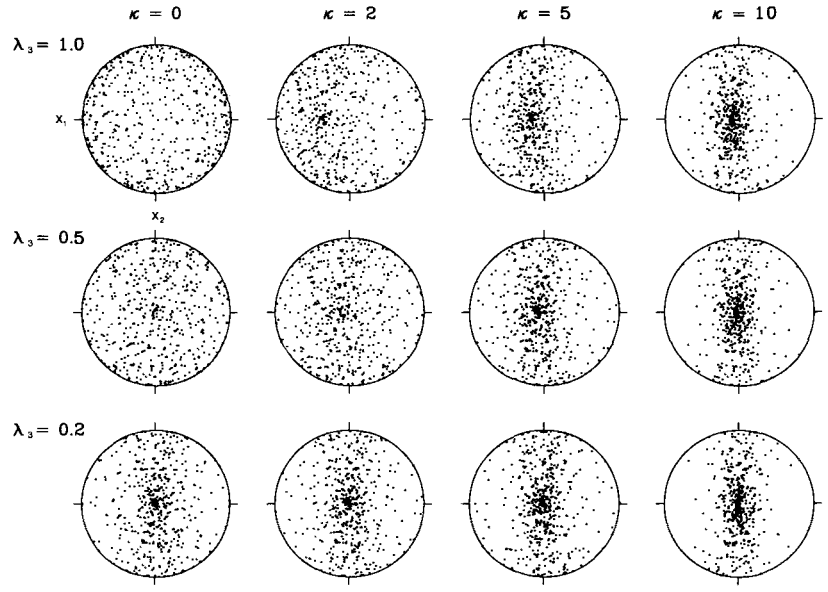

Fig. 5. Diagrams of the $c-$axis orientations demonstrating the fabric development with shear strain κ in simple shearing in the Ox_1x_3 plane following different initial axial deformations given by the stretch λ_3.

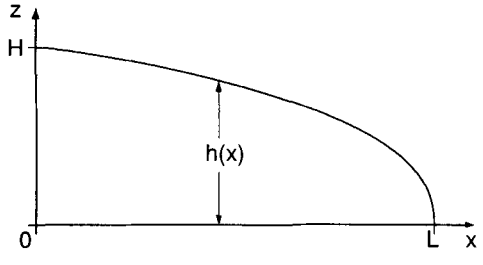

Fig. 6. Cross-section of an idealised symmetric ice sheet with the ice divide thickness H and the half-width L.

The flow problem has been solved numerically by the finite-element method for the ice sheet surface elevation defined by a parabola

$$\frac{h}{H} + \left(\frac{x}{L}\right)^2 = 1. \tag{32}$$

The calculations have been carried out for the aspect ratio $H/L = 0.01$, and the model parameters describing the limit behaviour of ice have been chosen again as $A = 3$ and $S = 0.2$. The results presented below are obtained for the response function (21) with $m = 1.5$. In Figure 7 the normalised horizontal and vertical velocities at the free surface, u_s and w_s, and the

accumulation ratio q, calculated for the anisotropic and isotropic ice, are compared. It is seen that the anisotropy significantly accelerates the flow of ice. Maximum velocities, in both directions, are increased by a factor of about 4 to 5 compared to the isotropic ice, and this increase is approximately of the magnitude of the shear enhancement factor ($1/S = 5$) adopted in the simulations.

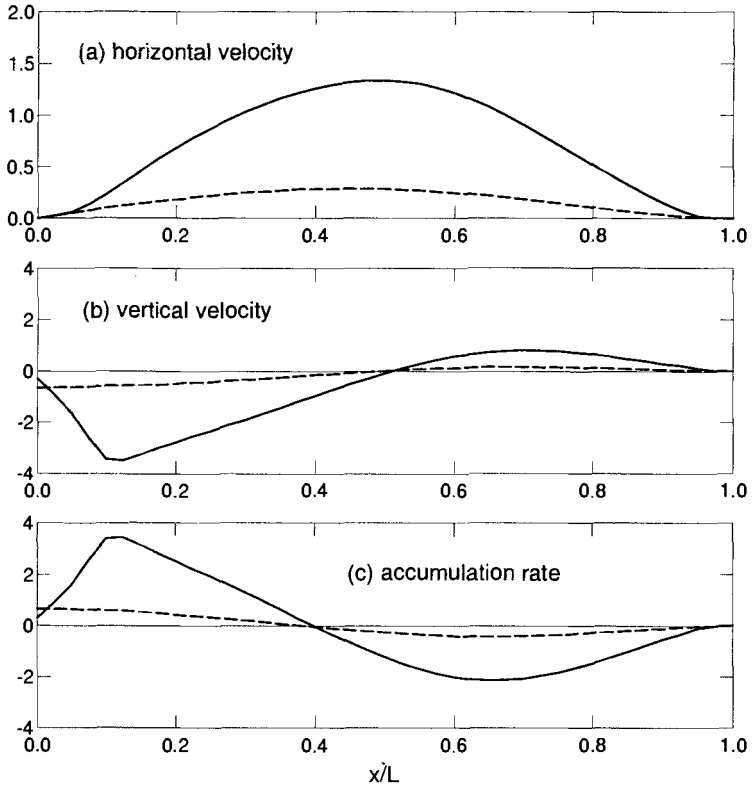

Fig. 7. Free surface horizontal velocities (a), vertical velocities (b), and accumulation rate (c) for the anisotropic ice (solid lines) and the isotropic ice (dashed lines).

Finally, Figure 8 illustrates normalised depth profiles of the velocities u/u_s and w/w_s at different locations x/L for the anisotropic ice (lines) and the isotropic ice (circles). In (a) the profile for the isotropic ice is common for all locations. In (b) the profiles for the isotropic ice vary with x/L, but they are close to the profiles for the anisotropic case, therefore only the plots for $x/L = 0$ (open circles) and $x/L = 0.8$ (solid circles) are shown.

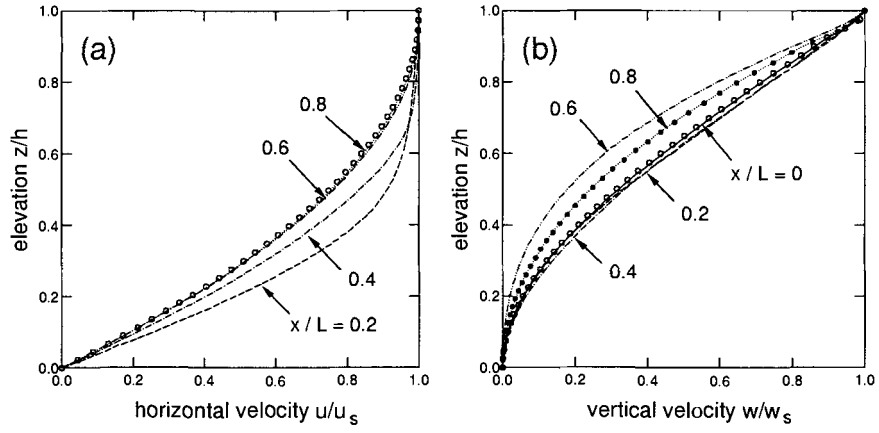

Fig. 8. Depth profiles of normalised horizontal (a) and vertical (b) velocities at different locations x/L for the anisotropic ice (lines) and the isotropic ice (circles).

References

1. Svendsen, B. and Hutter, K. (1996) A continuum approach for modelling induced anisotropy in glaciers and ice sheets. *Ann. Glaciol.* **23**, 262–269
2. Meyssonnier, J. and Philip, A. (1996) A model for tangent viscous behaviour of anisotropic polar ice. *Ann. Glaciol.* **23**, 253–261
3. Gagliardini, O. and Meyssonnier, J. (1999) Analytical derivations for the behaviour and fabric evolution of a linear orthotropic ice polycrystal. *J. Geophys. Res.* In press.
4. Morland, L.W. and Staroszczyk, R. (1998) Viscous response of polar ice with evolving fabric. *Continuum Mech. Thermodyn.* **10** (3), 135–152
5. Staroszczyk, R. and Morland, L.W. (1999) Orthotropic viscous response of polar ice. *J. Eng. Math.* In press.
6. Boehler, J.P. (1987) *Applications of Tensor Functions in Solid Mechanics.* Springer, Wien – New York
7. Budd, W.F. and Jacka, T.H. (1989) A review of ice rheology for ice sheet modelling. *Cold Reg. Sci. Technol.* **16**, 107–144
8. Pimienta, P., Duval, P. and Lipenkov, V.Y. (1987) Mechanical behavior of anisotropic polar ice. In *International Association of Hydrological Sciences Publication* no. 170, p. 57–66. (Symposium on *Physical Basis of Ice Sheet Modelling*, Vancouver 1987).
9. Mangeney, A., Califano, F. and Castelnau, O. (1996) Isothermal flow of an anisotropic ice sheet in the vicinity of an ice divide. *J. Geophys. Res.* **101** (B12), 28,189–28,204
10. Thorsteinsson, T., Kipfstuhl, J. and Miller, H. (1997) Textures and fabrics in the GRIP ice core. *J. Geophys. Res.* **102** (C12), 26,583–26,599
11. Staroszczyk, R. and Gagliardini, O. (1999) Two orthotropic models for the strain-induced anisotropy of polar ice. *J. Glaciol.* Submitted.

(Received 18 Dec. 1998, accepted 23 Feb. 1999)

Tertiary Flow Relations for Compression and Shear Components in Combined Stress Tests on Ice

Roland C. Warner[1 2], T.H. Jacka[1 2], Li Jun[1 2], and W.F. Budd[1]

[1] Antarctic CRC, Box 252-80, Hobart, Tasmania 7001, Australia
[2] Australian Antarctic Division

Abstract. The attainment of tertiary flow in ice involves the nonlinear response to the combination of applied stresses and the alteration of both the ice crystals and the polycrystalline aggregate. Tertiary flow rates for individual component strain rates from a series of ice deformation experiments under combined shear and compression stresses are presented, and the departure from the predictions of isotropic flow relations is quantified. A simple generalisation of the flow relations is suggested.

1 Introduction

The nature of the flow relations for ice undergoing tertiary creep, with the attendant complication of the development of anisotropic crystal fabrics and changes in crystal size etc. is of more than academic interest. The quantitative description of the flow under a range of combined stresses and a range of temperatures is of central importance to the study of the dynamics of glaciers and ice sheets. We present here a summary of a comprehensive series of combined stress experiments involving shear and confined compression (details will be presented elsewhere [1]) and indicate how the results motivate a simple generalisation of the canonical flow law for isotropic ice.

The pioneering work of Glen [2–5] and Steinemann [6] established the power law nature of the flow relation between an applied stress and the corresponding strain-rate largely from independent experiments on polycrystalline ice with random crystal fabrics, subjected to either unconfined compression or simple shear. It was recognised [6,7] that higher tertiary strain-rates and the development of anisotropic crystal fabrics occurred at high strains but the secondary flow rates for isotropic ice tended to be the basis for comparing the laboratory results with each other and with the flow of natural ice masses. In applying laboratory ice flow data to analysis of the shear rates observed in glaciers Nye [8] proposed that the rates might be related using the second invariants of the strain rate tensor $\dot{\varepsilon}_{ij}$ and the deviatoric stress tensor S_{ij}, and this was further analysed by Glen [9]. The resulting flow relation, which can be regarded as an expression of the isotropic nature of the polycrystalline ice takes the form

$$\dot{\varepsilon}_{ij} = BS_{ij}, \tag{1}$$

where, for a given temperature and ice type, B is a function only of the second invariant of the deviatoric stress tensor $I_2 = \sum_{ij} S_{ij}S_{ij}$ or the octahedral shear stress $\tau_o = \left(\frac{1}{3}I_2\right)^{1/2}$. The power law behaviour observed in the compression and shear experiments then becomes compatible with $B = k_o\tau_o^{n-1}$. Various researchers (e.g. [9–14]) have demonstrated that minimum strain rates from independent shear tests and unconfined compression tests on isotropic laboratory ice show convergence to a common relation between octahedral stress and strain rates with an exponent $n = 3$.

Some researchers (e.g. [6,11]) have suggested exponent values as high as 4 for isotropic ice at stresses greater than about 0.5 MPa. These higher stress values however are of little relevance to our primary interest – the flow of natural ice sheets and glaciers. Furthermore, at the resultant strain rates ($> 10^{-7}s^{-1}$ in the temperature range $> -10^o\,C$) micro-crack propagation is likely to have occurred [15] resulting in higher strain rates.

At stresses < 0.2 MPa flow law exponents $n < 3$ have been reported (e.g. [6,10,11]). While there is still some discussion concerning flow rates at the lower temperatures and stresses there is little doubt that the earlier tests failed to attain minimum isotropic strain rate. These laboratory tests were not carried out for the time required (many years) to reach minimum strain rate.

In grounded ice sheets the most important mode of ice deformation is an approximately horizontal shear which increases towards the bed. In areas of ice accumulation this is accompanied by vertical compression and there are generally both longitudinal and transverse extensive or compressive strain rates. The relative magnitudes of these latter strain rates depend mainly on the convergence or divergence of the flow. The applied stresses are usually considered to involve a transition from a zone dominated by vertical compression with negligible horizontal shear stress in the upper portion of the ice column to a predominant shear stress in the central and lower regions.

In the laboratory the appropriate experiments are accordingly those which combine a compressive stress (τ_{zz}) and a shear stress (τ_{xz}). The range of motions which might be encountered in natural ice masses longitudinal and transverse to such an orientation of coordinates should be accommodated to a great extent by considering extreme cases such as unconfined compression ($\dot{\varepsilon}_{xx} = \dot{\varepsilon}_{yy} = -1/2\,\dot{\varepsilon}_{zz}$), or compression confined in the longitudinal ($\dot{\varepsilon}_{xx} = 0$, $\dot{\varepsilon}_{yy} = -\dot{\varepsilon}_{zz}$) or transverse ($\dot{\varepsilon}_{xx} = -\dot{\varepsilon}_{zz}$, $\dot{\varepsilon}_{yy} = 0$) directions. We present here analyses based on experiments where, as discussed below, the ice flow is under longitudinally confined compression as a consequence of ice sample geometry – the case of transverse confinement would be more difficult to set up with the present apparatus.

Laboratory and field experiments [14,16–23] show different enhancement factors, determined from the ratios of tertiary anisotropic strain rates relative to minimum isotropic strain rates, for a variety of stress configurations. This indicates that in tertiary flow the simple unification of individual component flow relations in the Glen–Nye type of flow law does not apply. Thus the flow rates for the different components of the strain rate tensor must be expected to depend on the stress configuration, the movement picture and the rotations. These conditions also determine the steady state crystal orientation fabrics which also evolve with the transition to tertiary flow. Our only present concern is with the establishment of a steady-state tertiary flow regime, and what can accordingly be referred to as a "compatible" anisotropic crystal fabric. The present set of combined stress experiments provides an experimental basis for theorising about the form of flow law that should apply in tertiary flow under combined stresses.

2 Experiments and Laboratory Apparatus

The apparatus and laboratory techniques used for these experiments have been discussed previously [22]. The most appropriate sample shapes for tests involving shear alone are long rectangular prisms with the elongation in the direction of shear, and this shape has also proved suitable for combined stress experiments with confined compression tests, where the aspect ratio of the sample leads to negligible extension along the shear direction ($\dot{\varepsilon}_{xx} \simeq 0$). A large number of tests have now been carried out with samples of this type, reaching tertiary flow rates in combined experiments. These results, together with simple shear alone and confined compression alone have been accumulated over many years, because of the long time required to reach the large strains necessary for steady-state tertiary flow to be well established. The results discussed here, from twenty-five experiments, cover a range of deviatoric compression stresses and shear stresses between zero and 1 MPa, in various combinations. They were all carried out at $-2^{o}\,C$ and have been continued out to steady tertiary flow, generally in excess of 20 % strain. Separate experiments have been done to examine the effects of sample geometry and distortion on the results. The main point of concern has been that horizontal shear tests on rectangular prisms lead to some vertical contraction of the sample even in the absence of an applied compressive stress. This has been reduced by using longer samples and also by starting with a parallelogram cross section shape which passes through the rectangular shape before deforming further under continuing shear. This technique, referred to as starting with "back-cut" samples, starts with a slight vertical extensive strain, and is intended to reach a rectangular profile in tertiary flow. Only a few "back-cut" samples have been included in the data used in the present paper so that the measured vertical strain rates for low compressive loads should perhaps be

treated with some caution. At the conclusion of the tests the ice crystal sizes and orientation fabrics were measured and will be discussed elsewhere.

3 Enhanced Tertiary Flow

Li and Jacka [24] showed that the cubic power flow law relating octahedral shear strain rate at minimum creep and τ_o holds for a range of combined shear and compression experiments. It is clear from experiments involving shear or compression that the tertiary flow rates of deforming ice are "enhanced" compared to the minimum creep rates for isotropic ice, and that the extent of enhancement is greater for shear than for compression (e.g. [6,7,14]). This can be denoted by introducing an enhancement factor E, into the flow relation

$$\dot{\varepsilon}_o = E k_o \tau_o^3 \tag{2}$$

where the temperature dependent constant k_o describes minimum flow rates and E the appropriate enhancement factor E_s or E_c according to the nature of the applied stress. In single stress experiments this really describes the enhancement of a flow relation component of the form

$$\dot{\varepsilon}_{xz} = \tfrac{2}{3} E_s k_o S_{xz}^3, \qquad \text{or} \qquad \dot{\varepsilon}_{zz} = \tfrac{2}{3} E_c k_o S_{zz}^3 \tag{3}$$

Laboratory results have consistently indicated that tertiary anisotropic flow rates are enhanced over the minimum isotropic rates by an amount which appears independent of the magnitude of the applied stress, although it depends on the nature of that stress (e.g. compression or shear). The enhanced flow accordingly involves a change in the rate factor and not a change in the power law exponent, compared to the values found at minimum creep. Steinemann [6] found an enhancement, E_c of 3 to 4 for compression over a range of stresses. Thirty years later, Jacka and Maccagnan [18] found $E_c = 3$ for a different stress and temperature range. Steinemann [7], Russell-Head and Budd [17], Budd and Jacka [14] and others all report values of E_s near 10 for shear over a large range of temperature and stress.

While these enhancement studies mainly involve separate shear and compression experiments, some combined stress experiments reported by Li et al [22] have already indicated that E varies smoothly as the proportions of shear and compression contributing to τ_o change.

In tertiary creep the ice crystal orientation fabrics show marked anisotropy – varying from small circle girdle fabrics under compression to single maximum fabrics under shear stress. This departure from isotropy clearly removes one of the theoretical underpinnings of the Glen–Nye flow law, and it is not immediately clear what component flow relations are bound together in (2). More general flow law descriptions have been proposed as generalisations of the Glen–Nye form, introducing a preferred direction $\hat{n}$ and allowing the coefficient function B in (1) to depend on the various second-order invariant

tensors that can be constructed from S_{ij} and n_k, in what is sometimes referred to as the transverse isotropic case [25,26]. The geometry of the present experiments is even less symmetric than that, so we restrict ourselves to exhibiting the deviation of the results of combined stress experiments from the simple Glen–Nye form, and presenting a simple generalisation which gives a reasonable description of the observations. There are also various microscopic approaches to describing the component flow relations based on summing single crystal responses to applied stresses [16,20,26–29], either directly using crystal vectors, or in some parameterised form using an orientation distribution function. Crystal fabrics from the present set of combined stress experiments, together with the individual measured component strain rates could provide useful testing grounds for such theories, but we content ourselves with presenting the results in a way that suggests a simple generalisation of the Glen–Nye flow relations.

4 Interdependence of Shear and Normal Compression

The experimental results allow us to examine how the shear strain rate at constant shear stress is influenced by increasing normal stress, and conversely, how the compression strain rate at constant compressive stress is affected by increasing the shear strain. Given that the separate stress experiments support the cubic form of the flow relation, it appears appropriate to study the variations in the quantities $\dot{\varepsilon}_{xz}/S_{xz}^3$ and $\dot{\varepsilon}_{zz}/S_{zz}^3$ for increasing compressive stress and shear stress respectively. Li et al [22] considered the variation in the aggregated octahedral ratio $\dot{\varepsilon}_o/S_o^3$ as a function of the compression fraction (λ_c) and shear fraction (λ_s)

$$\lambda_c = \frac{S_{zz}}{\sqrt{S_{zz}^2 + S_{xz}^2}}, \tag{4a}$$

$$\lambda_s = \frac{S_{xz}}{\sqrt{S_{zz}^2 + S_{xz}^2}}, \tag{4b}$$

but we find that for examining the individual component responses a more symmetrical representation of the relative proportions of shear and compression can be made using the variables r_c and r_s, where

$$r_c = \frac{2}{\pi}\arctan(S_{zz}/S_{xz}), \tag{5a}$$

$$r_s = \frac{2}{\pi}\arctan(S_{xz}/S_{zz}), \tag{5b}$$

where clearly $r_c + r_s = 1$. For the present pattern of stresses (with non-zero deviators S_{xz} and $S_{zz} = -S_{yy}$) $\pi/2\, r_s$ is the angle between the principal compressive stress direction and the vertical (compression) direction.

The λ or r variables include the effects of rotation. They can distinguish, for example, between simple shear and pure confined compression even

though these may have the same principal stress deviators. The special feature of simple shear is that there is a principal shear plane which does not rotate. This results in the development of the strong single maximum crystal orientation fabric and the high tertiary flow rates (with mean enhancements $\sim$ 10–12) unique to simple shear.

In Fig. 1 the quantities $K_s = \dot{\varepsilon}_{xz}/S_{xz}^3$ and $K_c = \dot{\varepsilon}_{zz}/S_{zz}^3$, normalised by their values when the second stress is absent, are plotted using a log scale, against increasing relative compression S_{zz}/S_{xz} or increasing relative shear S_{xz}/S_{zz} as appropriate, using r_c, and r_s respectively. K_s and K_c may be thought of as flow relation coefficients or proportionalities.

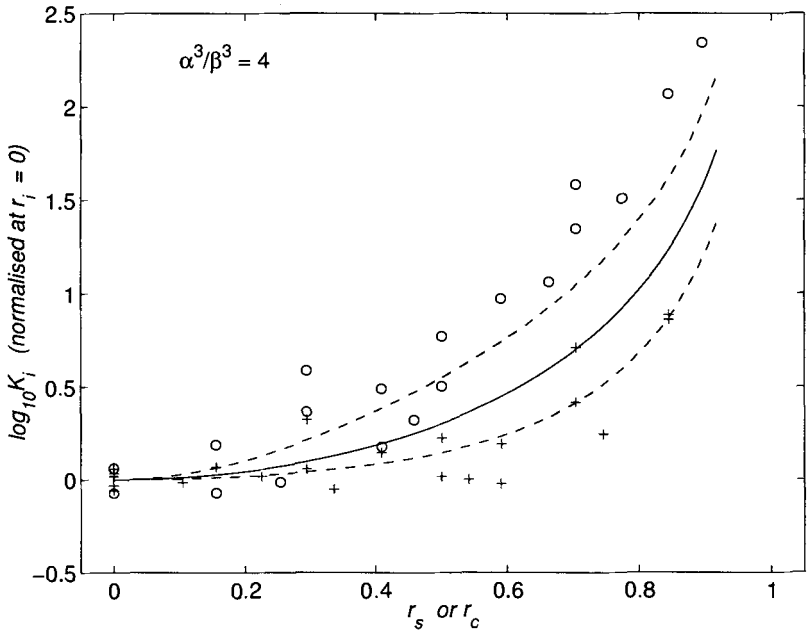

Fig. 1. The influence of increasing compression on the shear rate and increasing shear on the compression rate for steady state tertiary flow. The normalised proportionalities of the component strain rates to the cube of the component stresses, $K_s = \dot{\varepsilon}_{xz}/S_{xz}^3$ for shear (*crosses*) and $K_c = \dot{\varepsilon}_{zz}/S_{zz}^3$ for compression (*open circles*), are plotted on a log scale against increasing relative proportion of the other component stress, parameterised by r_c and r_s respectively. The prediction of the Glen–Nye flow law (*solid curve*) and the suggestions (12a, 12b) of the present study (*dashed curves*) are also shown

The prediction of the Glen–Nye flow relations is that for a given shear stress S_{xz} the addition of a compression with a deviator S_{zz} increases the

strain rate above the value for shear alone as

$$\tfrac{3}{2}k_o^{-1}\left(\dot{\varepsilon}_{xz}/S_{xz}^3\right) = 1 + S_{zz}^2/S_{xz}^2 = 1/\lambda_s^2 = 1 + \tan^2(\tfrac{\pi}{2}r_c), \tag{6}$$

while the addition of a shear stress S_{xz} would increase the compression rate by

$$\tfrac{3}{2}k_o^{-1}\left(\dot{\varepsilon}_{zz}/S_{zz}^3\right) = 1 + S_{xz}^2/S_{zz}^2 = 1/\lambda_c^2 = 1 + \tan^2(\tfrac{\pi}{2}r_s). \tag{7}$$

With our choice of variables these predictions both correspond to the solid curve in Fig. 1, which is observed to lie between the two quite separated sets of data points. The normalisations at $r = 0$ expose the deviations from cubic dependence due to the presence of the other stress components. A considerable degree of scatter can be expected from experimental data over such a broad range of stresses and strain rates, but in spite of this there is a clear indication that the strain rate values for compression (circles) on average lie well above the Glen–Nye flow law curve while the values for shear (crosses) lie well below it, particularly for higher values of the relevant angles, i.e. for strong influence of the second component stress. This means that the addition of shear stress increases the tertiary compression rate more than the isotropic law would suggest, while the addition of compression increases the tertiary shear rate less than suggested. Note that normalising the curves at $r = 0$ has suppressed the fact that the tertiary shear flow is enhanced by a factor of approximately four compared to the compressive response to the corresponding deviatoric stress. There is relatively little effect of the additional stress in either case until the two deviators are comparable (i.e. $r \sim 1/2$), but for larger values the discrepancy becomes more marked. It should be noted that the experimental values of the proportionalities K_s and K_c displayed in Fig. 1 become less reliable as r approaches unity. This is because the corresponding component strain rates are generally rather small, since large values of r_s or r_c typically indicate a dominance due to one stress being small, rather than the other being very large.

Before considering a simple generalisation of the flow relations which might parameterise these deviations, we briefly consider the dependence of the tertiary octahedral shear stress on the proportion of shear to compression. The variation in tertiary octahedral strain rates over the full range of the data is seen in Fig. 2 where the proportionality K_o defined by $K_o = \dot{\varepsilon}_o^{ter}/S_o^3$, normalised at zero shear stress, is plotted against increasing relative shear using r_s.

In spite of the scatter there is a clear trend to increasing values with increasing proportions of shear, smoothly approaching the ratio of the enhancement factors for shear and compression alone, E_s/E_c, as r_s approaches 1.

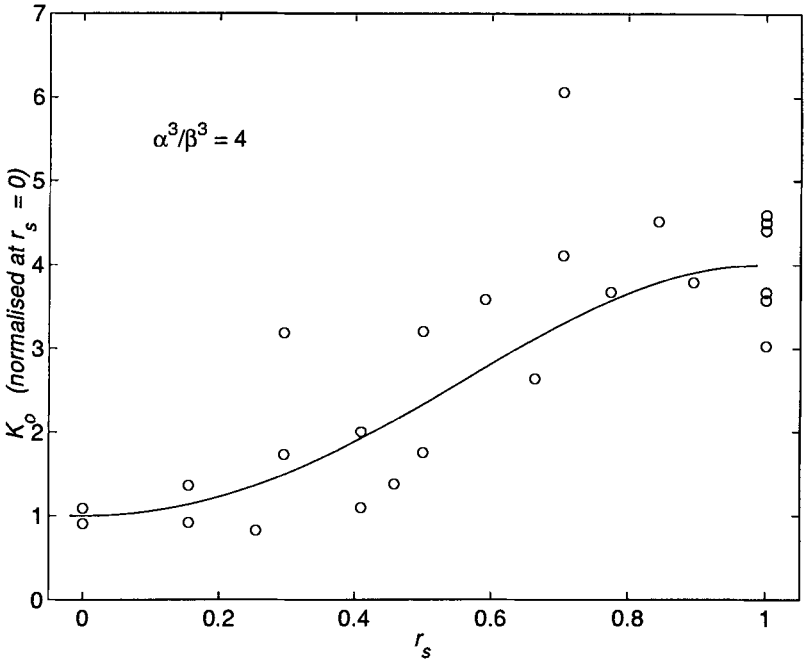

Fig. 2. The proportionality between octahedral shear strain rate and the cube of octahedral shear stress ($K_o = \dot{\varepsilon}_o/\tau_o^3$) is plotted (*open circles*) against increasing relative shear, parameterised by r_s. The suggestion (12c) of the present study (*solid curve*) is also shown

5 A Simple Generalised Flow Relation for Combined Stresses

As discussed earlier, the results for enhancement of flow for shear or compression stresses acting alone can be written in a form (3) which makes it explicit that these enhancements really only inform us about the single stress experiments.

One could of course choose to retain the dependence on τ_o by making the component enhancement factors functions which depend on the relative proportions of shear and compressive stresses. One particularly simple possibility would be if the flow relations (3) applied, with constant E_s and E_c values set by the independent shear and compression experiments, for all the combined experiments as well:

$$\dot{\varepsilon}_{xz} = E_s k_o \tau_o^2 S_{xz}, \tag{8a}$$

$$\dot{\varepsilon}_{zz} = E_c k_o \tau_o^2 S_{zz}. \tag{8b}$$

This would give a smoothly interpolating curve for the octahedral strain rate in Fig. 2

$$\dot{\varepsilon}_o^{ter}/S_o^3 \sim \left(\cos^2(\frac{\pi}{2}r_s) + \frac{E_s^2}{E_c^2}\sin^2(\frac{\pi}{2}r_s)\right)^{1/2}, \tag{9}$$

but it would not explain the different dependencies on stress proportions displayed in Fig. 1.

Since for $E_s \neq E_c$ one no longer expects a simple connection between $\dot{\varepsilon}_o$ and τ_o this leads us to consider that there may no longer be any dynamical significance in the octahedral shear stress in an anisotropic situation. This suggests that it may be more useful to consider a weighted expression of the form

$$\dot{\varepsilon}_{xz} = \tfrac{2}{3}k_o\alpha(\alpha^2 S_{xz}^2 + \beta^2 S_{zz}^2)S_{xz}, \tag{10a}$$

$$\dot{\varepsilon}_{zz} = \tfrac{2}{3}k_o\beta(\alpha^2 S_{xz}^2 + \beta^2 S_{zz}^2)S_{zz}, \tag{10b}$$

where $\alpha = E_s^{1/3}$ and $\beta = E_c^{1/3}$ are taken as constants. One could consider $T_o^2 = \frac{2}{3}(\alpha^2 S_{xz}^2 + \beta^2 S_{zz}^2)$ as defining an anisotropic mean shear stress in the sense that

$$\dot{\varepsilon}_o = k_o T_o^3 \tag{11}$$

replaces the usual Glen relation which holds for minimum creep rates and isotropic ice.

This formalism, for $E_s/E_c = 4$, provides the dashed curves in Fig. 1 and the curve in Fig. 2, corresponding to

$$\frac{\dot{\varepsilon}_{xz}}{S_{xz}^3} \sim 1 + \frac{\beta^2}{\alpha^2}\tan^2(\frac{\pi}{2}r_c), \tag{12a}$$

$$\frac{\dot{\varepsilon}_{zz}}{S_{zz}^3} \sim 1 + \frac{\alpha^2}{\beta^2}\tan^2(\frac{\pi}{2}r_s), \tag{12b}$$

$$\frac{\dot{\varepsilon}_o}{\tau_o^3} \sim \left(\cos^2(\frac{\pi}{2}r_s) + \frac{\alpha^2}{\beta^2}\sin^2(\frac{\pi}{2}r_s)\right)^{3/2}. \tag{12c}$$

These simple relations, constrained by the ratio of the enhancement factors, E_s and E_c, observed for the limiting tests ($r_s = 0$ and $r_c = 0$) in the present set of experiments, provide predictions for the proportionalities displayed in Figs. 1 and 2 that are a substantial improvement over the simple Glen–Nye type flow relations.

6 Conclusions

The flow properties displayed in Figs. 1 and 2, and represented by the suggested flow relations (10) contain both the direct influence of combined stresses

expected from a non-linear flow law, and the enhancements that are partially related to the development in tertiary flow of "compatible" ice crystal orientation fabrics (the "induced anisotropy").

The Glen–Nye flow law predicts an increase in component strain rates, for increases in the other component stress, through the corresponding increase in the octahedral shear stress. From the experiments, the increase in tertiary compression rates from increasing shear stress is greater than the Glen–Nye law prediction, whereas the influence on tertiary shear rates of increasing compressive stress is less.

A simple generalisation of the flow law for this particular geometry is suggested, which provides a description of the component flow relations that may be useful for ice sheet modelling. In this formulation the tertiary strain rates in combined shear and compression can be expressed in terms of the enhancement factors in shear alone and compression alone, through the parameters α and β, and the octahedral shear strain rate at minimum creep. This suggests that for ice sheet models which only consider $\dot{\varepsilon}_{xz}$ to calculate the vertical profile of horizontal velocity through the ice sheet (the shallow ice approximation [30,31]) it may only be necessary to make efforts to include the effects of other stresses, compared to simply using S^3_{xz}, when they are large relative to S_{xz}.

The present experimental geometry would have direct applicability to steadily divergent flow in ice caps such as Law Dome, East Antarctica, where for the flow line from the summit to Cape Folger the vertical compression appears to be mainly accompanied by transverse rather than longitudinal extension [32].

A question still remains whether the relatively weak dependence of tertiary shear strain rates on compressive stress seen here applies for other combinations of vertical compression with horizontal extension, such as the unconfined compression case. Since the tertiary "induced" or "compatible" crystal orientation fabrics will differ from the present cases, when unconfined compressive stresses are applied, there may well be changes in the magnitude of shear strain rates, even if the direct influence of the additional compressive and extensive stresses is once again small.

The fabrics produced by the confinement of compression in the shear direction appear more favourable for the shear flow than those produced by unconfined compression or transverse confinement. This means for these other cases the effect of compression in addition to the shear may be expected to increase the shear rate even less than in the longitudinally confined case addressed here.

While the present results provide some insights into the combined stress situation with induced anisotropy, it will clearly be necessary to experimentally explore other combinations of shear and compressive stresses relevant to the stresses found in ice sheets, such as the unconfined and transversely

confined geometries previously discussed. A representative range of these can be studied by experiments with different ice sample geometries.

In this paper we have presented just one facet of the results from a substantial series of ice flow experiments. For example it would also be possible to extract from the present data the dependence of enhancement functions for the component flow relations (generalising E_s and E_c) on the relative stress parameters r_s or r_c, to suit the forms of (3) or (8). There is clearly much scope for analysing the relationships between stresses, crystal properties, orientation fabrics and strain rates, and for examining the transition to the tertiary flow regime.

References

1. Budd W. F., Jacka, T. H., Li Jun, and Warner, R. C. Ice flow relations for individual components in combined shear and compression. in preparation
2. Glen J. W. (1952) Experiments on the deformation of ice. *Journal of Glaciology* **2**, (12), 111–114
3. Glen J. W. (1953) *Mechanical properties of ice and their relation to glacier flow.* Dissertation. Cambridge, 1953
4. Glen J. W. (1953) Rate of flow of polycrystalline ice. *Nature* **172**, (4381), 721–722
5. Glen J. W. (1955) The creep of polycrystalline ice, *Proceedings of the Royal Society, Series A* **228**, (1175), 519–538
6. Steinemann S. (1954) Flow and recrystallisation of ice. *IUGG General Assembly of Rome. IAHS Publication* **39**, 449–462
7. Steinemann S. (1958) Resultats experimentaux sur la dynamique de la glace et leurs correlations avec le mouvement et la petrographie des glaciers. *IUGG/IAHS Symposium of Chamonix. IAHS Publication* **47**, 184–198
8. Nye J. F. (1953) The flow of ice from measurements in glacier tunnels, laboratory experiments and the Jungfraufirn bore hole experiment. *Proceedings of the Royal Society, Series A.* **219**, (1139), 477–489
9. Glen J. W. (1958) The flow law of ice. *IUGG/IAHS Symposium of Chamonix. IAHS Publication* **47**, 171–183
10. Mellor M., and Testa, R. (1969) Effect of temperature on the creep of ice. *Journal of Glaciology* **8**, (52), 131–145
11. Barnes P., Tabor, D. and Walker, J. C. F. (1971) The friction and creep of polycrystalline ice. *Proceedings of the Royal Society, Series A* **324**, 127–155
12. Duval P. (1976) Lois de fluage transitoire ou permanent de la glace polycrystalline pours divers etats de contrainte. *Ann. Geophysique* **32**, 4, 335–360
13. Paterson W. S. B., and Budd, W. F., (1982) Flow Parameters for ice sheet modelling. *Cold Regions Science and Technology* **6**, 175–177
14. Budd W. F. and Jacka, T. H. (1989) A review of ice rheology for ice sheet modelling. *Cold Regions Science and Technology* **16**, (2), 107–144
15. Cole D. M. (1987) Strain-rate and grain-size effects in ice. *Journal of Glaciology* **33**, (115), 274–280
16. Lile R. C. (1978) The effect of anisotropy on the creep of polycrystalline ice. *Journal of Glaciology* **21**, (85), 475–483

17. Russell-Head D. S. and Budd, W. F (1979) Ice sheet flow properties derived from bore-hole shear measurements combined with ice-core studies. *Journal of Glaciology* **24**, (90), 117–130
18. Jacka T. H., and Maccagnan, M. (1984) Ice crystallographic and strain rate changes with strain in compression and extension. *Cold Regions Science and Technology* **8**, 269–286
19. Azuma N., and Higashi, A. (1984) Mechanical properties of Dye 3 Greenland deep ice cores. *Annals of Glaciology* **4**, 1–8
20. Lile R. C. (1984) The flow law for isotropic and anisotropic ice at low strain rates. *ANARE Reports, Publication No. 132, Australian Antarctic Division*, 93p
21. Dahl-Jensen D. and Gundestrup, N. S. (1987) Constitutive properties of ice at Dye 3, Greenland. *Proceedings of the Vancouver Symposium. IAHS Publication No.* **170**, 31–43.
22. Li Jun, Jacka, T. H. and Budd, W. F. (1996) Deformation rates in combined compression and shear for ice which is initially isotropic and after the development of strong anisotropy. *Annals of Glaciology* **23**, 247–252.
23. Li Jun and Jacka, T. H. (1998) Horizontal shear rate of ice initially exhibiting vertical compression fabrics. *Journal of Glaciology*, **44**, (148), 670–672
24. Li Jun and Jacka, T. H. (1996) Isotropic ice flow rates derived from deformation tests in simultaneous shear and compression. *IAHR Proceedings of the 13th International Symposium on Ice. Beijing, 27-31 August 1996.* **3**, 937–947.
25. Johnson A. F. (1977) Creep characterisation of transversely-isotropic metallic crystals. *Jour. Mech. Phys. Solids* **25**, 117–126.
26. Liboutry L. A. (1987) *Very Slow Flows of Solids*, Martinus Nijhoff Publishers, Dordrecht
27. Liboutry L. A. and Duval P., (1985) Various isotropic and anisotropic ices found in glaciers and polar ice caps and their corresponding rheologies. *Annales Geophysicae* **3**, 207–224.
28. Azuma N. and Goto-Azuma, K. (1996) An anisotropic flow law for ice-sheet ice and its implications. *Annals of Glaciology* **23**, 202–208.
29. Svendsen B. and Hutter, K. (1996) A continuum approach for modelling induced anisotropy in glaciers and ice sheets. *Annals of Glaciology* **23**, 262–269.
30. Hutter K. (1983) *Theoretical Glaciology: material science of ice and the mechanics of glaciers and ice sheets.* Reidel Publishing Co., Dordrecht.
31. Morland L. W. (1984) Thermomechanical balances of ice sheet flows. *Geophys. Astrophys. Fluid Dyn.*, **29**, 237–266
32. Pfitzner M. L. (1980) The Wilkes Ice Cap Project, 1966. *ANARE Scientific Reports, Series A (4) Glaciology, Publication No.* **127**, 133p

(Received 8 June 1999, accepted 12 June 1999)

An Iterative Solution Procedure for Shallow Stokes Flows. The Shallow Ice Approximation Revisited

Dambaru Raj Baral and Kolumban Hutter

Institute of Mechanics, Darmstadt University of Technology, Hochschulstr. 1, 64289 Darmstadt, Germany

Abstract. The shallow ice approximation (SIA) is a popular scheme in glaciology by which non-linear Stokes flow in shallow geometries is approximately solved. The pseudoplastic thermomechanically coupled material behaviour is decoupled from the heat equation determining the temperature field. The remaining force balance and constitutive relations for the stress deviator are iteratively solved for given geometry and temperature field using the SIA as a starting solution and iteratively correcting it for the terms ignored in the SIA. The method is *exact*, i. e., the iteration scheme, if convergent, generates the exact Stokes flow solution to the given geometry and temperature field. Singularities close to the ice divide and the free surface are avoided.

1 Introduction

Virtually all numerical codes that determine the three-dimensional velocity (and temperature) distribution(s) in large ice sheets use the shallow ice approximation (SIA) [10,11,13–15,19,20]. This approximation is the asymptotic limit of the Stokes flow equations if these equations are properly scaled and reduced to the lowest order limit in the *aspect ratio parameter*

$$\epsilon := \frac{\text{typical depth}}{\text{typical longitudinal extent}}.$$

A regular perturbation expansion of the velocity and stress fields in ϵ is known not to be uniformly valid; when an infinite viscosity law at zero strain rate (e. g. Glen's flow law) is used, then domes exhibit infinite mean curvature of the free surface at the zeroth order (see e. g., [3,21]). Furthermore, under the same conditions first order stress corrections become singular at the free surface if the SIA is tried to be improved [14,16]. Both deficiencies can be remedied by introducing an finite viscosity law as suggested by many theoretical and experimental glaciologists [4,8,13–15,17,20], but this regularization does not, in general, produce solutions which are sufficiently close to the exact solution. Inclusion of $\mathcal{O}(\epsilon^2)$-solutions are needed to achieve sufficiently accurate results [3,18]. This makes the formal perturbation expansion fairly complicated and rather questionable as a means to improve the SIA-solution.

The amendation of the SIA has been tried during the last twenty years by a number of authors [2,5–7,9,13,14,21], but many proposed schemes are incomplete by omitting certain terms [2,5,9] claimed to be small; however, the procedures arriving at the respective inferences are often at variance among different authors, or certain schemes are simply ad hoc, not generalizable to three dimensional flows or not extendable to higher order accuracy [6,7]. A systematic iterative procedure, that is particularly apt to numerical integration, does nevertheless exist; it starts essentially with the SIA and improves on it by successive iterations, making effective use in this integration procedure of the advantatages of the SIA strategy.

Thermomechanical coupling can be handled, i. e., the geometry, velocity, stress and temperature fields be determined. The advantage of the solution technique is, that for given geometry and temperature field, the velocity and stress fields can be computed on the basis of differentiations and quadratures alone. Only the evolution of the temperature and free surface geometry requires solutions of parabolic differential equations.

The suggested integration procedure is not as systematical as the perturbation scheme usually proposed [1,21], but if convergent this iteration method allows construction of the exact solution (which is formally never the case with the perturbation scheme). Furthermore, formulas are much simpler when this iteration scheme is used.

2 The Mechanical Problem

In what follows we shall restrict ourselves to the purely mechanical problem, i.e., we suppose the geometry of the ice sheet and the temperature distribution to be given (e. g., from an earlier time step of the complete problem). This is done so here as a matter of convenience because of space limitations. The difficulty of the SIA lies with the determination of the stress and velocity fields rather than that of the temperature and free surface evolution.

The basis of the ensuing analysis is the set of scaled field equations and boundary conditions of stress and velocity. In the non-dimensional variables introduced by Greve [12] and Baral [1], the momentum equations of the Stokes flow take the forms

$$-\frac{\partial p}{\partial x}+\frac{\partial t^D_{xz}}{\partial z}=\epsilon^2 T_x, \quad -\frac{\partial p}{\partial y}+\frac{\partial t^D_{yz}}{\partial z}=\epsilon^2 T_y, \quad \frac{\partial p}{\partial z}+1=\epsilon^2 P_z, \tag{1}$$

in which

$$\begin{aligned} \epsilon^2 T_x &:= -\epsilon^2\left(\frac{\partial t^D_{xx}}{\partial x}+\frac{\partial t^D_{xy}}{\partial y}\right), \qquad \epsilon^2 T_y := -\epsilon^2\left(\frac{\partial t^D_{xy}}{\partial x}+\frac{\partial t^D_{yy}}{\partial y}\right), \\ \epsilon^2 P_z &:= \epsilon^2\left(\frac{\partial t^D_{xz}}{\partial x}+\frac{\partial t^D_{yz}}{\partial y}+\frac{\partial t^D_{zz}}{\partial z}\right). \end{aligned} \tag{2}$$

In these equations, p, t^D_{ij} are the pressure and the deviatoric stress components and (x, y, z) are the horizontal and vertical directions of a Cartesian coordinate system; moreover, T_x, T_y and P_z are abbreviations defined in (2) and ϵ is the aspect ratio parameter; all quantitites are dimensionless. Equations (1) and (2) hold in the ice region between $z = b(x, y, t)$ and $z = h(x, y, t)$, where the functions b and $h \geq b$ describe the base and free surface, respectively.

Note that when $\epsilon \to 0$, (1) reduce to the zeroth order force balance equations in the SIA. If we now regard the quantities (2) as prescribed, then (1) can be solved, i. e., integrated in the z-direction as in the SIA. The boundary conditions needed for this integration can be written as follows

$$p = \epsilon^2 P_h, \quad t^D_{xz} = \epsilon^2 T_{xh}, \quad t^D_{yz} = \epsilon^2 T_{yh}, \qquad \text{at} \quad z = h(x, y, t), \tag{3}$$

with

$$\begin{aligned} \epsilon^2 P_h &:= \epsilon^2 (-t^D_{xz} \frac{\partial h}{\partial x} - t^D_{yz} \frac{\partial h}{\partial y} + t^D_{zz}), \\ \epsilon^2 T_{xh} &:= (-p + \epsilon^2 t^D_{xx}) \frac{\partial h}{\partial x} + \epsilon^2 t^D_{xy} \frac{\partial h}{\partial y}, \qquad \text{at} \quad z = h(x, y, t). \\ \epsilon^2 T_{yh} &:= \epsilon^2 t^D_{xy} \frac{\partial h}{\partial x} + (-p + \epsilon^2 t^D_{yy}) \frac{\partial h}{\partial y}. \end{aligned} \tag{4}$$

Integrating $(1)_3$ between $\bar{z} = z$ and $\bar{z} = h(.)$ subjected to the boundary condition $(3)_1$ yields

$$p(., z) = (h(.) - z) + p^{corr}(., z), \tag{5}$$

$$p^{corr}(., z) := \epsilon^2 \left(P_h(.) - \int_z^{h(.)} P_z(., \bar{z}) d\bar{z} \right), \tag{6}$$

in which the argument (.) stands for (x, y, t), where t is time. This notation will be maintained throughout the paper.

In the same way the remaining equations $(1)_{1,2}$ can be integrated. We illustrate the procedure for the determination of t^D_{xz} and shall then only list the result obtained for t^D_{yz}. The first step is to differentiate (5) with respect to x, which yields

$$\frac{\partial p}{\partial x} = \frac{\partial h}{\partial x} + \epsilon^2 \frac{\partial P_h}{\partial x} - \epsilon^2 \frac{\partial}{\partial x} \int_z^{h(.)} P_z(., \bar{z}) d\bar{z}. \tag{7}$$

Using this in $(1)_1$ yields

$$\frac{\partial t^D_{xz}}{\partial z} = \frac{\partial h}{\partial x} + \epsilon^2 \frac{\partial P_h}{\partial x} - \epsilon^2 \frac{\partial}{\partial x} \int_z^{h(.)} P_z(., \bar{z}) d\bar{z} + \epsilon^2 T_x, \tag{8}$$

or, after an integration with respect to z

$$t^D_{xz}(.,z) = \frac{\partial h(.)}{\partial x} z + \epsilon^2 \frac{\partial P_h(.)}{\partial x} z - \epsilon^2 \int_{b(.)}^{z} \frac{\partial}{\partial x} \int_{\bar{z}}^{h(.)} P_z(.,\bar{\bar{z}}) d\,\bar{\bar{z}}\, d\bar{z} + \epsilon^2 \int_{b(.)}^{z} T_x(.,\bar{z}) d\bar{z} + K_x(.)$$

of which the integration function $K_x(.)$ can be determined by invoking the boundary conditions $(3)_2, (4)_2$. The final result, complemented by that for $t^D_{yz}(.,z)$, is

$$t^D_{xz}(.,z) = -\frac{\partial h(.)}{\partial x}(h(.) - z) + t^{D\ corr}_{xz}(.,z), \tag{9}$$

$$t^D_{yz}(.,z) = -\frac{\partial h(.)}{\partial y}(h(.) - z) + t^{D\ corr}_{yz}(.,z), \tag{10}$$

where

$$t^{D\ corr}_{xz}(.,z) = -\epsilon^2 \frac{\partial P_h(.)}{\partial x}(h(.) - z) + \epsilon^2 T_{xh}(.) - \epsilon^2 \int_{z}^{h(.)} T_x(.,\bar{z}) d\bar{z} + \epsilon^2 \int_{z}^{h(.)} \frac{\partial}{\partial x} \int_{\bar{z}}^{h(.)} P_z(.,\bar{\bar{z}}) d\,\bar{\bar{z}}\, d\bar{z}, \tag{11}$$

$$t^{D\ corr}_{yz}(.,z) = -\epsilon^2 \frac{\partial P_h(.)}{\partial y}(h(.) - z) + \epsilon^2 T_{yh}(.) - \epsilon^2 \int_{z}^{h(.)} T_y(.,\bar{z}) d\bar{z} + \epsilon^2 \int_{z}^{h(.)} \frac{\partial}{\partial y} \int_{\bar{z}}^{h(.)} P_z(.,\bar{\bar{z}}) d\,\bar{\bar{z}}\, d\bar{z} \tag{12}$$

are obviously the "longitudinal stress effects", correcting the SIA. The quotation marks are used because according to (2) and (4) the longitudinal stresses contribute to these corrections, but these are not the only amendations to these terms.

Next, we wish to determine the velocity field such that it is corrected for the longitudinal stress effects. To this end, we write the constitutive relations for the horizontal shears and the continuity equation as follows

$$\frac{\partial v_x}{\partial z} = 2\mathcal{K} t^D_{xz} A(\theta') f(\sigma) - \epsilon^2 \frac{\partial v_z}{\partial x}, \qquad \frac{\partial v_y}{\partial z} = 2\mathcal{K} t^D_{yz} A(\theta') f(\sigma) - \epsilon^2 \frac{\partial v_z}{\partial y},$$

$$\frac{\partial v_z}{\partial z} = -\left(\frac{\partial v_x}{\partial x} + \frac{\partial v_y}{\partial y}\right), \tag{13}$$

where the dimensionless temperature relative to the pressure melting point, θ', is assumed to be a known function of position and time, and σ is the effective stress defined by

$$\sigma^2 = (t^D_{xz})^2 + (t^D_{yz})^2 + \underbrace{\tfrac{1}{2}\epsilon^2 \left[(t^D_{xx})^2 + (t^D_{yy})^2 + (t^D_{zz})^2 + 2(t^D_{xy})^2\right]}_{\sigma^2{}_{corr}}. \tag{14}$$

Integrating (13) with respect to z yields

$$v_x(.,z) = 2\mathcal{K}\int_{b(.)}^{z} t_{xz}^D(.,\bar{z})A(\theta'(.,\bar{z}))f(\sigma(.,\bar{z}))d\bar{z} - \epsilon^2\int_{b(.)}^{z}\frac{\partial v_z(.,\bar{z})}{\partial x}d\bar{z} + v_{x,b}(.), \tag{15}$$

$$v_y(.,z) = 2\mathcal{K}\int_{b(.)}^{z} t_{yz}^D(.,\bar{z})A(\theta'(.,\bar{z}))f(\sigma(.,\bar{z}))d\bar{z} - \epsilon^2\int_{b(.)}^{z}\frac{\partial v_z(.,\bar{z})}{\partial y}d\bar{z} + v_{y,b}(.), \tag{16}$$

$$v_z(.,z) = -\int_{b(.)}^{z}\left(\frac{\partial v_x(.,\bar{z})}{\partial x} + \frac{\partial v_y(.,\bar{z})}{\partial y}\right)d\bar{z} + v_{z,b}(.), \tag{17}$$

in which $v_{x,b}, v_{y,b}$ and $v_{z,b}$ are the components of the sliding velocity at the base. For the no-slip condition, $v_{x,b} = v_x^+$, etc., where $\boldsymbol{v}^+$ is the velocity immediately below the base. The form of $\boldsymbol{v}^+$ depends upon the interaction model between the ice, the lithosphere and the asthenosphere. Here we request that

$$v_x^+ = v_y^+ = 0; \quad v_z^+ = \frac{\partial b(.)}{\partial t} = -\frac{1}{\mathcal{T}_r}\left(b - b_{st} + \frac{\rho}{\rho_a}H\right) \tag{18}$$

where $\mathcal{T}_r$ is the dimensionless isostatic, relaxation time, about 0.3 (corresponding to 3000 years), $b_{st}(x,y)$ is the stationary bedrock at no ice cover, $H(.) = h(.) - b(.)$ and $\rho_a \approx 3300$ kgm^{-3} is the density of the asthenosphere.

When basal sliding occurs, then $\boldsymbol{v}_{,b}(.)$ can be computed from the following relationships, see Baral [1]:

$$v_{x,b}(.) = v_x^+ + \frac{\mathcal{F}C}{N_b}\left(p\frac{\partial b}{\partial x} + t_{xz}^D + \frac{1}{N_b^2}p\frac{\partial b}{\partial x}\right) + (v_{sl})_x{}^{corr} - \Delta v_x{}^{corr}, \tag{19}$$

$$v_{y,b}(.) = v_y^+ + \frac{\mathcal{F}C}{N_b}\left(p\frac{\partial b}{\partial y} + t_{yz}^D + \frac{1}{N_b^2}p\frac{\partial b}{\partial y}\right) + (v_{sl})_y{}^{corr} - \Delta v_y{}^{corr}, \tag{20}$$

$$v_{z,b}(.) = \left(1 - \frac{1}{N_b^2}\right)^{-1}\left\{v_z^+ - \frac{1}{N_b^2}\left[\left(v_{x,b}(.) - v_x^+\right)\frac{\partial b}{\partial x} + \left(v_{y,b}(.) - v_y^+\right)\frac{\partial b}{\partial y} + v_z^+\right] + \mathcal{F}C\left(t_{xz}^D\frac{\partial b}{\partial x} + t_{yz}^D\frac{\partial b}{\partial y}\right) + (v_{sl})_z{}^{corr}\right\}, \tag{21}$$

where

$$N_b = \sqrt{1 + \epsilon^2\left(\frac{\partial b}{\partial x}\right)^2 + \epsilon^2\left(\frac{\partial b}{\partial y}\right)^2}, \tag{22}$$

$$(v_{sl})_x{}^{corr} := -\epsilon^2 \frac{\mathcal{FC}}{N_b}\left[t^D_{xx}\frac{\partial b}{\partial x} + t^D_{xy}\frac{\partial b}{\partial y} - \frac{1}{N_b^2}\left\{\left(-p+\epsilon^2 t^D_{xx}\right)\left(\frac{\partial b}{\partial x}\right)^3 + \left(-p+\epsilon^2 t^D_{yy}\right)\frac{\partial b}{\partial x}\left(\frac{\partial b}{\partial y}\right)^2 + t^D_{zz}\frac{\partial b}{\partial x} + 2\epsilon^2 t^D_{xy}\left(\frac{\partial b}{\partial x}\right)^2\frac{\partial b}{\partial y} - 2t^D_{xz}\left(\frac{\partial b}{\partial x}\right)^2 - 2t^D_{yz}\frac{\partial b}{\partial x}\frac{\partial b}{\partial y}\right\}\right], \tag{23}$$

$$(v_{sl})_y{}^{corr} := -\epsilon^2 \frac{\mathcal{FC}}{N_b}\left[t^D_{xy}\frac{\partial b}{\partial x} + t^D_{yy}\frac{\partial b}{\partial y} - \frac{1}{N_b^2}\left\{\left(-p+\epsilon^2 t^D_{xx}\right)\left(\frac{\partial b}{\partial x}\right)^2\frac{\partial b}{\partial y} + \left(-p+\epsilon^2 t^D_{yy}\right)\left(\frac{\partial b}{\partial y}\right)^3 + t^D_{zz}\frac{\partial b}{\partial y} + 2\epsilon^2 t^D_{xy}\frac{\partial b}{\partial x}\left(\frac{\partial b}{\partial y}\right)^2 - 2t^D_{xz}\frac{\partial b}{\partial x}\frac{\partial b}{\partial y} - 2t^D_{yz}\left(\frac{\partial b}{\partial y}\right)^2\right\}\right], \tag{24}$$

$$(v_{sl})_z{}^{corr} := -\epsilon^2 \mathcal{FC}\left[t^D_{xx}\left(\frac{\partial b}{\partial x}\right)^2 + t^D_{yy}\left(\frac{\partial b}{\partial y}\right)^2 + 2t^D_{xy}\frac{\partial b}{\partial x}\frac{\partial b}{\partial y} + \left(\left(\frac{\partial b}{\partial x}\right)^2 + \left(\frac{\partial b}{\partial y}\right)^2\right)\left\{p\left(\left(\frac{\partial b}{\partial x}\right)^2 + \left(\frac{\partial b}{\partial y}\right)^2\right) + \frac{5}{2}t^D_{xz}\frac{\partial b}{\partial x} + \frac{5}{2}t^D_{yz}\frac{\partial b}{\partial y} - t^D_{zz}\right\}\right], \tag{25}$$

$$\Delta v_x{}^{corr} := -\frac{\epsilon^2}{N_b^2}\left[\left(v_{x,b}(.) - v_x^+\right)\frac{\partial b}{\partial x} + \left(v_{y,b}(.) - v_y^+\right)\frac{\partial b}{\partial y} - \left(v_{z,b}(.) - v_z^+\right)\right]\frac{\partial b}{\partial x}, \tag{26}$$

$$\Delta v_y{}^{corr} := -\frac{\epsilon^2}{N_b^2}\left[\left(v_{x,b}(.) - v_x^+\right)\frac{\partial b}{\partial x} + \left(v_{y,b}(.) - v_y^+\right)\frac{\partial b}{\partial y} - \left(v_{z,b}(.) - v_z^+\right)\right]\frac{\partial b}{\partial y}, \tag{27}$$

in which $\mathcal{FC}$ is a frictional coefficient and all formulas hold for $z = b(.)$. The formulas (19)-(27) describe a *complete and exact* interaction model between the Stokes flow of the ice sheet and the deforming lithosphere.

It is understood that $v_{x,b}$ and $v_{y,b}$ as obtained from (19) and (20) are used in the evaluation of $v_{z,b}$ in (21). Notice that all variables $(.)^{corr}$ are of order ϵ^2; however, by omitting these terms, the remainig equations (19)-(21) do not correspond to the shallow ice approximation because some terms involving ϵ do arise. Nevertheless, when all these additional ϵ-terms are also omitted then the emerging equations are equivalent to the corresponding equations

in the shallow ice approximation. Furthermore, it is not possible to additively decompose the velocity components (15)-(17) into SIA contributions and corrections of these unless all functions containing the small parameter ϵ are expanded in Taylor series expansions of ϵ. Here we abstain from doing this, as an iterative solution procedure is suggested.

How this iteration is performed will be explained below. Here, we proceed for the moment and take the position that the velocity field according to (15)-(17) is known. Then we may use the remaining stress-strain-rate relationships to evaluate the longitudinal deviatoric stresses $t^D_{xx}, t^D_{yy}, t^D_{zz}$ and the shear stress t^D_{xy} as follows

$$\begin{aligned} t^D_{xx} &= \frac{1}{\mathcal{K}A(\theta')f(\sigma)}\frac{\partial v_x}{\partial x}, & t^D_{yy} &= \frac{1}{\mathcal{K}A(\theta')f(\sigma)}\frac{\partial v_y}{\partial y}, \\ t^D_{zz} &= -(t^D_{xx} + t^D_{yy}), & t^D_{xy} &= \frac{1}{2\mathcal{K}A(\theta')f(\sigma)}\left(\frac{\partial v_y}{\partial x} + \frac{\partial v_x}{\partial y}\right). \end{aligned} \tag{28}$$

In these expressions, because of the nonlinear function $f(\sigma)$, an additive decomposition of these deviatoric stresses in SIA contributions and corrections of these is not possible.

This completes the derivation of the mechanical equations. For given geometry of the moving ice mass, i.e., for given $b(.)$ and $h(.)$ as well as for given temperature or moisture fields all equations are exact ! Approximations are introduced by the iterative solution procedure suggested below.

3 The Iteration Scheme

The guideline is that the starting solution should be the zeroth order approximation of the SIA or possibly a solution even closer to the exact solution than this. Before explaining this in detail, notice that in the above formulas (28) singular behaviour may arise whenever $f(\sigma) = 0$ for $\sigma = 0$. This happens for all infinite-viscosity creep laws such as Glen's flow law $f(\sigma) = \sigma^{n-1}, n > 1$ and must be avoided. It occurs at the free surface and at ice divides when σ^2_{corr} is not accounted for. So to avoid computational singularities, non-vanishing σ^2_{corr} must be implemented at the very first computational step, or a finite viscosity law must be applied.

In what follows two iteration steps will be nested into each other in order to extend the SIA to incorporate the "longitudinal stress deviator effects" and non-shallowness contributions. The purpose of the inner iteration is to quickly move away from the singular behaviour of a possible infinite viscosity law by forcing σ^2 to be different from zero. The outer iteration then accounts for the "non-shallowness". A complete separation of the two effects is not strictly possible (and not intended); they both are associated with the ϵ-terms. We now describe how the iteration model operates.

Step 1: To initialize the iteration, we set all variables equal to zero, in particular

$$\begin{aligned} &v_x(.,z) = v_y(.,z) = v_z(.,z) = \frac{\partial v_z}{\partial x}(.,z) = \frac{\partial v_z}{\partial y}(.,z) = 0, \\ &p^{corr}(.,z) = t_{xz}^{D\ corr}(.,z) = t_{yz}^{D\ corr}(.,z) = 0, \\ &(v_{sl})_x{}^{corr}(.,b) = (v_{sl})_y{}^{corr}(.,b) = (v_{sl})_z{}^{corr}(.,b) = 0, \\ &\Delta v_x{}^{corr}(.,b) = \Delta v_y{}^{corr}(.,b) = 0, \end{aligned} \tag{29}$$

and we assume the functions

$$z = h(.), \qquad z = b(.), \qquad \theta' = \theta'(.,z) \tag{30}$$

to be prescribed. We also assign values to the following control variables

$$\underline{\text{small1}} := 10^{-4}, \quad \underline{\text{small2}} := 10^{-4}, \quad \underline{\text{con}} := 0, \tag{31}$$

and initialize σ^2_{corr} (to avoid possible singularities) as follows

$$\sigma^2_{corr} = \begin{cases} 0, \text{ if a finite viscosity law is used,} \\ \underline{\text{small1}}, \text{ for Glen's flow law.} \end{cases} \tag{32}$$

Step 2: Evaluation of the near SIA-stresses (which carry the label *old*)

$$\begin{aligned} &t_{xz}^{D\ old}(.,z) = -\frac{\partial h(.)}{\partial x}(h(.) - z), \quad t_{yz}^{D\ old}(.,z) = -\frac{\partial h(.)}{\partial y}(h(.) - z), \\ &p^{old}(.,z) = (h(.) - z). \end{aligned} \tag{33}$$

These stresses are not necessarily identical to the corresponding zeroth order stresses in the SIA, because $h(.)$ may be the unfiltered function of the free surface.

Step 3: Avoid singular behaviour and account for longitudinal stress deviator effects,

$$\begin{aligned} t_{xz}^D &= t_{xz}^{D\ old} + t_{xz}^{D\ corr}, \\ t_{yz}^D &= t_{yz}^{D\ old} + t_{yz}^{D\ corr}, \\ \sigma^2_{old} &= (t_{xz}^D)^2 + (t_{yz}^D)^2, \\ p &= p^{old} + p^{corr}. \end{aligned} \tag{34}$$

Next we compute the sliding velocity components according to (19)-(21).

Step 4: $\sigma^2 = \sigma^2_{old} + \sigma^2_{corr}$.
With known initial stresses (34) the velocity field as given in (15)-(17) can be

computed, but they will differently be denoted (by attaching the label new) as

$$\begin{aligned} v_x^{new}(.,z) &= 2\mathcal{K}\int_{b(.)}^{z} t_{xz}^D(.,\bar{z})A(\theta'(.,\bar{z}))f(\sigma(.,\bar{z}))d\bar{z} \\ &\quad - \epsilon^2\int_{b(.)}^{z}\frac{\partial v_z(.,\bar{z})}{\partial x}d\bar{z} + v_{x,b}(.), \\ v_y^{new}(.,z) &= 2\mathcal{K}\int_{b(.)}^{z} t_{yz}^D(.,\bar{z})A(\theta'(.,\bar{z}))f(\sigma(.,\bar{z}))d\bar{z} \\ &\quad - \epsilon^2\int_{b(.)}^{z}\frac{\partial v_z(.,\bar{z})}{\partial y}d\bar{z} + v_{y,b}(.), \\ v_z^{new}(.,z) &= -\int_{b(.)}^{z}\left(\frac{\partial v_x(.,\bar{z})}{\partial x} + \frac{\partial v_y(.,\bar{z})}{\partial y}\right)d\bar{z} + v_{z,b}(.). \end{aligned} \tag{35}$$

Notice that these contain ϵ^2-corrections both explicitly and implicitly (in the definition of σ).

Step 5: As the formulas (35) and the corresponding unprimed quantities are iteratives, a measure is needed to interpret this iteration. So, let

$$d^2 := \int_{Domain}\left[(v_x^{new}-v_x)^2 + (v_y^{new}-v_y)^2 + (v_z^{new}-v_z)^2\right]dx^3, \tag{36}$$

where *Domain* is the entire ice sheet domain. So

if $d^2 \leq$ small2 and con= 0 then go to **Step 7** else continue
if $d^2 \leq$ small2 and con= 1 then go to **Step 8** else continue

Step 6: Having determined the velocities (35), the gradients

$$\begin{aligned} &\frac{\partial v_x^{new}(.,z)}{\partial x}, \quad \frac{\partial v_x^{new}(.,z)}{\partial y}, \quad \frac{\partial v_y^{new}(.,z)}{\partial x}, \\ &\frac{\partial v_y^{new}(.,z)}{\partial y}, \quad \frac{\partial v_z^{new}(.,z)}{\partial x}, \quad \frac{\partial v_z^{new}(.,z)}{\partial y} \end{aligned} \tag{37}$$

can be computed, and with their help the deviatoric stresses

$$\begin{aligned} t_{xx}^D &= \frac{1}{\mathcal{K}A(\theta')f(\sigma)}\frac{\partial v_x{}^{new}}{\partial x}, & t_{zz}^D &= -(t_{xx}^D + t_{yy}^D), \\ t_{yy}^D &= \frac{1}{\mathcal{K}A(\theta')f(\sigma)}\frac{\partial v_y{}^{new}}{\partial y}, & t_{xy}^D &= \frac{1}{2\mathcal{K}A(\theta')f(\sigma)}\left(\frac{\partial v_y{}^{new}}{\partial x} + \frac{\partial v_x{}^{new}}{\partial y}\right) \end{aligned} \tag{38}$$

be calculated. Because $\sigma \neq 0$ ab initio, there is no danger that (38) may become infinitely large. Next, σ_{corr}^2 can be updated,

$$\sigma_{corr}^2 = \tfrac{1}{2}\epsilon^2\left((t_{xx}^D)^2 + (t_{yy}^D)^2 + (t_{zz}^D)^2 + 2(t_{xy}^D)^2\right), \tag{39}$$

and velocities renamed

$$v_x(.,z) := v_x^{new}(.,z), \quad v_y(.,z) := v_y^{new}(.,z), \quad v_z(.,z) := v_z^{new}(.,z). \quad (40)$$

If con= 1 go to **Step 7** else go to **Step 4**.

Step 7: Having performed this iteration the longitudinal-stress-deviator effects are duly accounted for as far as they affect the creep response function (this is the most significant contribution), however their effect in the equilibrium equations has so far been set aside. So the quantities $p^{corr}(.,z), t_{xz}^{D\ corr}(.,z), t_{yz}^{D\ corr}(.,z)$ must now be updated. To this end, one needs first to calculate

$$\frac{\partial t_{xx}^D}{\partial x}, \quad \frac{\partial t_{xy}^D}{\partial x}, \quad \frac{\partial t_{yy}^D}{\partial y}, \quad \frac{\partial t_{xy}^D}{\partial y}, \quad \frac{\partial t_{xz}^D}{\partial x}, \quad \frac{\partial t_{yz}^D}{\partial y}, \quad \frac{\partial t_{zz}^D}{\partial z}. \quad (41)$$

These quantities are needed to compute the fields

$$\begin{aligned} &\epsilon^2 T_x(.,z), \quad \epsilon^2 T_y(.,z), \quad \epsilon^2 P_z(.,z), \\ &\epsilon^2 P_h(.,z), \quad \epsilon^2 T_{xh}(.,z), \quad \epsilon^2 T_{yh}(.,z), \end{aligned} \quad (42)$$

with the aid of which, using quadratures only, new values for the fields

$$p^{corr}(.,z), \qquad t_{xz}^{D\ corr}(.,z), \qquad t_{yz}^{D\ corr}(.,z) \quad (43)$$

can be deduced. It is important to realize that these operations only involve quadratures. We then update $(\boldsymbol{v}_{sl})^{corr}$ and $\Delta \boldsymbol{v}^{corr}$ according to (23)-(27).

Having all these functions available we set

$$\text{con} := 1,$$

which means that the inner iteration loop is completed, and then go to **Step 3**. i.e., the same iteration is performed again.

Step 8: Now both iterations are complete.

The above program module is adequate for computations when the geometry and the temperature field is prescribed. If convergent, it generates the exact solution to the Stokes problem. Some additional approximations are possible by ignoring certain terms, however, the decision whether certain terms can be ignored must come from explicit computations.

Acknowledgement: We thank R. Greve and an anonymous referee for helpful comments of an earlier version of this paper.

References

1. Baral, D. R., 1999. *Asymptotic theories of large scale motion, temperature and moisture distributions in land based polythermal ice shields and in floating ice shelves: A critical review and new development.* Pending Ph. D. dissertation, Institut für Mechanik, Technische Universität Darmstadt, Germany
2. Blatter, H., Clarke, G. K. C. and Colinge, J., 1998. Stress and velocity fields in glaciers: Part II. Sliding and basal stress distribution. *J. Glaciology*, **44**(148), 457-466.
3. Calov, R. and Hutter, K., 1997. Large scale motion and temperature distributions in land-based ice shields; the Greenland Ice Sheet in response to various climate scenarios. *Arch. Mech.,*, **49**(5), 919-962.
4. Colbeck, S. C. and Evans, R. J., 1973. A flow law for temperate glaciers. *J. Glaciology*, **12**, 71-86.
5. Colinge, J. and Blatter, H., 1998. Stress and velocity fields in glaciers: Part I. Finite-Difference schemes for higher-order glacier models. *J. Glaciology*, **44**(148), 448-456.
6. Dahl-Jensen, D., 1989a. Steady thermomechanical flow along two- dimensional flow lines in large grounded ice sheets. *J. Geophys. Res.*, **94**(B8), 10,355-10,362.
7. Dahl-Jensen, D., 1989b. Two-dimensional thermo-mechanical modelling of flow and depth-age profiles near the ice divide in central Greenland. *Ann. Glaciol.*, **12**, 31-36.
8. Doake, C. S. M. and Wolff, E. W., 1985. Flow law for ice in polar ice sheets. *Nature*, **314** (6008), 255-257.
9. Echelmeyer, K. A. and Kamb, B., 1986. Stress-gradient coupling in glacier flow: II. Longitudinal averaging of the flow response to small perturbations in ice thickness and and surface slopes. *J. Glaciology*, **32** (111), 285-298.
10. Fowler, A. C. and D. A. Larson., 1978. On the flow of polythermal glaciers. I. Model and preliminary analysis. *Proc. R. Soc. Lond.*, **A 363**, 217-242.
11. Fowler, A. C., 1992. Modelling ice sheet dynamics. *Geophys. Astrophys. Fluid. Dyn.*,**63**, 29-65.
12. Greve, R., 1997a. A continuum-mechanical formulation for shallow polythermal ice sheets. *Philosophical transactions of the Royal Society London*, A**355**, 921-974.
13. Hutter, K. 1981. The effect of longitudinal strain on the shear stress of an ice sheet. In defense of using stretched coordinates. *Ann. Glaciol.*, **27** (95), 39-56.
14. Hutter, K. 1983. Theoretical glaciology; material science of ice and the mechanics of glaciers and ice sheets. D. Reidel Publishing Company, Dordrecht, Holland, 510pp.
15. Hutter, K. 1993. Thermo-mechanically coupled ice sheet response. Cold, polythermal, temperate. *J. Glaciol.*, **39** (131), 65-86.
16. Jóhannesson, T., 1992. Landscape of temperate ice caps. Ph. D. dissertation, Geophysics program, University of Washington, 288 pp.
17. Lliboutry, L., 1969. The dynamics of temperate glaciers from the detailed viewpoint. *J. Glaciol.*, **8**(53), 185-205.
18. Mangeney, A., Califano, F. and Hutter, K., 1997. A numerical study of anisotropic, low Reynolds number, free surface flow for ice sheet modelling. *J. Geophys. Res.*, **102** (B10), 22749-22764.

19. Morland, L. W. and Johnson, I. R., 1980. Steady motion of ice sheets. *J. Glaciology*, **25** (92), 229-246.
20. Morland, L. W. 1984. Thermo-mechanical balances of ice sheet flows. *J. Geophys. Astrophys. Fluid Dyn.*, **29**, 237-266.
21. Szidarovszky, F., Hutter, K. and Yakowitz, S., 1989. Computational ice-divide analysis of a cold plane ice sheet under steady conditions. *Ann. Glaciol.*, **12**, 170-177.

(Received 10. April 1999, accepted 31. May 1999)

Nested High-Resolution Modelling of the Greenland Summit Region

Ralf Greve[1], Bernd Mügge[1], Dambaru Baral[1], Olaf Albrecht[2], and Alexey Savvin[1]

[1]Institut für Mechanik III, Technische Universität Darmstadt, Hochschulstraße 1, D-64289 Darmstadt, Germany
[2]Geographisches Institut, Eidgenössische Technische Hochschule Zürich, Winterthurerstrasse 190, CH-8057 Zürich, Switzerland

Abstract. The dynamics and thermodynamics of the vicinity of Summit, the highest point of the Greenland ice sheet at 72° 34′ N, 37° 38′ W, is simulated over two climate cycles until the present with a high-resolution regional model coupled to a large-scale model of the entire Greenland ice sheet. For the computation of the age of ice, two different methods are applied, an Eulerian scheme which solves the advective age equation in a frame fixed in space and requires some artificial diffusion, and a Lagrangian particle-tracing scheme which follows the motion of ice particles and is diffusion-free. The transient simulation is based on the shallow-ice approximation which neglects normal stress deviators and shear stresses in vertical planes. For the simulated modern ice sheet, the velocity and stress fields are then re-computed in the Summit region by a first-order algorithm which includes these stresses. The measured ice topography as well as the temperature profiles of the boreholes GRIP and GISP2 are reproduced very well. The simulated Summit motion of 16 ice thicknesses during the last 250,000 years gives a clue for understanding the origin of irregularities observed in the GRIP and GISP2 cores. In a 50 km region around Summit, all stresses are of the same order of magnitude, so that a very precise modelling of the ice dynamics, which is necessary for an accurate ice-core dating, requires that the shallow-ice approximation be locally abandoned.

1 Introduction

Summit is the highest point of the Greenland ice sheet (Fig. 1), situated at 72° 34′ N, 37° 38′ W, with an elevation of 3233 meters above the mean present sea level and an ice thickness of 3029 meters. In the early 1990's, two deep ice cores were drilled down to the bedrock in the region of Summit, the European core GRIP (Greenland Ice Core Project) directly at Summit, and the American core GISP2 (Greenland Ice Sheet Project) 28 kilometers west of Summit. These cores provided a climate archive which reaches back more than 200,000 years and comprises information about past surface temperature, atmospheric composition etc. Further, the surrounding surface and bedrock topography was surveyed very precisely, and the measured present temperature profiles of the core columns can be used to validate simulation results computed by dynamic/thermodynamic ice-sheet models.

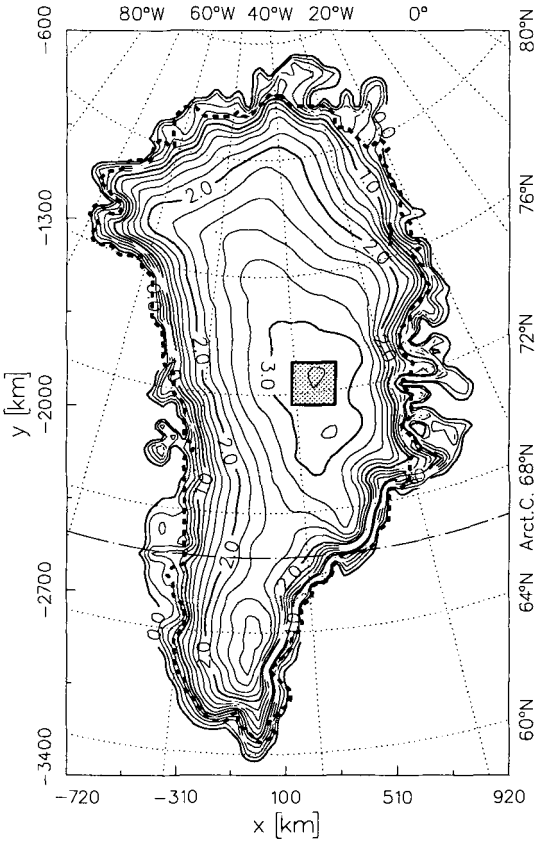

Fig. 1. Surface topography of the modern Greenland ice sheet, by Letréguilly et al. [22] (in km a.s.l., contour spacing 200 m). Shaded square: 160 × 160 km region around Summit for which the nesting procedure is applied. The heavy dashed line indicates the ice margin.

A major problem is to relate the depth of the ice core to the age of the ice ("dating"). In principle it is possible to measure the age stratigraphically by following the seasonal cycle of suitable tracers; however, this method is limited by ice-layer thinning. Therefore, it is common practice to date the lower parts of an ice core by modelling the ice flow. The traditionally applied flow models are of the Dansgaard-Johnson type (Dansgaard and Johnsen [8]). The parameters of these one-dimensional, purely vertical models are adjusted to the conditions in the borehole using the ice velocity and snowfall derived from the borehole as input, and steady-state conditions are usually assumed.

In this study, we apply the three-dimensional dynamic/thermodynamic ice-sheet model SICOPOLIS (SImulation COde for POLythermal Ice Sheets,

Greve [13]) to the Greenland ice sheet as a whole in order to model the present state of the ice sheet as accurately as possible. A 160×160 km region around Summit, for which the precise surface and bedrock data by Hodge et al. [16] are available, is modelled on a nested subgrid with the very high horizontal resolution of 4 km. This provides a detailed velocity field, which is then used to compute age-depth profiles for GRIP and GISP2 with an Eulerian scheme (fixed in space) as well as a Lagrangian, particle-tracing method. The simulated motion of the Summit in the course of time gives some hints to the origin of observed stratigraphic disturbances in the GRIP and GISP2 cores such as strongly inclined layers and overturned folds (Alley et al. [2]).

In addition, a diagnostic run with the FOA (first-order approximation) algorithm by Blatter [4] and Albrecht [1] is carried out for the modern time slice of the model output of SICOPOLIS. This algorithm solves the stress equilibrium balances under inclusion of deviatoric normal stresses and shear stresses in vertical planes which are neglected in SICOPOLIS, so that the relevance of these stresses for the ice-sheet dynamics in the Summit region can be assessed.

2 Modelling Approach for the Greenland Ice Sheet

2.1 Governing equations in the shallow-ice approximation

The large-scale dynamic and thermodynamic behaviour of ice sheets is described by a continuum-mechanical theory of polythermal ice masses, which makes use of the small depth-to-length ratio ($\sim 10^{-3}$) in typical ice sheets ("shallow-ice approximation", SIA); cf. Fowler and Larson [10], Greve [12], Hutter [18,19]. The main consequences of this limit are the neglection of normal stress deviators, horizontal shear in vertical planes and horizontal changes of temperature and water content on the large scale. Further, inertia forces are negligible compared to pressure and stress gradients, so that the momentum balance reduces to a balance of forces:

$$\begin{aligned} -\frac{\partial p}{\partial x} + \frac{\partial t_{xz}}{\partial z} &= 0, \\ -\frac{\partial p}{\partial y} + \frac{\partial t_{yz}}{\partial z} &= 0, \\ -\frac{\partial p}{\partial z} &= \rho g, \end{aligned} \tag{1}$$

where x, y, z are Cartesian coordinates (x and y span the horizontal plane, z is the vertical coordinate), p is the pressure, t_{xz} and t_{yz} are the horizontal shear stresses in horizontal planes, ρ is the ice density and g the gravity acceleration. By vertically integrating these equations from an arbitrary position

z to the free surface $z = h(x, y, t)$ and implying stress-free conditions there, one obtains first from $(1)_3$ the hydrostatic pressure distribution

$$p = \rho g(h - z), \tag{2}$$

and then from $(1)_{1,2}$ the simple expressions

$$t_{xz} = -\rho g \frac{\partial h}{\partial x}(h - z), \qquad t_{yz} = -\rho g \frac{\partial h}{\partial y}(h - z) \tag{3}$$

for the shear stresses.

Rheologically, ice is described as a viscous fluid with a nonlinear, temperature- and water-content-dependent viscosity. The two relevant components of the stress-stretching relation are

$$\frac{\partial v_x}{\partial z} = 2EA(T', \omega)\, f(\sigma)\, t_{xz}, \quad \frac{\partial v_y}{\partial z} = 2EA(T', \omega)\, f(\sigma)\, t_{yz}, \tag{4}$$

where v_x and v_y are the horizontal velocity components, T' is the homologous temperature (relative to pressure melting), ω the water content, $A(T', \omega)$ the rate factor, E the flow-enhancement factor, σ the effective stress (square root of the second invariant of the Cauchy stress tensor) and $f(\sigma)$ the creep function, for which

$$\sigma = \left(t_{xz}^2 + t_{yz}^2\right)^{1/2} \tag{5}$$

and

$$f(\sigma) = \sigma^{n-1} \quad \text{with} \quad n = 3 \tag{6}$$

hold. The latter is known in the glaciological literature as Glen's flow law (Glen [11], Nye [25]).

The horizontal velocity vector $\boldsymbol{v}_\mathrm{h} = (v_x, v_y)$ follows from Eqs. (3), (4) and a vertical integration from the ice base $z = b(x, y, t)$ to an arbitrary z,

$$\boldsymbol{v}_\mathrm{h} = \boldsymbol{v}_\mathrm{b} - \mathcal{C}\{T'(z), \omega(z), (h - z); \|\nabla h\|\} \times \nabla h; \tag{7}$$

the integral functional $\mathcal{C}$ is not explicitly given here. The basal sliding velocity $\boldsymbol{v}_\mathrm{b}$ must be prescribed as a boundary condition, and the deformational part of the ice flow, $\boldsymbol{v}_\mathrm{h} - \boldsymbol{v}_\mathrm{b}$, follows the direction of steepest surface descent, independent of the basal topography.

The vertical velocity v_z can then be inferred from the continuity equation for density-preserving materials,

$$\frac{\partial v_x}{\partial x} + \frac{\partial v_y}{\partial y} + \frac{\partial v_z}{\partial z} = 0. \tag{8}$$

By integration from the ice base to the surface and application of suitable kinematic boundary conditions, it yields further the evolution equation for the ice thickness H,

$$\frac{\partial H}{\partial t} = -\nabla \cdot \boldsymbol{q} + a_s - a_b, \tag{9}$$

where t is the time, $\boldsymbol{q}$ the vertically integrated horizontal velocity (mass flux), a_s the surface mass balance (accumulation minus ablation) and a_b the basal melting rate.

Further evolution equations hold for the temperature in cold ice (temperature below pressure melting), the water content in temperate ice (temperature at pressure melting), the temperature in the underlying lithosphere and the vertical motion of the lithosphere due to the varying ice load; these shall not be given here (see Greve [12]).

2.2 Large-scale ice-sheet model SICOPOLIS

SICOPOLIS is a 3-d dynamic/thermodynamic ice-sheet model based on the continuum-mechanical theory of polythermal ice masses as sketched above. It simulates the time-dependent extent, thickness, velocity, temperature, water-content and age for a grounded ice sheet in response to external forcing. Further, possible basal layers of temperate ice (ice at pressure melting point) are detected with high vertical resolution by fulfilling the Stefan-type conditions at the cold-temperate-transition surface. External forcing is specified by (i) mean annual air temperature above the ice, (ii) surface mass balance (accumulation, surface melting), (iii) sea level surrounding the ice sheet and (iv) geothermal heat flux from below. The model has been described more extensively in the predecessors of this study (Greve [13,14], Greve et al. [15]).

The model domain for the Greenland ice sheet consists of a 1640×2800 km rectangle in the stereographic plane with standard parallel 71°S, spanned by the coordinates x, y. Horizontal resolution is 40 km, so that the domain is discretized by 42×71 grid points. Vertical resolution is 51 grid points in the cold-ice column, 11 grid points in the temperate-ice column (if existing) and 11 grid points in the lithosphere column. Time steps are 5 years for the dynamic evolution (topography, velocity) and 50 years for the thermodynamic evolution (temperature, water content, age).

2.3 Nesting for the Summit region

As the aim of this study is to investigate in detail the dynamics and thermodynamics of the Greenland ice sheet in the vicinity of Summit, a refined subgrid is applied for the 160×160 km square around Summit shown in Fig. 1. In this region, the surface topography, bedrock and ice thickness has been surveyed in detail at 2 km spatial resolution (Hodge et al. [16]; Fig. 2). The

resolution of the numerical subgrid is 4 km (refinement factor 10 with respect to the coarse grid), so that the subgrid domain is discretized by 41 × 41 grid points. It is coupled to the coarse grid by boundary conditions at its margin which are interpolated field quantities of the coarse grid, and, in turn, it gives back the computed topography to the coarse grid at positions where coarse-grid and refined-grid points fall together (Savvin [29]). The time steps for the refined computations are 0.05 years for the dynamic evolution and 0.5 years for the thermodynamic evolution.

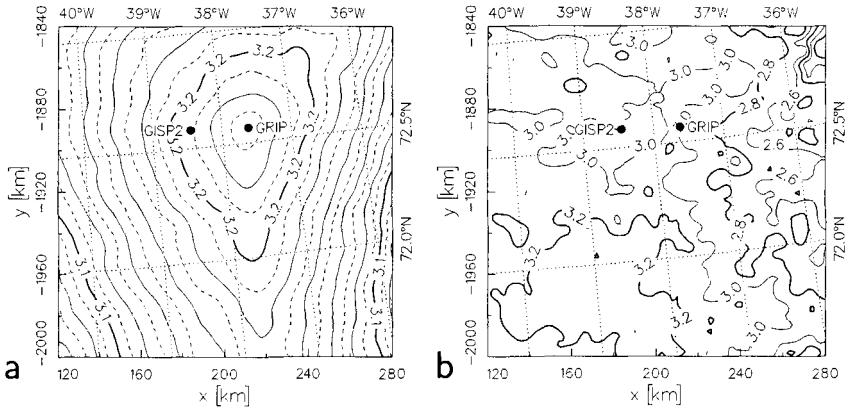

Fig. 2. Zoom of the Summit region marked in Fig. 1, data by Hodge et al. [16]. (a) surface topography (contours, in km a.s.l., spacing 10 m). (b) ice thickness (in km, spacing 200 m).

2.4 Eulerian age computation

For the age of ice (the elapsed time since the ice particles settled on the surface as snowflakes), $\mathcal{A}$, the purely advective (hyperbolic) evolution equation

$$\frac{d\mathcal{A}}{dt} = 1 \tag{10}$$

holds (d/dt denotes the material time derivative which incorporates ice movement), with the corresponding Dirichlet-type boundary condition

$$\mathcal{A}(z = h_{\mathrm{acc}}) = 0 \tag{11}$$

in the accumulation zones at the free surface $h_{\mathrm{acc}}(x, y, t)$. If regions of temperate ice exist, at the cold-temperate transition surface (CTS) the age is continuous.

Integration of Eq. (10) in the Eulerian frame of the numerical grid requires first to re-write it with the local time derivative $\partial/\partial t$ and explicit advection terms,

$$\frac{\partial \mathcal{A}}{\partial t} + v_x \frac{\partial \mathcal{A}}{\partial x} + v_y \frac{\partial \mathcal{A}}{\partial y} + v_z \frac{\partial \mathcal{A}}{\partial z} = 1 + D_\mathrm{A} \frac{\partial^2 \mathcal{A}}{\partial z^2}. \tag{12}$$

In order to achieve stable integration, the artificial vertical diffusion term $D_\mathrm{A}\,(\partial^2 \mathcal{A}/\partial z^2)$ is added on the right-hand side (Greve [13], Huybrechts [20]) and for the diffusivity D_A the small value $5 \cdot 10^{-8}$ m^2 s^{-1} is used.

As the type of the age evolution equation has now changed from hyperbolic to parabolic, artificial boundary conditions for the ablation zones of the free surface, $h_\mathrm{abl}(x, y, t)$, and the entire ice base, $b(x, y, t)$, must be prescribed. Following Greve et al. [15], we use the Neumann-type conditions

$$\frac{\partial \mathcal{A}}{\partial z}(z = h_\mathrm{abl}) = 0, \qquad \frac{\partial \mathcal{A}}{\partial z}(z = b) = -\frac{m_\mathrm{age}}{S_\mathrm{mean}}, \tag{13}$$

where $S_\mathrm{mean} \approx 30$ cm ice equiv. a^{-1} is the mean snowfall rate and $m_\mathrm{age} = 200$ the thinning factor.

The system (11), (12), (13) is integrated with an FTCS (forward time centered space) scheme and upstream discretization of the horizontal advection terms. This is the standard age computation method of SICOPOLIS; however, its disadvantage is that below approximately 85% depth the influence of the diffusion term overrides the solution of the physical equation (10), so that near the bedrock the results are not reliable (Calov et al. [6], Greve et al. [15]).

2.5 Lagrangian age computation (particle tracing)

The Eulerian age computation does not make efficient use of the very simple nature of Eq. (10). In the Lagrangian frame which follows the ice particles, this equation can be discretized in a straightforward way without any artificial diffusion, and its solution becomes trivial. The numerical work in this approach is to find out for which positions in the ice body the solution holds, that is, to compute the paths $\boldsymbol{x}(t)$ ($\boldsymbol{x}$ is the position vector) of the ice particles travelling through the ice sheet. The corresponding evolution equation is

$$\frac{d\boldsymbol{x}}{dt} = \boldsymbol{v}(x, y, z, t), \tag{14}$$

where $\boldsymbol{v}$ denotes the velocity field in the ice sheet.

The system of equations (10), (11), (14) is now solved directly in the cold-ice domain (temperature below pressure melting). We exclude the small regions of temperate ice for numerical simplicity, and because the presence of liquid water disturbs the well-defined stratigraphy anyway. The solution of Eq. (10) is very simple and leads to the statement that in one year an

ice particle becomes one year older. However, the integration of Eq. (14) requires more numerical effort, it is performed by the conventional fourth-order Runge-Kutta scheme (Mügge [24]). The initial condition for Eq. (14) is that the trajectory of an ice particle deposited at time t_0 in the accumulation zone of the ice sheet starts at the free surface, that is

$$\boldsymbol{x}(t_0) = \Big(x_0,\, y_0,\, z = h_{\mathrm{acc}}(x_0, y_0, t_0)\Big). \tag{15}$$

The end of a trajectory is reached when the ice particle leaves the cold-ice region by either crossing the free surface from below (ablation), or crossing the ice base (basal melting) or the CTS (if the cold ice is underlain by a layer of temperate ice). Further, for numerical reasons the tracing of a particle trajectory is stopped when the particle reaches a region with less than 500 m ice thickness, which occurs close to the margin of the ice sheet.

Evidently, in order to solve Eq. (14) for particle trajectories, the three-dimensional velocity field $\boldsymbol{v}(\boldsymbol{x}, t)$ as well as the topography (free surface, bedrock, CTS) of the ice body must be known. As SICOPOLIS provides these quantities only at the nodes of the numerical grid, which, in general, do not fall together with the positions $\boldsymbol{x}$ of the traced particles, a suitable interpolation procedure must be applied. For this, we use the values of the nearest-neighbour grid points and average them with weights proportional to the inverse distance to the position $\boldsymbol{x}$.

In this study, the particle-tracing algorithm is run diagnostically with the SICOPOLIS output for the modern time slice only. This implies that the time dependence of the velocity and topography is neglected, and we compute trajectories and ages in a quasi-steady-state approximation based on modern streamlines instead of real trajectories. In order to avoid interpolating the spatially-scattered particle ages back on the numerical grid, the algorithm is further run backward in time, that is, the particles of any ice column whose age is computed are traced back to the ice surface by applying the negative velocity field. As a by-product this method yields the geographic origin of the ice in a given column.

Full coupling between SICOPOLIS and the particle-tracing algorithm with consideration of the time-dependent velocity field and re-interpolation of the computed ages from the cloud of particles on the numerical grid has not yet been implemented. This will be done in the near future.

2.6 Diagnostic first-order approximation

Blatter [4] and Albrecht [1] developed an algorithm which allows the computation of the force equilibrium in a glacier or an ice sheet of given topography and temperature beyond the shallow-ice approximation (SIA), that is, under inclusion of normal stress deviators and shear stresses in vertical planes. This algorithm is based on Blatter's [4] first-order approximation (FOA), in which

the momentum balance is

$$\begin{aligned} 2\frac{\partial t^{\mathrm{D}}_{xx}}{\partial x} + \frac{\partial t^{\mathrm{D}}_{yy}}{\partial x} + \frac{\partial t_{xy}}{\partial y} + \frac{\partial t_{xz}}{\partial z} &= \rho g \frac{\partial h}{\partial x}, \\ 2\frac{\partial t^{\mathrm{D}}_{yy}}{\partial y} + \frac{\partial t^{\mathrm{D}}_{xx}}{\partial y} + \frac{\partial t_{xy}}{\partial x} + \frac{\partial t_{yz}}{\partial z} &= \rho g \frac{\partial h}{\partial y}, \end{aligned} \tag{16}$$

where t^{D}_{xx}, t^{D}_{yy} are the normal stress deviators, and t_{xy} is the horizontal shear stress in vertical planes. The stress-stretching relation in FOA is

$$\begin{aligned} \frac{\partial v_x}{\partial x} &= EA(T',\omega)\, f(\sigma)\, t^{\mathrm{D}}_{xx}, \\ \frac{\partial v_y}{\partial y} &= EA(T',\omega)\, f(\sigma)\, t^{\mathrm{D}}_{yy}, \\ \frac{\partial v_x}{\partial y} + \frac{\partial v_y}{\partial x} &= 2EA(T',\omega)\, f(\sigma)\, t_{xy}, \\ \frac{\partial v_x}{\partial z} &= 2EA(T',\omega)\, f(\sigma)\, t_{xz}, \\ \frac{\partial v_y}{\partial z} &= 2EA(T',\omega)\, f(\sigma)\, t_{yz}, \end{aligned} \tag{17}$$

with the effective stress

$$\sigma = \left((t^{\mathrm{D}}_{xx})^2 + (t^{\mathrm{D}}_{yy})^2 + t^{\mathrm{D}}_{xx} t^{\mathrm{D}}_{yy} + t^2_{xy} + t^2_{xz} + t^2_{yz}\right)^{1/2}, \tag{18}$$

and the creep function

$$f(\sigma) = (\sigma^2 + \sigma^2_{\mathrm{res}})^{(n-1)/2} \quad \text{with} \quad n = 3 \tag{19}$$

(modified Glen's flow law with finite viscosity at zero stress, the residual stress σ_{res} is taken as 31.6 kPa, see Albrecht [1]).

Provided the fields of temperature and water content are known, eqs. (16), (17) are seven equations for the seven unknown fields v_x, v_y, t^{D}_{xx}, t^{D}_{yy}, t_{xy}, t_{xz}, t_{yz}, which are completed by stress-free boundary conditions at the free surface,

$$\begin{aligned} t_{xz} - \frac{\partial h}{\partial x}\left(2t^{\mathrm{D}}_{xx} + t^{\mathrm{D}}_{yy}\right) - \frac{\partial h}{\partial y} t_{xy}\Big|_{z=h} &= 0, \\ t_{yz} - \frac{\partial h}{\partial y}\left(2t^{\mathrm{D}}_{yy} + t^{\mathrm{D}}_{xx}\right) - \frac{\partial h}{\partial x} t_{xy}\Big|_{z=h} &= 0, \end{aligned} \tag{20}$$

and a prescribed basal velocity (for instance, no-slip conditions).

The FOA algorithm solves these equations by first discretizing the horizontal derivatives, and then applying a second-order Runge-Kutta scheme for the vertical derivatives of eqs. (16), $(17)_{4,5}$. The Runge-Kutta scheme starts at the base and integrates the equations upward. Satisfaction of the surface condition (20) is achieved by iteratively determining appropriate values for the basal stresses. The FOA algorithm is used here to re-compute diagnostically the velocity and stress fields originally computed by SICOPOLIS in the nested Summit region for the modern state of the Greenland ice sheet.

3 Simulation Set-up

The past evolution of the Greenland ice sheet as well as its present state are simulated with the paleoclimatic simulation gf004 from 250,000 years BP until today, initialized by a previous 100,000-year steady-state run for the conditions at 250,000 years BP. The simulation is driven by the surface-temperature history inferred from the GRIP ice core (Johnsen et al. [21]) and the piecewise linear sea-level scenario by Greve et al. [15], and for the present reference state of the surface temperature the parameterization given by Reeh [28] is used. The accumulation input is based on the data by Bolzan and Strobel [5], Ohmura and Reeh [26] and Wilhelms [31] (gridded by Greve et al. [15]), modified by a time-dependent factor coupled linearly to the surface-temperature deviation from today (Greve [14]). Surface melting is modelled by a degree-day approach (Reeh [28]) with the parameters $\beta_{\mathrm{snow}} = 3$ mm w.e. $\mathrm{d}^{-1}\mathrm{K}^{-1}$ (snow melt), $\beta_{\mathrm{ice}} = 7 \ldots 10$ mm w.e. $\mathrm{d}^{-1}\mathrm{K}^{-1}$ (ice melt, linear increase from 60°N to 80°N), $P_{\max} = 60\%$ (firn saturation rate) and $\hat{T}_{\mathrm{air}} = 10 \ldots 21$ K (amplitude of the annual surface-temperature variation, linear increase from 60°N to 80°N) (Greve et al. [15]). Bedrock topography is by Letréguilly et al. [22], complemented by Hodge's et al. [16] high-resolution data for the Summit region. Further model parameters are listed in Table 1.

The particle-tracing algorithm is fed by the topography and velocity field of the simulated present ice sheet, and it is integrated over 500,000 years with a time step of 5 years. As explained above, this yields the age profiles for selected ice columns in quasi-steady-state approximation.

A diagnostic run with the FOA algorithm is performed for the modern time slice in the refined region around Summit (simulation gf013). This yields high-resolution velocity and stress fields including the normal stress deviators, t^{D}_{xx}, t^{D}_{yy}, and the shear stress in vertical planes, t_{xy}, which are neglected in the SIA on which SICOPOLIS is based.

4 Results and Discussion

4.1 Simulation gf004: shallow-ice approximation

The set-up of simulation gf004 results from the optimization process carried out by Greve [14], Greve et al. [15] in order to achieve optimum agreement between the simulated and the real modern Greenland ice sheet. Therefore, the simulated large-scale properties of the ice sheet fit the measured ones in an excellent fashion, which is demonstrated in Table 2 for the total ice volume, V_{tot}, the maximum elevation of the ice surface above the present sea level, $h_{\max}$, the ice-covered basal area, $A_{\mathrm{i,b}}$, the distance between the simulated Summit and GRIP, d_{GRIP}, the ice thickness at GRIP, H_{GRIP}, the age of the basal ice at GRIP, $\mathcal{A}_{\mathrm{GRIP}}$, the basal temperature at GRIP, T_{GRIP}, the basal temperature at Camp Century, T_{CC}, the basal temperature at Dye3, T_{Dye3} and the surface velocities at EGIG stations T4, TA15 and TA31, v_{T4},

Table 1. Physical parameters used in the simulations.

Quantity	Value
Gravity acceleration, g	$9.81\ \mathrm{m\,s^{-2}}$
Density of ice, ρ	$910\ \mathrm{kg\,m^{-3}}$
Power-law exponent, n	3
Rate factor, $A(T', \omega)$	Cold ice: Arrhenius law[1]
	Temperate ice: *linear dependence on* ω[1]
Flow-enhancement factor, E	1 (interglacial ice), 3 (glacial ice)
Heat conductivity of ice, κ	$9.828\, e^{-0.0057\, T[\mathrm{K}]}\ \mathrm{W\,m^{-1}K^{-1}}$
Specific heat of ice, c	$(146.3 + 7.253\, T[\mathrm{K}])\ \mathrm{J\,kg^{-1}K^{-1}}$
Latent heat of ice, L	$335\ \mathrm{kJ\,kg^{-1}}$
Clausius-Clapeyron gradient, β	$8.7 \cdot 10^{-4}\ \mathrm{K\,m^{-1}}$
Basal sliding velocity, v_b	Cold base: no-slip
	Temperate base: Weertman-type sliding[1]
Geothermal heat flux, q_geo	$65\ \mathrm{mW\,m^{-2}}$
Isostatic *time* lag, τ_V	3000 a
Asthenosphere density, ρ_a	$3300\ \mathrm{kg\,m^{-3}}$
Density × specific heat of the lithosphere, $\rho_\mathrm{r} c_\mathrm{r}$	$2000\ \mathrm{kJ\,m^{-3}\,K^{-1}}$
Heat conductivity of the lithosphere, κ_r	$3\ \mathrm{W\,m^{-1}K^{-1}}$

[1]For details see Greve et al. [15].

v_{TA15} and v_{TA31} (Hofmann [17]). The poor agreement for T_{Dye3} was already reported by Greve et al. [15] and is probably due to a local phenomenon not included in the model, for instance an exceptionally low geothermal heat flux.

Fig. 3 depicts for simulation gf004 the air-temperature forcing ΔT_ma, the sea-level forcing z_sl, the ice thicknesses H at GRIP and at GISP2, H_{GRIP} and H_{GISP2}, and the basal temperatures T_b at GRIP and GISP2, T_{GRIP} and T_{GISP2}. The results are very similar to those of Greve [14], which were based on a coarse-grid spacing of 20 km without a high-resolution subgrid in the Summit region. The thicknesses follow the air-temperature forcing in phase, because central Greenland is virtually not affected by ablation, but reacts most sensitively to changes of the accumulation rate which is larger during warm climates. However, owing to the lagged response of the ice sheet to these changes, the rapid climate oscillations during the Wisconsin ice age are filtered out to a large extent. By contrast, the basal temperatures show an anticyclic behaviour, that is, they are lowest during the warm Eemian and Holocene interglacials. This is so because ice flow is more pronounced during interglacial conditions, which leads to a larger advection of cold surface ice downward. The variation is only 3°C for the entire period of 250,000 model years, so that the surface signal which varies by as much as 27.7°C is strongly

damped. The simulated basal temperature at GISP2 is always some tenth degrees higher than that of GRIP.

Table 2. Simulated (gf004) and measured data for the modern Greenland ice sheet.

	Simulation	Data
V_{tot} [10^6 km^3]	2.815	2.828
h_{max} [km a.s.l.]	3.214	3.233
$A_{\mathrm{i,b}}$ [10^6 km^2]	1.672	1.682
d_{GRIP} [km]	30.88	0.0
H_{GRIP} [km]	2.955	3.029
$\mathcal{A}_{\mathrm{GRIP}}$ [ka]	257.13	~ 250
T_{GRIP} [°C]	−8.92	−8.56
T_{CC} [°C]	−10.05	−13.0
T_{Dye3} [°C]	−2.72	−13.22
v_{T4} [m a^{-1}]	123.64	102.98
v_{TA15} [m a^{-1}]	48.89	47.75
v_{TA31} [m a^{-1}]	14.43	14.85

The simulated V_{tot}, $A_{\mathrm{i,b}}$, T_{CC}, T_{Dye3}, v_{T4}, v_{TA15}, v_{TA31} are based on the coarse-grid computation, h_{max}, d_{GRIP}, H_{GRIP}, $\mathcal{A}_{\mathrm{GRIP}}$, T_{GRIP} on the refined-subgrid computation for the Summit region.

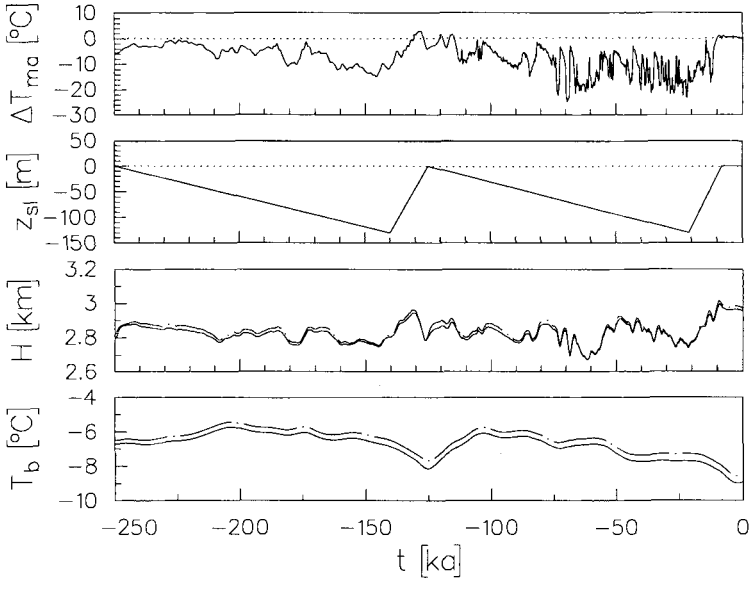

Fig. 3. Simulation gf004: Air-temperature forcing ΔT_{ma}, sea-level forcing z_{sl}, ice thicknesses H at GRIP (solid) and GISP2 (dash-dotted), basal temperatures T_{b} at GRIP (solid) and GISP2 (dash-dotted).

The simulated surface topography and ice thickness in the Summit region are shown in Fig. 4. Comparison with the data of Fig. 2 reveals a very good agreement for the surface and an excellent agreement for the thickness. The simulated Summit is situated approximately 31 km north-north-west of the real Summit at GRIP, and the maximum discrepancy for the ice surface is 40 m in the south-western corner of the region, which is slightly more than 1% of the typical ice thickness. Due to the high numerical resolution of 4 km, even many fine-structures of the ice thickness are reproduced in an unprecedented way.

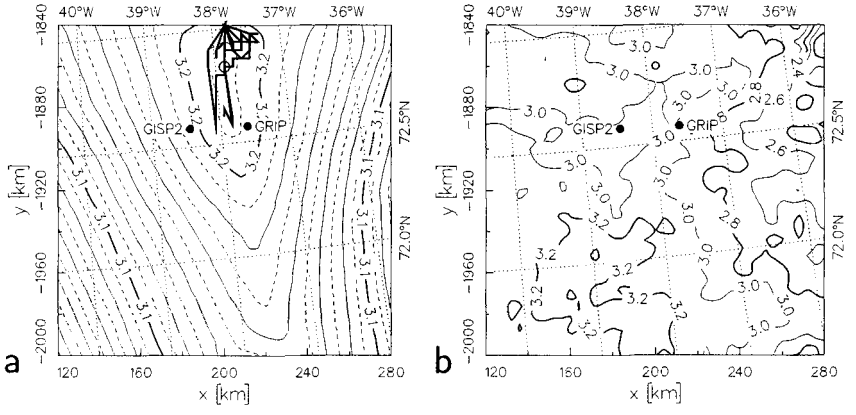

Fig. 4. Simulation gf004: The present vicinity of Summit. (a) simulated surface topography (contours, in km a.s.l., spacing 10 m), Summit path during the model time $t = -250 \ldots 0$ ka (thick line). (b) simulated ice thickness (in km, spacing 200 m). Open circles denote the simulated modern Summit position $\sim$ 31 km north-north-west of GRIP.

The path of the simulated Summit position during the 250,000 model years, which is also plotted in Fig. 4, shows a total variation of 24 km (eight ice thicknesses) in west-east direction, and 48 km (sixteen ice thicknesses) in north-south direction. As a consequence, the recent ice column at Summit experienced strongly varying three-dimensional flow conditions in the past, reaching from vertical compression and horizontal extension (pure shear, at times when the Summit was very close to the present one) to simple-shear conditions in virtually all directions (at times when the Summit was some ice thicknesses away). Therefore, this divide migration may contribute to the formation of irregularities such as strongly inclined layers and, perhaps, overturned folds, which have been observed in the GRIP and GISP2 cores (Alley et al. [2]) and destroy potentially the stratigraphy.

These varying flow conditions at Summit are further illustrated by Figs. 5, 6, which show the high-resolution velocity field for west-east and north-

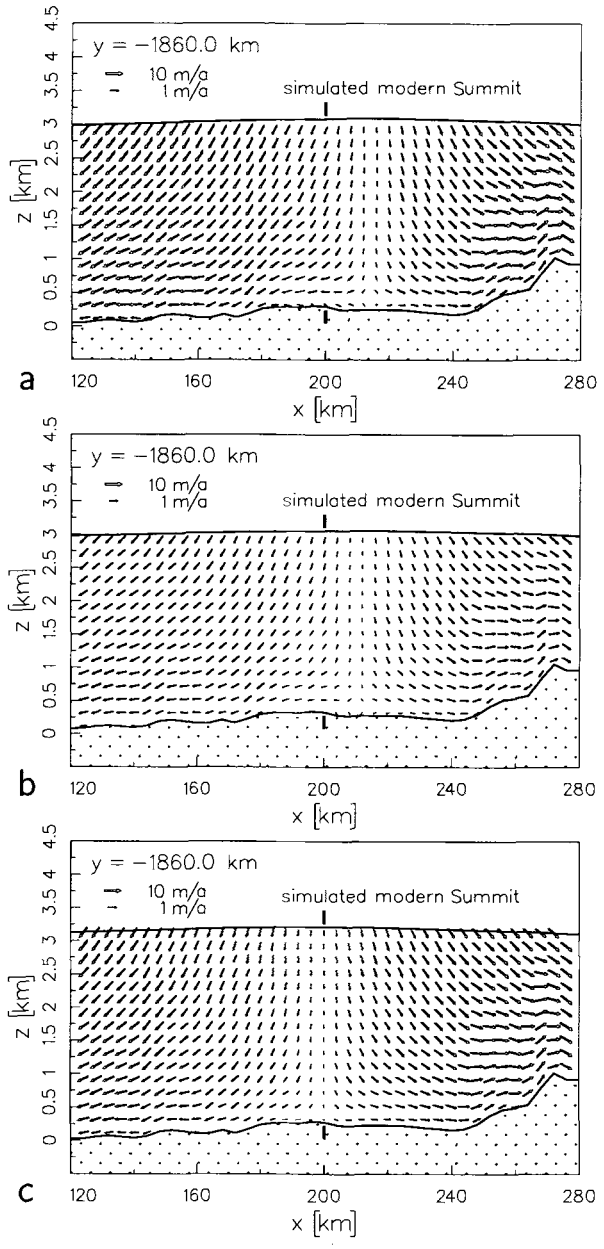

Fig. 5. Simulated (gf004) ice velocities in the refined-subgrid region, for a west-east transect across the simulated modern Summit. Time slices at 127,000 years BP (EIVM, panel a), 21,000 years BP (LGM, panel b) and the present (panel c). The simulated *present* Summit position is indicated by the heavy lines.

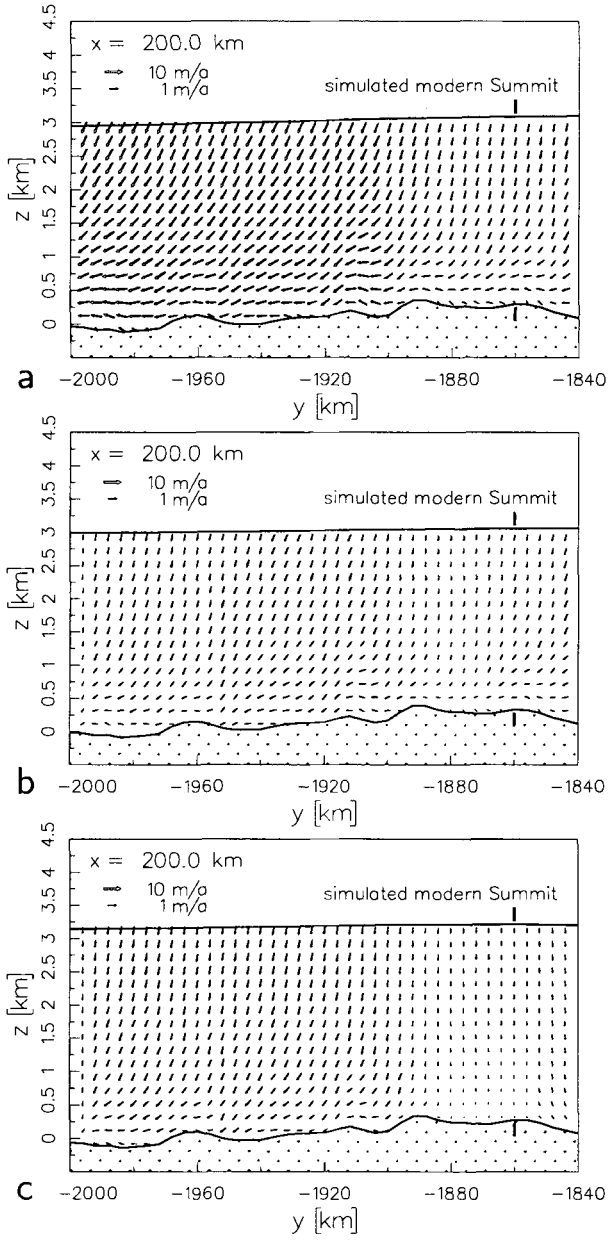

Fig. 6. Simulated (gf004) ice velocities in the refined-subgrid region, for a north-south transect across the simulated modern Summit. Time slices at 127,000 years BP (EIVM, panel a), 21,000 years BP (LGM, panel b) and the present (panel c). The simulated *present* Summit position is indicated by the heavy lines.

south transects across the simulated modern Summit and for time slices at 127,000 years BP (EIVM), 21,000 years BP (LGM) and the present. Naturally, the modern ice flow at the Summit column is of dome type, that is, pure shear with the velocity vector pointing downward throughout the column. In the EIVM and the LGM, however, the ice flow at the present Summit has a distinct component westward and southward, so that simple shear prevails.

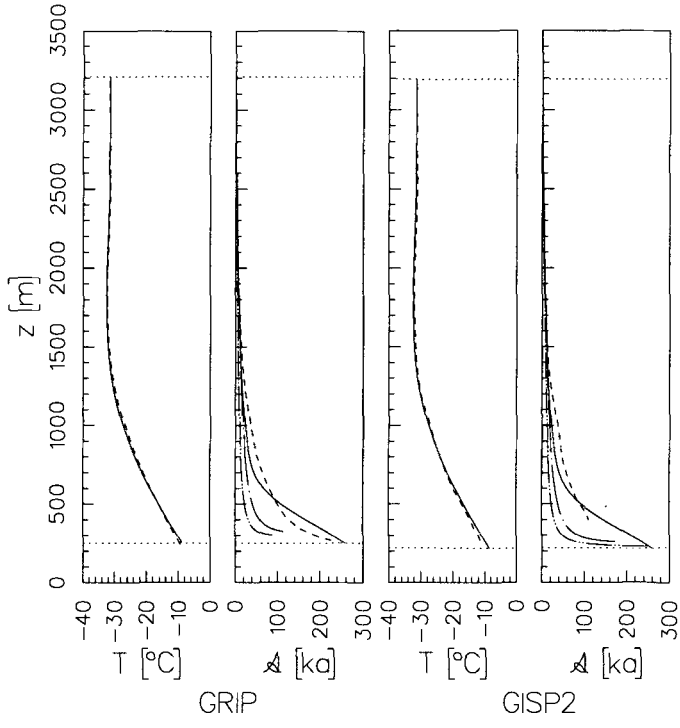

Fig. 7. Temperature-depth and age-depth profiles for GRIP and GISP2. Solid temperatures: computed by simulation gf004. Dashed temperatures: measured profiles (Cuffey et al. [7], Johnsen et al. [21]). Solid ages: computed by simulation gf004, Eulerian method. Dash-dotted ages: computed by simulation gf004, quasi-steady-state particle-tracing method. Dash-dot-dotted ages: computed by simulation gf013, quasi-steady-state particle-tracing method. Dashed ages: current profiles by Dansgaard et al. [9], Meese et al. [23], Sowers et al. [30].

Fig. 7 depicts the computed temperature and age profiles (the latter with the Eulerian and particle-tracing method, below referred to as "EM" and "PT", respectively) for GRIP and GISP2, and compares them with measured temperature profiles (Cuffey et al. [7], Johnsen et al. [21]) and current datings which stem from a combination of stratigraphic techniques and simple ice-flow modelling (Dansgaard et al. [9], Meese et al. [23], Sowers et al. [30];

below referred to as "ST/SIFM"). The agreement for the temperature, which has already been very good in the previous study by Greve [14], is now almost perfect as a consequence of the high-resolution subgrid; maximum discrepancies are less than 1°C. This demonstrates that the ice flow (which affects the temperature field strongly due to horizontal and vertical advection) is captured very adequately in the Summit region, a necessary prerequisite for reasonable age computations.

For the upper 1500 meters of the two cores, the three shown datings EM, PT and ST/SIFM fall together very closely. Here, ST/SIFM is based on annual-layer counting and therefore very precise; the good agreement with EM and PT is therefore a further validation for the computed flow field. Further down, both EM and PT provide ages approximately one third less than ST/SIFM. Even though some care is required in interpreting these findings, the large accuracy for the temperature profile indicates that the EM and PT results may be more realistic than the previous ST/SIFM results based on less sophisticated modelling approaches.

Large discrepancies become evident for the lowest 500 meters of the cores. In these parts, EM suffers from the applied numerical diffusion (section 2.4; cf. also Calov et al. [6]), even though the choice of m_{age} yields a basal age very close to the value of ST/SIFM (see also Table 2). As discussed in section 2.5, PT does not have this disadvantage due to the Lagrangian approach. However, its accuracy is still limited by the quasi-steady-state mode which provides too small ages because the ice particles are traced on the basis of modern ice velocities only which are rather large due to the interglacial climate conditions. A fully coupled SICOPOLIS/PT simulation in which the ice particles experience smaller velocities during glacial periods would certainly provide larger ages in the lower parts of the core columns. Thus, once the coupling between SICOPOLIS and PT is achieved, PT has the potential to provide very accurate ages also close to the bedrock where EM becomes unreliable.

4.2 Simulation gf013: diagnostic first-order approximation

The velocities and stresses computed with the diagnostic FOA simulation gf013 for the modern time slice are shown in Figs. 8, 9. The velocity distributions in the two transects look very similar to those of the SIA simulation gf004 (Figs. 5c, 6c). However, in the immediate vicinity of the Summit, the absolute values are larger as a consequence of the contribution of t^{D}_{xx}, t^{D}_{yy} and t_{xy} to the effective shear stress (18), which makes the ice softer. In Fig. 8a, a slight numerical instability becomes evident close to the western and eastern margin of the domain, which consists of a flip-flop behaviour of the velocity vectors between adjacent grid points.

The horizontal shear stresses, t_{xz}, t_{yz}, do not deviate distinctly from the SIA solution, which consists of a linear increase with depth and a proportionality to the local surface slope. By contrast, the normal stress deviators,

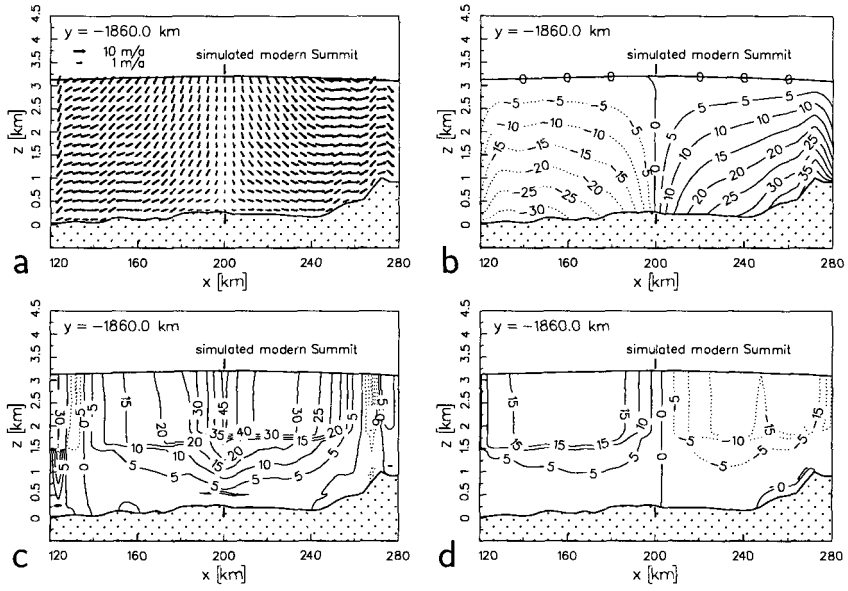

Fig. 8. Simulation gf013: (a) modern ice velocity, (b) horizontal shear stress t_{xz}, (c) normal stress deviator t^{D}_{xx}, (d) shear stress in vertical planes t_{xy} in the refined-subgrid region, for a west-east transect across the simulated modern Summit. Stresses in kPa, positive (negative) values are indicated by solid (dotted) contours.

t^{D}_{xx}, t^{D}_{yy}, and the horizontal shear stress in vertical planes, t_{xy}, which do not play a role in the SIA, are generally larger in the upper parts of the ice sheet because of larger horizontal velocity gradients. Figs. 8c, d reveal very clearly that these non-SIA stresses are most significant within a ca. 50 km circle around Summit, where they exceed 10 kPa and are of the same order of magnitude as the horizontal shear stresses. Very close to the margins, the computed stresses become partly spurious, which is certainly related to the numerical velocity wiggles reported above.

As a further illustration of the relevance of non-SIA contributions to the ice dynamics, the profiles of the horizontal velocities, the horizontal shear stresses and the normal stress deviators are presented in Fig. 10 for the Summit of simulation gf013. In the SIA, v_x, v_y, t_{xz} and t_{yz} are zero over the entire profile at an ice dome, whereas the computed FOA solution yields small, yet non-vanishing values of up to 0.1 $\mathrm{m\,a^{-1}}$ for v_x, v_y, and of up to 1.5 kPa for t_{xz}, t_{yz}. These stresses are far outweighed by t^{D}_{xx} and t^{D}_{yy} with maximum values of 45 kPa and 7 kPa, respectively, in the upper part of the Summit column.

In addition to the EM and PT age profiles of simulation gf004 discussed in the previous section, Fig. 7 also shows the age profiles for GRIP and GISP2 computed with PT using the output of simulation gf013. Evidently,

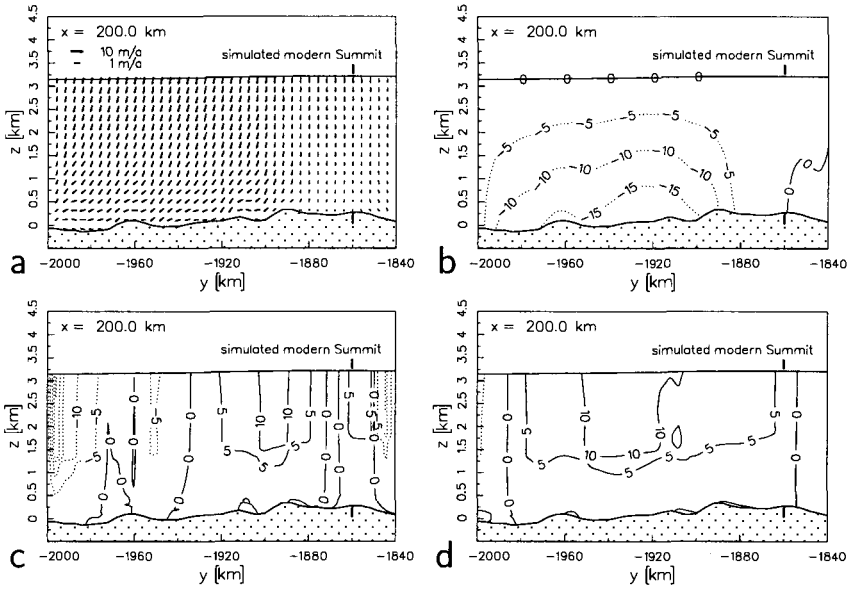

Fig. 9. Simulation gf013: (a) modern ice velocity, (b) horizontal shear stress t_{yz}, (c) normal stress deviator t^{D}_{yy}, (d) shear stress in vertical planes t_{xy} in the refined-subgrid region, for a north-south transect across the simulated modern Summit. Stresses in kPa, positive (negative) values are indicated by solid (dotted) contours.

the computed ages are approximately one third smaller than the PT ages of simulation gf004, which is due to the larger FOA velocities in the Summit region. Even though the absolute values are certainly unrealistic due to the quasi-steady-state mode which is also applied here, this demonstrates that the inclusion of normal-stress effects in the determination of the velocity field has a non-negligible influence on computed ages in the Summit region. In the lowest ca. 50 meters of the core columns, the PT scheme produces heavily oscillating, meaningless ages due to limitations of the spatial resolution of the velocity field; these oscillations are not depicted.

5 Conclusions

The dynamics and thermodynamics of the Greenland ice sheet was simulated with the three-dimensional ice-sheet model SICOPOLIS. For a 160 × 160 km region around Summit, a nesting procedure was applied which allows a high-resolution treatment of this region. Main results are:

- Very good to excellent agreement between the simulated and the measured ice sheet geometry.
- During the last 250,000 years, the basal temperature in the Summit region varied only slightly, and was always below pressure melting.

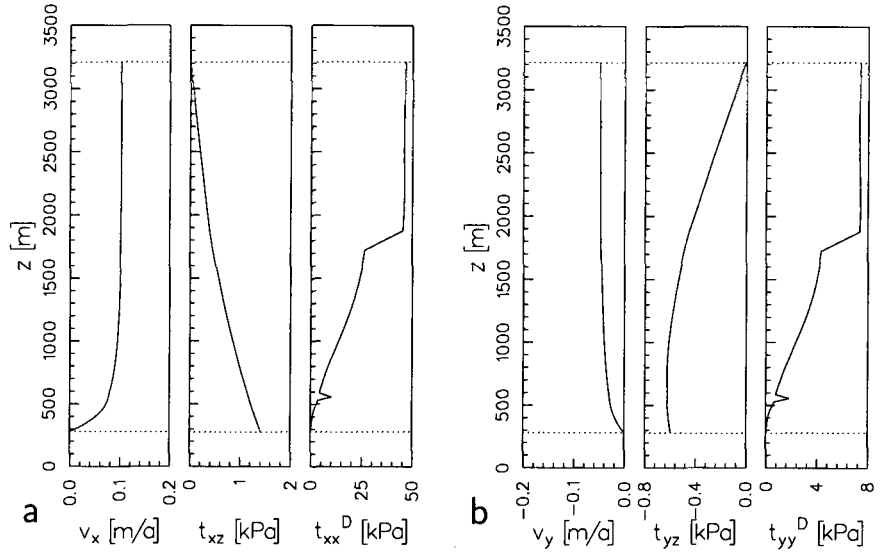

Fig. 10. Simulation gf013: Profiles of (a) the horizontal velocity v_x, the horizontal shear stress t_{xz} and the normal stress deviator t^{D}_{xx}, (b) the horizontal velocity v_y, the horizontal shear stress t_{yz} and the normal stress deviator t^{D}_{yy}, for the simulated modern Summit.

- The Summit moved by 16 ice thicknesses in this period. This entails strongly varying flow conditions for the modern Summit position.
- The computed datings for GRIP and GISP2 agree well with current datings (Dansgaard et al. [9], Meese et al. [23], Sowers et al. [30]) down to 1500 meters depth. Further down, our results indicate by approximately one third lower ages. For the last ca. 400 meters above the bedrock, the EM ages are falsified by artificial diffusion, and the PT ages suffer from the quasi-steady-state approximation applied for this method.
- Normal stress deviators and shear stresses in vertical planes, which are neglected in the widely used shallow-ice approximation, are important in a ca. 50 km circle around Summit. They tend to increase the ice velocities and should thus be accounted for when attempting to compute precise datings for GRIP and GISP2.

Future work will therefore comprise the full coupling between SICOPOLIS and the particle-tracing algorithm in order to capture the impact of the time-dependent velocity field on the particle paths. Once this is achieved, a very precise method will be at hand in order to compute diffusion-free age-depth profiles down to the bedrock. Furthermore, a simpler and more efficient algorithm for the inclusion of non-SIA stresses in the Summit region, based on a perturbation analysis of the model equations for ice sheets (Baral [3]), is currently under development. This will allow to carry out time-dependent

simulations over long periods under inclusion of non-SIA stresses, instead of the diagnostic assessment conducted here with the extremely CPU-time-consuming FOA algorithm.

Acknowledgements: The FOA algorithm was programmed by H. Blatter and O. Albrecht, the nesting algorithm by R. Calov and A. Savvin, partly during a visit of A. Savvin at the Geographisches Institut, ETH Zürich, funded by an EISMINT exchange grant of the European Science Foundation. This work was further supported by the Deutsche Forschungsgemeinschaft under project no. Hu 412/14-2, for which K. Hutter was acting as project leader. Comments of K. Hutter on an earlier version of this paper improved its quality considerably.

References

1. Albrecht, O. (1999) *Dynamics of glaciers and ice sheets: a numerical model study.* Ph.D. thesis in preparation, Geographisches Institut, Eidgenössische Technische Hochschule Zürich, Switzerland.
2. Alley, R. B., A. J. Gow, S. J. Johnsen, J. Kipfstuhl, D. A. Meese and T. Thorsteinsson (1995) Comparison of deep ice cores. *Nature*, **373**, 393-394.
3. Baral, D. R. (1999) *Asymptotic theories of large-scale motion, temperature and moisture distributions in land-based polythermal ice shields and in floating ice shelves - A critical review and new developments.* Ph.D. thesis in preparation, Institut für Mechanik, Technische Universität Darmstadt, Germany.
4. Blatter, H. (1995) Velocity and stress fields in grounded glaciers: a simple algorithm for including deviatoric stress gradients. *J. Glaciol.*, **41** (138), 333-344.
5. Bolzan, J. F. and M. Strobel (1994) Accumulation-rate variations around Summit, Greenland. *J. Glaciol.*, **40** (134), 56-66.
6. Calov, R., A. Savvin, R. Greve, I. Hansen and K. Hutter (1998) Simulation of the Antarctic ice sheet with a three-dimensional polythermal ice-sheet model, in support of the EPICA project. *Ann. Glaciol.*, **27**, 201-206.
7. Cuffey, K. M., G. D. Clow, R. B. Alley, M. Stuiver, E. D. Waddington and R. W. Saltus (1995) Large Arctic temperature change at the Wisconsin-Holocene glacial transition. *Science*, **270**, 455-458.
8. Dansgaard, W. and S. J. Johnsen (1969) A flow model and a time scale for the ice core from Camp Century, Greenland. *J. Glaciol.*, **8** (53), 215-223.
9. Dansgaard, W., S. J. Johnsen, H. B. Clausen, D. Dahl-Jensen, N. S. Gundestrup, C. U. Hammer, C. S. Hvidberg, J. P. Steffensen, A. E. Sveinbjörnsdottir, J. Jouzel and G. Bond (1993) Evidence for general instability of past climate from a 250-kyr ice-core record. *Nature*, **364**, 218-220.
10. Fowler, A. C. and D. A. Larson (1978) On the flow of polythermal glaciers. I. Model and preliminary analysis. *Proc. R. Soc. Lond.*, A **363**, 217-242.
11. Glen, J. W. (1955) The creep of polycrystalline ice. *Proc. R. Soc. Lond.*, A **228**, 519-538.
12. Greve, R. (1997a) A continuum-mechanical formulation for shallow polythermal ice sheets. *Phil. Trans. R. Soc. Lond.*, A **355**, 921-974.

13. Greve, R. (1997b) Application of a polythermal three-dimensional ice sheet model to the Greenland Ice Sheet: Response to steady-state and transient climate scenarios. *J. Climate*, **10** (5), 901-918.
14. Greve, R. (1997c) Large-scale ice-sheet modelling as a means of dating deep ice cores in Greenland *J. Glaciol.*, **43** (144), 307-310; Erratum **43** (145), 597-600.
15. Greve, R., M. Weis and K. Hutter (1998) Palaeoclimatic evolution and present conditions of the Greenland Ice Sheet in the vicinity of Summit: An approach by large-scale modelling. *Paleoclimates*, **2** (2-3), 133-161.
16. Hodge, S. M., D. L. Wright, J. A. Bradley, R. W. Jacobel, N. Skou and B. Vaughan (1990) Determination of the surface and bed topography in Central Greenland. *J. Glaciol.*, **36** (122), 17-30.
17. Hofmann, W. (1974) Die Internationale Glaziologische Grönland-Expedition EGIG. *Z. Gletscherkd. Glazialgeol.*, **5**, 217-224.
18. Hutter, K. (1982) A mathematical model of polythermal glaciers and ice sheets. *J. Geophys. Astrophys. Fluid Dyn.*, **21**, 201-224.
19. Hutter, K. (1993) Thermo-mechanically coupled ice sheet response. Cold, polythermal, temperate. *J. Glaciol.*, **39** (131), 65-86.
20. Huybrechts, P. (1994) The present evolution of the Greenland ice sheet: an assessment by modelling. *Global Planet. Change*, **9**, 39-51.
21. Johnsen, S. J., D. Dahl-Jensen, W. Dansgaard and N. Gundestrup (1995) Greenland palaeotemperatures derived from GRIP borehole temperature and ice core isotope profiles. *Tellus*, **47B**, 624-629.
22. Letréguilly, A., P. Huybrechts and N. Reeh (1991) Steady-state characteristics of the Greenland ice sheet under different climates. *J. Glaciol.* **37** (125), 149-157.
23. Meese, D., R. Alley, T. Gow, P. M. Grootes, P. Mayewski, M. Ram, K. Taylor, E. Waddington and G. Zielinski (1994) Preliminary depth-age scale of the GISP2 ice core. CRREL Special Report 94-1.
24. Mügge, B. (1998) *Eisalterbeerchnung im antarktischen Eisschild mit einem Algorithmus zur Teilchenverfolgung.* Diploma thesis, Institut für Mechanik, Technische Universität Darmstadt, Germany.
25. Nye, J. F. (1957) The distribution of stress and velocity in glaciers and ice sheets. *Proc. R. Soc. Lond.*, A **239**, 113-133.
26. Ohmura, A. and N. Reeh (1991) New precipitation and accumulation maps for Greenland. *J. Glaciol.*, **37**, 140-148.
27. Paterson, W. S. B. (1994) *The physics of glaciers.* Third edition. Oxford etc., Pergamon Press, 480 pp.
28. Reeh, N. (1991) Parameterization of melt rate and surface temperature on the Greenland Ice Sheet. *Polarforschung*, **59** (3), 113-128.
29. Savvin, A. (1999) *Grenzschichttheorie nichtlinearer Kriechströmungen und ihre Anwendung auf das EPICA-Vorhaben.* Ph.D. thesis, Institut für Mechanik, Technische Universität Darmstadt, Germany.
30. Sowers, T., M. Bender, L. Labeyrie, D. Martinson, J. Jouzel, D. Raynaud, J. J. Pichon and Y. Korotkevich (1993) 135,000 year Vostok-SPECMAP common temporal framework. *Paleoceanography*, **8**, 737-766.
31. Wilhelms, F. (1996) Leitfähigkeits- und Dichtemessung an Eisbohrkernen. *Ber. Polarforschung*, **191**, 224 pp.

(Received 04 June 1999, accepted 12 June 1999)

Numerical Age Computation of the Antarctic Ice Sheet for Dating Deep Ice Cores

Bernd Mügge[1], Alexey Savvin[1], Reinhard Calov[2], and Ralf Greve[1]

[1]Institut für Mechanik III, Technische Universität Darmstadt, Hochschulstraße 1, D-64289 Darmstadt, Germany
[2]Potsdam-Institut für Klimafolgenforschung, Postfach 601203, D-14412 Potsdam, Germany

Abstract. The application of two different methods for the computation of the age of ice is discussed within the frame of numerical ice sheet modelling. The first method solves the purely advective equation for the age field in the Eulerian frame, which requires the addition of a numerical diffusion term to stabilize the solution and therefore produces arbitrary results in a near-basal boundary layer. The second method makes more efficient use of the simplicity of the equation in the Lagrangian frame by tracing particle paths in the flowing ice body, and it does without artificial diffusion.

We compute the age field for the Antarctic ice sheet with both methods for a time-dependent simulation driven by a 242200 year surface temperature history derived from stable isotope data of the Vostok deep ice core, and discuss the differences of the age computation schemes. Emphasis is put on two regions: (i) western Dronning Maud Land (DML), where reconnaissance for a deep ice core within the European Project for Ice Coring in Antarctica (EPICA) is currently carried out, and (ii) the eastern part of central East Antarctica with the deep-ice-core locations Vostok and Dome C (the former completed, the latter currently drilled within EPICA). The Eulerian scheme provides good results except for the lower parts of the ice sheet where the numerical diffusion falsifies the computed ages. The particle-tracing scheme does not show this shortcoming; however, it yields ages generally somewhat too small because it does not yet account for the time-dependence of the ice flow.

1 Introduction

Ice cores are a valuable archive of the past climate containing data on the CO_2, CH_4 and dust contents of the atmosphere as well as proxy data on the atmospheric temperature. One major problem is to relate the depth of the ice core to the age of the ice, which is called dating of ice cores. In principle it is possible to measure the age stratigraphically by following the seasonal cycle of suitable tracers; however, this method is limited by ice-layer thinning. Therefore it is common practice to date the deeper parts of an ice core with the help of an ice-flow model. The traditionally applied flow models are of the Dansgaard-Johnson type [3]. The parameters of these one-dimensional, purely vertical models are adjusted to the conditions in the borehole using the

ice velocity and snowfall derived from the borehole as input, and steady-state conditions are usually assumed.

In this study, we discuss an alternative approach to ice-core dating based on the application of a transient, three-dimensional, dynamic/thermodynamic ice-sheet model (SICOPOLIS, Greve [6]). This model *computes* the englacial velocity field and therefore need not be driven by velocity *measurements* in the borehole. A further advantage is that an ice core can be dated preliminarily before it has actually been drilled.

Two different age-computation schemes are implemented in SICOPOLIS:

- Solution of the advective age equation in the Eulerian frame with the aid of some numerical diffusion (Huybrechts [11], Calov et al. [2]).
- Tracing of ice particles along their flowlines, connected with the age computation in the Lagrangian frame (Mügge [16]).

We compare both methods for a simulation of the Antarctic ice sheet. The attention is hereby focussed on two regions, namely (i) western Dronning Maud Land (DML), where ongoing field work prepares an ice core within the European Project for Ice Coring in Antarctica (EPICA, Jouzel et al. [14]), and (ii) the eastern part of central East Antarctica, where the ice cores Vostok (completed) and Dome C (EPICA, currently drilled) are situated (Fig. 1). For Vostok, the computed age profiles are further compared with the "Geophysical Metronome Time Scale" provided by Salamatin et al. [18].

2 Modelling of the Antarctic Ice Sheet

2.1 Ice-sheet model SICOPOLIS

SICOPOLIS is a 3-d dynamic/thermodynamic ice-sheet model based on the continuum-mechanical theory of polythermal ice masses [1,5,8,9]. It simulates the time-dependent extent, thickness, velocity, temperature, water-content and age for a grounded ice sheet in response to external forcing. Further, possible basal layers of temperate ice (ice at pressure melting point) are detected with high vertical resolution by fulfilling the Stefan-type conditions at the cold-temperate-transition surface. External forcing is specified by (i) mean annual air temperature above the ice, (ii) surface mass balance (accumulation, surface melting), (iii) sea level surrounding the ice sheet and (iv) geothermal heat flux from below. A more detailed description of SICOPOLIS can be found in Greve [6], Greve et al. [7].

The model domain for the Antarctic ice sheet consists of a 5341×4796 km rectangle in the stereographic plane with standard parallel 71°S, spanned by Cartesian coordinates x, y (the vertical coordinate is z). Horizontal resolution is 109 km, so that the domain is discretized by 50×45 grid points. Vertical resolution is 51 grid points in the cold-ice column, 11 grid points in the temperate-ice column (if existing) and 11 grid points in the lithosphere

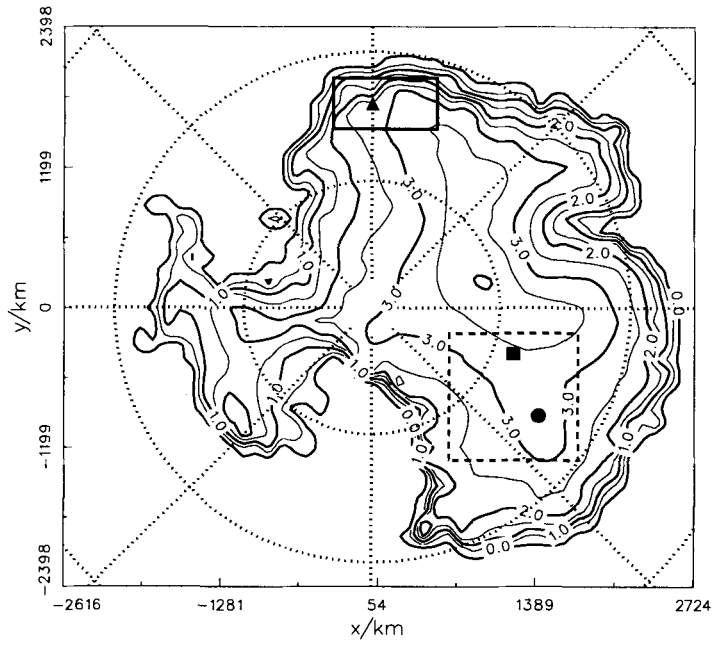

Fig. 1. Surface topography of the modern Antarctic ice sheet, by Drewry [4] (without ice shelves; in km a.s.l., contour spacing 500 m). Solid rectangle: DML; the small triangle within marks the proposal by Savvin et al. [20] for the EPICA drillsite position. Dashed square: Eastern part of central East Antarctica with the ice core positions Vostok (small square) and Dome C (small circle).

column. Time steps are 2.5 years for the dynamic evolution (topography, velocity) and 50 years for the thermodynamic evolution (temperature, water content, age).

2.2 Nesting for Dronning Maud Land

In order to provide model support for the planned EPICA core in DML, Savvin et al. [20] introduced a refined subgrid for the 872 × 436 km rectangle shown in Fig. 1, which is also applied here. Horizontal resolution of the subgrid is 10.9 km (refinement factor 10), so that the subgrid domain is discretized by 81 × 41 grid points. It is coupled to the coarse grid by boundary conditions at its margin which are interpolated field quantities of the coarse grid, and, in turn, it gives back the computed topography to the coarse grid at positions where coarse-grid and refined-grid points fall together (Savvin, [19]). The time steps for the refined DML computations are 0.1 years for the dynamic evolution and 1 year for the thermodynamic evolution.

2.3 Eulerian age computation

For the age of ice (the elapsed time since the ice particles settled on the surface as snowflakes), A, the purely advective (hyperbolic) evolution equation

$$\frac{dA}{dt} = 1 \tag{1}$$

holds (t is time, d/dt denotes the material time derivative which incorporates ice movement), with the corresponding Dirichlet-type boundary condition

$$A(z = h_{\mathrm{acc}}) = 0 \tag{2}$$

in the accumulation zones at the free surface $h_{\mathrm{acc}}(x, y, t)$. If regions of temperate ice exist, at the cold-temperate transition surface (CTS) the age is continuous.

Integration of Eq. (1) in the Eulerian frame of the numerical grid requires first to re-write it with the local time derivative $\partial/\partial t$ and explicit advection terms,

$$\frac{\partial A}{\partial t} + v_x \frac{\partial A}{\partial x} + v_y \frac{\partial A}{\partial y} + v_z \frac{\partial A}{\partial z} = 1 + D_{\mathrm{A}} \frac{\partial^2 A}{\partial z^2}, \tag{3}$$

where $v_{x,y,z}$ are the velocity components in x-, y- and z-direction. In order to achieve stable integration, the artificial vertical diffusion term $D_{\mathrm{A}}\,(\partial^2 A/\partial z^2)$ is added on the right-hand side [6,11], and for the diffusivity D_{A} the small value $5 \cdot 10^{-8}\,\mathrm{m^2\,s^{-1}}$ is used.

As the type of the age evolution equation has now changed from hyperbolic to parabolic, artificial boundary conditions for the ablation zones of the free surface, $h_{\mathrm{abl}}(x, y, t)$, and the entire ice base, $b(x, y, t)$, must be prescribed. Following Greve et al. [7], we use the Neumann-type conditions

$$\frac{\partial A}{\partial z}(z = h_{\mathrm{abl}}) = 0, \qquad \frac{\partial A}{\partial z}(z = b) = -\frac{m_{\mathrm{age}}}{S_{\mathrm{mean}}}, \tag{4}$$

where $S_{\mathrm{mean}} = 2.4\,\mathrm{cm}$ ice equiv. $\mathrm{a^{-1}}$ is the mean snowfall rate and $m_{\mathrm{age}} = 200$ the thinning factor.

The system (2), (3), (4) is integrated with an FTCS (forward time centered space) scheme and upstream discretization of the horizontal advection terms. This is the standard age computation method of SICOPOLIS; however, its disadvantage is that below approximately 85% depth the influence of the diffusion term overrides the solution of the physical equation (1), so that near the bedrock the results are not reliable (Calov et al. [2], Greve et al. [7]).

2.4 Lagrangian age computation (particle tracing)

The Eulerian age computation does not make efficient use of the very simple nature of Eq. (1). In the Lagrangian frame which follows the ice particles,

this equation can be discretized in a straightforward way without any artificial diffusion, and its solution becomes trivial. The numerical work in this approach is to find out for which positions in the ice body the solution holds, that is, to compute the particle paths $\boldsymbol{x}(t)$ ($\boldsymbol{x}$ is the position vector, see Fig. 2). The corresponding evolution equation is

$$\frac{d\boldsymbol{x}}{dt} = \boldsymbol{v}(x, y, z, t), \tag{5}$$

where $\boldsymbol{v}$ denotes the velocity field in the ice sheet.

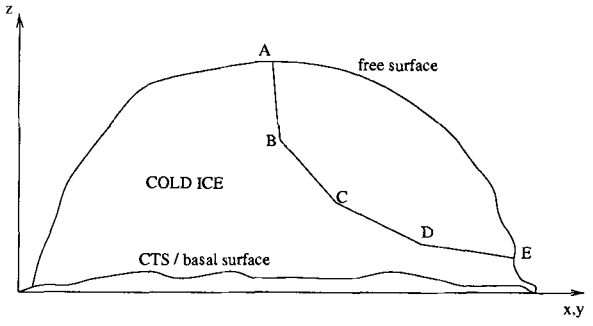

Fig. 2. Path of an ice particle through an ice sheet, starting from the deposition point A on the surface, along the positions B, C, D, until position E where the particle leaves the ice sheet by melting or calving.

The system of equations (1), (2), (5) is now solved directly in the cold-ice domain (temperature below pressure melting). We exclude the small regions of temperate ice for numerical simplicity, and because the presence of liquid water disturbs the well-defined stratigraphy anyway. The solution of Eq. (1) is very simple and leads to the statement that in one year an ice particle becomes one year older. However, the integration of Eq. (5) requires more numerical effort, it is performed by the conventional fourth-order Runge-Kutta scheme (Törnig & Spellucci [22]). The initial condition for Eq. (5) is that the trajectory of an ice particle deposited at time t_0 in the accumulation zone of the ice sheet starts at the free surface, that is

$$\boldsymbol{x}(t_0) = \Big(x_0,\, y_0,\, z = h_{\mathrm{acc}}(x_0, y_0, t_0)\Big). \tag{6}$$

The end of a trajectory is reached when the ice particle leaves the cold-ice region by either crossing the free surface from below (ablation), or crossing the ice base (basal melting) or the CTS (if the cold ice is underlain by a layer of temperate ice). Further, for numerical reasons the tracing of a particle trajectory is stopped when the particle reaches a region with less than 500 m ice thickness, which occurs close to the margin of the ice sheet.

Evidently, in order to solve Eq. (5) for particle trajectories, the three-dimensional velocity field $\boldsymbol{v}(\boldsymbol{x}, t)$ as well as the topography (free surface, bedrock, CTS) of the ice body must be known. As SICOPOLIS provides these quantities only at the nodes of the numerical grid, which, in general, do not fall together with the positions $\boldsymbol{x}$ of the traced particles, a suitable interpolation procedure must be applied. For this, we use the values of the nearest-neighbour grid points and average them with weights proportional to the inverse distance to the position $\boldsymbol{x}$.

In this study, the particle-tracing algorithm is run diagnostically with the SICOPOLIS output for the modern time slice only. This implies that the time dependence of the velocity and topography is neglected, and we compute trajectories and ages in a quasi-steady-state approximation based on modern streamlines instead of real trajectories. In order to avoid interpolating the spatially-scattered particle ages back on the numerical grid, the algorithm is further run backward in time, that is, the particles of any ice column whose age is computed are traced back to the ice surface by applying the negative velocity field. As a by-product this method yields the geographic origin of the ice in a given column.

Full coupling between SICOPOLIS and the particle-tracing algorithm with consideration of the time-dependent velocity field and re-interpolation of the computed ages from the cloud of particles on the numerical grid has not yet been implemented. This will be done in the near future.

2.5 Simulation set-up

The present state of the Antarctic ice sheet is modelled as the result of a paleoclimatic simulation from 242200 years BP until today, initialized by a previous 100000-year steady-state run for the conditions at 242200 years BP. The simulation is driven by surface-temperature and sea-level histories derived from the Vostok ice core (Jouzel et al. [13,15]) and the SPECMAP sea-level record (Imbrie et al. [12]), respectively, and for the present reference state of the surface temperature the parameterizations given by Huybrechts [10] are used. The accumulation input is based on the modern dataset by Giovinetto, Zwally and Bentley (personal communication, 1997; publication in preparation), modified by a time-dependent factor coupled linearly to the surface-temperature deviation from today (Calov et al. [2]). Surface melting is modelled by a degree-day approach with the parameters $\beta_{\mathrm{snow}} = 3\,\mathrm{mm\,w.e.\,d^{-1}K^{-1}}$ (snow melt), $\beta_{\mathrm{ice}} = 8\,\mathrm{mm\,w.e.\,d^{-1}K^{-1}}$ (ice melt), $P_{\mathrm{max}} = 60\%$ (firn saturation rate) and $\sigma_{\mathrm{stat}} = 5°\mathrm{C}$ (standard deviation for statistical air-temperature fluctuations) (Reeh [17]). Bedrock topography is by Drewry [4], complemented by recent high-resolution radio-echo-sounding data for DML measured and evaluated by the Alfred-Wegener-Institut für Polar- und Meeresforschung, Bremerhaven, Germany (Steinhage [21], Savvin et al. [20]). Further model parameters are listed in Table 1.

The particle-tracing algorithm is fed by the topography and velocity field of the simulated present ice sheet, and it is integrated over 500000 years with a time step of 50 years. As explained above, this yields the age profiles for selected ice columns in quasi-steady-state approximation.

For the nested DML domain the particle-tracing method operates on the refined grid. Particle-tracing results in this region are therefore based on the 10.9-km resolution instead of the coarse 109-km resolution of the entire ice sheet.

Table 1. Physical parameters used in the simulation of the Antarctic ice sheet.

Quantity	Value
gravity acceleration, g	$9.81\,\mathrm{m\,s^{-2}}$
density of ice, ρ	$910\,\mathrm{kg\,m^{-3}}$
power-law exponent, n	3
rate factor, $A(T',\omega)$[1]	cold ice: Arrhenius law[2] temperate ice: linear dependence on ω^2
flow-enhancement factor, E	5
heat conductivity of ice, κ	$9.828\,e^{-0.0057\,T[\mathrm{K}]}\,\mathrm{W\,m^{-1}K^{-1}}$
specific heat of ice, c	$(146.3 + 7.253\,T[\mathrm{K}])\,\mathrm{J\,kg^{-1}K^{-1}}$
latent heat of ice, L	$335\,\mathrm{kJ\,kg^{-1}}$
Clausius-Clapeyron gradient, β	$8.7 \cdot 10^{-4}\,\mathrm{K\,m^{-1}}$
basal sliding velocity, v_b	cold base: no-slip temperate base: Weertman-type sliding[2]
geothermal heat flux, q_geo	$54.6\,\mathrm{mW\,m^{-2}}$
isostatic time lag, τ_V	3 ka
asthenosphere density, ρ_a	$3300\,\mathrm{kg\,m^{-3}}$
density × specific heat of the lithosphere, $\rho_\mathrm{r} c_\mathrm{r}$	$2000\,\mathrm{kJ\,m^{-3}K^{-1}}$
heat conductivity of the lithosphere, κ_r	$3\,\mathrm{W\,m^{-1}K^{-1}}$

[1]Homologous temperature T' (relative to pressure melting), water content ω (mass fraction).
[2]For details see Greve et al. [7].

3 Results and Discussion

In the following we discuss age-depth profiles for the two ice cores Vostok, Dome C, and the EPICA DML drillsite proposed by Savvin et al. [20] (Fig. 1), computed with both the Eulerian and the Lagrangian particle-tracing method (henceforth referred to as "EM" and "PTM", respectively). For Vostok, the results can further be compared with the "Geophysical Metronome Time

Scale" (GMTS) by Salamatin et al. [18], which was obtained by first inferring a surface-temperature history from the measured temperature profile by transient 1-d modelling, and then matching this history to the measured deuterium (δD) profile.

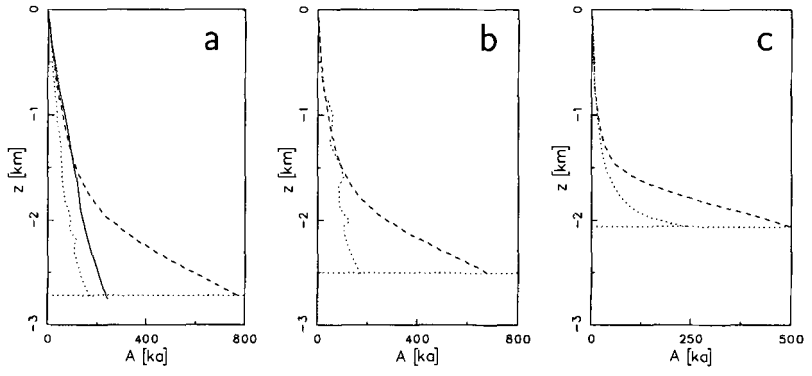

Fig. 3. Simulated age profiles at (a) Vostok, (b) Dome C, (c) EPICA DML drillsite proposed by Savvin et al. [20]. Dashed lines: Eulerian scheme. Dotted lines: particle-tracing method. Solid line in panel (a): GMTS age profile by Salamatin et al. [18]. The origins of the vertical coordinate, $z = 0$, correspond to the ice surface, the ice base is represented by the horizontal dotted lines.

Fig. 3a shows the age profiles computed with EM and PTM and the GMTS profile. The shape of the PTM curve agrees well with GMTS; however, it provides ages by approximately one third smaller. This difference can be explained with the quasi-steady-state assumption of PTM which uses only modern interglacial, rather large ice velocities to compute the age. In reality the deeper parts of the ice sheet have stored lower glacial temperatures and therefore smaller velocities, which leads to larger ages. By contrast, EM and GMTS agree quantitatively very well down to 1500 m depth due to the transient nature of the EM-based age computations. Further down EM yields much larger ages which reach as much as 780 ka at the base.

A similar behaviour becomes also evident for Dome C (Fig. 3b). Here EM and PTM fall closely together down to 1500 m depth, whereas further down EM ages become very (unrealistically?) large, and at the base the disagreement between the two methods reaches 500 ka. A probable explanation is that the applied thinning factor $m_{\mathrm{age}} = 200$ in the artificial basal boundary condition $(4)_2$, which does very well for Summit in central Greenland (Greve et al. [7]), is too large for central Antarctic locations. This points out very clearly the problem with the added numerical diffusion in the age equation (3) and the associated unphysical basal boundary condition.

For the EPICA DML drillsite proposed by Savvin et al. [20], situated at 73° 59′ S, 00° 00′ E, the computed EM and PTM ages (Fig. 3c) agree better

with each other than at Vostok and Dome C, the discrepancy at the base being approximately half of the values themselves. As the quasi-steady-state PTM ages tend to be somewhat too low in general (see above), the EM curve is probably more realistic also in the lower part of the ice column.

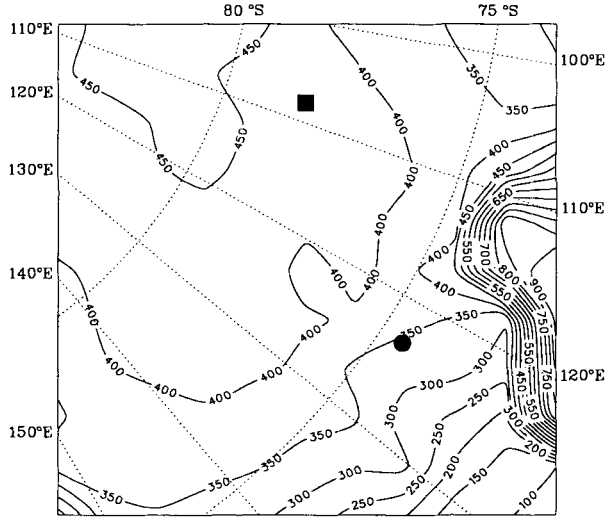

Fig. 4. Age at 85% depth (in ka) in the eastern part of central East Antarctica, computed with the Eulerian scheme. Square: Vostok. Circle: Dome C.

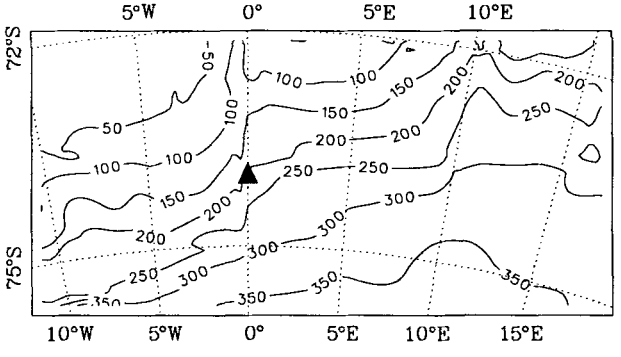

Fig. 5. Age at 85% depth (in ka) in DML, computed with the Eulerian scheme on the refined subgrid. Triangle: EPICA DML drillsite proposed by Savvin et al. [20].

In Figs. 4, 5 the EM ages at 85% depth are presented for the eastern part of central East Antarctica and DML, respectively. In the former case, the computed age is relatively uniform south of 75°S and decreases further north (coastward). A conspicuous exception to this is the zone between approximately 105°E and 125°E where the age increases sharply within a band

of 150 km width, probably an effect of the Aurora and Vincennes subglacial basins in this region. By contrast, the computed DML age distribution shows a more even decrease from the ice interior to the coast.

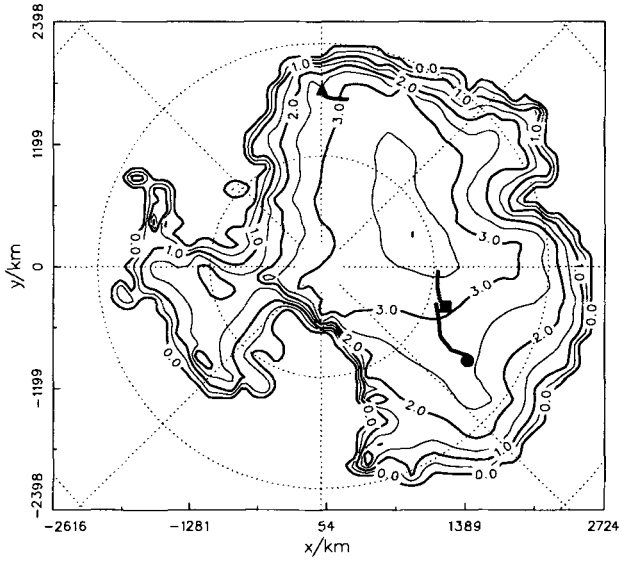

Fig. 6. Thick lines: Simulated geographical origin of the present ice columns at the EPICA DML drillsite proposed by Savvin et al. [20] (triangle), Vostok (square) and Dome C (circle). Background contours: simulated surface elevation, in km a.s.l.

A further interesting application of the particle-tracing method is to determine the geographical origin of a given borehole ice column, that is, the positions where the ice particles in the column were deposited on the surface as snowfall. Fig. 6 depicts the corresponding results for Vostok, Dome C and the EPICA DML drillsite proposed by Savvin et al. [20]. Evidently, for Vostok and Dome C the deeper ice was accumulated rather far from its present position, namely by approximately 500 km and 1000 km upstream toward Dome Argus (the highest point of the Antarctic ice sheet), respectively. However, the result for Dome C is doubtful because the local ice-elevation maximum is not reproduced by the simulation at this position, so that the simulated flow regime in the vicinity of Dome C is not that of an ice dome. For DML, the ice-origin line extends approximately 320 km upstream, so that the entire 2060 m thick column stems from within the DML domain marked in Fig. 1.

4 Conclusion and Outlook

Two numerical methods for the age computation in ice sheets, a Eulerian scheme with artificial diffusion and a Lagrangian particle-tracing scheme,

were applied to the Antarctic ice sheet. The Eulerian scheme works well in the upper parts of the ice sheet, but becomes increasingly unreliable further down because of the influence of the numerical diffusion. The particle-tracing method circumvents this shortcoming; however, it has been implemented only in a quasi-steady-state mode by now which leads to an underprediction of the ages.

The particle-tracing method has the potential to yield very accurate solutions to the age evolution problem. The next step will be to replace the diagnostic, quasi-steady-state mode by a real coupling with the ice-sheet model SICOPOLIS so that the trajectories are computed on the basis of the time-dependent velocity field. This entails the necessity to interpolate the computed particle ages back on the numerical grid, which can be achieved by triangulation of layers with equal particle ages (isochrones) and vertical interpolation between those layers.

Acknowledgments: We thank H. Miller and D. Steinhage of the Alfred-Wegener-Institut für Polar- und Meeresforschung, Bremerhaven, Germany, for permission to use the radio-echo-sounding data of Dronning Maud Land. The support by the Deutsche Forschungsgemeinschaft under project no. Hu 412/19-3 is gratefully acknowledged.

References

1. Calov, R. and K. Hutter (1997) Large scale motion and temperature distributions in land based ice shields – the Greenland Ice Sheet in response to various climatic scenarios. *Arch. Mech.*, **49** (5), 919-962.
2. Calov, R., A. Savvin, R. Greve, I. Hansen and K. Hutter (1998) Simulation of the Antarctic ice sheet with a three-dimensional polythermal ice sheet model, in support of the EPICA project. *Ann. Glaciol.*, **27**, 201-206.
3. Dansgaard, W. and S. J. Johnsen (1969) A flow model and a time scale for the ice core from Camp Century, Greenland. *J. Glaciol.*, **8** (53), 215-223.
4. Drewry, D. J. (1983) *Antarctica: Glaciological and geophysical folio.* Scott Polar Research Institute, University of Cambridge.
5. Greve, R. (1997a) A continuum-mechanical formulation for shallow polythermal ice sheets. *Phil. Trans. R. Soc. Lond.*, A **355**, 921-974.
6. Greve, R. (1997b) Application of a polythermal three-dimensional ice sheet model to the Greenland Ice Sheet: Response to steady-state and transient climate scenarios. *J. Climate*, **10** (5), 901-918.
7. Greve, R., M. Weis and K. Hutter (1998) Palaeoclimatic evolution and present conditions of the Greenland ice sheet in the vicinity of Summit: An approach by large-scale modelling. *Paleoclimates*, **2** (2-3), 133-161.
8. Hutter, K. (1982) A mathematical model of polythermal glaciers and ice sheets. *J. Geophys. Astrophys. Fluid Dyn.* **21**, 201-224.
9. Hutter, K. (1993) Thermo-mechanically coupled ice sheet response. Cold, polythermal, temperate. *J. Glaciol.*, **39** (131), 65-86.
10. Huybrechts, P. (1993) Glaciological modelling of the Late Cenozoic East Antarctic ice sheet: stability or dynamism? *Geografiska Annaler*, **75 A** (4), 221-238.

11. Huybrechts, P. (1994) The present evolution of the Greenland ice sheet: an assessment by modelling. *Global Planet. Change*, **9**, 39-51.
12. Imbrie, J., J. D. Hays, D. G. Martinson, A. McIntyre, A. C. Mix, J. J. Morley, N. G. Pisias, W. L. Prell and N. J. Shackleton (1984) The orbital theory of Pleistocene climate: Support from a revised chronology of the marine $\delta^{18}O$ record. In: A. Berger et. al. (eds.), *Milankovitch and climate, part I*, D. Reidel Publishing Company, Dordrecht, Holland, 269-305 (NATO ASI Series C: Mathematical and Physical Sciences 126).
13. Jouzel, J. and 16 others (1993) Extending the Vostok ice-core record of paleoclimate to the penultimate glacial period. *Nature*, **364**, 407-412.
14. Jouzel, J., K. Hammer, H. Miller, G. Orombelli, D. Peel and B. Stauffer (1994) European project for ice coring in Antarctica. Science Plan. [Available from Laboratoire de Modélisation du Climat et de l'Environnement, CEA/DSM SE Saclay, F-91191 Gif sur Yvette Cedex, France.]
15. Jouzel, J. and 14 others (1996) Climatic interpretation of the recently extended Vostok ice records. *Climate Dynamics*, **12**, 513-521.
16. Mügge, B. (1998) *Eisalterberechnung im antarktischen Eisschild mit einem Algorithmus zur Teilchenverfolgung.* Diploma thesis, Institut für Mechanik, Technische Universität Darmstadt, Germany.
17. Reeh, N. (1991) Parameterization of melt rate and surface temperature on the Greenland Ice Sheet. *Polarforschung*, **59** (3), 113-128.
18. Salamatin, A. N., V. Y. Lipenkov, N. I. Barkov, J. Jouzel, J. R. Petit and D. Raynaud (1998) Ice core age dating and paleothermometer calibrations based on isotope and temperature profiles from deep boreholes at Vostok Station (East Antarctica). *J. Geophys. Res.*, **103** (D8), 8963-8977.
19. Savvin, A. (1999) *Grenzschichttheorie nichtlinearer Kriechströmungen und ihre Anwendung auf das EPICA-Vorhaben.* Ph.D. thesis, Institut für Mechanik, Technische Universität Darmstadt, Germany (received 14 April 1999, accepted 28 April 1999).
20. Savvin, A., R. Greve, R. Calov, B. Mügge and K. Hutter (1999) Simulation of the Antarctic ice sheet with a 3-d polythermal ice-sheet model, in support of the EPICA project. Part II: Nested high-resolution treatment of Dronning Maud Land. *Ann. Glaciol.*, **30** (submitted).
21. Steinhage, D. (1999) Ph.D. thesis in preparation, Alfred-Wegener-Institut für Polar- und Meeresforschung, Bremerhaven, Germany.
22. Törnig, W. and P. Spellucci (1990) *Numerische Mathematik für Ingenieure und Physiker. Band 2: Numerische Methoden der Analysis.* Springer-Verlag.

(Received 14 April 1999, accepted 16 April 1999)

Three-Dimensional Isothermal Boundary Layer Solutions of Slow Creeping Ice Flows Based on the Shallow Ice Approximation

Alexey A. Savvin[1], Kolumban Hutter[1], and Alexander A. Dorfmann[2]

[1]Institute of Mechanics III, University of Technology Darmstadt, Hochschulstraße 1, D-64289 Darmstadt, Germany
[2]International Academy of Information, Harnackring 69, D-21031 Hamburg, Germany

Abstract. We study creeping, isothermal free surface flows of a non-linear power law fluid subject to gravity along straight or curved inclined basal surfaces and having a free surface that is subject to prescribed accumulation/ablation sources. The boundary-layer approximation of the Stokes equations corresponds to the equations in the Shallow-Ice Approximation (SIA), but here they are presented in a Cartesian co-ordinate setting as well as in topography-following orthogonal co-ordinates. Under isothermal conditions the govering equations, using Glen-type power law rheology, allow semi-analytical representation of the solutions of the three-dimensional ice flows. For plane flow explicit analytic solutions can be constructed. These solutions depend on the slope angle and the mass flux, the integrated accumulation/ablation function. We graphically represent depth profiles, streamwise and normal velocity components and shear stresses and illustrate how these quantities react to variations in the two parameters.

1 Introduction

Slow creeping flow of a non-Newtonial fluid under the action of gravity along straight or curved inclined surfaces is analysed under isothermal conditions and when the radii of curvature of the basal surface are large, so that boundary layer approximations are applicable. The model equations are pertinent to shallow ice flow in nearly temperate glaciers and ice sheets. The model equations stay in-between the one-dimensional kinematic models such as that of Dansgaard and Johnsen [2] which allow a fast but rough estimation of the mechanical behaviour of the ice sheet flow, and the more detailed three-dimensional (polythermal) models [3,5] which account for the spatially and temporally varying climatic input and deliver a fairly realistic representation of a glacier or ice sheet through time.

We propose here a class of models which lies between these two extremes, but also improves to some extent on the latter models. More specifically the govering equations of the Stokes flow of a rheologically non-linear fluid are presented in orthogonal curvilinear co-ordinates. If two sets of co-ordinate

lines of this system are chosen to lie within the basal surface and the third is orthogonal to these, and if at any surface point the principal curvature radii are large in comparison to the local ice thickness, and if the flow is essentially parallel to the basal surface, then the prerequisites of a boundary layer formulation are fulfilled. Thus curvilinear boundary layer equations of rheologically non-linear Stokes flow are derived; they are the analogues to the shallow ice equations in Cartesian co-ordinates [4]. For the general non-isothermal situation these equations allow a numerical solution technique akin to the shallow ice procedure.

Here we limit attention to the steady isothermal situation. It allows an elegant description of the flow with analytical representation of the solution (if the rheological behaviour is limited to power law behaviour). The results for the thickness and velocity distributions are expressible in two parameters, an inclination angle of the basal surface and a dimensionless accumulation flux; some cases are graphically represented, and it is shown how the solutions react to the variation of these parameters.

2 Asymptotic Model

Consider slow creeping flow under steady isothermal conditions of a non-Newtonian fluid with free surface subject to gravity (fig. 1). The mathematics of such Stokes flows is simplified by the assumption that field variables vary primarily perpendicular to the main flow direction and much less in the direction of the flow. In fluid mechanics the reduced equations describing this situation are the boundary layer equations, formulated in Cartesian or topography following co-ordinates; in models describing ice flow in ice sheets, these equations correspond to those of the shallow ice approximation (SIA), i.e. the asymptotic limit of vanishing aspect ratio of a typical height to length of the considered ice masses.

We treat the isothermal case as an approximation to the fully temperate situation or as a first rough estimate for the non-isothermal case, and consider power law behaviour for which analytical or at least semi-analytical solutions can be constructed. Extension to non-isothermal situations with prescribed temperature is possible, but solutions are then only numerically constructable.

2.1 Flow along an inclined plane

Let $\mathbf{x} = (x_{1,2}, z)$ be a Cartesian co-ordinate system with $x_{1,2}$ being in the plane and z perpendicular to it. Let, moreover, α be the angle of inclination of the plane and choose x_1 to lie in the direction of steepest descent. In the ensuing analysis we shall employ the short-hand notation for the following ordered pairs of physical quantities:

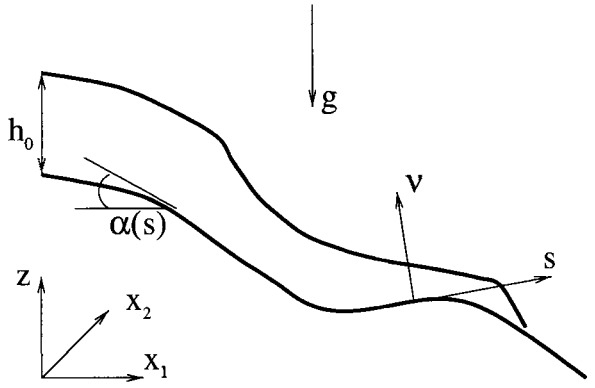

Fig. 1. Schematic representation of an ice tongue on a curved bed.

$$
\begin{aligned}
&\boldsymbol{\tau} = (\tau_{x_1 z},\ \tau_{x_2 z}) && \text{shear stresses,}\\
&\nabla = \left(\frac{\partial}{\partial x_1},\ \frac{\partial}{\partial x_2}\right) && \text{in-plane Nabla operator,}\\
&\mathbf{g}_1 = (g \sin\alpha,\ 0) && \text{in-plane gravity component,}\\
&\mathbf{u} = (u,\ v) && \text{in-plane velocity components.}
\end{aligned}
\tag{1}
$$

The model will also involve the variables

$$
\begin{aligned}
&\rho && \text{density,}\\
&p && \text{pressure,}\\
&w && \text{velocity component perpendicular to plane,}\\
&g_2 = g\cos\alpha && \text{gravity component perpendicular to plane.}
\end{aligned}
\tag{2}
$$

The equations of motion in the boundary layer or SIA-approximation are

$$\frac{\partial \boldsymbol{\tau}}{\partial z} - \nabla p + \rho \mathbf{g}_1 = \mathbf{0}, \tag{3}$$

$$-\frac{\partial p}{\partial z} - \rho g_2 = 0. \tag{4}$$

They ignore in-plane longitudinal stress deviator effects. The material law relating stretching and stress deviator takes the form

$$\frac{\partial \mathbf{u}}{\partial z} = K f(|\boldsymbol{\tau}|)\boldsymbol{\tau},\ f(|\boldsymbol{\tau}|) = |\boldsymbol{\tau}|^{n-1},\ n \in (0,\ \infty), \tag{5}$$

where f is the creep response function (a fluidity), K is a constant and the power law representation is used here for illustration in view of the glaciological application. We suppose the fluid to be density preserving, so that

$$\frac{\partial w}{\partial z} + \nabla \cdot \mathbf{u} = 0; \tag{6}$$

i.e., the normal velocity w is diagnostically determined from the in-plane velocity components.

We impose the no-slip condition at the base, $z = 0$, the stress free condition at the free surface, $z = h(x_1, x_2)$, and the kinematic condition accounting for accumulation, viz.,

$$z = h: \quad p = \boldsymbol{\tau} = 0, \quad \mathbf{u}\nabla h - w = a, \tag{7}$$

$$z = 0: \quad \mathbf{u} = \mathbf{0}, \quad w = 0. \tag{8}$$

The union of (3)-(8) defines the boundary value problem of the shallow free surface flow over an inclined plane.

2.2 Transformation of the equations

It is a routine matter to derive the integrated mass balance law via a depth integration of the continuity equation (6) and by imposing the kinematic boundary conditions (7_2) and (8), to arrive at

$$\nabla \cdot \mathbf{U} = a, \quad \text{where } \mathbf{U} := \int_0^{h(x_1,x_2)} \mathbf{u} dz. \tag{9}$$

$\mathbf{U}$ is called the integrated transport and so, depending whether a is positive or negative, this transport is either diverging or contracting. Futhermore, by integrating the hydrostatic pressure equation (4) subject to the boundary condition (7_1) yields

$$p = \rho g_2 (h - z), \tag{10}$$

so that (3) becomes

$$\frac{\partial \boldsymbol{\tau}}{\partial z} + \boldsymbol{\phi} = 0, \tag{11}$$

where

$$\boldsymbol{\phi} = \rho g(\mathbf{G}_1 - G_2 \nabla h), \ (\mathbf{G}_1;\ G_2) = (\mathbf{g}_1;\ g_2)/g. \tag{12}$$

Note that $\boldsymbol{\phi}$ is only a function of $x_{1,2}$ and t, but not z; thus (11) together with the no-shear boundary condition at the upper surface yields

$$\boldsymbol{\tau} = \boldsymbol{\phi}(h - z), \tag{13}$$

implying

$$\frac{\partial \mathbf{u}}{\partial z} = K\, |\boldsymbol{\phi}|^{n-1} (h - z)^n \boldsymbol{\phi}. \tag{14}$$

A further integration subject to the boundary condition (8_1) leads to the in-plane velocity field,

$$\mathbf{u} = \frac{K}{n+1} |\boldsymbol{\phi}|^{n-1} \boldsymbol{\phi} \left[h^{n+1} - (h-z)^{n+1}\right], \tag{15}$$

from which

$$\mathbf{U} = \frac{K}{n+2} |\boldsymbol{\phi}|^{n-1} \boldsymbol{\phi} h^{n+2} \tag{16}$$

may be deduced. This equation determines the transport, if the distribution of the height is known. The latter follows if (16) is substituted into (9),

$$\nabla \cdot \left(|\boldsymbol{\beta}|^{n-1} \boldsymbol{\beta} h^{n+2}\right) = \frac{(n+2)a}{K(\rho g)^n}, \tag{17}$$

or

$$\begin{aligned} &|\boldsymbol{\beta}|^{n-1} h^{n+2} \nabla \boldsymbol{\beta} + 2(n+2) |\boldsymbol{\beta}|^{n-1} \boldsymbol{\beta} h^{n+1} \nabla h \\ &+(n-1) |\boldsymbol{\beta}|^{n-2} \boldsymbol{\beta} h^{n+2} \nabla |\boldsymbol{\beta}| = \frac{(n+2)a}{K(\rho g)^n}, \end{aligned} \tag{18}$$

where

$$\boldsymbol{\beta} = \boldsymbol{\phi}/\rho g = \mathbf{G}_1 - G_2 \nabla h, \tag{19}$$

from which, using (12_2), (1) and (2), we deduce

$$\begin{aligned} &\nabla \boldsymbol{\beta} = -\cos\alpha \Delta h, \quad |\boldsymbol{\beta}| = \sqrt{\left(\sin\alpha - \cos\alpha \frac{\partial h}{\partial x}\right)^2 + \left(\cos\alpha \frac{\partial h}{\partial y}\right)^2}, \\ &\nabla |\boldsymbol{\beta}| = \frac{\cos\alpha}{|\boldsymbol{\beta}|} \left(-\frac{\partial^2 h}{\partial x^2} + \frac{\partial^2 h}{\partial x \partial y}, -\frac{\partial^2 h}{\partial x \partial y} + \frac{\partial^2 h}{\partial y^2}\right); \end{aligned} \tag{20}$$

$\Delta(\cdot)$ is the plane Laplacian. For a Newtonian fluid ($n = 1$) equation (18) takes the form

$$h^3 \Delta h + 3h^2 \left((\nabla h)^2 - \tan\alpha \frac{\partial h}{\partial x}\right) = -\frac{3a}{K\rho g \cos\alpha}. \tag{21}$$

Finally note that the divergence equation (9) may be transformed to global form by integrating both sides of (9) over an arbitrary closed domain Ω of the ice layer with boundary $\partial\Omega$; together with the divergence theorem this yields

$$\int_\Omega \nabla \cdot \mathbf{U} dx^2 = \int_{\partial\Omega} \mathbf{U} \cdot \mathbf{n} ds = \int_\Omega a dx^2 =: Q, \tag{22}$$

in which dx^2 is the area element, ds the arc length along $\partial\Omega$ and $\mathbf{n}$ the unit vector perpendicular to $\partial\Omega$.

Equation (17) is a nonlinear partial differential equation of elliptic type and second order for which equation (22) serves as a constraint condition.

2.3 Exact analytical solution of the plane problem

Assume that no field variable possesses an x_2-dependence, $\partial(\cdot)/\partial x_2 = 0$. Consider the interval $x \in [0, x_\bullet]$ and look for a solution of the one-dimensional analogue of (17),

$$\frac{d}{dx}\left(\beta^n h^{n+2}\right) = \frac{(n+2)a}{K(\rho g)^n}, \tag{23}$$

which after integration between $x = 0$ and $x = x_\bullet$ becomes

$$\beta^n h^{n+2} = \frac{(n+2)Q}{K(\rho g)^n}, \quad \text{where } Q = \int_0^{x_\bullet} a(x)dx, \tag{24}$$

with

$$\beta = \sin\alpha - \cos\alpha h', \quad \text{where } h' := \frac{dh}{dx}. \tag{25}$$

Substituting (25) into (24) and solving the resulting equation for h' yields

$$h' = \tan\alpha - \frac{1}{\cos\alpha}\left[\frac{(n+2)Q}{K(\rho g h)^n h^2}\right]^{\frac{1}{n}}. \tag{26}$$

This ODE of first order describes the x-dependence of h. Non-dimensionalizing by

$$\bar{h} = \frac{h}{h_0}, \quad \bar{x} = \frac{x}{h_0}, \tag{27}$$

where $h_0 = h(x = 0)$, yields

$$\frac{d\bar{h}}{d\bar{x}} = \tan\alpha\left(1 - \left(\frac{\bar{h}_*}{\bar{h}}\right)^{\frac{n+2}{n}}\right), \tag{28}$$

$$\bar{h}_* := \left(\frac{1}{\sin\alpha}\right)^{\frac{n}{n+2}}\left(\frac{(n+2)Q}{K(\rho g)^n h_0^{n+2}}\right)^{\frac{1}{n+2}}. \tag{29}$$

Equation (28) shows that there are basically three distinct flow configurations, namely

$$\begin{aligned} &1.\ \ \bar{h} = \bar{h}_*, \quad \bar{h}' = 0, \quad h = Const, \\ &2.\ \ \bar{h} > \bar{h}_*, \quad \bar{h}' > 0, \quad h \nearrow, \\ &3.\ \ \bar{h} < \bar{h}_*, \quad \bar{h}' < 0, \quad h \searrow. \end{aligned} \tag{30}$$

Case (3) corresponds to a snout configuration with $\bar{h}$ monotonically decreasing with $\bar{x}$ until the snout $\bar{h} = 0$ is reached. In the immediate neighbourhood of the snout the validity of the model is questionable since $\bar{h}'$ is large and

the SIA assumptions are no longer satisfied. Case (2) yields a monotonically inceasing $\bar{h}$, not corresponding to a realistic situation, whereas $\bar{h} = \bar{h}_*$ (case (1)) corresponds to the slab solution.

The formal integral of (28) subject to the initial condition $\bar{h}(0) = 1$ is

$$\bar{x} \tan \alpha = \bar{h}_* \int_{\bar{h}/\bar{h}_*}^{1} \frac{\psi^{\frac{n+2}{n}} d\psi}{1 - \psi^{\frac{n+2}{n}}}, \tag{31}$$

from which the snout position $\bar{x}_\bullet$ follows by putting $\bar{h} = 0$,

$$\bar{x}_\bullet \tan \alpha = \bar{h}_* \int_{0}^{1} \frac{\psi^{\frac{n+2}{n}} d\psi}{1 - \psi^{\frac{n+2}{n}}}. \tag{32}$$

The integrals (31) or (32) are meaningful for $\psi \in [0, 1]$, and the singularity arising at $\psi = 1$ is integrable for all $n > 0$. Writing finally $\xi = \psi^{(n+2)/n}$, equation (32) takes a standard form, expressible in terms of the Gaussian hypergeometric function ${}_2F_1$ [1,9], viz.,

$$\bar{x}_\bullet \tan \alpha = \bar{h}_*^{-1} \frac{n}{2(n+1)} \, {}_2F_1 \left(1, \frac{2(n+1)}{n+2}; \frac{3n+4}{n+2}; \frac{1}{\bar{h}_*^{\frac{n+2}{n}}} \right). \tag{33}$$

Similarly,

$$\begin{aligned} (\bar{x}_\bullet - \bar{x}) \tan \alpha &= \bar{h}_* \int_{0}^{\bar{h}/\bar{h}_*} \frac{\psi^{\frac{n+2}{n}} d\psi}{1 - \psi^{\frac{n+2}{n}}} = \\ &= \bar{h}_*^{-1} \frac{n}{2(n+1)} \, {}_2F_1 \left(1, \frac{2(n+1)}{n+2}; \frac{3n+4}{n+2}; \left(\frac{\bar{h}}{\bar{h}_*} \right)^{\frac{n+2}{n}} \right) \end{aligned} \tag{34}$$

describes the distance from the snout as a function of $\bar{h}$ and $\bar{h}_*$. Inverting (34) yields

$$\bar{h} = \bar{h}_* \left({}_2F_1^{-1} \left[(\bar{x}_\bullet - \bar{x}) \, \bar{h}_* \frac{2(n+1)}{n} \tan \alpha, n \right] \right)^{\frac{n}{n+2}}, \tag{35}$$

in which ${}_2F_1^{-1}$ is the inverse function of ${}_2F_1$, describing $\bar{h}$ as a function of $\bar{h}_*$ and $\bar{x}_\bullet - \bar{x}$.

Graphical representation of the solution (35) will be shown below. Here it may suffice to state that for $n = 1$ and $n = 2$ solutions can be expressed in terms of elementary functions [9],

for n=1

$$\bar{x}_\bullet \tan\alpha = \left\{ \frac{\bar{h}_*}{\sqrt{3}} \arctan\frac{2+\bar{h}_*}{\sqrt{3}\bar{h}_*} - \left[1 + \frac{\bar{h}_*}{3} \ln\frac{\bar{h}_* - 1}{\sqrt{1+\bar{h}_*+\bar{h}_*^2}} + \frac{\pi\bar{h}_*}{6\sqrt{3}} \right] \right\}, \quad (36)$$

$$(\bar{x}_\bullet - \bar{x}) \tan\alpha = \frac{\bar{h}_*}{\sqrt{3}} \arctan\frac{2\bar{h}+\bar{h}_*}{\sqrt{3}\bar{h}_*} -$$

$$- \left[\bar{h} + \frac{\bar{h}_*}{3} \ln\frac{\bar{h}_* - \bar{h}}{\sqrt{\bar{h}^2+\bar{h}\bar{h}_*+\bar{h}_*^2}} + \frac{\pi\bar{h}_*}{6\sqrt{3}} \right]; \quad (37)$$

and for $n = 2$

$$\bar{x}_\bullet \tan\alpha = \left[\frac{\bar{h}_*}{2} \ln\left|\frac{1+\bar{h}_*}{1-\bar{h}_*}\right| - 1 \right], \quad (38)$$

$$(\bar{x}_\bullet - \bar{x}) \tan\alpha = \left[\frac{\bar{h}_*}{2} \ln\left|\frac{\bar{h}+\bar{h}_*}{\bar{h}-\bar{h}_*}\right| - \bar{h} \right]. \quad (39)$$

2.4 Motion along a curved bedrock

Consider now an uneven basal surface with mean and Gaussian curvatures that are small such that principal radii of curvature are of the order of the horizontal extent of the ice sheet. Under such conditions it is meaningful to use a curvilinear co-ordinate setting q_i $(i = 1, 2, 3)$ with orthogonal metric. Such co-ordinates are characterized by the Lamé metric coefficients H_i [6]. In these coordinates the equations of motion, the continuity equation and the strain rate-stress relationship take the forms

$$\rho F_i - \frac{1}{H_i}\frac{\partial p}{\partial q_i} +$$

$$+ \frac{1}{H_i} \sum_{k=1}^{3} \left\{ \frac{1}{H_1 H_2 H_3} \frac{\partial}{\partial q_k} \left(\frac{H_1 H_2 H_3 H_i}{H_k} \tau_{ik} \right) - \tau_{kk} \frac{\partial \ln H_k}{\partial q_i} \right\} = 0, \quad (40)$$

$$\sum_{k=1}^{3} \frac{\partial}{\partial q_k} \left(\frac{v_k H_1 H_2 H_3}{H_k} \right) = 0, \quad (41)$$

$$\hat{\varepsilon} = K |\hat{\tau}|^{n-1} \hat{\tau}, \quad (42)$$

in which F_i are the physical components of the gravity force; $\hat{\varepsilon}$, $\hat{\tau}$ and $|\hat{\tau}|$ are, respectively, the strain rate tensor, the stress deviator and the root of its second invariant. The components of the strain rate tensor are

$$\varepsilon_{ik} = \frac{1}{H_k}\frac{\partial v_i}{\partial q_k} + \frac{1}{H_i}\frac{\partial v_k}{\partial q_i} -$$

$$- \frac{1}{H_k H_i} \left(v_i \frac{\partial H_i}{\partial q_k} + v_k \frac{\partial H_k}{\partial q_i} \right) + 2\delta_{ik} \sum_{n=1}^{3} \frac{v_n}{H_n} \frac{\partial \ln H_i}{\partial q_n}, \quad (43)$$

in which δ_{ik} is the Kronecer symbol and v_n $(n = 1, 2, 3)$ are the physical components of the velocity field.

Suppose that the base is a sufficiently smooth surface. Within this surface we choose a set of orthogonal geodetic curves and denote these by $\mathbf{s} = (s_1, s_2)$ [7]. At any surface point the normal vector defines the third spatial direction, here denoted by ν. Thus,

$$\mathbf{x} \to (\mathbf{s} = (s_1, s_2), \nu), \quad \mathbf{v} \to (\mathbf{u} = (u_1, u_2), w) \tag{44}$$

define the position in $\mathbb{R}^3$ and the vector $\mathbf{v}$. Because of the orthogonality of the metric, the line increment is given by

$$(ds)^2 = H_1^2(ds_1)^2 + H_2^2(ds_2)^2 + H_3^2(d\nu)^2 \tag{45}$$

with the Lamé coefficients

$$H_1 = 1 + k_{11}(\mathbf{s})\nu, \quad H_2 = 1 + k_{22}(\mathbf{s})\nu, \quad H_3 = 1, \tag{46}$$

in which $k_{ij} = \partial\alpha_i/\partial s_j$ are the curvatures of the geodetic lines. Referred to the geodetic lines, the components of the gravity field take the forms

$$\mathbf{g}_1 = g \begin{Bmatrix} \sin\alpha_1 \cos\alpha_2 \\ \cos\alpha_1 \sin\alpha_2 \end{Bmatrix}, \quad g_2 = g \cos\alpha_1 \cos\alpha_2. \tag{47}$$

Finally we note that the metric (45), (46) is only meaningful as long as normals erected at neighbouring points of the surface do not intersect, i.e., as long as local ice thicknesses measured in the direction of ν are smaller than the smaller of the two radii of curvature of the geodetic lines.

Subjecting the system of equations (40)-(43) to the scaling of the boundary layer theory [8], i.e., letting

$$\begin{gathered} \nu \sim h_0, \; s \sim L, \; u_s \sim u_0, \; u_\nu \sim u_0 \frac{h_0}{L}, \\ \tau_{\nu s} \sim \tau_{ss} \sim \tau_{\nu\nu} \sim \tau_0, \; \frac{\partial}{\partial \nu} \sim \frac{1}{h_0}, \; \frac{\partial}{\partial s} \sim \frac{1}{L}, \end{gathered} \tag{48}$$

where h_0, u_0, τ_0, L are typical values of height, streamwise velocity, stress and length, and supposing that $h_0/L << 1$ and $h_0 k_{ij} << 1$, boundary layer equations much like those presented above for the Cartesian setting are deduced. We are using here the integrating procedure of boundary layer theory in the same way as for the flow along an inclined plane [10] to reach the equation (17) with

$$\begin{gathered} U = \int_0^h u d\nu, \quad \nabla = \left(\frac{\partial}{\partial s_1}, \frac{\partial}{\partial s_2} \right), \\ \mathbf{G}_1 = \begin{Bmatrix} \sin\alpha_1 \cos\alpha_2 \\ \cos\alpha_1 \sin\alpha_2 \end{Bmatrix}, \; G_2 = \cos\alpha_1 \cos\alpha_2. \end{gathered} \tag{49}$$

In this case the equation $(20)_2$ takes the following form

$$|\beta| = \cos\alpha_1 \cos\alpha_2 \times$$
$$\times\sqrt{(\tan^2\alpha_1 + \tan^2\alpha_2) - 2\left(\tan\alpha_1 \frac{\partial h}{\partial s_1} + \tan\alpha_2 \frac{\partial h}{\partial s_2}\right) + (\nabla h)^2}. \tag{50}$$

For Newtonian fluids ($n = 1$), equation (17) reduces to

$$h^3 \Delta h + 3h^2(\nabla h)^2 - h^2 \left\{ \frac{\partial h}{\partial s_1} [3\tan\alpha_1 + h(k_{11}\tan\alpha_1 + k_{21}\tan\alpha_2)] \right.$$
$$\left. + \frac{\partial h}{\partial s_2} [3\tan\alpha_2 + h(k_{12}\tan\alpha_1 + k_{22}\tan\alpha_2)] \right\} = -\frac{3a}{K\rho g \cos\alpha_1 \cos\alpha_2}. \tag{51}$$

For 2-d flows we may choose $\alpha_2 = 0$, $\partial(\cdot)/\partial s_2 = 0$, and then deduce

$$\frac{d\bar{h}}{d\bar{s}} = \tan\alpha \left(1 - \left(\frac{\bar{h}_*}{\bar{h}}\right)^{\frac{n+2}{n}}\right); \tag{52}$$

thus, the same equation as (28) with $\bar{x}$ replaced by $\bar{s}$ and the constant α replaced by the function $\alpha(\bar{s})$ is obtained. $\bar{h}_*$ is also given by (29), but

$$Q = \int_0^{s_\bullet} a(\bar{s}, t) d\bar{s}. \tag{53}$$

2.5 Axisymmetric flow

This is the simplest nontrivial case for which orthogonal curvilinear coordinates are employed. Let $\bar{s}$ be the length measured along the generator $r(\bar{s})$ of the axisymmetric bedrock. With $(u_s,\ u_\nu)$ being the physical components of the velocity field in the radial planes, the continuity equation takes the form

$$\frac{\partial r u_s}{\partial s} + \frac{\partial r u_\nu}{\partial \nu} = 0, \tag{54}$$

or, after an integration in ν,

$$u_\nu = -\frac{1}{r}\int_0^\nu \frac{\partial (r u_s)}{\partial s} d\nu. \tag{55}$$

Substituting this into $(7)_2$, or

$$r u_s \frac{\partial u}{\partial s} - r u_\nu = r a,$$

yields, after a simple computation,

$$\frac{d}{ds}\int_0^h r(s)u_s d\nu = ar, \tag{56}$$

which upon a further integration in s becomes

$$\underbrace{\int_0^h r(s)u_s(s,\nu)d\nu}_{U_1=r(s)U} = \underbrace{\int_0^{s_\bullet} a(s)r(s)ds}_{:=Q_1}, \tag{57}$$

with

$$U = \frac{K(\rho g)^n \beta^n}{n+2} h^{n+2}, \quad \beta = \sin\alpha - \frac{dh}{ds}\cos\alpha. \tag{58}$$

Therefore,

$$\beta = \left(\frac{Q_1(n+2)}{r(\bar{s})K[h(\bar{s})]^{n+2}(\rho g)^n}\right)^{\frac{1}{n}}, \tag{59}$$

or

$$\frac{d\bar{h}}{d\bar{s}} = \tan\alpha\left[1 - \left(\frac{1}{\bar{r}(\bar{s})}\right)^{\frac{1}{n}}\left(\frac{\bar{h}_*}{\bar{h}}\right)^{\frac{n+2}{n}}\right], \tag{60}$$

with

$$\bar{h}_* = \left[\left(\frac{1}{\sin\alpha}\right)^n \frac{(n+2)Q_1}{K(\rho g)^n}\right]^{\frac{1}{n+2}}. \tag{61}$$

Once the bedrock profile is given, equation (61) describes the free surface profile. The discussion of existence of monotonically decreasing profiles parallels that given earlier and will not be repeated here.

3 Results and Discussion

Consider first plane flow of ice down an inclined plane. Fig. 2 displays dimensionless thickness profiles $\bar{h}(\bar{x})$ for $\alpha = 5°$ and $30°$, respectively and four different values of $\bar{h}_*$ as indicated in the figure caption. It is evident that with decreasing value of $\bar{h}_*$ the length profile of the ice approches more and more the slab solution that is attained for $\bar{h}_* = 1$. It is also observable that the snout is reached by the profile with a vertical tangent; indeed (28) possesses the local near-snout solution of which the derivative is infinite.

Clearly, if $\bar{h}_* < 1$, then the sheet thickness will grow with growing $\bar{x}$-coordinate, a situation that is physically not relevant, because the ice thickness

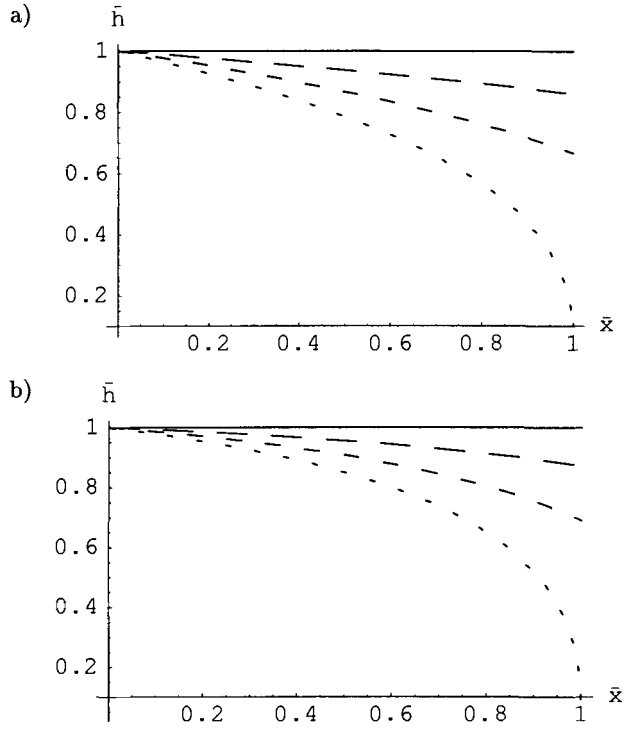

Fig. 2. Ice thickness profiles for a) $\alpha = 5°$ and $\bar{h}_* = 0.089$ (solid), 0.202 (long dashed), 0.315 (dashed) and 0.428 (dotted); b) $\alpha = 30°$ and $\bar{h}_* = 0.5$ (solid), 0.558 (long dashed), 0.616 (dashed) and 0.676 (dotted).

would grow to infinity as $\bar{x} \to \infty$; this simply follows from equation (28) since $d\bar{h}/d\bar{x} > 0$ in this case. Physically this case corresponds to large slope angles and small Q. When $\bar{h}_* > 1$, the thickness and total length of the layer are bounded. For this case the streamwise and normal velocity components and the shear stress components are displayed in Figs. 3 and 4, respectively. Accoding to these figures the absolute values of the velocity components grow with increasing $\bar{x}$. On the other hand, the shear stresses are lineary distributed, as expected.

Next consider plane boundary layer flow along a curved bed, of which the inclination angle is given by

$$\alpha(\bar{s}) = A\left(B - \bar{s}^C\right) \tag{62}$$

in which C determines the shape of the base, AB gives the initial value of α and A measures the difference $\alpha|_{\bar{s}=0} - \alpha|_{\bar{s}=1}$. Fig. 5 displays the thickness distribution $\bar{h} = \bar{h}(\bar{s})$ for different angles α (different values of the coefficient B) but fixed $\bar{h}_* = 0.3$ (panel a) and for different values of $\bar{h}_*$ but fixed

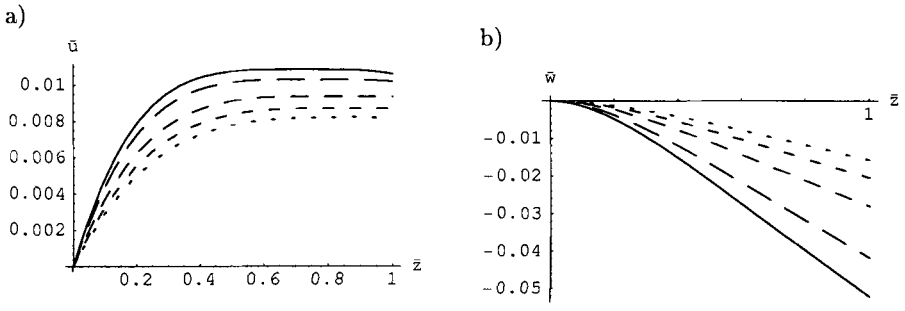

Fig. 3. Velocity profiles for $\alpha = 5°$ and $\bar{h}_* = 0.315$ a) streamwise velocity, b) velocity perpendicular to the base. Here the following notation is used: $\bar{x} = 0.9$ (solid), 0.8 (long dashed), 0.6 (medium dashed), 0.4 (short dashed) and 0.2 (dotted).

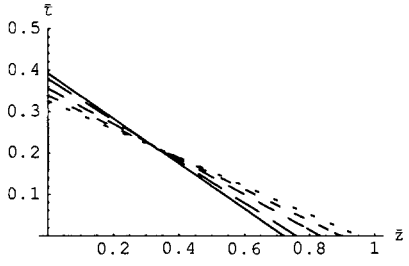

Fig. 4. Depth profiles of the shear stresses for $\alpha = 5°$ and $\bar{h}_* = 0.315$. Here the following notation is used: $\bar{x} = 0.9$ (solid), 0.8 (long dashed), 0.6 (medium dashed), 0.4 (short dashed) and 0.2 (dotted).

bed profiles $\alpha(\bar{s})$ (panels b, c, d). This demonstrates that the choice of the parameter $\bar{h}_*$ affects the solution for all geometries in a qualitatively similar fashion.

Acknowledgement: We thank Dr. Ralf Greve for his careful review of an earlier version of this paper.

References

1. Abramowitz, M. and I. A. Stegun, 1965. *Handbook of Mathematical Functions.* Dover. New York.
2. Dansgaard, W. and S. J. Johnsen, 1969. A flow model and a time scale for the ice core from Camp Century, Greenland, *Journal of Glaciology*, **8**, No. 53, p. 215-223.
3. Greve, R., 1997. A continuum-mechanical formulation for shallow polythermal ice sheets, *Phil. Trans. R. Soc. Lond.*, A **355**, p. 921-974.

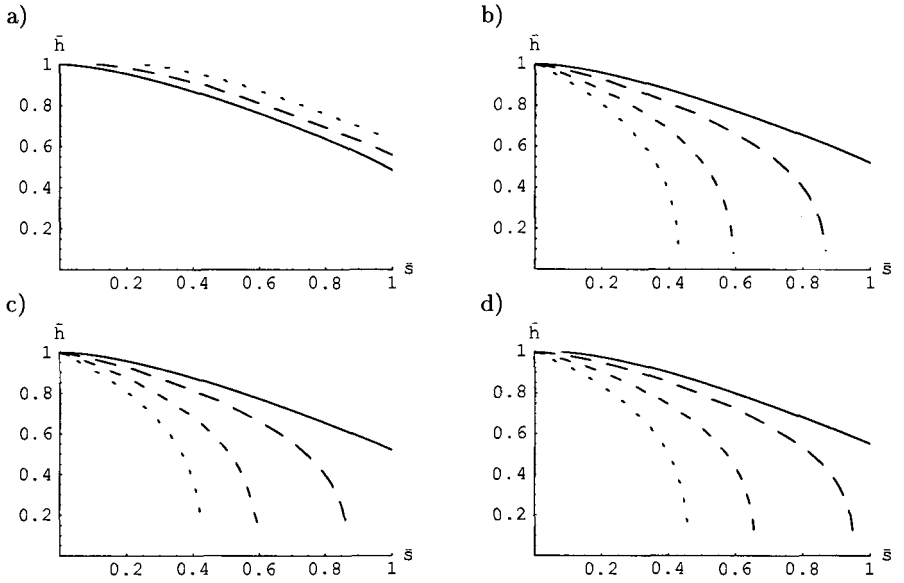

Fig. 5. Distribution of the thickness $\bar{h}$ as a function of $\bar{s} \in [0,1]$: a) for different values of the inclination $\alpha = (15-\bar{s})$ (solid), $(30-\bar{s})$ [°](dashed), $(45-\bar{s})$ [°](dotted) and $\bar{h}_* = 0.3$; b) for $\alpha = (15-\bar{s})$ [°]; c) for $\alpha = (15-\bar{s}^2)$ [°]; d) for $\alpha = 5(5-\bar{s}^2)$ [°] (in b, c, d is $\bar{h}_* = 0.25$ (solid), 0.5 (long dashed), 0.75 (dashed) and 1.0 (dotted)).

4. Hutter, K., 1983. *Theoretical Glaciology; material science of ice and the mechanics of glaciers and ice sheets.* D. Reidel Publishing Company, Utrecht.
5. Hutter, K., 1985. Mathematical foundation of flow of glaciers and large ice masses. Mathematical models and methods in mechanics. *Banach Center Publications*, No. 15, p. 278-321.
6. Kibel, I. A., N. E. Kotschin und N. W. Rose, 1963. *Theoretische Strömungsmechanik.* Band 2, Moscow.
7. Korn, G and T. Korn, 1961. *Mathematical Handbook for Scientists and Engineers.* McGraw-Hill. New York.
8. Schlichting, H., 1979. *Boundary layer theory.* McGraw - Hill. New-York.
9. Prudnikov, A. P., J. A. Brichkov and O. I. Marichev, 1981. *Integrals and Series. Elementar Functions.* New-York.
10. Savvin, A. A., 1999. *Grenzschichttheorie nichtlinearer Kriechströmungen und ihre Anwendung auf das EPICA-Vorhaben. Ph.D. Thesis.* Institut für Mechanik, TU Darmstadt, submitted.

(Received 21 May 1999, accepted 7 June 1999)

A Comparison Study Between Two Visco-Plastic Sea-Ice Models

Louis-Bruno Tremblay

Lamont-Doherty Earth Observatory of Columbia University, Palisades NY 10964-8000, USA

Abstract. A comparative study between two visco-plastic sea-ice models is presented. The two models are (i) the standard visco-plastic (SVP) approach with an elliptical yield curve and a normal flow rule and (ii) a granular material (GRAM) approach with a Mohr-Coulomb yield curve and a double-sliding deformation law with dilatancy included. Various numerical experiments in simple domains and forced with uniform winds are presented to illustrate the behaviour of each model and clearly see the influence of the ice interaction term on the flow field. The results highlight some irregularities with the SVP model, and with the GRAM approach when dilatation effects are not considered. In particular, simulated velocity fields from the SVP model in the presence of large thickness or concentration gradient, are sometimes not realistic; in the standard GRAM approach (without dilatation), the shear resistance of the material tend to be too low and the mobility of the pack ice too large. When dilatation effects are included, the internal ice pressure and shear viscosity increase and the simulated velocity fields are more realistic than the one obtained from the SVP model. The main difference between the two approaches (more important than the choice of yield curve or flow rule) lies in the way the internal ice pressure is calculated. In the SVP model, the internal ice pressure is specified independently of the sea ice deformation field (as a function of ice thickness and concentration), as opposed to the the GRAM approach where the specification of the ice pressure follows naturally from the double-sliding deformation law and does not depend on parameterization. In general, irregularities associated with the SVP model are subtle and do not prevent realistic simulations of the large scale sea-ice characteristics. However, the physical basis of the GRAM approach is considered more sound and therefore provides a better starting point for further model development. Whether drift pattern and ice thickness/concentration characteristics are sensitive to such details of the rheology remains to be determined.

1 Introduction

The presence of sea ice at high latitudes plays an important role in the present state and the variability of the global climate through various processes and feedback mechanisms. These include the ice-albedo feedback, the ventilation of the relatively warm ocean through leads in winter, the drastic change in the surface albedo associated with the formation of melt ponds and opening of leads, the fluxes of salt and fresh water implied when ocean water freezes in one location while the ice melts in some other location, and the insulation effect of sea ice which reduces the heat flux and momentum transfer

between the atmosphere and the ocean. Of the above, a majority are directly or indirectly (through the coupling between the thermodynamic and dynamic processes) influenced by dynamic effects. Model simulations of global warming scenarios are also very sensitive to the inclusion of a dynamic component in the sea ice models [1,2].

Dynamic modelling of sea-ice is based on the principles of the conservation of mass and momentum, and requires knowledge of the various forces acting on the ice floes. These include the Coriolis effect, water drag, air drag, gravitational pull due to the sea surface tilt and the internal ice stresses resulting from the interaction between different ice floes. In the Arctic, where the sea-ice motion is restricted by the presence of continental boundaries, strong interactions between ice floes take place and influence the basin-wide ice circulation; this makes the internal ice stress term important in the momentum balance. In the Antarctic, interactions do take place at certain locations and times; however, on average, the sea ice flow is divergent and ice interactions play a smaller role. The mathematical description of the Coriolis and the sea surface tilt terms are simple; the air and water drag on the ice floes depend on the free-stream velocity, boundary layer stability and surface roughness and so far, a number of existing parameterizations have been used successfully [3,4, for example]. The best way to model the internal ice stress term, on the other hand, is less clear and many different approaches have been proposed in the past 25 years. In the following, we refer to different sea-ice models as models which treat the ice interaction term differently.

It is generally accepted that the plastic approach to sea ice modelling is the most suitable. A plastic model implies that permanent (plastic) deformation only occurs when the load on the ice has reached a critical value in compression, tension or shear. If the load is less than the critical values, small elastic recoverable deformation takes place. For this reason, Coon [5] proposed to model ice as an elastic-plastic material. However, elastic deformation is a reversible process and hence the strain history of the ice must be stored, making the numerical treatment of the equations complicated. Since elastic deformations are negligibly small compared to plastic deformations and because they only occur in a small fraction of the physical domain at any one time, Hibler [6] proposed modelling the elastic deformation as a creeping flow (i.e. viscous behaviour). This made the numerical solution of the problem much simpler and more efficient and led to the widely used visco-plastic sea ice model of Hibler [7, referred to as the standard visco-plastic (SVP) model hereafter]. More recently, Hunke and Dukowicz [8] included an elastic stress term in the SVP rheology to further improve its numerical efficiency. In this model, elastic waves (whose speed is a function of a tunable parameter) allow for a faster propagation of information in the solution domain and a faster convergence. This elastic adjustment process takes place on very short time scales; for longer time scale (associated with wind and ocean forcing), the elastic term becomes negligible and the model reduces to the standard visco-

plastic model. This model also allows for an explicit numerical scheme and is well suited for parallel machines. Other visco-plastic models, with different yield curves and flow rules, also exist; amongst these is the Mohr-Coulomb yield curve with a double-sliding deformation law [9]. This type of model was successfully applied to the deformation of other materials showing similar deformation patterns to sea ice (eg. sand, land slides etc.). In this model, the ice is assumed to be a collection of granules (floes) in slow continuous deformation with friction acting between the floes and retarding its motion. In the following, we refer to this approach as the granular material (GRAM) approach.

In the next section, a review of previous sea-ice-model comparison studies is presented. In section 3, we give a general description of the SVP and GRAM models, elaborating upon the similarities and the differences. In section 5 results from simple numerical experiments highlighting the advantages and disadvantages of each approach are presented. Conclusions are summarized in the last section.

2 Previous Work

Ip et al. [10] presented a comparison study between four different sea ice models: (1) a visco-plastic model with an elliptical yield curve and normal flow rule [7], (2) a visco-plastic model with a Mohr-Coulomb yield criterion and a deformation law consisting of pure shear deformation (equivalent to the double sliding deformation law), convergent flow when the maximum ice compressive strength is reached, or free drift when the tensile strength limit is reached (3) a visco-plastic model with a square yield curve and normal flow rule, and (4) a cavitating fluid model. Similarities were found in both drift pattern and ice thickness buildup between the models using a square and elliptical yield curves, and between the Mohr-Coulomb and cavitating fluid models. Results showed that the models with square and elliptical yield curve gave more realistic drift distances than the Mohr-Coulomb and cavitating fluid models when compared with buoy drift data, but it was concluded that the monthly buoy drift statistics on which these considerations were based are inadequate to distinguish between different rheologies: daily buoy drift data were recommended for future studies. In their study, all the different rheologies used the same large scale compressive strength of sea ice, P^* (described below). This P^* was originally set to obtain the right proportion between ridging and shearing deformation for the visco-plastic sea ice model with elliptical yield curve [7] (Flato, personal communication). For the Mohr-Coulomb yield curve where the shear strength of the ice is generally much smaller when compared to the elliptical (Fig. 2) or square yield curve, it is expected that a higher compressive ice strength should be used to maintain the proper relative amount of ridging and shearing in the ice field. Also, for the Mohr-Coulomb yield curve, the internal sea ice pressure (p) is calculated

as opposed to the elliptical and square yield curve where it is specified as a function of thickness and concentration. This leads to significant differences in the resulting sea-ice pressure, and since the coefficients of viscosity are linearly related to p, differences in the velocity field are also expected. These two factors could explain the similarity found by the authors between the Mohr-Coulomb yield curve and the cavitating fluid rheology which has no shear resistance to sea ice motion. In this paper, we concentrate mainly on the implications of specifying the internal ice pressure differently, between the SVP and GRAM models.

More recently, the Sea Ice Intercomparison Project (SIMIP) was designed to produce a standard forcing and verification data set, and to test and evaluate a hierarchy of different sea ice models against observations. SIMIP presented the results of a similar study, comparing four different sea ice models: 1- a visco-plastic [7], 2- cavitating fluid [11], 3- a compressible Newtonian fluid [12] and 4- a freedrift sea ice model with blockage, all having very different levels of complexity. The first model, based on the Arctic Ice Dynamic Joint EXperiment (AIDJEX) recommendations [5], treats the ice as a plastic material with a finite compressive and shear strength, and with little tensile strength. The other three models either, ignore the shear strength of the material (2), consider ice as a simple Newtonian fluid[1] (3) or, ignore the interaction between the floes altogether (4). The conclusion of the study is that the most comprehensive (standard visco-plastic) approach performed best with the smallest root-mean-square (rms) error between the predicted sea ice drift pattern and the buoy position.

The SVP approach however, still has some counter-intuitive features present in its formulation, i.e., high resistance to shear motion is present even when the flow is divergent and the average normal stress is very small, and the presence of non-zero ice velocities with both winds and ocean currents set to zero, when thickness or concentration gradients are present. These will be described in more detail in the results section.

3 Model Description

Both models are visco-plastic in nature, and since there are two modes of deformation present (viscous and plastic), a criterion is required to mark the transition between the two. For small loads, negligibly small deformation occurs and sea ice is modelled as a very viscous fluid (creeping flow). When the load reaches some maximum allowable value, the material fails and large scale deformations take place (it flows plastically). This criterion marking the transition between the viscous and plastic behaviour is called the failure

[1] For Newtonian fluid, stresses are proportional to strain rates rather than independent of strain rates as for plastic material. It also resists both divergent and convergent motions contrary to what is observed for ice, i.e. ice offers very little resistance to divergence motion.

(yield) criterion and the rule that sets the type of deformation subsequent to failure is called the flow rule. In the plastic regime, different yield curves and flow rules can be used and since most of the time and over most of the domain, deformation takes place in this regime, it is important to identify the best plasticity theory (yield curve and flow rule) that one should use in sea ice modelling.

3.1 Yield criterion

The yield criterion is most easily described in terms of the principal stresses or stress invariants. In Fig. 1a, a general state of stress at a point in the ice is shown. Since the stress tensor is symmetric, it can be diagonalized with a pure rotation of the coordinate axes (see Fig. 1b). The stresses acting on the

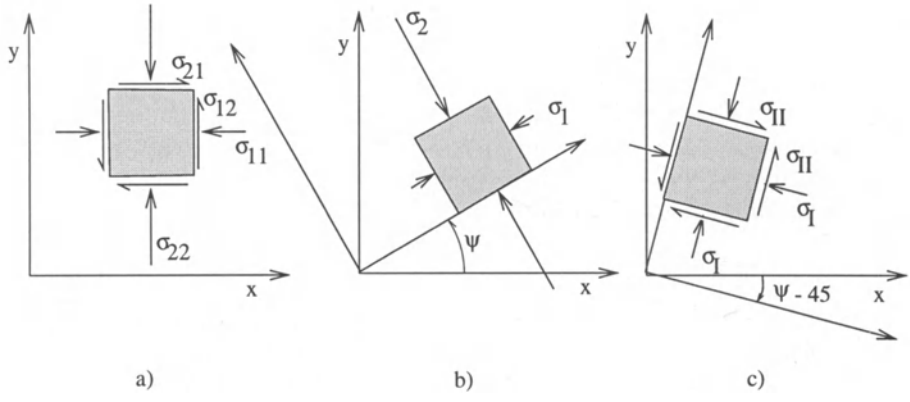

Fig. 1. State of stress at a point in model coordinates (a), principal stress coordinates (b), and stress invariant coordinates (c)

rotated element are the maximum and minimum normal stresses acting at a point and are called the principal stresses[2] (σ_1 and σ_2); the shear stresses acting on the rotated element vanish identically. Another useful frame of reference to describe the yield curve are the stress invariant axes. Physically, the two stress invariants (σ_I and σ_{II}) can be interpreted as the average normal stress at a point (or the internal ice pressure), and the maximum

[2] The principal stresses can also be interpreted as the eigenvalues of the stress tensor matrix and the angle of rotation ψ between the two coordinate systems can be deduced from the rotation matrix composed of the two normalized eigenvectors associated with the eigenvalues.

shear stress at a point. They are acting on mutually perpendicular planes oriented at an angle of 45 degrees from the principal stress axes (Fig. 1b-c). Note that all three representations of the state of stress at a given point are exactly equivalent. The only difference is the orientation of the set of axes chosen to study the problem. Although all three representation are equivalent, the principal and stress invariant frames of reference are certainly more useful since they reduce the number of variables from three (σ_{ij}) to two (σ_1 and σ_2, or σ_I and σ_{II}), and those stresses have a particular significance: they give the maximum (σ_2) and minimum (σ_1) normal stress at a point, or the maximum shear stress (σ_{II}) and internal ice pressure (σ_I). Since the material usually fails (and flows plastically) when σ_2, σ_1 or σ_{II} reach critical values in compression, tension or shear, these new coordinate axes provide a useful reference for determining the failure criterion of a given material.

A yield curve can be constructed experimentally by applying a given normal load to a sample and increasing the shear load until the material fails. This experiment is repeated for the entire possible range of normal load, and the data are plotted on a normal stress–shear stress diagram. In Fig. 2, the results of such a mental experiment are shown for both models (SVP and GRAM models) along with the 'ice-cream-cone' or 'tear-drop' yield curve of Coon for comparison. It shows the maximum-shear-stress (σ_{II}) sea ice can support before it fails and flows plastically as a function of the internal ice pressure (σ_I). The ice-cream-cone yield curve was proposed based on the AIDJEX observations campaign and is very similar to the yield curve derived from a discrete particle model proposed by Hopkins [13].

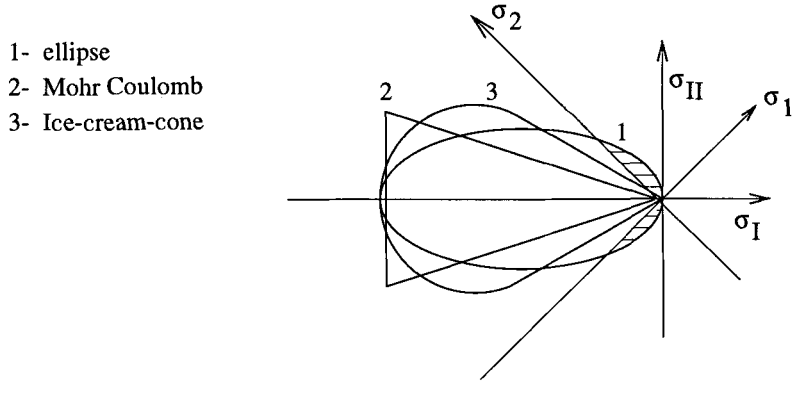

Fig. 2. Elliptical yield curve (1), Mohr-Coulomb yield curve (2), and ice-cream-cone yield curve (3) in stress invariant space (principal stress axes are also shown as a reference). In this drawing, all yield curves have the same maximum ice strength, P^*

In the SVP approach, the yield curve is an ellipse; in the granular material approach, the yield curve is a triangle (Mohr-Coulomb). The elliptical yield curve [7] was chosen in an attempt to represent the ice-cream-cone yield curve of Coon, yet keeping mathematical simplicity and computational efficiency, while the Mohr-Coulomb was originally proposed to model other types of granular materials that show similar patterns of deformation as sea ice. The ellipse is a good representation of the ice-cream-cone yield curve for large internal ice pressure (σ_I), however for small σ_I, the shear strength (σ_{II}) is much higher. Irregularities associated with this feature will be presented in the results section. Gray and Killworth [14] have suggested that the elliptical yield curve also suffers from additional complexities. They argue that the tensile strength associated with stress-states in the first and third quadrant of the principal stress axes (shaded in Fig. 2), leads to unstable flow states. In these cases, the originally hyperbolic initial value problem becomes elliptical in space and time and the problem is ill-posed. The Mohr-Coulomb failure criterion is identical to the ice-cream-cone yield curve for small to moderate σ_I. At high σ_I however, the two curves differ.

3.2 Flow rule

To determine the type of deformation subsequent to a failure (the flow rule), both approaches assume that the principal axes of stress (σ_1, σ_2) and the principal axes of strain rate ($\dot{\epsilon}_1, \dot{\epsilon}_2$) coincide. This implies that on the planes where the maximum (minimum) axial stress occurs (principal stress axes), so will the maximum (minimum) axial strain rate. No shear stress and shear strain rate are present in this frame of reference (Fig. 3a). Similarly, where the average normal stress and maximum shear stress occur (stress invariant axes), the average axial strain rate (divergence/2) and maximum shear strain

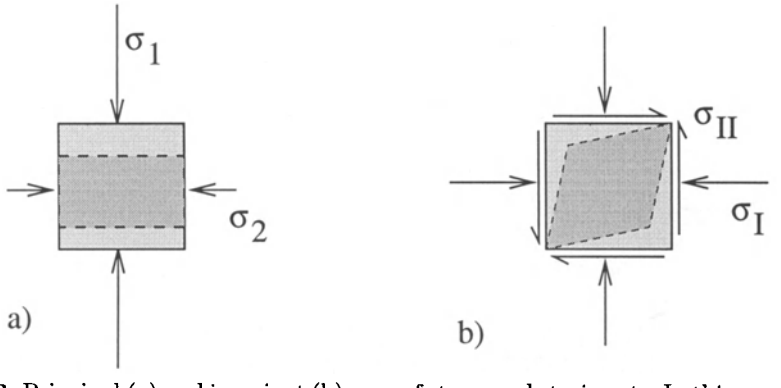

Fig. 3. Principal (a) and invariant (b) axes of stress and strain rate. In this example, the maximum compressive (a) or shear (b) load is reached, and the maximum axial (a) or shear (b) strain that develops to release the load is shown as a dotted line. In the principal stress space (a), no shear stress or shear strain are present

rate will also occur (Fig. 3b). This statement makes intuitive sense and is used in both models.

One difference between the two approaches is related to the choice of deformation law. In the SVP approach, the normal flow rule is used in conjunction with the elliptical yield curve (see Fig. 4a). With the normal flow rule, the strain rate vector is normal to the yield curve. Since the principal axes of stress coincide with the principal axes of strain rate, the projection of this vector on the x-y coordinates defines (when appropriately scaled) the two strain rate invariants of the flow ($\dot{\epsilon}_I, \dot{\epsilon}_{II}$) and therefore the deformation.

It can be seen that for stress states moving from one end of the ellipse to the other, the deformation field will go from purely convergent (far left of the ellipse) to purely divergent (far right of the ellipse) passing through a region of shear deformation with more or less divergence (convergence). Sea ice deformation fields derived from 3-day averaged satellite data [15] show that deformations in the pack ice consist mainly of shear deformation with some divergence or convergence associated with the shearing motion. This range is shown as a broad grey band on Fig. 4a. When the stress state lies to the right of this region, shear resistance is still present in the SVP model even though relatively large divergence is present (in divergence, little ice interaction and a free drift of the floes is expected). In the standard granular approach [10,11,9,16] pure shear deformation is present when the internal ice pressure lies between 0 and the maximum compressive strength. When the pressure reaches the critical value in compression (tension), convergent (divergent) motion is present in the flow field. When dilatation is included in the granular approach (Fig. 4b), shear flows with more or less divergence (convergence) are present when the stress state lies on the two limbs of the yield curve (see arrows). This convergence (divergence) comes from the reorganization of the floes as they roll and slide against one another in the shear zones. This effect is parameterized through an angle of dilatancy which determines the amount of opening (closing) as a function of the shear strain rate. Evolution equations for the angle of dilatancy can be used [17] to take into account the deformation history of the material at a given point. A detailed description of the dilatancy effect can be found in Tremblay and Mysak [9].

4 Governing Equations

In this section, the governing equation for the SVP and GRAM model is presented. The two-dimensional horizontal motion of sea ice can be described by

$$\rho_i h \frac{d\boldsymbol{u}_i}{dt} = -\rho_i h f \boldsymbol{k} \times \boldsymbol{u}_i + \boldsymbol{\tau}_a - \boldsymbol{\tau}_w + \nabla \cdot \boldsymbol{\sigma} - \rho_i h g \nabla H_d, \tag{1}$$

where ρ_i is the sea-ice density, h the mean ice thickness, f the Coriolis parameter, $\boldsymbol{k}$ a unit vector normal to the ice surface, $\boldsymbol{u}_i$ the ice velocity, $\boldsymbol{\tau}_a$ the

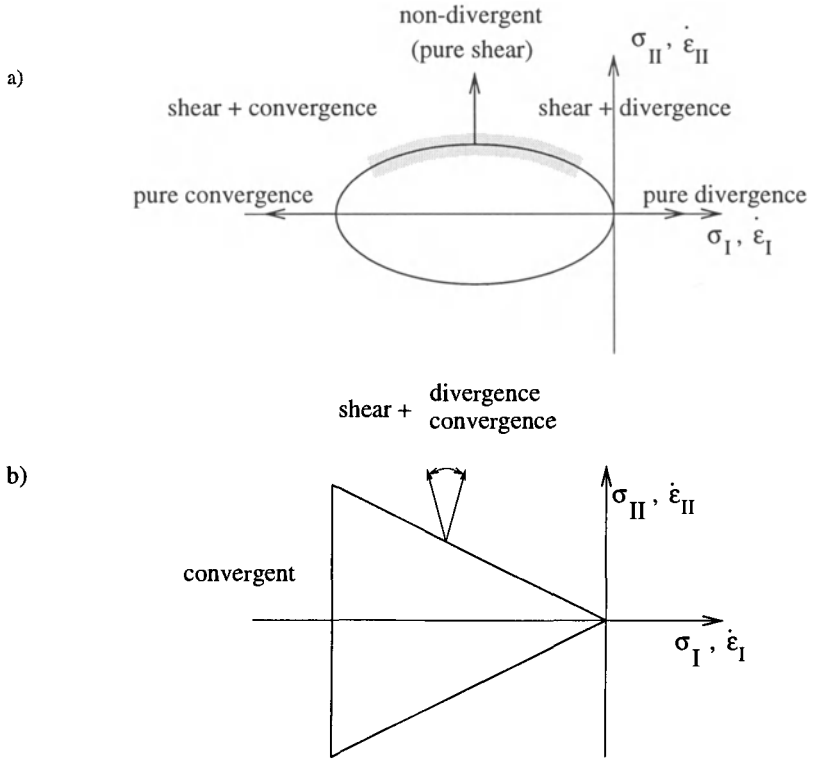

Fig. 4. Normal flow rule for the elliptical yield curve (a). Since the principal axes of stress and strain rate coincide, when the arrow has no projection on the horizontal axis ($\dot{\epsilon}_I$), the flow is non-divergent. For the Mohr-Coulomb yield curve without dilatation (b), the normal flow rule is not used. Instead, pure shear deformation is present when the stress states lie on the two sides of the triangle and convergent motion is present when the stress states lie on the cap of the triangle. If the effect of dilatation is included, shear deformation along with divergence (convergence) is obtained when the stress state lies on the two limbs of the triangle. This is shown by the two arrows in Fig. 4b for the case where some negative and positive dilatation is included.

wind shear stress on the top ice surface, $\boldsymbol{\tau}_w$ the ocean drag on the sea-ice flow, $\boldsymbol{\sigma}$ (σ_{ij}) the vertically integrated internal ice stress (normal or shear) acting on a plane which is perpendicular to the i-axis and in the j-direction, g the gravitational acceleration and H_d the sea-surface dynamic height. The air ($\boldsymbol{\tau}_a$) and water ($\boldsymbol{\tau}_w$) stresses are obtained from a simple quadratic law

with constant turning angle [3],

$$\boldsymbol{\tau}_a = \rho_a C_{da} |\boldsymbol{u}_a^g| \ (\boldsymbol{u}_a^g \cos\theta_a + \boldsymbol{k} \times \boldsymbol{u}_a^g \sin\theta_a), \tag{2}$$

$$\boldsymbol{\tau}_w = \rho_w C_{dw} |\boldsymbol{u}_i - \boldsymbol{u}_w^g| \ \left[(\boldsymbol{u}_i - \boldsymbol{u}_w^g)\cos\theta_w + \boldsymbol{k} \times (\boldsymbol{u}_i - \boldsymbol{u}_w^g)\sin\theta_w\right], \tag{3}$$

where ρ_a and ρ_w are the air and water densities, C_{da} and C_{dw} the air and water drag coefficients, $\boldsymbol{u}_a^g$ and $\boldsymbol{u}_w^g$ the geostrophic wind and ocean current and θ_a and θ_w the wind and water turning angles. In the above equation for the wind shear stress, the ice speed is considered small compared to the wind speed and is therefore neglected.

In the momentum equation (1), the internal ice stress $\boldsymbol{\sigma}$ can be written as follows [7,11,9]:

$$\sigma_{ij} = \begin{cases} 2\eta\dot{\epsilon}_{i,j} + (\zeta - \eta)\dot{\epsilon}_{kk}\delta_{ij} - p\delta_{ij}/2, & \text{SVP model,} \\ 2\eta\dot{\epsilon}_{i,j} \qquad - \eta\ \dot{\epsilon}_{kk}\delta_{ij} - p\delta_{ij}, & \text{GRAM model,} \end{cases} \tag{4}$$

where

$$\zeta = \min\left(\frac{p}{2\Delta}, \zeta_{max}\right), \ \eta = \min\left(\frac{\zeta}{e^2}, \eta_{max}\right), \tag{5}$$

$$\tag{6}$$

and

$$\Delta = \sqrt{(\dot{\epsilon}_{11}^2 + \dot{\epsilon}_{22}^2)(1 + \frac{1}{e^2}) + \frac{4}{e^2}\dot{\epsilon}_{12}^2 + 2\dot{\epsilon}_{11}\dot{\epsilon}_{22}(1 - \frac{1}{e^2})}$$

for the SVP model and,

$$\eta = \min\left(\frac{p\ \sin\phi}{\sqrt{(\dot{\epsilon}_{11} - \dot{\epsilon}_{22})^2 + 4\dot{\epsilon}_{12}^2}}, \eta_{max}\right) \tag{7}$$

for the granular material approach. In the above equation for Δ, e is the ratio of the principal axes of the elliptical yield curve (a measure of the shear resistance relative to the compressive strength of the ice). For small deformation ($\dot{\epsilon}_{ij}$), the coefficients of friction are capped to $\eta = \eta_{max}$ and $\zeta = \zeta_{max}$, and sea ice behaves as a very viscous fluid.

In the SVP model, the internal ice pressure p is fixed for a given ice thickness and concentration by the following empirical relation [7]:

$$p = P^* h\ \mathrm{e}^{[-C(1-A)]}, \tag{8}$$

where P^* is the ice strength per meter ice thickness, C is the ice concentration parameter, and A the ice concentration (percentage of a grid cell covered by ice). In the GRAM approach, the pressure p is calculated from the relation

$$\nabla \cdot \boldsymbol{u}_i = 2\dot{\gamma}\ \tan\delta, \ \text{when} \quad 0 < p < P_{max}, \tag{9}$$

where $\dot{\gamma}$ is the maximum shear strain rate at a point, δ is the angle of dilatancy and P_{max} is defined by (8) (see [9] for more details). Note that the SVP rheology has the same form as that of a compressible Newtonian fluid (except that η and ζ are non-linear functions of the strain rates), whereas the GRAM rheology has the form of an incompressible Newtonian fluid ($\zeta = 0$) with non-linear shear viscosity. However, since p is capped to P_{max}, compressibility in the GRAM approach is still present.

The specification (or calculation) of the internal ice pressure is important as it influences the sea ice deformation both through the pressure gradient term and the viscous term (the coefficient of viscosities are linearly related to p, see (5) and (7). Probably the most important difference between the SVP and the GRAM model lies in the way the internal pressure is specified. In the SVP model, the choice of flow rule does not impose any constraint on the internal ice pressure (i.e. there is a specific state of stress for a given state of strain, independent of the value of the sea ice pressure). For this reason, the internal ice pressure can be fixed to any arbitrary value independently of the state of strain (i.e. whether it is divergent or convergent). For the GRAM approach, the specification of the sea ice pressure follows naturally from the double-sliding deformation law, i.e. the flow is assumed to consist of pure shear deformation (sliding) along sliding lines roughly aligned with the stress characteristics in the material and the pressure is adjusted in order to meet this criterion. If the required pressure exceeds the maximum compressive strength of the ice (P_{max}), then p is set equal to P_{max} and convergence occurs; if it falls below the tensile strength (P=0), p is set to zero and divergence occurs. If dilatation is included, the pressure is adjusted so that some shear-induced divergence [15] is present. As discussed later, a calculated ice pressure is a desirable feature and often provides a more realistic internal ice pressure field and deformation field since the coefficient of viscosity is related to p (provided dilatation is included). Irregularities associated with a parameterized sea ice pressure as in the SVP model will be presented in the next section.

5 Results

In this section, results from a series of simple numerical experiments are presented in order to highlight certain features and irregularities in the behaviour of each model under different forcing conditions and in different physical domains. In particular, the flow of sea ice under weak forcing conditions (case A) and the flow of ice in a channel (case B1-2) is considered.

In case A, a Cartesian mesh with a grid resolution of 100 km is used on a simple rectangular domain (30 x 51 grid cell) with an island at the center (see Fig. 5). Open boundary conditions are used on all the sides in this simulation. In case B, a rectangular grid (30 x 21) with solid walls on both sides and open boundaries at the top and bottom is used. In order to highlight

the influence of the different rheologies on the simulation results, the Coriolis and thermodynamic effects are ignored, and the air and water turning angles are set to zero ((2) and (3)). The boundary conditions for the ice dynamic equation are zero normal and tangential velocity at a solid boundary (side wall, case B1-2) and free outflow (p = 0) at an open boundary (all boundaries in case A and downstream boundary in case B1-2). In all cases, the northerly winds on the upstream boundary advect a continuous flow of sea ice into the domain.

The model was integrated for a period of 2 days using a time step of 12 hours. In the next two sections, we highlight differences in behaviour associated with the two approaches. First, we concentrate on the influence of the pressure gradient term in the momentum equation (case A) and, secondly, on the viscous term in a shear flow situation (case B1-2). A summary of initial conditions and ice compressive strength used in all simulations is given in table 5.

Table 1. Initial condition (IC) and ice compressive strength used in the simulations

Case	h, IC (m)	A, IC (%)	P^* (N m^{-2})
A	1-3	100	25×10^3
B-1	1	100	5×10^3
B-2	2	100	20×10^3

5.1 Relaxation flow

In this simulation, the effect of the thickness and concentration gradients on the sea-ice velocity field is examined. In the SVP approach, the internal ice pressure is specified uniquely from the ice thickness and concentration, independently of the sea ice velocity field. A consequence of this assumption is that for 0 m s^{-1} winds and ocean currents (assuming the Coriolis effect and sea surface tilt are zero for simplicity), a 0 m s^{-1} ice velocity field is only a solution of the momentum equation provided that there are no ice thickness or concentration gradients (or $\nabla P = 0$). If a gradient is present, a flow field will develop in an attempt to eliminate it. A simple scaling analysis of the sea ice momentum equation (1) shows that the pressure gradient term is of the same order of magnitude as the wind stress term for a 1m thickness gradient [H] over 100 km [L], assuming $C_{da} = 1.2 \times 10^{-3}$, $[U_a] = 10$ m s^{-1} and $P^* = 20 \times 10^3$ N m^{-2} (see (1), (2) and (4)),

$$\rho_a C_{da} [U_a]^2 = \frac{P^*[H]}{[L]}.$$

Such gradients can occur close to land where convergence is sometimes present, and also at ice edges, but generally speaking, they occupy a small fractional area of a typical domain. Also, ice flow resulting from such thickness or concentration gradients are only apparent in regions where the wind speed is small; in these situations the deformations are small and the viscosities (inversely proportional to deformation, see (5) and (7)) are large, resulting in small ice velocities.

In order to demonstrate this irregularity with the SVP approach, the following situation is considered. The winds are blowing from the top to the bottom at 1 m s^{-1}. The initial conditions for the simulation are 1m ice thickness and 100% ice concentration everywhere except for a band of ice (one grid cell wide) in front of the island where the ice thickness is 3m. the ice concentration is 100 % and P_{max} is set to 25×10^3 N m^{-2}. Such a situation could be observed after a storm when wind piled up thicker ice in front of an island, and calm conditions returned.

Fig. 5a shows the ice velocity field for the visco-plastic model for this situation. Clearly, the pressure gradient (associated with the thickness gradient) in front of the island sets up a flow in a direction opposite to the winds. The speed of the flow is maximum in front of the island (0.5 cm s^{-1}), and after several iterations, the velocity vectors align themselves with the wind and the situation returns to normal. This behaviour is similar to that of a fluid and follows from the setting of the pressure p solely in terms of h and A. For a plastic material, the initial deformation should remain, i.e. the material should not relax back to its original state. For the GRAM model, the calculated pressure in the front of the island is just sufficiently large to prevent convergence (it does not reach P_{max}), and the velocity field is in line with the winds at all times (Fig. 5b). The calculated sea-ice pressure in this case is also shown in the background. This irregularity associated with the SVP model formulation leads to small ice velocities and could only become significant if the atmospheric and oceanic forcing remained small for an extended period of time.

Another situation in which this can be observed is when the wind start blowing ice of uniform thickness against an obstruction; at first the ice piles up against the land and the resulting thickness gradient can cause the ice to move against the wind. After a few time steps, the situation becomes more regular and the ice velocity is in the same direction as the wind (David Holland, personal communication).

5.2 Flow down a channel

In both visco-plastic models, the shear viscosity is linearly related to the internal ice pressure. For this reason, the mobility of the pack ice for a given wind and oceanic forcing is dependent of the way the internal ice pressure is calculated. With the elliptical yield curve and normal flow rule, the internal ice pressure is parameterized as a function of ice thickness, ice concentration

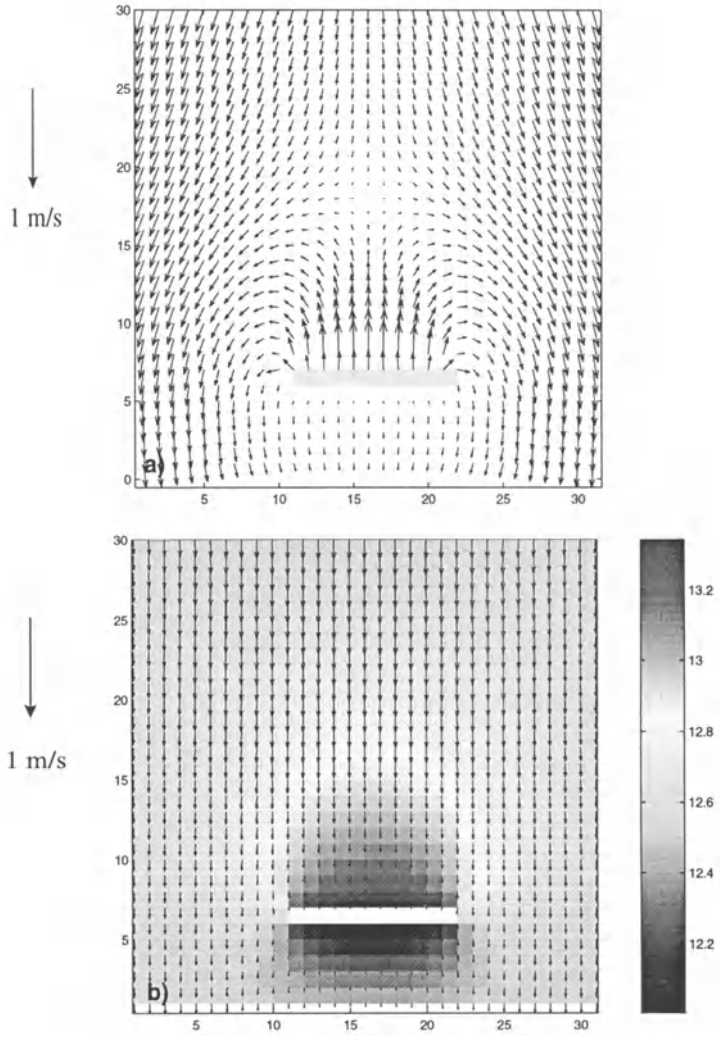

Fig. 5. Velocity field after one day for the SVP model (a) and the GRAM model (b). A color map of the internal ice pressure is shown in the background for the GRAM simulation (in KN m^{-1}); for the SVP model, the internal ice pressure are 12.5 KN m^{-1} everywhere except in front of the island where they are 37.5 KN m^{-1}. Wind is blowing uniformly in space and Heavyside in time from the top to the bottom at 1 m s^{-1}. The initial conditions for both simulations are 1m ice thickness and 100% ice concentration everywhere except for a band of ice (one grid cell wide) in front of the island where the ice thickness is 3m and the ice concentration is 100 %. The numerical domain in this simulation was larger than what is shown here (by two island length) in order to remove the influence of the boundary conditions on the interior solution. As a reference, the velocities in front of the island are 0.5 cm s^{-1}.

and two empirical constants (P^* and C, see (8)). For the Mohr-Coulomb yield criterion and double-sliding deformation law, the internal ice pressure is calculated and can lie anywhere between zero (in divergent flow) and P_{max} (convergent flow), with P_{max} defined by (8). In this section, results are presented for the ice flow in a channel (shear flow) using both models in order to highlight differences in the flow field from the two different internal ice pressure calculations. In this simulation, the initial conditions for ice thickness and concentration are $h = 1\text{m}$, $A = 100\ \%$ and P^* is set equal to 5×10^3 N m^{-2}.

Fig. 6 shows the velocity and internal ice pressure profiles across the channel for the SVP model and the GRAM model with and without dilatation. For the SVP model, the internal ice pressure is constant (P^*h, since $A = 1$), and the viscosity coefficients, inversely proportional to some function of the strain rates, are non-zero everywhere. For this reason, high velocity gradients are present close to the wall (large strain and small viscosities) and the effect of viscosity in the interior of the channel is small (small strain and large viscosities). For the GRAM model without dilatation, the internal ice pressure is zero everywhere inside the channel since the winds are non-divergent and the coast is aligned with the winds (in this model, convergent motion in the flow field is responsible for sea-ice pressure build up). For this reason, the shear viscosity is zero everywhere in the interior and the flow field is the same as that of a free drift solution. In general, the internal ice pressure calculated in a GRAM model without dilatation [10,11,9] is likely to be much smaller than the maximum internal sea ice pressure (P_{max}, used in the SVP model) in regions where large scale winds are non-divergent and far away from the presence of a coastline. In the Arctic, this includes most of the regions except north of the Canadian Arctic Archipelago (when looking at the time averaged winds). Since the coefficient of shear viscosity is linearly proportional to p, this leads to a very mobile pack ice which behaves similarly to a cavitating fluid. It is believed to be mainly for this reason (and to a smaller extent due to the fact that the shear stress for small internal ice pressure is smaller for the Mohr-Coulomb yield curve than for the elliptical yield curve), that the study of Ip et al. [10] shows a very similar behaviour between the Mohr-Coulomb yield curve and the cavitating fluid rheology in their Arctic simulation study. This behaviour in shear is not realistic, as one would expect significant ice floe interaction even with large-scale non-divergent wind fields (far from the influence of continental boundaries), since ice floes are irregular in shape and size, and shear deformation will lead to ice floe interactions and dilatation, causing the internal ice pressure to build up.

In order to take this into account, shear-induced dilatation of the material is included (see Fig. 6). Fig. 6b (circles) shows a pressure build-up against the coast due to local shear induced dilatation ($\delta = 1.5$) and the internal ice pressure decreases toward the center of the channel. In this case the internal ice pressure (and shear viscosity) are non-zero and the presence of the

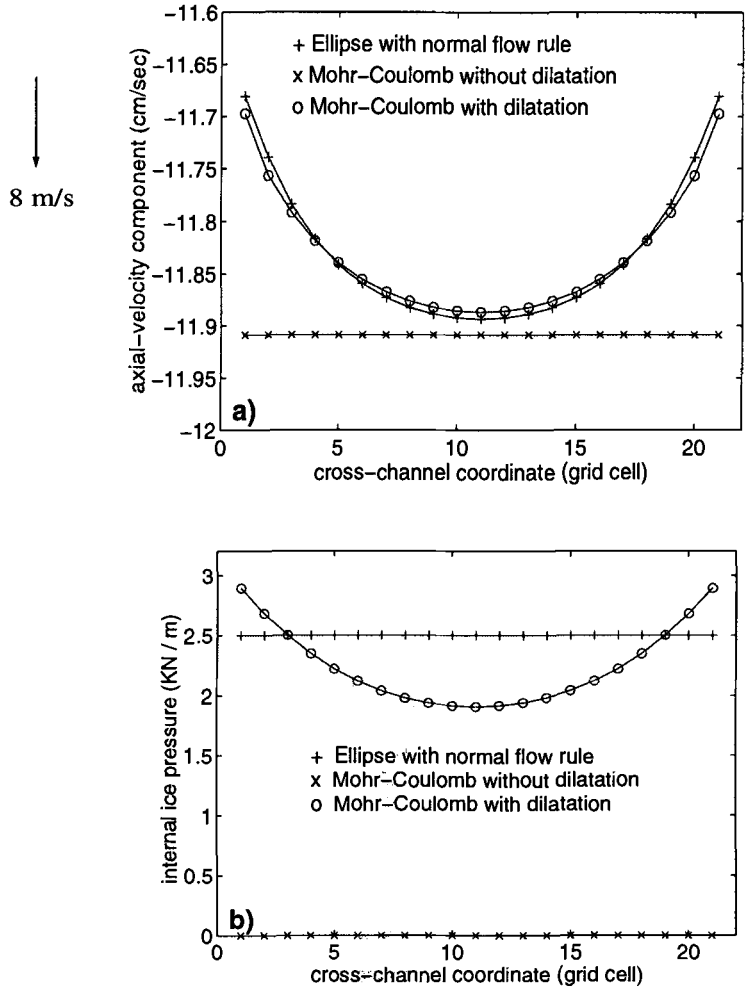

Fig. 6. Axial component of the velocity (a) and the internal ice pressure profile (b) across the channel for the SVP model and GRAM model with and without dilatation. Note that the velocity at the wall is not shown here in order to see the gradient in the interior more clearly

boundary is felt deeper inside the channel in a manner similar to the SVP model.

A disadvantage to specifying the internal ice pressure, independently of the deformation state in the ice field (as in the SVP model) is that ice will have shear resistance and resistance to tensile load even when the flow field is divergent. Intuitively, the internal ice pressure is expected to go to zero when the sea ice flow field is largely divergent. To illustrate this behaviour, the same channel flow experiment is analyzed with wind blowing at an angle

with respect to the coastline. In this case, the wind speed is set at 8 m s^{-1} at an angle of 25 degrees with the coastline. The initial conditions for this simulation are 2m ice thickness and 100% ice concentration. The sea-ice compressive strength used in this run is 20×10^3 N m^{-2}, a typical value used for large scale sea-ice studies forced with daily varying winds. In this case, the boundary flow on the left of the domain will be subjected to shear and divergence and that on the right of the domain, to shear and convergence. The axial velocity and internal ice pressure profile across the channel for this case in shown in Fig. 7.

For the SVP model, the internal ice pressure is constant (since h and A are constant) and shear resistance is present across the entire channel (even on the left wall where divergence is present). This is seen from the velocity profile (Fig. 7a) where a boundary layer of slow moving ice is present on both sides of the channel (the discontinuity in slope present near the side walls is due to the capping of the viscosity coefficients marking the transition from the plastic to the viscous behaviour). In the GRAM model (with dilatation included, $\delta = 1.5$) the internal ice pressure remains zero on the left wall due to the divergent flow field (Fig. 7b). The pressure increases slowly towards the right wall where convergence is present. The corresponding axial velocity profile has no boundary layer on the left and a more developed boundary layer on the right wall where the internal ice pressure (and the shear viscosity) is high. These results make more intuitive sense (no shear resistance when divergent flow is present) and constitute one of the advantages of calculating the internal ice pressure field. Finally, it should also be noted that (9) can not be used to calculate the internal ice pressure for the SVP model as it derives directly from the double-sliding deformation law and would lead to a velocity field incompatible with the normal flow rule.

6 Conclusions

In this paper, a general description of two visco-plastic sea-ice models is presented. The two models are the standard visco-plastic (SVP) approach with an elliptical yield curve and a normal flow rule, and a granular material (GRAM) approach with a Mohr-Coulomb yield curve and a double-sliding deformation law with dilatancy included. The SVP model requires the specification of a yield curve, a flow rule and an empirical relation defining the internal ice pressure. The GRAM model, on the other hand, only requires the specification of a yield curve and a flow rule; the specification of the internal ice pressure follows from the choice of flow rule. A key difference between the SVP and the GRAM model lies in the way the internal ice pressure is calculated. In the SVP model, the ice pressure is specified independently of the ice deformation. This leads to irregularities when large thickness or concentration gradients are present in the domain and in some shear flow situation. In the GRAM model, without dilatation included, irregularities are also present in

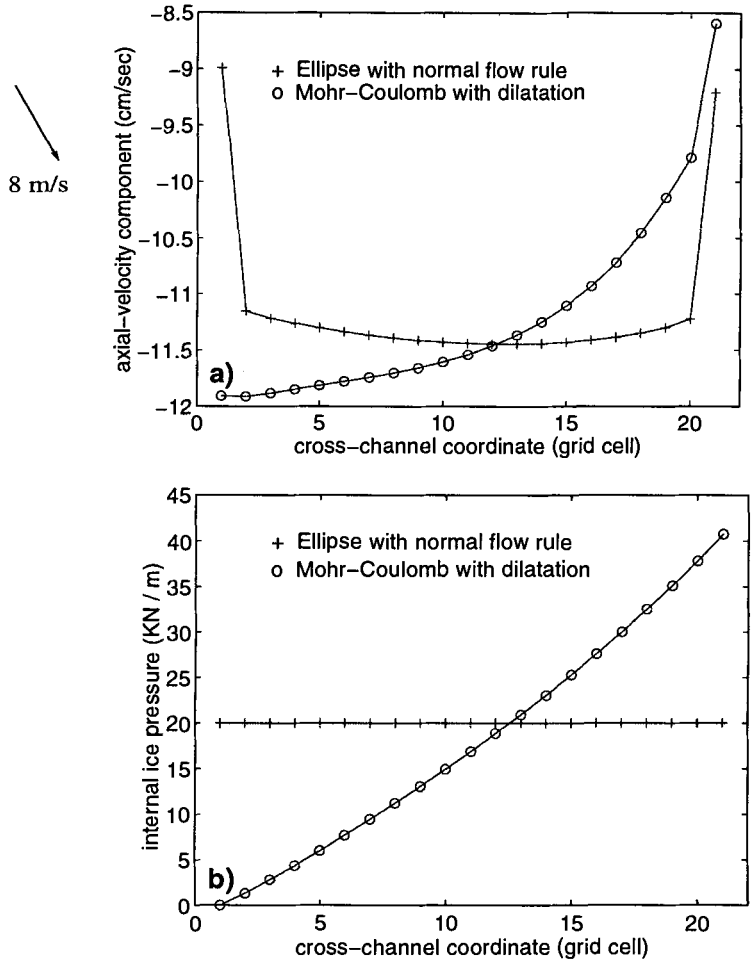

Fig. 7. Axial component of the velocity (a) and internal ice pressure profile (b) across the channel for the SVP model and the GRAM model with and without dilatation. In this experiment, the winds are 8 m s^{-1} at an angle of 25 degrees with the coastline

simple shear flow where the shear resistance is abnormally low. With dilatation included, this problem disappears. Although both models are capable of realistic large-scale sea-ice simulations [7,18,9,19], the physical basis of the GRAM model is considered more sound and should provide a better starting point for further model development.

Acknowledgment: I am grateful to Prof. K. Hutter, Dr G.A. Schmidt and Dr R. Hohmann for the careful review of the manuscript and suggestions for its improvements. During this work, I was partly supported by a NOAA Postdoctoral Fellowship in Climate and Global Change administered by the UCAR Visiting Science Program, and by the National Science Foundation through Grant OPP-9818711.

References

1. Hibler III, W. D. (1984) The role of sea ice dynamics in modeling CO_2 increases. Geophysical Monograph 29, American Geophysical Union. 238–253
2. Lemke, P., Owens, W. B., Hibler III, W. D. (1990) A coupled sea ice-mixed layer-pycnocline model for the Weddell Sea. Journal of Geophysical Research. **95**, 9513–9525
3. McPhee, M. G. (1975) Ice-ocean momentum transfer for the AIDJEX ice model. AIDJEX Bulletin. **29**, 93–111
4. Stössel, A., Claussen M. (1993) On the momentum forcing of a large-scale sea-ice model. Climate Dynamics. **9**, 71–80
5. Coon, M. D., Maykut, S. A. et al. (1974) Modelling the pack ice as an elastic plastic material. AIDJEX Bulletin. **24**, 1–105
6. Hibler III, W. D. (1977) A viscous sea ice law as a stochastic average of plasticity. Journal of Geophysical Research. **82**, 3932–3938
7. Hibler III, W. D. (1979) A dynamic thermodynamic sea ice model. Journal of Physical Oceanography. **9**, 815–846
8. Hunke, E. C., Dukowicz, J. K. (1996) An elastic-viscous-plastic model for sea ice dynamics. Journal of Physical Oceanography. **27**, 1849–1867
9. Tremblay, L.-B., Mysak, L. A. (1997) Modelling sea ice as a granular material including the dilatancy effect. Journal of Physical Oceanography. **27**, 2342–2360
10. Ip, C. F., Hibler III, W. D., Flato, G. M. (1991) On the effect of rheology on seasonal sea-ice simulations. Annals of Glaciology. **15**, 17–25
11. Flato, G. M., Hibler III, W. D. (1992) Modeling Pack Ice as a Cavitating Fluid. Journal of Physical Oceanography. **22**, 626–651
12. Campbell, W. J. (1965) The wind-driven circulation of ice and water in the Polar Ocean. Journal of Geophysical Research. **70**, 3279–3301
13. Hopkins, M. A. (1994) On the ridging of intact lead ice. Journal of Geophysical Research. **99**, 16351–16360
14. Gray, J. M. N. T., Killworth, P. D. (1995) Stability of the viscous-plastic sea-ice rheology, Journal of Physocal Oceanography. **25**, 971–978
15. Stern, H. L., Rothrock, D. A., Kwok, R (1995) Open water production in Arctic sea ice: satellite measurements and model parameterizations. Journal of Geophysical Research. **100**, 20601–20612
16. Gutfraind, R, Savage, S. B. (1997) Smoothed particle hydrodynamics for the simulation of broken-ice fields: Mohr-Coulomb-type rheology and frictional boundary conditions. Journal of Computational Physics. **134**, 203–215
17. Balendran B., Nemat-Nasser S. (1993) Double sliding model for cyclic deformation of granular materials, including dilatancy effects. Journal of the Mechanics and Physics of Solids. **41**, 573–612

18. Holland D. M., Ingram, R. G, Mysak L. A., Oberhuber J. M. (1995) A numerical-simulation of the sea-ice cover in the Northern Greenland Sea . Journal of Geophysical Research-Ocean. **100**, 4751–4760
19. Arfeuille G., Mysak L. A., Tremblay L.-B. (1999) A numerical simulation of the seasonal variation of the Arctic sea ice cover. Climate Dynamics, accepted for publication.

(Received 1 June 1999, accepted 18 June 1999)

Influence of Ice Accumulation Distribution on Ice Sheet Stability

Alexander V. Wilchinsky

Institute of Mathematics and Mechanics, Kazan State University, Kazan 420008, Russia

Abstract. The stability of a two-dimensional isothermal ice sheet with stationary margin is studied when the ice flow is described by Glen's flow law. The ice accumulation rate is assumed to depend on the elevation and the span. Surface perturbation is searched for as a normal mode, which determines a singular eigenvalue problem. The singularity of the perturbation at the margin can be treated by application of the method of matched asymptotic expansions. Numerical solution of the eigenvalue problem shows that the dependence of the accumulation rate on the elevation contributes strongly to the ice sheet instability. Positive downstream slope prevents stable solutions. Negative downstream inclination of the equilibrium line often equally leads to instability.

1 Introduction

Steady flow of an ice sheet is possible not only when there exists a steady-state solution of the corresponding mathematical model, but also when this solution is stable. While ice sheets and glaciers are characterized by diverse conditions of motion, and their steady-state profiles are very sensitive to these conditions (e.g Weertman, 1961, Oerlemans, 1996), analysis of ice sheet stability has been generally performed for the case when the ice accumulation rate at the upper surface depends only on the span (Bodvardsson, 1955; Nye, 1959; Fowler, 1992; Hindmarsh, 1996, 1997). The situation when the accumulation rate depends on the elevation was studied by Wilchinsky (submitted), who considered the ice as a Newtonian fluid, whereas more realistically its rheology should be described by the power law (Glen, 1955).

Assuming a power-law rheology of the ice and using the "shallow ice approximation" (Hutter, 1983), the evolution equation of the ice sheet can be found as a non-linear parabolic equation (Fowler and Larson, 1978; Morland and Johnson, 1980; Hutter, 1983; Salamatin and Mazo, 1984). If the ice sheet margin is assumed to be stationary, then the common approach to study the ice sheet stability is to perturb the evolution equation. Then separation of variables for this perturbation yields a singular Sturm-Liouville problem for the eigenvalues (Nye, 1959; Fowler, 1992; Hindmarsh, 1997). If the ice sheet margin moves, the method of separation of variables is generally not applicable (Wilchinsky, submitted).

In this paper we consider the two-dimensional isothermal motion of a continental ice sheet with fixed margin (Fig. 1). The slope of the bed is

comparable with that of the upper surface. The accumulation rate at the upper surface is assumed to depend on the span and elevation, and ice is a non-Newtonian fluid.

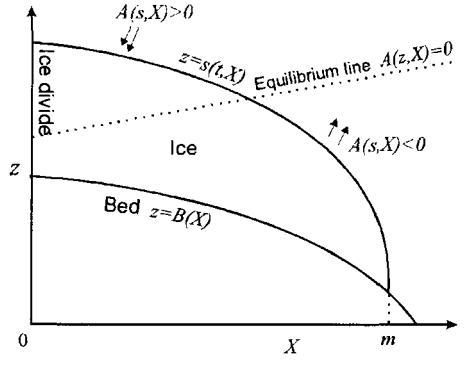

Fig. 1. Continental ice sheet

2 Analytical and Numerical Analysis

2.1 Evolution equation

In this work the ice is assumed to be an incompressible isothermal fluid with power-law rheology (Glen, 1955) under slow creeping motion. Therefore its (two-dimensional) flow is described by the Stokes equations. We consider the situation when at the bed the ice does not melt and thus we apply the no-slip condition.

The common approach to simplify the Stokes equations for ice sheets is to use the "shallow ice approximation" (Hutter, 1983); it is based on the fact that the ice sheet aspect ratio δ – ratio of typical ice thickness to ice sheet length – is a small quantity. Therefore, the boundary layer approximation allows us to derive the ice-sheet-evolution equation in relatively simple form (Fowler and Larson, 1978; Morland and Johnson, 1980; Hutter, 1983; Salamatin and Mazo, 1984). Here we show this derivation briefly.

We will use the following notations for the dimensional variables: $(\bar{X}, \bar{z})$ are the horizontal and upward vertical spatial coordinates, $\bar{t}$ is time, $\bar{u}$ and $\bar{w}$ are the horizontal and vertical velocities, $\bar{p}$ is the pressure, $\bar{B}$ and $\bar{s}$ are the bed and surface elevations, g is gravitational acceleration, $\bar{h} = \bar{s} - \bar{B}$ is the ice thickness, $\bar{A}$ is the accumulation rate at the upper surface, which is assumed not to depend on time, ϱ is the ice density, μ is the ice effective viscosity, η the flow law constant and n the flow law exponent. Letter subscripts denote partial derivatives.

Because the ice flow is shearing, scales can be chosen as $[\bar{w}] = [\bar{A}], [\bar{u}] = [\bar{w}]/\delta, [\bar{p}] = [\bar{z}]\varrho g, [\bar{t}] = [\bar{z}]/[\bar{A}], \delta = [\bar{z}]/[\bar{X}]$ (see discussion by Fowler, 1992). In dimensionless variables (without bars) the Stokes equations take the form

$$p_X = \gamma[(\mu u_z)_z + O(\delta^2)], \quad p_z + O(\gamma\delta^2) = -1, \tag{1}$$

where

$$\mu = |u_z|^{(1-n)/n} + O(\delta^2), \quad \gamma = \eta[\bar{A}]^{1/n}[\bar{X}]^{(n+1)/n}/(\varrho g[\bar{z}]^{2(n+1)/n}).$$

The stress-free conditions at the upper surface imply

$$\mu u_z = O(\gamma\delta^2), \quad p = O(\delta^2) \tag{2}$$

and the mass conservation equation becomes

$$h_t + q_X = A, \quad q = \int_B^s u dz, \tag{3}$$

where q is the horizontal mass flux. Letting $\gamma = 1$, we can find $[\bar{z}]$ when $[\bar{X}]$ is known (Salamatin and Mazo, 1984).

Neglecting the terms of order $O(\delta^2)$ and integrating of $(1)_1$ and $(1)_2$ with respect to z, we obtain

$$p = s - z, \quad u = sign(s_X)\,|s_X|^n\,[(s-z)^{n+1} - h^{n+1}]/(n+1). \tag{4}$$

Substitution of $(4)_2$ for u into the mass conservation equation (3) yields the evolution equation

$$\begin{gathered} h_t + q_X = A(s,X), \quad q = -sign(s_X)h^{n+2}\,|s_X|^n/(n+2), \quad 0 < X < m, \\ q = 0 \text{ at } X = 0, \quad q|_{t=0} = h = 0 \text{ at } X = m, \end{gathered} \tag{5}$$

where m is the margin position. Note that $A(s,X)$ is supposed not to depend on time.

Equation (5) is of parabolic type one (Courant and Hilbert, 1953). It requires two boundary and one initial conditions. If the ice sheet spreads freely then the third boundary condition is used to determine the margin position m, which is not known. In imposing the boundary conditions, we assume that the horizontal mass flux is zero at the ice divide ($X = 0$) – this is a vertical line at the position of maximal surface elevation. The other boundary conditions prescribe the ice thickness and the horizontal mass flux at the margin. For freely spreading continental ice sheets, both values are set to zero. If the ice sheet length is known and fixed in time due to the bed topography, then the only one condition at the margin is to prescribe the ice thickness. It was shown (Wilchinsky, submitted) that the method

of separation of variables is not applicable when the ice sheet margin moves. Therefore *we will study the motion of a continental ice sheet with fixed margin* (and boundary conditions $q(0) = h(m) = 0$); this motion is the result of a perturbation of a stationary ice sheet with free margin (and boundary conditions $q(0) = q(m) = h(m) = 0$).

In this study we shall assume that solutions of (5) do indeed exist and that A is a smooth function of its arguments. We consider only situations, when $h \geq 0$ and s is monotone ($s_X \leq 0$). We shall neither treat the singularity of the solution of (5) at the ice divide (for details see e.g. Wilchinsky and Chugunov, 1997).

2.2 Analytical steady-state solutions

If the bed is a horizontal plane and the accumulation rate function does not depend on the elevation ($A_s \equiv B \equiv 0$), then the steady-state solution of (5) can be found in terms of quadratures and is called Vialov-Nye solution (Vialov, 1958; Nye, 1959)

$$h(X) = \left\{ -\frac{2n+2}{n} \int_X^m \left[(n+2) \int_0^{X_*} A dX^* \right]^{1/n} dX_* \right\}^{n/(2n+2)}. \tag{6}$$

The margin position m is determined from the condition that the mass flux is zero at the margin

$$\int_0^m A(X) dX = 0. \tag{7}$$

If $A \equiv const$ then (6) yields

$$h(X) = \left\{ -2(n+2)^{1/n} A^{1/n} \left(m^{(n+1)/n} - X^{(n+1)/n} \right) \right\}^{n/(2n+2)}. \tag{8}$$

If $A_X \equiv B \equiv 0$, but $A_s \neq 0$, then the steady-state solution of (5) can be found in inverse form as the function $X(h^{2(n+1)/n})$:

$$X = \frac{n}{2(n+1)} \int_f^{f(0)} \left(-(n+2) \int_0^{f'} A^*(f_*) df_*/2 \right)^{-1/(n+1)} df', \tag{9}$$

where $f = h^{2(n+1)/n}$, $A^*(f) = A(h)$ and $f(0)$ is determined from the equation

$$\int_0^{f(0)} A^* df_* = 0. \tag{10}$$

In particular, when $n = 3$ and $A = a_1 h^2 - a_2$ we can derive the solution in the form

$$h = \sqrt{[7/(4a_1)]\left\{a_2 - [(6a_1/7)(5/2)^{1/4}X]^{4/3}\right\}}. \tag{11}$$

Here $a_1 > 0$ and $a_2 > 0$ are constant.

2.3 Perturbation analysis

For the subsequent analysis it is convenient to introduce new variables, in which the ice sheet length is equal to 1 and the margin is situated at the origin of the coordinate system;

$$x = 1 - X/m, \quad \tau = t.$$

With these, the evolution equation (5) takes the form

$$\begin{gathered} h_\tau = q_x/m + A(s, m(1-x)), \quad q = h^{n+2}s_x^n/[(n+2)m^n], \quad 0 < x < 1, \\ q|_{\tau=0} = h = 0 \quad \text{at } x = 0, \quad q = 0 \quad \text{at } x = 1. \end{gathered} \tag{12}$$

Let h_0, m be a steady-state solution of (12) describing a freely spreading ice sheet (its margin position is determined from the condition that the mass flux is zero there). To find a time dependent solution of (12) describing the flow of the ice sheet with a fixed margin as a perturbation about the steady-state solution in separated form, we use the expansion

$$\begin{gathered} h = h_0 + \varepsilon e^{-\lambda\tau}h_1 + O(\varepsilon^2), \quad s = b + h_0 + \varepsilon e^{-\lambda\tau}h_1 + O(\varepsilon^2), \\ q/m = q_0 + \varepsilon e^{-\lambda\tau}q_1 + O(\varepsilon^2), \quad A(s, m(1-x)) = a + \varepsilon e^{-\lambda\tau}a_s h_1 + O(\varepsilon^2), \end{gathered} \tag{13}$$

where $a(s_0, x) = A(s_0, m(1-x)), a_s = A_s(s_0, m(1-x)), b(x) = B(X)$. Substituting (13) into (12) we derive the leading order problem

$$\begin{gathered} q_{0x} + a(s_0, x) = 0, \quad q_0 = h_0^{n+2}s_{0x}^n/[(n+2)m^{n+1}], \quad 0 < x < 1, \\ q_0 = h_0 = 0 \quad \text{at } x = 0, \quad q_0 = 0 \quad \text{at } x = 1. \end{gathered} \tag{14}$$

Let us denote $a^{(m)} = a(b(0), 0)$ and $c = -m^{n+1}(n+2)a^{(m)}$. The steady-state solution with zero mass flux at the margin has the following asymptotic behaviour

$$h_0 = (2^n c)^{1/(2n+2)}x^{1/2} + O(x^k), \tag{15}$$

where $k = 3/2$ when $a_s \equiv 0$, and $k = 1$ else. On the other hand, if the horizontal mass flux at the margin (denoted by $-q^{(m)}m$, where $q^m = q|_{x=0}/m$) is not zero, then a solution of (5) has the behaviour

$$h \sim x^{n/(2n+2)}\left\{(n+2)m^{n+1}[(2n+2)/n]^n q^{(m)}\right\}^{1/(2n+2)}. \tag{16}$$

For the first order terms we obtain

$$\begin{gathered} q_{1x} + (a_s + \lambda)h_1 = 0, \quad 0 < x < 1, \\ q_1 = h_0^{n+1} s_{0x}^n h_1 / m^{n+1} + n h_0^{n+2} s_{0x}^{n-1} h_{1x} / [(n+2)m^{n+1}], \\ h_1 = 0 \quad \text{at } x = 0, \quad q_1 = 0 \quad \text{at } x = 1. \end{gathered} \tag{17}$$

The first order problem is a linear second order Sturm–Liouville problem (Courant and Hilbert, 1953). Finding solutions of (14),(17) analytically requires complex mathematical analysis and is outside the scope of this paper. However, when $n = 1$ (ice is a Newtonian fluid) we can find the eigenvalues as (Wilchinsky, submitted)

$$\lambda = \left\{ \int_0^1 \left[w_x^2 - (\gamma_x/2 + 3m_0^2 a_s / h_0^3) w^2 \right] dx \right\} \Big/ \int_0^1 3m_0^2 (w^2/h_0^3) dx, \tag{18}$$

where $w = h_0^3 h_1, \gamma = 3b_x/h_0$. This yields as sufficient condition of stability $\gamma_x/2 + 3m_0^2 a_s/h_0^3 \leq 0$ when $0 < x < 1$. If $b(x) \equiv const$, then this condition takes the form $a_s \leq 0$ when $0 < x < 1$, which is not informative, because for ice sheets we assume $a_s \geq 0$.

Integrating (17) with respect to x from 0 to 1 we derive the relation

$$q_1|_{x=0} - \int_0^0 a_s h_1 dx = \lambda \int_0^1 h_1 dx. \tag{19}$$

Equation (19) has an evident mechanical meaning: if the mass flux at the margin (q_1) is larger than the additional accumulation rate due to the changed surface elevation (the second term in (19)) then the steady-state solution is stable, otherwise it is not.

2.4 Singularity at the margin

If the mass flux at the margin $q^{(m)} \neq 0 \quad \forall \tau$, then it follows from (16) that $h_0 \simeq x^{n/(2n+2)}$ and from (17) we derive $h_1 \simeq x^{n/(2n+2)}$. Hence the expansion (13) is uniformly valid, that is the first order term of the expansion (13) is much smaller than the leading order term for any x, because $h_1/h_0 = O(1)$ as $x \to 0$. If the mass flux at the margin $q^{(m)} = 0$ when $\tau = 0$, then (15) yields $h_0 \simeq x^{1/2}$ and from (17) we derive $h_1 = \alpha x^{-1/2} + O(1) \to \infty$ as $x \to 0$, where α is an arbitrary constant. Hence, h_1 is unbounded and the expansion is not uniformly valid: $h_0 \ll \varepsilon h_1$ as $x \to 0$.

Let us consider a particular case when $b \equiv a_s \equiv 0$ to show that the singularity can be treated using the method of matched asymptotic expansions (Van Dyke, 1975). There are two causes to break the validity of the expansion (13). First, $h_0 \simeq \varepsilon$ when $x \simeq \varepsilon^2$. Second, the functions h and h_0 have different asymptotic behaviours as $x \to 0$. In the latter case, in order to find

the thickness of the boundary layer near the margin, where the expansion (13) is not valid, we integrate (12) with respect to x from 0 to 1 to obtain

$$q^{(m)} = -\int_0^1 h_\tau dx = O(\varepsilon). \tag{20}$$

Hence, from (16) we derive $h \simeq (\varepsilon x^n)^{1/(2n+2)}, x \to 0$. Because $h_0 \simeq x^{1/2}$, we have $h_0/h \simeq (x/\varepsilon)^{1/(2n+2)}$. Therefore $(h - h_0) \simeq h$, when $x \simeq \varepsilon$. On the other hand, $h_0 \simeq \varepsilon h_1 \simeq \varepsilon^{1/2}$, when $x \simeq \varepsilon$. In the other words, the inaccuracy of (13) is sensible when $x \simeq \varepsilon$.

To find the inner solution in the vicinity of the margin, we introduce the inner variable and function $\xi = x/\varepsilon, H = h/\varepsilon^{1/2}$. In these new variables the evolution equation takes the form

$$\begin{gathered}\varepsilon^{1/2} H_\tau = (H^{n+2} H_\xi^n)_\xi / [(n+2) m^{n+1}] + a^{(m)} + O(\varepsilon), \quad \xi > 0, \\ H = 0 \quad \text{at} \quad \xi = 0.\end{gathered} \tag{21}$$

Expanding $H = H_0 + O(\varepsilon^{1/2})$, we derive for the leading order term

$$H_0 = \chi \left\{ [Q - (n+2) m^{n+1} a^{(m)} \xi]^{(n+1)/n} - Q^{(n+1)/n} \right\}^{n/(2n+2)}, \tag{22}$$

where $\chi = (2/c)^{n/(2n+2)}$ and Q is a parameter to be determined by the matching procedure.

The inner solution is

$$\begin{gathered}h = H\varepsilon^{1/2} = \varepsilon^{1/2} [2^{n/(2n+2)} c^{1/(2n+2)} \xi^{1/2} + \\ + 2^{-(n+2)/(2n+2)} c^{-(2n+1)/(2n+2)} Q \xi^{-1/2}] + \\ + \varepsilon^{1/2} O(\xi^{-(n+2)/(2n)}) + O(\varepsilon).\end{gathered} \tag{23}$$

The outer solution is

$$h = (2^n c)^{1/(2n+2)} x^{1/2} + \varepsilon e^{-\lambda\tau} [\alpha x^{-1/2} + O(1)] + O(x^{3/2}) + O(\varepsilon^2). \tag{24}$$

Matching requires $Q = 2^{(n+2)/(2n+2)} c^{(2n+1)/(2n+2)} \alpha e^{-\lambda\tau}$.

Hence, the singularity arising in the expansion of the ice thickness about the steady-state solution can be treated by applying the method of matched asymptotic expansions. The singularity of the expansion (13) near the margin does not affect the eigenvalues λ and therefore is passive.

2.5 Numerical algorithm

Analytical solutions of (14) and (17) are difficult to find; therefore let us consider numerical methods of solving these equations. Two points must be taken into account: first, solutions of these equations have singular behaviour

($h_{0x} = O(x^{-1/2}), h_1 = O(x^{-1/2})$); second, h_0 can be unstable, therefore some iterational approaches of solving (14) may not be covergent.

In order to remove the singularities, we introduce new independent variable and smooth functions $y = x^{1/2}, u = h_1 y, v = h_0/y$ and integrate (14),(17) with respect to y from 0 to y. The problem for the zeroth-order solution takes the form (subscript y denotes derivative)

$$\begin{gathered} v^{n+2}(yv+b)_y^n + (2m)^{n+1}(n+2)\int\limits_0^y y_* a(b+y_*v, y_*^2)dy_*/y^2 = 0, \\ v = 2^{n/(2n+2)}c^{1/(2n+2)} \quad \text{at } y=0, \quad v^{n+2}(yv+b)_y^n = 0 \quad \text{at } y=1. \end{gathered} \tag{25}$$

We introduce the discretization length $\Delta = 1/n$ and $n+1$ nodes $y_i, i = 0, 1, .., n$ to obtain

$$\begin{gathered} v_{i+1/2}^{n+2}[(b_{i+1} + y_{i+1}v_{i+1} - b_i - y_i v_i)/\Delta]^n + \\ +(2m)^{n+1}(n+2)y_{i+1/2}^{-2}\left[(ya)_{i+1}\Delta/8 + (ya)_i\Delta 3/8 + \sum_{j=0}^{j=i-1}(ya)_{i+1/2}\Delta\right] = \\ = O(\Delta^2/(i\Delta)); \quad r_{i+1/2} = (r_i + r_{i+1})/2, \quad r = v, y, ay. \end{gathered} \tag{26}$$

This numerical scheme has approximation accuracy of $O(\Delta)$ near the margin and $O(\Delta^2)$ for $i\Delta \simeq 1$. This numerical algorithm represents an implicit Euler scheme and does not require iterations in determining the function v starting from some initial approximation. The developped algorithm was tested with the analytical solution (11), and convergence of the numerical scheme was shown for it.

The considered algorithm permits us to find v for any m. The ice sheet length m can be determined from the boundary condition at the ice divide ($y = 1$).

After integration, the eigenvalue problem (17) in new variables is written as

$$\begin{gathered} \phi u_y + \psi u + \int\limits_0^y \mu u dy^* = 2v_0^{2n+1}u_0, \quad 0 < y < 1, \\ \phi u_y + \psi u = 0 \quad \text{at } y = 1, \end{gathered} \tag{27}$$

where

$$\begin{gathered} \phi = ynv^{n+2}(b+yv)_y^{n-1}, \quad \mu = (2m)^{n+1}(n+2)(a_s + \lambda), \\ \psi = (n+2)v^{n+1}(b+yv)_y^n - nv^{n+2}(b+yv)_y^{n-1}. \end{gathered} \tag{28}$$

Here $u(0)$ is arbitrary. The numerical approximation is developped as it was done for the determination of v. However, the accuracy is now uniformly $O(\Delta^2)$, and we have developped an explicit Euler scheme. The parameter λ is determined from the boundary condition at the divide. This numerical scheme was tested with the analytical solution of the inhomogeneous equation (27), and covergence of the scheme was demonstrated.

2.6 Experiments

To study the ice sheet stability the following functions were chosen: $B = b_1X^2, A = a_1s + a_2 + a_3X$, where b_1, a_1, a_2, a_3 are constants. Parameters $b_1, a_1, -a_3/a_1$ represent the (typical) bed slope, the vertical gradient of the mass balance and the equilibrium line inclination (line at which $A = 0$), respectively. The equilibrium line altitude is given by the formula $z = -(a_2 + a_3X)/a_1$. In the numerical experiments, the minimum value of λ as a function of one of these parameters is found, while the other parameters are fixed. The numerical experiments showed that in many cases there exist two solutions of the leading-order problem (14) with different m. In Figs.2-3 we will show direction of the increase of m by arrows.

The dependence of λ on b_1 is presented in Fig. 2. Six curves are shown. Curves $1, 2, 3$ are determined by $a_3 = 0, -0.2, 0.2$, respectively, while $a_1 = 1, a_2 = -0.5, n = 1$ are taken fixed as common values. Curves $4, 5, 6$ are determined by the same values as curves $1, 2, 3$ except the parameter $n = 3$. When $b_1 < 0$, there are two steady-state solutions – stable and unstable. These solutions coincide at the axis $\lambda = 0$ determining neutral equilibrium. It can be seen that positive downstream bed slope ($b_1 > 0$) leads to the absence of stable solutions.

Dependence of λ on a_3 is depicted in Fig. 3. Six cases are again considered. Curves $1, 2, 3$ are determined by $b_1 = 0, -0.2, 0.2$, respectively. The other parameters are taken as $a_1 = 1, a_2 = -0.5, n = 1$. Curves $4, 5, 6$ are determined by the same values as curves $1, 2, 3$ except the parameter $n = 3$. For the cases 1,4 (for $a_3 < 0$) and 2,5 there are two steady-state solutions – stable and unstable. In particular, for $n = 3$ there are two (stable and unstable) solutions when $b_1 < 0.03$. If the bed slope is larger, then there are no stable solutions.

If $b_1 \equiv a_3 \equiv 0$, then a change of the parameters a_1, a_2 does not affect the stability. This can be derived with the help of similarity theory. Let $\hat{h}$ be a solution of the equation

$$\hat{h}_{\hat{\tau}} + (\hat{h}^{n+2}\left|\hat{s}_{\hat{X}}\right|^n)_{\hat{X}}/(n+2) = \hat{A}(\hat{s}, \hat{X}), \quad \hat{s} = \hat{h} + \hat{B}, \tag{29}$$

where

$$\begin{gathered}\hat{B}(\hat{X}) = B(X_*\hat{X})/h_*, \quad \hat{A}(\hat{s}, \hat{X}) = A(h_*\hat{s}, X_*\hat{X})X_*^{n+1}/h_*^{2n+2}, \\ \hat{X} = X/X_*, \quad \hat{h} = h/h_*, \quad \hat{\tau} = \tau h_*^{2n+1}/X_*^{n+1},\end{gathered} \tag{30}$$

and $X_*, h_* = const$. If h is a steady-state solution of (5), then $\hat{h}(\hat{X}) = h(X_*\hat{X})/h_*$ is a solution of (29).

For the case considered, we have $\hat{B}(\hat{X}) = \hat{b}_1\hat{X}^2$, where $\hat{b}_1 = b_1X_*^2/h_*$, and $\hat{A} = \hat{a}_1\hat{s} + \hat{a}_2 + \hat{a}_3\hat{X}$ with $\hat{a}_1 = a_1X_*^{n+1}/h_*^{2n+1}, \hat{a}_2 = a_2X_*^{n+1}/h_*^{2n+2}, \hat{a}_3 = a_3X_*^{n+2}/h_*^{2n+2}$.

If $b_1 \equiv a_3 \equiv 0, a_1 > 0, a_2 < 0$ and h is the solution found for particular values $a_1 = \tilde{a}_1, a_2 = \tilde{a}_2$, then for any values a_1, a_2 equating $\hat{a}_1 = \tilde{a}_1, \hat{a}_2 = \tilde{a}_2$

gives us two equations for the determination of h_*, X_*, which determines $\hat{h}(\hat{X}, \hat{\tau}) = h(\hat{X}, \hat{\tau})$. Therefore, in variables $\hat{h}, \hat{X}, \hat{\tau}$ we have the same solutions and the same eigenvalues for any $a_1 > 0, a_2 < 0$.

Experiments showed stability of the ice sheets when $a_1 = 0, a_2 = 0.5, a_3 = -1$ and b_1 is arbitrary (solution $h(X, \tau, b_1)$). In this case equating $\hat{a}_2 = 0.5, \hat{a}_3 = -1$ for any $a_2 > 0, a_3 < 0$ allows us to find X_*, h_* and $\hat{b}_1 = b_1 X_*^2 / h_*$, such that $\hat{h}(\hat{X}, \hat{\tau}) = h(\hat{X}, \hat{\tau}, \hat{b}_1)$. Therefore, the ice sheets are stable when $a_1 = 0$, while $a_2 > 0, a_3 < 0, b_1$ are arbitrary.

For interpretation of the numerical experiments let us turn to (19), from which it follows that if the mass flux at the margin is larger than the additional accumulation rate due to the changed surface elevation, then the steady-state solution is stable, otherwise it is not. Evidently, conditions making the ice flow "easier" will lead to a larger mass flux at the margin and, hence, to stability. Here, the intuitive term "easier" cannot be substituted by the term "faster", because the ice sheet length and its geometry also influence the stability.

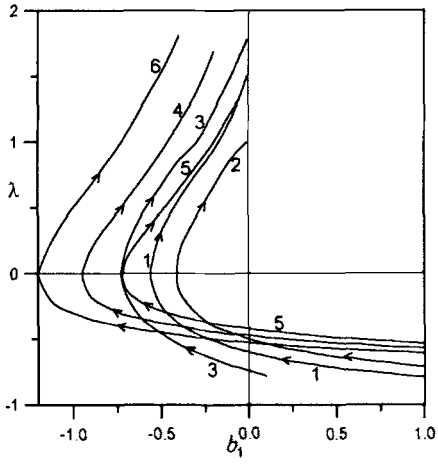

Fig. 2. The dependence of the minimum eigenvalue λ on the typical bed slope b_1

Physically, the larger the (negative) bed slope is in comparison with the average ice thickness gradient, the "easier" will be the ice flow and vice versa. Moreover, the higher the equilibrium line inclination is, the "easier" will also be the ice flow. If in the numerical experiments there are two (stable and unstable) solutions for the same data set, then the stable ice sheet is longer than the unstable one. On the other hand, the longer the ice sheet, the smaller the average ice thickness gradient. Thus, the longer the ice sheet is, the stronger will be the influence of the bed slope. Therefore, when the bed slope changes in the experiments, two mechanisms interact: the changing

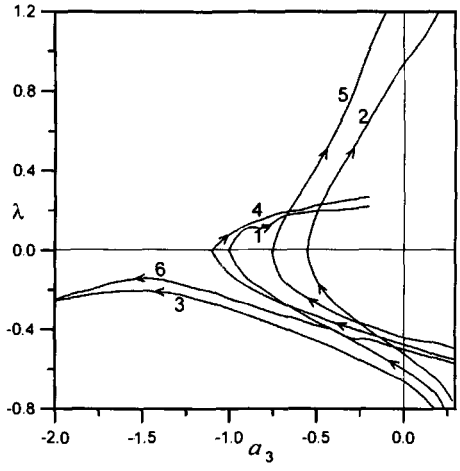

Fig. 3. The dependence of the minimum eigenvalue λ on the equilibrium line inclination a_3

bed slope and the changing ice sheet length. The experiments show that small changes of the bed slope lead to large changes of the stable-ice-sheet length. Therefore, an increase of the (negative) bed slope causes a decrease of the minimum eigenvalue of the stable ice sheets. At the same time, when the ice sheet is unstable, then an increase of the (negative) bed slope leads to an increase of λ. Similar results can be derived for the influence of the equilibrium line inclination. However, as the experiments show, the bed slope has stronger influence on the stability, than the equilibrium line inclination. For example, when $b_1 > 0.03, n = 3$ there are no stable solutions. In this case an increase of the (positive) equilibrium line inclination leads to an increase of the ice sheet length, and, hence, to a stronger influence of the (positive) bed slope leading to instability. Therefore, stability cannot be achieved. On the other hand, when the bed slope is negative, then there is a stable solution even if the equilibrium line inclination is positive, which could lead to instability.

3 Conclusions

The accumulation rate distribution has a strong influence on the ice sheet stability. If the accumulation rate does not depend on elevation then steady-state solutions are stable. If it does depend on elevation, then stability is determined by bed slope and equilibrium line inclination. Positive downstream bed slope causes instability. Again, if the bed is a horizontal plane, then a negative downstream inclination of the equilibrium line also causes instability. In many cases there exist two steady-state solutions – stable and unstable – they are in neutral equilibrium when they coincide for certain values of the

parameters. A change of the flow law exponent has only a quantitative (but not qualitative) influence on the ice sheet stability.

The singularity of the perturbation at the margin can be treated by the application of the method of matched asymptotic expansions and does not affect the eigenvalues.

Acknowledgement: I thank the editor Prof. K. Hutter and both referees Dr. R. Greve and A. Savvin for useful remarks.

References

1. Bodvardsson G. (1955) On the flow of ice sheets and glaciers. *Jökull.* **5**, 1-8
2. Courant R., Hilbert D. (1953) *Methods of Mathematical Physics.* Vol. I. Wiley-Interscience
3. Fowler A. C. (1992) Modelling ice sheet dynamics. *Geophys. Astrophys. Fluid Dyn.* **63**, 29-65
4. Fowler A. C. , Larson D. A. (1978) On the flow of polythermal glaciers I: model and preliminary analysis. *Proc. R. Soc. Lond.* **A363**, 217-242
5. Fowler A. C. , Larson D. A. (1980) On the flow of polythermal glaciers II: surface wave analysis. *Proc. R. Soc. Lond.* **A370**, 155-171
6. Glen J. W. (1955) The creep of polycrystalline ice. *Proc. R. Soc. Lond.* **A228**, 519-538
7. Hindmarsh R. C. A. (1996) Stochastic perturbation of divide position. *Ann. Glaciol.* **23**, 94-104
8. Hindmarsh R. C. A., Normal modes of an ice sheet. *J. Fluid Mech.* **335**, 393-413
9. Hutter K. (1983) *Theoretical glaciology.* Reidel, Dordrecht
10. Morland L. W. , Johnson I. R. (1980) Steady motion of ice sheets. *J. Glaciol.* **28**, 229-246
11. Nye J. F. (1959) The motion of ice sheets and glaciers. *J. Glaciol.* **3**(26), 493-507
12. Oerlemans J. (1996) Modelling the response of valley glaciers to climatic change, In: Boutron C. (Ed.) *Physics and chemistry of the atmospheres of the Earth and other objects of the solar system*, ERCA, Vol. II, 91-123
13. Salamatin A. N., Mazo A.B. (1984) Similarity analysis of the general mathematical model of an ice-cap glacier. *J. Sov. Math.* **44**(5), 664-672
14. Vialov S. S. (1958) Regularities of ice deformation. In: *International Assosiation of Scientific Hydrology Symposium at Chamonix 1958* – Physics of the Movement of Ice, publ. 47, 383-391
15. Van Dyke M. (1975) *Perturbation methods in fluid mechanics.* Parabolic Press, Stanford, California
16. Weertman J. (1961) Stability of ice-age ice sheets. *J. Geophys. Res.* **66**, 3783-92
17. Wilchinsky A.V. (submitted) Studying ice sheet stability using method of separation of variables. *Geophys., Astrophys. Fluid Dynamics*
18. Wilchinsky A. V., Chugunov V.A. (1997) Modelling ice-divide dynamics by perturbation methods. *J. Glaciol.* **43**(114), 352-358

(Received 4 Jan. 1999, accepted 14 Feb. 1999)

A Computational Procedure for Instationary Temperature-Dependent Snow Creep

Perry Bartelt[1] **and Marc Christen**[2]

[1] Head Avalanche Dynamics and Numerics, Swiss Federal Institute for Snow and Avalanche Research, CH 7260 Davos Dorf, Switzerland, bartelt@slf.ch
[2] Engineer,Swiss Federal Institute for Snow and Avalanche Research, CH 7260 Davos Dorf, Switzerland, christen@slf.ch

Abstract. A computational procedure to model instationary creep movements in alpine snowpacks is presented. The model allows the study of large volumetric and shear strains (new snowfall), temperature dependent material behaviour (sudden warming) and progressive creep fracture. These processes are all important factors in natural avalanche release. A viscoelastic material model for snow is proposed in which the constitutive properties are characterized on planes of various orientations within the material. This model is conceptually simple because it does not employ complicated tensorial arguments. It is, however, capable of modelling the highly nonlinear and complex material behaviour of snow including the influence of material microstructure. The model requires only a few parameters which can be determined from simple uniaxial or triaxial experiments. The new constitutive model and numerical procedure is verified using two field and laboratory experiments.

1 Introduction

The purpose of this paper is to present a finite element based computational procedure to calculate instationary viscoelastic creep movements in alpine snowpacks. The procedure can model: (1) large volumetric and shear strains (0.50 to 1.00) and strain-rates (up to $10^{-3}s^{-1}$) to allow the study of snowpack movements after a heavy snowfall and the settlement of new snow, (2) temperature dependent material behaviour (including phase change) to allow the study of sudden variations in meteorological conditions, such as a quick rise in temperature with strong winds (Föhn), (3) fracture or progressive creep damage of weak snow layers based on the crystal morphology of those layers and (4) the creep forces exerted on avalanche retaining structures.

We would like to emphasize that these modelling requirements are posed by avalanche warning specialists at our institute who are now beginning to use physical snowpack models on a day-to-day operational basis [1], [2]. The determination of the maximum creep force exerted on defense structures is also an important engineering task for the safety of many mountain communities.

The finite element method has been employed to simulate snowpacks [3], [4], [5], [6]; however, these calculations have all made the assumption of

stationary strain-rates and small deformations and strains. They are not adequate to postulate and quantify theories of avalanche formation, especially immediately after a new snowfall when the snowpack creep velocities are clearly instationary. In the snow settlement experiments of de Quervain, 1945, [7], which are modelled in this paper, snow increased in density from 120 [kgm^{-3}] to over 300 [kgm^{-3}] from self-weight alone in a period of 100 days. The experiments clearly showed that the settlement velocities reached a constant deformation velocity only after 70 days. Moreover, instationary creep behaviour dominated the duration of the experiments.

The greatest difficulty in the modelling of these processes is to formulate a constitutive law for snow that is both simple, i.e. it can be well understood intuitively, while, at the same time, it is elaborate enough to treat highly nonlinear and complex material behaviour. These goals are clearly at odds with each other. A further requirement is that the constitutive theory be expanded to consider the influence of snow micro-structure on material response. Of particular importance is the modelling of the strength of the snow-crystal bonds or necks. Of course, the law must also be directly verifiable by both field and laboratory experiments.

In the first part of this paper the constitutive model and the large-strain, rate-dependent plane strain finite element numerics are presented. The constitutive model does not employ over-complicated theories to describe viscoelastic snow behaviour [8], [9] or fracture [10]. These theories are both conceptually difficult and require complex experiments (shear tests) to determine the material parameters. Furthermore, they neglect the influence of snow microstructure.

In our approach the constitutive properties are characterized using simple one-dimensional material laws on planes with various orientations within the material. The overall material response, including shear resistance, is found by superimposing the response of the individual directions. This facilitates a better understanding of the material behaviour and, most importantly, the constitutive law requires fewer parameters which can be determined using simple temperature dependent uniaxial or triaxial tests. (Traxial creep tests using a specially designed triaxial apparatus for snow are presently being performed at our institute.) Finally, since the material laws are one-dimensional it is much easier to introduce microstructural parameters (grain size and shape, bond strength, neck length) into the constitutive model. Above all, fracture criteria based on snow microstructure can be easily formulated. The proposed model is based on so-called "microplane" models that have been successfully used to simulate progressive tensile fracturing and/or damage of aggregate materials such as concrete and rock [11], [12], [13].

The model is verified using both field and laboratory experiments. The 100-day creep experiments of de Quervain [7] and the snow settlement experiments of Kojima [14] are simulated with a high degree of accuracy.

2 Microplane Material Laws for Snow

Snow is a porous material consisting of ice grains and air. The ice grains have different shape and size depending on the thermodynamical and mechanical history of the snow. The ice grains are bonded together at so-called necks to form complex load carrying chains. The response of snow under loading is primarily a function of (1) the number of chains, which is usually described by the snow density, (2) the strength of the individual grain bonds, (3) the grain size and (4) the neck length. The deformation rate plays an important role on overall material behaviour since the ability of snow to form new load carrying chains and the strength of the ice bonds is rate dependent. In summary, the mechanical behaviour of snow is strongly dependent on the microstructural parameters of the ice matrix and the rate of applied loading. The constitutive modelling, however, is made even more difficult by the fact that the microstructure parameters are persistently changing under an applied temperature gradient and overburden pressure. Fig. 1 shows an idealized schematic representation of snow consisting of ice grains, grain bonds and load chains.

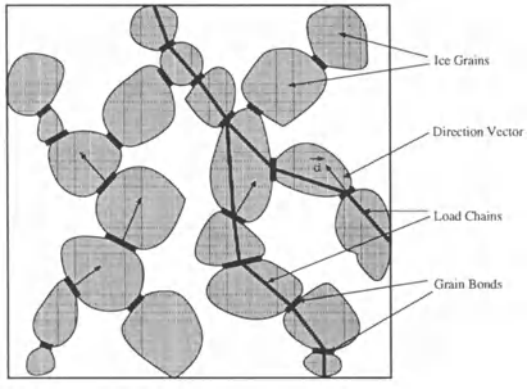

Fig. 1. Snow microstructure with microplane directions

In our model for snow creep and fracture, the constitutive laws are defined on planes of various orientations within the material. Bazant [11] called these planes "microplanes" because the inelastic material behaviour of each plane is based on the mechanics of the material microstructure. He introduced the prefix "micro" in order to emphasize the fact that for many materials the mechanical behaviour, especially fracture and damage, is best characterized on weak planes that are found in the material microstructure, specifically the interaggregate contact planes which, for the case of snow, are the ice grain bonds and necks.

The behaviour of the individual microplanes is described by simple one-dimensional rheological material laws relating the normal stresses and strains in a single direction. We postulate that the mechanical behaviour and strength of the ice grain chains is more realistically and more simply described by the N-directional one-dimensional laws than complicated tensorial constitutive laws with many parameters. In a first approximation shear strains in the microplane directions are unopposed. However, this does not imply that the material as a whole has no shear stiffness: shear deformations are resisted by the normal stiffness of each microplane. The total material response is found by superimposing the contributions from all directions.

The strain on any microplane n is the resolved component of the macroscopic strain E_{ij} defined with respect to a Cartesian coordinate system. For plain strain:

$$\epsilon_n = d_{in} d_{jn} E_{ij} \qquad \text{for} \qquad i,j = 1,2 \qquad \text{(No sum on n)}, \tag{1}$$

where d_{1n} and d_{2n} are the components of the $n-th$ unit direction vector d_n, see Fig. 2, and are defined according to

$$d_n = \left\{ \begin{matrix} d_{1n} \\ d_{2n} \end{matrix} \right\} = \left\{ \begin{matrix} \cos(\phi - \frac{(n-1)\pi}{N}) \\ \sin(\phi - \frac{(n-1)\pi}{N}) \end{matrix} \right\}. \tag{2}$$

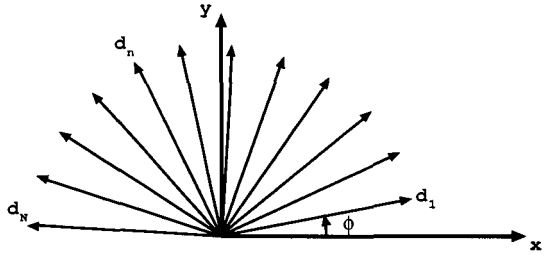

Fig. 2. The direction vectors d_n for $n = 1$ to N. As a first approximation, we assume that snow is an isotropic material and that the direction vectors are equally distributed.

We term ϵ_n the microstructure strain or the N-directional strain. In matrix form (1) can be written as

$$\{\epsilon\} = [D]\,\{E\}\,. \tag{3}$$

Relation (1) is termed a kinematic constraint since the strain in the $n-th$ direction is related to the macroscopic state of deformation. According to

Bazant [11], this approach physically models the behaviour of brittle aggregate materials better than by assumming that the microstresses in the N-directions correspond to the macroscopic stress. The stresses in a porous granular material like snow are far from uniform having very high stress concentrations at the snow crystal bonds: the microscopic stress state varies significantly from the macroscopic stress field. The kinematic constraint (1), however, ensures that the relative displacements between the ice crystals are approxiamated by the macroscopic strain field. This is a much better assumption, especially when formulating constitutive laws with fracture.

A further constraint is introduced into the microplane constitutive formulation. Namely that the N-directional stress components σ_n and Cartesian components S_{ij} which are work conjugate to the strains, ϵ_n and E_{ij}, respectively, must fulfill the scalar work equation,

$$S_{ij}E_{ij} = \sum_{n=1}^{N} \sigma_n \epsilon_n = \sum_{n=1}^{N} \sigma_n d_{in} d_{jn} E_{ij}. \tag{4}$$

The macroscopic Cartesian stress is thus related to the N-directional stress according to

$$S_{ij} = \sum_{n=1}^{N} d_{in} d_{jn} \sigma_n. \tag{5}$$

The above equation implies that the macroscopic state of stress, S_{ij} is found by superimposing the N-directional stresses. The stress σ_n represents the one-dimensional stress in the $n-th$ direction.

The vector d_n is defined in the undeformed coordinate system x_i. The angle ϕ is an arbitrary angle, usually set to $\phi = 0°$.

3 Viscoelastic N-Directional Material Models

In this section we formulate several one-dimensional, scalar material laws relating σ_n to ϵ_n (and not the tensors S_{ij} and E_{ij}). The N-directional constitutive formulation must meet a simple requirement: small strain linear isotropic elasticity will be modelled exactly. In this case the stress S_{ij} is related to the elastic strain E_{ij} according to the well known relation

$$S_{ij} = 2\mu E_{ij} + \lambda\gamma \tag{6}$$

where μ and λ are the Lamé constants and γ is the volumetric strain. The corresponding N-directional material law is

$$\sigma_n = \alpha\epsilon_n^e + \beta\gamma^e; \tag{7}$$

where α and β are material constants with the values

$$\alpha = \frac{8\mu}{N} = \frac{4C}{N(1+\nu)} \tag{8}$$

and

$$\beta = \frac{2\lambda - \mu}{N} = \frac{C}{N}\frac{4\nu - 1}{(1+\nu)(1-2\nu)} \tag{9}$$

The superscript e has been introduced to denote that the quantities ϵ_n and γ refer to the elastic N-directional and volumetric strains. The symbol C denotes the modulus of elasticity and ν Poisson's ratio. Note that when $\nu = 0.25$ then $\beta = 0$ and $\alpha = \frac{16}{5}\frac{C}{N}$. According to Mellor [15], $\nu = 0.25$ for medium to high density snow ($300 \leq \rho \leq 500$). For smaller densities ($\rho \leq 300$), $\nu \approx 0.20$.

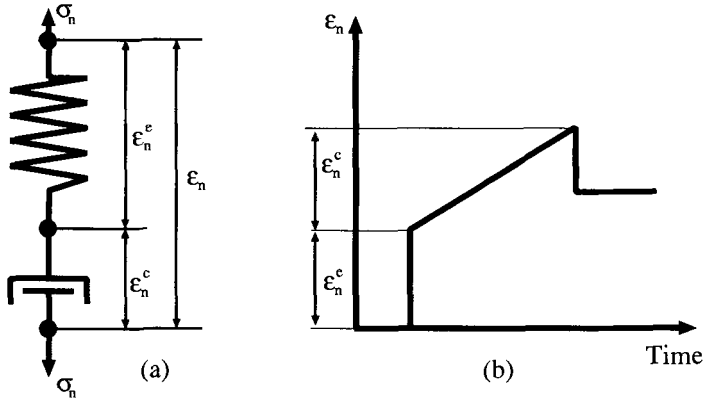

Fig. 3. (a) A visco-elastic Maxwell model describes the stress-strain relation in the $n-th$ direction. (b) Strain response of a Maxwell model under constant load.

Viscous behaviour (creep) is introduced into the N-directional material model by assuming that the total strain in the $n-th$ direction is composed of elastic and viscous parts, i.e.,

$$\epsilon_n = \epsilon_n^e + \epsilon_n^c. \tag{10}$$

Also, the total volumetric strain is likewise decomposed into elastic and viscous parts of

$$\gamma = \gamma^e + \gamma^c. \tag{11}$$

Thus, the N-directional material law (7) is rewritten as

$$\sigma_n = \alpha(\epsilon_n - \epsilon_n^c) + \beta(\gamma - \gamma^c). \tag{12}$$

Moreover, a simple Maxwell model is used to describe viscoelastic material behaviour. Of course, more complicated models are possible. Our motivation behind using this simple model in a first approximation is to demonstrate that even long time creep experiments and field tests can be modelled adequately with this law. The Maxwell model defines the viscous strain rate according to

$$\dot{\epsilon}_n^c = \frac{\sigma_n}{\eta} \tag{13}$$

The parameter η is termed the snow viscosity (with dimensions Pa s). Usually, the viscosity is defined as a function of the snow density and temperature $\eta = f(\rho, T)$. Several of the different laws are listed in the Table 1.

Table 1. Different constitutive laws for the compactive viscosity η.

Author (Year)	Viscosity [Pa s]
Kojima (1974) [14]	$\eta = 8.64(10^6)e^{0.021\rho}$
Mellor (1975) [15]	$\eta = 5.0(10^7)e^{0.022\rho}$
Claus (1978) [16]	$\eta = 6.57(10^7)e^{0.014\rho}$
Gubler (1994) [17]	$\eta = 1.86(10^{-6})e^{0.02\rho+8100/T}$
Morris (1994) [18]	$\eta = 5.38(10^{-3})e^{0.024\rho+\frac{6042}{T}}$
Loth (1993) [19]	$\eta = 3.70(10^7)e^{8.10(10^{-2})(273.15-T)}e^{2.10(10^{-2})\rho}$

* In the formulas T and ρ are to be substituted in Kelvin and kgm^{-3}

4 N-dimensional Constant Strain Triangular Elements

In this section the principle of virtual work (see, for example, Crisfield [20]),

$$W = W_i - W_e = \int_V \{S\}^T \{\delta E\}\, dV - W_e \tag{14}$$

is invoked in order to derive the tangent stiffness matrix and internal force vector of the N-directional plane strain triangular elements. In the equation above, W is the virtural work, W_i is the internal virtual work and W_e is the external virtual work. The internal virtual work is presently expressed in terms of the energy conjugate virtual Green's strains, δE, and the second Piola-Kirchhoff stress, S, which are both defined in a Cartesian coordinate system.

In the following the virtual work expression will be rewritten using the N-directional stress and strain measures presented in the previous section. As stated in the introduction, our goal is to develop a continuum finite element

that employs simple one-dimensional visco-elastic constitutive relations. This implies finding the N-directional virtual strains.

Viscous creep deformations are produced by introducing creep forces on the right-hand side of the equilibrium equations. These "pseudo-loads" enforce the viscous strain rates predicted by the viscous creep law. Thus, another important task of this section is to derive the creep "pseudo-load" vector.

In the next section, the computational procedure used to solve the global finite element equations, which is found by assembling the element stiffness matrices and force vectors, will be discussed.

Unlike the usual finite element formulation where the strains are found from the element-deformation gradient in the Cartesian directions, in this formulation the strains are calculated from the element side deformations. This is computationally efficient; however, it does introduce notational difficulties since a third strain measure arises. In the following a small e is used to denote the finite element side strains. Since the strains in the N-directions ϵ are finally used in the constitutive formulation, it does not matter whether the Cartesian strains E or element-side strains e are resolved into the N-directions.

As in the previous section, the superscripts e and v will be used to distinguish between the elastic and viscous strains in the N-directions, ϵ^e and ϵ^v, respectively. Also, the subscripts s and n are used to denote an element side and the $n-th$ direction. The superscript t will be used to define the element configuration at time t and the superscript 0 will be used to denote the undeformed element configuration, $t = 0$.

Consider Fig. 4 which depicts a finite element triangle with area A.

For the deformed state at time $t > 0$ the Green-Lagrange strain of element side s is:

$$e_s = \frac{{}^tL_s^2 - {}^0L_s^2}{2({}^0L_s^2)} = \frac{\Delta x_s^2 + \Delta y_s^2 - {}^0L_s^2}{2({}^0L_s^2)} \qquad \text{for} \qquad s = 1,2,3. \tag{15}$$

where ${}^0L_s^2$ and ${}^tL_s^2$ are the lengths of side s at the beginning of the analysis and time t, respectively. Note that for a pure rigid-body rotation the side strains are $e_s = 0$ for $s = 1,2,3$. The values Δx_s and Δy_s are found according to

$$\Delta x_s = {}^tx_i - {}^tx_j \quad \text{and} \quad \Delta y_s = {}^ty_j - {}^ty_i \quad \text{for} \quad i = 3,1,2 \quad \text{and} \quad j = 2,3,1. \tag{16}$$

The Green-Lagrange side strains are found with respect to the undeformed side lengths ${}^0L_s^2$. The element side strains e_s are related to the Cartesian Green-Lagrange strains E_{ij} by

$$\{e\} = \begin{Bmatrix} e_1 \\ e_2 \\ e_3 \end{Bmatrix} = \begin{bmatrix} \frac{\Delta x_1^2}{L_1^2} & \frac{\Delta y_1^2}{L_1^2} & \frac{2\Delta x_1 \Delta y_1}{L_1^2} \\ \frac{\Delta x_2^2}{L_2^2} & \frac{\Delta y_2^2}{L_2^2} & \frac{2\Delta x_2 \Delta y_2}{L_2^2} \\ \frac{\Delta y_3^2}{L_3^2} & \frac{\Delta y_3^2}{L_3^2} & \frac{2\Delta x_3 \Delta y_3}{L_3^2} \end{bmatrix} \begin{Bmatrix} E_{11} \\ E_{22} \\ E_{12} \end{Bmatrix} = [F]\{E\} \tag{17}$$

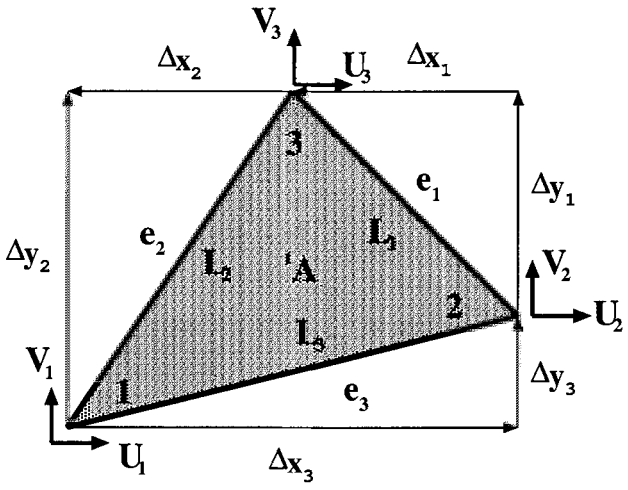

Fig. 4. Constant strain triangle.

From (3) the relationship between the side strains and N-directional strains can then be established

$$\{\epsilon\} = [D]\{E\} = [D][F]^{-1}\{e\} = [T_{ns}]\{e\}\,. \tag{18}$$

The N x 3 matrix $[T_{ns}]$ resolves the side strains into the N-directions. Note that the elements of this matrix are only functions of the element shape at time $t = 0$, the undeformed configuration. It must be determined only once at the beginning of each calculation.

If a set of virtual nodal displacements,

$$\{\delta a\}^T = \{\delta U_1, \delta V_1, \delta U_2, \delta V_2, \delta U_3, \delta V_3\} \tag{19}$$

is applied to the finite element, the virtual side strains are

$$\delta e_s = \frac{\Delta x_s}{{}^0L_s^2}\delta\Delta x_s + \frac{\Delta y_s}{{}^0L_s^2}\delta\Delta y_s = x_s(\delta U_i - \delta U_j) + y_s(\delta V_j - \delta V_i). \tag{20}$$

where x_s and y_s are defined by setting

$$x_s = \frac{\Delta x_s}{{}^0L_s^2} \qquad \text{and} \qquad y_s = \frac{\Delta y_s}{{}^0L_s^2} \tag{21}$$

Thus, the virtual strains can be expressed in matrix form as

$$\{\delta e\} = \begin{Bmatrix} \delta e_1 \\ \delta e_2 \\ \delta e_3 \end{Bmatrix} = \begin{bmatrix} 0 & 0 & -x_1 & -y_1 & x_1 & -y_1 \\ x_2 & -y_2 & 0 & 0 & -x_2 & y_2 \\ x_3 & y_3 & x_3 & -y_3 & 0 & 0 \end{bmatrix} \begin{Bmatrix} \delta U_1 \\ \delta V_1 \\ \delta U_2 \\ \delta V_2 \\ \delta U_3 \\ \delta V_3 \end{Bmatrix} = [{}^t\bar{B}]\{\delta a\}\,. \tag{22}$$

The superscript t is placed on the $[\bar{B}]$ matrix to emphasize that it is a function of the deformed element configuration. The virtual N-directional strains are subsequently related to the virtual finite element displacements according to

$$\{\delta\epsilon\} = [T_{ns}]\{\delta e\} = [T_{ns}]\left[{}^t\bar{B}\right]\{\delta a\} = \left[{}^tB\right]\{\delta a\}. \tag{23}$$

Rewriting the internal virtual work by using the N-directional stress and strain measures and then substituting the above epression relating the virtual element displacments to the virtual strains allows the definition of the finite element internal nodal forces $\{{}^tp_i\}$ at time t:

$$\begin{aligned} W_i &= \int_A \{S\}^T \{\delta E\}\, dA = \int_A \{\sigma\}^T \{\delta\epsilon\}\, dA \\ &= \{\delta a\}^T \int_A \left[{}^tB\right]^T \left\{{}^t\sigma\right\} dA = \{\delta a\}^T \left\{{}^tp_i\right\}. \end{aligned} \tag{24}$$

Moreover,

$$\left\{{}^tp_i\right\} = \left[{}^tB\right]^T \left\{{}^t\sigma\right\} {}^tA. \tag{25}$$

The tangent-element-stiffness matrix $[K_T]$ is found by differentiating the internal forces (see Crisfield [20]), i.e.

$$d\left\{{}^tp_i\right\} = \left(d\left[{}^tB\right]^T \left\{{}^t\sigma\right\} + \left[{}^tB\right]^T d\left\{{}^t\sigma\right\}\right) {}^tA = [K_T]\, d\{a\}. \tag{26}$$

In the numerical calculations we neglect the geometric stiffness contribution, that is,

$$d\left[{}^tB\right]^T \left\{{}^t\sigma\right\} \approx 0. \tag{27}$$

The increment in stress is found from the N-directional stress strain relationship (7),

$$d\{\sigma\} = d\left(\alpha\epsilon^e + \beta\gamma^e\right) = \left(\frac{d\alpha}{d\epsilon^e}\epsilon^e + \alpha + \frac{d\beta}{d\epsilon^e}\gamma^e\right) d\epsilon^e + \beta \sum_{n=1}^{N} \frac{d\gamma^e}{d\epsilon_n^e} d\epsilon_n^e. \tag{28}$$

Assuming that the last term of the above equation is small,

$$\beta \sum_{n=1}^{N} \frac{d\gamma^e}{d\epsilon_n^e} d\epsilon_n^e \approx 0, \tag{29}$$

the diagonal elements C_n of an NxN material matrix $[C_T]$ can be defined by

$$C_n = \left(\frac{d\alpha}{d\epsilon_n^e}\epsilon_n^e + \alpha + \frac{d\beta}{d\epsilon_n^e}\gamma^e\right). \tag{30}$$

The N-directional incremental stress-strain relationship is then

$$d\{{}^t\sigma\} = [{}^tC_T]\, d\epsilon^e = [{}^tC_T]\,[{}^tB]\, d\{a\}\,. \tag{31}$$

This equation can be substituted into (26) to find

$$d\{{}^tp_i\} = \left[[{}^tB]^T\,[{}^tC_T]\,[{}^tB]\,{}^tA\right] d\{a\}\,. \tag{32}$$

The element stiffness matrix is then by definition

$$[K_T] = [{}^tB]^T\,[{}^tC_T]\,[{}^tB]\,{}^tA. \tag{33}$$

The approximations (27) and (29) are not significant for the accuracy of the numerical calculations since the stiffness matrix is used only to approximate the internal stress state. As will be shown in the next section, the equilibrium between the internal and external forces is always strictly enforced. However, the approximations could influence the number of computational iterations required to find equilibrium. In the numerical calculations a Poisson's ratio for snow of $\nu = 0.25$ is assumed, thus, $\beta = 0$ and (29) is exactly zero.

The increment in load produced by a creep deformation is

$$d\{{}^tp_c\} = [{}^tB]^T\,[{}^tC_T]\, d\{\epsilon^v\}\,{}^tA. \tag{34}$$

These forces are applied to the finite element mesh in order to produce creep deformations corresponding to the time dependent viscous strain rates. In the calculation procedure we use an explicit scheme to find d $\{\epsilon^v\}$:

$$d\{\epsilon^v\} = \{\dot{\epsilon}^v\}\,\Delta t, \tag{35}$$

where Δt is the time step increment of the time integration scheme.

Finally, a self-weight load, $\{{}^tp_e\}$, always acts on the system. This element force vector is calculated according to

$$\{{}^tp_e\}^T = \left\{0, -\frac{\rho g A}{3}, 0, -\frac{\rho g A}{3}, 0, -\frac{\rho g A}{3}\right\}, \tag{36}$$

where g is the gravitational acceleration and ρ the density of the finite element. This vector is constant since the mass of each element remains unchanged during the calculation.

5 Solution of the Equilibrium Equations

The equations of equilibrium which must be satisfied at any instant of time t are the balance between internal and external nodal forces,

$$\{{}^tp_i\} + \{{}^tp_e\} = \int_A [{}^tB]^T\,\{{}^t\sigma\}\, dA + \{{}^tp_e\} = 0. \tag{37}$$

These equations can also be posited in incremental form

$$d\{{}^t p_i\} + d\{{}^t p_e\} = \int_A [{}^t B]^T \, d\{{}^t \sigma\} \, dA + d\{{}^t p_e\} = 0, \tag{38}$$

in which $d\{{}^t p_e\}$ is the change in external load during the time interval Δt. For our case, $d\{{}^t p_e\}$ is usually zero, except in the beginning of the analysis or during a new snowfall.

The displacement increment $d\{a\}$ which is calculated for the time step Δt is found according to

$$d\{a\} = [{}^t K_T]^{-1} \, d\{R\}, \tag{39}$$

where $d\{R\}$ is called the incremental pseudo-load vector containing the influence of the instationary creep effects of

$$d\{R\} = d\{{}^t p_c\} + d\{{}^t p_e\} = \int_A [{}^t B]^T \, [{}^t C_T] \, \{{}^t \dot{\epsilon}^v\} \, \Delta t dA + d\{{}^t p_e\}. \tag{40}$$

These calculations require the formation of the $[{}^t B]^T$ matrix for every element at every time step. This is not computationally demanding since the calclation of $[{}^t \bar{B}]$ needs only a few floating point operations, (22). It is then multiplied with the Nx3 matrix $[T_{ns}]$, see (23). This transformation matrix is formed only once at the beginning of a computation.

Because the calculation (40) is based on the linearized form of the equilibrium equations, (39), they will not satsify the equilibrium condition (38) exactly. Thus, several iterations may be required to satisfy (40) within some specified convergence criterion. The out-of-balance forces at the end of the time step are always added to the applied force increment $d\{{}^t p_e\}$ at the next time step.

In summary, the computational procedure is as follows:

(1) At time t, the displacements $\{{}^t a\}$, N-directional stress $\{{}^t \sigma\}$ and external forces $\{{}^t p_e\}$ are known. To begin at $t = 0$, we set $\{{}^0 a\} = 0$. The initial stress state $\{{}^0 \sigma\}$ is determined from a small strain elastic analysis. The external load is self-weight.

(2) The creep-strain rate in N-strain-directions is determined for every element,

$$\{{}^t \dot{\epsilon}^v\} = f\left({}^t \sigma_n, {}^t T, {}^t \rho\right), \tag{41}$$

according to a vicous law listed in Table 1. The creep strain increment in the nth-direction is thus

$$d\{\epsilon^v\} = \{{}^t \dot{\epsilon}^v\} \, \Delta t. \tag{42}$$

(3) Find the NxN diagonal elasticity matrix $[C_T]$ from (30).

(4) Construct the incremenatal creep force vector $d\{p_c\}$ according to (34) and add it to the incremental external load vector $d\{p_e\}$ to obtain the pseudo-load vector $d\{R\}$.
(5) Construct the tangent stiffness matrix $[{}^tK_T]$ according to (33).
(6) Calculate the increment in displacements $d\{a\}$ according to (39).
(7) Calculate the increment in total strain and stress in N-directions for each element

$$d\{\epsilon\} = [{}^tB]\, d\{a\}\,. \tag{43}$$

$$d\{\sigma\} = [C_T]\,(d\{\epsilon\} - \{\dot{\epsilon}^v\}\,\Delta t)\,. \tag{44}$$

(8) Update the stress

$$\{{}^{t+\Delta t}\sigma\} = \{{}^t\sigma\} + d\{\sigma_n\}\,. \tag{45}$$

(9) Update the displacements

$$\{{}^{t+\Delta t}a\} = \{{}^ta\} + d\{a\}\,. \tag{46}$$

Finally, note that the determination of the increment in creep strains $d\{\epsilon^v\}$ is based on an Euler time integration; that is, it is determined by the conditions existing at time t. This procedure is not unconditionally stable. Therefore, both the stability and the numerical results depend on the time step size Δt.

6 One-Hundred Day Laboratory Settlement Experiments of M. de Quervain, 1945

In order to determine long-term, temperature dependent snow settlement curves, De Quervain (1945) [7] filled eight wooden boxes (20cm x 20cm x 100cm) with 90 cm of sieved snow (grain size of 0.3mm) and measured the snow displacement and density distribution daily, see Fig. 5a and Fig. 5b. The experiment lasted 100 days, the first 40 days being investigated in this example. The experimental results are extremely well documented and are ideal first examples to test the computational procedure described in the first part of this paper.

De Quervain used the experiments to develop empirical settlement curves for inhomogeneous (multi-layer) snowpacks. At the time this was an improvement over the existing theory of Haefeli (1942) [21], which considered only homogeneous snow (single layer snowpacks) and was based on a purely empirical formula.

Although De Quervain realized that snow metamorphism and sublimation produced a settlement and mass loss, he was primarily interested in the time dependent mechanical deformation caused by self-weight and wind loads. He

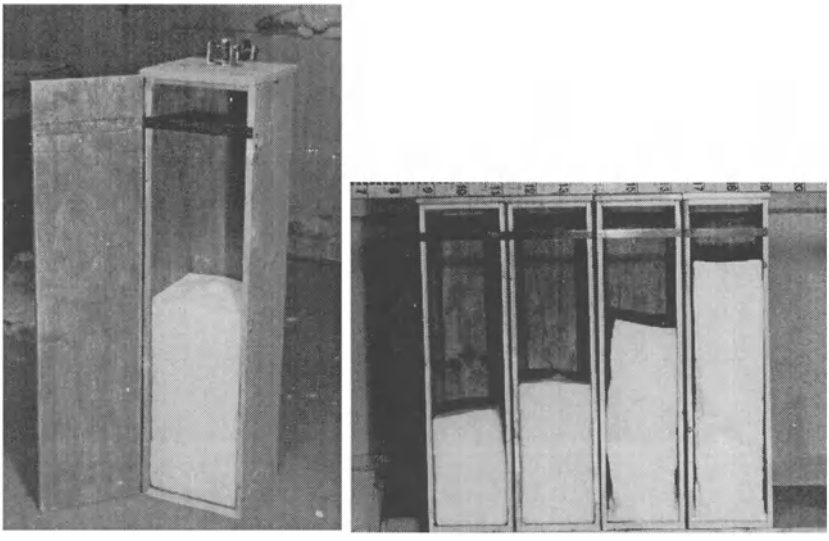

a b

Fig. 5. a) Open wooden box showing the settlement measuring instrument on top of it; b) Wooden boxes after the 100 days settlement period, temperature boundary being -2C, -10C, -18.5C and -32.5C (from left to right).

believed that the deformation of new snow was primarily caused by overburden stress, and not ice crystal changes, which occur at a much slower rate. For this reason De Quervain performed the experiments in the laboratory with homogeneous snow under constant temperature. The initial snow density was approximately 115 [kgm^{-3}]; the snow settled up to 50 cm and compacted to densities over 300 [kgm^{-3}], depending on the test temperature. Four different temperatures were used: -2 C, -10 C, -18.5 C and -32.5 C. Ski-wax was used to mimimize the side wall friction of the wooden boxes.

Calculations were carried out, using different viscosity laws (see Table 1), and comparing them to the measured values. A 'best-fit' viscosity law (*Christen* viscosity law) was developed,

$$\eta = 2.0(10^{-8})\rho^{7.9}, \quad \text{[Pa s]}, \qquad (\rho \text{ in [kgm}^{-3}\text{]}) \tag{47}$$

yielding very good results in this special experiment (see Table 3), but failing when used with other problems. Table 3 compares the measured and simulated settlement and density results.

Table 2. Initial simulation data

Simulation Begin/End [days]	0 - 40
Initial Mesh Height [cm]	90
Initial Density [kgm^{-3}]	115
Initial Temperature [C]	-10

Table 3. Simulation results.

Simulation time	5 Days		40 Days	
Viscosity	Settlement [cm] Δh	Density [kgm^{-3}] Top/Base	Settlement [cm] Δh	Density [kgm^{-3}] Top/Base
Measurements	20.0	150/188	39.8	186/288
Kojima	54.8	125/496	-	-
Mellor	25.7	116/210	55.4	131/509
Claus	11.6	115/144	50.9	121/551
Gubler	34.6	115/292	59.3	119/596
Morris	19.6	115/174	51.3	117/441
Christen	19.7	115/164	40.5	120/275

7 Kojima's Field Experiments on the Densification of Natural Snow Layers, 1974

Simple field experiments were performed by Kojima (1974) [14] in order to determine the densification strain-rates of natural snow layers under load. Kojima wanted to demonstrate with his experiments that snow load, and not the metamorphism of snow crystals and grains, is the driving mechanism behind layer densification.

Kojima measured the settlement of several layers of a natural snowpack. The layer densities in Kojima's studies varied between 100 and 300 [kgm^{-3}]. He added and subtracted snow at different locations in order to vary the overburden stress. Subsequently, the layers densified at different rates. By analyzing the initial and final layer densities, it was then possible to determine an average settlement strain-rate as a function of the stress. This information was used to formulate a viscosity law for low density snow,

$$\eta = 8.64(10^6)e^{0.021\rho} \quad \text{[Pa s]}, \qquad (\rho \text{ in [kgm}^{-3}\text{]}). \tag{48}$$

In this section, the load subtraction tests of Kojima are simulated using this viscosity law. The notation used by Kojima to designate the tests and layer positions, as well as the initial densities will be taken directly from the original paper.

In the load subtraction experiments a 5 x 1.5 m wide and 1 m deep trench was dug in a level snowpack near Sapporo. On one side of the trench four points were selected where 70 x 70 cm hollows were made by removing snow in the upper part of the snowpack. Each hollow had a different depth. Thus, the snow beneath each hallow was subjected to a different overburden stress. The subtracted loads at the hollows (denoted S-1 to S-4) was 0.16 kPa, 0.33 kPa, 0.67 kPa and 1.07kPa. The points, S-a, S-b, etc., refer to the positions were densification measurements were made.

Kojima provides numerical values of initial and final snow density, time interval (six days for the load subtraction tests), average strain rate, load and settlement at the locations S-b, S-c and S-d. Temperatures were not measured. A comparison between the measured and calculated final layer densities and the total settlement is presented in Table 4.

Table 4. Measured and simulated layer densities and settlements.

Snow Layer	Hallow	Initial Snow Density $[kgm^{-3}]$	Measured Final Density $[kgm^{-3}]$	Sim. Final Density $[kgm^{-3}]$	Measured Settlement [cm]	Sim. Settlement [cm]
S-b	N	138	218	350	13.3	18.0
	S-1	138	197	250	10.7	14.0
	S-2	138	169	195	9.8	11.5
S-c	N	184	250	310	7.5	10.1
	S-1	184	236	265	6.2	7.7
	S-2	184	222	250	6.1	7.4
S-d	N	237	286	310	5.8	7.0
	S-1	237	280	305	5.1	5.2
	S-2	237	282	282	5.0	5.1
	S-3	237	257	257	3.1	3.0

The simulation results for snow layer S-d, located near the bottem of the snowpack, show a very good agreement with the measurements (both densities and settlements). This layer has the highest initial density. The deviation

of the simulation results from the measurements worsens with decreasing initial density. The poorest agreement is at position S-b which is located only 20 cm below the snowpack surface.

In Table 5 a comparison is made between the measured and calculated average strain rates.

Table 5. Measured and simulated average strain rates.

Snow Layer	Hallow	Measured Average Strain Rate $10^{-7}(s^{-1})$	Simulated Average Strain Rate $10^{-7}(s^{-1})$
S-b	N	8.87	7.19
	S-1	6.88	6.65
	S-2	3.91	4.16
S-c	N	5.93	6.04
	S-1	4.81	5.39
	S-2	3.65	4.36
S-d	N	3.65	3.68
	S-1	3.20	3.21
	S-2	2.80	2.75
	S-3	1.22	1.14

8 Conclusions

In this paper we have presented a computational procedure to model instationary creep movements in alpine snowpacks. The model allows the treatment of large deformations, strains and strain rates. These processes have never been modelled - or experimentally verified - in any existing 2-D finite element model.

At the present time we are employing a simple Maxwell model to describe the viscous behaviour of snow. This model can only describe snow creep under constant loading. Altough we have shown that the model can simulate the experimental tests of DeQuervain and Kojima, more complicated models must clearly be formulated. For example, the model does not describe snow relaxation under decreasing loading. Therefore, it could never be used to

study the formulation of wet snow avalanches during periods of snow melt. Presently, the model also does not take into account snow microstructure.

Because the procedure is based on the concept of micro-planes, it can be used to model snow fracture and avalanche formation. However, fracture laws are presently failing.

The model employs Green strains and Piola-Kirchhoff stress measures to describe material behaviour. Other stress and strain measures are possible. For example, logarithmic or natural strain measures could be employed in the n-directions. The choice of strain and stress measures will certainly have an influence on the calulated material parameters.

In our validation studies we have found that different viscosity laws are only valid for a particular density and strain rate range. Considerable care must therefore be applied when using the viscosity formulations presented in this article.

We have performed many computational tests with varying number of directions, N. We have found that at around $N = 10$, there is no significant change in simulation results. However, this conclusion might change as more complicated material laws are implemented. For example, when highly nonlinear material laws with differing response in tension and compression or material fracture are introduced, the number of material directions N might increase in order to model avalanche formation.

References

1. Lehning, M., Bartelt, P. and Brown, R. (1998). Operational Use of a Snowpack Model for the Avalanche Warning Service in Switzerland: Model Development and First Experiences, *Proceedings of the NGI Anniversary Conference, Norwegian Geotechnical Institute*, May 1998, 169–174
2. Russi, T., Ammann, W., Brabec, B., Lehning, M. and Meister, R. (1998). Avalanche Warning 2000, *Proc. of the int. snow science workshop (ISSW 1998)*, Sunriver, Oregon
3. Smith, F. and Sommerfeld, R. (1971). Finite-Element Stress Analysis of Avalanche Snowpacks, Short Note, *Journal of Glaciology*, Vol. **10**, No. 60, 401–405
4. Curtis, J. and Smith, F. (1974). Material Property and Boundary Condition Effects in Avalanche Snow-Packs, *Journal of Glaciology*, Vol. **13**, No. 67, 99–108
5. Lang, T. and Sommerfeld, R. (1977). The Modeling and Measurement of the Deformation of a Sloping Snow-Pack, *Journal of Glaciology*, Vol. **19**, No. 81, 153–163
6. Bader, H.P., Gubler, H.U. and Salm, B. (1989). Distributions of stresses and strain-rates in snowpacks, *Proceedings of the Conference: Numerical Methods in Geomechanics, edited by Swoboda*, (Innsbruck 1988)
7. de Quervain, M. (1945). Die Setzung der Schneedecke, *Interner Bericht Nr. 11, Eidgenössisches Institut für Schnee- und Lawinenforschung, Davos*, September 1945
8. Salm, B. (1975). A constitutive equation for creeping snow, *IAHS-AISH Publication No. 114, Snow Mechanics Symposium, held at Grindelwald, Switzerland*, April 1974, 222–235

9. Desrues, J., Darve, F., Flavigny, E., Navarre, J. and Taillefer, A. (1980). An Incremental Formulation of Constitutive Equations for Deposited Snow, *Journal of Glaciology*, Vol. **25**, No. 92, 289–307
10. Brown, R. (1977). A Fracture Criterion for Snow, *Journal of Glaciology*, Vol. **19**, No. 81, 111–121
11. Bazant, Z. and Oh, B. (1985). Microplane Model for Progressive Fracture of Concrete and Rock, *ASCE Journal of Engineering Mechanics*, Vol. **111**, No. 4, April 1985, 559–582
12. Bazant, Z. and Prat, P. (1988). Microplane Model for Brittle-Plastic Material: I. Theory, *ASCE Journal of Engineering Mechanics*, Vol. **114**, No. 10, October 1988, 1673–1688
13. Bazant, Z. and Prat, P. (1988). Microplane Model for Brittle-Plastic Material: II. Verification, *ASCE Journal of Engineering Mechanics*, Vol. **114**, No. 10, October 1988, 1689–1702
14. Kojima, K. (1974). A field experiment on the rate of densification of natural snow layers under low stress, *IAHS-AISH Publication No. 114, Snow Mechanics Symposium, held at Grindelwald, Switzerland*, April 1974, 298–308
15. Mellor, M. (1975). A review of basic snow mechanics, *IAHS-AISH Publication No. 114, Snow Mechanics Symposium, held at Grindelwald, Switzerland*, April 1974, 251–291
16. Claus, B. (1978). Compactive viscosity of snow from settlement gauge measurements, *Interner Bericht Nr. 565, Eidgenössisches Institut für Schnee- und Lawinenforschung, Davos*, August 1978
17. Gubler, H.U. (1994). Physik von Schnee, *Interne Herausgebung, Eidgenössisches Institut für Schnee- und Lawinenforschung, Davos*
18. Morris, E.M. (1994). Modelling mass and energy exchange over polar snow using the DAISY model, *IAHS Publication* No. **223**, 53–60
19. Loth, B. and Graf, H.F. (1998), Snow Cover Model for Global Climate Simulations, *Journal of Geophysical Research*, Vol. **98**, No. D6, 10,451–10,464
20. Crisfield, M. (1991). Non-linear Finite Element Analysis of Solids and Structures. Volume 1: Essentials, John Wiley and Sons, Inc., 605 Third Avenue, New York, NY 10158-0012, USA.
21. Haefeli, R. (1942). Spannungs- und Platizitätserscheinungen in der Schneedecke. *Mitteilungen aus der Versuchsanstalt für Wasserbau an der Eidg. Technische Hochschule (Zürich)*, Nr. 2.
22. Jansson, M. (1901). Ueber die Wärmeleitfähigkeit des Schnees, *Ofversigt af Kongl. Vetenskaps-Akademiens Forhandlinger*, Vol. **58**, 207–222
23. Devaux, J. (1933). L'économie radio-thermique des champs de neige et des glaciers, *Ann. Chim. Phys.*,Vol. **20**, 5–67
24. Sturm, M., Holmgren, J., Knig, M. and Morris, K. (1997). The thermal conductivity of seasonal snow, *Journal of Glaciology*, Vol. **43**, No. 143, 26–41
25. Bartelt, P., Christen, M. and Wittwer, S. (1999). HAEFELI, a 2D-snowpack-simulation program - documentation and examples, *Interner Bericht (unveröffentlicht), Eidgenössisches Institut für Schnee- und Lawinenforschung, Davos*, Herbst 1999
26. Salm, B. (1977). Snow Forces, *Journal of Glaciology*, Vol. **19**, No. 81, 67–100
27. Salm, B. (1971). On the Rheological Behavior of Snow under High Stresses, *Contributions from the Institute of Low Temperature Science, Series A* No. **23**, *Hokkaido University, Sapporo Japan*, 1–43

28. Salm, B. (1967). An Attempt to Clarify Triaxial Creep Mechanics of Snow, *from Physics of Snow and Ice, Proceedings of the International Conference on Low Temperature Science*, Volume **I**, Part 2, Edited by Hirobumi Oura

(Received 18 May 1999, accepted 10 June 1999)

Transformation of the Snow Crystal to a Particle of Ice

Elena Guseva-Lozinski

Immenhoferstr. 38, 70180 Stuttgart, Germany

Abstract. To study the physical properties of snow under different meteorological conditions a mathematical model and numerical computer program were created and applied for some numerical modelling estimates. The non-linear mathematical model consists of partial differential equations and can be subdivided into a thermal part with phase changes in porous media, diffusion, structural transformation and mechanical parts. The model was applied to simulate the evolution of structural, thermal and mechanical parameters in a snow profile subject to meteorological parameters (air temperature and moisture, wind velocity, precipitation, density). The snow structure is very sensitive to the temporal variations of all external parameters: temperature, humidity, precipitation and wind-pumping. Snow deposited in cold weather conditions is transformed through densification, metamorphism and recrystallisation. Snow crystals have unstable shapes. The tendency for mass and heat to be redistributed through sublimation is to minimise the surface free energy. The result of these processes is to change the shape of a snow crystal to that of a sphere. The transformation of the initial singular stellar crystal to a number of small grains with the same mass as the original crystal is described mathematically. It gives the rates of the transformations. Based on this mathematical approach we can predict changes of the crystal shapes, number of crystals and other physical properties inside a snowpack subject to different meteorological conditions.

1 Introduction

Snowflakes falling on the Earth's surface have a mono-crystalline, idiomorphic form (dendrite, for example) or polycrystalline elements with crystals ranging in sizes from 0.1–0.4 mm [1] at very low air temperatures (-50°C – -70°C) to several millimetres at air temperature around 0°C. Depending on the weather conditions (air temperature, moisture, wind velocity) the snowpack is formed under windless conditions from lamellar snowflakes with an initial snow density of 10-80 kgm^{-3} and idiomorphic contours, or from snowflake 0.2–0.3mm sized fragments formed under windy conditions with a density of about 200-300 kgm^{-3}.

The crystallisation process involves a change of phase of the initial substance to a phase with lesser free energy. The main conditions controlling the crystallisation are the water vapour oversaturation or supercooling of the initial medium (water vapour in air). Both these processes are necessary for crystallisation and are characterised by the departure from thermodynamic equilibrium. The simplest growth form is polyhedral. The sizes of separate facets strongly depend on growth conditions. Oversaturation is higher around

apices and ribs and lesser in the central parts of facets. That is one reason for the formation of the skeletal and arborescent, dendritic grain forms; another is rapid growth of crystals.

The initial state of the freshly deposited snow depends on the combination of the wind condition and crystal type at the moment of deposition. A freshly deposited snowpack consists of different crystal forms. Most of the crystals deposited under windless conditions, have a dendritic form. If the oversaturation above the central facets part of the crystal is less then the vertices come to play a dominant role in the crystal growth process. This is a primary reason for the skeletal and dendritic crystal appearance. Dendritic and skeletal crystal construction can be divided into smaller elements (Fig. 1).

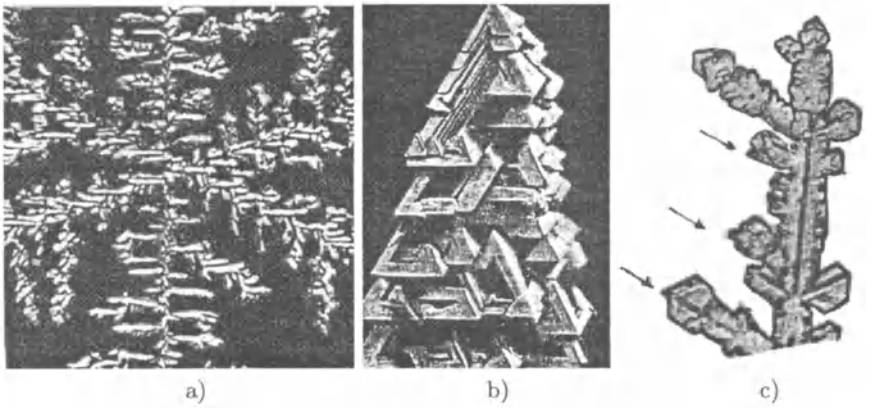

Fig. 1. a) A dendritic crystal; b) A skeletal crystal; c) A crystal branch of multilayered construction. It consists of several small elements. Arrows show rimed droplets at edges or corners [17]

The snowpack can be visualized as a porous medium composed of a network. The snow crystals lose their stability in the upper layers of the snowcover. As a result of the crystal instability, sublimation processes begin leading to internal transformation of the ice crystal network. The result of these metamorphic transformations is the establishment of the thermodynamic equilibrium of the snow crystals within the snowpack and decrease of the surface free energy. The changes of grain form and grain size within the snowpack results from superposition of both isothermal metamorphism and temperature metamorphism. A roundish form of snow grains, roundness of thin ring of the separate dendritic crystal branches are the direct result of this metamorphism. The grains draw together the interior snow-pack, and bonds are formed in the crystal contacts area. These metamorphic processes are accompanied by snow densification and by the increasing of the strength of the grain bonds.

2 Crystal Shapes and Metamorphism

Metamorphic processes occur very quickly within a freshly deposited layer of snow. Within 1-3 days, depending on temperature and initial conditions, after deposition, snowflakes are transformed into polyhedral and oval grains due to high degree of supersaturating, temperature gradients and destructive metamorphic processes. In the case of a stand-alone crystal more time is needed, about 60 days [2,3]. The velocity of metamorphism slows down appreciably during subsequent stages. From crystallization theory we know, that $\mu_c = \mu_0$ is the equilibrium condition in close proximity to a flat interface surface, where μ_c, μ_0 are the chemical potentials of the substance in vapour and in crystal forms respectively,

$$\mu_c = \mu_0 + \frac{\Omega}{R_1}\left(\alpha + \frac{\partial^2 \alpha}{\partial \varphi_1^2}\right) + \frac{\Omega}{R_2}\left(\alpha + \frac{\partial^2 \alpha}{\partial \varphi_2^2}\right), \tag{1}$$

where Ω is the specific volume of one particle, α is a specific free interface surface energy, R_1,R_2 are the main surface curvatures at a point of the interface surface, φ_1,φ_2 are angles defined through the crystallographic oriented surface. $(\mu_c - \mu_0)$ is positive, for crystal growth, and it is negative, when the crystals are undergoing sublimation. The real crystal form with its volume V is transformed to its equilibrium crystal form. This tendency to minimise the surface energy $E_{v=const}$ is described by the Gibbs-Curie-Wolf principle

$$E_{v=const} = \sum_{i=1}^{n} \sigma_i Si = min. \tag{2}$$

According to the Glaciological Vocabulary [2] the initial diameters of snowflakes depend on the air temperature: -6°C $r = 1.5 - 2$ mm; -8°C $r = 1$ mm; -12°C $r = 0.5 - 1$ mm. The flakes were mostly stars, with plates and prisms being rare above -20°C. Snowflakes are modified during their fall through the atmosphere due to over-riming. In other words, the snowflake surface is covered by numerous small crystals. The size of these new crystals is one hundred times smaller than the host snowflake. The number of small crystals so formed can reach to several hundreds. Thus the simple form of a snowflake can convert to the very complicated dendritic form of snowflakes due to over-riming. Those surfaces with small crystals attached can be described as a combination of trihedral fracture angles.

The geometry of the initial crystal surface can be defined as a combination of polyhedron faces with edges and vertices. Using Eq. (1) and principle (2), the average value of water vapour around crystal $\bar{e}$ with n faces and m edges and k vertexes can be written as follows:

$$\bar{e} = e_0 n \frac{S_g}{S_c} + e_d m \frac{S_e}{S_c} + e_x k \frac{S_x}{S_c}, \tag{3}$$

where e_0, e_d, e_x are the water vapour pressures above the flat ice surface, above edges and above vertices and where S_c, S_g, S_e, S_x are the surface area

of a polyhedron, of the flat part of a face, of the area near edge and of the area above a vertex respectively (Fig. 2). The shaded area in Fig. 2 is the area of higher water vapour pressure due to surface heterogeneity. According to the Physical Encyclopedical Vocabulary [4], the thickness l_d of this area is $\approx \bar{l}10^{-2}$, where $\bar{l} = 10^{-5}m$ is the average free path length of the gas (water vapour) molecules. The water vapour pressure above an edge can be rewritten as $e_d = e_0 + \Delta e_d$ and above a vertex as $e_x = e_0 + \Delta e_x$. It is known [5], that the cohesion work $\sigma = 2\sigma_0$ for light mobile phase boundaries, where σ_0 is the tension surface of flat ice $\sigma_0 = 130din/cm$. Using the Thomson-Kelvin Equation for the case of not too small radius of curvature and Eq. (1), the following expressions can be written for the water vapour pressure and the ice,

$$\Delta e_e = \frac{\rho_0}{\rho_i}\frac{\sigma_e}{l_d} \quad \text{and} \quad \Delta e_x = \frac{\rho_0}{\rho_i}\frac{2\sigma_x}{l_d}, \tag{4}$$

where ρ_0 is the water vapour saturation pressure and ρ_i is the ice density.

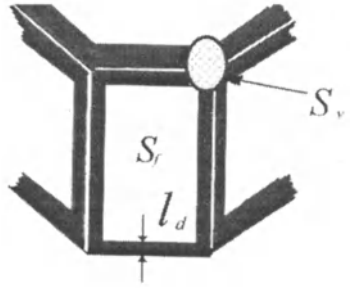

Fig. 2. Hexagonal crystal. S_g is a facet surface area, l_d is the thickness with the higher water vapor pressure near the edges, S_v is the area above a vertex. The shaded areas are the areas with higher water vapor pressure above a surface heterogeneity

An estimate of the average value of water vapour around a polyhedral crystal $\bar{e}$ can be written as

$$\bar{e} = e_0\left(1 + n\frac{10^{-6}}{\bar{R}}\right), \tag{5}$$

where $n > 4$, e_0 is the water vapour pressure above the flat ice surface at temperature T and $\bar{R}$ is the average size of the polyhedron.

The roughness mono-crystal shapes have a big density of incoming trihedral fracture angles. In these points the addition of new particles to a crystal is very easy. It did not request the overcoming of the potential barrier. The growth limit is defined by the degree of oversaturation and temperature gradients. Some simple forms of snowflakes give the very complicated forms of snowflakes due to over-riming. r_f, m_f are the radius and mass of a dendritic crystal, r_c is the radius of the central hexagonal plate, r_t is the size of

crystal element (Fig. 3). We estimate the fracture number k_t due to the form of the snowflake as follows:

$$k_t = \frac{1}{r_t^2} \frac{\left(m_f/r_f - 4\pi\rho_i r_c^2\right)}{\rho_i} \left(1 + 10^{-2} k_t^*\right) \text{ and } \bar{e} \approx e_0 \left(1 + k_t \frac{10^{-6}}{\bar{R}}\right), \quad (6)$$

where k_t^* is a rime droplet parameter. The surface over-riming process increases the fracture number k_t. Most common snowflakes are a flat plate ten times larger in diameter than in thickness [6]: $d_0 = 10^{-1} r_f$. The water vapour pressure e_v above elements of the structure at temperature T is defined by the Magnus relation

$$\mathrm{e}_v(T, r') = e_0 \exp\left(\frac{17T}{T + 235}\right)\left(1 + \frac{F}{r'}\right), \quad (7)$$

where r' is the radius of surface curvature of the elements of the ice matrix, where the water vapour pressure above a flat surface at $T = 0°\mathrm{C}$ is e_0, and where F is a shape parameter. Using (3)-(6), this parameter was calculated as $F = 2 \times 10^{-5}$ for depth hoar layers and for fresh snow layers. The shape parameter is corrected for an excess of water vapour pressure both above an inhomogeneous surface and above a smooth surface. Snowflakes incorporated in the snow-cover become rounded and the branches of dendrites undergo evaporation. The rapid sublimation of the dendritic branches can be explained by sublimation due to surface curvature effects [7,8]. Colbeck [1], Hobbs and Mason [9] show, that the main process of bond growth between grains is vapour diffusion due to curvature difference of the different structural elements.

In the initial stage grain possess an oval form; in the second stage they become spherical. The grains within the snowpack are close packed. Bonds originate in the contact areas of grains due to capillary processes and to oversaturation near these contacts. Depth hoar is the result of post-depositional

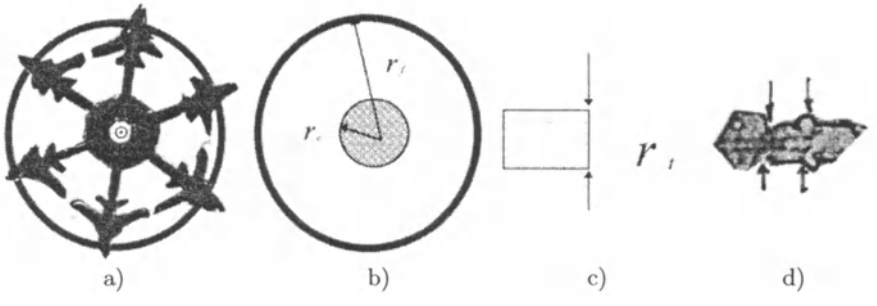

Fig. 3. a) Here is shown one of the typical forms of dendritic snowflake form with a circumscribed circle around the dendritic crystal. b) r_f is the radius of a circumscribed circle around the dendritic crystal and r_c is the radius of a central hexagonal plate. c) r_t is the surface size of a crystal element. d) a part of the dendritic crystal from Fig. 1

metamorphic processes. It is characterised by secondary idiomorphic and skeletal crystal forms. Surfaces of crystals have a step composition. The reason for step formation is the screw dislocation. In this widespread case the crystal growth is defined through the step moving. Steps interact together through their own thermo- and diffusion- fields and intermolecular forces. The result of the step confluence is higher steps. Sometimes macroscopic steps can also fall apart.

3 Mathematical Approach

Every layer of snow within the snowpack corresponds to individual snowfall. The mathematical model for a non-uniform stratified snow-cover with wind-pumping, snow densification and transformation of its thermo-mechanical and structural properties was investigated in the papers [10–13]. The present mathematical model focuses on the modelling of the mass-transfer and structural transformation of freshly deposited snow in the snowpack. Temperature T is determined as follows:

$$C_s \frac{\partial T}{\partial t} - C_a \boldsymbol{V}_a \cdot \nabla T = \nabla \cdot (K_s \nabla T) + f(x) + Lj, \tag{8}$$

where K_s,C_s are the coefficients of heat conductivity and capacity, t is time, $f(x)$ is the absorbed sun radiation distribution (Buger-Lambert-Beer Equation), L is the heat of sublimation for transition from vapour to ice, j is the sublimation rate, $\boldsymbol{V}_a$ is the Darcy flow. Heat conductivity and capacity coefficients depends linearly on the snow density ρ_s. Determination of temporal density changes, due to viscous snow-pack densification, were based on papers by Yosida [8]. The radial growth rate of the ice-matrix elements is given by the Arrhenius equation [14,15]

$$\frac{dr'}{dt} = K_0 \exp\left(\frac{-E}{RT}\right), \qquad r' \mid_{t=0} = r_0, \tag{9}$$

where r', r_0 are the current and initial curvature radii of different structural elements. Each layer of snow within the snowpack consists of N snowflakes with centres and Nk_t elements. We can consider a snowflake as consisting of a central part with radiate rays. These rays consist of elements. We can operate with two kinds of grains: grains with radius r_c and smaller grains with r_t. Using the Arrhenius relation for the ice-matrix elements growth in snow and ice, in conjunction with the Darcy relation for airflow velocity and the Magnus condition, it is possible to write the conditions for the rate of sublimation/condensation on the surface of the grains j_c and j_t as follows:

$$j_c = S_c(e_v - e_c)K_0 \exp(-E/RT)N + S_c V_a \frac{\partial e_c}{\partial z} N, \tag{10}$$

$$j_t = S_t(e_v - e_t)K_0 \exp(-E/RT)NK_t + S_t V_a \frac{\partial e_t}{\partial z} NK_t, \tag{11}$$

$$j = j_c + j_t. \tag{12}$$

The rate of sublimation-evaporation is defined through the processes of diffusion and wind-pumping in the porous space

$$j = -\frac{\partial e_v}{\partial t} + \frac{\partial}{\partial z}\left(D_{ef}\frac{\partial e_v}{\partial r_c}\frac{\partial r_c}{\partial z} + D_{ef}\frac{\partial e_v}{\partial r_t}\frac{\partial r_t}{\partial z} + D_s\frac{\partial e_v}{\partial T}\frac{\partial T}{\partial z}\right) + S_f V_a \frac{\partial e_v}{\partial z}, \quad (13)$$

where $j = j^+ + j^-$ is the sum of the positive part of the mass transfer (corresponding to condensation) and negative part of the mass transfer (corresponding to evaporation) above the common sublimation/condensation surface S_f of the grains per one unit of volume. The water-vapor pressure above grains e_c and e_t is described by (7). Here we use the hypothesis that the sublimation rate on the surface of ice-matrix elements is the result of equalizing the difference between the average water-vapor pressure in the pore space and the concentration above the structural elements and sublimation/evaporation through wind-pumping. Grain diameter changes (Magnus relation) occur as a result of the growth of coarse grains through evaporation of fine parts of the ice matrix and sublimation rate (Eqs. (10)-(13))

$$\frac{dr_c}{dt} = \frac{j_c}{4\rho_i N k_t \pi r_c^2} + K_0 \exp\left(\frac{-E}{RT}\right), \quad (14)$$

$$\frac{dr_t}{dt} = \frac{j_t}{4\pi\rho_i N k_t r_t^2}. \quad (15)$$

The grain number per unit volume changes with time, and by using (6), is determined as

$$\mathrm{k}_t(t) = \frac{1}{\pi}\frac{0.75\rho_s - N\rho_i r_c^3}{N\rho_i r_t^3} \text{ and } \mathrm{r}_t(t) > 0. \quad (16)$$

The boundary conditions for (8) and (13) are similar to those given in [12]. The initial data and surface boundary conditions are defined from meteorological data.

Mathematical modeling of the connection between the snow strength and temperature, density and structural parameters for two-dimensional stratified snow/firn with bonded structure within the snowpack was done in paper [13].

4 Conclusion

The thermo-mechanical mathematical model of structure formation and its changes allows study of the main characteristics of the non-uniform stratified snow and firn. This approach and mathematical model describes the temporal evolution of the properties of freshly deposited snow. The present mathematical model describes the recrystallisation processes and structural changes occurring within a fresh snow layer inside the snowpack and must be extended through the semi-empirical equations. This model is based on the mathematical model for snow/firn [12], the theory of mass- and heat transfer

in the polycrystalline solids [16], thermodynamic rules and on semi-empirical over-crystallisation theory of the snow structure. For the study of the physical properties of snow subject to different meteorological conditions some numerical modelling calculations were made using the mathematical model and numerical computer program given in papers [10–13].

References

1. S.C.Colbeck (Ed.). 1980 *Dynamics of snow and ice masses*, Academic Press, a Subsidiary of Harcourt Brace Jovanovich Publishers.
2. V.M. Kotljakov (Ed.). 1984 *Glaciological vocabulary*, Gidrometeoizdat, Leningrad.
3. E.R. LaChapelle. 1992 *Field Guide to Snow Crystals*, International Glaciological Society, Cambridge.
4. 1983 *Physical encyclopedical vocabulary*, Nauka, Moscow.
5. V.Gnielinski, A.Mersmann, F.Thurner. 1993 *Verdampfung, Kristallisation, Trocknung*, Friedr. Vieweg & Sohn Verlagsgesellschaft mbH, Braunschweig, Wiesbaden.
6. G.Seligman, 1980 *Snow structure and ski fields*, Printed in England by Foister & Jagg LTD, Cambridge.
7. R.Perla, 1978 *Temperature-gradient and Equi-temperature Metamorphism of Dry Snow*, Paper presented at Deuxieme Rencontre Internationale sur la Neige et les Avalanches. Assoc. Pour l'Etude de la Neige et des Avalanches, France
8. Z.Yosida, 1963 Physical properties of snow. In: Kingery, W.D., (ed.) *Ice and snow: properties processes, and applications.* Cambridge, Massachusetts, The M.I.T. Press, 485-527.
9. P.V.Hobbs and B.J. Mason, 1964 , Philos.Mag. [8] 9, 181-197.
10. E.V.Guseva, V.N.Golubev. 1989 Thermomechanical mathematical model of the formation of the structure and properties of the snowcover, *Geojournal* **19**(2), 193-200.
11. E.V.Guseva, V.N.Golubev. 1990 *Matematicheskaja model formirovanija stroyenijya i svoystv snezhnogo pokrova [Mathematical model of the properties and structure of the snowcover]*, Issued., 68, 18-26. [In Russian with English summary.]
12. E.V.Guseva, V.N.Golubev. 1997 Mathematical modelling of temporal changes in snow-firn properties in cold period, *Annals of Glaciology*, **24**, 89 – 92
13. E.V.Guseva, 1998 Evolution of Snow-Firn Properties: A thermomechanical approach, *Proceedings of the 9 International Symposium on Continuum Models and Discrete Systems*, 29-38.
14. P.J.Stefenson. 1967 Some considerations of snow metamorphism in the Antarctic Ice sheet in the light of ice crystal studies. *Phys. Snow and Ice.*, **2**, 725-740
15. A.J.Gow. 1969 On the rates of growth of grains and crystals in South Polar firn, *Journal of Glaciology* **8**(53), 241-252.
16. U.Gösele, W.Frank, A.Seeger. 1980 Mechanism and Kinetics of the Diffusion of Gold in Silicon, *Appl. Phys.* **23**, 361-368.
17. A.Yamashita , A.Asano, T.Ohno, 1985 Comparison of ice crystals grown from vapour in varying conditions, *Annals of Glaciology* **6**,242-245.

(Received 22 Feb. 1999, accepted 15 June 1999)

Temperature and Temperature Gradient Dependence of Snow Recrystallization in Depth Hoar Snow

Yasushi Kamata[1], Sergey A. Sokratov[1,2], and Atsushi Sato[1]

[1] National Research Institute for Earth Science and Disaster Prevention, Shinjo Branch of Snow and Ice Studies; Tokamachi 1400, Shinjo, Yamagata 996–0091, Japan

[2] Institute of Geography, Russian Academy of Science; Staromonetnyi 29, Moscow, 109017, Russia

Abstract. Under extremely low temperatures (ranging from $-65°C$ to $-15°C$), an experiment on temperature gradient metamorphism with 500 Km^{-1} was carried out for three days. Heat fluxes were produced in snow in either upward or downward directions. The effects of temperature, temperature gradient and its direction on crystal growth were investigated. The experiment showed that the growth rate was larger in layers where the average for the layer temperature was higher, even if the temperature gradient was small. The relationship of the calculated water-vapor flux and crystal growth to temperature was examined, and good correlation was found. It was concluded that crystal growth primarily depends on temperature, and secondarily on temperature gradient.

1 Introduction

Because of its significance as a cause for avalanche formation, dry snow metamorphism has recently been an intensive research topic in snow science. In Polar Regions, these processes are now also often included into the studies of the snow-cover interaction with the climate. It is also known that in cold environments the snow cover is characterized by highly developed depth-hoar layers. The purpose of the experimental work that we are going to present here is to investigate the growth of depth-hoar-crystals in cold dry snow. The results that are reported, are at variance with results presented by others.

It is known that snow metamorphism results from the processes of evaporation and condensation on the surfaces of the snow grains, giving rise to a water-vapor flux essentially from locations of evaporation to those of condensation [1–3].

It is an accepted understanding that under isothermal conditions the driving force for snow recrystallization is the difference of curvature between the crystals [4,5]. Likewise, it is widely believed though not uniformly accepted that when a temperature gradient is applied the main influencing activity of

the snow recrystallization is this temperature gradient. Akitaya [2,3] reported that conditions for depth-hoar crystals to develop are, first, the magnitude of the temperature gradient and, second, the existence of a sufficient fraction of pore space. Fukuzawa and Akitaya [6,7] explicitly spoke out that the growth rate of the depth-hoar crystals is proportional to the magnitude of the temperature gradient. However, the temperature range of these studies was from -20°C to 0°C making it difficult to estimate the influence of the (mean) temperature on the process. In addition, there were very few experimental studies under extremely low temperatures. So the question remains open as to how the temperature itself affects the recrystallization processes in snow.

It was found that the depth-hoar-growth rate is also affected by the snow density. In fact experimental studies showed that depth hoar was not formed under high temperature gradients in snow samples with high density; however, they were formed under the same conditions in low density snow samples [8–10]. Generally, the larger the snow density was, the smaller the growth of depth hoar.

It is known that the shape of snow flakes is determined by the temperature and supersaturation of water vapor. This fact was constructively used by us to shape the depth hoar crystals accordingly; similar types of depth hoar crystals developed in the same temperature ranges as for the snow flakes [1,8].

In the present study, the crystal growth was observed under extremely low temperatures (ranging from -65°C to -15°C). The experiments were carried out with temperature gradients of about 500 Km^{-1} and lasted three days. Two samples, discussed here, were subjected to the same conditions except that the heat fluxes imposed on the snow were opposite in direction, upward and downward. Since we monitor both the (mean) temperature and the temperature gradient, the present study proposes a relationship for the growth rate of the depth-hoar crystals involving the temperature and temperature gradient.

2 Experimental Method

2.1 Snow sample

Lightly compacted snow (initially with density 290 kgm^{-3}) was used (Fig. 1 (**a**)), which was made in the Cryospheric Environment Simulator (CES) in Shinjo Branch, NIED and kept in a cold room (-15°C) for a month. Its average diameter is that of an equivalent circle of the grains' cross-sectional area which was calculated to be 2.56×10^{-4} m.

2.2 Apparatus

A scheme of the experimental apparatus is shown in Fig. 2. A thermo-insulated container ($0.6 \times 0.7 \times 1.2$ m) was installed in a cold room. The

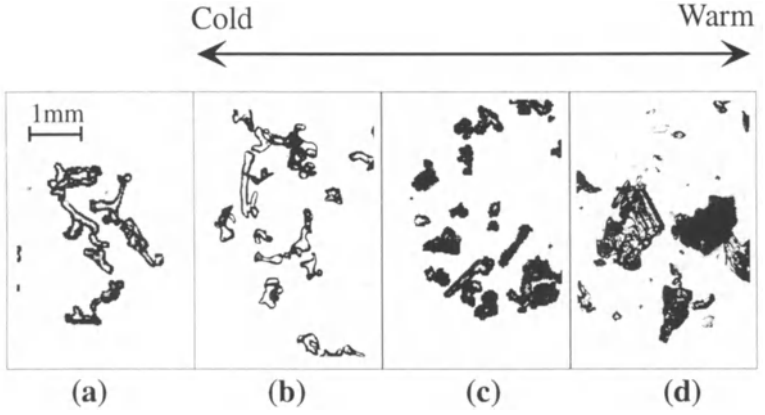

Fig. 1. Comparison of initial disaggregated grains with grains of each layer after experiments : (**a**) initial, (**b**) cold layer (about −65°C to −45°C), (**c**) middle (about −45°C to −25°C), (**d**) warm (about −25°C to −15°C)

inside temperature of the container was kept at −15°C by a heater and a fan that was automatically regulated. Snow was sifted into the sample box made with 0.1 m foam plastic walls, with the inside space for snow of 0.25 × 0.25 × 0.1 m. Those two sample boxes with snow were positioned in the thermo-insulated container as shown in Fig. 2. A cold plate of circulating thermostat was put between the samples. The opposite sides of the samples were in contact with iron plates. The temperature of the cold plate was kept to within an accuracy of ±0.05°C. The temperature of the iron plates was varied between ±0.2°C. In this way the samples ("**a**" – the "upper" one and "**b**" – the "lower" one) had temperature gradients with opposite directions. Six copper-constantan thermocouples were measuring the temperature in each sample every 1 minute, on the central axis parallel to the heat fluxes produced in the snow at intervals of about 0.02 m.

2.3 Method

Once a uniform temperature of −15°C was achieved throughout both samples, the temperature of the cold plate was changed to −65°C. So the samples were subjected to a strong temperature gradient of about 500 Km^{-1}. The temperature distributions in the samples were measured continuously and soon achieved quasi–steady state conditions (i.e. there was no longer any temperature change according to the accuracy of the measurements). After three days of fixed thermal conditions each snow sample with thickness 0.1 m was divided into three layers: "Top" (0.067–0.097 m), "Middle" (0.034–0.067 m), and "Bottom" (0–0.033 m from the bottom face), as shown in Fig. 2.

Photographs of the disaggregated grains for each layer were taken using a microscope. The cross-sectional area of the digitized grains was determined

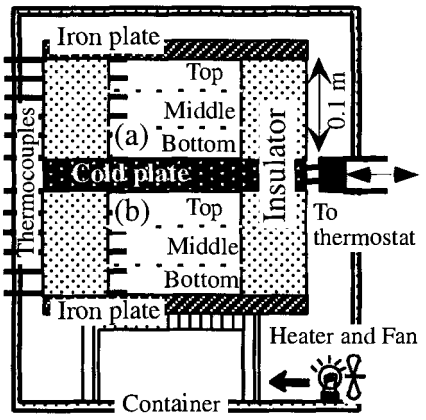

Fig. 2. Scheme of the experimental apparatus

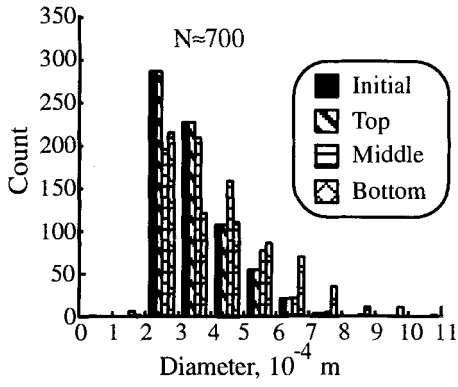

Fig. 3. Diameter distribution in each layer of the "lower" sample. N is the total number of crystals.

and the diameter of a circle with an equivalent area was computed. The diameter distribution of each layer after the experiment was compared with the initial diameters. This gave the relationships between the crystal growth rate and the temperatures, temperature gradients, and its direction.

3 Results

We found no difference in crystal shapes of the upper and the lower samples. Crystal shapes in the layers near the cold plate did not change from their initial state (Fig. 1**b**). As the average temperatures of the layers increased, crystals developed to solid type in the both "Middle" layers and to skeleton type depth hoar near the cold plate. Over the process the diameter of the crystal also increased (Fig. 1**c**, **d**).

Fig. 3 shows the diameter distribution of each layer for the "**b**"-sample in Fig. 2. We see that the initial distribution of the crystals (ranging between 1.1–6.8 $\times$ 10^{-4} m) had a peak between 2 and 3 $\times$ 10^{-4} m.

The distribution in the "Top" layer (crystal size range 0.94–5.8 $\times$ 10^{-4} m), being in contact with the cold plate, indicated little change from the initial one. The "Middle" (crystal size range 0.62–7.1 $\times$ 10^{-4} m) and the "Bottom" (0.36–9.3 $\times$ 10^{-4} m) layers, whose temperatures increased in turn, showed smaller peaks than the initial reading and were widely distributed over a larger diameter. Small radii grains had to sacrifice as the large radii grains acquired mass from the smaller grains [4].

Fig. 4 shows quasi-steady state temperatures and calculated temperature gradients of each position. The temperature distributions were not linear

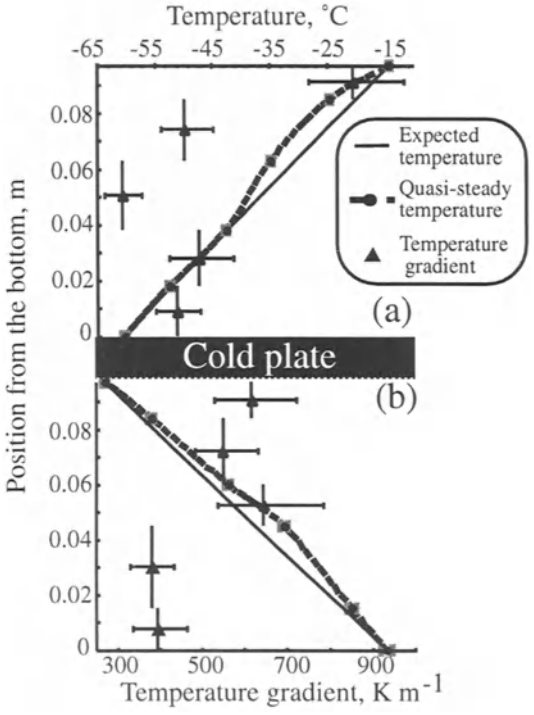

Fig. 4. Quasi–steady state temperature and calculated temperature gradients with vertical downward (**a**) and upward (**b**) heat fluxes.

in either of the samples and differed between the "upper" and the "lower" sample. A more detailed analysis of temperature distributions is given in [11].

Neither of the temperature gradients calculated from the observed temperature distributions were uniform in the two samples. Their change was within the accuracy of the measurements in those parts of the snow samples where temperatures were below −40°C. Above −40°C temperature gradients increased in the "upper" but decreased in the "lower" sample as the temperature increased.

Average crystal diameters in each layer with the mean temperatures and the mean temperature gradients are shown in Table 1. Akitaya [1] reported that the surface of the warmer snow grain evaporated sublimatically and then condensed sublimatically on the surface of the colder grain. However, our results showed in both samples that crystals of the warmest layer developed more than those in the other layers.

Fukuzawa et al. [6] reported that the growth rate of depth hoar was proportional to the magnitude of the temperature gradient. Contrary to this, crystals of the "Bottom" layer in the "lower" sample, whose temperature gradient was the smallest, had the highest growth rate of the sample.

Table 1. Average diameter of each layer with its temperatures and temperature gradients (Fig. 2)

Sample	Layer	Temperature °C	Temperature gradient ° m^{-1}	Crystal diameter $\times 10^{-4}$ m
"upper"	Top	-25	810	4.19
	Middle	-40	310	2.94
	Bottom	-53	460	2.86
"lower"	Top	-57	590	2.66
	Middle	-37	640	2.84
	Bottom	-23	400	3.33

4 Discussion and Conclusions

The results shown above contradict those previously reported. It is necessary for the development of the depth-hoar crystals to be supplied with water vapor. We assume that the water vapor in the porous space is saturated, and this depends on temperature. For example, the saturated water-vapor concentration in the porous space had to be 2.2×10^{-6} kgm^{-3} at $-65°C$, and 1.4×10^{-3} kgm^{-3} at $-15°C$, i.e. the water-vapor concentration at $-15°C$ was about thousand times larger than at $-65°C$. The theoretically possible water-vapor flux in the porous space was calculated by multiplying the water-vapor-concentration gradient with the temperature dependent water-vapor-diffusion coefficient, both obtained from the temperature measurements.

Fig. 5 shows the relationship between this water-vapor flux and the crystal growth in each layer. In the "upper" sample the fluxes of the "Middle" and the "Bottom" layers were small, and that of the "Top" layer, whose temperature was high, increased abruptly. While in the "lower" sample the flux increased gradually from the "Top", the "Middle" to the "Bottom" layer. Thus, the flux did not show a symmetrical distribution.

The possible reason for such non-symmetry could be convection. In the "upper" sample the bottom plate was cold and the top plate was warm making this condition stable against convection. However, in the "lower" sample the bottom plate was warm and the top plate was cold making convection possible. It is generally accepted that the dimensionless Rayleigh number is used to estimate under what conditions convection will occur in snow [12–14]. This Rayleigh number (Ra) is

$$Ra = \frac{g\beta(\rho c)_f \Delta T h k_i}{\nu k_m}, \tag{1}$$

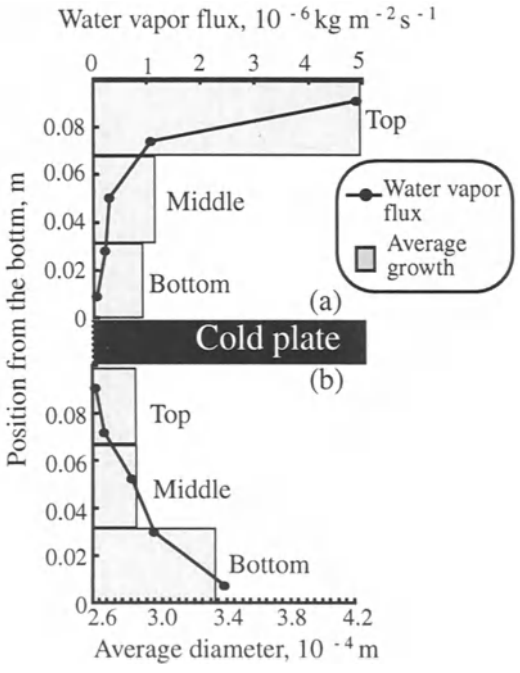

Fig. 5. Relationship between the water vapor flux and the crystal growth in each layer. Left end of diameter axis indicates average diameter of initial snow and then columns shows the growth of each layer.

where g is the acceleration due to gravity, β is the isobaric coefficient of thermal expansion, $(\rho c)_f$ is the volumetric heat capacity of the fluid (moist air), ΔT is the temperature difference across the sample, h is the thickness of the sample, k_i is the coefficient of air permeability, ν is the kinematic viscosity, and k_m is the thermal conductivity of the porous medium. We computed Ra roughly and compared it to a critical value (Ra_{cr}). It seems that convection will occur when $Ra > Ra_{cr}$. Ra_{cr} for snow is usually assumed to be between 18 and 40 [13,14]. In this experiment, Ra was 7.6. This value is lower than Ra_{cr}. However, Sturm et al. [14] observed convection at Rayleigh numbers as low as 4, and their temperature difference was smaller than in this experiment. This is why one can expect that convection could take place and influence the process of recrystallization under present conditions.

The diameters of the crystals increased with an increase in the magnitude of the flux. Crystals developed in the layers where the flux was large because of high temperature. The growth was small where the temperatures were low even if the temperature gradients were large, since the amount of water vapor was small.

Next, as an example of the effect of the temperature gradient, the "Top" layer of the "upper" with the "Bottom" layer of the "lower" sample can be compared. Both layers had similar temperatures but the temperature gradient in the "Top" layer was twice as large as in the "Bottom" layer. The

growth in the "Top" layer was also twice as large as that in the "Bottom" layer.

We conclude that the temperature, which determines the water vapor amount in the porous space, is the most important factor for the depth hoar growth. The magnitude of the temperature gradient also affects the growth rate but not primarily, a fact that can be seen when temperatures are similar.

Acknowledgements: The work was partly supported by the Japan Science and Technology Agency through JST and JISTEC.

References

1. Akitaya, E. (1964) Studies of depth hoar I. *Low Temp. Sci., Ser. A* **23**, 67–74
2. Akitaya, E. (1967) Studies of depth hoar II. *Low Temp. Sci., Ser. A* **25**, 37–47
3. Akitaya, E. (1974) Studies on depth hoar. *Contrib. Inst. Low Temp. Sci., Ser. A* **26**, 1–67
4. Brown, R. L., Edens, M. Q., and Sato, A. (1994) Metamorphism of fine-grained snow due to surface curvature differences. *Ann. Glaciol.* **19**, 69-76
5. Sato, A., Adams, E. E., Brown, R. L. (1994) Effect of microstructure on heat and vapor transport in snow composed of uniform fine ice spheres. *Proc. ISSW* 1994, 176–184
6. Fukuzawa, T. Akitaya, E. (1991) An experimental study on the growth rates of depth hoar crystals at high temperature gradients (I). *Low Temp. Sci., Ser. A* **50**, 9–14
7. Fukuzawa, T., Akitaya, E. (1992) An experimental study on the growth rates of depth hoar crystals at high temperature gradients (II). *Low Temp. Sci., Ser. A* **51**, 23–30
8. Marbouty, D. (1980) An experimental study of temperature-gradient metamorphism. *J. Glaciol.*, **26**(94), 303–312
9. Perla, R., Ommanney, C. S. L. (1985) Snow in strong or weak temperature gradients. Part I: Experiments and qualitative observations. *Cold Reg. Sci. Tech.* **11**, 23–35
10. Perla, R. (1985) Snow in strong or weak temperature gradients. Part II: Section-plane analysis. *Cold Reg. Sci. Tech.* **11**, 181–186
11. Sokratov, S. A., Kamata, Y., Sato A. (1999) Relation of temperature gradient to heat transfer in snow. In: Hutter, K., Wang, Y. and Beer, H. (eds) *Advances in Cold Regions Thermal Engineering and Sciences*, Springer Verlag, 409–414
12. Palm, E., Tveitereid, M. (1979) On heat and mass flux through dry snow. *J. Geophys. Res.* **84**(C2), 745–749
13. Powers, D. J., Colbeck, S. C., O'Neill, K. (1985) Thermal convection in snow. *CRREL Report* 85-9
14. Sturm, M., Johnson, J. B. (1991) Natural convection in the subarctic snow cover. *J. Geophys. Res.* **96**(B7), 11657–11671

(Received 17 Feb. 1999, accepted 15 May 1999)

On Creep Flow of Snow and Firn

Bernhard Meussen

Vedior Engineering+Consulting GmbH, Wendenstrasse 23, D-20097 Hamburg, Germany

Abstract. The exploration and exploitation of polar regions requires the ability to work in and with the firn layer, which is the topmost layer of the continental ice sheet. A firn layer consists of meteoric snow which changes by metamorphosis from original snow flakes to a stable firn body. As the firn is compressed by subsequent layers of snow, a porous granular material evolves with density that is increasing with depth. This leads to polycrystalline ice in the bottom layers. The porous structure of the firn gives rise to volumetric viscous behaviour. Its granular build-up leads to an increase of volume under shearing conditions (dilatation). Furthermore, firn exists at high homologous temperatures, thus it shows creep behaviour.

A material law for snow and firn is proposed, which accounts for these characteristic features of the material. Following the approach by von Mises, it is based on the assumption of an elastic and a viscous potential. The dilatation is described by the third invariant of the stress tensor to model a strain orthogonal to the shearing direction. Creep experiments are used to evaluate the material parameters.

1 Introduction

The prediction of the flow of large polar ice masses is an important contribution to the geophysical simulation of polar regions. As measurements of the natural flow are only available for about the last hundred years, the necessity of the simulation of the flow of large ice masses over thousands of years is obvious.

The simulation of large glaciers or ice sheets is based on the framework of continuum mechanics and the supposition of non-linear viscous rheology, Hutter [1]. The assumption of the continuously distributed matter is utilized to formulate equations which govern kinematics and balance relations for mass, linear momentum, moment of momentum, energy and entropy Haupt, [2]. These formulations are equally valid for all materials, however, they do not suffice to determine the material behaviour. Further *constitutive relations* are required. It is the aim of this investigation to find such constitutive relations for the deformation of polar firn.

A material element has six degrees of freedom in Cartesian space, if Boltzmann's continuum is applied. The constitutive relation in question then has to link six strains with six stresses. The constitutive relation can be written in matrix form, linking the strains with the stresses in a system of equations. The components of the matrix can be determined from creep experiments.

Further information on the material behaviour can be gathered from the investigation of the structure of the material. These investigations may give hints as to whether to expect anisotropy or kinematical couplings between degrees of freedom, or other characteristics.

As time scales of several thousand years can not be covered in the laboratory, the interaction between the evolution of the firn cover and the deformation will not be investigated. Furthermore, the influence of chemical agents or microscopic impurities is not considered because of the limited number of experiments.

2 Structural Properties of Snow and Firn

The samples used in the creep experiments were made of snow and antarctic firn. In order to ensure comparability of the results and to document the properties of the samples on a commonly accepted basis, the *International Classification for Seasonal Snow on the Ground* (Colbeck *et al.* [3]) is applied. The firn samples were retrieved from different depths out of a core drilled into the Filchner-Ronne-Ice Shelf by the Alfred-Wegener-Institut für Polar und Meeresforschung in Bremerhaven, Germany, and were made available for this investigation. Table 1 gives the above mentioned classification of these samples. For the tested samples, no specific orientation of the c-axes could be detected. Therefore, the samples are assumed to be isotropic. Samples were chosen from the core to be as homogenous in density and structure as possible. Characteristic bends in the snow density profiles over depth of polar firn layers are related to specific states of particle arrangement (Ebinuma and Maeno [4]). At a density of 0.55Mg m^{-3}, the particles reach a stable mechanical packing. The firn reaches an optimal packing structure at a density of 0.73Mg m^{-3}. The transition from snow to ice is reached at a density of about 0.83Mg m^{-3}. From this observation, it is concluded that the most important parameter to describe the mechanical behaviour of firn is its density. The density of the firn is linked to the state of mechanical packing of its particles, the grains. The material with the optimal mechanical packing is referred to as the *consolidated material*, one with smaller density will be called *under consolidated material*. A density higher than that of the consolidated material can not be achieved by particle rearrangement alone.

In addition to the Antarctic firn samples, artificial snow samples were prepared. They were made of fresh fallen snow, which was stored at -10° C until use. The snow was sieved and filled in cylindrical forms. The snow was then compressed until the desired initial density was reached. The samples were retrieved from the forms and stored again at -10 ° C for at least a month in order to allow a structure to evolve. To ensure the quality of the samples, thin cuts were prepared and investigated under a microscope. Fig. 1 shows photographs of these samples. The upper part of these figures shows the thin section in cross polarized light to show the crystalographic structure. The

Table 1. Classification of the Antarctic Firn Samples

category	4.5 m	7.5 m	10.5 m	28 m	41 m	51 m
density [Mgm^{-3}]	0.40	0.48	0.55	0.72	0.76	0.82
porosity [%]	56.4	47.7	40.1	21.6	17.2	10.7
grain shape	3sr	3sr	3lr	3 lr	3 lr	3 lr
grain size	fine	fine	medium	coarse	coarse	very coarse
liquid water content	dry	dry	dry	dry	dry	dry
impurities	-	-	-	-	-	-
hardness	very low	low	low	medium	high	very high
temperature [°C]	−22.0	−22.0	−22.0	−22.0	−21.5	−21.0

lower part of the figures shows the samples in unpolarized light and displays the pores. The pores were filled with plaster for better visualization. Table 2 gives the classification of the snow samples.

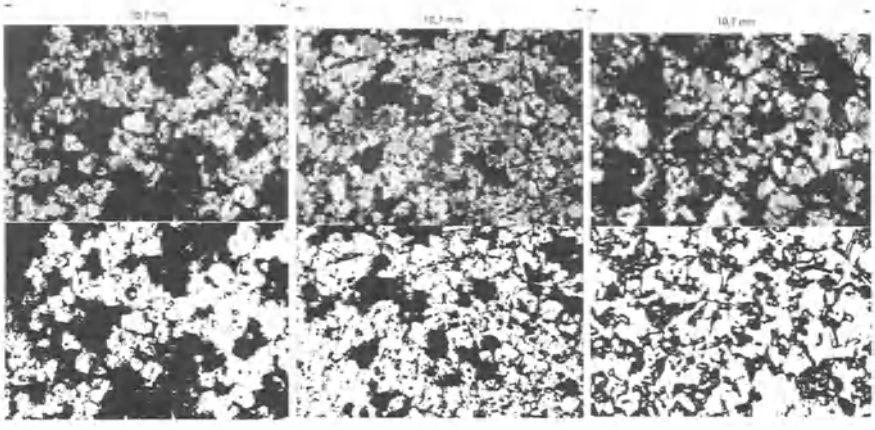

Fig. 1. Samples (from left: $\rho = 0.46\text{Mg m}^{-3}$, $= 0.55\text{Mg m}^{-3}$, $= 0.79\text{Mg m}^{-3}$)

3 Material Law for Snow and Firn

Mahrenholtz, Wu and Enss [5] successfully described the settlement of a snow cover under distributed loading. Following their line of thinking, the strain tensor ε_{ij} is divided into an elastic ($\varepsilon_{ij}^{(e)}$) and a viscous strain ($\varepsilon_{ij}^{(v)}$)

$$\varepsilon_{ij} = \varepsilon_{ij}^{(e)} + \varepsilon_{ij}^{(v)}. \tag{1}$$

Table 2. Classification of the Snow Samples

Categories	artificial snow	natural snow
density [Mgm^{-3}]	0.51 to 0.84	0.55 to 0.86
porosity [%]	44 to 8.4	40 to 6.3
grain shape	-	3 sr
grain size [mm]	0.40 (fine)	0.28 (fine)
liquid content	dry	dry
impurities	none	aerosols
hardness	low - very high	low - very high
temperature [°C]	-1 to -20	-1 to -20

The elastic strain is calculated from Hooke's law

$$\varepsilon_{ij}^{(e)} = \frac{1}{E}((1+\mu)\sigma_{ij} - \mu\sigma_{kk}\delta_{ij}), \tag{2}$$

where E is Young's modulus, μ Poisson's ratio and σ_{ij} are the components of the stress tensor. The viscous part of the strain rate is written as

$$\dot{\varepsilon}_{ij}^{(v)} = \frac{1}{E^v}((1+\mu)\sigma_{ij} - \mu\sigma_{kk}\delta_{ij}) - \frac{1}{D^v} \cdot (\sigma_{ik}\sigma_{kj} - \sigma_{(ij)}\sigma_{(ij)})\delta_{(ij)}. \tag{3}$$

The brackets around indices are used to indicate where Einstein's summation convention is not to be applied. The first term in this equation models the volumetric and shape behaviour of snow and firn. In the second term, D^v is a dilatation parameter which evaluates the dilatational strain rate caused by the corresponding orthogonal shear stress. Fig. 2 illustrates the mechanism observed in biaxial creep experiments. During shearing, the sample becomes elongated. This is due to the granular structure of the material. The stiff grains move relative to each other, leaving the optimal structure with an increase of the volume of the samples. $E^{(v)}$ denotes the viscous modulus. Young's modulus of ice is given by Michel [6] to be

$$E_{ice} = 9500\text{MPa}. \tag{4}$$

The elastic modulus of snow and firn is assumed to be depending on the load carrying ice matrix alone. Assuming proprtionality to the volume fraction yields

$$E(\rho) = E_{ice} \cdot \frac{\rho}{\rho_{ice}}. \tag{5}$$

The density of polycrystaline ice ρ_{ice} is 0.9 Mgm^{-3}. The Poisson's ratio is assumed to follow the equation (Mahrenholtz, Wu and Enss [5]):

$$\mu(\rho) = 0.15\text{m}^3(\text{Mg}^{-1}) \cdot \rho + 0.2. \tag{6}$$

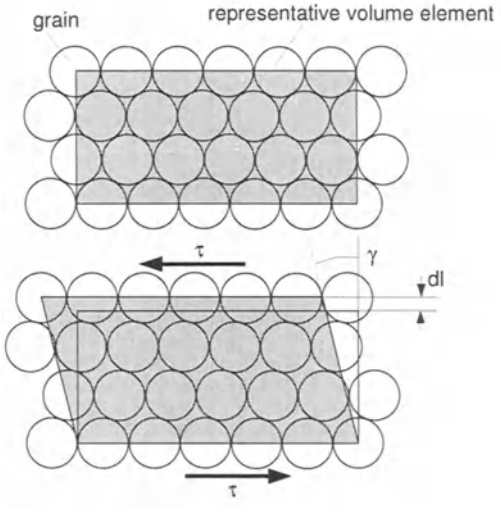

Fig. 2. Mechanism of Dilatation

The viscous modulus $E^{(v)}$ has been determined from uniaxial creep tests. These tests were performed with tensile and compressive loading of the samples. The loading and the temperature during the test were held constant throughout the test, but they were varied from test to test. More than 50 tests with different snow types and initial densities were considered to evaluate $E^{(v)}$. For compressive loadings, $E^{(v)}$ has been determined to be

$$E^v(\rho,T) = K_{type}[\text{MPa h}]\cdot(1-T[\text{K}]/273\text{K})^{0.65}(\rho_o/\rho_{ice})^9\cdot(\sigma_v[\text{MPa}]/\text{MPa})^{-2.57}, \tag{7}$$

for tensile loadings, $E^{(v)}$ has been determined to follow the equation

$$E^v(\rho,T) = K_{type}[\text{MPa h}]\cdot(1-T[\text{K}]/273\text{K})^{0.65}(\rho_o/\rho_{ice})^4\cdot(\sigma_v[\text{MPa}]/\text{MPa})^{-2.57}. \tag{8}$$

K_{type} is given in Table 3 for the materials investigated here. D^v is calculated from biaxial creep tests as follows

$$D^v = 8.734\cdot 10^{-3}\text{MPa}\left(1.21 - \frac{\rho}{0.74\ \text{Mg m}^{-3}}\right)^{-1}\cdot\frac{E^v}{2(1+\mu)}. \tag{9}$$

4 Conclusion

This report deals with the mechanical behaviour of snow and firn. The structural analysis of the samples showed the porous, granular fabric of the firn. This fabric causes a voluminal viscous and dilatational material behaviour

Table 3. Values of K_{type}

material	$K_{type}/(\mathrm{MPa \cdot h})$	σ/MPa
artificial snow	2750	< 0
natural snow	10000	< 0
natural snow	16000	> 0
antarctic firn	20000	< 0
antarctic firn	1200	> 0

under a three-dimensional state of stress. Depending on the depth of retrieval of the samples, the structure of the firn changes. Firn and snow of a density below 0.73 Mg m$^-$3 may be referred to as underconsolidated material, firn of a density of 0.73 Mg m^{-3} may be referred to as consolidated material. The consolidated firn shows the strongest dilatational behaviour. Firn of higher density shows a behaviour more similar to that of polycrystalline ice. From the findings presented here, a three dimensional material law is derived which models the material behaviour of firn using von Mises potentials. The volume viscous behaviour under isotropic stress is modelled by a bulk viscosity. The dilatational behaviour due to shearing is modelled by linking the shear deformation to the third invariant of the stress tensor, this gives rise to an axial deformation being normal to the shear plane. The material parameters presented here were calculated from creep tests lasting for 80 hours.

References

1. Hutter, K. (1983): *Theoretical Glaciology.* D. Reidel Publishing Co., Dordrecht Boston Lancaster.
2. Haupt, P. (1993): Foundation of continuum mechanics. In K. Hutter, editor, *Continuum Mechanics in Environmental Sciences and Geophysics*, chapter 1, pages 1–77. CISM Courses and Lectures No. 337.
3. Colbeck, S.; Akitaya E.; Armstrong, R.; Gubler, H.; Lafeuille, J.; Lied, K.; McClung, D. und Morris, E. (1990): The International Classification for Seasonal Snow on the Ground. Technical report, The International Commission on Snow and Ice of the International Association of Scientific Hydrology.
4. Ebinuma, T. und Maeno, N. (1987): Particle rearrangement and dislocation creep in a snow-densification process. *Journal de Physique*,C1–263 – C1–269.
5. Mahrenholtz, O.; Wu, Z. und Enss, D. (1993): Time-dependent subsidence of snow-ground under distributed loading. In *Beiträge zur Mechanik: Festschrift zum 65. Geburtstag von Prof. Dr. Rudolf Trostel.* 2. Institut für Mechanik der Technischen Universität Berlin, 170 – 179.
6. Michel, B. (1978):*Ice Mechanics.* Les Presses De L'Universite Laval, Quebec, Canada.

(Received 16 Feb. 1999, accepted 31 May 1999)

Relation of Temperature Gradient to Heat Transfer in Snow

Sergey A. Sokratov[1,2], Yasushi Kamata[1], and Atsushi Sato[1]

[1] National Research Institute for Earth Science and Disaster Prevention, Shinjo Branch of Snow and Ice Studies; Shinjo, Yamagata 996–0091, Japan
[2] Institute of Geography, Russian Academy of Science; Staromonetnyi 29, Moscow, 109017, Russia

Abstract. Temperature distributions in snow, measured in the laboratory and the field are always used as a basis for the calculation of snow-heat conduction and water-vapor-diffusion characteristics. According to recently obtained experimental data temperature distributions are not linear even under steady conditions and thus do not fit into present theories of the simultaneous heat and mass-transfer mechanisms. The temperature distributions are related to the heat-transfer processes in a much more complicated way than is presently accepted. They must be the result of latent heat release in snow recrystallization that is superimposed on the balance between the evaporation and condensation processes, regulated by the specific surface area of the ice matrix, snow structure, and potentiality of the porous space for water-vapor transfer.

1 Previous Investigations

The quantities that today still chiefly characterize the snow conditions are the temperature and its gradient deduced from temperature measurements at several points; at the same time, these are the easiest to measure. They are used in almost any equation describing the processes of heat and mass transfer in snow and are included in any modeling of snow metamorphism.

The heat flux in snow is constructed by the heat conduction in the ice matrix, the heat transport by water-vapor flux and the heat transferred by air flux. The temperature distributions observed must be the result of the coexistence of these three terms [1]. For pure conduction a steady-state temperature distribution must be linear throughout homogeneous snow. When part of the heat is transported by water vapor (estimated to contribute up to 50% into the effective heat-conductivity coefficient of snow [2,3]), nonlinear temperature profiles can be expected. However, according to the presently accepted physical theory of simultaneous heat and mass transfer in snow, the water-vapor flux can only change the profile by less than 2% from the linear one [4]. Presence of air convection changes the temperature distribution tremendously [5]; it becomes the main mechanism of the temperature-profile construction [4].

There exist more than a dozen models of simultaneous heat and mass transfer in snow and snow recrystallization. The main difference between

most of them is the presentation of the snow structure: de Quervain [6] tried to consider the set of ice plates parallel or perpendicular to the direction of heat and mass transfer. Sommerfeld [7] constructed his "branch grain theory" of crystal growth, where evaporated material condensed on specific grains further away from a heat source. Gubler [8] designed a model which included interparticle structures. Adams and Sato [1,3] considered the relation of heat conduction to microstructure, interpreting snow crystals as ice spheres. Successful modeling was also done without involving stereological properties of snow [9]. Of course each model was a simplification of the real natural processes, and a combination of different factors included and different assumptions made, usually resulted in achieving quite a good agreement between modeled and observed data.

The above mentioned and other published models used the same physical interpretation of the mass-transfer phenomenon, described in [10]. The temperature of the ice matrix and the porous air were equated for each point of a snow sequence, and supersaturation (or non-saturation) in the snow was accepted to be smaller than the diffusion driving density difference [8]. These assumptions, coupled with the fact that (except in [9]) the volumetric heat production related to the non-zero density balance in the snow was omitted from the heat-transfer equations, indeed resulting in almost linear steady-state modeled temperature distributions.

The tomographic reconstruction from optical interferometric data on ice-crystal growth in supercooled water [11] and in air [12] showed temperature gradients up to 500°C m^{-1} around growing crystals over distances in the order of the crystal size. Under conditions always called "isothermal" the temperature of the ice was up to 2°C higher than the temperature in the surrounding pore space. This raised doubt in the validity of equating the ice matrix and the porous air temperatures when constructing the heat-transfer or snow-metamorphism models. More than this, these temperature gradients are of the same order as the gradients commonly applied to snow in known heat and mass-transfer experiments. That is why usage of the water-vapor concentration close to its saturated value can also not be correct.

It is traditionally stated that the intensity of the water-vapor transfer depends on the temperature gradient. However experimental data did not reveal a relation between these two characteristics [13]. The relationship found was a dependence of the water-vapor flux on the water-vapor-concentration gradient, related primarily to the temperature and secondarily to the temperature gradient. Finding a stronger water-vapor-flux dependence on the temperature than could be expected from the theoretical model [14] also supports this.

The quasi-steady-state temperature distributions actually observed [15] were always far from linear. As the obtained data could hardly be explained on the basis of the above sited interpretation of heat and mass-flux coexistence, additional experiments were done to find which processes could form such non-linear behavior.

2 Present Experimental Results

Heat and mass fluxes in the snow were produced by keeping opposite faces of 0.1 m long snow samples under different temperatures. The temperature was measured on the central axis parallel to the direction of the heat and mass fluxes. A more detailed description of the experimental apparatus and the results of crystal-size determination are given in [16]. The temperature distributions were accepted to represent quasi-steady-state conditions after the temperature change with time was no longer visible within the accuracy of the present measurements (±0.1°C). The results shown here are a combination of the data obtained before and partly shown in [17] (19 snow samples) and results of recently performed experiments (17 snow and glass bead samples).

The thin lines on the following figures are the linear temperature distributions, which could be expected in the case that the heat was transferred by conduction only. Bars represent the range of the temperature varying during steady-state conditions, corresponding to the temperature regulation in the experimental set–up and not changing shape of the graphs.

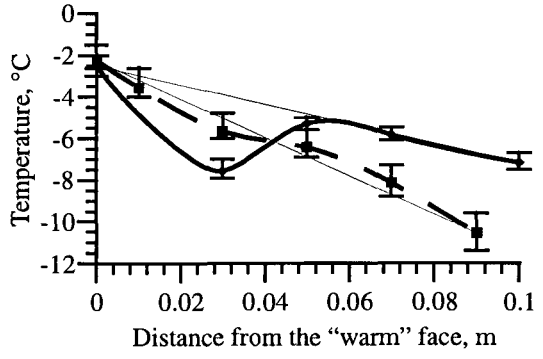

Fig. 1. Quasi-steady-state temperature distributions in snow samples with horizontal heat and mass fluxes; natural compacted (*dashed line*) and sifted (*solid line*) snow

Fig. 1 shows examples of the quasi-steady state temperature distributions obtained with horizontally produced heat and mass fluxes in a sample made from naturally compacted snow (snow density 325 kgm^{-3}), and when naturally compacted snow was sifted through a wire net for sample preparation (in this case the snow density became 458 kgm^{-3} and the crystal size range 1.11–8.34 $\times$ 10^{-4} m). The non-linearity (concave to the "warm" face) is present in both samples, but in sifted snow the temperature gradient in the central part of the sample was opposite to those applied externally.

Fig. 2 shows examples of the quasi-steady state temperature distributions in two similar snow samples made from sifted new snow (snow density 290 kgm^{-3}, crystal size range 1.1–6.8$\times$ 10^{-4} m) with vertically produced heat and mass fluxes. The character of the temperature distributions is similar – a

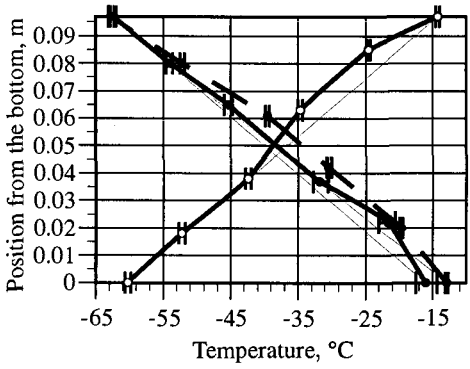

Fig. 2. Quasi-steady-state temperature distributions in snow (*solid lines*) and steady state temperature distribution in glass bead samples (*dashed line*) with vertical heat and mass fluxes; ○ – downward, ● – upward fluxes

non-linear profile is formed in the part of the snow sample with temperatures higher than −40 to −30°C, and the distributions are almost linear in the colder parts of the samples. This must be related to the maximum possible water-vapor concentration in the porous space, decreasing with the temperature decrease. However in the snow samples with "upward heat flux" the temperature distributions in the "warm" parts were convex to the "warm" face, which required other mechanisms of the water-vapor transfer than in the snow samples with "horizontal" and "downward" heat flux. The dashed line presents the temperature distribution with upward heat flux produced in a sample made from glass beads ($1.2–2.0 \times 10^{-3}$ m grain size) in the same temperature range. A considerable difference from linearity is seen throughout the whole sample, not restricted to the "warm" part as in the snow sample. It ought to be noted that the downward heat flux formed a linear temperature distribution in the glass bead sample.

Fig. 3 shows an example of temperature distribution in a sample from the same snow as used for the snow samples shown in Fig. 2, but with smaller

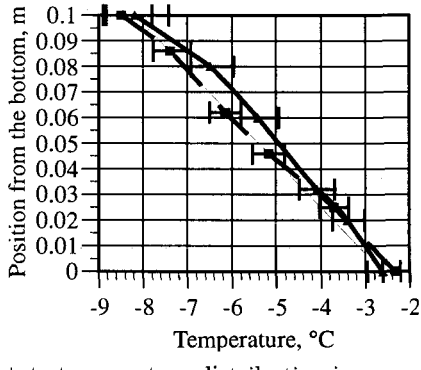

Fig. 3. Quasi-steady state temperature distribution in snow (*solid line*) and steady state temperature distribution in glass bead samples (*dashed line*) with vertical upward heat and mass fluxes

applied temperature difference. A convex temperature distribution was also formed; the whole temperature range corresponded to the "warm" part of the temperature distributions in Fig. 2. The dashed line shows an almost linear temperature distribution found in the glass bead sample under the same conditions.

3 Conclusions

These results of our experimental work drive us to conclude that the simultaneous heat and mass transfer modeled on the basis of presently used theoretical treatments of the phenomenon [4] are not able to explain the experimentally observed quasi-steady state temperature distributions in snow.

It is possible that the temperature measured in the snow is the temperature of the ice grains contacting a thermocouple – higher in zones where condensation prevails [11,12], and lower than the temperature of the porous air in zones where evaporation prevails. However, in this case the attempts to relate the observed to the theoretically expected temperature distributions need assumptions other than presently accepted for modeling the process. More than this, the temperature of grains with different size can also be different, and the actual "temperature range" in each "point" of the measurement can be broader, the wider the crystal size range is.

When relating the observed non-linearity of temperature distributions to alternations of evaporation and condensation processes [15], it can be concluded that the latent heat release had higher impact on the observed temperature distributions in case of sifted snow, characterized by wider range of crystal sizes and higher specific surface area of the ice matrix, and thus possibly more active process of mass exchange between neighboring grains, i.e. recrystallization. The non-linearity shows a clear dependence on the temperature; this means that it is related to the water vapor in the porous space formed by the recrystallization process.

In low density snow and when the heat flux is upward, the temperature distributions could be affected by convection superimposed on the prevailing evaporation and condensation zoning (Fig. 2). But under our experimental conditions the convection more likely enforced not air but only water-vapor transport (Fig. 3).

All the above considerations lead to the conclusion that the measured temperature gradients do not represent the amount of heat and water vapor transferred in snow even under quasi-steady state conditions. The temperature distributions in snow are the result of the mass and energy exchange between neighboring grains, regulated on the one hand by the specific surface area of the ice matrix, the crystal size range, the snow porosity and the tortuosity, limiting the amount of water vapor transferred by the externally applied temperature gradient; and decreasing, on the other hand, with decreasing temperature.

As the source of the water-vapor transfer consists mostly of material evaporated from the surface of the grains, it can be expected that the activity of

snow metamorphism should also primarily correlate to temperature and only secondarily to the temperature gradient that is present in snow, which is in agreement with our experimental results shown in [16].

Acknowledgments: The work was partly supported by the Japan Science and Technology Agency through JST and JISTEC.

References

1. Adams, E. E., Sato, A. (1993) Model for effective thermal conductivity of a dry snow cover composed of uniform ice spheres. *Ann. Glaciol.* **18**, 300–304
2. Woodside, W. (1958) Calculation of the thermal conductivity of porous media. *Can. J. Phys.* **36**, 815–823
3. Sato, A., Adams, E. E. (1995) Influence of microstructure on effective thermal conductivity of snow cover composed of ice spheres. *Seppyo* **57**(2), 133–140
4. Albert, M. R., McGilvary, W. R. (1992) Thermal effects due to air flow and vapor transport in dry snow. *J. Glaciol.* **38**(129), 273–281
5. Yen, Y. -C. (1963) Heat transfer by vapor transfer in ventilated snow. *J. Geophys. Res.* **68**(4), 1093–1101
6. de Quervain, M. R. (1972) Snow structure, heat, and mass flux through snow. *Symp. on the role of snow and ice in hydrology, Banff* **1**, 203–226
7. Sommerfeld, R. A. (1983) A branch grain theory of temperature gradient metamorphism in snow. *J. Geophys. Res.* **88**(C2), 1484–1494
8. Gubler, H. (1985) Model for Dry Snow Metamorphism by Interparticle Vapor Flux. *J. Geophys. Res.* **90**(D5), 8081–8092
9. Gray, J. M. N. T., Morland, L. W. et al. (1995) A Phase–changing dry snowpack model. *J. Glaciol.* **41**(137), 11–29
10. Colbeck, S. C. (1983) Theory of Metamorphism of dry snow. *J. Geophys. Res.* **88**(C9), 5475–5482
11. Braslavsky, I., Lipson S. G. (1998) Interferometric measurement of the temperature field in the vicinity of ice crystals growing from supercooled water. *Physica A* **249**, 190–195
12. Fujino, T., Tsushima, K. (1998) Growth of snow crystal in the view of thermally. Preprints 1998. *Conf. Jap. Soc. Sn. Ice*, 175
13. Fedoseeva, V. I., Fedoseev N. F. (1988) Otsenka koeffitsienta diffuzii vodyanogo para v snezhnom pokrove [Estimation of water vapor diffusion coefficient in snow cover]. *Meteorologiya i Gidrologiya* [Meteorology and Hydrology] (2), 132–135
14. Colbeck, S. C. (1993) The vapor diffusion coefficient for snow. *Water Resources Res.* **29**(1), 109–115
15. Sokratov, S. A., Maeno, N. (1998) Wavy temperature and density distributions formed in snow. *Ann. Glaciol.* **26**, 73–76
16. Kamata, Y., Sokratov S. A., Sato A. (1999) Temperature and temperature gradient dependence of snow recrystallization in depth hoar snow. In: Hutter, K., Wang, Y. and Beer, H. (eds) *Advances in Cold Regions Thermal Engineering and Sciences*, Springer Verlag, 395–402
17. Sokratov, S. A., Maeno, N. (1997) Heat and mass transport in snow under a temperature gradient. In: *Snow Engineering: Recent Advances.* Balkema Publ., 49–54

(Received 14 Feb. 1999, accepted 15 May 1999)

Methods of Similitude in Granular Avalanche Flows

Yih-Chin Tai, Yongqi Wang, J.M.N.T. Gray, and Kolumban Hutter

Institute of Mechanics, Darmstadt University of Technology, Hochschulstraße 1, 64289 Darmstadt, Germany

Abstract. Snow avalanches are relatively dry and dense granular flows for which the Savage-Hutter (SH) equations have been demonstrated to be an adequate mathematical model. We review these equations and point out for which cases the equations have been tested against laboratory experiments. Since the equations are scale invariant and because agreement with experiments is good, laboratory experiments can be used to test realistic flows. This is detailed in this paper. We demonstrate how shocks are formed when dilatational flow states merge into compacting states and show that shock formation is an essential mechanism in flows against obstructions. We finally apply the theory of similitude to the design of a projected avalanche protection structure of the Schneefernerhaus at the Zugspitze.

1 Introduction

It is now ten years since Savage and Hutter (SH) [11] presented their mathematical model of granular avalanche flow; in many subsequent papers [3–14] the equations proved to form an adequate mathematical model for dense flows of cohesionless granular materials, provided the moving masses were smaller than a few million cubic metres. For those masses observations showed that the Pauschalgefälle[1] is independent of mass, a property shared by the SH-equations, which are scale invariant.

Snow and ice avalanches as well as land slides and pyroclastic flows can be classified into two limiting cases, both of which have granular structure: (*i*) the *dense gravity driven flow* of a cohesionless granular material in which the interstitial fluid plays a negligible role and can be discarded and (*ii*) the *air borne powder snow avalanches*, which are turbulent boundary layer flows of a binary mixture of air and suspended solid particles [6]. In real avalanches these two limiting cases seldom occur in their purest form; mixed forms are the rule, in which either the dense granular or the powder flow component is predominant, but the dense flow avalanche is by far more frequent than the powder avalanche.

In this paper we are exclusively concerned with flow avalanches. We performed a number of experiments involving the flow of granular materials

[1] "Pauschalgefälle" is the slope angle of a line connecting the centers of gravity of an avalanching mass in its initial and final positions.

down complex topographies from initiation to runout and proved by comparison with numerical solutions that the SH-equations are adequate to model rapid flows of granular materials [3–15]. Inferences deduced from such experiments to the size in nature are therefore trustworthy, in particular since the SH-equations are scale invariant.

On this basis, laboratory experiments were performed to study the rapid flow of granular materials around obstructions. For certain geometries these flows show shocks being formed much like in channelized water waves, which can easily be visualized. Using photographic techniques the key features of the motion can be identified; the experimental technique can also be used in the optimal design of the flow around avalanche protection structures in mountainous regions. In particular, we try to make propaganda here for an experimental technique in the laboratory which can be effectively used in the design of avalanche protection constructions and in the determination of endangered zones of inhabited regions with a potential to be hit by possible avalanches. We first present the equations (§ 2), then point out where the equations proved to be in conformity with experiments (§ 3), show how shocks are formed (§ 4) and then demonstrate the application of laboratory experiments (§ 5).

2 The Equations of the SH-Model

Flow avalanches are mathematically described as incompressible fluids, of which the rheological behaviour obeys a Mohr-Coulomb type plastic flow law with a constant internal angle of friction ϕ, which can, roughly, be identified with the limiting slope angle of a triangular heap at rest. Observations indicate that the Pauschalgefälle is always smaller than the internal angle of friction of the granular material; the reason is the mechanical fluidization by the collisions of the particles in the strongly sheared basal-near layer. The flow in this thin fluidized layer can be represented by a Mohr-Coulomb type friction law with a bed friction angle $\delta < \phi$.

The model assumes shallow geometries in the sense that the avalanche thickness is very much smaller than its extent parallel to the bed. The fundamental equations are the balance laws of mass and momentum, kinematic boundary conditions at the free surface and the base as well as the stress free condition at the free surface and the Mohr-Coulomb sliding law at the base. These equations are simplified by integrating them over the avalanche thickness. What emerges is a free boundary value problem for the avalanche depth and the two velocity components parallel to the bed. In dimensionless form these equations take the form [3], see also Fig. 1.

$$\frac{\partial h}{\partial t} + \frac{\partial}{\partial x}(hu) + \frac{\partial}{\partial y}(hv) = 0, \tag{1}$$

$$\frac{\partial u}{\partial t} + u\frac{\partial u}{\partial x} + v\frac{\partial u}{\partial y} = \sin\zeta - \frac{u}{|\boldsymbol{u}|}\tan\delta(\cos\zeta + \lambda\kappa u^2) - \epsilon\cos\zeta\left(K_x\frac{\partial h}{\partial x} + \frac{\partial b}{\partial x}\right), \tag{2}$$

$$\frac{\partial v}{\partial t} + u\frac{\partial v}{\partial x} + v\frac{\partial v}{\partial y} = \quad - \frac{v}{|\boldsymbol{u}|}\tan\delta(\cos\zeta + \lambda\kappa u^2) - \epsilon\cos\zeta\left(K_y\frac{\partial h}{\partial y} + \frac{\partial b}{\partial y}\right), \tag{3}$$

$$K_{x_{act/pass}} = 2\sec^2\phi\left(1 \mp (1 - \cos^2\phi\sec^2\delta)^{1/2}\right) - 1, \tag{4}$$

$$K^x_{y_{act/pass}} = \frac{1}{2}\left(K_x + 1 \mp \left((K_x - 1)^2 + 4\tan^2\delta\right)^{1/2}\right), \tag{5}$$

subject to the initial conditions

$$\begin{aligned} h(x, y, 0) &= h_0(x, y), \\ u(x, y, 0) &= u_0(x, y), \\ v(x, y, 0) &= v_0(x, y). \end{aligned} \tag{6}$$

Equation (1) is the depth integrated mass balance, (2), (3) are two components of the momentum balance parallel to the bed and (4), (5) define the active and passive earth pressure coefficients. In the momentum balance (based on Newton's fundamental law) the individual terms on the right side represent the following effects:

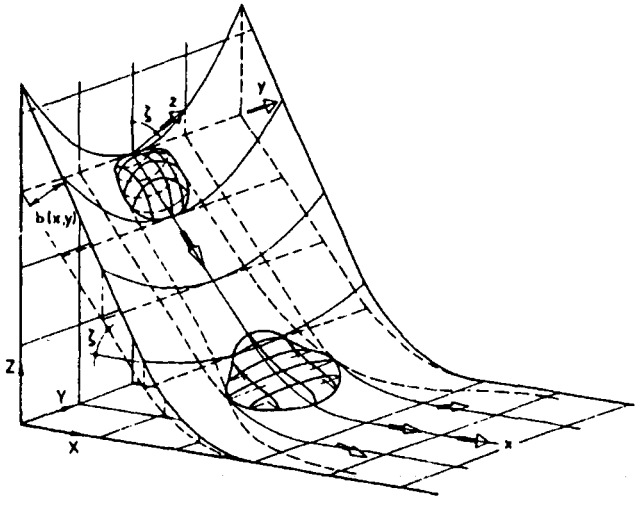

Fig. 1. Sketch of a avalanche slope: a parabolic channel merges into a horizontal plane. Curvilinear coordinates are x, y, z in the direction of steepest descent, horizontal and perpendicular to these. ζ is the slope angle and $b(x, y) = z$ forms the basal profile.

- the first term (which acts only in the direction parallel to the dominant flow) represents the gravity force component along the principal flow direction;
- the second term represents the friction with the solid ground; it is proportional to the pressure on the ground (which is equal to the superimposed pressure plus centrifugal force);
- the last term represents the variation of the integrated normal pressure (in the axial and transverse directions).

ζ and $\lambda\kappa$ are the slope angle and the curvature of the coordinate line in the flow direction, respectively. $K^{x,y}_{act/pass}$ are the active and passive earth pressure coefficients, respectively. These coefficients link the normal pressures in the down and cross flow directions with the overburden pressure. The active or passive components become effective when the avalanche extends or contracts in either the down and cross flow direction, respectively. These coefficients are functions of the friction angles δ and ϕ.

The equations include only two empirically determined phenomenological parameters, δ and ϕ. They are scalar invariants and therefore cannot describe the relationship between the runout distance of the sliding material and the total mass of the avalanche. However, this scale invariance proves that experiments performed in the laboratory at a small size can be transferred to the size of the prototype, if the friction angles δ and ϕ are the same.

3 Laboratory Tests in Chute and Slope Flows

Laboratory experiments were conducted on flows down inclines of various forms as well as idealized gullies and granular avalanches followed from initiation to run-out, Fig. 2. The following configurations were tested and are documented in detail in the literature.

Chutes, 10 cm wide and of 2 to 3 m length with a finite granular mass of triangular shape released behind a gate that was suddenly opened.

- Straight inclined chute merging via a circular segment into the horizontal [9, 12].
- Chute continuously curved of exponential form [8].
- Curved chute with a bump along its track, allowing for a separation of a single granular mass to be separated into two deposits, one possibly above the bump, the other below the bump [4].

Idealized slopes, approximately 1 m wide and 2 to 3 m long with a finite granular mass released from a spherical cap that was suddenly tilted.

- Inclined plane with 45°–60° slope angle [5, 6].
- Straight inclined plane merging via a curved segment into a horizontal plane [10].

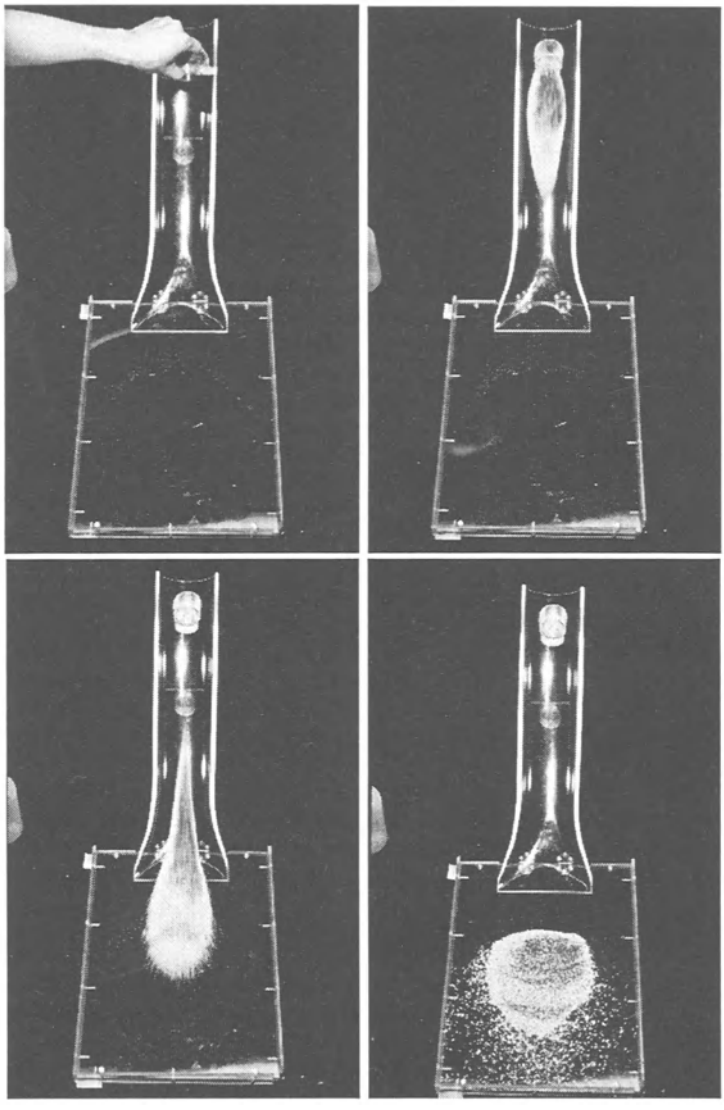

Fig. 2. Demonstration model of an idealized avalanche gully with snapshots of a granular avalanche (mustard seeds) on its track from initiation to run-out.

- Parabolic channel with straight talweg placed on an inclined plane merging continuously into a horizontal plane [3, 15].
- Parabolic channel with sinusoidally sidewise curved talweg merging into a plane [2], see Fig. 3.

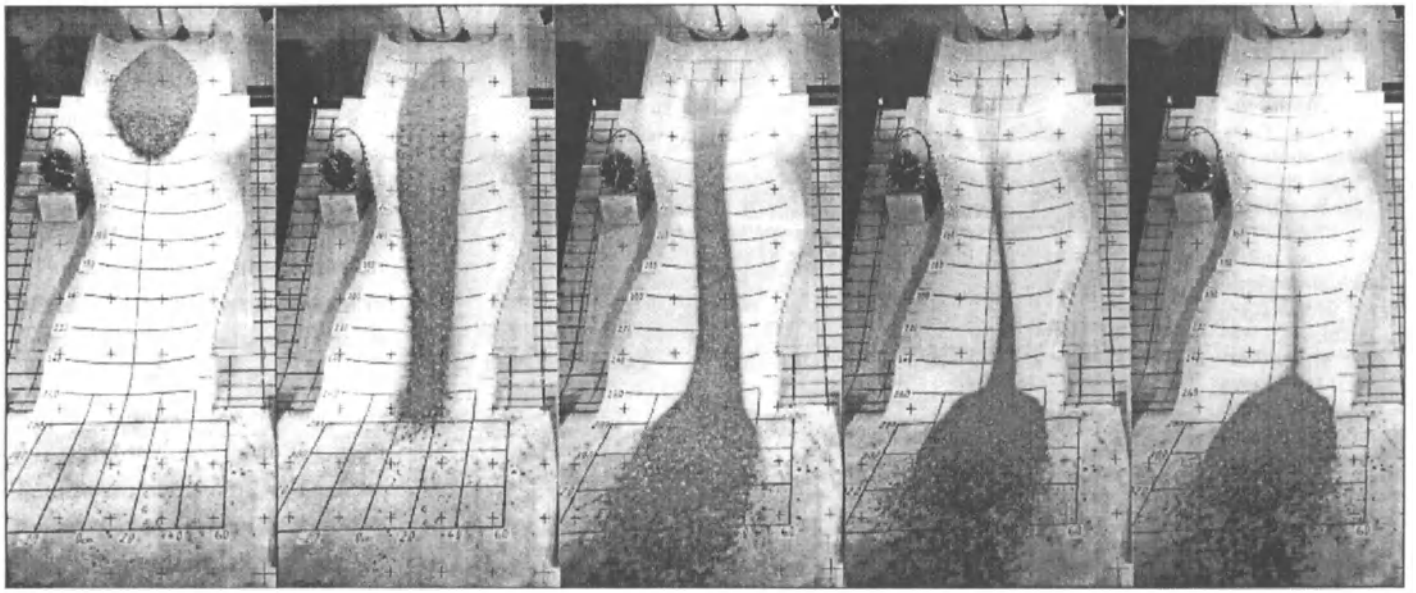

Fig. 3. Laboratory gully for simulations of granular avalanches: On a plane inclined by 40° against the horizontal a parabolically shaped channel is mounted of which the talweg deviates sinusoidally from the direction of steepest descent. A mixture of 40 kg sand and gravel is released from a plexiglass spherical cap at the upper edge of the photographs. A clock (on the left in the pictures) measures the time; its arm performs one revolution per second. The photographs show five shots of the moving avalanche. Note that the originally well mixed gravel mass is demixed with the coarse pariticles in the front and the small ones in the rear. (From [2], by permission.)

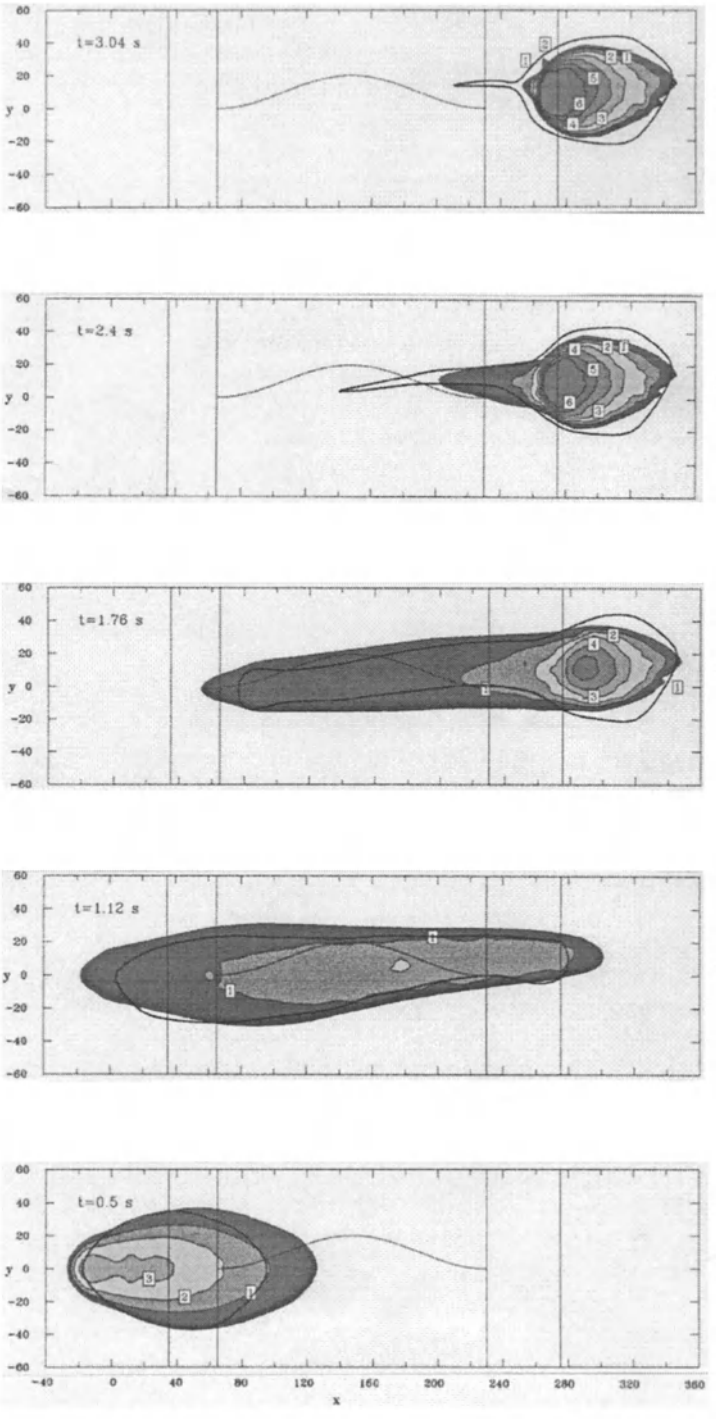

Fig. 4. Plan view onto the plane of the unrolled chute of Fig. 3 with the avalanche motion from top to bottom. The horizontal lined show where sinusoidal talweg begins (above at $x = 65$ cm), ends (at $x = 230$ cm) and where the horizontal plane begins (below $x = 275$ cm). The times in the panels indicate the moments since the avalanche wa released from rest. The graphs show the topographies in different shadings (with numbers indicating the thickness in cm), as obtained via nummerical computations. The black solid line shows the margins of the avalanche piles as declared from the photographs (From [2], by permission.)

The incline angle and the flowing material (quartz, marble, sand, plastic beads, sugar, mustard seeds, etc) were both varied, as was the coating on the gully surface to vary the effective bed friction angle. High speed photography was used to track the deformed granulate as it flowed. Stereo-photography was also used to probe the three-dimensionality of the avalanche. The free boundary problem (1)–(6) was numerically solved for the configurations realized in the experiments, and the geometry of the avalanche from initiation to run-out was tracked as well as the velocity field determined and compared with the corresponding results obtained from the experiments. Fig. 4 illustrates this comparison; the agreement between the theoretical and experimental results as detailed in the mentioned literature is very good.

The fact that equations (1)–(6) are scale invariant, and since the theory has been demonstrated to adequately reproduce experiments under laboratory conditions, makes it possible that the model equations are indeed able to predict avalanche flows at all those scales for which the pauschalgefälle has been demonstrated to be independent of the moving granular mass, i. e., for $M \leq 10^6 \mathrm{m}^3$. Of course, there remain uncertainties in this upscaling process for real avalanches. Conditions of shallow geometry are for montain slopes not always satisfied, and the granular cohesionless behaviour of the snow is still conjectured and may sometimes be violated. Furthermore, the friction angles δ and ϕ must be correctly reproduced — correct values for δ are more critical than those for ϕ — which may be difficult. In particular, variations of the bed friction angle along the mountain track for real avalanches may not be reproduced adequately in the laboratory experiments, one reason being that it may simply be difficult to determine them. Nevertheless, to within these provisos the extrapolation to the prototype size is reliable.

Laboratory experiments are thus a competitive tool in estimating the potential impact of flow avalanches and may be employed in estimating avalanche zoning schemes, avalanche protection designs, etc.

4 Formation of Shocks

The earth pressure coefficients (4) and (5) may suffer a jump in the course of the motion whenever the flow switches from a state of dilatation to that of contraction. This implies that internal shocks must form whenever this happens. Numerical integration procedures should account for this, however they are very complicated and difficult to implement. In the spirit of a first approximation we performed a smoothing operation for the earth pressure coefficient from its active to its passive values and thus were able to avoid the use of shock capturing numerical integration procedures [3, 15]. Conceptually this is tantamount to locally changing the constitutive behaviour in an uncontrolled manner, but the approach is defendable when the activation of this smoothing operation is restricted. This is the case in most situations treated above.

For an avalanche flow of a finite granular mass from an inclined gully to a horizontal run-out plane internal shocks are formed in the transition region from dilatational to contracting flow states in the region immediately before and at settlement. Fig. 5 shows the geometry of the deposited granular mass from an experiment similar to the one shown in Fig. 2 as computed with the regularized earth pressure coefficient. Regularization of the transition of the active and passive earth pressure coefficients has done no harm in this situation. Computation with shock-capturing techniques is under way [13]. One may, from a realistic point of view, even defend the use of the regularization procedure because upslope travelling shocks in experiments of granular flows down heaps disclosed a rather diffuse shock structure of several particle diameters [1, 2].

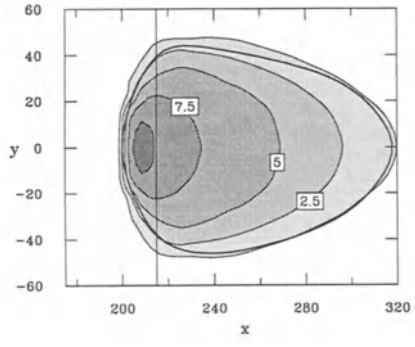

Fig. 5. Deposit of a finite granular mass after its motion through a straight channel of parabolic cross section inclined by 45° and merging into a horizontal plane. The direction of flow was from left to right. The graphs show the settled heap with level lines at 0.5 cm intervals as computed with the regularized procedure described in the main text.

The formation of shocks is a dominant phenomenon when e. g. a rapidly flowing granular mass is diverted and redistributed by structural devices (fences, walls). Classical avalanche protection constructions for structures are often used in this way. If a uniform layer of rapidly flowing granular material down an inclined plane is encountering a vertical wall forming an angle α with the direction of steepest descent, Fig. 6ab, then a straight shock will form at an angle β. Above the shock the undisturbed flow is supercritical with a given height h_1 and velocity v_1, behind the shock it is subcritical with different thickness $h_2 > h_1$ and different velocity $v_2 < v_1$. The situation is analogous to the sub- and supercritical flows in hydraulics of free surface channel flow. If the retaining wall is curved, the steady shock that is formed will also be curved, Fig. 6c. Given the upstream flow conditions (velocity, height) the downstream conditions can be computed. Structurally significant for instance is the determination of the pressure at the wall. Similar experiments can, of course, also be performed on slopes with varying topography or around bodies as shown in Fig. 7. Shocks are also formed in this case.

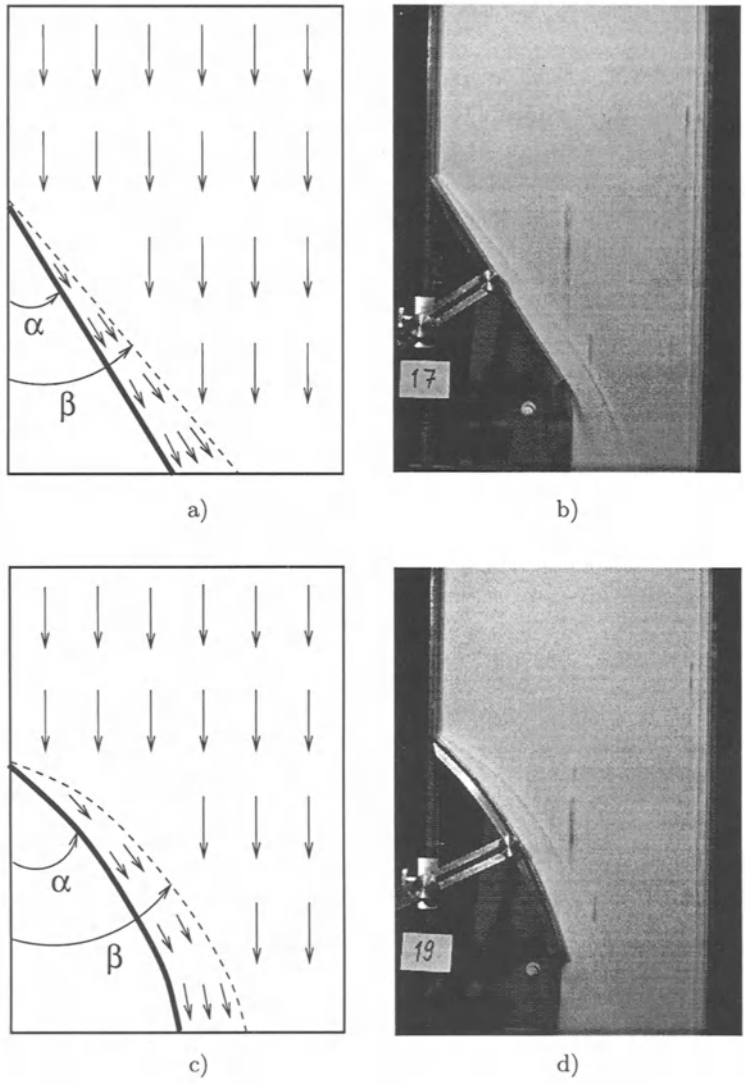

Fig. 6. A layer of granular material having thickness h_1, supercritical downstream velocity v_1 and moving down an inclined plane is encountering a wall (straight in panel a) and inclined at angle α, curved in panel c)). The induced cross flow generates a shock (straight in panel a) and inclined at angle β, curved in panel c)) with layer thickness h_2 and subcritical velocity v_2. The photos in panels b), d) show the same situation in the laboratory experiment.

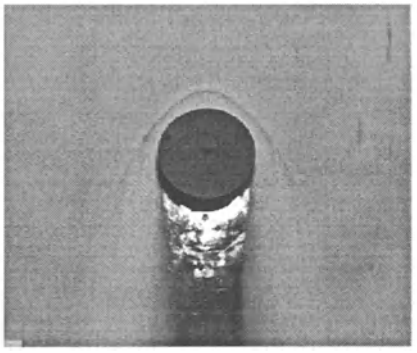

Fig. 7. Rapid flow of a granular layer down an inclined plane and around an obstruction of circular cylindrical shape. A detached curved shock is formed with supercritical flow above it and subcritical flow below it.

5 Model Studies of Avalanche Protections

From the example of the flow-diverting wall in Fig. 6 it is only a small step towards the small scale reproduction of the flow of an avalanche around an obstruction designed to protect a structure from being hit by the avalanche. We have done this for the "Schneefernerhaus at the Zugspitze" an old Hotel renovated and transferred into a research laboratory for environmental and climatological research. The building is situated at 2700 m.a.s. on a rather flat mountain slope inclined by approximately 45°. A number of masts equipped with meteorological instruments will be erected on the roof of the building and should be protected from avalanches throughout the year. Several avalanches pass and/or overflow the building every year so that a protection for a 100 year event is mandatory. According to expert studies the largest avalanche with a 100 year recurrence is a moving snow layer of slightly more than 8 m depth down the mountain. In a first study of protecting the building against such an event a tetrahedral wedge was constructed that should divert the flow and guide the snow to pass the building on either side of it. Fig. 8a,b shows a photograph of the Schneefernerhaus, and the tetrahedral wedge was positioned above the building at an optimal distance determined by trial and error.

The experiments were performed with two models of scales 1 : 100 and 1 : 300, using as "snow" plastic beads of 2.5 mm and semolina and white sugar of app. 0.8 mm diameter, respectively. As slope planes metallic and plexiglass sheets were used. These materials gave internal and bed friction angles approximately 35–45 and 15–25 degrees which lie in the range appropriate for snow. Fig. 9 displays the experimental set-up in the two scales, and Fig. 10 shows three snapshots of the motion of a layer of semolina down the slope, past and around the wedge and the Schneefernerhaus at three stages. The snow depth corresponds here to the motion of an 8 m layer. One can clearly see how the side flanks of the wedge divert the flow; a shock is formed at the wedge tip that extends on both sides of the flanks of the wedge.

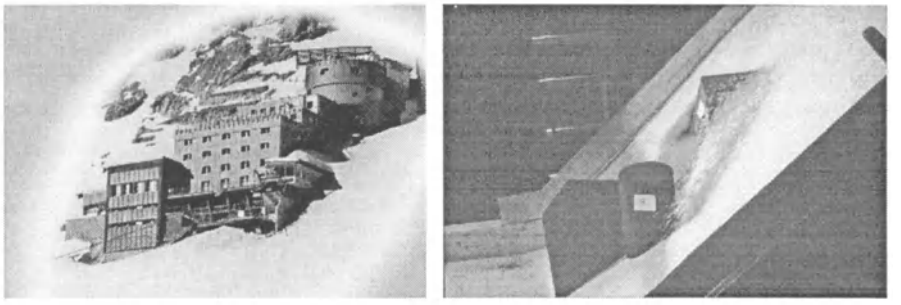

a) b)

Fig. 8. a) Schneefernerhaus at the Zugspitze at 2700 m.a.s. and b) its model reproduction together with a tetrahedral wedge type avalanche protection structure.

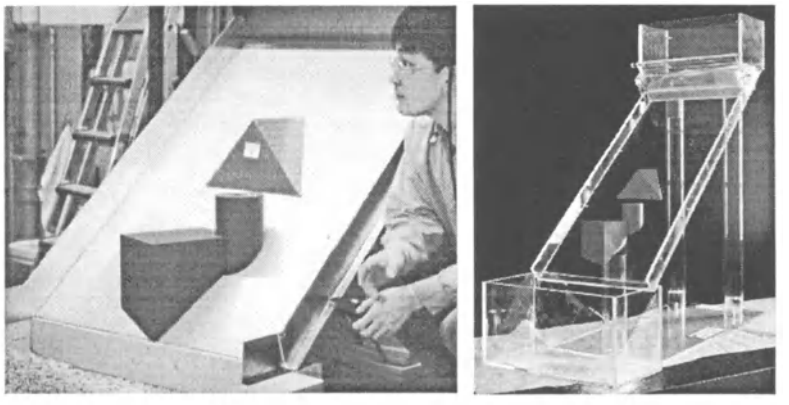

a) b)

Fig. 9. Incline with the Schneefernerhaus and the avalanche protection wedge, a) scale 1 : 100, b) scale 1 : 300.

One advantage of the model experiments is the fact that various different event scenarios can be tested, and thus the effectiveness of the protective structure estimated. A frequent scenario is when a layer of new snow is deposited on a hard and stable layer of old snow, and this new layer becomes unstable and forms an avalanche. Such cases are illustrated in Fig. 11. The plexiglass surface is now identified with the upper surface of the hard layer, here corresponding to a 5 m deep layer, and the moving granular mass corresponds to the new snow layer, here 3 m and (unrealistically large) 8 m, thus amounting to 13 m snow cover. It is evident that the wedge suffices for the first scenario but is not sufficiently shielding the building for the second; this can be no surprise, as total shielding was neither intended nor achieved in this case.

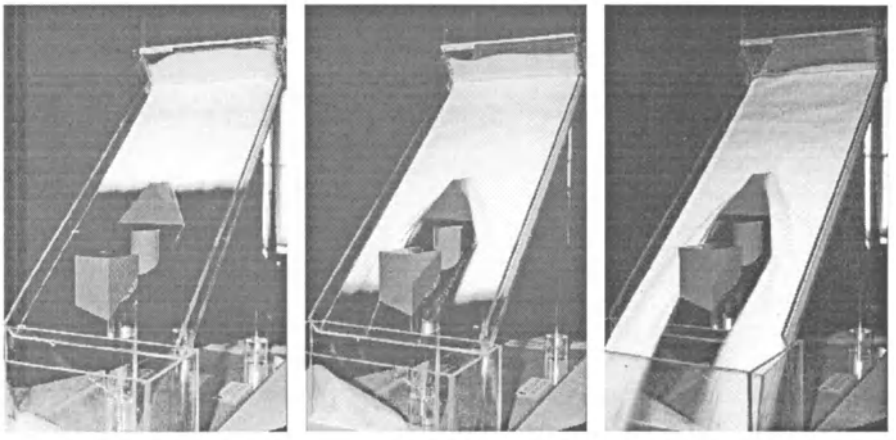

Fig. 10. Flow of a layer of semolina down a plane of 45° inclination, past the tetrahedral wedge and around the building that must be protected.

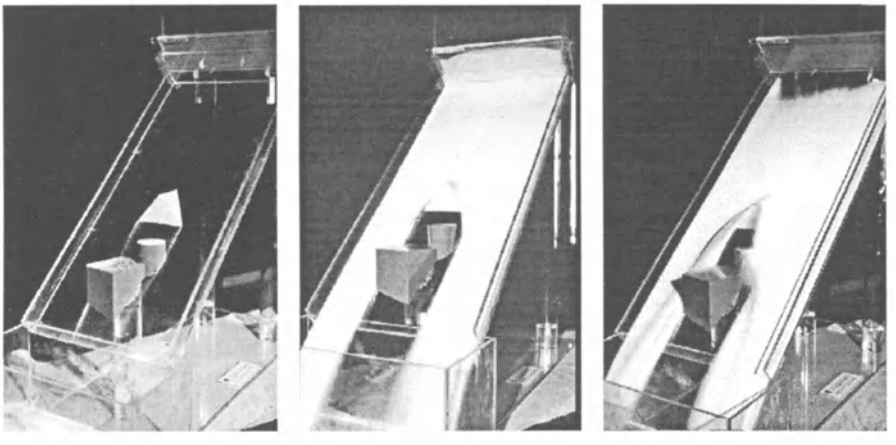

Fig. 11. a) Model of the Schneefernerhaus and the tetrahedral wedge protecting it against avalanches, here with the assumption that 5 m hard snow is stably deposited. The plexiglass surface corresponds to the upper level of this snow cover; motion of a 2 m b) and an 8 m c) layer of snow, here semolina. To differentiate this case from those of Figs. 9 and 10 the wedge is shown in light gray.

Acknowledgement: We thank Ms Danner for her help in typing this manuscript. This work was supported by the Deutsche Forschungsgemeinschaft through the Sonderforschungsbereich 298, "Deformation and Failure of Metallic and Granular Media.

References

1. Gray, J. M. N. T. and Hutter, K., Pattern formation in granular avalanches, *Continuum Mechanics and Thermodynamics*, **9** (1997), 341 - 345
2. Gray, J. M. N. T. and Hutter, K., Physik granularer Lawinen, *Physikalische Blätter*, **54** (1998), 37 - 44
3. Gray, J. M. N. T., Wieland, M. and Hutter, K., Gravity driven free surface flow of granular avalanches over complex basal topography, *Proc. R. Soc. London* (in press)
4. Greve, R. and Hutter, K., Motion of a granular avalanche in a convex and concave curved chute: experiments and theoretical predictions, *Phil. Trans. R. Soc. London*, **A342** (1993), 573 - 600)
5. Greve, R., Koch, T. and Hutter, K., Unconfined flow of granular avalanches along a partly curved surface - Part I: Theory, *Proc. Royal Soc. London*, **445A** (1994), 399 - 413
6. Hutter, K., Avalanche Dynamics, A Review, In: *Hydrology of Disasters* (V. P. Singh, ed.), Kluwer Academic, Amsterdam, 1996, pp. 313 - 390
7. Hutter, K. and Greve, R., Two-dimensional similarity solutions for finite mass granular avalanches with Coulomb and viscous-type frictional resistance, *J. Glaciology* **39**, 357 - 372 (1993)
8. Hutter, K. and Koch, T., Motion of a granular avalanche in an exponentially curved chute: Experiments and theoretical predictions, *Phil. Trans. Royal Soc. London*, **A334** (1991): 93 - 138
9. Hutter, K., Koch, T., Plüss, C. and Savage, S. B., Dynamics of avalanches of granular materials from initiation to runout, Part II: Laboratory experiments, *Acta Mechanica* **109** (1995), 127 - 165
10. Koch, T., Greve, R. and Hutter, K., Unconfined flow of granular avalanches along a partly curved surface - Part II: Experiments and numerical computations, *Proc. Royal Soc. London*, **445A** (1994), 415 - 435
11. Savage, S. B. and Hutter, K., The motion of a finite mass of granular material down a rough incline, *J. Fluid Mech.* **199** (1989): 177 - 215
12. Savage, S. B. and Hutter, K., Dynamics of avalanches of granular materials from initiation to runout, Part: Analysis, *Acta Mechanica*, **86** (1991): 201 - 223
13. Tai, Y.C. An application of shock-capturing numerical schemes to the dynamics of granular material. Dissertation for the doctoral degree, TU Darmstadt, (in preparation).
14. Tai, Y.C., Gray, J.M.N.T. and Noelle, S., Front-tracking method with Non-oscilatory Central Scheme for the free moving boundary problem., (in preparation).
15. Wieland, M., Gray, J. M. N. T. and Hutter, K., Channelised free surface flow of cohesionless granular avalanche in a chute with shallow lateral curvature, *J. Fluid Mech.* (in press)

(Received 10 June 1999, accepted 22 June 1999)

Experimental Study of Gas Hydrate Formation in Porous Media

Evgeny M. Chuvilin[1], Vladimir S. Yakushev[2], and Elena V. Perlova[1]

[1] Departament of Geocryology, Faculty of Geology,Vorobyevy Gory, Moscow State University, Moscow, 119899, Russia
[2] Russian Research Institute of Natural Gases and Gas Technologies, Moscow Region, p.Razvilka, 142717,Russia

Abstract. The experimental discovery of gas-hydrate self-preservation phenomenon made it possible to establish gas hydrates as one of the permafrost components such as ice, unfrozen water and gas. However, this component is so far poorly investigated. Little is known about conditions of formation and decomposition of gas hydrates in dispersed rocks. Special experimental chambers are used by the authors for the simulation of hydrate formation/decomposition processes in porous media and the study of different factors influencing the hydrate formation in dispersed rocks. Our experimental research reveals new data on kinetics and P, T- conditions of hydrate formation and decomposition in dispersed rocks. The experimental data show, that the process of hydrate formation in porous media depends on composition and structure of dispersed rocks and also on some external condition.

1 Introduction

Natural gas hydrate formation is a global phenomenon, exceeding the ice formation on the Earth crust. Hydrates are crystalline clathrate compounds of gas and water spread in permafrost regions and in the ocean floor (at water depth below 500 m). Their instability at atmospheric pressure makes their experimental study very difficult, especially in dispersed media. Experimental discovery and field studies of metastable permafrost gas hydrates (about 10 years ago) make it possible to consider gas hydrates as one of the main components of frozen rocks such as unfrozen water, ice and gas (Ershov E. D. et al. [2]). Moreover, discovery of this self-preservation phenomenon, when hydrates exist at non-equilibrium thermodynamic conditions, has opened new possibilities for the experimental study of hydrate-enriched deposits. During the last years the Geocryology Department of the Moscow State University conducted experimental studies targeted to the determination of the clay-particle influence on the process of hydrate-formation within dispersed rocks. This problem has so far not been studied, although there are some theoretical predictions and sporadic experimental data. Sometimes they are in contradiction with each other. For example, Y. Makogon [4] theoretically predicts an increase of the equilibrium hydrate formation pressure when the dispersed rock particle size decreases. S. B. Cha et.al. [1] have experimentally shown the

opposite phenomenon, namely that hydrate formation within a suspension of bentonite in water starts at pressures lower than equilibrium in the system free gas-liquid water. But experimental data of V. Yakushev [9], T. Uchida et al. [7] were in agreement with the theoretical prediction of Y.Makogon.

Unfortunately, data received earlier do not allow us to establish the physical and chemical nature of the described phenomena. Also, there are no data on the influence of clay particles on the micro and macro structure of hydrate-containing sediments during hydrate accumulation; this is very important for the understanding of the origin of natural hydrate textures in sediments. There are many uncertainties in the experimental data on water migration during methane hydrate formation in clays. V. Yakushev [9] reported absence of considerable water transfer during hydrate formation in heavy clays; at the same time, V. P. Melnikov and A. N. Nesterov [5] observed a thick propane hydrate rim on the top surface of the water-enriched heavy clay.

In this work we study the influence of different contents of clay particles on the phase equilibrium, water transfer and structure changes in the course of methane-hydrate formation in fine-grained quartz sand.

2 Procedure

2.1 Experimental equipment

The experimental chamber constructed jointly with researchers from the Geological Survey of Canada (F.Wright et al. [8]), was used for the hydrate formation and the study in the soil samples. This high pressure chamber, made of stainless steel, was equipped by a manometer, pressure and temperature sensors and valves for gas injection and withdrawal. Its general construction is the same as described in the paper of Ershov E.D. and Yakushev V.S. [3]. P-, T- data are recorded by a data logger and transmitted to a computer in accordance with the time step. Data documentation was controlled by "Sciemetric" software.

The experimental equipment included a cold room (temperature down to - 10°C), a methane cylinder (pressure 15 MPa, 99,9% methane), a laboratory for sample preparation and study, and freezers of "Grunland" type.

2.2 Experimental soil sample parameters and procedure of their preparation

Quartz sand of marine genesis was used as base soil. The sand was of light-gray color, with smoothed surface and homogeneously sorted. According to E. M. Sergeev's sand classification it is a fine-medium grained sand, see Table 1. Mineral composition, in accordance with the results of optical immerse analysis, is represented by quartz (more than 90%) and feldspat (10 %) and

Table 1. Particle size distribution of the soils used [%]

Particle diameter [mm]	1 ≀ 0.5	0.5 ≀ 0.25	0.25 ≀ 0.1	0.1 ≀ 0.05	0.05 ≀ 0.01	0.01 ≀ 0.005	0.005 ≀ 0.001	<0.001
Qartz sand	1	53	45	1	-	-	-	-
Montmorillonite clay	0.0	0.0	0.2	0.1	18.8	7.3	20.1	53.5

density 2.65 gcm^{-3}. The soil is characterized by low specific area - about 0.02 m^2g^{-1}.

Montmorillonite (bentonite) clay was of eluvial genesis. According to V. V. Okhotin's classification it was a heavy clay (Table 1). Montmorillonite prevails in clay fraction by more than 80%. The specific soil area is huge, about 620 m^2g^{-1}.

The clay content of the sand was 0, 2, 3, 5, 7 and 9% of the total sample mass. The initial water content (Wo) of the samples was the same in all experiments, 17%, and it was approximately equal to the optimum water content for most intensive hydrate accumulation (2/3 of the maximum water content). Distilled water was used.

In each experimental run two samples of the same composition and properties were prepared by the "layer-by-layer" compression method. One sample was for the experimental chamber, the second was the control sample; it was positioned near the chamber for temperature control and structure-change comparison.

2.3 Experimental procedure

The kinetics of the hydrate formation and the dissociation within the samples was documented when the temperature of the sample was varried in the hermetically closed pressurized chamber with hydrate-formation conditions. A sample was prepared (clay and water content, density control) and loaded to generate special conditions of the inner container of the chamber. Thereafter, the chamber was closed and blown through by methane to eliminate air. All this was done at room temperature. Then, the pressure inside the chamber was slowly increased up to 7–8 MPa and the chamber was put into a freezer with temperature +2 – +4°C. Once the hydrate formation process was finished (registered by the pressure change), the temperature in the freezer was lowered down to -6 – -7°C and the sample was frozen and then recovered from the chamber.

When the cyclic hydrate formation was under study, the temperature within the freezer rose up back to room temperature, and then the hydrate

formation cycle was repeated without depressurization. Pressure changes during all experiments were regular and corresponded to the temperature change and the hydrate formation/decomposition.

When the chamber was opened at temperatures below 0°C (in the cold room), all samples were stable due to the self-preservation phenomenon (Ershov E.D. and Yakushev V.S., [3]); so there was a favorable possibility to study the structure changes of the samples during the hydrate formation. Recovered hydrate-containing samples were described, cut into 4 cylindrical pieces and water, gas, and hydrate content of each piece as well as density were determined.

3 Results of Experimental Study

3.1 Kinetics of hydrate formation and dissociation in the samples

The study of the pressure and temperature changes with time allows us to determine when and how much hydrates form within the sample. The total character of the pressure and temperature curves was the same in all experiments (Fig. 1). It is partly described by F. Wright et al. [8].

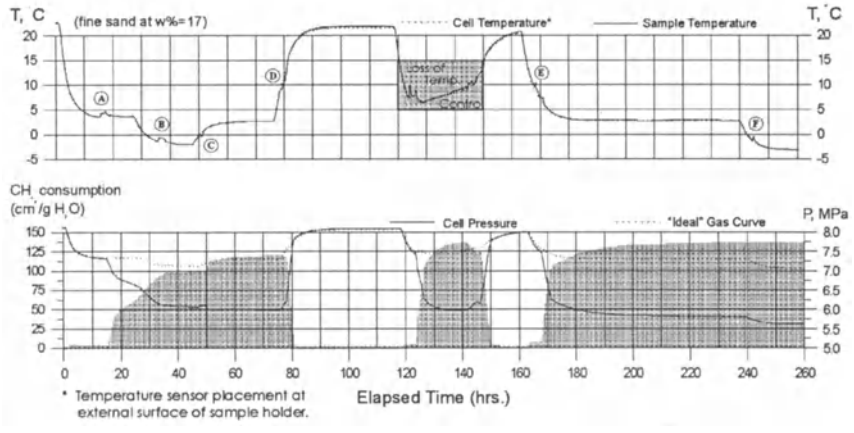

Fig. 1. Typical pressure/temperature record during experiments (according to F. Wright et al, [8])

Point A (Fig. 1) corresponds to the initial hydrate formation within the sample. Point B indicates sample freezing. Usually, the sample recovered subsequently, but in some cases, when cyclic hydrate formation was under study, a sample was heated and cooled again. In this case point C corresponded to secondary hydrate formation during ice melting within the sample. Point D

makes the final hydrate decomposition in the first cycle of hydrate formation/decomposition. Point E shows the initial hydrate formation during the second cycle and point F indicates the residual water freezing during the second cycle. Shadowed areas in the lower part of Fig. 1 reflect recalculated methane consumption into hydrate phase according to the pressure drop within the chamber.

The experiments have shown a considerable influence of freezing and cyclic repetition on equilibrium conditions and kinetics of hydrate formation within dispersed rocks. Equilibrium conditions of initial hydrate formation during the first cycle (A) were considerably different from the same conditions during the second cycle (E). Further repetition of hydrate formation produced no difference from the second cycle data. Secondary hydrate formation during the first cycle (point C) was unexpected and is explained by new possibilities for gas-water contact created by ice melting under hydrate-formation conditions.

The main methodical result obtained during the measurements of the kinetics was the correspondence between second-cycle-initial-hydrate-formation conditions and natural hydrate-formation conditions in sediments of the same properties and composition. So, probably, there is no longer any need to take into account supercooling needed for initiation of hydrate formation in nature. Equilibrium parameters of initial hydrate formation in natural sediments could be determined experimentally during the second cycle of hydrate formation. Equilibrium conditions of hydrate formation in dispersed rocks are different from the same conditions for pure water-free gas systems. They are shifted into thermodynamic conditions of higher pressures and lower temperatures, and this difference is growing with the rock-particle size and a decrease in the water content.

It is also worth mentioning that addition of clay particles to sand usually shifted equilibrium parameters of hydrate formation to higher pressures and lower temperatures, but sometimes a small pressure drop began at pressures lower than equilibrium for the system methane-pure water. This phenomenon still requires its explanation.

3.2 Structure and properties of hydrate-containing samples

In many samples recovered from the chamber hydrate caps of different thicknesses were observed at the top-exposed sides of the samples. In pure sand this cap was thickest and reached 12 mm. It was represented by white, relatively dense hydrate accumulation with inclusions of monolithic semi-transparent hydrate. This cap reflects strong water transfer in quartz sand during hydrate formation. However, addition of clay in proportion, (as small as 2% of the total weight) considerably decreased this cap formation and prevented water transfer along the soil samples. Thin caps (no more than 5mm thickness) were observed in samples with 2 and 3% of clay content, and in samples with 5, 7 and 9% of clay content this cap was practically absent.

At the same time, a clay-content increase resulted in more intensive hydrate-texture formation along the samples. In pure sand there is massive hydrate texture (hydrate-cement), in samples with 2 and 3% of clay some visible hydrate inclusions are formed. Further increase of clay content resulted in lens-like and porphyry-like (V. Yakushev [9]) hydrate-texture formation with thickness up to 1,5 mm and length up to 5-6mm.

Measurement of the final water content in samples showed considerable differences in the water distribution along samples in pure sands and those with clay (Figs 2, 3, 4, 5). In pure sand the water transfer was registered by drying of the central part (Fig. 2). Addition of montmorillonite clay reduced the water transfer very strongly, and with a clay content of more than 5% water transfer during hydrate formation was negligible.

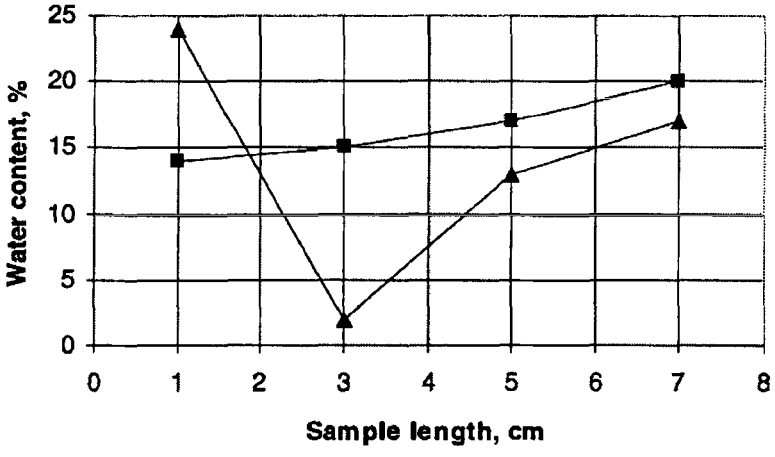

Fig. 2. Water content distribution along sand samples (Ac = 0%, Wo = 17%). ■ – control sample; ▲ – hydrate-containing sample

Gas (hydrate) content distribution within the samples was dependent on the water content and increased with the clay-content increase up to 7%. In pure sands, due to the low water content, the gas content is small and does not exceed 1 cm^3g^{-1} (Fig. 6). Addition of clay in small volumes (clay content (Ac) = 2%) does not change the gas content considerably. This is probably related to quick formation of an insulating hydrate film on water-gas contact within the sample and a reduction of the hydrate formation velocity. A further increase of the clay content results in more intensive hydrate accumulation, and the gas content is growing to approximately 5 cm^3g^{-1} at Ac = 7%. However, a further increase of the clay content decreases the gas content which could be attributed to decreasing the sample reservoir para-

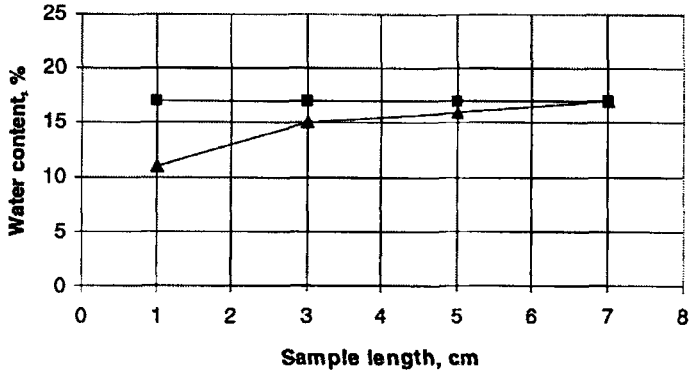

Fig. 3. Water content distribution along sand samples (Ac = 2%, Wo = 17%). ■ – control sample; ▲ – hydrate-containing sample

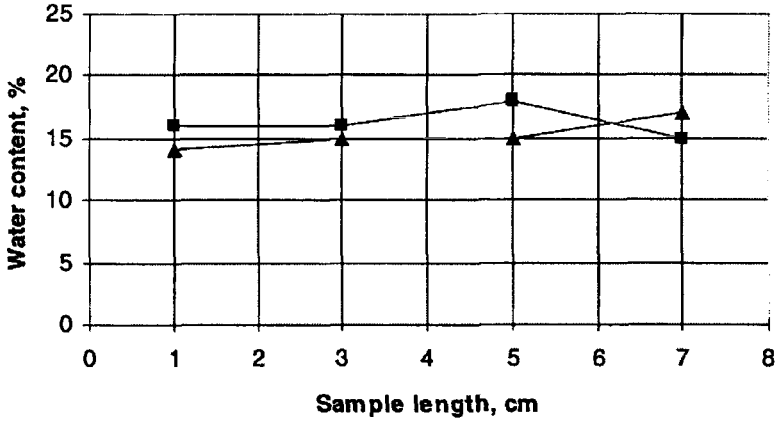

Fig. 4. Water content distribution along sand samples (Ac = 7%, Wo = 17%). ■ – control sample; ▲ – hydrate-containing sample

meters which influence the growing bonded water content. So, probably for each permeable soil, there is an optimum value of the clay content at constant water content for maximum hydrate accumulation.

4 Conclusion

The experiments conducted allow the following conclusions:

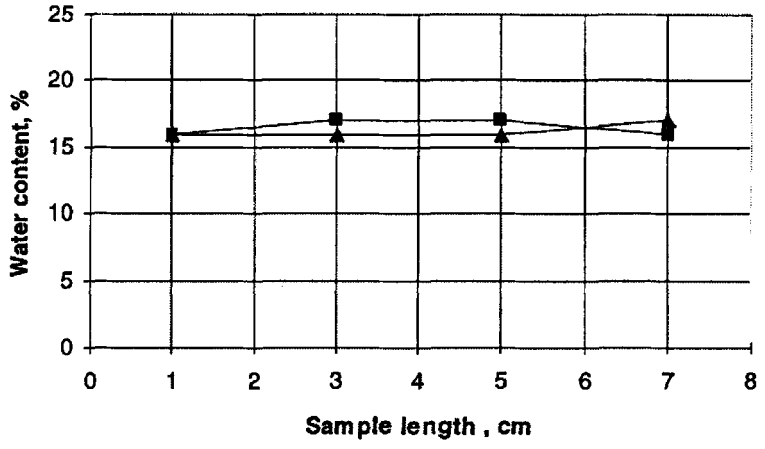

Fig. 5. Water content distribution along sand samples (Ac = 9%, Wo = 17%). ■ – control sample; ▲ – hydrate-containing sample

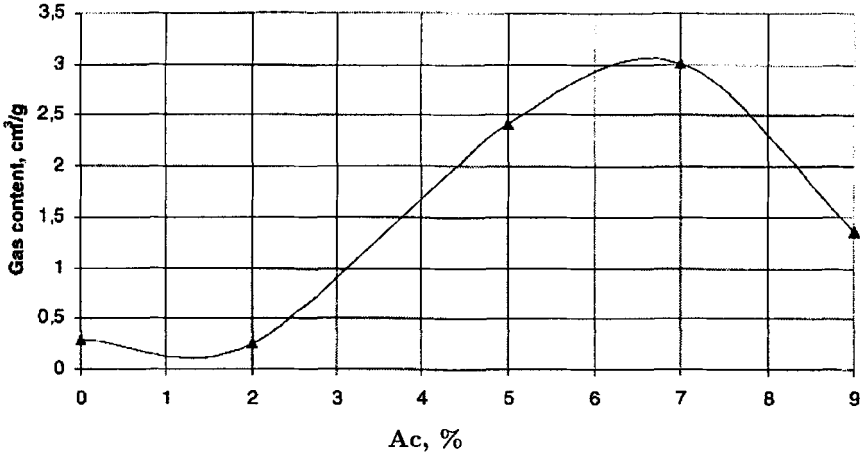

Fig. 6. Experimentally determined average gas (hydrate) content of sand samples of the same initial water content (Wo = 17%) with different clay content (Ac)

(1) Equilibrium conditions of hydrate formation in dispersed rocks are different from conditions for pure water-free gas system. The difference is growing with rock particle size and decreasing water content.

(2) Equilibrium conditions of hydrate formation in natural dispersed rocks can be determined experimentally during the second cycle of hydrate formation/decomposition; whereas the equilibrium conditions of hydrate

decomposition can be determined during the first cycle of hydrate formation/decomposition.

(3) If dispersed rock is frozen at hydrate-formation conditions, ice melting causes secondary hydrate formation, and hydrate content of the rock can grow considerably (Fig. 2).

(4) The second cycle of hydrate formation in dispersed rocks causes more intensive hydrate accumulation than first ones.

(5) Appearance of clay particles in sands strongly changes the character of hydrate accumulation decreasing water transfer during hydrate formation.

(6) The hydrate content of consolidated permeable sands is growing with the clay-content increase to an optimum value. Further increase of clay content considerably decreases the possibility for hydrate accumulation.

In addition the following result was found. Self-preservation phenomenon, when hydrates do not decompose completely at temperatures below 0°C, after a pressure drop due to isolating ice-film formation on their surface, can be successfully applied when natural sample storage is needed and experimental studies of hydrate-containing rock structure are conducted. Recently published experimental results on superheated ice storage in hydrate envelope (L.Stern et.al. [6]) further the development of self-preservation phenomenon study; it can be applied to frozen rock storage and experimental studies at temperatures above 0°C, if the ice within the rock is covered by hydrates existing at atmospheric pressure (for example, tetrahydrofuran hydrate). This is very important for the transport of the frozen samples from drill sites to the laboratory, when there is no possibility for constinuing cooling of the samples recovered.

References

1. Cha, S.B., Ouar, H., Wildeman T.R., Sloan E.D. (1988). A Third-Surface Effect on Hydrate Formation. *J. Phys Chem.* **92**, 6492-6494.
2. Ershov.E.D., Lebedenko, Yu.P., Chuvilin, E.M., Istomin, V.A., Yakushev, V.S. (1991). Peculiarities of gas hydrate existence in the permafrost zone. *Doklady Akademii Nauk S.S.S.R.* **321**, 788-791,(in Russian).
3. Ershov, E.D.and Yakushev, V.S. (1992). Experimental research on gas hydrate decomposition in frozen rocks. *Cold Reg Sci Tech.* **20**,147-156.
4. Makogon Yu.F. (1974). *Hydrates of Natural Gases.* Nedra, Moscow (in Russian).
5. Melnikov, V.P., Nesterov A.N. (1997) Water migration during gas hydrate formation in porous media. In: Knutsson (Ed.) *Ground Freezing, Balkema*, Belgium, 391-395.
6. Stern, L., Kirby S.H., Durham, W.B. (1996) Peculiarities of methane clathrate hydrate formation and solid-state deformation, including possible superheating of water ice. *Science* **273**, 18431848.

7. Uchida T., Ebinuma T., Ishizaki T. (1998). Dissociation Pressure Measurement of Methane Hydrates in Porous Media. In: Methane Hydrates: Resources in the Near Future? *International Symposium in Chiba-city, Japan, October 20-22, 1998. JNOC*, 253-258.
8. Wright, J.F., Chuvilin, E.M., Dallimore, S.R., Yakushev, V.S., Nixon, F.M. (1998). Methane hydrate formation and dissociation in fine sands at temperature near 0 0 . In: Allard M., Lewkowicz A. (Eds.), *7-th International Conference on Permafrost at Yellowknife, Canada. June 23-28, 1998*, 1147-1153.
9. Yakushev V.S. (1990). Peculiarities of mass-transfer in dispersed rocks during hydrate formation. In: Gritsenko A.I., Istomin V.A. (Eds.) *Natural and Technogenic Gas Hydrates. VNIIGAZ, Moscow*, 174-187. (in Russian).

(Received 6 April 1999, accepted 1. June 1999)

Electroacoustic Technique to Study Changes in the Liquid Phase State of Frozen Soils

Anatoly D. Frolov, Vadim B. Kravchenko, Andrei S. Pavlov

Scientific Council on Earth Cryology, Russian Academy of Sciences, Fersman St 11, Moscow, 117312, Russia

Abstract. We discuss experimental data, measuring techniques and interpretation of the electromechanical energy conversions in frozen soils. These conversions clearly depend on the unfrozen liquid state, its content, bulk distribution, initial concentration and ionic composition of the saturating pore solution. For saline frozen sand saturated with solutions of various compositions in the concentration range from 10^{-4} to 1 molel^{-1} the collected data on the peculiarities of electroacoustic conversions reflect the presence of the unfrozen liquid phase and changes of its content and state in the wide temperature range from the beginning of freezing to the corresponding eutectic point, and even below it. The established features are the basis of a new physical method to study and control liquid phase changes in frozen soils during freezing and thawing processes.

1 Introduction

Porous soils and rocks containing a liquid phase (which is always a solution of some concentration) represent original natural chemotrones, which fonction as electrokinetic energy converters. The physical causes of these conversions are the presence of electric double layers (EDL) at the boundaries of the solid-liquid phases and displacements of the phases relative to each other under external actions such as a pressure gradient in the liquid phase or an electric potential difference. As a result the electric charges separate in EDL by diffusion, implying bulk polarization of the medium and, hence, through electro-mechanical coupling, elastic deformations. If the penetrable porous medium is sufficiently rigid these energy conversions give rise to two electrokinetic phenomena: filtration potential and electro-osmosis. Both of them are well known and in the static regime studied in electrochemistry.

In soils the dynamic analogues of these energy conversions were discovered by American and Russian scientists in the 30-40s, and in geophysics they are called the *seismic-electric effect - E*, and the *electro-seismic effect*, respectively. The first designates the appearance of an electromagnetic field when an elastic wave propagates through the wet sandy-clayey or terrigenous-carbonate soils. It is correlated with the dynamic analogue of the filtration potential. The second denotes an elastic wave that accompanies an applied time varying electromagnetic field. This coupling is correlated with the dynamic analogue of electro-osmosis. To reproduce these effects in the laboratory, the

fields vary usually in the sonic and the nearest ultrasonic frequency ranges; therefore, it is logical to apply the more general terms *acoustic-electrical conversion (AEC)* and *electro-acoustic conversion (EAC)*, which we will use in this paper.

There are a lot of studies of these phenomena in the field and laboratory for temperatures above the freezing point of moist soils (see for instance the bibliography in Parkhomenko [19, 20]; Kokorev et al [11]; Migunov and Kokorev [16]; Migunov [18]). The results of the studies allowed to determine many features, mainly for AEC. However, the existence of AEC and EAC in frozen grounds were doubted for a long time, since the liquid phase content is small, and therefore difficult to differentiate from the unfrozen pore liquid phase, let alone to quantify its structure and energy state.

Below, we deal with the physical approaches to AEC and EAC, the measuring techniques, the experimental results and the EAC applied aspects in studies of phase changes in frozen soils.

2 Theoretical Approaches to Describe the Phenomena

Up to now, a full quantitative AEC and EAC theory has not been developed; instead much attention was devoted to the experimental studies of these phenomena. However, some of the theoretical approaches have been worked on. Let us consider briefly the essence of them.

The first attempt to create the AEC theory in a moist porous medium was a model offered by Frenkel [3]. He examined the dynamic analogue of the filtration potential in the tub-capillary porous medium by considering that their walls deform during the elastic wave propagation. As a result, the linear correlation of the electric field intensity E and displacement of the solid, L was obtained in the form $E = aL$, where the parameter "a" is a function of the porosity, permeability, ζ-potential, dielectric permittivity (ε), electric conductivity (σ), dynamic viscosity (η) and average flow velocity of a pore liquid, the velocity of a solid skeleton oscillations and other factors of filtration and electro-osmosis. However, calculations according to Frenkel's formula allows to obtain only qualitative agreement with experimental results.

The theory was further developed by Migunov [17, 18]. He considered the influence of the electrokinetic peculiarities of the medium on the velocity and the attenuation of elastic waves and introduced the notion of the electrokinetic sensitivity of the medium. This parameter establishes a correspondence between the appearing electric potential difference and the pressure gradient in the pore liquid, which (in the stationary regime) is $\chi_{AEC} = \Delta\varphi/\Delta P \approx \varepsilon\zeta/\eta\sigma$. In the dynamic regime the correlation between the amplitudes of E and P (or stress) can be obtained via the modulus of the seismic-electrical complex sensitivity (s) which is defined by the χ_{AEC} value as well as by the wave frequency (ω), velocity (V) and attenuation coefficient (δ)

$$| s | = E/P = [(\omega/V)^2 + \delta^2]^{1/2}\chi_{AEC}.$$

Physically interpreted, this modulus is a function of the mobility, the number of ion transfers and their concentration in the pore solution, as well as the tortuosity of the pore space, the adsorptive properties of the soil-solid matrices (mineral and ice), the extent of the pore saturation with the liquid phase and other parameters which are difficult to define directly. In the whole, it was found that the soil seismic-electrical modulus is far less than, for instance, the piezoelectric modulus of quartz.

However, to explain the nature of the energy conversion in soils only by the filtration potential and electro-osmosis in a permeable medium is not enough. Especially, it is related to the low-wet thawed soils as well as the frozen soils. Therefore we offered another model, which takes into consideration the existence of an allotropy of the pore liquid phase in soils. The essence of this model is as follows. In any soil the irregularities of the adsorption activity (spots, zones of active centres) and morphology (microhollows, cracks etc.) of grain surfaces cause energetic inhomogeneities and diversified degree of freedom in the movement of the liquid phase. As a result a sufficient number of bounded (semi-bounded) domains of pore liquid are formed. The application of external force fields leads in these discret domains to an ion migration, which generates electric macro dipoles, whence a large effective dielectric permittivity of the medium at relatively low frequencies ($< 50kHz$) is achieved [5]. When an elastic wave or a mechanical stress impulse propagates through such a medium the ions of the different masses and solvate envelopes shift, causing the displacements of the positive and negative charge centres within the liquid phase domains, so electric macro dipole moments are generated. These lead to bulk electric polarization, which vary in time with the frequency of the exciting acoustic field, i.e. this is the EAC-E appearance. In low moist porous media with an increased degree of the pore liquid phase separation, the effect of macro dipole polarization may become the prevailing effect in AEC compared with the conventional filtration potential.

In the case of electric excitation, the migration of ions to domain walls ("rigid" boundaries) occurs twice during the period of the applied electric field; this will in turn stipulate a pressure drive to the walls of the porous medium, and consequently cause deformations variable in time and space, - a wave with doubled frequency. So, in this case, with sufficient intensity of the exciting electric field, the wave of mechanical stresses arising at doubled frequency presents the effect of the electro-mechanical energy conversion, i.e. the basis of EAC. Thus in a medium with some permeability the EAC should manifest itself in the form of two types of signals

1) the electro-osmotic component, registering at the frequency of the exciting electric field - EAC-A_1;
2) the macro dipole component, registering at the doubled frequency of the exciting electric field - EAC-A_2.

It is obvious that higher the degree of the liquid phase separation is the greater should be the EAC-A_2 intensity; i.e. in low moist clayey soils at pos-

itive temperatures and in frozen sandy-clayey soils (according to the initial concentration and composition of the pore solutions) the last type of EAC may be prevailing. Thereto, according to the theory of Frenkel and Migunov for AEC and thanks of the reversibility of the filtration potential and the electro-osmosis phenomena the EAC-A_1 intensity should be linearly correlated with the magnitude of the exciting field E. However, due to appearing the concentration gradient and because of the ion displacements in the domains of the liquid phase (which entails the opposite ion diffusion) and the ion-ion interactions, the EAC-A_2 value should depend non-lineary on the magnitude of E. Thus, in the general case the mechanical deformation in the soil, conditioned by electric excitation is a relatively complicated function of the exciting field E

$$L_j = \sum a_{ij} E^{k_j},$$

where $j = 1, 2, 3, 4, 5, 6$; $i = 1, 2, 3\,(x, y, z)$ and the exponents k_j have positive values beginning with 1 and growing (the values are not necessarily integers due to the complicated process of the electro-mechanical energy conversion in moist soils). By now, the experiments have verified two possible values of the exponent $k_1 = 1$ and $1 < k_2 < 2$ (Fig. 1).

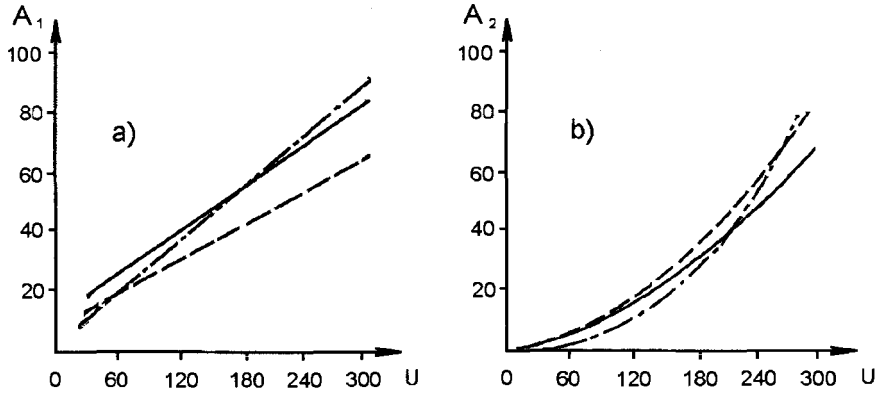

Fig. 1. Typical examples of the $EAC - A1$ (a) and $A2$ (b) dependence on the magnitude of exciting electric voltage; solid, dashed and dashed-doted lines correspond to the samples of various kinds of bricks saturated with $NaCl$ solution, $C = 10^{-1}$ mole/l , temperature was $+20°C$.

3 Results of the Previous Tests

The first laboratory experiments carried out in the wide temperature range (down to $-30°C$) on the samples of porous soils saturated with fresh water [5, 11], showed that it is possible to measure the AEC signal in the frozen state with a reliability of 5 - 7% (Fig. 2). These tests proved that the variation of the AEC value as a function of temperature is similar in frozen quartz sand,

kimberlite and limestone; this value is determined by the kinetics of freezing of the liquid phase in them.

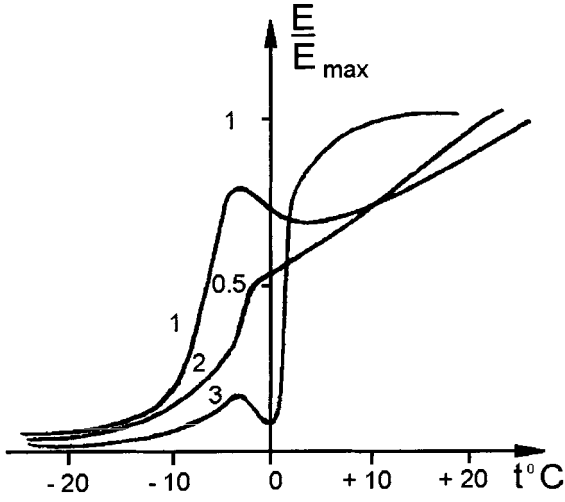

Fig. 2. Normalized *AEC* values in moist soils vs temperature: 1-productive kimberlit (Yakutiya); 2-carbonate non-productive kimberlit formations; 3-quartz sand

The effect actually vanishes in the frozen quartz sand approximately at $-28°C$ (practically the end of the liquid phase freezing), which is consistent with the results of the dielectric studies of this sand [4]. The *AEC* temperature dependence for frozen soils was most clearly observed in these experiments at the frequencies of the exciting acoustic signal (7-8 and 17-20 kHz). No dependence of the AEC value on the ice content was noted in the frozen sand. The highest AEC intensity in the frozen state was obtained in these experiments for productive kimberlities of Yakutia (Fig. 2, Curve 1), a soil consisting of clayey formations with higher content of admixtures such as radioactive isotopes (especially Th and F^{+3}).

Thus, despite the evident absence of permeability and whence filtration potential (especially in frozen sand), the existence of the *AEC* signal down to fairly low temperatures supports our hypothesis about its probable macro dipolar nature. This is also confirmed by the characteristic *AEC* maximum slightly below 0°C, when the samples pass into the frozen state (Fig. 2), due to an increase of the degree of the liquid phase separation thanks to the ice formation in the pores. Later (see for instance Migunov [18]), the seismic-electric effect was registered in frozen kimberlite pipes in the field (Western Yakutia).

The tests on low-moist (air-dry) samples of loam, limestone and sandstone at room temperature were performed by Chernyak [1, 2]. His results were: first, the occurence of both *EAC* and *AEC* also in the absence of the permeability of the studied soils; second, a doubling of the registered signal frequency of the elastic vibrations compared to the frequency of the exciting

electric field; third, a non-linear (close to quadratic) dependence of the EAC amplitude on the intensity of the exciting field and a non-polarity of EAC. However, the author's explanation of the results, including the identification of the EAC with electrostriction, was wrong [15]. We think that these experimental results are also in complete agreement with our model and the prevailing role of the domain-macro dipolar polarization in low-moist soils.

The further experiments performed by us with the moist samples of sand, brick, cement etc. made it possible to justify the idea of the prominent contribution of macro dipolar polarization in EAC, which under certain conditions becomes prevailing. Particularly, in contrast to Chermyak's tests, two types of electro-acoustic effects were established at room temperature: linear (electro-osmotic) behaviour at the frequency of the exciting field, the EAC-A_1, and a non-linear (macro dipolar) response, at doubled frequency, the EAC-A_2.

The intensity of the linear EAC-A_1 effect in samples of quartz sand saturated with the salt solutions of very low concentrations ($C_i < 10^{-3}$ mole l^{-1}) was nearly by an order greater than that of the non-linear EAC-A_2 effect. The concentration of the pore solution increased the EAC-A_1 magnitude, the difference between the A_1 and A_2 values decrease and at $C_i = 10^{-}1$ mole l^{-1} this difference was only about twofold. A decrease of the EAC-A_1 value, while the concentration of the pore solution grows, is conditioned by a decrease of the thickness of the diffuse parts of the EDL. This fact has considerably hampered the realization of filtration potentials but only weakly influenced the contribution of macro dipolar polarization. When $C_i \geq 1$ mole l^{-1} the general level of the EAC intensity fell by approximately an order of magnitude while preserving the above mentioned difference between the A_1 and A_2 values from two to about ten folds according to the composition of the A_2 saturating solution. Note that the dependence $A_2(U)$ evidently digresses from the quadratic behavior, i.e. the exponent of the electric voltage U (or of the field E) was less than 2, approximately as in Fig. 1b.

In these experiments we also proved the nonpolarity of EAC-A_2, however there was a fixed non-identity of the reaction of the liquid phase in domains on the sign of the exciting electric field changes, which is associated with the inertia of the concentration gradient arising under ion migration. This non-identity is illustrated by the asymmetric Lissagoux's figures for exciting and responsive signals (Fig. 3).

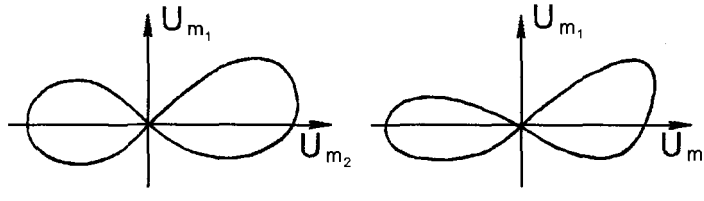

Fig. 3. Example of the Lissagoux figures for signals of exciting field and receiving doublet frequency EAC-A_2.

4 Measuring Technique

In principle, performance of AEC and EAC measurements in the laboratory is relatively simple and comprises of the following items:

a) a cell made of a good insulator (preferably of cylindrical shape), contains the sample, the ends of which are to be made as electrodes adjoining the soil, and a calibrated piezoceramic transducer emitting (or receiving) the acoustic signal in (or from) the sample; this whole cell must be be screened electromagnetically;
b) a generator of electric signals (pulse or periodic) with regulated output voltage power, pulse extension and (or) periodic voltage frequency;
c) a selective amplifier and a measuring unit which may be either an analogue (as a selective microvoltmeter) or digital device and is connected with a PC.

The possibility of visual control is considered necessary for comparison of the shapes of the exciting and registered signals on display.

So, to study *AEC* the exciting signal from the generator is transmitted to the piezoelectric emitter while the electric component of responsive signal is detected by the electrodes. Trial experiments showed the possibility to measure the magnetic component of responsive signal too by using a small spark-inductor (preferably of toroidal shape). In the *EAC* studies a voltage from the generator is applied to the electrodes and the acoustic responsive signal is taken by a calibrated piezoreceiver. The information about the tested medium received using *AEC* or *EAC* is approximataly equivalent, however, in the laboratory studies of frozen soils the *EAC* use is preferable as it delivers more reliable results. The latter is conditioned by the necessity in the *AEC* measurements: to damp the various interferences (including micro vibrations), the impedance matching of the sample and the gauge etc.

In EAC studies of frozen soils there are two major difficulties: the high transient resistance of the sample-electrode and the effect of heating the sample in the subelectrode zone, because for reliable registration of the responsive signal an exciting electric field of relatively large intensity and power is necessary. Therefore, a sharp reduction of the time of the exciting field application (approximately within 1- 2 seconds) and use of measuring units with high input resistance ($> 30 - 50$ MOhm) are needed.

For methodological studies and to establish the basic regularities we took a soil with the simplest mineral matrix - pure (washed many times), fine grained quartz sand (fraction 0.05 - 0,1 mm) which was saturated with various salt solutions at the initial concentration C_i from 10^{-4} to 1 molel^{-1}. Cylindrical cells with radius and height of 20 mm, containing a sample of a certain degree of moisture (2 - 18 %) and an assigned mass concentration and ion composition of the pore solution were used. The saturations with these solutions were used to define the peculiarities of the appearance of macro dipoles and their influence on the chemotronic effect in the frozen soils and also to get wider temperature ranges of phase changes, modeling

the freezing kinetics of the saline and clayey soils. With these aims solutions of a number of salts (different anions, cations) with consequently falling eutectic temperatures (t_{eu}) were chosen: KCl, $NaCl$, $MgCl_2$ and K_2CO_3. The samples prepared in measuring cells with electrodes were frozen at the temperature $-50\,\mathrm{div}\,-60°\mathrm{C}$ under loading $3-4$ kg to provide the simpliest massive cryotexture and to prevent frost heave. Measurements were taken in a mode of successive warming at 10-15 fixed temperatures. At each setting temperature the samples were held for a long time (8 - 36 hours) to achieve a state of quasi-equilibrium. This holding time increased as the measuring temperature came closer to the melting point or t_{eu}. The measurements were carried out at the optimal frequency (7 - 8 kHz) of the periodical exciting electric field.

5 Results and Dicsussion

The tests of the frozen soils resulted in temperature and concentration dependencies of EAC-A_1 and A_2 as given in Fig. 4. The data show the following features:

1. Existence of a critical initial concentration of pore solutions C_{cr}, exceeding it entails substantial deviations in the freezing kinetics of the liquid phase compared to the one known for fresh frozen sands. $C_{cr} \cong 5 \cdot 10^{-3}$ mole l^{-1} for sands which corresponds to the concentration obtained by the dielectric method [6, 7, 10].

2. Occurrence of both kinds of EAC (A_1 and A_2) in frozen saline soils is clear, however, their temperature dependence is considerably different: EAC-A_1 always decreases, while EAC-A_2 increases sharply, in the transition zone from the unfrozen to the frozen state. When the temperature of the frozen soil decreases, A_1 continues to decrease while A_2 can either grow or fall depending on the initial concentration of the pore solution, $C_i > C_{cr}$.

3. When $C_i < C_{cr}$ the major phase changes in the frozen sand occur in the temperature interval $0\,\mathrm{div}\,-2°C$, i.e. like in sands saturated with fresh water. This interval was not studied in our experiments in detail due to a lack of opportunity to keep our samples under thermostatic conditions with an accuracy of $\pm 0,1°C$ within the mentioned temperature interval. However, a number of samples with these C_i values showed an abrupt increase of the EAC-A_2 magnitude and, correspondingly, a fast drop of the EAC-A_1 value at negative temperatures near $0°C$.

4. Elevation of the initial concentration of the pore solution to $C_i < C_{cr}$ (saline soils) extends the temperature range of the EAC-A_1 and A_2 characteristic changes substantially and, consequently, alters the phase transformations in the frozen state, which indicates an increase of the liquid phase content and a change of its freezing kinetics.

5. During a temperature decrease of the frozen soil the freezing kinetics and the bulk separation of the unfrozen pore solution at $C_i = 10^{-2}, 10^{-1}$ and ≥ 1 mole l^{-1} are totally different from one another, Fig. 4.

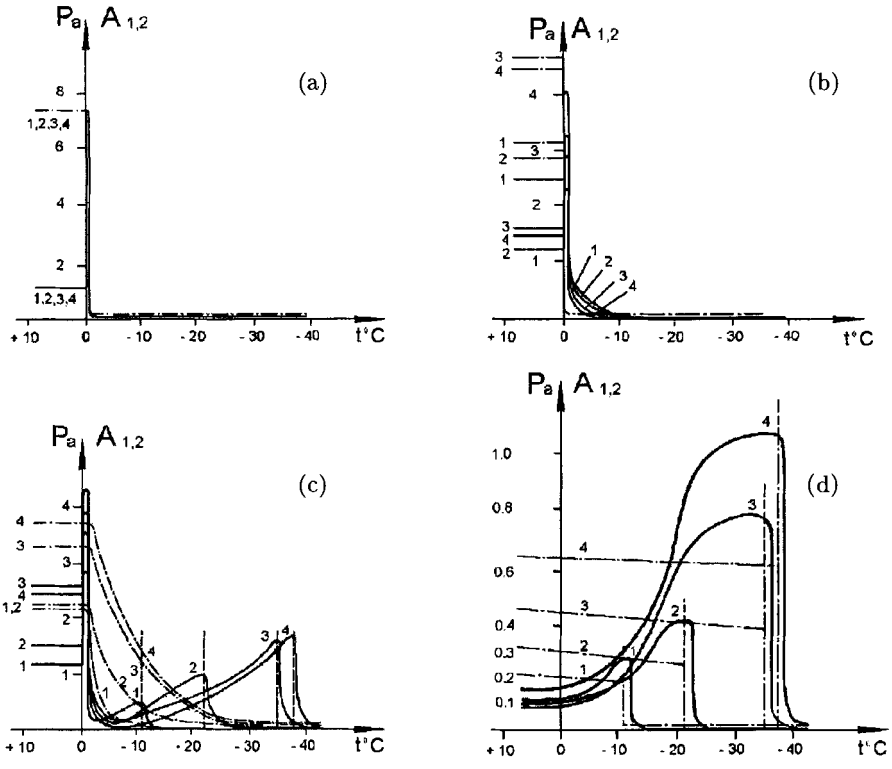

Fig. 4. Experimental data on EAC-A_1 and A_2 signals for various initial pore solution concentration (C_i) and composition: $C_i = 10^{-3}$ (a), 10^{-2} (b), 10^{-1} (c), 10^{0} (d) in molel^{-1}: 1 - KCl, 2 - $NaCl$, 3 - $MgCl_2$, 4 - K_2CO_3; solid line - A_2; dotted line - A_1; soil matrix is the fine grained quartz sand.

6. When either C_i, or the unfrozen liquid phase concentration increase, the diffusive parts of the EDL degenerate and, as a result, the greater part of the unfrozen pore solution in the domains passes in the quasi-free (from the influence of the surface of the solid soil matrix) state.

7. The latter essentially changes the character of the temperature dependences of the EAC-A_1 and A_2. The EAC-A_1 value practically decreases to zero in the frozen state where the soil permeability is absent, and the diffusive parts of the EDL in the unfrozen brine cells become degenerate (Fig. 4c). When $C_i \geq 1$ molel^{-1} this state occures only at the temperature near by t_{eu} (Fig. 4d). The decrease to zero of the EAC-A_2 values implies practically complete freezing of the liquid phase in the closed disseminated small cells (domains). This takes place at such a high salinity when the temperature is lower than t_{eu} by $15 - 20°C$. this is in conformity with the data of dielectric studies [6, 8, 9] and NMR tests [14, 23]. This experimental results are new because we know of no studies in physical chemistry of the eutectic state for

solutions in small separate cells, in which this state is extended and shifted to the lower temperatures.

8. The inversion of the EAC-A_2 temperature dependence was obtained when $C_i = 10^{-1}$ mole l^{-1} but the reduction of this kind of conversion occurs only at temperatures lower than t_{eu} for the corresponding composition of the pore solution (Fig. 4c).

9. At $C_i \geq 10^{-1}$ mole l^{-1} the known eutectic temperatures of the pore solutions are clearly noted by the EAC-A_2 value transmitted via the maximum combined with a further sharp drop.

All above mentioned peculiarities and regularities reflect in one way or another the content of the unfrozen liquid phase, the state of the frozen soils and the kinetics of its freezing partly described in several of our previous publications [9, 21, 22]. In this paper we discuss possible explanations of the physical causes of the found peculiaraties and their agreement with existing theoretical approaches. The detailed analyses of the results make it possible to give for the first time a rather detailed physical interpretation of the electroacoustic energy conversion in frozen soils.

Linear EAC: It is evident from Fig. 4 that the EAC-A_1 value diminishes when the soil passes to the frozen state and its temperature continues to fall. This drop is conditioned by the growth of the degree of the discrete destribution of the liquid phase in the bulk, a result of the pore ice formation and the precipitation of salt crystallohydrates. The result is a reduction of the medium permeability, and hence of the electro-osmosis intensity. The initial concentration of the pore solution primarily determines the degeneration of the EDL diffusive parts with a corresponding weakening of the electro-osmosis. The EAC-A_1 signal tends to zero when the unfrozen liquid phase passes to the disconnected discrete domain distribution. If the initial concentration of saturating pore solution is low (Fig. 4a, b) the principal phase changes occur in the temperature range approximately between 0 and $-2°C$. In highly saline ($C_i = 1$ mole l^{-1}) soil the EAC-A_1 value deminishes very slowly (Fig. 4d). The permeability and the high content of the unfrozen liquid phase (brine), the domains of which are not disconnected, persist up to t_{eu} of the pore solution in such soils. Only at a temperature close to t_{eu} a sharp domain size diminution and corresponding disconnection of the liquid phase occur as a result of intensive precipitation of salt crystallohydrates, and the EAC-A_1 value tends to zero. At intermediate concetrations, $C_i = 10^{-1}$ mole l^{-1}, an evident decrease of the EAC-A_1 value extended into the temperature range from freezing to the eutectic point with about 90 % of A_1 falling in the first half of this range (Fig. 4c).

On the whole, the dependence of the EAC-A_1 value on temperature and concentration is in good agreement with the electro-osmotic nature of this kind of conversion, and it is easy to judge by the signal magnitude about the degree of development (or degeneration) of the diffusive part of the EDL in the soil and in turn, by its dependence on the temperature, about the changes of the permeability of the frozen soil until its disappearence.

Non-linear EAC: The temperature dependence of the non-linear EAC-A_2 value is much more complicated which is clearly seen at the concentration $C_i = 10^{-1}$ mole1^{-1} (Fig. 4c). It is evident from this figure that there are two EAC-A_2 maxima: the first one is observed when the soil passes into the frozen state, and the second occurs near the eutectic temperature of the pore solution. Both maxima depend on the level of separation of the unfrozen pore solution as well as upon the increase of their concentration during the fall of the soil temperature. The first maximum (near $0°C$) is conditioned by the formation of pore ice, hence by the higher degree of the liquid phase separation than in the thawed state, but on the whole the medium is still permeable and some deffusive parts of the EDL are kept in this state, (because the EAC-A_1 value is considerable). As the temperature lowers further, the concentration of the unfrozen pore solution increases, whence, the EDL diffusive parts degenerate more and more, and thus the macro dipole effect related to the EDL inhomogenity and consequently the EAC-A_2 value both decrease. At temperatures corresponding to the EAC-A_2 minima the remaining part of the EDL is close to homogeneous and practically immobile, but a substantial portion of the unfrozen pore solution becomes quasi free, i.e. weakly bonded by the grain surfaces of the soil-solid matrix. A further decrease of the soil temperature results in an increase of the separation of the unfrozen liquid-phase domains and, hence, an increase of the macro dipole effect sets in thanks to the ion displacement in domains of the quasi-free solution. In this state, when the concentration of solution is sufficiently high the hydrate atmosphere of ions can be destroyed and the ion mobility increases. A decrease of the temperature and an increase of the concentration of the unfrozen pore solution in the domains lead to an increased probability of the process of ion association and formation of charged composite ions, which, in turn lead to an increase the solution electric conductivity [13]. These factors are responsible for the increase of the EAC-A_2 value up to the secound maximum at t_{eu} in spite of the domain size of the gradual diminution of the liquid phase. At $t < t_{eu}$ the sizes of the liquid phase domains are quickly decreased as a result of the increased salt precipitation of the crystallohydrates. This is reflected in the consequent quick decrease of the EAC-A_2 value in some temperature ranges (Fig. 4c, right part).

At $C_i < 10^{-1}$ mole1^{-1} (Fig. 4a,b) only the first EAC-A_2 maximum (near $0°C$) is observed. According to the kinetics of the soil freezing at $C \leq 10^{-2}$ mole1^{-1} the liquid phase almost fully crystallizes at temperatures higher than $-10°$C, and the stage, when the domains with the quasi-free solution are formed, does not occur. On the other hand, at $C_i \geq 1$ mole1^{-1}, only the second EAC-A_2 maximum at $t = t_{eu}$ is observed (Fig. 4d). This is connected with the fact that at so high initial concentrations of the pore solution the EDL diffusive parts turn out to be almost degenerated, a fact that is evident by the large decrease of the EAC-A_2 and A_1 signals immediately in the thawed state. The transition of the soil into the frozen state at such high

C_i- values occurs at temperatures below 0°C and hardly influences the state of the pore solution. Then, as the temperature is lowerd and the pore ice is gradually formed, the degree of separation of the unfrozen liquid phase grows, which is reflected in a continuous increase of the EAC-A_2 value (Fig. 4d). The soil permeability still remains sufficiently high up to the point $t = t_{eu}$ (the EAC-A_1 value is nearly independent of the temperature). However the increase of the EAC-A_2 value shows certain peculiarities in this case.

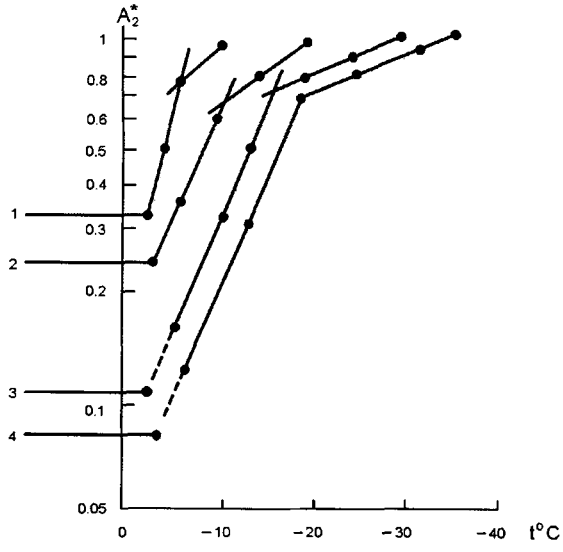

Fig. 5. Particularities of the increase of normalized EAC-A_2 values in the sand saturated with solution at $C_i = 1$ molel^{-1} vs temperature; 1,2,3,4 - see Fig. 4.

First, as is obvious from Fig. 5, the temperature dependence of the EAC-A_2 value in the frozen state for all compositions of the used saturating solutions is well expessed by the formula $A_2^* = a \cdot 10^{b|t|}$. Second, for all compositions at the approximate value $A_2 \sim (0.7 - 0.8)A_{2max}$ the slope of the $A_2^*(t)$ curve changes. This change may be caused by precipitation of salt crystallohydrates as the concentration of the unfrozen pore solution increases to a value higher than the limit for the given ion composition. Thus the size reduction of the half-limited domains is affecting the reduction of the increase of the EAC-A_2 value. Third, the increase of the EAC-A_2 value in the frozen state as compared with the corresponding values in the thawed state is conditioned by the ion composition of the pore solution. For instance, the EAC-A_2 value increases three times for KCl solution, whilst for K_2CO_3 this increase is more then 10 times. This may be caused by the formation of larger unfrozen liquid phase domains in frozen soils that are saturated with solutions with lower t_{eu}-values.

Thus, the results conform in general with the concept of the inhomogeneous liquid phase model in moist soil with discrete (semi-discrete) domain

formation, which display the macro dipole electric polarization under impact of external force fields. In frozen soils such domains can be inside the *EDL* diffusive parts or in the form of cells with quasi free pore solution of high concentration.

6 Conclusions

The experimental results allow to draw the following main inferences:

1. Moist soils, including frozen ones, are electrokinetic energy converters of electrical and mechanical oscillations. The signals of these conversions contain important informatiom about the energy state, concentration and ion composition of the saturating pore solutions, as well as about the kinetics of the changes of the liquid phase content in the soil during its freezing (or drying) processes.

2. It is found that in thawed and also in frozen soils existence of *AEC* and *EAC* is quite possible and measurable. In frozen soils of various salinity there are better outlooks for joint studies of the EAC-A_1 and A_2, which make up the bases for a new physical method to study and to control phase changes in these media both in the laboratory and in the field.

3. It is shown that to explain *AEC* and *EAC* in moist soils it is insufficiently to consider the dynamic analogues of the classical filtration potential and electro-osmosis conditioned by the presence of the *EDL* diffusive parts. The ion displacements in the limited liquid phase domains must also be taken into consideration. This gives rise to the macro dipolar effect, by which many experimentally found peculiarities (such as frequency doubling, non-linear dependences on temperature, effect of concentration and composition of pore solution, etc.) can be explained.

The results obtained by us are the first in this field, which is why it is necessary to develop further experimental and theoretical studies of electromechanical conversions in frozen soils. They will make it possible to comprehend their physical-chemical mechanisms and improve the fields of their practical applicability.

References

1. Chernyak G.Ya., 1975. About the direct and reverse seismic-electric effects in sediment soils at sinusoidal exciting. *Izvestiya Acad. of Sciences of USSR, Physics of Earth*, **7**, 117-121.
2. Chernyak G.Ya., 1976. On the physical nature of seismic-electric effects in rocks. *Izvestiya Acad. of Sciences of USSR, Physics of Earth*, **2**, 108-112.
3. Frenkel Ya.I., 1944. To the theory of seismic and seismic-electric phenomena in moist soils. *Izvestiya Acad. of Sciences of USSR, Geography and Geophysics*, **4**, 117-125.
4. Frolov A.D., 1976. *Electric and elastic properties of cryogenic formations.* Nedra Press, Moscow, 254 pp.
5. Frolov A.D., Dmitrieva T.A., 1976. Some results of seismic-electric effect study in frozen soils. *Permafrost studies*, **15**, MGU Press, Moscow, 250-252.

6. Frolov A.D., Gusev B.V., Fedyukin I.V., Massarskiy A.M., 1978. Dielectric properties of frozen soils saturated with KCl and NaCl solution. *Deponir. in VINITI, Moscow*, **1670-78**., 20 pp.
7. Frolov A.D., Fedyukin I.V., 1983. On the polarization of frozen dispersed soils in the time variable electromagnetic fields. *Izvestiya VUZov, Geology and Prospecting*, **6**, 90-96.
8. Frolov A.D., 1991. Peculiarities of phase changes in quartz sand saturated with salt solutions at 0 div $-40°$C. *Proc. III Intern. Symp. on Cold Region Heat Transfer, UAF, Fairbanks, USA*, 293 - 302.
9. Frolov A.D., Seguin M.K., 1993. Characteristiques de la Cinetique de Congelation de Sols Salins. *Permafrost and Periglacial Processes*, **4**, 311 - 325.
10. Frolov A.D., Fedyukin I.V., 1995. Dielectric properties of saline frozen sands. *Geophys. Investigations of Cryolithozone, Transactions*, **1**, PNC RAN Press,Moscow, 73 - 74.
11. Kokorev A.A., Migunov N.I., Frolov A.D., 1978. Seismic-electrric effect of kimberlities at negative temperatures. *Coll. Study of rocks by acoustic methods, VNIIYaGG Press, Moscow*, 44 - 49.
12. Kokorev A.A., Semionov G.S., Frolov A.D., 1981. Seismic-electric and acoustic studies of Siberian kimberlites. *Deponir. in VINITI, Moscow*, **1548-81**, 20 pp.
13. Krasnov K.S. (Ed), 1982. *Physical Chemistry.* Visshaya Shkola Press, Moscow, 675 pp.
14. Kvlyvidze V.I., Krasnushkin A.V., Zlochevskaya R.I., 1988. Properties of water superficial films and layers. *Call. Bonded water in dispersing systems*, **7**, MGU Press, Moscow, 48 - 66.
15. Migunov N.I., Sobolev G.A., Frolov A.D., 1976. About the seismic-electric effect amplification by static electric field. *Izvestia Acad. of Sciences of USSR, Physics of Earth*, **10**, 110 - 112.
16. Migunov N.I., Kokorev A.A., 1977. Dynamic features of seismic-electric effect in water saturated rocks. *Izvestiya Acad. of Sciences of USSR, Physics of Earth*, **6**, 114 - 118.
17. Migunov N.I., 1984. Use the seismic-electric phenomena to study a strained state of saturated soiles. *Izvestiya Acad. of Sciences USSR, Physics of Earth*, **9**, 76 - 85.
18. Migunov N.I., 1987. On the seismic-electric effect of ore bodies. *Izvestiya Acad. of Sciences of USSR, Physics of Earth*, **5**, 99 - 107.
19. Parkhomenko E.I., 1968. *The phenomena of electrification in soils and rocks.* Nauka Press, 240pp.
20. Parkhomenko E.I., 1978. Basic regularities of seismic-electric effect in rocks and his use in geophysics. *Coll. Physical properties of rocks and minerals at high pressures and temperatures. Nanka Press, Moscow*, 110 - 117.
21. Pavlov A.S., Frolov A.D., 1988. Electric-acoustic effect in frozen soils. *Proc. V-th Int. Conf. on Permafrost, Trondheim, Norway*, **1**, 431 - 435.
22. Pavlov A.S., Frolov A.D., 1990. On the application of electric-acoustic effect to study of saline soils freezing. *Coll. Saline frozen soils as a foundations of constructions. Nauka Press, Moscow*, 136 - 143.
23. Zhang Lixin, Xu Xiaozu, Tao Zhaoxiang, Deng Yousheng, 1993. Analysis of the second phase transition of sodium chloride solution in freezing soil. Permafrost. *Proc. Sixth Int. Conf. Beijing, China*, **1**, 773-777.

(Received 16 Feb. 1999, accepted 5 June 1999)

Permeability Effects on Winter-Time Natural Convection in Gravel Embankments

Douglas J. Goering and Pankaj Kumar

Department of Mechanical Engineering, University of Alaska,
Fairbanks AK 99775, USA

Abstract. Winter-time natural convection in open-graded gravel embankments has been suggested as a technique which can be used to provide passive cooling and thereby avoid thaw- settlement of roadways located in permafrost areas (Goering and Kumar [1]). The present paper examines the ability of these embankments to maintain the structural integrity of thaw-unstable permafrost which often underlies roadway or airport embankments in northern climates. As a result of low ambient temperatures acting on the embankment surface during winter months, an unstable density stratification develops in the embankment. Buoyancy-driven convection of the pore air occurs in reaction to the density gradient. The convection enhances the upward transport of heat out of the embankment during winter months, thus cooling the lower portions of the embankment and underlying foundation soil. During summer months the density stratification is stable and convection does not occur. Consequently, summer-time heat transfer is dominated by thermal conduction which transports heat less effectively. The results of the present study show that the winter-time convection can lower foundation soil temperatures beneath open-graded embankments by as much as 6°C on an annual average basis compared to standard sand and gravel embankments. Time varying temperatures and pore air velocities are calculated for different embankment permeabilities and the results are visualized in the form of isotherm and velocity vector plots for different times of the year.

1 Introduction

Natural convection in porous materials is a subject that has received much attention in recent years. This is a result of the interesting fluid flow and heat transfer characteristics of such systems as well as the numerous practical applications. One configuration of particular interest is a horizontal layer of porous material that is heated from below. It is well known that such a system will experience natural convection of the pore fluid so long as a critical temperate difference between the upper and lower boundaries is exceeded, Nield and Bejan [6]. If these systems are exposed to time-dependent boundary conditions, it is possible for convection to occur in an unsteady fashion only during the portion of the cycle when the upper boundary is at a relatively low temperature. Because convection is a much more efficient heat transfer mechanism than thermal conduction, the resulting unsteady periodic convection leads to the possibility of producing a passive cooling or 'thermal

diode' effect. In geotechnical applications such a cooling effect may be either advantageous or problematic, depending on the circumstances.

Various methods of providing cooling have been examined for use in maintaining the structural integrity of engineered structures which are located in permafrost regions. Because permafrost is often ice-rich and may be quite close to its melting temperature, it can cause great difficulty when building structures or roadway embankments are constructed. Such construction often produces a warming of the ground surface which eventually warms the underlying permafrost and causes thaw settlement. Large maintenance costs or abandonment of the structure are typically the result.

Previous research has resulted in a number of techniques which can be utilized to protect roadway or airport embankments from thaw settlement. In general, these techniques can be grouped into three categories; 1) those that modify conditions at the embankment surface in an effort to reduce the mean surface temperature, 2) those that augment the removal of heat from the embankment structure during winter months, and 3) those that employ insulation within or beneath the embankment. Methods 1) and 2) produce a cooling effect which, if strong enough, can eliminate thaw settlement, while method 3) uses insulation to slow the rate of thaw settlement to manageable levels. Surface modifications that have been studied include painting of the asphalt surface to increase the albedo, Reckard [7], and the use of snow sheds and snow removal on embankment side slopes, Zarling and Braley [8]. Both air duct circulation systems and thermosyphons have been utilized to augment winter-time cooling of embankments. Zarling et al. [9] reported on the operation of an experimental air duct system and Zarling and Braley [8] discussed the use of thermosyphons in roadway embankments. Esch [4] reviewed the use of foam insulation in roadway and airfield embankments.

In the present study the fluid mechanical and thermal characteristics of highly porous roadway embankments, known as air convection embankments, are examined as a function of embankment permeability. These embankments have fundamental characteristics which are similar to those of a two-dimensional horizontal porous layer. During the winter, the embankment is cooled at its upper surface due to low ambient air temperatures. If the cooling is strong enough and the embankment material is of sufficient permeability, natural convection of the pore air will occur during winter months. During summer the pore-air density gradient is stable and convection does not occur. Thus the embankment acts as a sort of one-way heat transfer device or thermal diode which effectively removes heat from the embankment and underlying foundation material during winter without re-injecting heat during subsequent summers. This passive cooling effect can prevent thaw of underlying permafrost, thus eliminating thaw settlement. In more temperate regions which are not underlain by permafrost, the natural convection can cause enhanced seasonal freezing beneath embankments and exacerbate problems with frost heave in the foundation soils.

Previously Goering and Kumar [1], Goering [2], and Goering [3] have reported experimental and numerical data which demonstrates the passive cooling capability of air convection embankments. In the present study a two-dimensional unsteady finite element model is used to examine the characteristics of these embankments as the air permeability of the embankment material is varied from 1.86×10^{-6} to 6.32×10^{-8} m^2. The results show large differences in the mean annual temperature at the embankment base as the permeability changes.

2 Mathematical Representation

2.1 Physical and computational domain

The physical domain chosen for the present study consists of the roadway embankment and foundation soil with dimensions shown in Fig. 1. Note that only the left half of the domain is shown in the figure due to the symmetry of the problem. This geometry corresponds to a roadway embankment with a driving surface width of 6 m, a height of 2.5 m, and 2:1 side-slopes. The lower boundary of the computational domain is located 9 m beneath the native ground surface and the left boundary is 17 m from the centerline. The embankment material consists of a rock/gravel matrix with the interstitial spaces filled with air. The resulting embankment has a large air permeability (which is varied in the current study) compared to those constructed of typical materials. The foundation soil is a uniform silt with high moisture content. An impermeable barrier is assumed to cover the embankment at its upper surfaces. On the driving surface this cover would consist of an asphalt-concrete pavement layer and on the side slopes an impermeable geotextile with a thin covering of top soil could be employed.

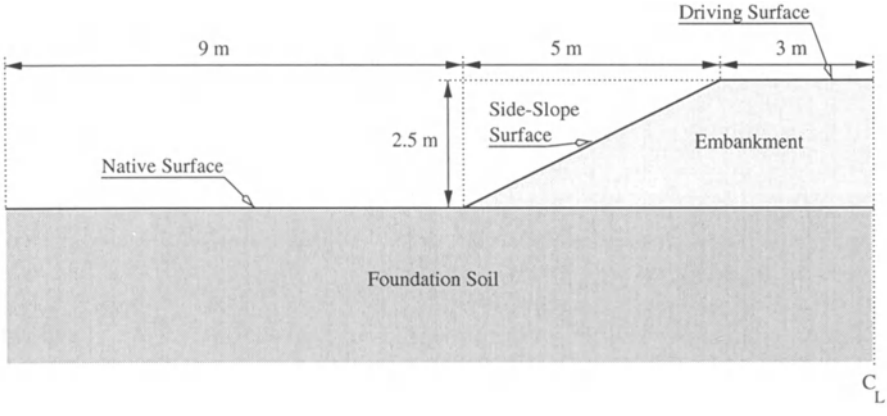

Fig. 1. Physical domain used for numerical modeling

2.2 Governing equations and numerical model

Equations governing unsteady energy transport and fluid motion in a two-phase system consisting of a porous matrix saturated with a single mobile fluid are summarized in the present section. See Goering and Kumar [1] for a complete description of the governing equations, and numerical model utilized in this study. The present section summarizes the governing equations for a two-phase system consisting of pore air moving through a porous gravel embankment. It is assumed that the pore air is in thermal equilibrium with the solid matrix and that Darcy's law can be used to relate the pore air velocities to pressure. With these assumptions the following conservation equations can be used for mass, momentum and energy:

continuity:

$$\nabla \cdot \boldsymbol{v} = 0 \tag{1}$$

momentum:

$$\frac{\mu}{K}\boldsymbol{v} = -\nabla P' + \rho \boldsymbol{g} \tag{2}$$

energy:

$$L\delta(T_f - T)\frac{\partial T}{\partial t} + C_m \frac{\partial T}{\partial t} + C_f \boldsymbol{v} \cdot \nabla T = k_m \nabla^2 T \tag{3}$$

where $\boldsymbol{v}$ is the average pore-air velocity, μ is the dynamic viscosity of the air, K is the intrinsic permeability of the porous matrix, ρ is the air density, C_m is the volumetric heat capacity of the medium, C_f is the volumetric heat capacity of the air, k_m is the thermal conductivity of the medium, T is the temperature, and L is the latent heat of freeze/thaw. The delta function appearing in Eq. 3 is used to represent the latent heat of the freeze/thaw process which is assumed to occur at the fusion temperature T_f (i.e. 0°C). The Bousinesq approximation is employed in order to couple Eqs. 2 and 3, resulting in the following equation for pressure:

$$\nabla \cdot \frac{K}{\mu}(\nabla P + \rho_o \beta T \boldsymbol{g}) = 0 \tag{4}$$

where:

$$P = P' + \rho_o(1 + \beta T_o)gy,$$

P is the non-hydrostatic component of pressure, β is the expansion coefficient for air, and ρ_o and T_o are reference density and temperature, respectively. Combining the definition of P with Eq. 2 results in the following expression for velocity:

$$\boldsymbol{v} = -\frac{K}{\mu}(\nabla P + \rho_o \beta T \boldsymbol{g}). \tag{5}$$

Equations 3, 4, and 5 represent a set of coupled, non-linear partial differential equations which must be solved simultaneously in order to obtain solutions to the embankment problem.

Numerical solutions to the governing equations described above are obtained via a two-dimensional unsteady finite element model as described in Goering and Kumar [1]. The model uses linear triangular finite elements and has been tested extensively and validated for problems of the type investigated in the present study. The spatial discretization is based on a Galerkin weighted residual integration over the problem domain. The resulting equations are integrated forward in time using a Galerkin time integration based on pore air velocities and thermal properties calculated at the present time level. This procedure results in the time history of temperature and pore air velocity throughout the grid as the boundary temperatures vary annually.

2.3 Boundary conditions and material properties

Before the solutions can be obtained for the governing equations described above, boundary conditions are required for pressure and temperature at each edge of the computational domain. Pressure boundary conditions are derived from the fact that there is no air flow across any of these surfaces (each is considered impermeable). As a consequence, Neuman boundary conditions can be applied for pressure at each surface.

The temperature boundary conditions consist of a combination of prescribed heat flux and prescribed temperature. Heat flux boundary conditions are used at the centerline, left, and lower boundaries. At the centerline, symmetry dictates a heat flux of zero. At the left-hand boundary the lateral (x-direction) temperature variations are negligible and, consequently, a heat flux of zero is specified. At the lower boundary, the geothermal heat flux of 0.06 wm^{-2} is imposed.

At the upper boundaries of the computational domain, which are exposed to the environment, yearly harmonic temperatures are prescribed. These boundaries include the driving surface, the gravel side slope, and the native ground surface, as indicated in Fig.1. The harmonic temperature functions have been calculated based on conditions which are typical of interior Alaska and are given in Table 1 where t is time in Julian days. Note that the yearly mean temperatures correspond to 1.1, 2.7, and -1.9 °C for the driving, gravel side slope, and native ground surfaces, respectively.

The foundation soil is taken to be a uniform ice-rich silt with a moisture content of 45% and a dry density of 1442 kgm^{-3}. Thermal properties include frozen and thawed thermal conductivities of 2.15 W/m °C and 2.00 $Wm^{-1}°C$, respectively, frozen and thawed specific heats of 1.64 $\times 10^6$ $Jm^{-3}°C$ and 2.01 $\times 10^6$ $Jm^{-3}°C$, respectively, and a latent heat of 26.2 $\times 10^6$ Jm^{-3}. For this type of material the effective air permeability is very small, and in the present simulations it is approximated as zero.

Table 1. Harmonic Temperature Boundary Conditions.

Surface	Thaw n-factor	Freeze n-factor	Temperature function (°C)
Driving surface	1.9	0.9	$1.1 - 26.1\cos(\frac{2\pi}{365}(t-9))$
Gravel side slope	1.7	0.6	$2.7 - 20.9\cos(\frac{2\pi}{365}(t-9))$
Native surface	0.5	0.5	$-1.9 - 10.0\cos(\frac{2\pi}{365}(t-9))$

With the exception of air permeability, the material properties for the embankment aggregate are identical for each of the cases examined in this study. Due to the fact that the embankment aggregate is highly permeable, it is assumed that the moisture content of this material is essentially zero. With this in mind the latent heat was taken as zero for this material. Also a thermal conductivity of 0.346 $Wm^{-1}°C$ and a specific heat of 1.02×10^6 $Jm^{-3}°C$ were used for both the frozen and thawed states.

3 Results and Discussion

In this section the results of three numerical simulations are presented and discussed. Each of the simulations were identical with the exception of the permeability of the embankment material which had values of 1.86×10^{-6}, 6.32×10^{-7} and 6.32×10^{-8} m^2 for case 1 (high permeability), case 2 (base permeability), and case 3 (low permeability), respectively. The simulations were carried out with a finite element grid consisting of 4898 triangular elements and 2560 nodes covering the domain shown in Fig. 1. A time step of 0.25 days was used with a total simulation time of 25 years. The 25 year simulation time was used in order to obtain the periodic annual cycle which eventually develops in response to the given boundary conditions and material properties. It is this long-term state which determines whether the roadway eventually thaws the foundation and fails.

Fig. 2 shows the velocity vectors within the embankment structure on January 31 as calculated by the model. The figure shows a complicated pattern of pore-air circulation within the embankment which consists of several individual cells. Perhaps the most distinctive feature of the flow field is a strong downward flowing plume beneath the center of the driving lane. The pattern shown in Fig. 2 is characteristic of winter behavior when a highly unstable air density gradient exists within the embankment. Note that the maximum velocity is 58.3 mhr^{-1}. Similar data for summer months (not shown here) reveals much weaker circulation with a maximum velocity on the order of a 1 mhr^{-1}. Also, January 31 data for case 2 and case 3 (also not shown here) reveals maximum pore-air velocities of 21.52 mhr^{-1} and 1.46 mhr^{-1}, respectively.

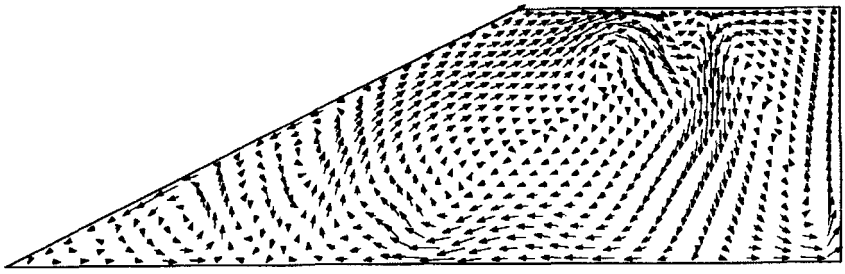

Fig. 2. Embankment velocity vectors for Case 1 on January 31. Maximum velocity is 58.3 mhr^{-1}.

Fig. 3 shows the dramatic effect that the circulation has on the isotherm shapes within the embankment. Isotherms in the foundation soil are generally horizontal and show a cooling from the top down, as we would expect during winter. Within the embankment, however, the isotherms are complex and display the characteristics of alternately upward and downward flowing plumes. These plumes are a direct consequence of the pore-air circulation taking place within the embankment. Note that the largest plume flows downward beneath the center of the driving lane and generates a strong cooling influence on the foundation soil by bringing low temperature pore air into close proximity with the base of the embankment.

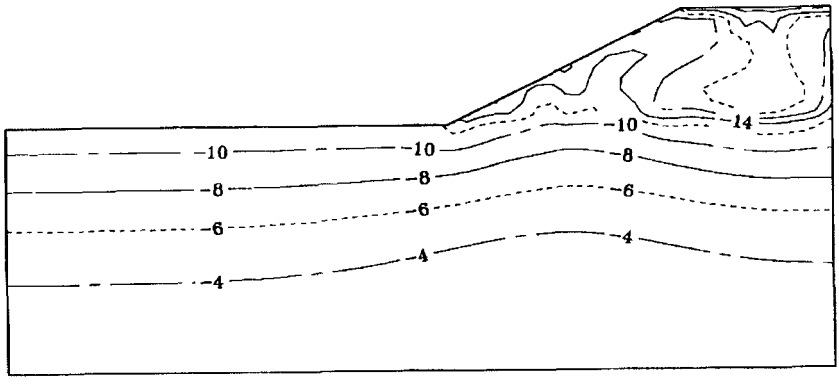

Fig. 3. Isotherms for Case 1 on January 31.

Isotherms for case 1 are shown in Fig. 4 for July 31. During summer the pore-air convection is too weak to have an impact on energy transport and, thus, the isotherm characteristics are determined by conduction alone. This is indicated by the lack of plume structures. An additional indication of this

is the large temperature difference (approx. 26°C) between the top and the bottom of the embankment which is illustrated in Fig. 4. Fig. 3 shows that this temperature difference is much smaller during winter months (approx. 10°C). This is due to the strong convective mixing occurring during winter which results in a more uniform temperature profile within the embankment.

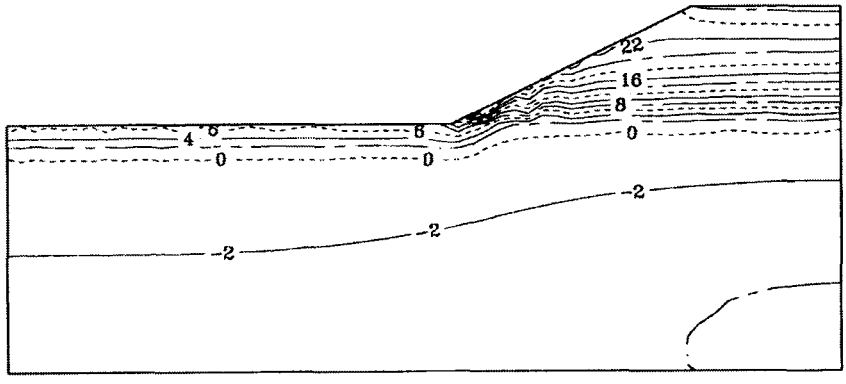

Fig. 4. Isotherms for Case 1 on July 31.

Figs. 5 and 6 show maximum annual temperature extremes for cases 1 and 3 (the high and low permeability cases). The position of the 0°C isotherm shows the maximum extent of the thaw and, thus, indicates the upper surface of the permafrost layer. For case 1 there is a clear upward displacement of the permafrost table beneath the embankment, whereas for case 3 the permafrost table has been displaced downward beneath the embankment. For case 3, Fig. 6 indicates a thaw depth which extends approx. 1.5 m deeper into the foundation soil beneath the embankment centerline than the thaw depth beneath the native surface.

Fig. 7 shows a comparison of the mean annual temperatures at the embankment base (calculated based on the simulated temperatures at the interface between the embankment and the foundation soil) for each of the three cases. The figure clearly shows that mean annual temperatures for cases 1 and 2 (high and base permeability) are well below 0°C over most of the embankment base. This is true despite the fact that mean temperatures at the upper surfaces of the embankment are 1.1°C for the driving surface and 2.7°C for the side slope. On the other hand, the data for case 3 (low permeability) shows a much less substantial cooling effect with mean annual temperatures which are slightly above the freezing point. In fact, the simulations showed that a talik formed beneath the embankment for case 3 which did not freeze back during the annual cycle.

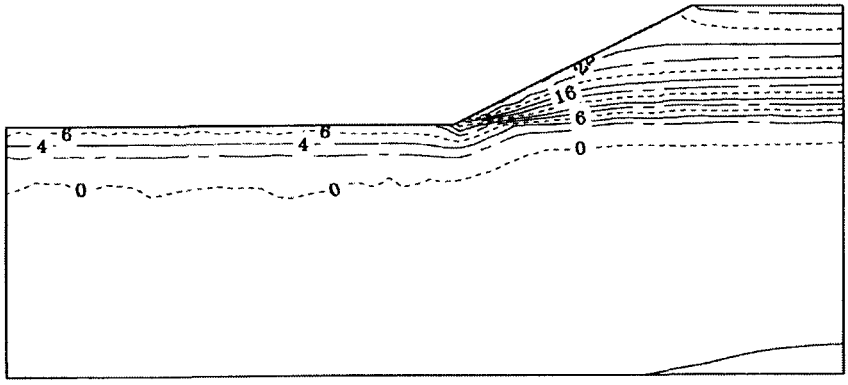

Fig. 5. Maximum annual temperature extremes for Case 1.

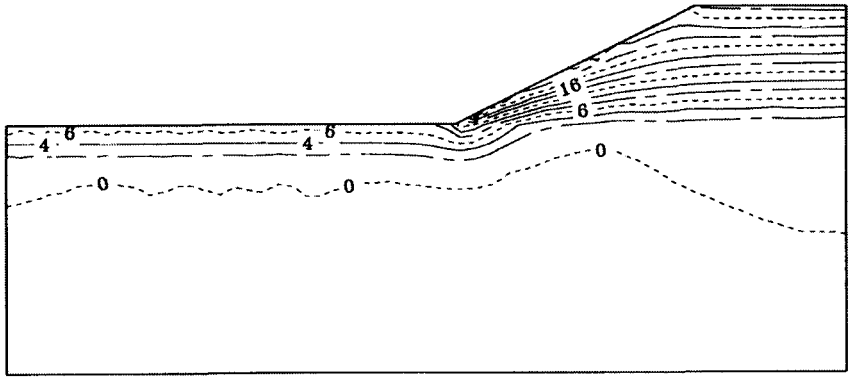

Fig. 6. Maximum annual temperature extremes for Case 3.

4 Conclusions

The results shown above indicate that both the high and base permeability cases (cases 1 and 2) are successful at producing a large cooling effect which decreases the mean annual temperature at the embankment base and agrades the permafrost table upward. On the other hand, the low permeability case produces much less effective cooling and allows some thaw of the previously frozen foundation soils. If these soils are ice rich, damage to the embankment structure is likely for case 3. Comparison of the maximum pore-air velocities on January 31 for the three cases indicates that these velocities scale linearly with the embankment permeability. This scaling feature may allow limited extrapolation of the present results to higher or lower permeabilities.

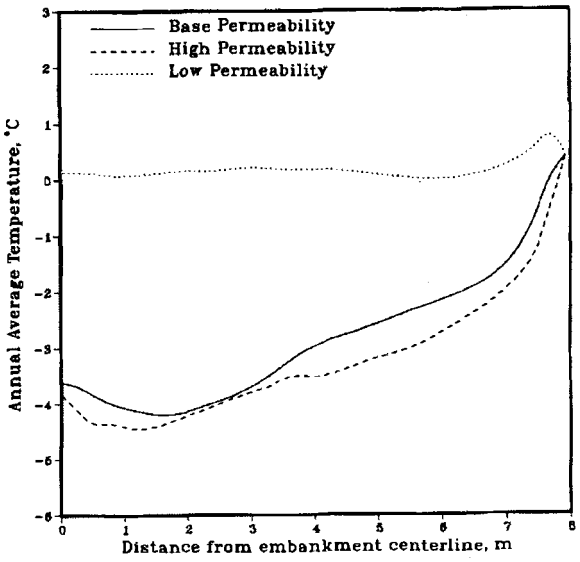

Fig. 7. Mean annual temperature at the location of the embankment/foundation soil interface.

References

1. Goering D.J., Kumar P. (1996) Winter-time convection in open-graded embankments. *Cold Reg. Sci. and Tech.* **24**, 57–74
2. Goering D.J. (1996) Air convection embankments for roadway construction in permafrost zones. *Proc. VIII Int. Conf. on Cold Reg. Engr.* 1–12
3. Goering D.J. (1998) Experimental investigation of air convection embankments for permafrost-resistant roadway design. *Proc. VII Int. Conf. Permafrost*, 319–326
4. Esch D.C. (1987) Insulation performance beneath roads and airfields in Alaska. *Transportation Research Record*, 1146
5. Lunardini V.J. (1981) *Heat Transfer in Cold Climates.* Van Nostrand Reinhold, New York
6. Neild D.A., Bejan A. (1992) *Convection in Porous Media.* Springer-Verlag, New York
7. Reckard M. (1985) White paint for highway thaw settlement control. *Federal Highway Administration Report* No. FHWA-AK-RD-85-16
8. Zarling J.P., Braley, W.A. (1986) Thaw stabilization of roadway embankments constructed over permafrost. *Federal Highway Administration Report* No. FHWA-AK-RD-87-20
9. Zarling J.P., Conner B., Goering D.J. (1983) Air duct systems for roadway stabilization over permafrost areas. *Proc. IV Int. Conf. Permafrost*, 1463–1468

(Received 12 Feb. 1999, accepted 17 Feb. 1999)

Barothermic Effect and Temperature Regime of Frozen Soil

Jacob B. Gorelik, Vladimir S. Kolunin, and Aleksy K. Reshetnikov

Earth's Cryosphere Institute SB RAS, 625000, Tyumen, P.b.1230, Russia

Abstract. A new phenomenon arising in frozen soil cooling under loading was identified by experiment. The frozen soil samples were placed into dry blotting-paper bush, thermostabilized at temperatures below 0 °C and subjected to an overburden pressure. The pressure was lower than is needed for melting volumetric ice at a given temperature. In the experiments the loading causes a decrease of the soil temperature by several tenth of a degree. This observation was called *barothermic effect.*

Equations of heat and mass transfer are proposed for the prediction of the temperature of frozen soil under loading. They are able to explain the observed phenomenon.

The barothermic effect is displayed by the anomalous temperature distribution in a frozen massif near the town Salechard, Tyumen region. The site is a relict frozen layer of 100–200 m thickness, situated 50 m beneath the unfrozen ground. The temperature distribution has a convex form, and its minimum is positioned approximately in the middle of the layer. Calculations show that the time of anomalous temperature distribution may be kept for hundreds of years.

1 Introduction

We have observed in experiments of frozen soil that loading the soil specimen lowered the temperature by a fraction of a degree. This phenomenon — called *barothermic effect* by us — is able to explain the temperature distribution in a frozen layer of ground in the Tyumen region. We demonstrate here that the phenomenon is connected with the lowering of the pressure melting point with the increase of the effective pressure. Indeed, variation of the pressure in the water phase shifts the equilibrium state of frozen soils in accordance with the generalised Clapeyron-Clausius equation. It may require a long lasting process of phase transition to make the phenomenon visible, and it is accompanied by a temperature change of the frozen soil.

Perfect and Williams [12] studied the thermally induced water migration in saturated frozen soil; they noted that the cylindrical sample with thickness of about 4 cm was relaxed to a stationary temperature state within 12 hours after contact with a lactose solution. The soil temperature was somewhat above that of the stationary state during this time. Such a long relaxation time is not only connected with the heat capacity of the sample, but is also due to an additional freezing process. The freezing was due to the decrease of the pressure in the unfrozen water of the frozen soil on account of the

osmotic effect. This viewpoint is confirmed by the outflow of the water from both ends of the sample during the relaxation period.

If we impose an increase of the pore water pressure at the contact of the sample with the external water resource we observe the opposite phenomenon: partial melting of the pore ice, water flow into the sample and a decrease of its temperature during the relaxation period.

Radd and Oertle [13] observed the melting of an ice lens in soil under an overburden pressure; they fixed the decrease of the temperature at both ends of the sample in this process. Since one side of the soil column had a positive temperature it is impossible to identify the melting zone inside the sample; one must define the correlation of the cooling effect with the acting load. Konrad and Morgenstern [9] experimentally determined that the temperature at the base of the growing ice lens decreased with an increase of the overburden pressure. However, the dynamics of the temperature change and of the ice lens-thawing process were not investigated in this work.

Frozen-soil cooling under an applied overburden pressure can likely be deduced from an analysis of the experimental results performed by Biermans et al. [2]. The melting regime of the ice body (placed on a filter surface) was investigated under a thermostat temperature below 0 °C. This process, induced by a decrease of the pressure in the liquid phase causes a heat flux toward the phase-transition surface. Therefore, the temperature at the contact of the ice body and the filter is lower than the temperature of the external medium. A similar effect may be achieved by applying an overburden pressure to the ice column instead of a water pressure decrease. Calculations show [5] that the temperature change is about 0.28 °C/MPa in this experiment, that is four times more than the melting point shifts for volumetric phases of water. Let us consider a multi-layer sandwich, each forming its own ice body as a porous continuum, being subjected to a steady temperature profile. This sandwich is a simplistic model of a frozen soil. If an additional overburden pressure (above the corresponding equlibrium value) is applied at its top and bottom ends, then melting will occur in all layers and consequently the temperatures (including those at boundaries) will decrease. Thus, the sandwiched layers will cool in accordance with the latent heat used for melting. This situation was analysed by Gorelik et al. [6] but the theoretical conclusions must be verified by the experiments.

2 Experiments

For the experimental study two soil specimens were selected. Their characteristics are given in Table 1. S is the specific area of the soil, defined by the adsorption method, k_u is the permeability coefficient of the unfrozen soil and t_0 is the melting point of the frozen soil. Values for k_u and t_0 were determined by standard methods under a compressive load of 20 kPa.

Table 1.

	weight percent to fraction size in [mm]					S,	k_u,	t_0,
	0.4–0.1	0.1–0.05	0.05–0.01	0.01–0.001	< 0.001	$[m^2g^{-1}]$	$[ms^{-1}]$	[°C]
Sandy loam	11.0	17.5	49.5	17.5	4.5	10.85	$0.5 \cdot 10^{-9}$	−0.08
Clay	0.5	3.5	18.5	25.5	52.0	77.22	$2 \cdot 10^{-11}$	−0.25

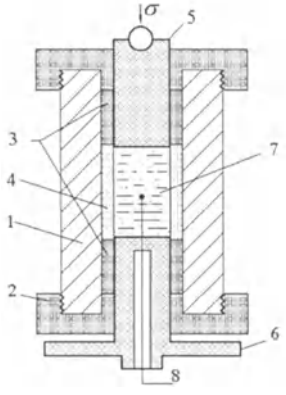

Fig. 1. Sketch of the experimental cell. 1 — body, 2 — cover, 3 — directional bushes, 4 — working bush, 5 — upper piston, 6 — lower piston, 7 — soil sample, 8 — thermocouple

Details of the experimental cell are shown in Fig. 1: A cylindrical body (1) with plexiglass walls, height 80 mm, outer and inner external diameters of 70 mm and 18 mm, respectively; directional, 4 mm thick teflon bushes (3) with inside diameter 10 mm and height 25 mm and restricting lids (2) made out of copper. This arrangement is holding the soil probe (7) in the cylindrical center which is covered from above and below by two textolite pistons (5, 6) of 10 mm diameter and sidewise by dry blotting paper (4) of 4 mm thickness, inside diameter 10 mm and height 30 mm. The thermocouple (8) was located in the center of the sample.

The saturated unfrozen soil was placed into a special capsule, consolidated under 20 kPa, frozen at −20 °C and put into the bush in a cold room. The frozen soil sample had cylindrical form with 10 mm diameter and 30 mm height. After assembling, the cell was thermostabilized at given temperature t_e below 0 °C withing 12 hours and then subjected to an overburden pressure. At the given temperature the value of the pressure was lower than is needed for melting of volumetric ice.

Examples of the temperature change in the frozen soil are presented on the recorder diagrams (Fig. 2). It is clear that the cooling begins at the moment when the pressure is applied and stops after a short relaxation upon

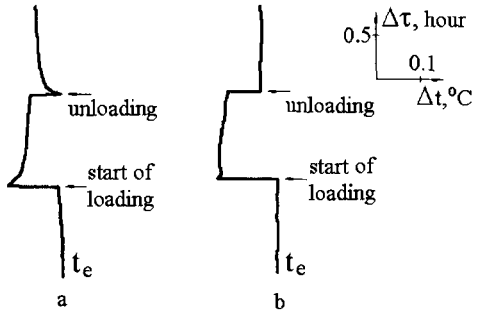

Fig. 2. Temperature change of frozen soils under overburden pressure ($\sigma = 3$ MPa). (**a**) Sandy loam, $t_e = -0.5\,^{\circ}$C. (**b**) Clay, $t_e = -0.75\,^{\circ}$C

cessation of the load application. The plateau on the diagrams characterises the phase transition in the frozen soil and is in accordance with the sample deformation, that is controlled by a special sensor (not shown in Fig. 1). At the plateau stage the thawing water is absorbed by the blotting-paper bush where it did not freeze due to the very thin pores of the bush.

The barothermic cooling is several tenth of a degree and depends on the initial temperature, the applied pressure and the water content in the soil. The hydroconductivity of the frozen soil essentially influences this effect. At small water content this effect changes the sign. Detailed results of this investigation will be published in another paper.

It may seem that conditions of the experiment described above are highly special for the display of the barothermic effect; however this is not so. In cold regions the saturated ground is subject to a vertical temperature field. The upper part of the ground is as a rule frozen. Its lower part is unfrozen and is connected with a water source. Every frozen layer is under the weight of the overlying bed. If the pressure of this bed is more than the pressure-melting equilibrium value (with respect to a given temperature), then the ice lenses will thaw and liquid will flow through the soil to the reservoir (as in the model by Radd and Oertle [13]).

3 Basic Equations

The basic equations of the heat and mass transfer must be written for the frozen soil containing the macroscopic inclusions of the ice. Therefore, the cryogenic texture parameters must be defined for a general case.

First, let us consider a model soil with a periodic distribution of macroscopic ice lenses into a porous medium containing only pore ice (Fig. 3). All ice lenses are identical and have a cylindrical form with radius R and height l. The distances between the lenses in the vertical and horizontal directions are d and D, respectively. This model soil is in contact with the water reservoir at the bottom (Fig. 3b). Vertical loading of the system causes melting of the ice lenses and movement of the water from their boundaries in the horizontal

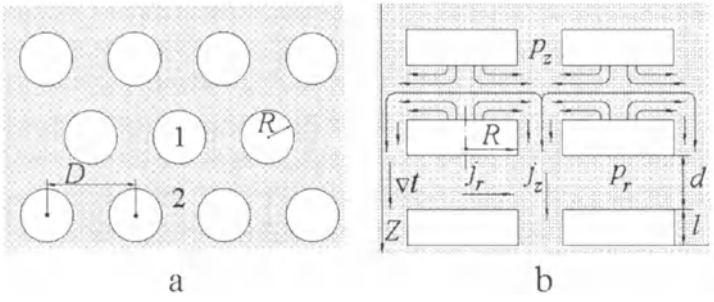

Fig. 3. Scheme of model frozen soil. (**a**) Upper view, 1 — ice, 2 — frozen soil without ice lenses. (**b**) Side view

directions to the vertical channels (the flow of j_r). This water will outflow from the system to the reservoir along the vertical channels (the flow of j_z).

For this model soil the set of equations has the following form:

$$\frac{\partial}{\partial\tau}\left(\theta_s\rho_s t\right) = \frac{\partial}{\partial z}\left(\lambda_f\frac{\partial t}{\partial z}\right) + \kappa\rho_i\frac{\partial i}{\partial\tau} - \kappa\rho_w\frac{\partial W}{\partial\tau}, \tag{1}$$

$$\rho_w\frac{\partial j_z}{\partial z} = -\rho_i\frac{\partial i}{\partial\tau} - \Delta\rho_{wi}\frac{\partial W}{\partial\tau}, \tag{2}$$

$$j_z = -\mu_s C_f\frac{\partial}{\partial z}\left(p_z - \rho_w g z\right), \quad \frac{\partial j_z}{\partial z} = \nu_s j_r, \tag{3}$$

$$j_r = \omega_s C_f(p_r - p_z), \quad \frac{p_i}{\rho_i} - \frac{p_r}{\rho_w} = -\frac{\kappa t}{T_0}. \tag{4}$$

Here θ_s, ρ_s, λ_f are the heat capacity, density and thermal conductivity of the soil averaged by volume, ρ_w, ρ_i are the water and ice densities and $\Delta\rho_{wi} = \rho_w - \rho_i$; κ is the latent heat of water-ice phase transition; g is acceleration due to gravity and $T_0 = 273.15\,\mathrm{K}$; i and W are the volumetric contents of the ice lenses and unfrozen water, respectively, t is the temperature in °C; p_z is the liquid pressure in the vertical channel averaged over the cross section; p_i the ice pressure; p_r the liquid pressure at the horizontal boundary of the ice lenses, averaged over the area (all pressures were taken relative to standard atmospheric pressure); C_f is the hydroconductivity of the frozen soil; furthermore, $\mu_s = (\sqrt{3}D^2 - 2\pi R^2)/(\sqrt{3}D^2)$; $\nu_s = 4\pi R/(\sqrt{3}D^2)$; $\omega_s = 4d/(R(d+l))$. Finally, τ and z are the time and space coordinates.

The hydroconductivity C_f is defined as [6]

$$C_f = C_s\left(-t - \frac{\Delta\rho_{wi}T_0}{\kappa\rho_w\rho_i}p_z\right)^{-3/2}, \tag{5}$$

where C_s is a constant. The last relation is theoretical, but it describes the experimental data by Horiguchi and Miller [8] with the same precision as does the empirical function of O'Neill and Miller [10]. Eq. (5) gives a value less than that measured, but the empirical function exceeds it approximately by the same amount. This difference is not principal for the calculation on the model soil. The unfrozen water content W is a function of the same argument as C_f in (5), i.e. it depends both on t and p_z [10,6].

The set (1)–(5), written for the model soil, may be extended to more general cases if the values of μ_s, ν_s, ω_s are interpreted as local characteristics of an arbitrary distribution of the lenses in a cryogenic texture.

The meaning of the separate equations is as follows: (1) describes heat transfer process with heat sources of which the intensity depends on the pressures in the water phases; (2) is mass balance; $(3)_1$ is Darcy's law for vertical flow, taking into account the liquid weight and channel narrowing; $(3)_2$ describes the continuity of the mass flows in the horizontal and vertical channels; $(4)_1$ is the definition of the water flow from the ice lens to the vertical channel; it was obtained from the solution of the task about filtration inside the horizontal gap between adjacent ice lenses; $(4)_2$ is the condition of thermodynamic equilibrium at the horizontal boundary of ice lens (generalized Clapeyron-Clausius equation).

Equations (1)–(4) describe the disturbance of the heat equilibrium in the soil due to the pressure change in the water phases at the system boundaries. (1) contains two kinds of bulk heat sources connected with the phase transformations of the ice lenses ($\partial i/\partial \tau$) and pore ice ($\partial W/\partial \tau$). If the ice lenses are absent ($\partial i/\partial \tau = 0$), then the water pressure alteration at the sample boundaries makes the unfrozen water content move to the equilibrium state and the temperature field inside the soil to become nonstationary (as in the test by Perfect and Williams [12]). In the opposite case ($\partial W/\partial \tau = 0$) the pressure change makes the ice lenses thaw or freeze. A quasi-steady temperature profile is eventually emerging in the sample as in the experiment by Biermans et al. [2]. The second case is more important for the solution of the problem presented in this paper.

The soil layer that contains the heat sources of the second kind is called active. A layer that includes only the first kind sources will be considered passive. Active layers are transformed to passive ones if all ice lenses have been melted.

The intensity of the melting of the ice lenses is largest near the boundaries of the active layer and decreases to its center because the hydraulic resistance of frozen soil rises toward the center. As a result during this process the passive layer grows near the boundaries of the active zone. Moreover, for a positive temperature of the environment the unfrozen layer grows near the soil boundary. Layers are disposed from the outer surface of the sample to its center in the following order: unfrozen, passive, active. At the contact of active and passive layers the heat and mass flows are continuous. Heat and

mass balance equations include the jump of the ice content at the contact of the unfrozen and passive zones:

$$\lambda_f \frac{\partial t}{\partial z}\bigg|_{z=z^*-0} - \lambda_u \frac{\partial t}{\partial z}\bigg|_{z=z^*+0} = \kappa \rho_i i_0 \frac{dz^*}{d\tau}, \tag{6}$$

$$C_f \frac{\partial (p_z - \rho_w g z)}{\partial z}\bigg|_{z=z^*-0} - C_u \frac{\partial (p_z - \rho_w g z)}{\partial z}\bigg|_{z=z^*+0} = -\frac{\Delta \rho_{wi}}{\rho_w} i_0 \frac{dz^*}{d\tau}. \tag{7}$$

Here i_0 is the volumetric pore-ice content at this boundary; λ_u, C_u are the coefficients of thermal conductivity and hydroconductivity of the unfrozen soil; z^* is the location of the phase boundary at which there is a connection of the temperature t^* and the pressure p_z^*

$$t^* = t_0 - \frac{\Delta \rho_{wi} T_0}{\kappa \rho_w \rho_i} p_z^*. \tag{8}$$

The standard equations of heat transfer and filtration without sources are valid for the unfrozen layer. The initial conditions are defined by distributions of $t(z)$, $p_z(z)$, and $i(z)$ at time $\tau = 0$. Boundary conditions prescribe for example the temperature and pressure p_z.

The set (1)–(8) must be complemented by a deformation law of the frozen part of the model soil and by conditions of the stress redistribution between the frozen soil of the vertical channel and the ice lens and its joint deformations (Fig. 3), but these problems are not considered here.

It should be noted that if the value of the overburden pressure is less than its equilibrium value for a given temperature, the presented equations will describe the following process: growth of ice lenses, water flow into the frozen soil and increase of its temperature. It gives the possibility to describe the growth of the ice lenses in the frozen zone, but not their growth in the frozen fringe only. This phenomenon was referred to in some works [3,11] but is not taken into account by modern mathematical models of texture formation [10].

4 Anomalous Temperature Distribution in Relict Frozen Layer

Duhin [4], Baulin [1] adduced the results of temperature measurements in special thermometric holes drilled through permafrost near the town Salechard, in the Tyumen region (see also: [7]). The important circumstances are as follows: the drilling was conducted without liquid washing and by a full sampling of the soil — it secured a visual control of the state of the rock. The holes were left untouched for some years before measurements were taken. A specially prepared equipment ensured measurement of the temperature with

a precision of 0.01 °C. The three-layer structure of the permafrost was opened by holes. Two frozen layers are separated by saturated unfrozen stratum with 50 m height. The geological structure of the lower frozen layer is inhomogeneous and includes interlayers with various dispersion of the soil. The water of the soil has rather low mineralization that does not alter the freezing point.

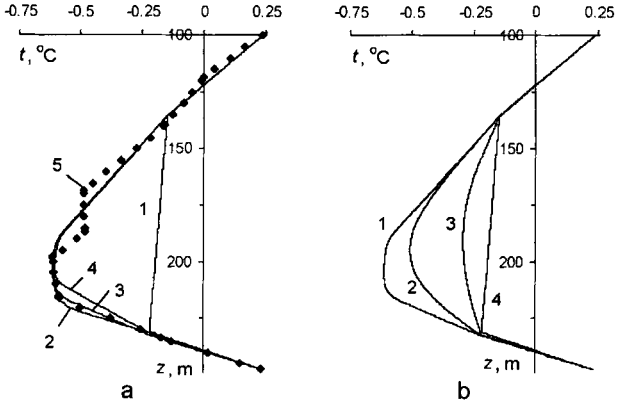

Fig. 4. Anomalous temperature profiles in frozen layer: (**a**) temperature distribution in hole #11. 1 — initial temperature (equilibrium state of frozen layer), 2 — after 100 years, 3 — after 500 years, 4 — after 1000 years, 5 — natural data; (**b**) temperature evolution in the massif without heat sources (hole #11). 1 — initial (real) temperature distribution, 2 — after 10 years, 3 — 50 years, 4 — equilibrium state of frozen layer

The data of the temperature measurements of one hole in the lower (relict) frozen layer that was in contact with the unfrozen strata are shown in Fig. 4a by dot symbols. The upper frozen layer is not shown. It is practically impossible to explain this temperature distribution by usual methods. For example, the relict frozen layer relaxes to the equilibrium state very rapidly if one considers it as a non-stationary process in the frame of usual heat transfer task. The temperature in this layer becomes equal to the temperature of the water-ice transformation (equilibrium state) (Fig. 4b). Neither climate change nor inhomogenity characteristics of the external surface of the massif can explain this distribution because the thick unfrozen stratum exists above the relict layer [14].

The set of equations (1)–(8) was used for the explanation that this temperature distribution can in principle be preserved so long. To simplify the calculation the frozen layer was considered homogeneous. In the absence of the detailed information about the parameters of the soil, they are taken as $\lambda_u = 1.5\,\mathrm{W\,m^{-1}K^{-1}}$; $\lambda_f = 2\,\mathrm{W\,m^{-1}K^{-1}}$; $\theta_s\rho_s = 2514\,\mathrm{kJ\,m^{-3}K^{-1}}$; $i_0 = 0.3$; $\mu_s = 0.3$; $\nu_s = 0.01\,\mathrm{m^{-1}}$; $\omega_s = 1\,\mathrm{m^{-1}}$; $C_u = 10^{-9}\,\mathrm{m^3s\,kg^{-1}}$; $C_s =$

$10^{-15}\,\mathrm{K}^{3/2}\mathrm{m}^3\mathrm{s}\,\mathrm{kg}^{-1}$. The value of p_i in $(4)_2$ may be defined as

$$p_i = \rho_s g z - \sigma_s, \tag{9}$$

where σ_s characterizes the hard connections between the soil particles in the vertical channel (Fig. 3). These connections take some part of the overburden pressure and protect the ice lenses from the total weight of the overlying ground. With the assumption that the value of σ_s is proportional to the thickness of the overlying bed equation (9) may be presented as

$$p_i = \rho_s' g z, \tag{10}$$

where ρ_s' is some fictitious density of the soil in the interval $\rho_i < \rho_s' < \rho_s$. The parameter ρ_s' is $1540\,\mathrm{kg\,m}^{-3}$, and it was selected so as to adapt the calculated results most efficiently to the actual temperature distribution. The real values of the temperature and the hydrostatic pressure of water into unfrozen strata on either end of the relict layer were accepted as boundary conditions. The equilibrium temperature distribution inside the relict layer was taken as initial condition. This distribution has a slope in accordance with the water hydrostatic pressure (Fig. 4a). The calculation makes clear that the temperature distribution quickly approaches the quasi-steady state that may be kept for many hundreds years (Fig. 4a). A few decades are needed to reach this regime. Ice melting occurs inside the frozen massif and the ice content changes in the course of time (Fig. 5a). The direction of the water

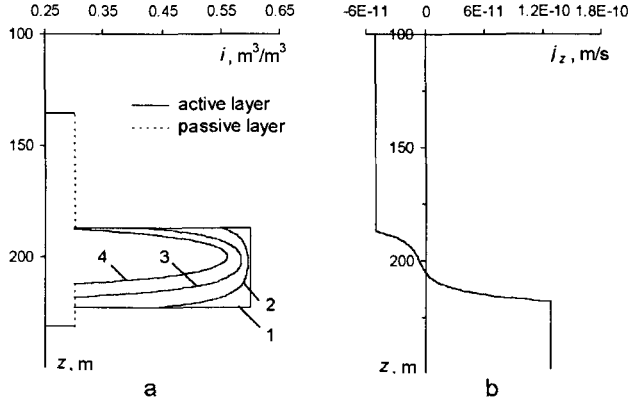

Fig. 5. Bulk characteristics of the melting massif: (**a**) Ice content distribution. 1 — initial, 2 — after 100 years, 3 — after 500 years, 4 — after 1000 years. (**b**) Water flow in frozen soil after 500 years

flow depends on the position in space: at the upper part of the relict layer the water moves to the overlying unfrozen stratum and, at the lower part, to

the opposite direction (Fig. 5b). Knowledge of the flows on the boundaries permits calculation of the deformation of the massif although the equations of the presented model do not take it into account.

Acknowledgements: We thank Professor K. Hutter, Ph. D., Technische Universitat Darmstadt, for help in the preparation of this paper. This work was supported by Russian Fund of Fundamental Research (grant of 97-05-65044).

References

1. Baulin V.V., Belopuhova E.B., Dubikov G.I., Shmelev L.M. (1967) Geocryological Conditions of West-Siberian Plain, *Nauka*, Moscow
2. Biermans M.B.G.M., Dijkema K.M., de Vries D.A. (1978) Water Movement in Porous Media towards an Ice Front. *J. Hydrology*, **37**: 137–148
3. Chistotinov L.V. (1973) Water Migration in Freezing Unsaturated Soils, *Nauka*, Moscow
4. Duhin E.I. (1963) Some Factors Acting on Permafrost Thickness. Lectures notes on Frozen Zones of Earth's Crust. Pt. IX. Thermophysical Problems of Building on Frozen Ground, *Academy of Sciences of the USSR*, Moscow
5. Gorelik Y., Kolunin V. (1993). Mechanism of Layer Structures Growing during Ground Freezing. In: *Permafrost, 6th International Conference at Beijing*, China, July 5–9, V.1. South China University of Technology Press, 879–884
6. Gorelik J.B., Kolunin V.S., Reshetnikov A.K. (1997) Simplest Physical Models of Cryogenic Phenomena. *Cryosphere of Earth*, **1**, **3**: 19–29
7. Porhaev G.V.(Ed.) (1964) Thermal Physics of Freezing and Thawing Soils, *Nauka*, Moscow
8. Horiguchi K., Miller R.D. (1983) Hydraulic Conductivity Functions of Frozen Materials. In: *Permafrost, 4th International Conference at Fairbanks*, Alaska, July 17–22. *National Academy Press*, Washington, D.C., 504–508
9. Konrad J.-M., Morgenstern N.R. (1982) Effects of Applied Pressure on Freezing Soils. *Can. Geotech. J.* **19**. 4: 494–505
10. O'Neill K., Miller R.D. (1985) Exploration of a Rigid Ice Model of Frost Heave. *Water Resour. Res.* **21**. 3: 281–296
11. Ohrai T., Yamamoto H. (1985) Growth and Migration of Ice Lenses in Partially Frozen Soil. In: Kinosita S., Fukuda M. (Eds.) *Ground Freezing, 4th International Symposium at Sapporo*, Japan, August 5–7, 1985, V.1. *Balkema*, Rotterdam, Boston, 79–84
12. Perfect E., Williams P.J. (1980) Thermally Induced Water Migration in Frozen Soil. *Cold Regions Sci. Technology* **3**: 101–109
13. Radd F.J., Oertle D.H. (1973) Experimental Pressure Studies of Frost Heave Mechanisms and the Growth-Fusion Behavior of Ice. In: *Permafrost, 2nd International Conference at Yakutsk*, USSR, July 13–28. *National Academy of Sciences*, Washington, D.C., 377–384
14. Redozubov D.V. (1966) Geothermical Method of Permafrost Exploration, *Nauka*, Moscow

(Received 16 Feb. 1999, accepted 15 April 1999)

Detecting Alpine Permafrost Using Electro-Magnetic Methods

Christian Hauck and Daniel Vonder Mühll

Laboratory of Hydraulics, Hydrology and Glaciology (VAW), Federal Institute of Technology (ETH), CH-8092 Zürich, Switzerland

Abstract. In the European Alps, thawing permafrost caused by warmer temperatures has been recognised as a possible danger for slope instabilities in the past few years. The permanently frozen layer (permafrost) is often only a few metres thick. Consequently it is very vulnerable to small changes in local climate. Furthermore, the detection and localisation of such shallow permafrost sites is difficult. The heterogeneity of the material and the difficult access of the steep slopes make commonly used techniques such as reflection seismics or Ground Penetrating Radar (GPR) less adequate for alpine permafrost studies.

We present preliminary results from geophysical studies within the EU-project PACE (Permafrost and Climate in Europe) which focus on a non-contact electromagnetic method to detect the distribution of mountain permafrost. The method is quick and easy to apply even in difficult terrain and on snow-covered ground. The results show that shallow permafrost lenses can be detected with only a small amount of prior information.

1 Introduction

Mapping and characterising areas of permanently frozen ground (permafrost) has been an important task in construction work in the arctic and in high altitude mountain ranges for many years. In the European Alps, there has recently been an increased interest in mapping and monitoring permafrost because of possible risks to civilization arising from increased frequency of slope instability due to global warming. Therefore, efforts are being made to find suitable methods to delineate permafrost in mountain areas as a basis for the assessment of the potential of natural hazards due to thawing of permafrost bodies. As direct measurements in boreholes are costly, time-consuming and only valuable for the drill site, geophysical methods represent a powerful tool to map and characterise permafrost areas. These methods consist of measurements at the surface, hence, the data have to be interpreted using for example inversion models in order to yield information about the subsurface. Many different geophysical methods have been used for permafrost mapping in the past (for a review see [18]). Refraction seismics, direct current (DC) electrical resistivity, electromagnetic induction and Ground Penetrating Radar (GPR) have been succesfully applied especially in the Arctic (e.g. [1],[3],[4],[6],[9],[15]).

For many of these methods the assumption of locally homogeneous layering of the subsurface has to be made in order to interpret the data correctly. This assumption is usually valid for the vast and flat terrain of the arctic tundra. However, in low latitude mountain regions, such as the European Alps, permafrost occurrence depends strongly on incoming radiation. Hence, the permafrost distribution and characteristics may considerably change within small distances. Furthermore, many of the mountaineous regions are not accessible by vehicle, so equipment must be light, portable and robust. So far, geophysical surveys (mostly refraction seismics and vertical electrical soundings) have concentrated on obvious and visible permafrost features like rock glaciers (e.g. [8], [20], [21]).

On heterogeneous ground conditions with patchy permafrost distribution, e.g. glacier forefields or north facing valley slopes, it is still difficult to delineate permafrost lenses without additional information, such as borehole data. Possibilities are the application of refraction seismics and DC resistivity profiling with a Wenner electrode configuration (e.g. [12]). Another approach uses two-dimensional resistivity tomography, which combines the resistivity sounding and profiling method to yield a two-dimensional model section of the subsurface. Through a two-dimensional inversion of the data the ambiguity, usually inherent in resistivity surveys, is greatly reduced. Thus, the assumption of homogeneity of the subsurface layers is no longer necessary. This method was succesfully applied to map permafrost on laterally varying ground conditions ([2]). None of the methods is feasible for mapping large areas, because survey speed is limited since contact between the electrodes and the ground must be ascertained. This is especially difficult on debris covered ground with many voids, as it occurs in most high altitude alpine regions. Additionally, the snow cover often prohibits ground contact from autumn until late spring.

Electromagnetic induction methods solve this problem, because they use magnetic fields as a source to generate eddy currents in the subsurface and, hence, do not require ground contact. These methods have succesfully been applied in permafrost studies in the arctic (using the GEONICS EM31, EM34-3) (e.g. [3],[16]). Few attempts have been made to apply these methods on mountain permafrost ([17]). The aim of the study presented here is to test the feasibility of using a EM31 conductivity meter for mapping larger areas of shallow and variable permafrost in mountain regions. We will present results from the Swiss Alps, which were obtained within the EU-project PACE (Permafrost and Climate in Europe). The results are compared with data from two-dimensional resistivity tomography and refraction seismics.

2 Method

The Geonics EM31 is a light (12.4kg), one-man-portable conductivity meter with a penetration depth of about 6 metres. It consists of a 3.7 metres pole

with a transmitter coil at one end and a co-planar receiver coil at the other end. A current through the transmitter coil induces a magnetic field which is varied by an alternating current (9.8 kHz) and penetrates the subsurface. A changing magnetic field induces eddy currents in the subsurface which generate a secondary magnetic field, that can be detected by the receiver coil. Based on the difference between primary and secondary magnetic fields, the bulk conductivity (=1/resistivity) of the ground is calculated. For high resistive media (like frozen ground) and low frequencies this value is roughly proportional to the ratio between primary and secondary magnetic fields ([11]). The instrument can be used in two different polarisation modes, that differ in the effective depth of penetration. For vertical polarisation the penetration depth is about 6 metres, for the horizontal polarisation about 3 metres. Except for some sensitivity studies, only the vertical polarisation was used in this study. A complete description of the theory and the instrument is found in [11].

One major difference between mountain and arctic permafrost is the much higher resistivity values of the former. Resistivity values in the permafrost regions of the European Alps range typically between a few tens of kΩm (low ice content) and 1 MΩm (massive ice) ([20], [21]). In the arctic typical values are much smaller, between 1 and a few kΩm (e.g. [13],[19]). This is due to the much more conductive overburden and host sediments in arctic tundra regions. For conductivity measurements in mountain regions this causes problems, because the conductivity values are close to the accuracy limit of the EM31 instrument (0.1 mS/m). This leads to substantial noise in the data, as does the inhomogeneous overburden and the topography. To overcome these problems we use a three step procedure:

- Obtain a reference *ground truth* at one representative permafrost location in the target area. This was done by two-dimensional resistivity tomography and refraction seismics surveys.
- Repeat the survey line with the EM31 and compare the data with the resistivity values from step 1. With this a *permafrost signal* can be determined.
- Map the whole target area with the EM31 and plot the results as deviations from the measured mean value.

In Section 3 this procedure is illustrated by an example from a low altitude valley slope in the Eastern Swiss Alps. The resistivity tomography measurements were done using an ABEM Lund system with 41 electrodes and 5 metres electrode spacing (see [2]). The refraction seismics was performed with an Geometrics EG&S system with 12 channels and 5 metres geophone spacing.

3 Results

The investigation site is located in Val Bever, a small valley in the Upper Engadin in the Eastern Swiss Alps. It is situated on a 35° steep north-facing

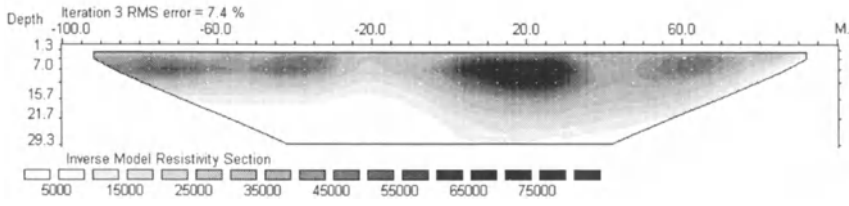

Fig. 1. Model results for resistivity section along a forest aisle on the Western boundary of the survey area in Val Bever, Upper Engadin, Eastern Swiss Alps. Uphill is on the left, downhill on the right. The dark shadings represent high specific resistivity values.

slope well below the tree line (1800 m asl). Results from a model simulating the permafrost distribution based on potential solar radiation and mean annual air temperature ([5]) predict limited permafrost occurrence. Consequently this site has been chosen to be the focus of several investigations using different methods e.g. BTS (bottom temperature of snow cover), ground temperature measurements and various geophysical methods ([7], [10]).

Fig. 1 shows the resistivity tomography model, which results from a 200 metres survey line along a forest aisle on the Western boundary of the survey area. The contoured values represent specific resistivities, which are calculated according to the measured apparent resistivities using the software package RES2DINV. There are values up to 80 KΩm (near station 20) in the top 15 metres of the section. A refraction seismics survey along the same line yielded P-wave velocities between 3000 and 3500 m/s for this layer, which are typical values for ice-rich permafrost ([14],[20]). Thus, the high resistivity areas are interpreted as permafrost lenses above unfrozen material.

For comparison the lower half of this survey line (station 0 – 100) was repeated with the EM31 with vertical polarisation (effective depth of penetration 6 metres). A measurement was taken each metre and a 5-point low-pass filter was applied to the raw data. Fig. 2 shows a comparison between the EM31 results and the apparent conductivity values for the corresponding depths range calculated from the DC resistivity raw data (Fig.1).

The EM31-data (Fig. 2a) are much noisier, even after the low-pass filtering. However, comparing the 10-point running mean with the DC resistivity data (Fig. 2b) both data sets show good agreement. However, note that the absolute numbers differ substantially, due to difficulties in calibrating the EM31 for highly resistive material.

A second example from a profile perpendicular to the first survey line is shown in Fig. 3. Here, the ground is even more heterogeneous and the conductivity values are changing on a scale smaller than the electrode spacing of the DC resistivity survey (5 metres). Consequently, the EM31 data (Fig. 3a) show more small-scale structure than the DC resistivity data (Fig. 3b)

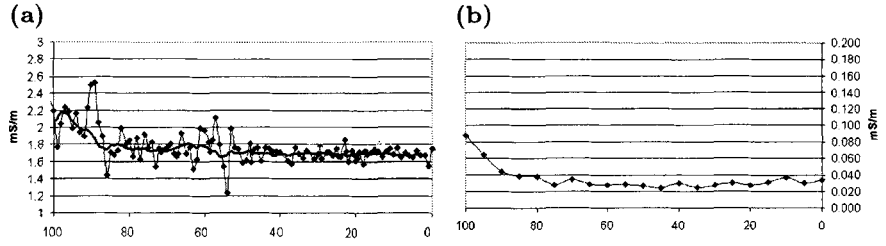

Fig. 2. Comparison of conductivity data **(a)** measured with the EM31 and **(b)** determined from the DC resistivity data from the southern half of the Western forest aisle, Val Bever, Upper Engadin, Eastern Swiss Alps. In **(a)** a 10-point running mean (*thick line* was calculated.

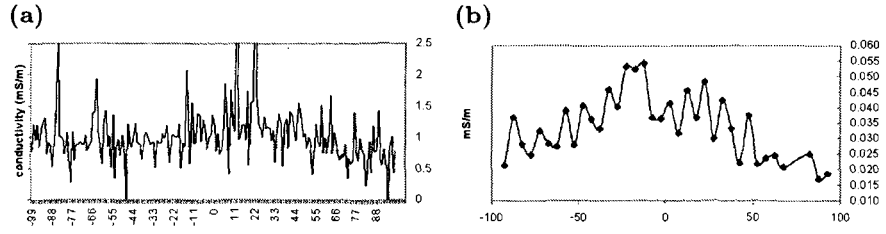

Fig. 3. Comparison of conductivity data **(a)** measured with the EM31 and **(b)** determined from the DC resistivity data from a survey line across the Western forest aisle, Val Bever, Upper Engadin, Eastern Swiss Alps.

and the agreement between the two methods is less obvious than in Fig. 2. Nevertheless, the positive and negative conductivity anomalies are still possible to distinguish and coincide within a few metres in both surveys. Therfore, to map areas of possible permafrost lenses (= negative conductivity anomalies) the EM31 can be applied inspite of the noisy data quality.

Fig. 4 shows a preliminary anomaly plot for the EM31 data of the whole survey area. The area is 300 m x 100 m wide, bounded by two forest aisles to the East and West (left and right hand side of the plot) and by a road to the north. The area slopes to the north with a difference in altitude of 70 to 90 metres. The survey line shown in Fig. 2 is located on the right hand side of Fig. 4. The permafrost areas can be clearly delineated from this contour map. These are located mainly in the upper part of the survey area, with a more patchy distribution further down. Apart from the two zones at both lateral ends of the area there is another region with large anomaly values in the centre of the map, coinciding with a large area of small tree growth.

To verify these results, further resistivity tomography measurements were performed. As an example Fig. 5 shows the results for the Eastern zone at

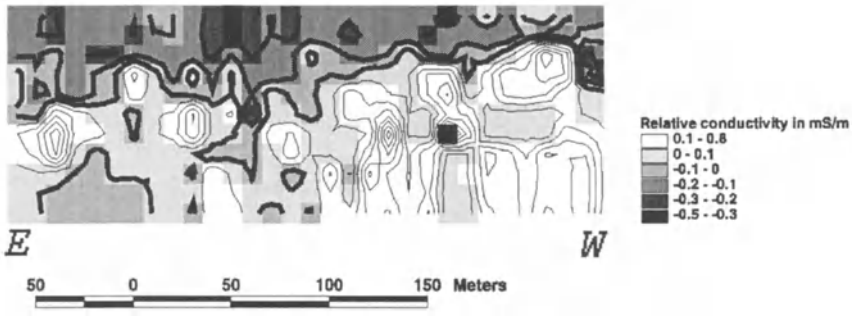

Fig. 4. Contour map of the survey area in Val Bever, Upper Engadin, Eastern Swiss Alps, with north at the bottom of the plot. The area is bounded by two forest aisles to the East and West and by a road to the North. Negative conductivity anomalies (calculated as deviations from the global mean) are shaded in grey and black and the thick black lines depict negative contours, thus bordering the areas of enhanced permafrost occurrence. The thin contours represent positive anomalies.

the left hand side of the anomaly plot (Fig. 4). Note that the top left corner of the anomaly plot coincides with station 20, the bottom left corner with station 100 of Fig. 5. Permafrost is very shallow in this area and is not present in the lower 50 metres of the line. This is in good agreement with the results from the EM31 anomaly plot (Fig. 4).

Influence of the snow cover

Sensitivity tests on snow covered ground showed that the snow cover does not change the results qualitatively. If the snow height is homogeneous the effect is similar to changing the instrument height above the ground. This affects all data points in a systematic way and does not change the anomaly distribution. However, difficulties arise if the snow height is heterogeneous or if the snow has a high liquid water content.

4 Conclusion

Mapping the distribution of ice-rich permafrost with a EM31 conductivity metre has been proven to be a reliable, fast, high resolution method for heterogeneous alpine terrain. As the method gives only qualitative results the data have to be compared using quantitative methods like two-dimensional resistivity tomography. The resulting anomaly plots are suited to localise the distribution of permafrost lenses on a scale of a few square-metres.

In the presented example of a steep, forested slope (1800 m asl) permafrost is present mainly in the upper part of the survey area, in forest aisles, clearings and on isolated patches further down. A homogeneous snow cover

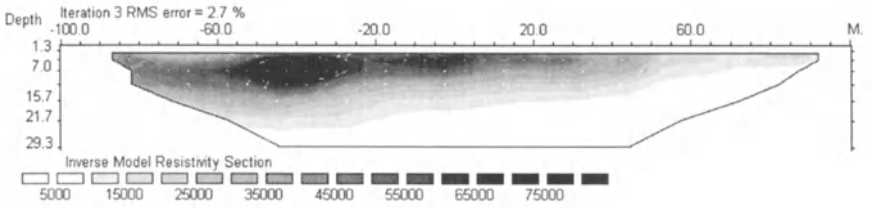

Fig. 5. Model results for resistivity section along the forest aisle on the Eastern boundary of the survey area in Val Bever, Upper Engadin, Eastern Swiss Alps. Uphill is on the left, downhill on the right. The dark shadings represent high specific resistivity values.

does not affect the results. However, difficulties arise, if the snow height varies significantly or if very wet snow is present.

This approach is likely to have wide application in the context of natural hazard assessment and ground investigations at higher altitude in the mountains of Europe.

Acknowledgements: We would like to thank C. Kneisel and F. Keller for local knowledge and help at the fieldwork site, the town of Bever for making this research possible, M. Hoelzle for help with the figures and K. Hutter, as well as two anonymous referees for useful comments. We thank especially the Institute for Applied and Environmental Geophysics, ETH Zürich (A. Green) for providing the EM-31. This study was financed through the PACE project (Contract Nr ENV4-CT97-0492 and BBW Nr 97.0054-1).

References

1. Arcone S. A., Lawson D. E., Delaney A. J., Strasser J. C., Strasser J. D. (1998) Ground-penetrating radar reflection profiling of groundwater and bedrock in an area of discontinuous permafrost. *Geophysics* **63**(5), 1573–1584
2. Hauck C., Vonder Mühll D. S. (1999) Using DC resistivity tomography to detect and characterise mountain permafrost. *Proc. 61th EAGE Annual Conf.*, Helsinki
3. Henderson J. D. (1980) Permafrost mapping along transportation corridors. *Proc. Symp. Permafrost Geophysics* (No. 5), Techn. Memorandum 128, 130–138
4. Hoekstra P., McNeill D. (1973) Electromagnetic probing of permafrost. *Proc. II. Int. Conf. on Permafrost*, Yakutsk, 517–526
5. Hoelzle M., Haeberli W. (1995) Simulating the effects of mean annual air-temperature changes on permafrost distribution and glacier size: an example from the Upper Engadin, Swiss Alps. *Annals of Glaciology* **21**, 399–405
6. Horvath C. L. (1998) An evaluation of ground penetrating radar for investigation of palsa evolution, MacMillan Pass, NWT, Canada. *Proc. VII. Int. Conf. on Permafrost*, Yellowknife, 473–478

7. Keller F., Kneisel C. (1997) Permafrost im Val Bever. *Bericht der Gemeinde Bever*, March 1997
8. King L., Fisch W., Haeberli W., Wächter H. P. (1987) Comparison of resistivity and radio-echo soundings on rock glacier permafrost. *Zeitschr. für Gletscherkunde und Glazialgeologie*, **23**(2), 77–97
9. King M. S., Garg O. P. (1980) Interpretation of seismic and resistivity measurements in permafrost in northern Quebec. *Proc. Symp. Permafrost Geophysics* (No. 5), Techn. Memorandum 128, 50–69
10. Kneisel C., Keller F., in preparation
11. McNeill J. D. (1980) Electromagnetic terrain conductivity measurement at low induction numbers. *Techn. Note TN-6 of Geonics Ltd*, Mississauga, Ontario, Canada
12. Naguel C. (1999) *Master thesis*, Department of Physical Geography, Universität Zürich, Switzerland
13. Osterkamp T. E., Jurick R. W. (1980) Geophysical investigations at the Engineer Creek Road Cut, Fairbanks, Alaska. *Proc. Symp. Permafrost Geophysics* (No. 5), Techn. Memorandum 128, 46–49
14. Röthlisberger H. (1972) Seismic exploration in cold regions. *Cold regions science and engineering*, Hanover. Monograph II-A2a. 139.
15. Rozenberg G., Henderson J. D., Sartorelli A. N. (1985) Some aspects of transient electromagnetic soundings for permafrost delineation. CRREL: *Special report 85-5*, 74–90
16. Sartorelli A. N., French R. B. (1982) Electromagnetic induction methods for mapping permafrost along northern pipeline corridors. *Proc. 4th Can. Permafrost Conf.*, Nat. Res. Counc. Canada, 283–298
17. Schmöller R., Fruhwirth R. K. (1996) Komplexgeophysikalische Untersuchung auf dem Dösener Blockgletscher (Hohe Tauern, Österreich). *In Beiträge zur Permafrostforschung in Österreich*, Arbeiten aus dem Institut für Geographie, Universität Graz, Band 33, 165–190
18. Scott W. J., Sellmann, P. V., Hunter, J. A. (1990) Geophysics in the study of permafrost. *Geotechnical and environmental geophysics* (ed. S. H. Ward), Soc. of Expl. Geoph., Tulsa, Oklahoma
19. Timofeev V. M., Rogozinski A. W., Hunter J. A., Douma M. (1994) A nmew ground resistivity method for engineering and environmental geophysics. *Proc. of Symp. on the application of geophysics to engineering and environmental problems*, 1994, 701–715
20. Vonder Mühll D. S. (1993) *Geophysikalische Untersuchungen im Permafrost des Oberengadins*. PhD-thesis, ETH Zürich, Switzerland
21. Vonder Mühll D. S., Schmid W. (1993) Geophysical and photogrammetrical investigations of rock glacier Muragl I, Engadin, Swiss Alps. *Proc. VI. Int. Conf. on Permafrost*, Beijing

(Received 19 Feb. 1999, accepted 22 March 1999)

Climatic Warming and Permafrost

Virgil J. Lunardini

US-Army Cold Regions Reaearch and Engineering Laboratory,
72 Lyme Road, Hanover NH USA 03755

Abstract. Permafrost is dependent upon the ambient temperature for its existence and is sensitive to climatic changes. Conduction heat transfer relations, with thawing and geothermal heat flow, are presented to predict the transient effects of surface temperature changes on the thermal state of permafrost. These relations can be used to examine past climate changes that could have resulted in the present permafrost thermal state. A number of phenomena may affect the thermal regime of permafrost, however some of these are not directly related to climate change, and may lead to spurious conclusions as to past climate warming. It is critical to understand the physical processes controlling the temperature and active layer of permafrost and to accurately relate them to past climate change. It is also possible to estimate the effect of climate change scenarios, manifested by air and surface temperature changes, on permafrost degradation. Realistic assessments require that the initial thermal regime of the permafrost be accurately known. Relatively small amounts of permafrost will disappear within 50-100 years due to the usual global warming scenarios.

1 Limitations on Use of Permafrost Temperatures to Detect Past Climate Change

There is considerable interest in predicting the surface temperature history at a location from the measured soil temperature profile, allowing these temperatures to be used to infer past global warming. However, there may be considerable error in such estimates if the perturbations in the temperature are due to causes other than Ground Surface Temperature Changes (GSTC) or if the soil parameters are not known in detail. In addition, GSTC associated with long term natural oscillations may be extremely difficult to interpret correctly using present temperature data. We will use some results for homogeneous and non-homogeneous soils to examine the difficulties associated with inferring past surface temperature increases from present soil temperatures.

1.1 Phenomena unrelated to GSTC

The following are some of the physical processes unrelated to GSTC that can cause temperature perturbations.

Many rocks contain minerals that release energy due to radioctive decay. The effect of this heat generation appears to be a cooling of the temperature

– increase in the thermal gradient – but is likely to be small, on the order of 0.01 – 0.02 K.

Uplift or subsidence, natural phenomena associated with mountain building, erosion, and sedimentation, can perturb the soil temperature profile. The effects are likely to be negligible if the surface movement is less than 0.1 mm yr^{-1}.

Terrain variation encompasses phenomena including vegetation distribution and temporal changes, snow cover, surface orientation and topography, and local lapse rate. These can be quantitatively discounted if information is available for a given borehole site.

Ground water flow causes convective heat transfer in addition to the dominant conduction. Downward percolation of water will be perceived as a warming effect, but will be limited if the percolation does not exceed 5 cm yr^{-1}. If the water flow exceeds this limit, it is probably prudent to abandon the site for climate change studies.

The temperature perturbation effect due to layering or stratigraphy of the soil/rock system must be removed before a reliable climate signal can be deduced. In particular, the ground thermal properties are very important.

1.2 Thermal properties and periodic GSTC

If moderate to long-term periodic GSTC are occurring, it may be difficult or impossible to correctly remove the effects of these natural variations from the present measured temperatures. This will make any climate change deductions, using borehole temperatures, less than desireable.

Two-layered soil Consider a semi-infinite soil overlain by a finite layer of different soil, for $X_2 \leq x \leq 0$. Initially, a steady state exists with a steady geothermal heat flow $q_g = k_2 G_2$ and a surface temperature T_{so}. The steady state temperatures are:

$$T_1(x) = T_{so} + k_{21} G_2 (x + X_2), \quad -X_2 \leq x \leq 0, \tag{1}$$

$$T_2(x) = T_{so} + G_2 (x + k_{21} X_2), \quad x \geq 0. \tag{2}$$

Depending upon the ratio of the thermal conductivities, k_{21}, the steady state temperatures in the two layers will be as sketched in Fig. 1. The temperature profiles can appear to reflect warming or cooling simply due to the thermal conductivities of the layers. Consider an instantaneous change of surface temperature to a new constant value T_s. The transient temperatures are given in Carslaw and Jaeger [3] as follows

$$T_1(x,t) = T_1(x,0) + (T_s - T_{so}) \sum_{n=0}^{\infty} \nu^n \left[\operatorname{erfc}\left(\frac{2n+1+\zeta}{\tau_1} \right) - \nu \operatorname{erfc}\left(\frac{2n+1-\zeta}{\tau_1} \right) \right], \tag{3}$$

$$T_2(x,t) = T_2(x,0) + \frac{2(T_s - T_{so})}{(1+\mu)} \sum_{n=0}^{\infty} \nu^n \operatorname{erfc}\left(\frac{2n+1+\eta\zeta}{\tau_1} \right), \tag{4}$$

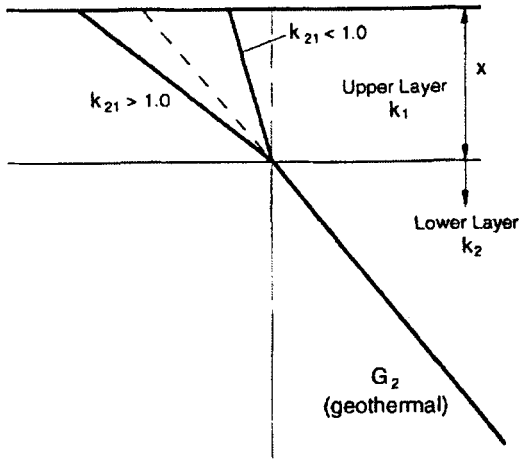

Fig. 1. Steady-state temperature, 2-layer soil

where $$\zeta = \frac{x}{X_2},\ \eta = \sqrt{\alpha_{12}},\ \mu = k_{21}\eta,\ \nu = \frac{\mu - 1}{\mu + 1},\ \tau_1 = \frac{2\sqrt{\alpha_1 t}}{X_2}.$$

If $X_2 \to 0$, we have the case of a homogeneous soil with a linear initial temperature and a step change of surface temperature

$$T(x,t) = T_s + G_2 x + (T_{so} - T_s)\mathrm{erf}\frac{x}{2\sqrt{\alpha_1 t}}. \tag{5}$$

Surface temperature history The simple results of the previous section can be used to quantitatively examine the effect of soil surface temperature changes (an assumed global warming) on the transient behavior of the soil mass. Since the present temperature of permafrost can be accurately measured, it may be possible to infer the surface temperature changes that could lead to the present temperature profiles, the well-known inverse conduction problem.

Many surface temperature variations are possible, but the simplest case is a homogeneous soil that underwent a step change in the surface temperature some time ago. The result is an example of a synthetic or "measured" temperature profile shown in Fig. 2. If we extrapolate the linear part of the measured temperature to the surface, we find the old surface temperature. Since the present surface temperature is T_s, we assume a temperature change of $T_s - T_{so}$ has occurred. The time required can be predicted by matching the calculated results from (5) to the measured values, using an inverse scheme. The best match would give an estimate of the magnitude and duration of the surface temperature change. This method is quite convincing for a homogeneous soil, but the results are far from clear if the soil is non-homogeneous.

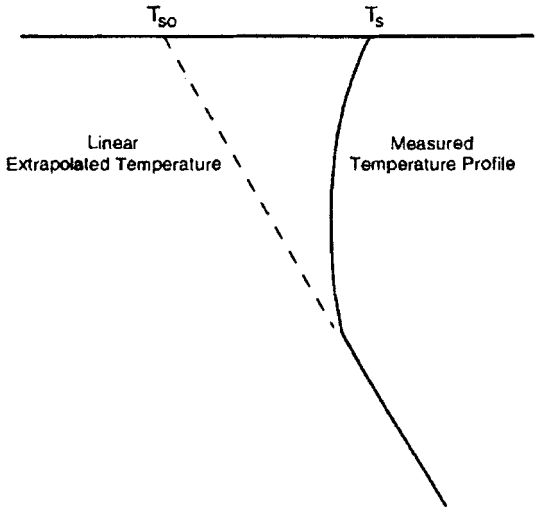

Fig. 2. Extrapolated surface temperature

Let a dry sand be overlain by 50 m of Prudhoe Bay soil, see Table 1 for properties. With $G = 0.0369°\mathrm{Cm}^{-1}$, assume the soil was originally at equilibrium with a surface temperature $T_{so} = -11°\mathrm{C}$ and fifty years ago the surface cooled to a constant value of $-11.25°\mathrm{C}$. Fig. 3 shows the initial temperature profile that existed fifty years ago. The present temperature was calculated with (3),(4) where $\eta = 1.3127$, $\mu = 0.6025$, $\nu = -0.2480$ and $\tau_1 = 2.1701$. This temperature profile is considered the present "measured" temperature, labeled as 0.25°C cooling, and it appears, from the shape of the profile, as if the soil has warmed from the surface although we know that it has actually cooled.

Table 1. Soil layer properties

	Prudhoe	Dry sand
k thermal cond. [$\mathrm{Wm}^{-1}°\mathrm{C}^{-1}$]	3.399	1.56
c specific heat [W-hr $\mathrm{kg}^{-1}°\mathrm{C}^{-1}$]	0.258	0.218
ρ dry density [$\mathrm{kg\,m}^{-3}$]	1960	1836
α thermal diffusivity [$\mathrm{m}^2\mathrm{hr}^{-1}$]	0.00672	0.0039

We wish to estimate a surface warming that would yield the "measured" curve just calculated. If we have no information on thermal properties, we could assume a homogeneous soil with $\alpha = 0.0039\mathrm{m}^2\mathrm{hr}^{-1}$ (value for the overlying sand) and $T_s = -11.25°\mathrm{C}$. Any combination of surface temperature

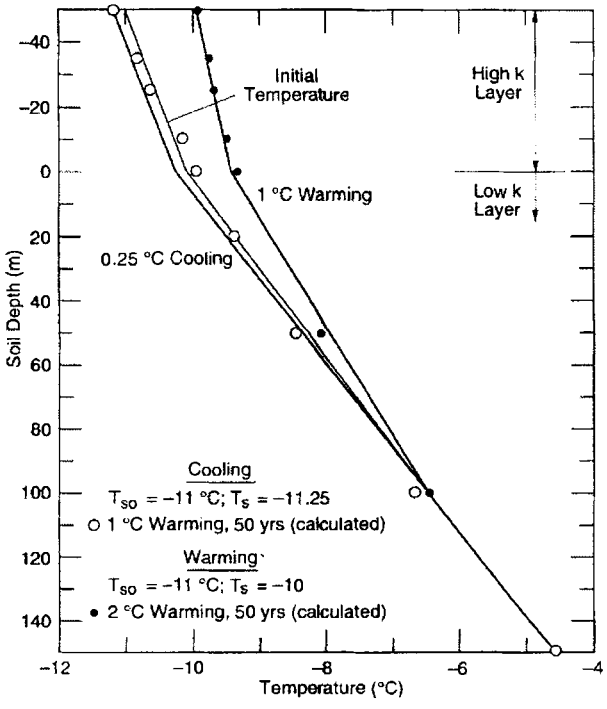

Fig. 3. Prudhoe soil over 50m dry sand.

warming and time duration can be used with (5) to calculate the temperature profile after some time. Fig. 4 shows the effect of 1°C and 3/4°C surface temperature increases for fifty years. The results are suggestive of the present "measured" temperature profile, however, since we are free to choose any soil properties, let $\alpha = 0.001\text{m}^2\text{hr}^{-1}$. Then we can obtain a closer fit to the present temperature as shown in Fig. 4. With arbitrary, choices of T_{so}, α, and time duration, a fit as close as desired could be attained.

Starting with the same initial temperature and properties as before, let us now assume a 1°C warming for fifty years, plotted on Fig. 3 as the warming curve. This "measured" temperature variation will now be matched, as before, for surface warming. The results of a 2°C surface temperature warming for fifty years are also plotted on Fig. 3. Clearly the inferred surface warming of 2°C matches the present temperature profile quite well, although this is actually double the surface warming used to produce the synthetic present temperature. To deduce surface paleotemperature fluctuations from present temperature data, good values of the variation of soil thermal conductivity and diffusivity are necessary.

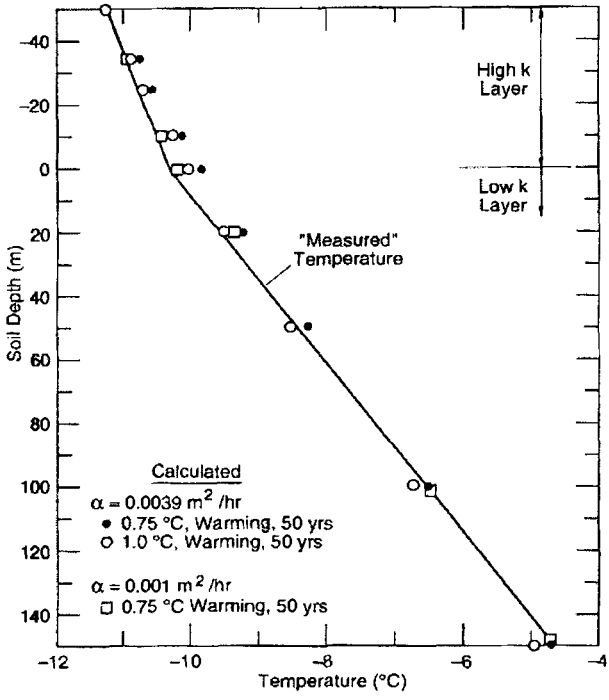

Fig. 4. Surface warming 2-layer soil

Thermal conductivity effect on temperature If the thermal conductivity varies with depth, the temperature profiles can lead to erroneous conclusions as to whether the soil temperature is increasing or decreasing with time, or if it is actually at steady-state. This ambiguity can be resolved if the variation of k with depth is known. The energy equation is

$$\frac{\partial}{\partial x}\left(k(x)\frac{\partial T}{\partial x}\right) = \rho c \frac{\partial T}{\partial t}. \tag{6}$$

Introduce a new variable to replace x

$$\xi = \int_0^x \frac{d\beta}{k(\beta)}. \tag{7}$$

Equation (6) now becomes

$$\frac{\partial^2 T}{\partial \xi^2} = k[x(\xi)]\rho c \frac{\partial T}{\partial t}. \tag{8}$$

This is especially useful for steady-state problems since the temperature for any variation of k with depth will be a linear function of ξ.

The solution to the two-layer problem with the new coordinate ξ is

$$T = T_{so} + k_2 G_2 \xi. \tag{9}$$

The relation of the coordinate ξ to x depends upon the particular form of the $k(x)$ function. For this two-layer case

$$\xi = \begin{cases} (x + X_2)/k_1, & -X_2 < x < 0, \\ X_2/k_1 + x/k_2, & x > 0. \end{cases} \tag{10}$$

The temperature profile now appears as a linear curve labelled "undisturbed temperature" of Fig 5, along with the temperature profiles previously calculated for a 0.25°C cooling and a 1.0°C warming. We note that the cooling and the warming now appear as unambiguous effects, easily interpreted.

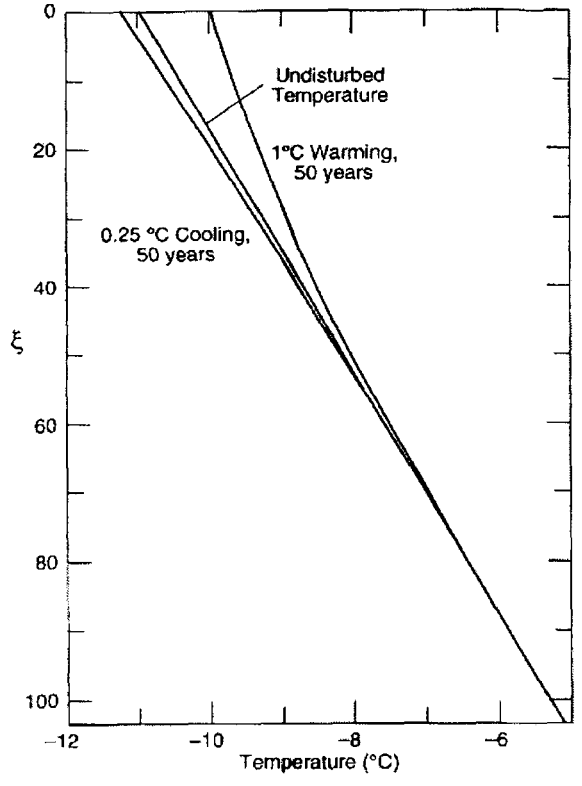

Fig. 5. Temperatures, transformed coordinates

The correct approach for interpreting temperature profiles is to plot the measured temperatures as a function of ξ rather than depth. Any systematic variation of the temperature from a linear profile in ξ would then be indicative of true surface temperature changes.

The geothermal heat flux must be constant if a true steady state exists, but its constancy over geological time periods is sometimes questioned. Fourier [7] and Kelvin [15] examined the cooling of a homogeneous earth with a constant initial temperature. The transient value of the geothermal gradient, near the surface, was predicted and its change over the entire Quaternary Period would not have been great enough to measure. The geothermal gradient decreased rapidly after the earth was formed but the changes now occurring are extremely small except for large variations due to tectonic and volcanic activity.

1.3 Long period surface temperature oscillations

Cycles of glacial length We can examine temperature oscillations on a glacial time scale by noting a reconstructed temperature cycle at Prudhoe Bay, Alaska as cited in [25]. The glacial cycle has a period of 120,000 years with a mean temperature of $-13.38°C$. It consists of a glacial interval of 105,000 years with average temperature of $-13.76°C$ and an interglacial time span of 15,000 years with average temperature of $-10.73°C$. We calculate the temperature distribution for the present time by considering a series of step changes in the surface temperature. We find that the temperature profiles are essentially linear. The apparent geothermal gradient is changing with time and the present temperature profile and gradient are very close to measured values. The very long term temperature oscillation will not be discernible in terms of near surface (< 500 m) temperatures. The true geothermal gradient may be somewhat different than the value determined from shallow temperature profiles.

A sinusoidal surface temperature with a 120,000 year period will also yield steady periodic profiles that appear linear with depth at any time. The mean temperature profile is $-13.38 + 0.0286x$ and the curve for $t = 38,696$ years looks very much like the present profile at Prudhoe Bay, Alaska, except that the geothermal gradient is $0.0278°\mathrm{Cm}^{-1}$. Very long periodic surface temperature oscillations will leave little measureable evidence in the present temperature profile, requiring thousands of years to detect the temperature variations of very lengthy periodic fluctuations.

100 Year Sinusoidal Surface Temperature Periodic surface temperature oscillations of long, but not glacial, duration can also lead to soil temperature profiles that can easily be misinterpreted. For a sinusoidal surface temperature oscillation and a homogeneous soil mass, the temperature is governed by

$$T = T_0 + A_0 \mathrm{e}^{-x\sqrt{\omega/2\alpha}} \sin\left(\omega t - x\sqrt{\omega/2\alpha}\right) + Gx, \tag{11}$$

where $\omega = 2\pi/P$, P is the period. Let $P = 100$ years, $\alpha = 0.0039\ \mathrm{m}^2\mathrm{hr}^{-1}$, $T_0 = -11°C$, $G_2 = 0.0369°\mathrm{Cm}^{-1}$, $A_0 = 1°C$. A measured soil temperature

profile at this location would yield values depending upon where the present time falls on the steady-periodic time scale of (11). For example, we might assume that the time at which measurements are made coincides with $t = 40$ years. The temperature profile calculated with (11) is shown on Fig. 6. The "measured" temperature profile seems to indicate a location that underwent a surface warming for a time and then cooled, while the temperature profile for $t = 95$ years now looks like surface cooling. This location is experiencing only periodic changes about a constant mean temperature.

A simple surface temperature scenario can produce the "measured temperature" profile at $t = 40$ years. Let the surface temperature be $-11°C$ and jump to $-9.9°C$ for 15.6 years, starting at $t = 0$. Then the temperature drops to $-10.41°C$ for an indefinite time. The average surface-temperature increase for 20 years is $0.99°C$. The temperature calculated from the inversion analysis with the above scenario is also shown on Fig. 6. The agreement is very good, but this again shows that the inversion procedure does not yield unique results. If the 40 year curve of Fig. 6 was actually field data, a reasonable interpretation of the cause of the apparent warming could be the surface warming given above. It seems that we can reproduce almost any present soil temperature profile by adjusting the past assumed surface temperatures and time durations.

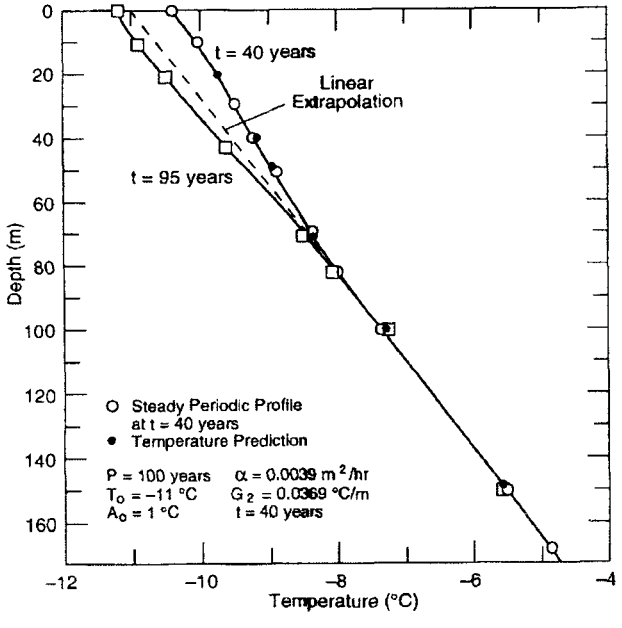

Fig. 6. 100yr surface temperature oscillation

1.4 Ramp increase of surface temperature

The long term increase of air temperature due to future global warming has been estimated at 1 to 5°C per 100 years, [12]. Let us examine the effect such increases would have on soil temperatures over periods of time during which field measurements might be made. We consider a linear increase of surface temperature with time and a linear initial temperature. The solution is

$$T(x,t) = T_0 + Gx + \delta_2 t \left[\left(1 + \frac{x^2}{2\alpha t} \right) \operatorname{erfc} \frac{x}{2\sqrt{\alpha t}} - \frac{x}{\sqrt{\pi \alpha t}} \exp\left(\frac{-x^2}{4\alpha t} \right) \right]. \quad (12)$$

Temperature changes were calculated for soils with a representative range of thermal diffusivity values ($44 < \alpha < 80$ m^2yr^{-1}) and a surface temperature change at the high end of speculation ($0.05°Cyr^{-1}$). We find that

1 After 5 years, temperature changes at 50m will be marginally detectable ($0.002 < \Delta T < 0.006$°C). These changes may be masked or confused by the annual temperature variations at depth.
2 After 10 years, temperature changes at 50m may be detectable ($0.015 < \Delta T < 0.043$°C).
3 After 20 years, the changes at 50m should be unmistakeable ($0.10 < \Delta T < 0.2$°C).
4 The measurement error due to incorrect depth determination should be less than 0.002°C ($G = 0.0286°Cm^{-1}$) if $\Delta x < 6$cm.

2 Active Layer as a Measure of Global Warming

The active layer is the limit of melt penetration and can vary each year. It is of interest with regard to global warming since it can be measured rather easily over large permafrost areas. A simple probe measurement once a year is quite cheap, but is the least reliable technique. Frost tubes are more expensive, but far more accurate.

Active layer thawing is governed by the net transfer of energy at the ground surface and at the top of the permafrost, the initial thermal state of the ground when thaw begins, the mode of energy transfer within the ground, the soil structure, the amount and distribution of water in the ground, and the soil thermal properties. The surface energy balance will be strongly affected by climatic change, but the other parameters will be significantly less susceptible to variation due to climate change. The assumption is usually made that global warming will induce an increase in air temperature, such an increase in air temperature will be accepted for this discussion. The surface thaw index is related to the air thaw index in a complicated way, but if the air index increases it can be assumed that the surface index will increase.

Is a change in the active layer a valid proxy for global change? The answer to the question is yes if the active layer change is due primarily to a change

in the air index. Accurate measurements of the active layer should then yield quantitative information on the changes in the air index. If the water content of the soil is uniform with depth and time, then the thermal properties will not vary and the active layer should respond in a one-to-one fashion to changes in the surface index. Clearly this will not be true if the amount of water (latent heat) varies from one year to the next. However, as will be shown, even if the water has the same magnitude and merely redistributes itself from season to season, the active layer will not be a reliable measure of global change. Other measurements must be taken with the active layer depth in order to relate it to global change.

2.1 Theory

Consider a layer of soil for which the soil skeleton does not vary with depth or time. The amount of water contained in the soil can vary and the saturation can change with depth as shown in Fig. 7a. The saturation function is assumed to vary over the depth X_0 in a linear fashion. The soil is initially frozen at the phase-change temperature and the thermal conductivity, latent heat, and specific heat of the soil will vary with depth. The functional form of the thermal conductivity will be specified by the geometric mean. Series and parallel geometries are also possible, but they tend to bracket values for the geometric mean. The mathematical forms for the thermal properties as functions of depth are given in Appendix A.

The quasi-steady approximation will be used since this is the basis for the Stefan equation, the equations governing the thaw process are as follows:

$$\frac{\partial}{\partial x}\left(k(x)\frac{\partial T}{\partial x}\right) = C(x)\frac{\partial T}{\partial t} = 0, \tag{13}$$

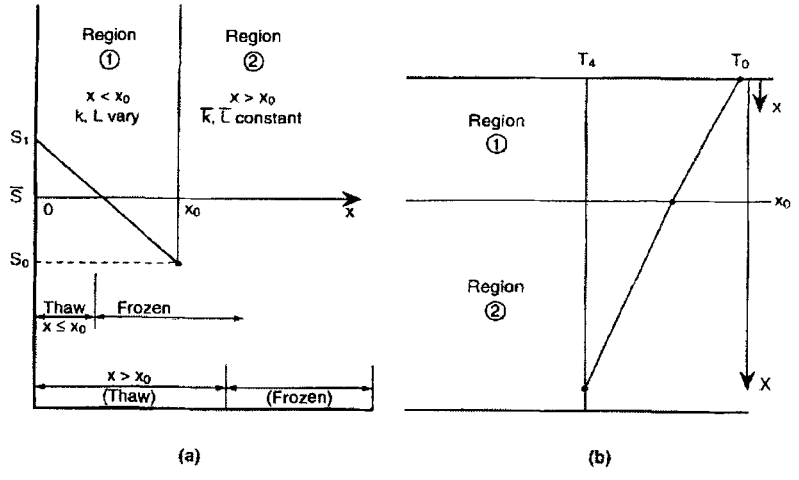

Fig. 7. Geometry for variable water content.

$$T(0,t) = T_s(t), \tag{13a}$$

$$T(X,t) = T_f. \tag{13b}$$

The Stefan condition is

$$k(X)\frac{\partial T(X,t)}{\partial x} = -L(X)\frac{dX}{dt}, \tag{14}$$

where X is the location of the thaw interface and the surface temperature can be a function of time. Integrating (13), using the functional relation for $k(x)$, (A.1), yields

$$T(x,t) - T_s = \frac{F(1 - B^{-bx})}{KB^{S_0} b \ln B}. \tag{15}$$

Using (13b), the form of $F(t)$ is

$$F(t) = \frac{bKB^{S_0}\ln B \Delta T}{B^{-bX} - 1}, \tag{16}$$

where $\Delta T = T_s(t) - T_f$. Application of the Stefan condition results in a relation for the thaw depth X versus time,

$$AI = S_0 X + bX^2/2 + \frac{1}{\ln B}\left[A_1\left(B^{-bX} - 1\right) + XB^{-bX}\right], \tag{17}$$

where the surface index is defined as

$$I = \int_0^t \Delta T dt', \; A = KB^{S_0} b \ln B / B_1, \; A_1 = (S_0 + 1/\ln B)/b.$$

The equation can also be written as

$$\frac{KI}{B_1 X_0^2} = \frac{1}{B^{S_0} M \ln B}\left[S_0\beta_2 + M\beta_2^2/2 + \frac{1}{\ln B}\left(B^{-M\beta_2}\{A_2/M + \beta_2\} - A_2/M\right)\right], \tag{18}$$

where

$$\beta_2 = X/X_0, \;\; A_2 = S_0 + \frac{1}{\ln B}.$$

It can be shown that the familiar constant property solution follows from the above equations in the limit as $b \to 0$,

$$X^2 = 2\bar{k}I/\bar{L}. \tag{19}$$

This relation, often called the Stefan Solution is the basis for the concept that the active layer is proportional to the square root of the surface index. However, since it is only valid for constant thermal properties, it can lead to significant errors when used to correlate field data. Equation (17) clearly shows that the thaw depth is not a function of the square root of the surface index.

Growth after thaw reaches X_0 When the thaw depth reaches the value of the layer of variable saturation soil, X_0, the thaw relation must be found for the underlying layer with constant thermal properties at mean saturation $\bar{S}$. The value of the surface index when $X = X_0$ is obtained from (17) as

$$I_0 = P_1 \bar{L} X_0^2 / \bar{k}, \tag{20}$$

where

$$A_3 = M \ln B, \quad A_4 = B^M - 1, \quad I_0 = \int_0^{t_0} \Delta T dt',$$

$$Q = S_0 + M/2 - \frac{1}{A_3 B^M}(A_2 A_4 - M), \quad P = \frac{A_4 Q}{A_3^2 \bar{S}},$$

and t_0 is the time to reach X_0. There are now two regions to consider, the first governed by the variable thermal property equations, and the second for constant properties. The Stefan relation is integrated from t_0 to t yielding the relation for the thaw rate X

$$\frac{k_2 I}{\bar{L} X_0^2} = \beta_2^2/2 + (D-1)\beta_2 + 1/2 + \frac{B^{M/2} Q}{\bar{S} A_3}. \tag{21}$$

This can be solved explicitly for β_2

$$\beta_2 = 1 - D + \sqrt{D^2 + 2R_1}, \tag{22}$$

where

$$R_1 = \frac{B^{M/2} K B^{S_0}(I - I_0)}{\bar{L} X_0^2} \quad \text{and} \quad D = \frac{B^M - 1}{B^{M/2} M \ln B}.$$

Variation of latent heat only The solution is much simpler if only the latent heat varies. The temperature is identical to that for the constant property Stefan solution and the Stefan condition leads immediately to

$$\frac{\bar{S} \bar{k} I}{\bar{L}} = X^2(S_0/2 + bX/3). \tag{23}$$

2.2 Discussion

To compare the effect of the variation in water content, the specific soil properties listed in Appendix A are used. The value of the thaw index when the thaw reaches the depth X_0 is illustrative. The relations for thaw depth can be written in the form of (20). Table 2 shows the results for some appropriate cases. All of the cases have the same water content in the top X_0 layer of soil and thus the latent heats are identical. The time (surface index) needed to reach a thaw depth X_0 varies remarkably for the different cases examined. A

Table 2. Value of thaw index when $X = X_0$

Case		P
Constant Property		0.50
Variation of k and L	a) water decreases with depth	0.264
	b) water increases with depth	0.926
Variation of L only	a) water decreases with depth	0.333
	b) water increases with depth	1.667

decreasing water content with depth ($M = -1$) differs greatly from that of increasing water content ($M = +1$). In the latter case the thaw rate initially is higher but then slows so that ultimately the thaw depth for a given surface index is much smaller. Table 2 lists only one value of the thaw index, the intermediate times vary according to the equations derived.

These results can be seen graphically in Fig. 8, where the plotted values of the thaw depth versus thaw index show that the cases differ significantly from the constant property results. For a surface index of 64°C-day all cases have a similar thaw, about 0.38m. As the thaw index increases the results diverge. At $I = 196$°C-day, the thaw depths are 0.58, 0.65, and 0.76m for the cases $M = 1, 0$, and -1. The active layer can differ by -11 to $+$ 17% compared to the Stefan solution at the same thaw index. If active layer depths of 0.58, 0.65, and 0.76m were measured in 3 consecutive years, it might be surmised that climatic warming was occurring. However, this is simply due

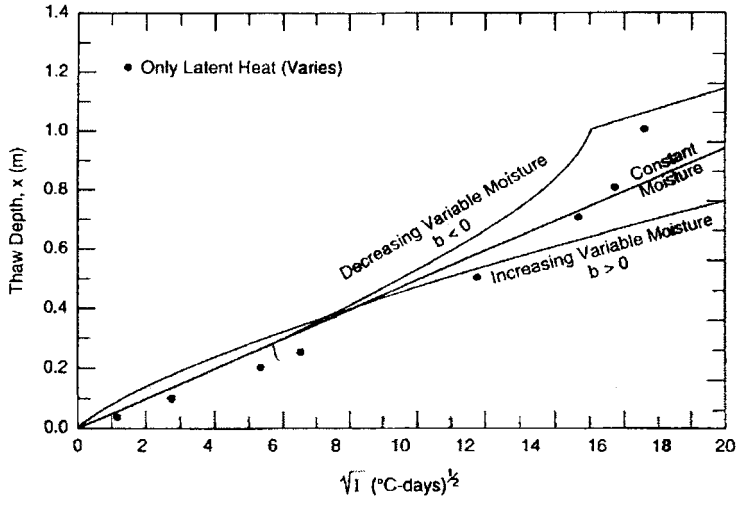

Fig. 8. Thaw depth vs thaw index, App. A soil

to the assumption that the thaw depth is related to the surface index by the Stefan relation for each year at the site. The active layer depth alone cannot be a unique measure of the surface index if moisture changes can take place within the active layer.

Figure 9 shows general non-dimensional relations and allows an estimate of the range of variability that could occur due simply to moisture redistribution and its effects on the thermal properties.

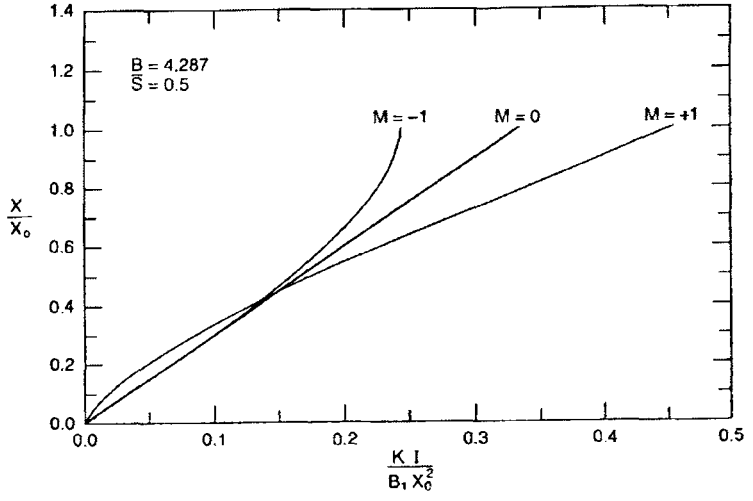

Fig. 9. Thaw depth vs thaw index general soil

3 Degradation of Warm Permafrost

Permafrost underlies many important engineering systems for transportation and human habitation. When the temperature of the permafrost increases, its ability to support a load decreases and if the permafrost totally melts, there may be a catastrophic loss of stuctural support. The threat of global warming and its effects upon the permafrost of the world have been widely discussed in the scientific community, [5]. Recent speculation on the effect of increasing greenhouse gases on world climates has raised numerous questions on the thermal stability and even the continued existence and ecological consequences of permafrost [1,4,6,11,12,22]. The International Panel on Climate Change [9] has presented scenarios on temperature increases to be expected in the future. Gavrilova [8] predicts that large areas of permafrost will vanish in the next 100 years. This is also forecast by Nelson et al. [20], however their method relies on a model which does not include the dynamics of permafrost change, assuming that the changes take place after sufficient time has passed to equilibriate with new climatic conditions, Nelson et al. [21]. This cannot

provide a reliable guide to the permafrost changes that will occur during times as short as 50 or 100 years. If governments intend to combat climate warming by implementing strategies that may have profound economic consequences, then it will be important to assess with confidence the near term changes that might occur in the permafrost regions due to various climatic prognostications.

Relict permafrost exists in regions where the present earth/atmosphere energy balance is not favorable for permafrost. It is the slowly degrading remnants of frozen volumes of earth materials that froze during harsher glacial periods, with a slowly growing layer of unfrozen soil over the permafrost. In order to quantitatively examine the warming threat it is necessary to specify values for the expected global temperature increases over time. We will use a surface temperature rate of change of $0.05°\text{Cyr}^{-1}$, which is the upper range of broadly accepted scenarios, although the IPCC (Intergovernmental Panel for Climate Change) has recently reduced its consensus temperature change scenario.

3.1 Climate change and permafrost thaw

A simple model to predict the maximum amount of permafrost that could melt under a given global warming scenario is given by Lunardini [16]. The increased surface temperature causes melting and thermal disturbance, while the lower boundary of the permafrost is unaffected, but eventually the permafrost starts to thaw at its base. Lunardini [16] calculated the temperature profiles, for a specific example, when the permafrost just starts to thaw at its base, using soil and climate change information reported for cold paleopermafrost in France, Lebret et al. [14]. Details on the formation process are given by Lunardini [17]. Even with a surface temperature change of +24°C, it takes about 130 years for the bottom of the permafrost to start to thaw. There will be no top melt at all if the surface temperature remains below the freezing value with the permafrost slowly adjusting its temperature with eventual bottom melt. Lachenbruch et al. [13] showed that the time scale of these changes for cold thick permafrost, is on the order of thousands of years. Thus, the expected disappearance of permafrost, in the next 100 years, will be limited to warm permafrost.

Time to Complete Thaw To maximize the thaw effects, the temperature changes occur instantly and translate, without attenuation, to the surface of the soil system. An approximate solution to this problem was obtained using the heat balance integral technique, which has been shown to be accurate by Lunardini [18]. Thaw will be complete when the sum of the top and bottom thaws equals the original permafrost thickness. The relation for the top thaw, at the completion of thaw is

$$(X-\gamma)^2 = X_1^2 + 2Q\left[\frac{\gamma^2}{6}\left(1+2\sqrt{2L/(C_u G_\gamma)}\right)+\gamma L/(GC_u)\right], \quad (24)$$

where

$$S_T = \frac{C_u}{L}(T_s - T_f), \quad R = \sqrt{2S_T + 1},$$

$$Q = 6(1 + 2S_T - R)/(5 + 2S_T + R), \quad \gamma = X_e - X,$$

and t is the time to reach X_1. The equations can be used to predict the thickness of permafrost at any time. The maximum thickness of the original permafrost that will melt after a given time Δt is

$$\delta_1 = q_g \Delta t / L + \sqrt{X_1^2 + 2\alpha_u Q \Delta t} - X_1. \tag{25}$$

Discussion We can bracket the estimates of the thaw depth by considering maximal and minimal property values, see Table 3, with instantaneous surface temperature change and a surface temperature that ramps linearly with time. We note from Fig. 10 that the amount of relict permafrost melted in 55 years could range from 9.3 to 17.9 meters, if the initial thawed surface layer is zero. For Alaska, the initial depth to relict permafrost is $5 - 25$ m, Brown et al. [2], thus the melted permafrost would be on the order of $3 - 13$ meters.

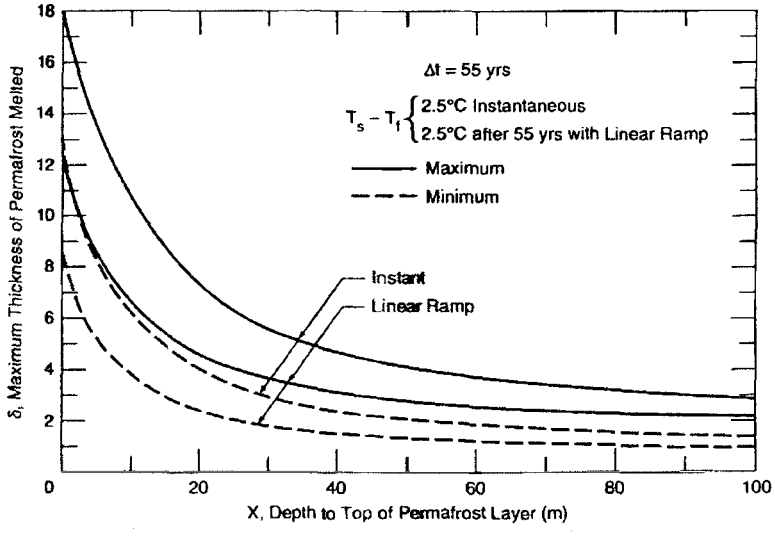

Fig. 10. Permafrost melt after warming 55 yrs

The case for $\Delta t = 100$ years and $T_s = 5°\text{C}$ resulted in a maximum value of the permafrost melted of 33 m, for $X_1 = 0$. Since relict permafrost will always lie at some finite depth X_1, the probability of significant permafrost

Table 3. Extreme property values permafrost melt case

	k_u [$Wm^{-1}K^{-1}$]	L [Jm^{-3}]	C_u [$Jm^{-3}K^{-1}$]	α_u [m^2yr^{-1}]	q_g [Wm^{-2}]
Maximum	3.0	9.7×10^7	2.49×10^6	38.16	8.4×10^{-2}
Minimum	2.0	1.17×10^8	2.63×10^6	24.05	4.2×10^{-2}

disappearance during the next 55 years in Alaska, is fairly small except at the southerly fringes of the discontinuous zone.

To predict the dynamic behavior of permafrost due to global warming, we need to know the original thermal state of the permafrost, its thermal properties, the geothermal heat flow, and the magnitude and timing of the warming. This information on the permafrost is sketchy while the warming relies on plausible global scenarios. While relatively small areas of permafrost will disappear in the next 55 years, this does not imply that significant warming of permafrost will be without engineering or environmental problems.

Appendix A.
Effect of Saturation on Soil Thermal Properties

Consider a soil with a void ratio ϵ and thermal conductivities of the soil constituents known. The soil skeleton is rigid so that the void ratio is constant. The constituents are soil solids, water, and air. The saturation of the soil will be a linear function of depth (other variations could be considered). The water saturation variation is linear with depth,

$$S = S_0 + bx, \tag{A.1}$$

where $0 \leq S \leq 1$. We will use the geometric mean for the soil thermal conductivity, Lunardini [19].

$$k = k_s^{1-\epsilon} k_w^{\epsilon S(x)} k_a^{\epsilon(1-S)} = K B^{S_0} B^{bx}, \tag{A.2}$$

$$L = \gamma_d \ell W/100 = \epsilon \rho_w \ell S = B_1 S(x), \tag{A.3}$$

$$C = C_s(1-\epsilon) + C_w \epsilon S + C_a \epsilon (1-S) = C_0 + C_1 x, \tag{A.4}$$

where γ_d is the dry unit weight.

The average properties over the soil depth X_0 are evaluated as follows:

$$\bar{k} = \frac{K B^{S_0}(B^{bX_0} - 1)}{bX_0 \ln B}, \tag{A.5}$$

$$\bar{L} = B_1 \bar{S} = [L(0) + L(X_0)]/2. \tag{A.6}$$

Representative values for the soil solids, water, and air constituents are: $k_s = 5$ $Wm^{-1}K^{-1}$, $k_w = 0.561$ $Wm^{-1}K^{-1}$, $k_a = 0.0237$ $Wm^{-1}K^{-1}$, $\epsilon = 0.46$, $K = 0.4264$ $Wm^{-1}K^{-1}$, $B = 4.287$, $B_1 = 1776.2$ W-day m^{-3}.

Nomenclature

A_0	amplitude of surface temperature oscillation	b	$2(\bar{S} - S_0)/X_0$
B_1	$\ell\epsilon\rho_w = \bar{L}/\bar{S}$	B	$(k_w/k_a)^\epsilon$
C	ρc specific heat capacity	c	specfic heat
I	surface thaw index	G	geothermal gradient
K	$(k_a/k_s)^\epsilon k_s$	k	thermal conductivity
L	$\rho\ell$, volumetric latent heat	l	latent heat of solidification
S	soil saturation	M	$bX_0 - 1 \leq M \leq +1$, for $M = 1$, $S_0 = S_1 = \bar{S}$
S_T	Stefan Number	t	time
t_1	time to melt permafrost to depth X_1	Δt	$t - t_1$
T_0	initial constant temperature	T	temperature
x	depth, Cartesian coordinate	T_s	surface temperature
X_B	bottom melt of permafrost	X	thawed thickness at permafrost top
X_e	$X_1 + \delta_1$	X_0	depth of soil over which S varies
X_1	initial thawed layer over permafrost	X_2	thickness of top layer in 2-layer problem
α	thermal diffusivity	β	δ/X
α_{12}	α_1/α_2	δ	depth of temperature disturbance
ϵ	void ratio of soil	δ_2	rate of surface temperature increase
δ_1	initial thickness of permafrost	τ	dimensionless time
ΔT	$T_s - T_f$		
ρ	density		

Subscripts

$1, 2$	different materials	a, s, w	air, soil solids, water
f, u	freeze, thaw	s	surface

References

1. Brigham, J.K., and G.H. Miller (1983) Paleo-temperature estimates of the Alaskan Arctic Coastal Plain during the last 125,000 years, *Proceedings of 4th Int Conference on Permafrost*, National Academy Press, 80-85.
2. Brown, R.J.E. and T.L. Pewe (1973) Distribu- tion of permafrost in North America and its relation to the environment: A review 1963-1973, *Proceedings of 2nd International Conference on Permafrost*, NAS Press, 71-100.
3. Carslaw, H.W. and J.C. Jaeger (1959) *Conduction of Heat in Solids*, Oxford Clarendon Press, 2nd edition.
4. COHMAP Members (1988) Climatic changes of the last 18,000 years: observations and model simulations, *Science* **241**, 1043-1052.
5. Dansgaard, W. and H. Oeschger (1989) Past en- vironmental long-term records from the Arctic in H. Oeschger and C.C. Langway(eds), *The Environmental Record in Glaciers and Ice Sheets* John Wiley and Sons, pp.288-317.
6. Folland, C.K., T.R. Karl, and K.YA. Vinnikov (1990) Observed climate variations and change Ch7,Climate Change in J.T. Houghton, G.J. Jenkins and J.J.Ephraums(eds), *The IPCC Scientific Assessment*, Cambridge Univ. Press.

7. Fourier, J.B. (1820) Extrait d'un Memoire sur le refroidissiment du globe terrestre, *Bull. Sci. par la Societe Philomathique de Paris.*
8. Gavrilova, M.K. (1993) Climate and permafrost *Permafrost and Periglacial Processes* **4**(2), 99- 111.
9. W.J. McTegart, G.W. Sheldon and D.C. Griffths (eds) (1990) Intergovernmental Panel on Climate Change: The IPCC Impacts Assessment, *Australian Gov Publishing Service*, Canberra.
10. J.T. Houghton, G.J. Jenkins, and J.J. Ephraum (eds) (1990) Intergovernmental Panel on Climate Change: Scientific Assessment, Working Group I Report,WMO&UNEP, *Cambridge U Press.*
11. Lachenbruch, A.H., T.T. Cladouhos, and R.W. Saltus (1988) Permafrost temperature and the changing climate, *Proceedings of the 5th Int Conference on Permafrost* **3**, Trondheim, 9-17.
12. Lachenbruch, A.H., and B.V. Marshall (1986) Changing climate: geothermal evidence from permafrost in the Alaskan Arctic, *Science* **234**, 689-696.
13. Lachenbruch, A.H., Sass, J.H., Marshall, B.V. and Moses, T.H., Jr. (1983) Permafrost, heat flow, and geothermal regimes at Prudhoe Bay, Alaska, *J Geophysical Res.* **87**(B11) 9301-9316.
14. Lebret, P., Dupas, A., Clet, M., Coutard, J.-P., Laudridou, J.-P., Courbouleix, S., Garcin M., Levy, M., and Van Vliet-Lanoe, B.(1994) Modelling of permafrost thickness during the late glacial stage in France, *Can. J. Earth Sci.* **31**,959-968.
15. Lord Kelvin (1864) The secular cooling of the earth,Trans. *Roy. Soc. Edin.* **23**, 157.
16. Lunardini, V.J. (1996) Climatic warming and the degradation of warm permafrost, *Permafrost and Periglacial Processes* **7**(4),311-320.
17. Lunardini, V.J. (1995) Permafrost formation time, *USACRREL Report 95-8*,Hanover, N.H.
18. Lunardini, V.J. (1991) *Heat Transfer with Freezing and Thawing*, Elsevier Science Publishers, Amsterdam, The Netherlands.
19. Lunardini, V.J. (1981) *Heat Transfer in Cold Climates*, Van Nostrand Reinhold,New York.
20. Nelson, F.E. and O.A. Anisimov (1993) Permfrost zonation in Russia under anthropogenic climatic change, *Permafrost and Periglacial Processes* **4**(2),137-148.
21. Nelson, F.E. and S.I. Outcalt (1987) A Computational method for prediction and regionalization of permafrost, *Arctic and Alpine Research* **19**(3),279-288.
22. Osterkamp, T.E. and J.P. Gosink (1991) Variations in permafrost thickness in response to changes in paleoclimate, *J. Geophysical Research* **96**B3,4423-4434.

(Received 14 June 1999, accepted 18 June 1999)

The Monitoring and Prediction of Permafrost Temperature, Distribution and Geocryological Processes Within Russia Under Global Climate Changes

Alexander Pavlov and Stanislav Grechishchev

Earth Cryosphere Institute SB RAS, Moscow dept, Vavilova street, 30/6, room 85, Moscow, 117982, Russia

Abstract. The recent changes of climate and permafrost conditions are studied on the basis of the data of northern meteorological and permafrost stations located in various regions of Russia.

Everywhere on Russian territory a warming of the Climate and the upper part of the Permafrost was observed since the middle of 1960s. The Permafrost Monitoring data indicate an increase of the permafrost temperature for the last 15-20 years up to 2-1.5 °C in 3 m depth and up to 1 °C in 10 m depth. The probable increase of the temperature of the upper part of the permafrost of Western Siberia will amount to about 1 °C by 2020, and 1.5-2 °C by 2050.

Calculations (up to the year 2025) and small scale map-schemes of predicted permafrost thawing, distribution and changes of cryogenic cracking of the soils within Russia under a global climate warming were carried out. Predictions were done for peaty, clayey and sandy types. The zones of degrading and stable permafrost for different stow types and areas of decreasing frost soil cracking are identified within the territory of Russia.

1 Introduction

Instrumental meteorological observations show that starting in the mid-1960s the climate was becoming warmer in all regions of the Northern Hemisphere. For the last 25-30 years, the air-temperature increase in the North of Russia was on the average estimated to be 1°C, whereas in Central Yakutia it was at most amounting to 1.9°C. The climate warming, and in a number of regions the growing height of the snow cover, induced an increase in the temperature of the upper horizons of frozen soils. Continuation of the trend towards climate warming in the North will, in the 21st century lead to adverse consequences: enhanced degradation of frozen soils over the area and profile, thawing of underground ice, decreasing of cryogenic cracking and long-term heaving, activation of destructive cryogenic geological processes (landslide flows, thermokarsts, and others), disturbance of the functioning of the natural and natural-technogenic geosystems of the permafrost zone. Climate warming influences human life-support systems and economic activities.

2 Trends in Contemporary Changes in Climatic Indicators at Northern Russia

Meteorological measurements revealed several warming-cooling cycles in the North of Russia. The most conspicuous warming ("Arctic Warming") by about 2°C took place during the period from the end of the 19^{th} century until the early 1940s. The subsequent slight cooling covered the period until the mid-1960s followed again by a warming. Throughout the period of instrumental records (150-185 years) a trend towards an air temperature increase in the Arctic regions of Russia has not been clearly manifested (Pavlov, 1994, 1996, 1998). In the Arctic and the neighbouring regions, the contemporary warming-cooling cycles remain within the range of natural secular climate cyclicity owing to the proximity of the Polar seas and a very low technogenic impact. On the other hand, in inland regions of the Russian permafrost zone, and especially in Central Yakutia, a clear-cut climate warming was observed during the period of meteorological observations. For Yakutsk it is 2.4°C (1830-1995).

The last distinct climate warming started everywhere in the North in the 1960s. In some areas of the Russian permafrost the air temperature increased by 1.8-2.3°C. The strongest trend towards highest mean annual air temperatures was observed in the North of West Siberia (Tazovskoe, Salekhard, Nadym) and in Yakutia (Lensk, Chul'man, Olekminsk, Yakutsk). The regional trend towards an increase if the mean annual air temperature for the last three decades was between 0.01 and 0.06°C $year^{-1}$. For the period 1960-1995, a mean annual air temperature increment of more than 1°C was recorded at a number of meteorological stations (Vilyuisk, cap Kamenny, Tadibeyakha, and others); on the other hand, at some other stations a slight summer cooling was observed. During this period, the highest regional increase of the mean summer (0.9°C) and winter (3.6°C) air temperatures were revealed in the North of West Siberia and Yakutia, respectively. For the North of Russia on the whole, as well as for its individual regions, the contemporary climate warming was characterized by a higher increase of the winter temperature in comparison with the increment of the summer temperature. Regional estimates obtained by generalization of data from individual meteorological stations show that the trend towards higher air temperature during the long cold period is 1.2-1.5 times higher than that during the short warm period.

3 Quantitative Estimation of the Evolution of Contemporary Permafrost Based on Monitoring Data

Data from perennial measurements of ground temperature as well as results of numerical modelling point to a wide occurrence of permafrost degradation

under contemporary conditions. It is induced by both an air temperature increase and a growth of snow cover (in some cases). Specifically, at the Marre Sale permafrost station (West Yamal) the increase in the soil temperature at a depth of 10 m (t_{10}) was found to vary from 0.1 to 1°C within the period 1980-1995 . The largest warming of frozen soil is characteristic of low-temperature tundra stows, while the smallest warming was observed in relatively high-temperature stows of low flood-plains and river valleys. Thus, the contrast range of the warming of the frozen ground increases with a decrease of their temperature. At the Marre Sale permafrost station of the trend of contemporary increase in the soil temperature at the 10-m depth reaches 0.07°C year^{-1} with a mean of 0.03°C year^{-1} for the station area. These and other field data (Pavlov, 1996) provide conclusive evidence of the rise of the ground temperature for the last 10-15 years in areas of the cryolithozone well studied under stationary conditions. This trend is clearly manifested even in the absence of technogenic impact. By reconstructing temperature profiles in deep wells, T. Zhang and T. Osterkamp (1993) revealed the growth of ground temperature (by 2-4°C on the surface) in Alaska which started 40-80 years ago and continued even during the period of the air temperature decrease. According to geothermal measurements in West Yakutia, modern warming of frozen grounds reaches the depth of 70-80 m.

In contrast to the soil temperature, the seasonal thaw depth, h_{th}, on the whole, responds poorly to contemporary climate warming. However, for a number of regions in the North a common trend towards a growth (though weak) of h_{th}-values was revealed for the 1978-1995 years (up to 0.7 cm year^{-1}); this was due to a slight increase of the air temperature during the summer seasons (Pavlov, 1996). Due to an abnormally cold summer period of 1997 the trend of increasing h_{th} for 1978-1998 practically stopped. Perennial studies (uninterrupted since 1978) of the seasonal thaw depth have been underway at Marre Sale permafrost station. According to these observations, the interseasonal variations of the seasonal thaw depth (h_{th}) on the greater part of the relief elements are more than 20%. The maximum variations of h_{th} are, as a rule, characteristic of soils of organic origin.

4 Prognostic Scenarios of Expected Climate Change and Permafrost Evolution in 2025-2050

Analysis of serial records of meteorological observations is one of the possible ways for predicting climate changes in the near future. Under the condition of preservation of the contemporary climate trend in the future an increase of the air temperature is predicted per year: in the North of Western Siberia by 1.3-1.5°C; in Yakutia by 1.4-1.6°C; and by the year 2050 in the North of Western Siberia by 2.4-2.6°C and in Yakutia in by 2.4-2.6°C. The expected air temperature increase in the North of Russia will not exceed 1.6°C by 2020 and 2.8°C by 2050.

Our studies show that the climate warming during the next 20-25 years will not lead to a radical restructuring of the permafrost conditions. The seasonal thaw depth will increase on the average 1.13 times by the years 2020-2025, while the temperature of the upper horizons of the frozen soil will rise by 0.5-1.1°C. The actual southern boundary of the continuous permafrost can move northward by that time by 30-80 km. However, thawing will occur at a distance of 200-450 km from todays southern boundary of sporadic permafrost (partially from above or completely). The area of intense thawing of sporadic permafrost from above for West Siberia will be more than 450,000 km^2 by the year 2025 (36 % of the total regional permafrost territory). By 2050, changes in permafrost conditions will become more substantial. Todays extent of the continuous permafrost will by then have decreased considerably because of the retreat of its southern boundary in the northward direction (by 150-200 km and more). The seasonal thaw depth will increase 1.23 times, on the average. In areas of contemporary low-temperature permafrost of West Siberia (Yamal, Gydan) the background temperatures of the frozen soils at the 10-m depth will increase on the average by 1.5-2°C (from -5 to -6°C to -3 to -4°C). During the period after the year 2050 there will be the danger of formation of low-temperature frozen soils even in Arctic regions.

5 Natural Geocryological Processes Under a Changing Climate

Climate warming will be accompanied by different geocryological processes the development of which in most cases adversely affects the economic activity. It should be emphasized that the point is about natural background processes which in general are slower and less noticeable than non-background geocryological technogenic processes induced by the direct impact of engineering activity on the geological environment.

Natural background processes develop under the influence of hydrometeorological factors in areas unaffected directly by human's economic activity. They occur under conditions of quasi-equilibrium of grounds with the environment as a result of slight deviations from it and are the expression of continuous evolutionary adaptation of geological environments to the more mobile water and air media. The advisability of timely prediction of background processes is dictated by environmental protection goals, as well as by the possible impact of such processes on engineering structures. So, for example, warming of permafrost may be conducive to degradation of buildings constructed with the preservation of permafrost in their bases, whereas the cessation of ground cracking would improve the operation conditions of roads, earth dams, buildings, etc.

It appears important to estimate the extent of the adverse effect of the expected climate warming on the permafrost for the period of direct practical interest, i.e. for the next 30-50 years.

The results of the prognosis of natural geocryological processes in connection with expected climate warming for the next three decades, i.e. approximately until the year 2025 are presented below. The predicted parameters are: depth and rate of permafrost thaw (i.e. the depth of its roof), approximate geographical position of areals of the break-off of the roof of permafrost from the sole of the seasonally thawing layer (STL), changes in the areals and depth of cryogenic cracking of the grounds. Cryogenic cracking was chosen as one of the geocryological processes for the prediction because of the availability of adequately developed computational methods necessary for the prognosis.

The scenario of possible climate warming and the rise of soil temperature was assumed in conformity with the analysis mentioned above according to which the soil surface temperature in the cryolithozone will rise by 1-2°C within the prediction period.

It was assumed that the soil, vegetation and snow covers are not subjected to direct technogenic destruction since we consider natural processes.

The principle of hierarchy of natural geosystems, according to which large geosystems – landscapes, localities – are composed of smaller geosystems: stows and facies were used for the interpretation of predicted changes. The latter are characterized by a homogeneous lithological composition of subsurface grounds which we divide, according to their attitude to the thaw-freeze cycles and other geocryological processes, into peaty, clay and sandy grounds. Rocks, semirocks and large-skeletal grounds, as well as the geosystems which comprise them, were not considered. We also left out of account the water geosystems since there are no data from direct observations of geocryological processes occurring in them and the virtual absence of respective physico-mathematical computational models.

The purpose of the initial database required for the schematic predictive computations and compilation of small-scale map-schemes was served by the information contained in small-scale (1:25 000 000) maps of "The Atlas of the USSR" (1984).

A schematic prediction of changes in the position of the permafrost boundary was performed with the determination of the rate of its thaw, i.e. the "break-off" of the permafrost roof from the sole of STL in peaty, clay and sandy stows. These boundaries were compared with the actual permafrost boundaries. Based on predictive estimates a schematic zoning of the prognostic geocryological situation was performed (Grechishchev, 1997).

The calculated southern boundaries of permafrost in peaty, clay and sandy soils were compared with the recent boundaries of sporadic, discontinuous and continuous permafrost. The southern boundary of peaty soils freezing is seen to nearly coincide with the southern boundary of sporadic permafrost, while the southern boundary of the freezing of clay soils coincides with the southern boundary of discontinuous permafrost, and the southern boundary of sands coincides with the southern boundary of continuous permafrost.

This allows geosystematic interpretation of such terms as "sporadic", "discontinuous" and "continuous" permafrost. The sporadic permafrost is the territory in which the peaty stows are frozen, while the clay and sandy stows remain basically unfrozen. The discontinuous permafrost is the territory in which the peaty and clay stows are frozen, while the sandy stows remain virtually unfrozen. The continuous permafrost in the territory in which all types of stows, including sandy ones, are frozen.

In fact, the "southern boundaries" of permafrost for each type of soil should be viewed as rather approximate because of long-term fluctuations of climatic parameters. In this context, for each ground type there should exist a characteristic region of persistent snowbanks with the corresponding freezing frequency. The problem of determination of such regions is not considered in this paper.

Prognosis of the permafrost thaw in grounds of different composition may be characterized by the rate of permafrost thaw V near the southern boundary and by the maximum (by the year 2025) "break-off" of the permafrost roof from the STL sole depth H also near its southern boundary.

As a result, the following mean prognostic estimates were obtained:

- in peat: $V = 0.05\mathrm{m\,year^{-1}}$, $H = 1.5\,\mathrm{m}$.
- in clay: $V = 0.10\mathrm{m\,year^{-1}}$, $H = 3.0\,\mathrm{m}$.
- in sands: $V = 0.14\mathrm{m\,year^{-1}}$, $H = 4.2\,\mathrm{m}$.

Summing up the results of the prognostic calculations, we should note that in the territory of Russian cryolithozone two large regions are differentiated: S - zone of conditionally stable permafrost (about 50% of modern permafrost area) and D - zone of its potential degradation (another 50% of modern permafrost area), each having three subzones. The designations used mean that if the global warming continues only until the year 2025 and the climatic conditions are not further changed for an indefinitely long time, then after a long time period (possibly in a few millennia) the permafrost in zone D will thaw in all types of soils, while it will be totally or partially preserved in zone S.

The subzones differentiated in the direction from south to north have the following meaning:

- D_1, complete thaw of permafrost by 2025;
- D_2, partial thaw: sandy and clay stows remain basically unfrozen; in peaty stows the permafrost roof lowers, by 2025 its "break-off" will be within the range from 1.5 to 0.5 m;
- D_3, slight thaw: sandy stows remain basically unfrozen; in clay stows the permafrost roof lowers, its "break-off" starts nowadays, by 2025 its "break-off" will be 3-1.5 m; in peaty stows the permafrost roof goes down, by 2025 its "break-off" will range from 0.5 to 0 m;
- S_1, sporadic permafrost: in sandy stows the permafrost roof is lowered, its "break-off" begins nowadays and will range from 4.2 to 2.2 m by 2025;

in clay stows the permafrost roof is lowered, its "break-off" will begin in 10 years and be 1.7-0 m by 2025; peaty stows will remain frozen;

- S_2, zone of discontinuous permafrost: in sandy stows the permafrost roof is lowered, its "break-off" will start in 15 years and reach 2-0 m by 2025; the permafrost will be preserved in clay and peaty stows;
- S_3, zone of continuous permafrost: the permafrost is preserved in all types of stows.

In all of the described regions the ground temperature at the 10-m depth will increase and this requires special prognostic estimates.

Cryogenic cracking was predicted using the technique proposed by Grechishchev et al. (1984). The input data for this computational procedure are: (a) climatic data including the air temperature and snow cover, (b) properties of grounds including physical, thermophysical and mechanical ones. The snow cover thickness was taken from the perennial meteorological data reported in the Climatic Handbook (1967).

To predict areals of frost cracking, critical minimal winter temperatures under the snow cover were determined for different soil types: for peat, -12°C; for clay, -14°C; for sand, -20°C. The areas of modern soil cracking were compared to those expected in 30 years, i.e. by 2025. In both cases the calculated boundaries correspond to the cracking frequency 0.2-0.3. Comparison shows that by 2025 one should expect a strong reduction of the cracking areals. Under natural conditions it will totally stop over vast territories. Specifically, this is pertinent to the Yamal peninsula. Calculations show a vast zone where the cracking of soils in the permafrost area will be reduced to the cracking of STL alone, since there in 2010-2015 the permafrost roof will start to break off from the STL sole.

Realistic estimates of possible changes in the permafrost distribution show that by 2025 its total thaw and disappearance is possible only within a 50-100 km wide band along its actual southern boundary that accounts for an insignificant share of the existing permafrost-bound territory. However, noticeable changes in the temperature, permafrost structure and manifestation of geocryological processes will occur over nearly 50% of the permafrost territory.

Special mention should be made of the occurrence of new specific processes in zone D (see above) associated with the appearance of a thawed layer between the lowering permafrost roof and the STL sole. In this watered layer there arises a seasonally oscillating cryogenic pressure of ground water which will lead to the formation of icings, frost mounds, partial flooding of cellars and underground parts of buildings, more complex conditions for drilling, etc.

A very important problem for the northern civil engineering is the probability of the thawing of massive underground ice bodies. Analysis shows that todays southern boundary of their distribution within Russia is in the S zone mentioned above, and evidently they will not thaw until 2025.

Acknowledgments: Analysis of the observational data for 1996-1998 of the active layer and of the thermal regime of the soil are carried out with support of the Russian Fundamental Research Foundation (Grant N 98-05-64633). The prediction of the permafrost distribution and geocryological processes (including thawing of massive ice bodies) were supported by John and Catherine MacArthur's Foundation (grant No. 97-47007-FSU/EKP) and the Russian Fundamental Research Foundation (grant No. 97-05-65967).

References

1. Atlas SSSR (Atlas of the USSR) (Moscow: Izd. GUGK, 1984) (in Russian).
2. Balobaev, V.T., Pavlov, A.V. (1998) Evolution of the cryolithozone of West Siberia under contemporary and expected climate changes, *DAN 363*, No. 1, 7-9 (in Russian).
3. Grechishchev S.E., Chistotinov L.V., Shur Yu.L. (1984). *Bases of modelling cryogenic physical processes*, Nauka P.H., M., pp.236.
4. Grechishchev S.E. (1997) Prediction of permafrost thawing and distribution and cryogenic cracking within the Rassian territory under global warming. *Earth Cryosphere*, **1**, 59-65, (in Russian).
5. *Handbook of the USSR climate.* (1967) Leningrad, Gydrometeoizdat, vol. 1-34, (in russian)
6. Mackay, J.R. (1995). Active Layer Change (1968-1993) following the Forest-Tundra file near Inuvik, N.W.T., Canada. - In: *Arctic and Alpine Research*, **27**, No 4, 323-336.
7. Pavlov A.V. (1994). Current Change of Climate and Permafrost in the Arctic and Sub-Arctic of Russia. *Permafrost and Periglacial Processes*, **5**, 101-110.
8. Pavlov A.V. (1996). Permafrost - Climatic monitoring of Russia: analysis of fild data and forecast. *Polar Geography*, **20**, N1, pp. 44-64.
9. Pavlov A.V. (1998) Evolution of Permafrost in Siberia at contemporary Climate Change. *Proceedings of Second International Workshop on Energy and Water Cycle* in GAME-Siberia, 1997. - Nagoya University COOP, N4.
10. Vyalov S.S.,Gerasimov A.S., Zolotar A.I., Fotiev, S.M. (1993) Ensuring structure stability and durability in permafrost ground areas at global warming of the Earth's climate. *Proc. Sixth Int. Conf. on Permafrost*, V. 1, South China University of Technology Press, Beijing, China, pp. 995-960.
11. Zhang, T., Osterkamp, T.W. (1993) Changing climate and permafrost temperatures in the Alaskan Arctic. *Proc. Sixth Int. Conf. on Permafrost*, V. 1, South China University of Technology Press, Beijing, China, pp. 783-788

(Received 01 March 1999, accepted 06 May 1999)

Thermally Induced Temporal Strain Variations in Rock Walls Observed at Subzero Temperatures

Matthias Wegmann and G. Hilmar Gudmundsson

Laboratory of Hydraulics, Hydrology and Glaciology (VAW)
ETH-Zentrum, CH-8092 Zürich

Abstract. It has been predicted theoretically that frost weathering may take place in rock material at subfreezing temperatures. These predictions have been confirmed in laboratory experiments. The importance of such frost weathering mechanisms in natural environments have, however, remained an unsettled question.

We present and discuss *in situ* measurements of temperature and strain conducted within permafrost rock walls at 3600 m asl, in the Jungfraujoch-Aletsch region (Valais, Switzerland). From the spatio-temporal variations of the temperature field, the rate of freezing and thawing is estimated. We find both freeze and thaw processes in the rock walls at negative temperatures. In fact, both freezing and melting of ice as well as concomitant temporal changes in strain regime are observed in regions were the bedrock is subjected to permafrost conditions.

The annual variations in rock temperatures correlate with the rock deformations. Extensions are observed during cooling and contractions during warming periods. Furthermore, the spatial variation in strain is affected, to some degree, by the presence of a mechanically active joint system.

1 Introduction

The breakdown of rocks due to frost action is considered to be of fundamental importance in the formation of landscapes in periglacial environments [1]. A number of different possible frost-cracking processes have been proposed. The traditional idea of frost weathering is based on the 9% volume expansion of water while freezing. This so-called *volume-expansion model* predicts, that numerous freeze-thaw cycles of the interstitial water will result in rock fatigue. Important requirements for this process to be effective are a high saturation level ($\geq$ 91%), a hydraulically closed pore system and a large number of freeze-thaw cycles [2] [3]. In nature, these conditions only exist in the vicinity of the rock surface, where diurnal and annual temperature variations are large.

Permafrost is widespread in high alpine rock walls. The term permafrost refers to the thermal state of a perennially frozen ground regardless of its composition or ice content. The maximum seasonal penetration of the 0°C isotherm defines the thickness of the active layer situated above the permafrost zone [4]. Frost weathering according to the volume expansion model must be expected in the active layer [2]. It has been a subject of debate

whether below the active layer, that is within the permafrost zone, frost weathering processes may also be expected.

A reappraisal of frost damage processes was first demanded by Mellor [5] on the basis of his observation of unfrozen mobile water in cold rocks. According to theoretical considerations, permafrost conditions are a requirement for frost weathering by segregation ice growth in microcracks [6] [7]. The *segregation-ice model* was also confirmed by a laboratory experiment on a sandstone sample subjected to a fixed temperature gradient [8].

A further weathering process for permafrost rocks was proposed by Thrap [9]. Seasonal meltwater intrusion in the joint system of permafrost rocks should refreeze at depth and enlarge the rock fissures. This *frost wedging* idea in solid rocks is theoretically described, however its effectiveness is still unclear.

Neither the segregation ice model nor the frost-wedging idea were investigated in natural surroundings. The existence, the relevance and the frequency of frost weathering processes in permafrost rocks has remained an unsettled question.

In this paper, we present and discuss *in situ* measurements of temperature and strain made within permafrost rock walls at the Jungfrau east ridge 3600 m asl [10]. We show, that freezing and thawing is not limited to the active layer, but also takes place within the permafrost zone itself. Furthermore, by analysing the temporal variation in the rate of thawing and freezing and the corresponding variation in strain, we find strong evidence for frost weathering within the permafrost zone.

2 The Study Site

On top of the Jungfrau east ridge, an antenna station (Fig. 1) is situated at 1 km distance from Europe's highest railway station at Jungfraujoch. The access to this antenna station is through a tunnel. At 3600 m asl two branch galleries lead to the surface on both sides of the mountain ridge. These branch galleries provide an easy access to the cliff surfaces on the north and the south sides of the ridge.

The atmospheric climatic conditions at Jungfraujoch are recorded by an automatic meteorological station operated by the Swiss weather office. The mean annual air temperature is approximately $-8°C$, and in the bedrock continuous permafrost is present. The lithologies at the investigation site consist of chlorite-sericite-gneiss of the Innertkirchen-Lauterbrunnen cristalline unit. These gneisses are close to a major thrust plane and are therefore tectonically strongly deformed and internally imbricated. The schistosity dips approximately 30° towards south. The dominant and mechanically active joint system strikes in a north-easternly direction and dips sub-vertically. As observed at a recent building construction site nearby Jungfraujoch, these joints are partly filled with ice [11]. Although these lithologies are tectonically strongly deformed by several orogeneses [12], they are nevertheless sound and massive.

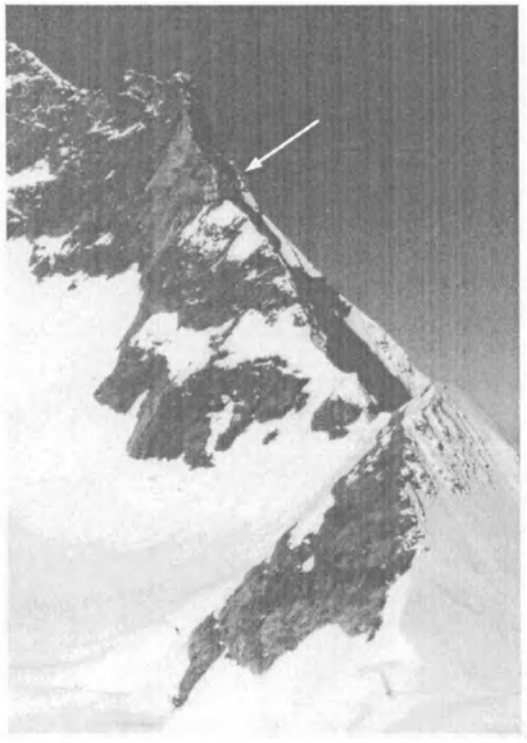

Fig. 1. Jungfrau east ridge with the antenna station. View from Jungfraujoch.

3 Measurements and Results

In Summer 1995, two twenty meters deep, slightly inclined boreholes were drilled out from the branch galleries towards the cliff surfaces. Each borehole was equipped with a six-point extensometer for measuring axial strain. In addition, eight thermistors were installed to monitor the rock temperatures. The thermistors were calibrated at five different temperatures and the absolute accuracy was a few hundredths of a Kelvin. The extensometers were factory-calibrated to a high accuracy (better than $\pm 0.02\,\mathrm{mm}$). The accuracy was further improved by accounting for the linear thermal expansion of the extensometer rod. All sensors were linked to a datalogger station and the readings were transmitted via telephone modem. Temperature and strain readings were recorded twelve times daily.

With an extensometer the axial displacement of the rock relative to a fixpoint is measured. The natural strain of the rock in an axial direction is calculated by $\varepsilon_{xx} = \ln(l_1/l_0)$, where l_0 is the initial distance between two extensometer fixpoints at time t_0 and l_1 the new distance at time $t_1 > t_0$.

The position of the boreholes and the sensors relative to the ridge surface were surveyed.

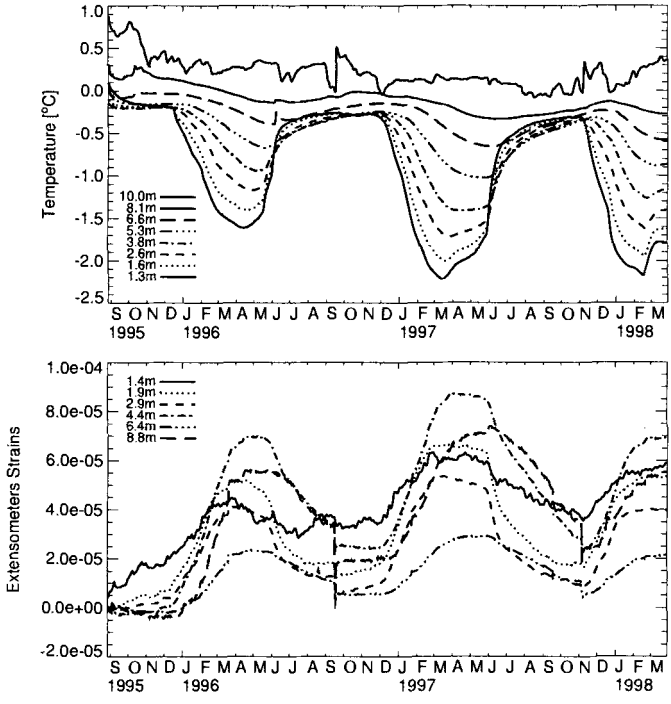

Fig. 2. Rock temperature and strain measurements in a borehole on the south side of the Jungfrau east ridge. The borehole crosses the mechanically active joint system at an acute angle and the deformations are therefore interpreted as joint opening and closing.

In Fig. 2 the strain and the temperature values measured by sensors installed in a borehole on the south side of the mountain ridge are plotted against time. The outermost thermistor is 1.3 m below the cliff surface. The rock temperature record shows clear annual variations at that depth. As expected, the amplitudes of the annual temperature wave decrease and the phase shifts with depth. The deepest sensor is at a depth of approximately 10 m. The temperature readings at this depth are affected by the proximity of a man-made air ventilated tunnel, from which the drillings were performed.

Annual recurring variations are seen in the strain record (Fig. 2). The temporal strain variation is correlated with the annual temperature variation. Extensions are observed during cooling and contractions during warming phases. This pattern can be explained by seasonal freezing of water and thawing of ice in rock fissures. The two constant shifts in the strain readings seen in Fig. 2 in September 1996 and November 1997 are artefacts caused by accidental mechanical impacts on the extensometer head.

The amount of water that freezes (or ice that melts) at a given depth can be estimated by separating the effects of conduction and latent-heat release. An analogous approach has been used to identify meltwater infiltration in a

snow cover [13] [14]. The one-dimensional heat conduction equation may be written as

$$\rho C \frac{\partial T}{\partial t} = \frac{\partial}{\partial z}\left(K \frac{\partial T}{\partial z}\right) + H, \tag{1}$$

where T is temperature, t time, K thermal conductivity, ρ density, C heat capacity, and H volumetric rate of local internal energy sources and sinks. The material properties of the rock (ρ, C, K) were determined from core samples [10]. The spatial gradient ∇T is, in general, variable in all three dimensions. The direction of the heat flow through the Jungfrau east ridge is, however, dominated by the topography and in the region of the borehole the heat flow direction is primarily perpendicular to the ridge surface [10]. The surface-perpendicular depths of the sensors have therefore been considered in the analysis.

The measured temperature field as a function of depth and time was interpolated by applying a two-dimensional, tensor-product spline interpolant (Fig. 3). Apart from a small region, where the readings are affected by the man-made tunnel, the temperatures are below the freezing point throughout the whole observation period. This thermally undisturbed region is completely within the permafrost zone, and none of the thermistors is within the active layer.

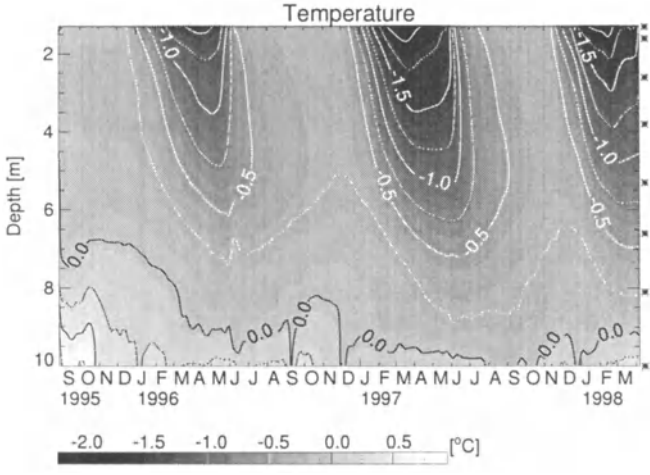

Fig. 3. Temperature as function of depth and time. Thermistor locations are indicated by a star on the right side.

On the basis of the temperature field (Fig. 3) the volumetric rate of local internal energy sources and sinks (Equation 1) was calculated. If the calculated energy rate (H) is the sole result of freezing and melting, then a refreezing rate can be calculated as $H\,L_f^{-1}$, where L_f is the latent heat of fusion ($L_f = 3.338 \times 10^5\,\mathrm{J\,kg^{-1}}$). In Fig. 4 the refreezing rate is plotted as a function of time and depth.

Between 1.3 m and 7 m depth (within the permafrost zone) an annually repeating pattern with positive and negative refreezing rates can be observed (Fig. 4). A cold wave starts to propagate downward from the surface in December of both years. Near the surface this freezing phase usually ends in February, but at a depth of approximately 6 m, the freezing period lasts one or two months longer. In early summer (June, July) a melting impulse can be observed, which penetrates almost instantaneously to a depth of some 5 m.

To compare the calculated refreezing rates with the extensometer measurements, a field of strain rates ($\dot{\varepsilon}$) as a function of depth and time is plotted in Fig. 5. The extensometers do not extend to the same depth as the thermistors, but for comparison the y axes in Figs. 4 and 5 have been plotted to cover the same range. Within the permafrost region, we observe a strongly correlated temporal and spatial variation in the calculated refreezing rates and the measured strain rates. Extensions are measured during freezing and contractions during melting conditions.

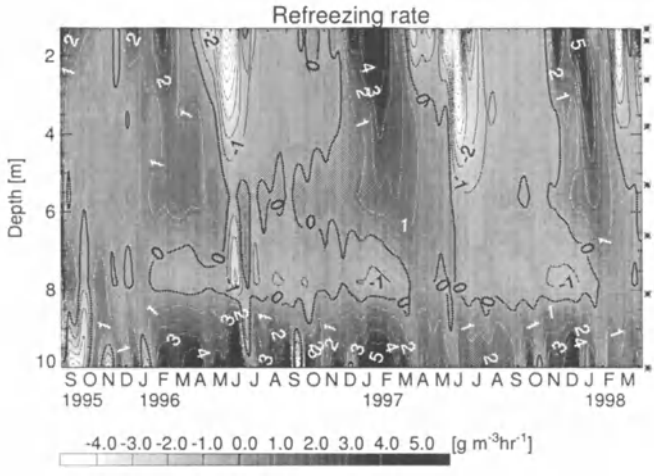

Fig. 4. Local internal refreezing rate as a function of depth and time as calculated from temperature gradients.

4 Conclusions

By estimating the effects of thermal diffusion using the one-dimensional heat conduction equation the rate of freezing and thawing was calculated (Fig. 4). Apart from a small region where the temperatures are affected by a man-made tunnel, an annually repeating pattern of freezing and thawing can be observed (Fig. 4). This gives rise to internal heat production and annihilation. Even in permafrost with a small ice content (some volume percent) changes in the permafrost distribution are strongly attenuated by such latent heat production [15].

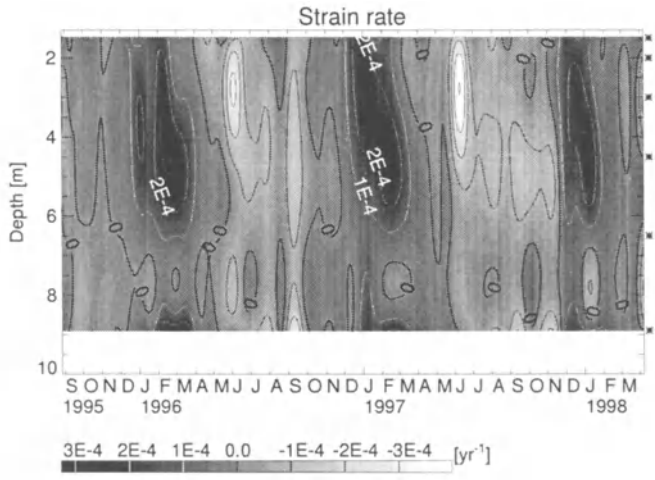

Fig. 5. Strain rate as a function of depth and time. The extensometer positions are indicated by a star on the right side.

In the winter months a freezing front slowly penetrates from the rock surface to the depth. On the other hand early summer melting advances very fast (Fig. 4). This melting impulse can be explained by the intrusion of snow melt water in the vertically-oriented dominant joint system. In the cold permafrost-rock material this water should immediately refreeze and result in a volume expansion (frost-wedging [9]). However, the strain measurements show the opposite, and the melting impulse results in a contraction in the bedrock (Fig. 5).

In the permafrost zone, the calculated refreezing rates (Fig. 4) and the measured strain rates (Fig. 5) show a strongly correlated temporal and spatial variation. Contraction rates were observed in melting regions and expansion rates at freezing locations. This is a clear indication of freeze-thaw processes in the permafrost rock walls. A similar thermo-mechanical behaviour was already observed at a construction site at Jungfraujoch [11]. We would expect such a strain behaviour as a result of the volume expansion model [2]. However, the maximal freezing rate is at a location where the bedrock is approximately $-1.5°C$ cold (Figs. 3, 4). These rock temperatures contradict the thermal requirements of the volume expansion model.

The observed thermo-mechanical behaviour could also be a result of ice segregation processes in the rock wall [7]. The thermal requirements for this assumption are met. Nevertheless, it is not possible to prove such an assumption on the basis of our measurements.

Although the presented temperature and strain measurements clearly indicate freezing and thawing processes in a permafrost rock wall, it is not possible to definitely identify the underlying processes. Of the two permafrost weathering models frost-wedging and ice-segregation the latter seems

more likely to describe our observations. Further field investigations are necessary to understand frost weathering processes in permafrost rock walls. In future investigations rock moisture measurements could help to detect water migration processes.

References

1. Embleton C. King C. A. M. (1975) *Glacial geomorphology.* John Wiley & Sons, New York. 573p
2. McGreevy J. P., Whalley W. B. (1982) The geomorphic significance of rock temperature variations in cold environments: A discussion. *Arctic and Alpine Research.* **14(2)**, 157–162
3. Matsuoka N. (1991) A model of the rate of frost shattering: Application of field data from Japan, Svalbard and Antarctica. *Permafrost and Periglacial Processes.* **2(4)**, 271–281
4. Burn C. R. (1998) The active layer: two contrasting definitions. *Permafrost and Periglacial Processes.* **9(4)**, 411–416
5. Mellor M. (1970) Phase composition of pore water in cold rocks. *CRREL report.* **292**, 61p
6. Walder J., Hallet B. (1985) A theoretical model of the fracture of rock during freezing. *Geological Society of America, Bulletin.* **96(3)**, 336–346
7. Walder J., Hallet B. (1986) The physical basis of frost weathering: Towards a more fundamental and unified perspective. *Arctic and Alpine Research.* **18**, 27–32
8. Hallet B., Walder J. S., Stubbs, C. W. (1991) Weathering by segregation ice growth in microcracks at sustained subzero temperatures: Verification from experimental study using acoustic emissions. *Permafrost and Periglacial Processes.* **2(4)**, 283–300
9. Thrap T. M. (1987) Conditions for crack propagation by frost wedging. *Geological Society of America, Bulletin.* **99(1)**, 94–102
10. Wegmann M. (1998) *Frostdynamik in hochalpinen Felsw¨anden am Beispiel der Region Jungfraujoch–Aletsch.* Mitteilungen No.161 der Versuchsanstalt f¨ur Wasserbau, Hydrologie und Glaziologie. Gloriastrasse 37-39, ETH-Zentrum, CH-8092 Z¨urich.
11. Wegmann M., Keusen H. R. (1998) Recent geophysical investigations at a high Alpine permafrost construction site in Switzerland. In *Proceedings of the 7th International Permafrost Conference,* Yellowknife, Canada. Nordicana Series. 1119–1124
12. Abrecht J. (1994) Geologic units of the Aar massiv: A critical review. *Schweizerische Mineralogische und Petrographische Mitteilungen.* **74(1)**, 5–27
13. Echelmeyer K., Harrison W. D., Clarke T. S., Benson C. (1992) Surficial glaciology of Jakobshavns Isbrae, West Greenland: Part II. Ablation, accumulation and temperature. *Journal of Glaciology.* **38(128)**, 169–181
14. Pfeffer W. T., Humphrey N. F. (1996) Determination of timing and location of water movement and ice-layer formation by temperature measurements in sub-freezing snow. *Journal of Glaciology.* **42(141)**, 292–304
15. Wegmann M., Gudmundsson G.H., Haeberli W. (1998) Permafrost changes in rock walls and the retreat of Alpine glaciers – thermal modelling approach. *Permafrost and Periglacial Processes.* **9(1)**, 23–33

(Received 29 March 1999, accepted 14 April 1999)

Soil Microstructure and the Thermodynamic Behaviour of Permafrost Affected Soils

Thomas Leslie White

Geotechnical Science Laboratories, Carleton University 1125 Colonel By Drive, Ottawa ON K1S 5B6 Canada

Abstract. The thermodynamic conditions within permafrost affected soils at temperatures below 0°C are such that there is continuing translocation of water in conjunction with the formation of ice and displacement of particles. The microstructure of freezing soils is largely responsible for the thermodynamic properties within permafrost. Microstructure controls the free energy of soil water for a given water content and the dependence of unfrozen water content or temperature. The thermal properties, strength and deformation, transport phenomena and other characteristics of frozen ground at the macroscopic level are determined by these relationships.

1 Introduction

The thermodynamic conditions within frozen ground at temperatures just below 0° are such that there is a continuing translocation of water in conjunction with ice formation and displacement of soil particles. Washburn [25], French [13] and White [26,27] put forward hypotheses to explain the upward and downward movement of soil particles (skeleton components and plasma) resulting from freezing and thawing. Corté [7] reported on separate experiments which involved cycles of freezing soil from the top or from the bottom up and then thawing from the top. He inferred from the grain size analysis of the soil samples that during the freezing cycles, there was a tendency for the fine particles ($<74\mu$m) to migrate downward from the freezing plane and for the coarser grains to move up. Van Vliet-Lanöe's [23] review of frost effects summarised the major factors for soil structure in cold environments, including ice lensing, frost heaving, soil solute concentration, degree of cryodessication and periglacial movements. Cryoturbation refers to processes which makes soil surfaces unstable. They are responsible for internal displacement and mixing of materials from different soil horizons.

Platy structure (Van Vliet-Lanöe, [23]; Gubin, [14]) is commonly associated with freeze-thaw processes and ice lens formation. Platy microstructure represents isoband and banded fabric (Brewer and Pawluck, [3]; White, [26,27]; McMillan and Mitchell, [19]; Dumanski and St. Arnaud, [8]). Distinct fabric types e.g., Fox and Protz [12], Fox [10], Smith et al., [22] and White and Fox [29] for Turbic Cryosols have been related to the influence of cryogenic processes active in soils exposed to seasonal freezing and for soils affected by permafrost. A fundamental consequence of the thermodynamic relations

is the development of cryosuction - a state of lowered pressure in the water phase which is responsible for water movements leading to frost heave, as well as for consolidation effects and the development of particle aggregates.

This paper compares cryogenic fabric types which have developed in response to prolonged periods of freezing (between 12 and 20 months) followed by shorter periods of thaw (two to three months) in a silt used in a large scale ground freezing experiment with fabrics which develop in small scale freeze-thaw experiments. These experiments have provided information on thermodynamic consequences of freezing on macroproperties such as hydraulic and thermal properties. The observed reorganisation of soil fabric components have been analysed for the cumulative effects of particle aggregation on unfrozen water content and thermal and hydraulic properties.

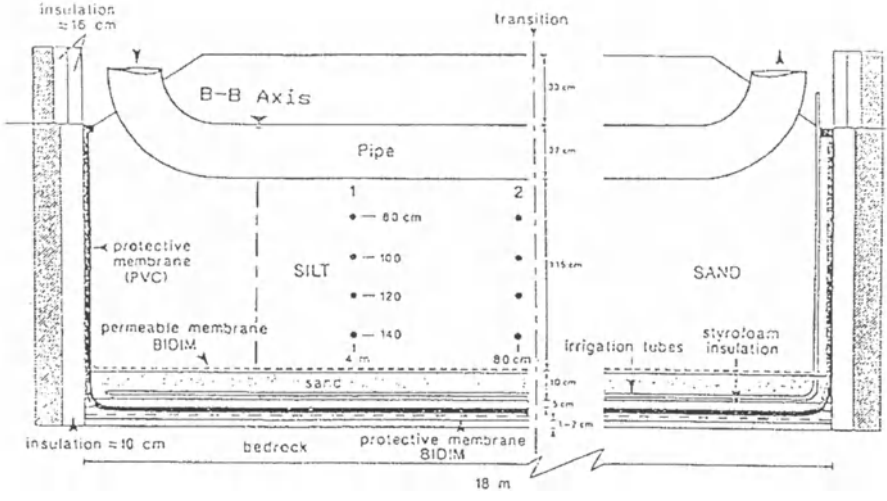

Fig. 1. Longitudinal cross-section of ground freezing experiment

2 Methods and Materials

The Canada-France Pipeline Ground Freezing study (Williams et al., [35]) was carried out in the controlled environment facility of the Centre de Géomorphologie, C.N.R.S., located in Caen, France. The totally enclosed, temperature controlled test facility was initially described by Burgess et al., [4] and after additional instrumentation, by Carleton University [6]. The refrigerated hall is 18 m long by 8 m wide and 5 m high and equipped with a 1.8 m deep basin. The test basin was specially prepared to isolate the thermal and hydraulic regimes and to carefully control experimental conditions. An 18 m

long by 27 cm diameter uninsulated steel pipe was buried in initially unfrozen soil to a depth of 60 cm below surface, so that it transected a frost-susceptible silt designated as MC (silt with low plasticity) by the Unified Soil Classification System and a non-frost-susceptible sand (Fig. 1). During freezing periods the air temperature was maintained at -0.75°C and pipe temperature at -2°C for the first cycle while the pipe temperature was maintained at -5°C for the subsequent three cycles of freezing.

3 Soil Samples and Preparation

After four cycles of freezing and thawing during which only part of the silt (Fig. 2) was frozen around the pipe and immediately adjacent to the pipe, 29 samples (8.5cm × 6.5cm × 5) were taken for micromorphological analysis.

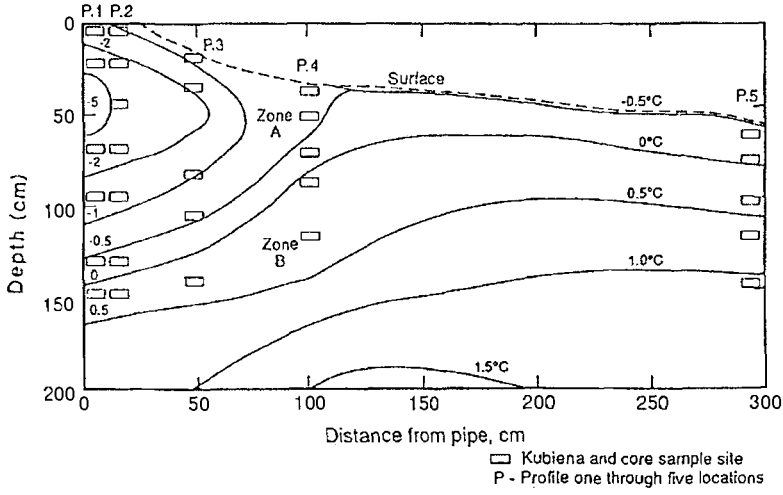

Fig. 2. Sampling locations and position of isotherms at the end of the fourth freeze cycle

The samples were from five locations in a hand dug trench, in the centre of the silt section of the experiment. The sampling was carried out according to procedures outlined in Fox et al. [11] and every effort was taken to obtain all samples in an undisturbed condition (that is, to minimise damage to the samples such as stress cracks).

Soil thin sections were prepared from the samples after they were impregnated with a polyester resin containing a fluorescent dye (Vvitex OB, Ciba-Geigy). The methodology for sample impregnation is widely documented by Fitzpatrick [9], Murphy [20] and Fox et al. [11]. Given the presence of an

identified swelling clay mineral smectite (White, [26]) which would lead to shrinkage cracks if air dried, soil water replacement was undertaken using acetone.

3.1 Effects of changes in soil microstructure

Soil micromorphology is the study of the arrangement of the soil constituents and associate pores in an undisturbed state of the soil at a particular time (Kubiena, [17]). Micromorphology of the thin sections was described following Brewer [2,3] and the glossary of micromorphological terminology by Howes and White [16]. Soil fabric descriptions were made for vertically oriented thin sections at 12 fold magnification. There is a tendency to regard a soil as simply a collection of mineral particles (grains) of easily defined sizes. The size distribution of these 'elementary particles' (to use a Russian term) leads, at least in engineering terminology, to the classification of a soil as a sand, silt or clay or some combination of these. It is also understood that the grain-size distribution largely determines the size of the pores, or, more precisely, the pore-size distribution. It is also fundamental, at least to the soils engineer, that when the particles are small, of clay size, they may be more or less densely packed, or consolidated (again, in engineering terminology). It is also known that the presence of certain substances in small quantity may effectively cement particles together-a state of affairs which, confusingly, geologists describe as 'consolidated' (Williams, [34]).

All this, however, is too simple a view, as pedologists have known for many years. In particular, elementary particles are often drawn together into aggregates which, in some respects, become the largest 'particles'. This aggregation necessarily will be associated with a large modification of the pore system. Instead of a pore-size distribution following directly from the size distribution of the elementary particles and the closeness of their packing, there is a pore size distribution that can be bimodal. There are then intra-aggregate pores and inter-aggregate pores. Within the two modes a range of pore sizes occurs (Williams, [34]).

3.2 Optical and scanning electron microscope observation of soil micromorphology

The microstructure of soils has been studied for decades, especially for agronomy and related topics. A widely used procedure is to impregnate a soil sample with resin such that thin sections of the strengthened material may be made. The thin sections can be examined with optical or electron microscopy. Examples of two soils which have never been frozen are shown in Plate 1 and Plate 3. The same soils after freezing and thawing are shown in Plate 2 and Plate 4. The microstructure of soils varies strikingly with their lithological nature. The same is true of soils exposed to freezing (Williams, [34]).

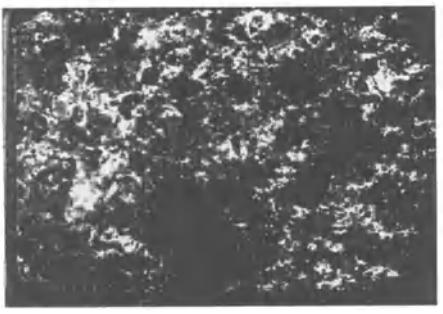

Plate 1. Microstructure of Tourville silt (unfrozen). The frame is 36 mm wide

Plate 2. Microstructure of Moley Clay (unfrozen). The frame is 36 mm wide

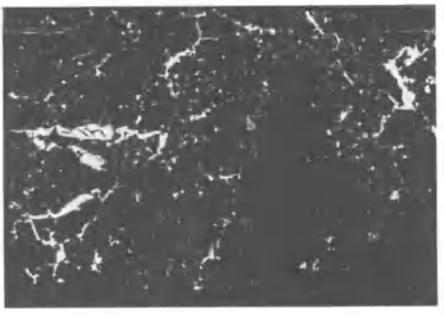

Plate 3. Microstructure of Tourville silt (after one freeze-thaw Cycle). The frame is 36 mm wide

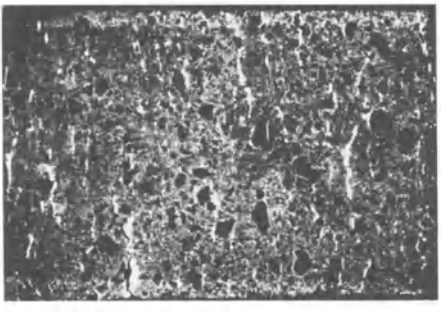

Plate 4. Microstructure of Moley Clay (after one freeze-thaw Cycle). The frame is 36 mm wide

3.3 Microstructure of soils exposed to freezing

Effects of freezing on the microstructure of a soil were investigated, using samples that were taken after thawing, by Harris [15], Bunting [5], Van Vliet Lanöe [23,24] and others. Until recently, however, the importance of these effects for properties of the frozen soil had not been analysed in detail. It has long been evident that freezing modifies geotechnical properties, but Pusch [21] appears to be the first to have directly related microstructure of a soil (as observed in a soil after thawing) to the unfrozen water content. He observed (using an electron microscope) that freezing of a remoulded clay (one in which the natural structure was destroyed by stirring) resulted in aggregation of the clay particles. The unfrozen water content was less, in second and subsequent freezings, over a range of temperature, and this can be understood from the reduction of total pore volume within the aggregates. The inter-aggregate pores on the other hand were enlarged with accumulating ice (Williams, [34]).

Over the last decade, Van Vliet Lanöe [23,24] has shown how modifying the procedures allows not only the study of the structure of newly-thawed

soils but even of the structure of the soil while frozen. In the latter case, a sample taken in the frozen state is effectively freeze-dried and taking care to avoid disturbance, the impregnation with resin is carried out. The sample shown in Plate 5 is impregnated in this way and is actually free of real ice.

The main difference between the newly-thawed soil and the frozen soil is that on melting of the ice bodies larger than pore size, there is a closing of the space which they occupied as the excess water drains away. The sites of the ice segregations do not close completely (certainly not over a short time interval) and persist as discontinuities and elongated enlarged pores. The overall soil volume decreases, although as far as can be ascertained without any significant change in the intra-aggregate porosity during the thaw and consolidation.

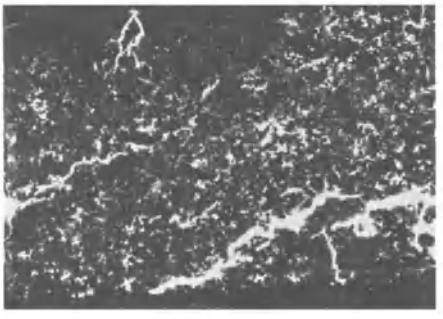

Plate 5. Microstructure of Tourville silt (after five freeze-thaw Cycle). The frame is 36 mm wide

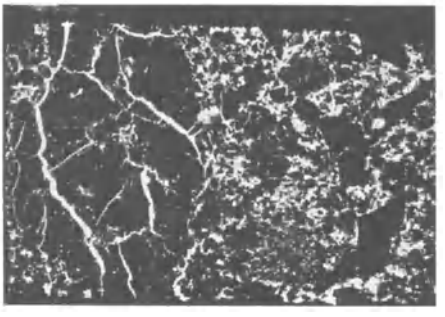

Plate 6. Microstructure of Tourville silt (after ten freeze-thaw Cycle). The frame is 36 mm wide

The aggregates may themselves be formed, or enhanced, by the freezing process as noted (compare Plate 1 and Plate 3) and the intra-aggregate porosity may continue to change with further freeze-thaw cycles (White and Williams [30]). Microstructural changes occur progressively although less marked for each succeeding cycle (compare Plates 5 and 6). After about ten cycles little change is seen in the microstructure. However Russian workers have observed that there can be breakdown of the elementary particles themselves over many cycles such that there is a gradual change in grain size distribution (Yershov, [37]).

Frequently there is a sorting of particles in the vicinity of ice accumulations with a closer packing of the particles towards the ice. The images, Plates 7 and 8, were obtained by scanning electron microscopy and accordingly are distinct in appearance (as well as in scale) from those obtained using transmitted light and optical microscopy. The packing of the particles is clearly seen.

When the Caen silt was saturated (that is, the soil pore space was essentially filled with water), a layered structure developed that did not dir-

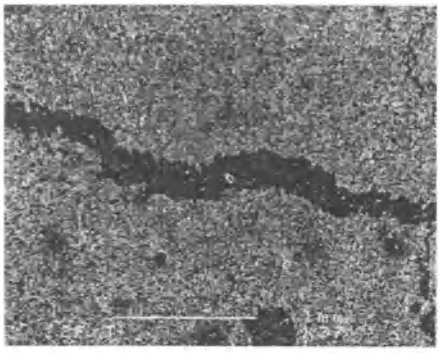

Plate 7. Scanning electron micrographs of packing of particles adjacent to lense

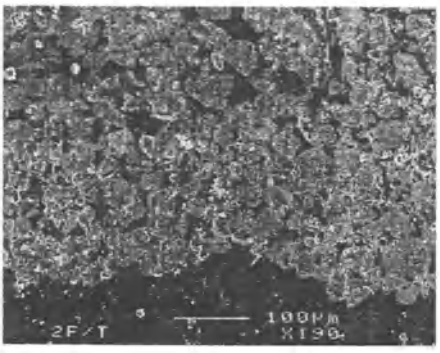

Plate 8. Scanning electron micrographs of silt and clay particles above planar pore

ectly correspond to the location of the ice layers. At least, the sorted layers of particles appeared to be more frequent than the ice layers even though the latter were numerous. Distinct gross morphologies were observed in the samples taken from the frozen soil annulus surrounding the buried chilled pipeline. White [26] Van Vliet-Lanöe and Dupas [24], White and Williams [30–32], and Williams [33] noted that the soil structure was altered directly in response to cryogenic and freezing-induced consolidation processes, and that the new cryogenic structures were essentially maintained through subsequent freeze-thaw cycles. White and Williams [31] furthermore showed progressive, less abrupt changes in soil aggregation and porosity (including the development of new pore shapes) as a function of the number of freeze-thaw cycles. They also showed that similar types of soil structure developed within a range of frost susceptible soils compacted to two dry densities.

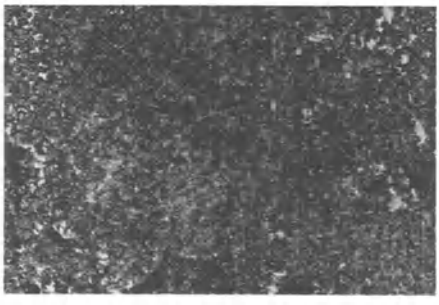

Plate 9. Granodic-porphyroskelic morphology of unfrozen Caen silt. The frame is 12 mm wide

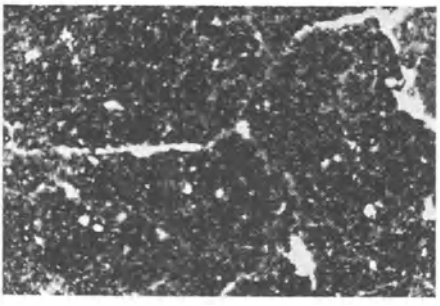

Plate 10. Fragmic morphology in Caen silt (after one freeze-thaw cycle). The frame is 12 mm wide

Plate 11. Fragmic morphology in Caen silt (after two freeze-thaw cycle). The frame is 12 mm wide

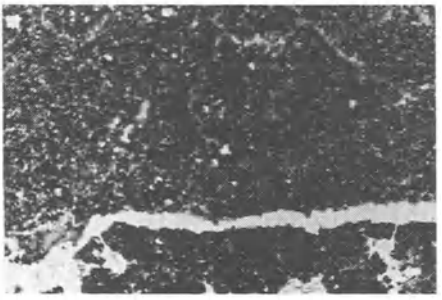

Plate 12. Fragmic morphology in Caen silt (after four freeze-thaw cycle). The frame is 12 mm wide

Two dominant morphologies were observed to have developed in the zone around and immediately adjacent to the buried chilled pipeline. Fragmic and fragmoidic fabrics developed from a granoidic- porphyroskelic intergrade (Plate 9) which has been created through compaction. Plate 10 shows the material after being subjected to only one cycle of freezing (to a temperature of -2°C) and thawing. The fragmic fabric designates morphology having compacted aggregates separated by planar pores. Further freeze-thaw cycles (Plate 11, after two cycles, and Plate 12 after four cycles) resulted in the development of a second distinct soil fabric. The fragmic fabric was observed to change to a fragmoidic fabric after exposure to an additional two to three freeze-thaw cycles. The fragmoidic fabric was characterised by planar pores and coalesced, often elongated soil units. These elongated pores (planar pores) develop at sites where ice segregation had taken place. Particle aggregation which occurs between planar pores is also observed to be modified in successive cycles. The progressive nature of the microstructure modifications with successive freeze-thaw cycles is of particular interest. Scanning Electron Microscope (SEM) observations of a planar pore created by an ice lens (Plate 8) shows that a well-defined zone of compaction developed along the upper boundary of the pore. Interparticle porosity within the 300m thick zone of compaction is much lower than that in the zone above. Ice segregation through its expansive pressure and water cryosuction are responsible for microcompaction and particle reorientation required to create planar pores. Maximum planar pore widths (up to 70m) were observed in the fragmic fabric which developed after exposure to one freeze-thaw cycle (White and Williams, [30]). Planar pore widths were observed to increase to a maximum of 200 m in the fragmoidic fabric which developed after exposure to subsequent freeze-thaw cycles.

The microstructural changes are, therefore, related to the thermodynamically imposed, effective stress which develops within freezing soil (differences of pressure between the phases, Williams and Smith, [35], Williams, [35]). Yershov [37] explains that they are responsible, too for the development of fis-

sures and other macroscopic discontinuities larger than the structures shown in the figures but small enough to be often overlooked when considering the mechanical and hydraulic properties (White and Williams, [31]; Williams, [34]).

3.4 Implications of microstructural alteration of soil structure on hydraulic and thermal properties

The special properties of soils at freezing temperatures arise because of the particular nature of the freezing and thawing process within a fine porous system (Williams and Smith, [36]). Most fundamental is the modification of the freezing point of the water. Because of capillarity and mineral surface adsorption forces, significant amount of the water in fine-grained soils remains unfrozen at temperatures down to several degrees below 0C. In thermodynamic terms the free energy of water in the soil is modified - a fact well-known in soils science and the unfrozen water contents (Fig. 3) are dependent on lithology and grain and pore size composition of the soil (Williams and Smith, [36]).

3.5 Changes of water content

There is no doubt that a layer of some molecules thickness and more of water molecules adsorbed on mineral surfaces undergoes modifications of properties, as well as a lowering of freezing "point". Water remaining unfrozen below -1°C is essentially within this layer (Williams, [34]). Measurements of surface area of the particles can be used to predict unfrozen water content (Anderson and Tice, [1]).

The development of new fabric morphology as a function of freeze-thaw cycles and in particular the reorganisation of soil particles through aggregation has a profound influence on water contents (Fig. 4) both the total water content at +10°C and the unfrozen water content at -2°C. Decreases in pore volume within aggregates has decreased the amount of unfrozen water from one freezing to the next. At a depth of 20 cm below the buried chilled pipe the Time Domain Reflectrometry (TDR) volumetric unfrozen water content of Caen silt at -2°C was observed to decrease from 15% after one cycle of freeze-thaw to 12% after a third freeze cycle. Also of interest is the decrease that took place in the thawed (and drained moisture content, 45% prior to the onset of the first freeze cycle became 36% prior to the second freeze cycle and finally, 32% prior to the third freeze cycle.

Alternation of the soil microstructure, in particular the geometry and size of the pore spaces has also had, it would appear, a profound impact on the amount of water and its chemical potential (free energy, J, per g) held by capillarity and adsorption at temperatures as low as -2°C. A reduction in volume of these soil pores which act as capillaries, due to aggregation, and the creation of larger planar pores has resulted in a net reduction in the

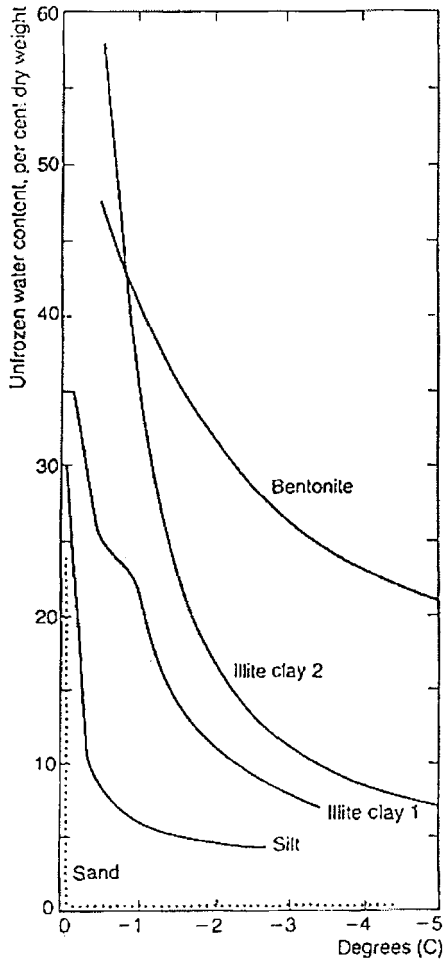

Fig. 3. Unfrozen water contents of saturated soils as a function of temperature

amount of water that Caen silt held prior to the onset of the next freeze-thaw cycle. The tiny pores within aggregates hold only a small volume of unfrozen water, present because of surface adsorption effects.

3.6 Effects of micromorphology on thermodynamic behaviour of permafrost affected soil

The depth of the active layer overlying permafrost and indeed, the exact distribution and extent of permafrost, depends on the thermal conductivity and thermal capacity of the soil, which are highly dependent on the relationships illustrated in Figs. 3 and 4. The thermal capacity of the freezing soil

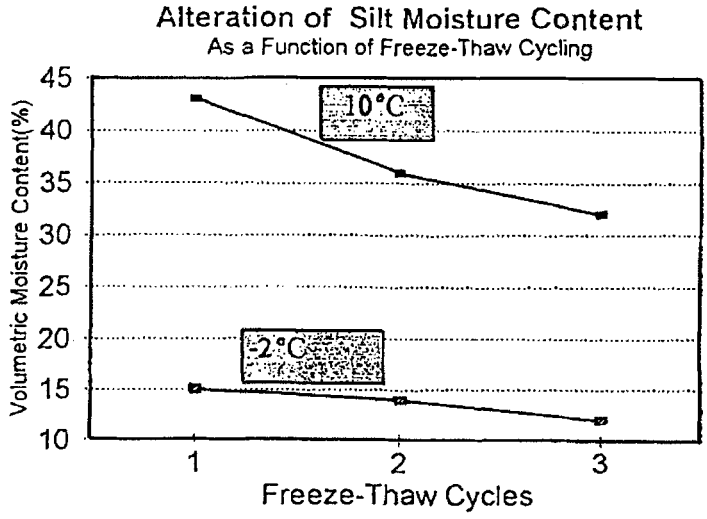

Fig. 4. Unfrozen water contents of Caen silt as a function of temperature and number of freeze-thaw cycles [6]

is primarily due to the latent heat of fusion, exchanged as the proportions of water and ice change with changing temperature. Fig. 5 shows the position of the 0°C isotherm at Day 100 of the ground freezing experiment for the second, third and fourth freeze cycles in the silt adjacent to the buried chilled pipe. The figure shows that the depth of frost penetration from cycles two through four has increased. From this it may be inferred that the silt's thermal diffusivity has increased, thus giving faster penetration of the 0°C isotherm. The thermal conductivity increases from one cycle to the next in response to consolidation of the silt and intense ice segregation (ice has higher conductivity that water). Probably more important though, is the decrease in total moisture content and thus in the heat of fusion, giving smaller heat capacity.

3.7 Soil microstructure as a controlling factor of changes in environmnetal conditions

The observations confirm what is intuitively reasonable. The soil microstructure, because it controls the fundamental thermodynamic behaviour of a freezing soil, and thus the soil's physical and geotechnical properties (density, frost heave, thermal properties etc.), controls the development of specific geocryological features. Depth of active layer, extent of permafrost, creep and solifluction and the forms of patterned ground are the soil's response to external conditions. The precise nature of the response is determined by the soil microstructure.

If the external conditions change for example, a change of climate, the release of a contaminant, or the construction of a pipeline then soil micro-

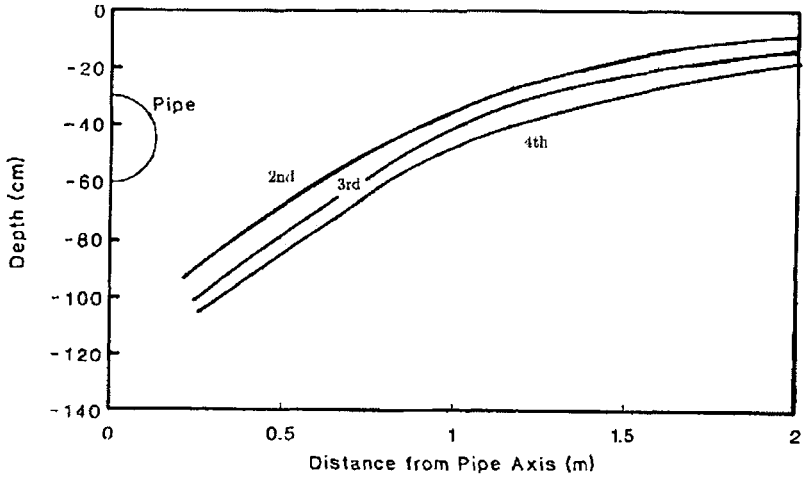

Fig. 5. Position of 0°C isotherm in Caen silt, Day 100 of 2nd, 3rd and 4th freeze cycles [6]

structural changes are to be expected (White and Williams, [32], White and Coutard, [28]). The modified microstructure will dictate the course of subsequent (macroscopic) changes in ground form and conditions. Thus the microstructure of freezing soils in both the product of the environmental conditions and also definitive for the future changes in ground conditions.

Geotechnical engineering in the cold regions largely consists of devising countermeasures to adverse conditions which develop over time. Thus for example building foundations must be designed so that thawing of the ground (as a result of the construction) does not cause damage. In problems of ground contamination the geotechnical engineer must prevent a harmful spreading of the contaminant. In both situations, the appropriate geotechnical response is dependent on predicting what may occur with the passage of time. Such prediction is only possible if the various geotechnical properties are understood and definable with sufficient precision.

4 Conclusions

Soil microstructure determines thermal and hydraulic properties of freezing soils. Experiments in a controlled environmental facility demonstrate this and also show the effects of both large and small scale freeze-thaw cycling experiments in modifying the microstructure.

The development of characteristic features such as hummocks and patterned ground in periglacial terrain are thus ultimately to be traced back to the microstructure of the specific materials and the properties of the soil which result. The behaviour of geotechnically engineered ground is to be similarly understood.

References

1. Anderson, D.M., Tice, A.R., 1972, Predicting unfrozen water contents in frozen soils from surface area measurements. *Highway Res. Rec.* **393**, 12-18.
2. Brewer, R. 1964, *Fabric and Mineral Analysis of Soils*, Wiley, New York.
3. Brewer, R. 1964 and Pawluk, S. 1975 Investigations of some soils developed in hummocks of the Canadian sub-arctic and southern-arctic regions. Morphology and Micromorphology. *Canadian Journal of Soil Science* **55**, 301-319.
4. Burgess, M., Lemaine, G., Smith, M.W., Williams, P.M., 1982, *Etude du gel des sols autour d'une conduite réfroidie enterré dans une station expérimentale.* Phase I. Pour Le Ministére d'Energie, Mines et Resources, Direction de la Physique du Globe, 62 p.
5. Bunting, B.T. 1983. High Arctic soils through the microscope: Prospect and Retrospect. *Annals Amer. Assoc. Geographers*, **73**,4: 609-616.
6. Carleton University, G.S.L., 1985, 1986 and 1988. *Report on the Canada-France Ground Freezing Experiment*, Geotechnical Science Laboratories, Carleton University, Ottawa.
7. Corté, A.E., 1966, Particle sorting by repeated freezing and thawing. *Buil. Peryglacjalny.* 175- 240.
8. Dumanski, J., St. Arnaud, R.J., 1966, A micropedological study of eluvial soil horizons. *Canadian Journal of Soil Science* **46**, 287-292.
9. Fitzpatrick, E.A., 1984, *The Morphology of Soils.* New York: Chapman and Hall Ltd.
10. Fox, C.A. 1983, Micromorphology of an Orthic Turbic Cryosol-a permafrost soil. *Soil Micromorpholgy*, Ed.,P.Bullock and C.P.Murphy, vol.2, 699-705.
11. Fox, C.A., Guertin, R.K., Dickson, E., Sweeney, S., Protz, R. and Mermut, A.R., 1993. Micromorphogy Methodology for inorganic Soils, from Carter, M.R.(ed), *Soil sampling and Methods of Analysis*, Canadian Society of Soil Science, Lewis Publisher, Boca Raton, Florida, pp686-709.
12. Fox, C.A., Protz, R., 1981, Definition of Fabric Distribution to Characterise the Rearrangement of Soil Particles in Turbic Cryosols, *Canadian Journal of Soil Science* **61**, 29
13. French, H.M., 1976, *The periglacial environment.* Longman, London, 309 p.
14. Gubin, S.V., 1993, Structure formation dynamics in Tundra Gryogenic Non-Gleyed Soils (Tundra Cryozems). Joint Russia-America Seminar on Cryopedology and Global Change. *Russia Academy of Science*, p. 201-213.
15. Harris, C. 1980, Micromorphology of soils in soliflucted materials, Okstindan, *Northern Norway. Geoderma*, **23**, 11-29.
16. Howes, J.E., White, T.L., 1991, *Glossary of Terminology for Soil Micromorphology.* Ottawa: Geotechnical Science Laboratories, IR-60, 39 p.
17. Kubiena, W.L., 1938, *Micropedology*, Collegiate Press, Ames, Iowa.
18. Ladanyi, B., Shen, M., 1993, Freezing pressure development on a buried chilled pipeline. *International Symposium on Frost in Geotechnical Engineering, Anchorage, Alaska*, pp. 23-34.
19. Millan, W.J. and Mitchell, J., 1953. Microscopic story of platy and concretionary structures in certain Saskatchewan soils. *Canadian Journal of Agriculture Science* **33**, 178-183.
20. Murphy, C.P., 1986, *Thin section preparation of soils and sediments. Berkhamsted*, Herts, England: AB Academic Publishers.

21. Pusch, R. 1979, Unfrozen water as a function of clay microstructure. *Engineering Geology*, **13**, 157-162.
22. Smith, C.A.S., Fox, C.A., Hargrave, A.E., 1991, Development of soil Structure in some turbic cryosols in the Canadian low Arctic, *Canadian Journal of Soil Science* **71**, 11-29.
23. Van Vliet-Lanöe, B., 1985, *Frost Effects in Soils in Quarternary Landscape Evolution* (J. Boardman, ed.). John Wiley and Sons Ltd., New York.
24. Van Vliet-Lanöe, B., Dupas, A., 1992, Development of soil fabric by freeze-thaw cycles. Its effects on frost heave. *Proceedings of the Fifth International Symposium on Ground Freezing, Beijing*, p. 189-195.
25. Washburn, A.L. 1973. Soil deformation resulting from some laboratory freeze-thaw experiments. *Proc. of the 2nd International Permafrost Conference*, pp. 757-762.
26. White, T.L., 1992, *Cryogenic Alteration of a Frost Susceptible Soil.* Ottawa: Carleton University.
27. White, T.L., 1996, *Cryogenic Alteration of Clay and Silt Microstructure, Implications for Geotechnical Properties.* Carleton University, Ottawa.
28. White, T.L., Coutard, J-P., 1999, Modfication of silt microstructure by hydrocarbon contamination in freezing ground. Contamination in Freezing Ground, Proc. of Conf., Cambridge, 1997. *Polar Record*, vol. **35**, no. 192, Jan 1999, p. 41-50.
29. White, T.L., Fox, C.A., 1996, Comparison of cryogenic features dominant in soils affected by permafrost with those produced experimentally. *Proceedings, 10th International Working Meeting of Soil Micromorphology*, Moscow, July 1996.
30. White, T.L., Williams, P.J., 1994, Cryogenic alteration of frost susceptible soils. *Proceedings of the 7th International Symposium on Ground Freezing*, Nancy, France, 17-24.
31. White, T.L., Williams, P.J., 1996, The Role of Microstructure - Geotechnical Properties of Freezing Soils. Ottawa: *Fifth International Symposium on Thermal Engineering and Science for Cold Regions*, p. 415-426.
32. White and Williams 1997,The influence of Soil microstructure on Hydraulic properties of hydrocarbon contaminated freezing ground. *Conference on Contaminates in Freezing Ground.* Cambridge University, July 9-12 1997.
33. Williams, P.J., 1997, The Freezing of Soils: Ice in a Porous Medium and Its Environmental Significance. *Proceedings: Nato Advanced Study Institute, Italy*, Springer Verlag, pp. 219- 231.
34. Williams, P.J., 1997, Contaminants and Microstructure in frozen ground. *Proceedings: NATO Advances Study Institute, Italy*, Springer Verlag.
35. Williams, P.J., Riseborough, D.W. and Smith D.W., 1993, The France-Canada joint study of , deformation of an experimental pipeline by differential frost heave. *Intern. Journ. Offshore and Polar Eng.*, Vol. **3**, 1, pp. 55-60.
36. Williams, P.J. and M.W. Smith, 1991. *The Frozen Earth.Fundamentals of Geocryology.* Cambridge Press. 306pp.
37. Yershov, E.D., 1998, *General Geocryology* (Translation from the Russian, Nedra 1990). Cambridge University Press, 580 p.

(Received 07 April 1999, accepted 16 April 1999)

Heat Transfer in Heat Storage Arrangements Under Melting

Vladimir A. Alexeev

Scientific and Research Institute of Precision Instruments, Yurlovsky proezd.6.1, Moscow 127490 Russia

Abstract. Heat storage arrangements (HSA) are devices containing a medium, which for appropriately prescribed outside energy source, may experience phase change processes and alternate between liquid and solid states. We present computational results that were obtained for HSAs of realistic form and size. The mathematical description of the model is given for two-dimensional heat conduction incorporating possible phase changes, when either melting or freezing occur. The numerical results are compared with the corresponding experiments for HSAs of different size and form. On the basis of the two-dimensional analysis it was then possible to construct a one-dimensional model with equivalent parameters and producing equivalent results. The investigation suggests to use the model for the design of energy-saving-heat-storage-battery systems.

1 Introduction

Our interest in the solution of melting processes in solid bodies confined to vessels is founded on the actuality of the problem to store heat, in industry and transportation in particular, and in many instances of modern life in general. As a rule, such solutions are obtained by solving a Stefan problem [1]. At early stages of the development one-dimensional problems were usually studied. Later, when designs of the operating elements, such as heat-storage batteries, became complicated, it was necessary to solve a multi-dimensional Stefan problem. This allows to closely analyse the principal physical factors, especially e. g. the dimension and form of the arrangements and their influence on the thermal parameters and the heat transfer performance.

One of the most practical approaches to the solution of such a difficult problem of phase transition is the so-called enthalpy method, [2]. In this paper an equivalence is established between the solutions of a solid-liquid phase-transition problem with moving interface as obtained with the enthalpy method and the classical energy conservation equation. The enthalpy method was then used with its finite difference representation to solve the freezing problem of a liquid in a cubic box, however without taking account of the thermal processes of the container itself.

We are in this paper interested in two main problems. In the first, a modified enthalpy model is employed to calculate for a rectangular cell of a heat-storage battery the thermal processes including the phase transition in

the medium [3]. Besides the phase-transition processes in the medium the model accounts for the heat contained in the wall, and rips of the cell. The second problem deals with an elaborate heat analysis of energy accumulation in a complex construction [4]. We remark that in [3, 4] the influence of the dimension of the body was not studied and neither were the thermal conditions of the entire arrangement as a whole. We make in this paper an attempt to discuss these questions. For that purpose we suggest to apply the finite volume balance to the enthalpy method and to state and solve the two-dimensional heat-transfer problem in a body subject to phase-transition processes, [2].

The advantage of the finite volume-balance technique is that it allows to write down at once the finite difference equations for the elemental cells, thus circumventing the strong local form of the equations yielding differential equations and complicated boundary conditions.

In what follows, the co-ordinates of the cells are fixed; when the temperature in any element reaches the phase-change temperature, the enthalpy method will be applied in this cell and the analysis proceeded with its use.

2 Statement of the Problem

Consider a heat-storage arrangement (HSA) such as displayed in Fig. 1. It consists of a lightly shaded metallic frame within which the body experiencing phase-transition is lcoated. From the outside, i. e. at the upper wall in Fig. 1 (dark shading) an *energy source* (ES) influences the arrangement, usually preriodically in time and provoking the melting process of the solid body.

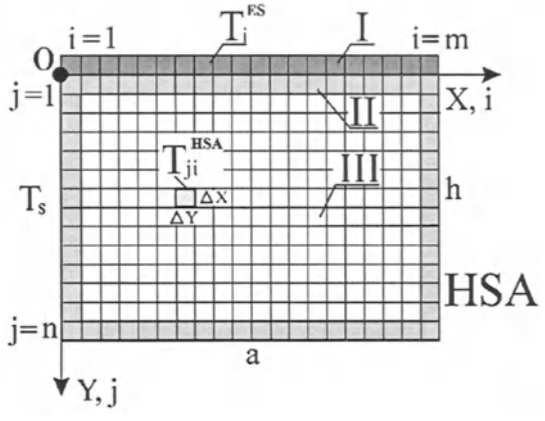

Fig. 1. Model of heat storage arrangement (HSA) with energy source (ES) at the upper edge. I, II and III denote, respectively, the energy source ES, frame of HSA and the operating medium of the HSA

This arrangement with the working medium inside is divided into elementary geometrical cells (volumes) with co-ordinates labeled by i, j. In the

limit as the number of these cells becomes large the variation of the temperature within such a cell becomes linear. Plane processes will be assumed, i. e., while the arrangement may have an extent perpendicular to the plane of Fig. 1 isothermal conditions are assumed to prevail in that direction. For simplicity we will also impose isothermal conditions in the transverse direction of the plane. X, Y, Z being Cartesian co-ordinates with the origin in the upper left corner of the arrangement, all quantities are then independent of Y and Z. So the device including the ES will be divided into cell elements only in the X-direction. The temperature for each cell as a function of time will be calculated by using a finite difference representation of the energy balance equation. Viscous effects were incorporated according to Newtonian behaviour and for heat conduction Fouriers law was used. For cells attaining the melting temperature the rate of internal energy is not given by the specific heat of the mass within the cell and the rate of temperature, but by the product of the cell mass and the latent heat of fusion.

The equations of balance of energy for the individual elementary cells are: (1) for ES-cells

$$
\begin{aligned}
C_i^{ES} \cdot \frac{\Delta T_i^{ES}}{\Delta \tau}\Big|_{i=1 \operatorname{div} m} &= P_{i=1 \operatorname{div} m} + \sigma_{1,i-1}^{ES} \cdot (T_{i-1}^{ES} - T_i^{ES})|_{i=2 \operatorname{div} m} \\
&+ \sigma_{1,i}^{ES} \cdot (T_{i+1}^{ES} - T_i^{ES})|_{i=1 \operatorname{div}(m-1)} \\
&+ \frac{1}{\frac{1}{\sigma_{2i}^{ES-HSA}} + \frac{\Delta Y_i}{2 \cdot S_{xi}^{ES-HSA}}} \cdot (T_{ji}^{HSA} - T_i^{ES})|_{j=1, i=1 \operatorname{div} m} \\
&+ \alpha_{xi}^{ES} \cdot S_{xi}^{ES-HSA} \cdot (T_s - T_i^{ES})|_{i=1 \operatorname{div} m} + \alpha_{yi}^{ES} \cdot S_{yi}^{ES} \cdot (T_s - T_i^{ES})|_{i=1 \operatorname{div} m}, \quad (1)
\end{aligned}
$$

in which $i = 1, 2, ..., m$ is the number of elementary cells ES (which coincides with the number of elementary cells of the HSA along the X-axis); $\Delta T_i^{ES} = \Delta T_i^{ES,k+1} - \Delta T_i^{ES,k}$ is the temperature difference at consecutive time steps, indicated by the label k, which is not shown on the right-hand side of (1); T_s is the tempeature of the environment. The remaining symbols are explained in the list of "Nomenclature". (2) for interior cells of the HSA, when the temperature is higher or lower than the temperature of the phase transition T_{cr} ($T_{cr} < T_{ji}$, or $T_{ji} < T_{cr}$),

$$
\begin{aligned}
C_{ji}^{HSA} \cdot \frac{\Delta T_{ji}^{HSA}}{\Delta \tau}\Big|_{j=1 \operatorname{div} n, i=1 \operatorname{div} m} &= \mathcal{A}(T_i^{ES} - T_{ji}^{HSA})|_{j=1, i=1 \operatorname{div} m} \\
&+ \mathcal{B}(T_{j-1,i}^{HSA} - T_{ji}^{HSA})|_{j=2 \operatorname{div} n, i=1 \operatorname{div} m} + \mathcal{C}(T_{j,i-1}^{HSA} - T_{ji}^{HSA})|_{j=1 \operatorname{div} n, i=2 \operatorname{div} m} \\
&+ \mathcal{D}(T_{j+1,i}^{HSA} - T_{ji}^{HSA})|_{j=1 \operatorname{div}(n-1), i=1 \operatorname{div} m} + \mathcal{E}(T_{j,i+1}^{HSA} - T_{ji}^{HSA})|_{j=1 \operatorname{div} n, i=1 \operatorname{div}(m-1)} \\
&+ \mathcal{F}(T_s - T_{ji}^{HSA})|_{j=n, i=1 \operatorname{div} m} + \mathcal{G}(T_s - T_{ji}^{HSA})|_{j=1 \operatorname{div} n; i=1,n}, \quad (2)
\end{aligned}
$$

where

$$\mathcal{A} = \frac{1}{\dfrac{1}{\sigma_{2i}^{ES-HSA}} + \dfrac{\Delta Y_j^{HSA}}{2 \cdot S_{xi}^{HSA} \cdot \lambda_{ji}^{HSA}}}, \qquad \mathcal{B} = \frac{2S_{xi}^{HSA}}{\dfrac{\Delta Y_{j-1}^{HSA}}{\lambda_{j-1,i}^{HSA}} + \dfrac{\Delta Y_j^{HSA}}{\lambda_{ji}^{HSA}}},$$

$$\mathcal{C} = \frac{2S_{yi}^{HSA}}{\dfrac{\Delta X_{i-1}^{HSA}}{\lambda_{j,i-1}^{HSA}} + \dfrac{\Delta X_j^{HSA}}{\lambda_{ji}^{HSA}}}, \qquad \mathcal{D} = \frac{2S_{xi}^{HSA}}{\dfrac{\Delta Y_j^{HSA}}{\lambda_{ji}^{HSA}} + \dfrac{\Delta Y_{j+1}^{HSA}}{\lambda_{j+1,i}^{HSA}}},$$

$$\mathcal{E} = \frac{2S_{yi}^{HSA}}{\dfrac{\Delta x_i^{HSA}}{\lambda_{ji}^{HSA}} + \dfrac{\Delta x_{i+1}^{HSA}}{\lambda_{j,i+1}^{HSA}}},$$

$$\mathcal{F} = \frac{1}{\dfrac{1}{\alpha_{xi}^{HSA} \cdot S_{xi}^{HSA} + \sigma_{kji}^{HSA}} + \dfrac{\Delta y_j^{HSA}}{2 \cdot S_{xi}^{ES-HSA} \cdot \lambda_{ji}^{HSA}}},$$

$$\mathcal{G} = \frac{1}{\dfrac{1}{\alpha_{yi}^{HSA} \cdot S_{yi}^{HSA} + \sigma_{kji}^{HSA}} + \dfrac{\Delta x_i^{HSA}}{2 \cdot S_{yi}^{HSA} \cdot \lambda_{ji}^{HSA}}},$$

and where $\Delta T_{ji}^{HSA} = \Delta T_{ji}^{HSA,k+1} - \Delta T_{ji}^{HSA,k}$. The quantities $\mathcal{A}$ to $\mathcal{C}$ are only introduced to make the formula less unwieldy.

If in an interior elementary cell with $j = 2\,\mathrm{div}(n-1)$; $i = 2\,\mathrm{div}(m-1)$ the temperature T reaches the melding temperature T_{cr}, $T_{ij} = T_{cr}$, then the left hand side in (2) is replaced by

$$\left.\frac{\Delta M_{lij} \cdot r}{\Delta \tau}\right|_{j=2\,\mathrm{div}(n-1), i=2\,\mathrm{div}(m-1)}, \tag{3}$$

where $\Delta M_{lji}/\Delta\tau$ is the mass melted within the elementary cell per unit time and r is the latent heat, both of the material contained in the cell ij. On the total mass ΔM_{ji} of the cell is conserved and given by

$$\Delta M_{ji} = \rho_{ji} \Delta x \Delta y \Delta z. \tag{4}$$

Once all solid mass has melted the calculation within the cell proceeds by using as left-hand side of (2) again the expression

$$C_{ji}^{HSA} \frac{\Delta T_{ji}^{HSA}}{\Delta \tau},$$

where C takes now values of the liquid phase. The same procedure also applies for solidification in the reverse way.

By solving the above (1) and (2) forward in time subject to prescribed temperature of the frame (T_s) the temperature and/or the solid/fluid masses

of each elementary cell could be computed. This then yields the temperature field within the HSA and the motion of the solid/liquid phase-interface from initiation to any subsequent time.

To estimate the reliability of the code for two-dimensional problems, the numerical results were compared with exact solutions of the Stefan problem and experimental results of a two dimensional HSA. Its design consists of an arrangement of L-shaped profiles with frames made out of aluminium alloy and having wall thickness of 0.001 mm; the butt-end surfaces along the Z-axis could be opened for filling the device with the working body. The energy source at the boundary was implemented by adhering a substrate of polycor to the external frame of the HSA, on the surface of which nickel-chromium resistive layers were evaporated. A form stable composite material, consisting of paraffine and a silicon binder component (to eliminate free convection in the melted phase) was used as working medium. Free convection in the melted phase never arose. The results obtained from the measurements and the calculations were in satisfactory agreement, providing confidence in the proposed mathematical model.

3 Significance of the Shape and Dimension of the HSA

To test the influence of the shape and dimension of the HSA on its thermal performance we consider arrangements of rectangular shape but different aspect ratios (from squares to elongated rectangles). Adopting the above mathematical model we are interested in the speed of melting of the material. The results then gave rise to analyses of further heat transfer processes involving melting and freezing.

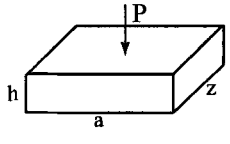

No	h/a	a, mm	h, mm	z, mm	V, mm^3	S, mm^2	q, W/m^2
1	1,0	10	10	100	10000	4000	1750
2	0,8	11,2	8,9	100	9968	4020	1741
3	0,6	13	7,7	100	10010	4140	1691
4	0,4	16	6,3	100	10080	4460	1570
5	0,2	22	4,5	100	9900	5300	1321

Fig. 2. The parameters of the heat storage arrangements

Fig. 2 lists the geometric data of the rectangular cells used in the study; they list aspect ratios from 1 to 0.2 and size parameters expressing volume and surface area. The figure also lists the specific energy source in Wm^{-2}. The cell frame is made out of aluminium alloy, the working body is paraffin. Calculations were made for constant heat flow from the top surface of the cell with the amounts also given in Fig. 2, and computations were performed by dividing the HSA into 81 cubic cells.

Fig. 3 illustrates how the solid-liquid interface propagates in time; it shows the position of the phase boundary at consecutive times after onset. Fig. 4

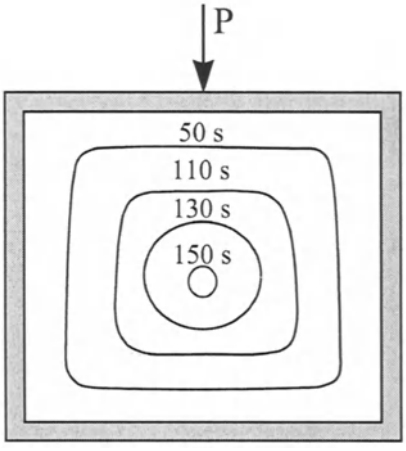

Fig. 3. Position of the interface between the solid and liquid phases at the indicated times after exposing the cell with an energy source of $P = 7W$ for $h/a = 1$

displays the temporal evolution of the frame temperature T and mass ratio

$$\xi_M = \frac{M_l}{M_\Sigma}$$

of the liquid and total mass within the arrangement for the five different cases listed in Fig. 2 and a specific energy source of $q = 1500\,\mathrm{Wm}^{-2}$ in the center of the HSA.

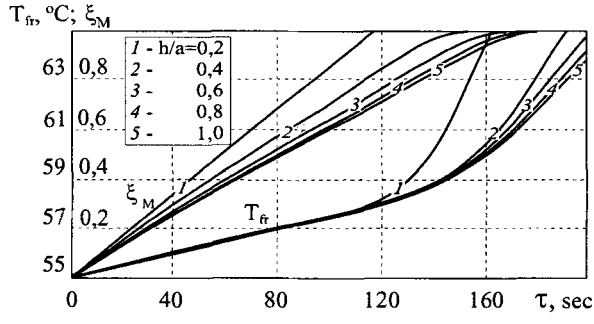

Fig. 4. Frame temperature and mass ratio for $q = 1500\,\mathrm{Wm}^{-2}$

Fig. 5 shows how the phase boundary in the middle of the specimen moves in time from above and below and when they meet; this motion is unsymmetric (the curves in Fig. 5 intersect below the middle) because of the temperature variation along the metallic frame due to the one-sided heat input from above.

Freezing being generally accompanied with contraction there may, in a HSA cell after solidification, result a gap between the upper boundary of the working material and the wall providing the heat from the ES. Such gaps

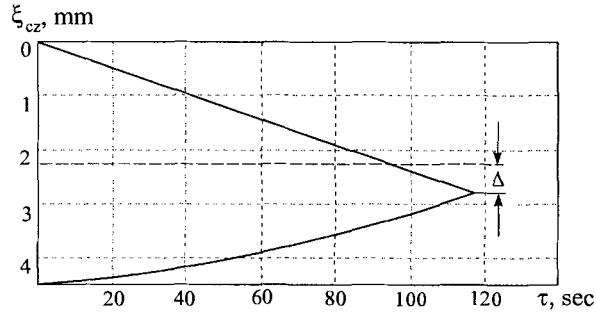

Fig. 5. Positions (z-coordinate) of the interfaces in the middle of the HSA-cell as they evolve in time from the lower to the upper boundary for $q = 1500\,\mathrm{Wm}^{-2}$ and $h/a = 0.2$

affect the performance of the HSA. If such a gap has formed and the ES is switched on a very strong overheating of the frame will occur at that place altering the onsetting melting process. The results of such a configuration are summarized in Fig. 6. It shows the time evolution of the frame temperature T_{fr} and the mass ratio M without (curves labeled 1) and with (curves labeled 2) the gap. The difference indicates that this effect must be taken into account when designing HSAs.

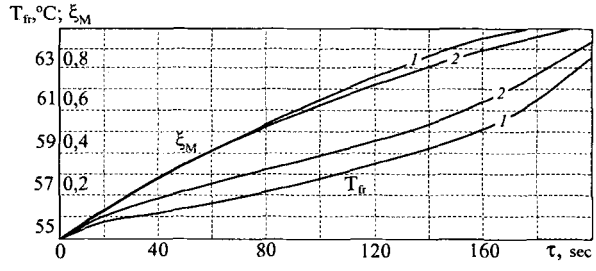

Fig. 6. Change of the frame temperature and the relative mass of the working media in case of the gap presence between them; $P = 6$ W, 1 - without the gap, 2 - with the gap

4 Conversion to a HSA-Equivalent One-Dimensional Model

Scrutiny of the numerical solutions has led us to propose an approximate computational method that is suitable for engineering purposes. If the temperature variations along the frame and the shrinkage due to solidification are ignored, then for approximate calculation of the influence of the size and form of the HSA on the heat transfer may be performed by replacing the real devices with complicated form by one-dimensional models with equivalent parameters. This "mapping" from the real arrangement to its one-

dimensional replacement requires that the following quantities remain unchanged:

- q_e heat flow from the ES,
- M_Σ total mass of the working body in the HSA,
- C_{fr} heat capacity of the frame,
- S_{fr} total area of the frame of the HSA in contact with the working body.

We then can write

$$q_e = \frac{P}{S_{fr}}, \tag{5}$$

$$l_e = \frac{M_\Sigma}{S_{fr} \cdot \rho}, \tag{6}$$

$$S_e = S_{fr}, \; \delta_e = \frac{M_{fr}}{\rho_{fr} S_{fr}}. \tag{7}$$

The simplified one-dimensinal arrangement is shown in Fig. 7, and analytical solution for the heat transfer and the evolution of the phase interface are published e. g. in [1, 2].

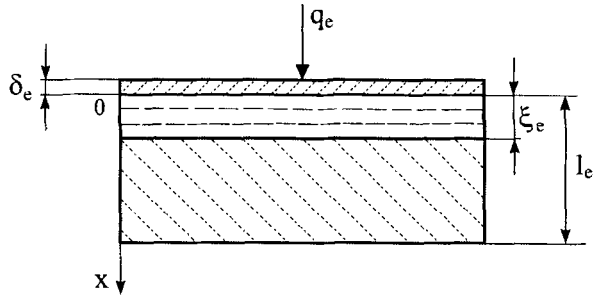

Fig. 7. An equivalent heat model of the arrangement

Below we show that the suggested approximate calculation of the heat conduction with phase changes is reliable. To this end a series of computations was carried out for the cubic cell model with different geometric characteristics as described above, and the results of these were compared with results from the equivalent one-dimensional model. The results are summarized in Figs. 8 and 9. These figures show the time evolution of the mass ratio M (of the melted mass relative to the total mass) for the aspect ratios $h/a = 0.2(0.2)1$ and for $p = 7\text{W}$ and $q = 1500\,\text{Wm}^{-2}$, respectively. The solid and dotted curves are valid for the two- and one-dimensional model, respectively.

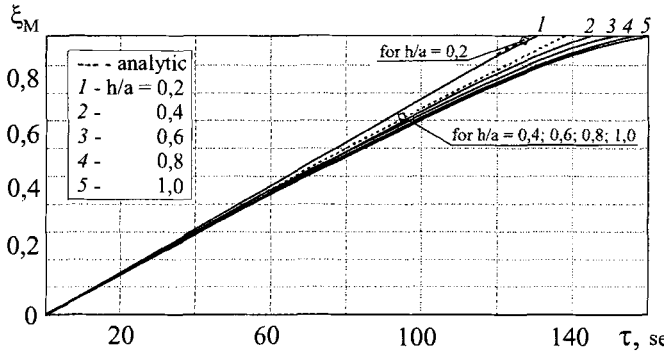

Fig. 8. Variation of the relative melted mass with time, when $P = 7$ W is constant and for the two-dimensional (solid) and one-dimensional (dashed) computation for the aspect ratios as indicated

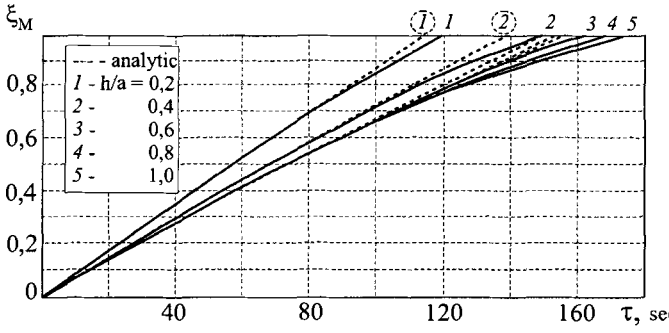

Fig. 9. Same as Fig. 8 but now for constant $q = 1500\,\mathrm{Wm}^{-2}$

The graphs of these two figures disclose that the speed of the working body, i. e., the melting rate ξ_M is constant for a reasonably long time and begins to increase only in the final part of the process when the effects of the finite size and form become more significant. This influence is maximum for the quadratic cell ($h/a = 1$) and is very low for small aspect ratios ($h/a \leq 0.2$), so that the one-dimensional equivalent model may be used in this case.

An average temperature of the frame, T_{fr}, when $h/a \leq 0.2$ can be taken to be quasistationary, independent of the position of the phase interface; it may be calculated as follows:

$$T_{fr} = T_s + \frac{Pl}{\lambda \cdot S_{fr}} \cdot \xi_M. \tag{8}$$

In all other cases, i. e. when $h/a \geq 0.2$ the two dimensionality of the system must be accounted for.

5 Conclusions

The findings of this study may be summarized as follows:

- We presented a finite volume discretization of the heat conduction problem in heat storage devices in which the working body may suffer a transition from its solid and fluid phases. The phase transition of melting and freezing is accomplished by setting the HSA in the proper thermal environment and providing a heat input from the outside via an energy source. The enthalpy method was used to determine the phase interface.
- The equations were solved for a working material placed within a metallic capacity of rectangular form. Various geometries (aspect ratios) and sizes of these cubic cells were subjected to external ESs. It was shown that both the form and the size affect the heat transfer process.
- It was shown that for cells with aspect ratios $h/a \leq 0.2$ an equivalent one-dimensional problem could be formulated with parameters deduceable from the two-dimensional arrangement, of which the result, i. e. the melting/freezing rates were in sufficient coincidence with the two-dimensional results.

Nomenclature

C: Heat capacity of an elementary cell time
T: Temperature
P: Dissipative power
σ: Heat transfer coefficient between interior cells and interior cells and the surrounding
S: Surface area
λ: Coefficient of heat conduction of a cell of the working medium
α: radiation coefficient in the surroundings of the boundary cells of the HSA
r: Latent heat of phase transformation of the working medium
M: Mass of the working medium

References

1. Carslaw H.S., Jaeger J.C., *Conduction of the head and solids*, London, 1947.
2. Shamsunder M., and Sparrow E.M., Analysis of multidimensional conduction phase change via the entropy model, *ASME journal of heat transfer*, **97**, N 4, August, 1975, p.p 333-340.
3. Schneider G.E. A numerical study of phase change energy transport in two-dimensional rectangular enclosures. "*AIAA Pap.*", 1983, N 321 1pp.
4. Abhat A., Dietrich G., Hage M., Study and design oh a modular phase change material thermal capacitor for application to spacelab payloads, *AJAA paper*, 1978,N 887, p.p.1-9.
5. Vanichev N.P., An approaching method of solution of problems of heat conduction in solid state. *AS USSA, OTN*, 1946, N 12
6. Alexeev V.A., *Cooling of radio electronics equipment using the melting substances*, Moscow, Energia, 1975, 88 p.
7. Alexeev V.A., Antonov V.V., Cooling of power supply sources using the melt working substances. In: Naivelt G. S. (ed.), *The sources of electrofeeding of radioelectronic apparatus*, Moscow, Radio and Svyaz, 1985, pp.562-568

(Received 2 March 1999, accepted 10 June 1999)

Microscale Analysis of Ice Crystals Made from Aqueous Solutions by Scanning Tunneling Microscope

Takaaki Inada[1], Akira Yabe[1], Tsuyoshi Saito[2], Shu-Shen Lu[3], Xu Zhang[1], Kenji Yoshimura[4], Makoto Tanaka[1], and Svein Grandum[5]

[1] Mechanical Engineering Laboratory, Tsukuba, Ibaraki, 305-8564, Japan
[2] University of Tsukuba, Tsukuba, Ibaraki, 305-0004, Japan
[3] South China University of Technology, Guangzhou, 510641, China
[4] Fukuoka Industrial Technology Center, Kitakyushu, 807-0831, Japan
[5] Institute for Energy Technology, Kjeller, 2007, Norway

Abstract. In order to clarify the growth of ice crystals in a solution of silane coupling agents (SCAs), a fundamental and microscale analysis has been conducted. We investigated the growth patterns of the ice crystals experimentally using an optical microscope. It was found that some SCAs that particularly have three hydrophilic groups in a molecule prevent the ice crystals from growing towards the a-axis direction. We also investigated the ice crystal surface using a Scanning Tunneling Microscope (STM) in order to determine the influence of SCA molecules on the microscale surface structure. Systematic grooves on the ice crystal surface were observed. This indicates that SCA molecules are adsorbed to the ice crystal surface preventing further crystal growth and recrystallization. Furthermore, we investigated ethylene glycol and polyvinyl alcohol in the same way. A specific microscale pattern on the ice crystal surface could not be found.

1 Introduction

Ice slurry is a promising working fluid for low temperature energy storage and transportation systems due to its flowability and large cooling capacity. Compared to conventional systems utilizing sensible heat, ice slurry systems will have a lower mass flow rate, reducing the system dimensions. In order to obtain good storage and transportation characteristics of the ice slurry, the ice creation process for optimizing the shape and size of the crystals is essential. Furthermore, methods for preventing ice from recrystallization during long term storage and long distance transportation should be developed.

Grandum et al. [1,2] have proposed a method for making ice slurry resistant to recrystallization by the use of Antifreeze Proteins (AFP). These are found in fish living in the Antarctic Ocean and have an ability to depress the freezing point of their blood in a noncolligative manner [3]. They showed that type 1 AFP, which is a long single α-helical molecule, is an effective additive in ice slurry systems with respect to the characteristics of thermal storage and flowability. However, AFP solutions have not been utilized for ice storage

systems commercially yet, mainly because AFP is relatively expensive itself and is easily affected by bacteria degradation. Therefore ice slurry systems utilizing substances which are cost-effective and are not easily affected by bacteria should be developed.

We focused on a silane coupling agent (SCA) as a substitute additive due to the similarity in molecular structure between SCA and AFP. The formation pattern of the ice crystals in SCA solutions was examined. Furthermore, the microscale structure of the ice crystal surface was analyzed by a Scanning Tunneling Microscope (STM) in order to determine the influence of SCA molecules on the microscale surface structure. Other additives such as ethylene glycol and polyvinyl alcohol were investigated in the same way.

2 Silane Coupling Agent (SCA)

SCA is a silicone monomer which has a good affinity for solvents. In Fig. 1a, OR is a hydrolyzable group making a bond with inorganic materials like glass and carbon after hydrolysis, while X is a functional group which reacts on organic materials. Therefore, SCA has the ability to connect chemically an organic material to an inorganic material. In water, SCA forms silanol (Si(OH)) as a result of the hydrolysis process. Consequently, one SCA molecule has three hydrophilic groups and one hydrophobic group, when the number of OR, n, is equal to 3. As time goes on, long chained molecules are generated after H_2O molecules are released, because silanols are unstable. Fig. 1b shows the schematic figure of a long chained SCA molecule adsorbed to the surface of an ice crystal. The distance between adjacent hydrophilic groups in a long chained SCA molecule is 0.30nm. Therefore, the SCA molecule will be adsorbed to a particular ice crystal plane where the distance between adjacent oxygen atoms is equal to a multiple of 0.30nm. When the SCA molecules are adsorbed to the ice crystal surface as shown in Fig. 1b, the hydrophobic groups will be faced outwards. The adsorbed SCA molecules will then inhibit the crystal growth and recrystallization.

3 Crystal Shape of Ice Made from SCA Solutions

3.1 Experimental procedure

The free growth of ice crystals in a supercooled solution of SCA was observed using the experimental apparatus as shown in Fig. 2. In order to minimize the temperature gradient inside the solution, the experimental apparatus was set in a cold room (0°C). The SCA solution was exposed to a cold surface, cooled by an ethanol flow. The solution temperature was controlled by the ethanol flow and was recorded by a thermistor. Observations were made by an optical microscope connected to a camera. Crystal growth was initiated by inserting a seed ice crystal when a desired steady state supercooling was

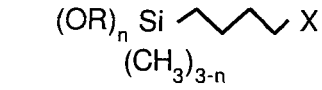

OR : Hydrolyzable group
CH_3O-, C_2H_5O-, $CH_3OC_2H_4O$-, etc.
X : Functional group
Vinyl, Epoxy, Amino, Mercapto, etc.

Hydrolysis (n=3)

$$X\text{-}Si(OR)_3 + 3H_2O \rightarrow X\text{-}Si(OH)_3 + 3ROH$$

(a)

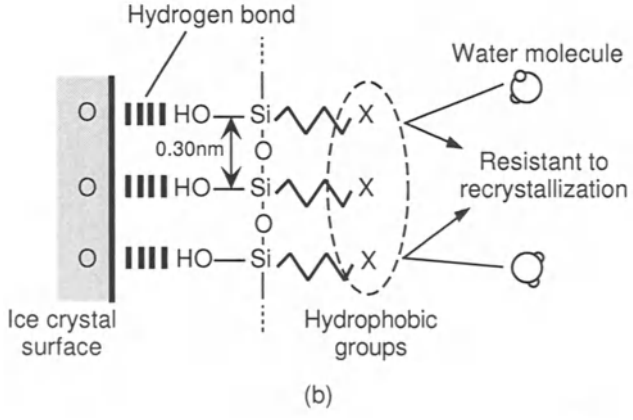

(b)

Fig. 1. The properties of SCA. (a) Structural formula of SCA and its hydrolysis process. (b) Model of SCA molecules adsorbed to an ice crystal surface

established. Experiments were performed at different degrees of supercooling and different solution concentrations.

3.2 Experimental results and discussion

Needle type ice crystals were observed as shown in Fig. 3 for a 2mg/ml solution of Vinyltriethoxysilane (VTES), which is one of the SCAs. Since the cross section of the needle type crystal had several edges, though it cannot be recognized from Fig. 2, the growing direction would be parallel to the c-axis direction. Each crystal grew independently without joining together. From the observations when varying the VTES concentration, the needle type crystals were observed between 2mg/ml and 10mg/ml, indicating that there is no gradual change in the growth pattern within this concentration range. For a 5mg/ml solution, the needle type crystals kept their shape when the

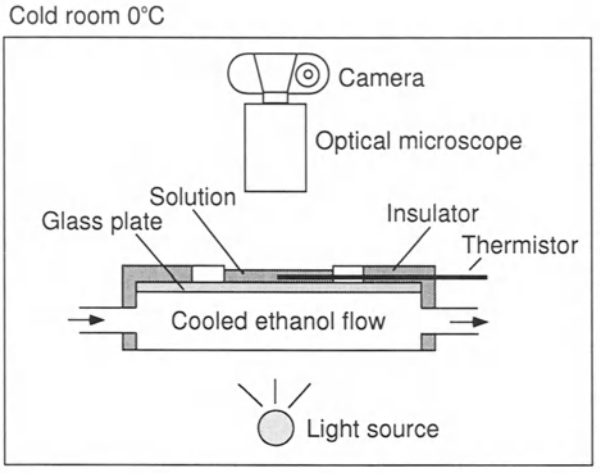

Fig. 2. Experimental apparatus for observation of crystal shape

temperature in the solution was between -0.4°C and 0.0°C, while the typical dendritic crystals were initiated below -0.4°C. Based on the assumption that SCA molecules are adsorbed to a specific crystallographic plane like AFP molecules do [2], this observation indicates that it would take some time for SCA molecules to align on the specific plane. When the degree of supercooling exceeds the critical value, the speed of addition of water molecules to the ice crystal surface will be faster than that of the systematic adsorption of SCA molecules. That is, SCA molecules are no longer effective for preventing the crystal growth and recrystallization. In the case of the 5mg/ml SCA solution, -0.4°C is the critical temperature.

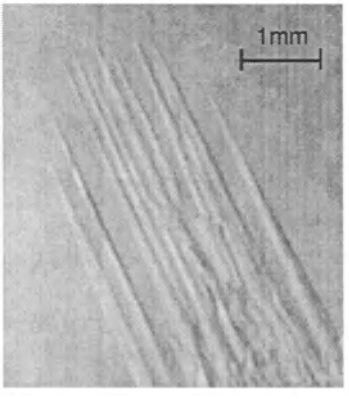

Fig. 3. Needle type crystal growth in a 2mg/ml VTES solution

Table 1 shows the results from the examination of the shape of ice crystals made from five SCA solutions each with different molecular structure. The needle type crystals were observed for VTES, 3-glycidoxypropyltriethoxysilane (3-GPTES), and 3-methacryloxypropyltriethoxysilane (3-MPTES) solutions which have three hydrophilic groups in a molecule. On the other hand, the dendritic crystals were observed for 3-glycidoxypropylmethyldiethoxysilane (3-GPMDES) and 3-aminopropyltriethoxysilane (3-APTES) solutions. Neither 3-GPMDES nor 3-APTES can form long chained molecules, because the former has only two hydrophilic groups and the latter is stable by the existence of an amino group. Therefore, long chained SCA molecules must be generated in order to be adsorbed to the ice crystal surface and to inhibit the ice crystal growth and recrystallization.

Table 1. Ice crystal growth patterns in SCA solutions

Chemical name	Structural formula	Functional group	Number of hydrolyzable groups	Ice crystal growth pattern
VTES	$CH_2 = CHSi(OC_2H_5)_3$	Vinyl	3	Needle
3-GPMDES	$CH_2(O)CHCH_2OC_3H_6 -SiCH_3(OC_2H_5)_2$	Epoxy	2	Dendrite
3-GPTES	$CH_2(O)CHCH_2OC_3H_6 -Si(OC_2H_5)_3$	Epoxy	3	Needle
3-MPTES	$CH_2 = CH(CH_3) -COOC_3H_6Si(OC_2H_5)_3$	Metha-cryloxy	3	Needle
3-APTES	$NH_2C_3H_6Si(OC_2H_5)_3$	Amino	3	Dendrite

4 STM Observation of Ice Crystal Surface

4.1 Experimental procedure

The surface of ice crystals made from SCA solutions was observed by an STM and the adsorbing mechanism for SCA molecules was investigated. Furthermore, the surface of ice crystals made from ethylene glycol and polyvinyl alcohol solutions was also observed. Since an STM tip does not touch the ice crystal surface, melting and deformation of the ice crystal can be avoided

during the observation. The STM was put inside a cold room, held at -7°C so that the surface structure of the ice crystal was not affected by sublimation. A droplet of supercooled pure water had been prepared on a sample stage before a needle type ice crystal made from a VTES solution was set to it. When the supercooled droplet received the ice crystal, the droplet froze immediately, binding the ice crystal to the sample stage tightly. In order to prevent the crystal from sublimation completely, the sample was covered by a thin oil layer as shown in Fig. 4.

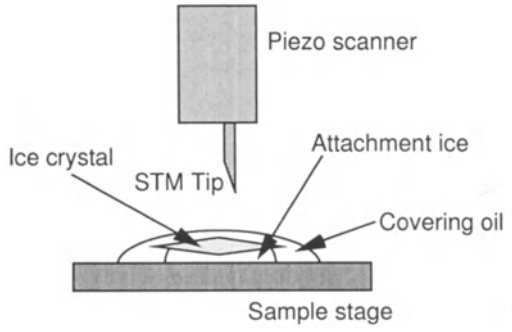

Fig. 4. Details of the ice crystal on the sample stage

4.2 Influence of oil covering ice crystal on STM image

The influence of the oil covering the ice crystal on the STM observation was investigated by using a graphite standard sample. Comparing the atomic images of the bare graphite and that covered by the oil, there was almost no difference in the same observed area. It indicates that the covering oil does not affect the STM observation.

4.3 Image of ice crystal surface containing adsorbed AFP molecules

In order to examine the reliability of the STM observation, we investigated the surface of an ice crystal adsorbed by type 1 AFP molecules, similar to the work of Grandum et al. [2]. The ice crystal used in this observation had hexagonal bipyramidal shape. Fig. 5 shows a typical surface plot of an ice crystal made from a 4mg/ml solution. The size of systematic grooves on the ice surface was 5nm long and 1nm wide, which corresponds to that of an AFP molecule. The grooves were about 15nm deep, and existed at 4-5 nm intervals. The grooves were aligned approximately 65-70° to one hexagonal side on a bipyramidal plane. This is proving that the AFP molecules are adsorbed

to the $\{20\bar{2}1\}$ planes along the $\langle 01\bar{1}2\rangle$ directions, preventing further crystal growth and recrystallization [2,4]. Fig. 6 represents one of the 12 equivalent bipyramidal $\{20\bar{2}1\}$ planes and one of the 12 equivalent $\langle 01\bar{1}2\rangle$ directions in a hexagonal system. Fig. 7 shows a surface plot of an ice crystal made from pure water. It was almost flat, though there were irregular small ridges existing. The maximum depth of the ridges was less than 5nm. These results are almost the same as Grandum et al. [2] obtained, moreover, the image obtained here is clearer. This indicates the reliability of the STM observation in this report.

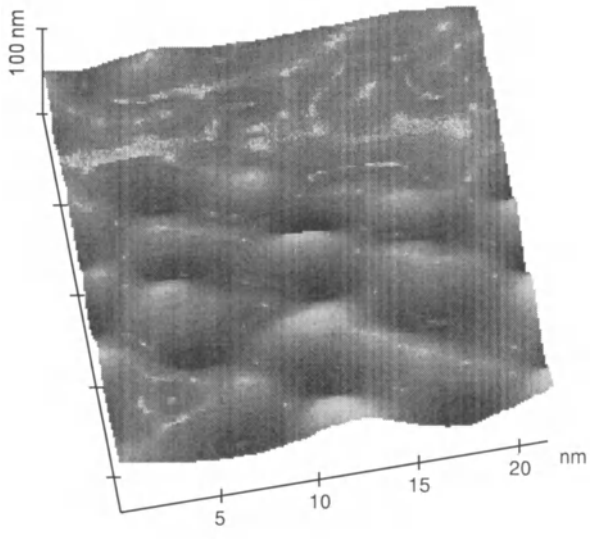

Fig. 5. STM surface plot indicating the ice surface curvature generated by adsorbed AFP molecules

4.4 Image of ice crystal surface containing adsorbed SCA molecules

Fig. 8 shows a typical STM surface plot of an ice crystal made from a VTES solution. Systematic grooves were at least 500nm long, 30-70nm deep, and existed at about 200nm intervals. For smaller area scan, less than 500nm-$\times$500nm, other particular patterns could not be observed. VTES molecules have obviously a great influence on the surface structure of an ice crystal, in comparison with the surface of an ice crystal made from pure water. This result indicates that long chained SCA molecules are adsorbed to the ice crystal surface along the grooves, preventing the crystal growth and recrystallization.

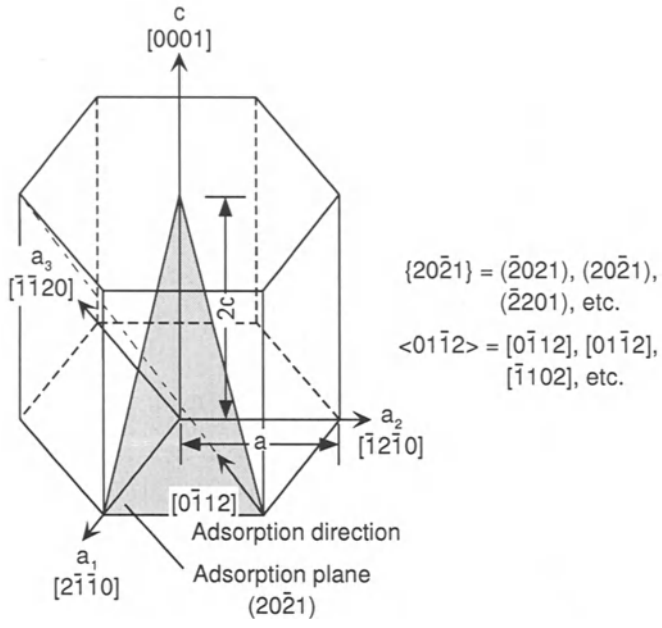

Fig. 6. Typical AFP adsorption plane and direction in a hexagonal system

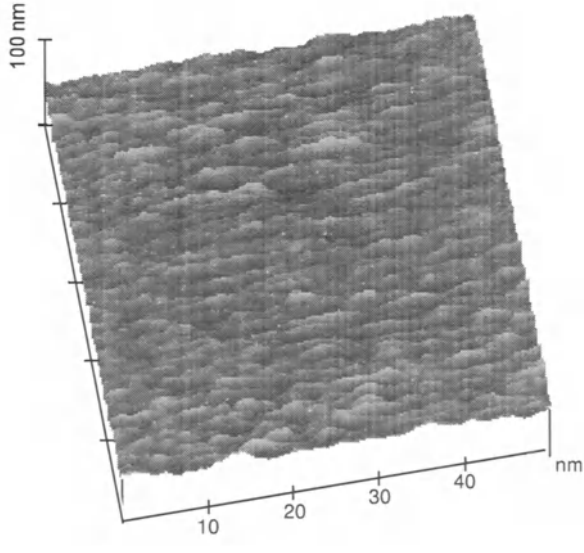

Fig. 7. STM surface plot for the ice surface made from pure water

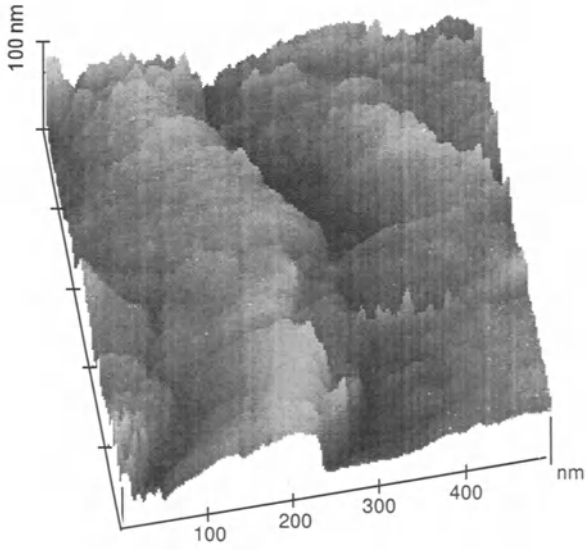

Fig. 8. STM surface plot indicating the ice surface curvature generated by adsorbed SCA molecules

4.5 Other substances

Ethylene glycol ($C_2H_4(OH)_2$) and polyvinyl alcohol ($[-CH_2CH(OH)-]_n$) were investigated as the substitute additives. Since they have simple molecular structures that consists of both hydrophilic and hydrophobic groups, there is a possibility that they will be adsorbed to the surface of an ice crystal, preventing the crystal growth and recrystallization. The STM observation was conducted for ice crystals made from ethylene glycol solutions and polyvinyl alcohol solutions within the concentration range of 0.1wt% and 5wt%. A specific microscale pattern on the ice crystal surface was never observed. The STM surface plot is almost similar to that of an ice crystal made from pure water. This indicates that ethylene glycol and polyvinyl alcohol molecules can not be adsorbed to the ice crystal surface. It would be an important factor for the adsorption that the distance between adjacent hydrophilic groups in the additives corresponds to that between adjacent oxygen atoms on the ice crystal surface. Therefore, in future work, we should find new substitute additives taking the distance into account.

5 Conclusion

We examined the formation pattern of ice crystals in SCA solutions. Furthermore, we investigated the microscale structure of the surface of ice crystals

made from AFP, SCA, ethylene glycol, and polyvinyl alcohol solutions by STM observations. The following results were obtained.

(1) Needle type ice crystals were observed in some SCA solutions. They have an ability to prevent recrystallization.

(2) The formation of long chained SCA molecules is essential to their adsorption to the ice crystal surface, preventing further crystal growth and recrystallization.

(3) In the STM observation, microscale systematic grooves were found on the surface of ice crystals made from AFP and SCA solutions, while a specific pattern could not be found on the surface of ice crystals made from ethylene glycol and polyvinyl alcohol solutions. These results indicate that AFP and long chained SCA molecules were adsorbed to the ice crystal surface, preventing the crystal growth and recrystallization. On the other hand, ethylene glycol and polyvinyl alcohol molecules could not be adsorbed to the ice crystal surface.

References

1. Grandum, S., Yabe, A., Tanaka, M., Takemura, F., Nakagomi, K. (1997) Characteristics of ice slurry containing antifreeze protein for ice storage applications. *J. Thermophys. Heat Transfer* **11**, 461–466
2. Grandum, S., Yabe, A., Nakagomi, K., Tanaka, M., Takemura, F., Kobayashi, Y., P. E. Frivik (1999) Analysis of ice crystal growth for a crystal surface containing adsorbed antifreeze proteins. *J. Crystal Growth* (in press)
3. Davies, P. L., Sykes, B. D. (1997) Antifreeze proteins. *Current Opinion Structural Biology* **7**, 828–834
4. Knight, C. A., Cheng, C. C., DeVries, A. L. (1991) Adsorption of α-helical antifreeze peptides on specific ice crystal surface planes. *Biophys. J.* **59**, 409–418

(Received 23 Feb. 1999, accepted 18 May 1999)

Development Study of a Novel Tower-Style Tank for Simultaneous Storing Warm Water and Ice

Kunihiko Kitamura[1], Keiji Kurokawa[2], Yasutoshi Inatomi[3], Itsunari Fukushima[3], and Osamu Miyatake[1]

[1] Department of Chemical Systems and Engineering, Faculty of Engineering, Kyushu University, 6-10-1 Hakozaki, Higashi-ku, Fukuoka 812-8581, Japan
[2] Thermal Storage Technical Department, West Japan Engineering Consultants Incorporation, 1-12-9 watanabe-dori, chuoku, Fukuoka 810-0004, Japan
[3] Environmental Engineering Division, Kyudenko Corporation, 1-23-35 Nanokawa, Minami-ku, Fukuoka 815-0081, Japan

Abstract. In February 1999, a unitary tower-style thermal storage tank was constructed in a building in Fukuoka City (1). This storage tank is designed such that the upper part is used as a warm water storage tank, while the lower part is used as an ice thermal storage tank. A piece of equipment called "Duo Stable" (which has two stabilizing functions) is installed in the middle of this storage tank. "Duo Stable", which is shaped as a "trap", is newly devised for keeping warm and cold water from mixing.

This study reports the results of the experiment, which was conducted with the focus of acquiring the necessary basic data for designing this thermal storage tank. The results indicate that the "Duo Stable" has a possibility to store warm water and ice inside a unitary thermal storage tank. Furthermore the validity of agitation during the process of ice making is clarified.

1 Introduction

It was about 1950 when engineers in Japan began to use thermal storage tanks for air conditioning in buildings. At that time the trend was to use water storage tanks built as double foundation slabs. Their usability is established and has also been substantiated (2)-(5). Later, these water storage tanks were changed into compact thermal storage tanks for ice. This was done so, because in high rise buildings the thermal storage tanks are generally centrally located and need be as small as possible. Another reason was that in the process of increased demands for the cooling of buildings also social demands for the electric power leveling increased; it led to a substantial reduction of the fees for electricity at night hours.

In addition, there are ongoing significant trends for improved thermal performance and increased internal heat gain in recent constructions of, and application to, buildings. These trends were also triggered by the demand for heating and cooling in cold regions and climates. Due to all these reasons

compact, tower-style thermal storage tanks have become popular in urban areas where only limited space is available. Because of the thermal stratification these storage tanks are devised to store warm water in the upper part and cold water in the lower part (6)-(7). This arrangement is naturally changed inside the existing tower-style thermal storage tanks which can store warm water and high density ice simultaneously. When producing ice in such a tank and the water temperature is below 4°C, then due to the anomaly of the temperature dependence of the density an unstable stratification will occur which results in a loss of efficiency because of the convective mixing processes that take place.

Therefore, in order to control this inversion phenomenon, the authors designed a piece of equipment, called "Duo Stable" which can stabilize the water with maximum density at 4°C at the top of the novel tower-style tank simultaneously with the ice below it. Duo stable achieves to maintain the thermal stratification within the warm water and the ice in a common unified thermal storage tank.

This is done by producing two stable conditions, one of which has 45°C warm and 4°C cold water and the other has 0°C and 4°C cold water. This novel tower-style tank itself is designed to be used for air conditioning, and an exhaust heat recovery type heat-pump is used for its heat source system. Also, the coefficient of performance in the whole air conditioning system can be improved by simultaneously providing heating and cooling energy into the storage tank. The performance is improved by agitating water-current or by bubbling inside the tank. In so doing the time of making ice can be shortened as compared to the case with no agitation (8). It is also meant that both agitation mechanisms are installed.

The objective of this study is to clarify the operating methods, of a novel tower-style tank for simultaneous storing warm water and ice. This is done by conducting experiments which examine the effect of agitation in the ice part, and in the "Duo Stable" part inside the tank, for the case of the temperature distribution as well as the case of forming ice, during the processes of storage and discharge.

2 The Experimental Apparatus, Method and Conditions

The experimental apparatus is shown in Fig. 1. It consists of two constant temperature baths as a heating and a cooling source, four pumps (for heating, cooling, water circulation and air circulation), a test thermal storage tank and a piping system with these systems. The test tank has rectangular shape. A staggered array of piping-heat exchangers for a warm water storage tank was placed in the upper part of this test tank and that for an ice thermal storage tank in the lower part, and a "Duo Stable" was placed in the middle of the

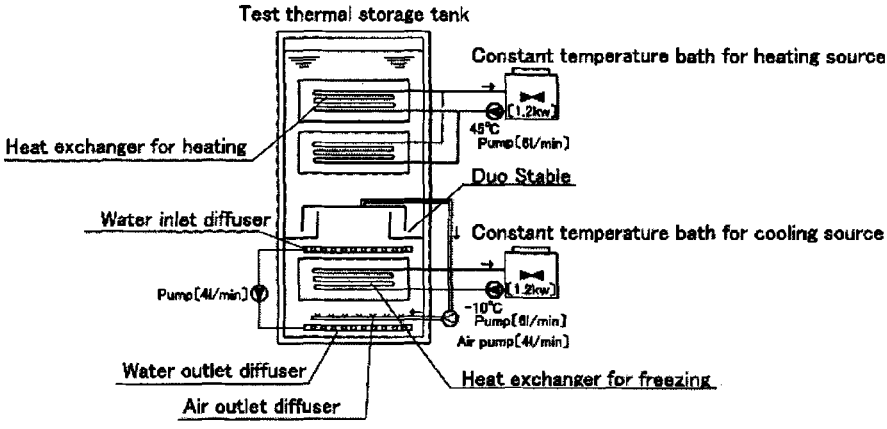

Fig. 1. Schematic of the experimental apparatus

tank. The experiment was conducted by using the following three patterns; no agitation, water-current agitation, and bubbling.

The water outlet diffuser for water-current agitation was devised by arranging two parallel perforated pipes of 10 [mm] diameter and 300[mm] length and placing it in the bottom of the heat exchanger of the ice thermal storage. The water inlet diffuser was of the same size and placed between the "Duo Stable" and the heat exchanger for the ice thermal storage. The water-current was agitated by circulating the water between the outlet diffuser and the inlet diffuser. The air outlet diffuser for bubbling consisted of three parallel perforated pipes (of 6[mm] diameter and 260[mm] length); and it is placed in the bottom part of the heat exchanger of the ice thermal storage. Bubbling was maintained by a circulation method, in which air of the air holder inside the "Duo Stable" was released creating bubbles, from the air outlet diffuser.

A test thermal storage device was made by using an acrylic board with thickness 15[mm]. The size inside the tank, as shown in Fig. 2a, is 350 × 200 × 780[mm]. The open part connecting the "Duo Stable" in the middle and the bottom part of the tank, is 210 × 100[mm]. Three heat exchangers were made by arranging copper pipes (outside diameter 8[mm], inside diameter 6.4[mm]) in 6 × 5 lines (260 × 141 × 104[mm]) . Two of them are set for the warm water storage and the other is set for the ice thermal storage.

In an experiment, heating was conducted by the heat exchangers for warm water storage, and, at the same time, cooling was done by the heat exchanger for the ice thermal storage, after the temperature inside the tank had been kept consistent by a heat source system.

In addition, the initial water temperature was set at 20 ~ 22°C, and the brine temperatures for the heat exchangers of heating and cooling were each set at 45°C and -10°C respectively. The temperatures were measured by positioning 16 K-type sheathed chromel-alumel thermocouples (the outside diameter of 0.5[mm] × 500[mm]) in the numbered places shown in Fig. 2b.

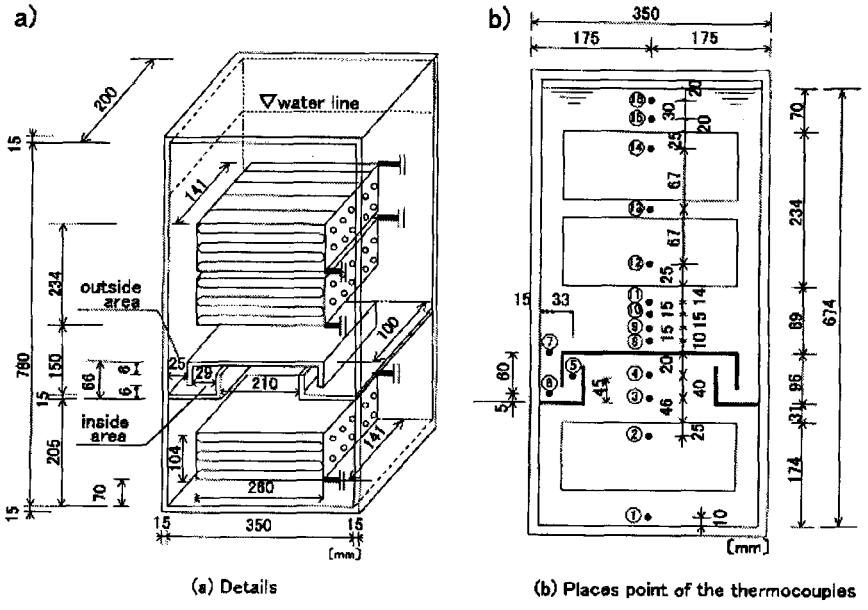

Fig. 2. Test thermal storage tank a) Details, b) Positions of thermocouples

3 Experimental Results and Numbered Considerations

3.1 Storage

Fig. 3 shows the changes in the temperatures inside the tank as functions of time. As these curves show at the places numbered ⑫ and ⑮, the three patterns; no agitation, water-current agitation, and bubbling, exhibit almost the same changes over time.

On the freezing side in the lower part of the tank, in the case without any agitation, there is some descending current occurring in parts of the heat exchanger ②, which is caused by the cooling functioning. This also causes decreasing temperature in the area below position ②, where the heat exchanger for the ice thermal storage is situated, ①. When the temperature at the bottom of the tank reaches 4°C, and below the density decreases, which causes the ascending current. At the same time, the water temperature at the upper part of the heat exchanger decreases gradually, and after about 100 minutes, the temperature at ④ starts decreasing and reaches 0°C after a total of 120 minutes. During this process, the water temperature in the bottom of the tank stabilizes at 4°C. As the time passes, the temperature decreases, ⑤; and the temperature at the bottom of "Duo Stable", ⑥ also levels in at 4°C. While this process is going on, the temperature at ② enters a super-cooling state below 0°C. When finally this super-cooling is released

160 minutes after the experiment was started, needle-shaped ice is forming at the heat exchanger and around it. As time goes on, the solid ice starts growing from the copper pipes of the heat exchanger. When this occurs, the temperature in the bottom of the tank is persistently kept at 4°C.

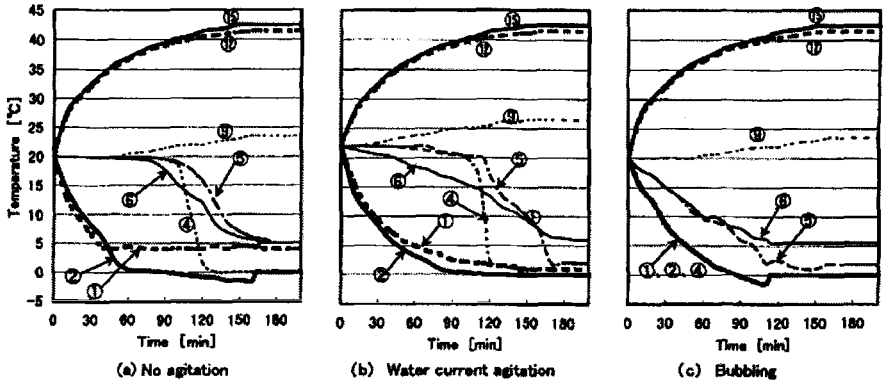

Fig. 3. Temperature in the test thermal storage tank. Encircled numbers correspond to those in Figure 2

With the water-current agitation, water between the outlet diffuser and the inlet diffuser in the bottom is slowly circulated in the upper direction by a circulation pump at 4[l/min], with current speed inside the tank of about 0.1[cm/s] (corresponding to one turn about every 4[min]). Because of this, the temperature in the area between the lower part of the outlet diffuser and the bottom part of the tank, slowly decreases at the same rate. Different from the case without agitation, the temperature around the heat exchanger ② is lower than the temperature in the bottom of the tank at all times. This is because the descending current caused by cooling at the beginning stage of this experiment was relieved by the ascending current due to the water-current agitation. Next, when the lower part of the water outlet diffuser was cooled off below 4°C, it made the density become small, and produced the ascending cold current, that reached ④, followed by spreading around ⑤, and then lastly arrived at the bottom of the "Duo Stable" ⑥ where it became stable at 4°C. During this process, the temperature at ② attained a supercooling state below 0°C. Then, when the supercooling was released 150[min] after this experiment started, needle-shaped ice was produced in the whole tank, and solid ice started growing around the cooling pipes. At this time, the temperature in the bottom part of the tank continuously decreased to 0°C.

In the case of bubbling, the temperatures at ①, ② and ④ in the lower part of "Duo Stable" decrease in the same way; this is different from the

other two cases, of Fig. 3. Due to the bubbling, the temperatures at ⑤ and ⑥ inside the "Duo Stable" decrease more rapidly in the initial stage, and the bottom of the "Duo Stable" ⑥ stabilizes quickly at 4°C. The temperatures at ② and ④ were simultaneously super-cooled below 0°C. When the super cooling was released 110[min] later, needle-shaped ice started forming in the whole tank, and then solid ice started growing around the cooling pipes.

3.2 Thermal storage capacity for cooling

Fig. 4 shows the result of the changes in the thermal storage capacity for cooling, which was estimated from changes of the temperature inside the tank as the time passed until the super cooling was released. Although there were no significant differences seen in the thermal storage capacity for cooling between the case with no agitation and that with water-current agitation, it was obvious that the heat transfer efficiency in the case of bubbling had improved. Moreover, in any of the three cases, it was when the thermal storage capacity for cooling in the bottom inside the tank reached about 1600[kJ] that super-cooling was released. The release times were 160[min] without any agitation, 150[min] with water-current agitation, and 110[min] in the case of bubbling. As a result, the super-cooling-release time in the case of bubbling was two-thirds shorter than that without agitation.

From the results mentioned above, the differences in the speeds of making ice can be estimated from the differences in the super cooling release times. Although the water-current agitation case could not shorten the cooling storage time when compared with the case without agitation, it was demonstrated in the case of bubbling.

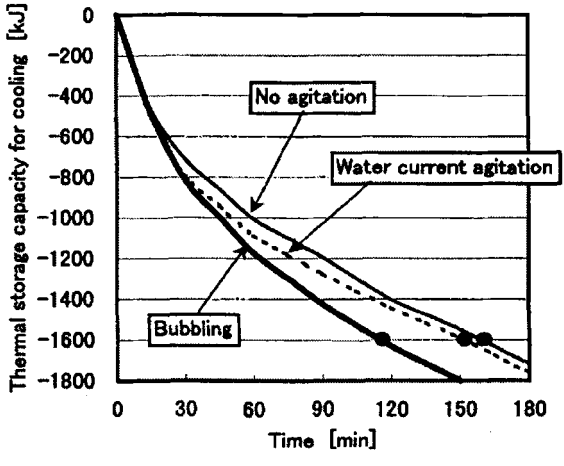

Fig. 4. Thermal storage capacity for cooling (estimated value). "• " Super cooling release point

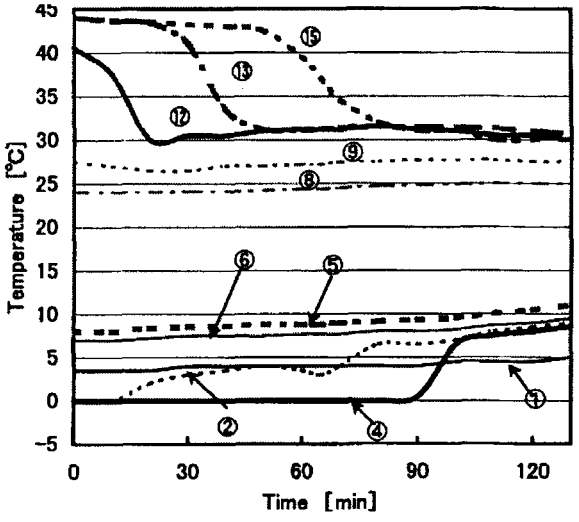

Fig. 5. Temperature in the test thermal storage tank during the process of discharge. Encircled numbers correspond to those in Figure 2

3.3 Discharge

Fig. 5 shows the experimental results of the temperature time series during a process of discharge. The discharge on the warm-water side was carried out by circulating warm water in the thermal storage tank and warm water in the constant temperature bath outside of it. The temperature of the bath was kept at 30°C. The discharge on the ice side was conducted by flowing the brine, which was kept at 10°C in the constant temperature bath, into the heat exchanger for ice thermal storage (internal fusion method). The discharge experiment was completed when the warm water in the tank became 30°C and the cold water 10°C. In addition to this, bubbling was not experimented on the ice side during this experiment.

The temperature on the warm water side was decreasing from the bottom part of the warm water tank, while the temperatures at ⑧ and ⑨ were kept almost constant. The temperatures at ⑫, ⑬ and ⑮ all approached about 30°C, 20[min] later for ⑫, 50[min] later for ⑬, and 80[min] later for ⑮. The water temperatures at ⑤ and ⑥ inside the "Duo Stable" remained stable during the process of discharge. The temperature inside the tank at the initial stage of discharge on the ice side was consistently kept at 0°C, except at the bottom part of the tank ①. It is understood that the 4°C water with the maximum density stays in the bottom part of the tank ①. 20[min] later, after the discharge was started, the water temperature ② around the heat exchanger for ice thermal storage rose, followed by ice fusion, which causes some ice floatations. The "Duo Stable" prevents this floating ice from streaming into the warm water side. Because of this, the temperature at the

upper part of the tank ④ is kept at 0°C until all the floating ice is fused. The floating ice is all fused of the 95[min].

4 Conclusions

In this experiment, coexistence of both warm water and ice in the same tank was substantiated by assuring that warm water is stored in the upper part of the tank, ice is made in the lower part, and by maintaining the two under stable conditions. The following statements were clarified by the experimental results.

- Warm water and ice can be stored simultaneously inside a single unified thermal storage tank.
- The bottom of "Duo Stable" is stable at 4°C during the storing process.
- Compared to the condition without agitation, the case with bubbling can shorten the time of making ice by a factor of two-thirds.
- "Duo Stable" has the ability to keep cold water from flowing into the warm water, which is caused not only by the inversion density but also by bubbling.
- "Duo Stable" is effective for preventing ice from surfacing in the process of discharge.

References

1. K.Kitamura, et al.;Development of Hybrid-Storage system. *HACTEC*, No. **12** (1998-11)
2. Y.Nakajima;Thermal storage tank(1)~(7). *SHASE* Vol. **54** No.6~11(1980-6~1980-11)
3. N.Nakahara;Real data for operating thermal storage system and improvement of the efficiency. *SHASE* Vol. **50** No.9(1976-9)
4. O.Miyatake, et al.;Thermal storage efficiency of a submerged Weir-Type hot water storage tank. *Transactions of SHASE* No. **29** (1985-10)
5. O.Miyatake, et al.;Studies on the internal characteristics of a temperature stratification-type thermal storage water tank. *Transactions of SHASE* No. **32-33-35**(1985-10,1987-2,10)
6. T.Sugimoto, et al.;Air conditioning system of IKEDA electric building. *SHASE* Vol. **70** No.12(1996-12)
7. J.Mabuchi, et al.;Air conditioning system of R&D center. *HACTEC* No. **2** (1993-12)
8. T.Takahashi, et al.;Experiment on accelerating methods of ice melting for ice storage equipment. *Transactions of SHASE Symposium in Sapporo* (1990-10)

(Received 14 April 1999, accepted 16 April 1999)

Latent Heat Storage in a Fixed-Bed Packed with Cross-Linked Polymer Particles

Hiroki Morita[1] and Osamu Miyatake[2]

[1] HVAC & Plumbing Engineering Department, Kyudenko Corporation, 1-23-35 Nanokawa, Minami-ku, Fukuoka 815-0081, Japan
[2] Department of Chemical Systems and Engineering, Graduate School of Engineering, Kyushu University, 6-10-1 Hakozaki, Higashi-ku, Fukuoka 812-8581, Japan

Abstract. Experimental and numerical analyses were carried out to investigate the discharge characteristics of a fixed-bed, using form-stable cross-linked cylindrical polymer particles as a phase change type of heat storage material and ethylene glycol as heat transfer fluid. Firstly, particle-to-fluid heat transfer coefficient in a fixed-bed, essential for analyzing the discharge characteristics of the latent heat storage column, were evaluated experimentally using Schumann's extended theory, and an empirical formula for estimating the heat transfer coefficient was presented. Secondly, by using the empirical formula, the transient temperature distribution in the column and the transient response of the outlet temperature of the heat transfer fluid were calculated numerically, and the latter was compared with measurements of the outlet temperature of the fluid. The numerical results were found to be in good agreement with the experimental results.

1 Introduction

The latent heat storage in cross-linked polymers is one of the promising storage methods that can be used for load levelling by utilizing off-peak electric power and various sources of waste heat. The cross-linked polymers, used as a phase change material (PCM), can retain their shapes when heated above the melting point and thus enable heat transfer by direct contact with the heat transfer fluid (HTF). The utilization and economical aspects of this storage method have already been analyzed. Experimental results on the charge and discharge characteristics of this method have been reported for various shapes of the PCM such as particles [1,2], cylindrical tubes [3] and cylindrical rods [4]. Numerical results on the charge and discharge characteristics of this method have also been reported for shapes such as cylindrical tubes [3] and cylindrical rods [5].

In the previous numerical analyses, however, the heat transfer coefficient between the PCM and HTF was not well investigated, which is an important factor in analyzing the charge and discharge characteristics. The previously available numerical methods were not necessarily general enough.

In this investigation, particle-to-fluid heat transfer coefficients in a fixed-bed packed with the cross-linked cylindrical polymer particles subjected to

the melt-freeze cycles were evaluated experimentally to obtain a formula for estimating the heat transfer coefficient. A numerical analysis was carried out to study the discharge characteristics of the latent heat storage columns by using the empirical formula, and the validity of the numerical analysis was verified by comparing the numerical results with the experimental results.

2 Principle of Evaluation of the Heat Transfer Coefficient

In the case of unsteady heat transfer from the particles to the fluid in a fixed-bed, Schumann [6] derived an analytical solution for the transient temperature distribution within the fixed-bed under the boundary condition that the inlet temperature of the fluid is constant. However, in most applications, a step-change of the inlet temperature of the fluid is not a realistic situation, because mixing space exists for the fluid at upstream positions of the fixed-bed. Accordingly, Cyuma et al. [7] derived the analytical solution,

$$\theta_f = 1 - e^{-\zeta} \int_0^\tau e^{-\tau} \mathbf{I}_0(2\sqrt{\zeta\tau}) d\tau + (1-\phi) e^{-\zeta-\phi\tau} \int_0^\tau e^{-(1-\phi)\tau} \mathbf{I}_0(2\sqrt{\zeta\tau}) d\tau, \tag{1}$$

with the boundary condition of the time-dependent inlet temperature of the fluid given by

$$T_{in} = T\,|_{z=0} = (T_0 - T_{in,\infty}) e^{-kt} + T_{in,\infty}. \tag{2}$$

(For definition of symbols see "Nomenclature" at the end)

When the value of the time constant, k, in Eq. (2) is obtained by the least squares method by fitting the experimental transient response of the inlet temperature of the fluid, T_{in}, the value of the heat transfer coefficient, h, is the only unknown quantity under given experimental conditions. Thus, the dimensionless theoretical curves calculated from Eq. (1) can be transformed into dimensional theoretical curves that express the relation between the temperature of the fluid, T_f, and time, t, with h as parameter, and then, the value of h can be determined by selecting the one from those dimensional theoretical curves which fits best with the experimental results. Since in this investigation, the outlet temperature of the fluid from the fixed-bed with a height H, $(= T_f\,|_{z=H})$, was measured, the best curve fit was selected from dimensional theoretical curves at $z = H$. Hereafter, the term "fixed-bed packed with the PCM" is described as "heat storage column".

3 Experimental Apparatus and Procedure

The experimental loop, as shown in Fig. 1, consists of two thermostatic baths holding high and low temperature HTF, a regulation heater, a gear pump,

a heat storage column, and a terminal tank. The storage column is 109.6 mm in inner diameter and is packed with the PCM of cross-linked cylindrical polymer particles.

At the beginning, fluid (HTF) maintained at a temperature above the melting point of the particles (PCM) is flown from the top to the bottom of the column, and the particles are melted. When a uniform distribution of temperature within the column is attained, fluid maintained at a temperature lower than the initial temperature of the column is flowing from the bottom to the top, and the transient response of the inlet and outlet temperatures of the fluid are measured, each with four thermocouples, placed in a horizontal plane at the top and bottom of the column. Ethylene glycol was used as HTF.

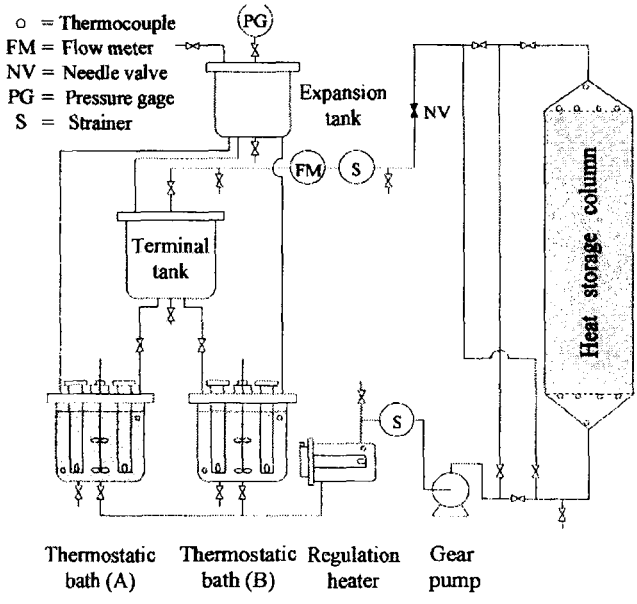

Fig. 1. Schmatic diagram of the experimental apparatus.

In the experiment on the evaluation of the heat transfer coefficients, the inlet temperature of the fluid was set above the crystallization point of the particles to keep the particles in their molten state so that the experiment was not affected by the occurrence of phase-change (latent heat) of the particles. In the experiment on the discharge characteristics of the heat storage column, the inlet temperature of the fluid was set below the crystallization point so that the process of crystallization of the particles can be involved.

As shown in Table 1, cylindrical polymer particles of two different kinds of polyethylene (Type : R1 and R2) having different dimensions were used as the PCM. R1 is a cross-linked polymer based on a high-density polyethylene. R2 is a cross-linked polymer based on the copolymer of ethylene vinyl acetate (the vinyl acetate content is 8wt. percent). The data of the apparent specific

heat of the cross-linked polymers containing the contribution of latent heat is shown in Fig. 2.

Table 1. Dimensions of polymer particles (at 20°C)

Particle symbol	Diameter [mm]	Length [mm]	Specific surface diameter [mm]
R1	3.4	9.8	4.3
R2-a	5.3	3.8	4.7
R2-b	1.9	3.1	2.2

Before conducting the experiments, fluids at high and low temperatures were flown into the heat storage column alternately more than ten times until the contraction of the column due to the melt adhesion of the particles was no longer recognized. During this time, the packing fraction of the particles in the column varied from 0.55 to 0.63 (evaluated at 20°C). The photograph of the particles, R1, subjected to the melt-freeze cycles are shown in Fig. 3. Although the particles appear to adhere tightly to one another, the degree of adhesion is not so strong and the particles can be easily detached by hand.

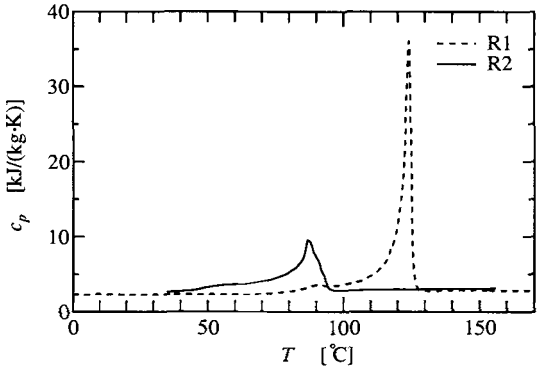

Fig. 2. Temperature dependence of the apparent specific heat of the cross-linked polymer.

4 Governing Equations and Analytical Procedure

The analytical system and coordinates are shown in Fig. 4. Fluid at a low temperature was introduced into the heat storage column, initially charged uniformly at a high temperature from the bottom, and the discharge is carried out by direct contact heat transfer between the particles and the fluid. For simplicity, the following assumptions are made in carrying out the analysis.

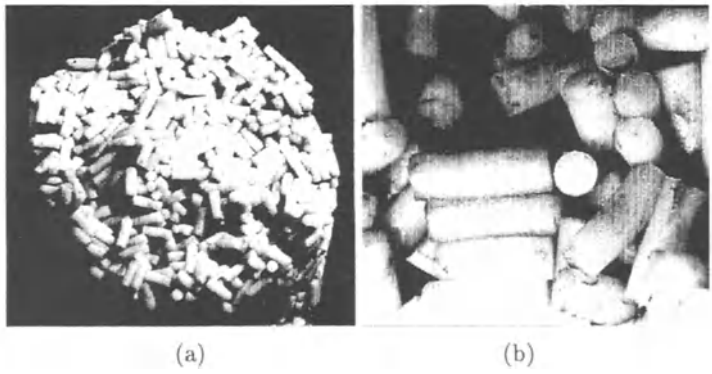

Fig. 3. Cross-linked polymer particles,R1, subjected to the melt-freeze cycles. (a) Whole aspect, (b) Local aspect

(a) The particle is considered to be of the shape of a sphere having the same specific surface diameter as that of the particle, and heat conduction occurs only in the radial direction within the sphere.
(b) All physical properties except the specific heat of the particle and fluid are considered constant and are evaluated at the mean temperature, $(T_0 + T_{in,\infty})/2$.
(c) Heat conduction between the adjacent particles is negligible, and heat conduction in the fluid along the direction of the bulk flow is also negligible compared with the convective heat transfer.
(d) The heat transfer coefficient between the particle and the fluid is uniform in the column.

Based on the above assumptions, the governing equations and the initial and boundary conditions become,

$$\rho_p c_p \frac{\partial T_p}{\partial t} = \lambda_p \frac{1}{r^2} \frac{\partial}{\partial r}\left(r^2 \frac{\partial T_p}{\partial r}\right), \tag{3}$$

$$\rho_f c_f \epsilon \left(\frac{\partial T_f}{\partial t} + v_m \frac{\partial T_f}{\partial z}\right) = ah(T_p \mid_{r=D/2} - T_f), \tag{4}$$

I.C. $T_p \mid_{t=0} = T_f \mid_{t=0} = T_0$ (5)

B.Cs. $(\partial T_p/\partial r) \mid_{r=0} = 0,$ (6)

$$-\lambda(\partial T_p/\partial r) \mid_{r=D/2} = h(T_p \mid_{r=D/2} - T_f), \tag{7}$$

$$T_f \mid_{z=0} = T_{in}. \tag{8}$$

The heat transfer velocity depends on the direction of particles. But, the direction of particles is random in the column. So, the particle is considered to be the spherical model on average.

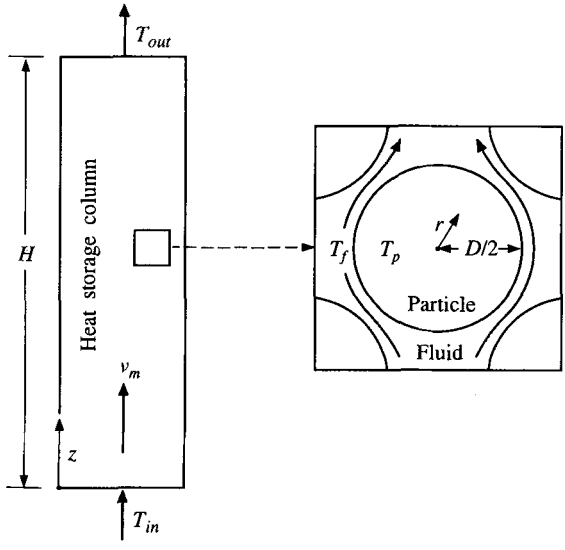

Fig. 4. Analytical system and coordinates.

The temperature distribution in the column can be calculated numerically by solving Eqs. (3) to (8) when physical properties of the particle and fluid, the operating conditions (the initial temperature of the column, T_0, the inlet temperature of the fluid, T_{in}, and the superficial mass velocity of the fluid, v_m) and the conditions of packing of the particles inside the heat storage column (the mass of the particles, M, and the height of the column, H) are given and the heat transfer coefficient, h, between the particles and the fluid is determined.

Equation (3) is discretized by the implicit finite difference method and Eq. (4) is discretized by the explicit finite difference method. The calculation continues until a difference of 0.001 between the outlet temperature of the fluid, $T_{out}(= T_f \mid_{z=H})$ and the inlet temperature, T_{in}, is attained. The time steps, the grid intervals within the particle in the radial direction and the grid intervals in the longitudinal direction of the column are selected sufficiently small so that the calculated amount of heat discharged from the column agrees with the amount of the theoretical heat stored initially in the heat storage column within 1 percent limits.

5 Experimental Results

5.1 Evaluation of the heat transfer coefficient

The transient response of T_{in} and T_{out} under typical experimental conditions is shown in Fig. 5. T_{in} changes with time mainly due to the mixing of the entering low temperature HTF and the small amount of high temperature

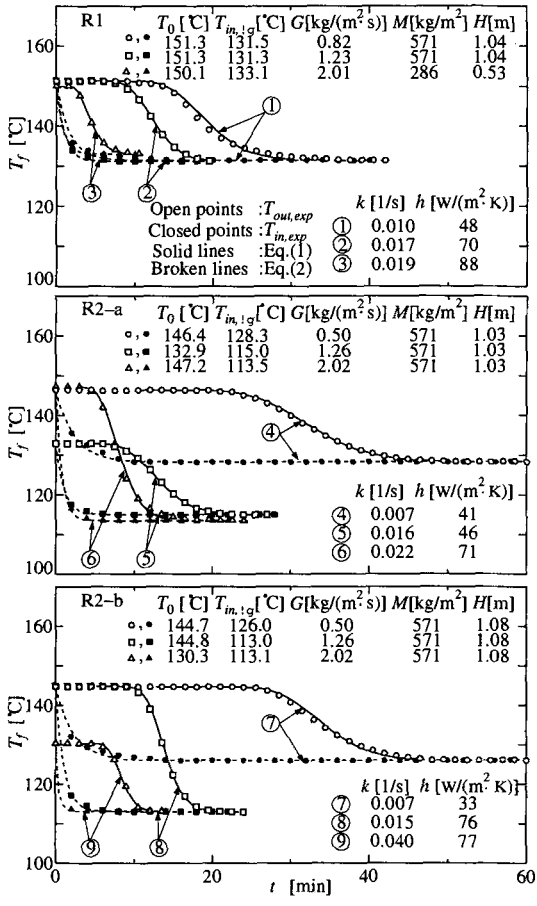

Fig. 5. Transient response of the temperature of HTF. (Experiments on the evaluation of the heat transfer coefficient.)

HTF that remains at the upstream side of the heat storage column at the end of charging. After discharging is started, T_{out} remains constant for a while as HTF at the charging temperature T_0 flows away from the column and entering HTF is also heated up to T_0 by heat transfer from the PCM. After that, T_{out} drops down to T_{in} as the sensible heat of the molten state of the PCM is removed.

The value of k is determined by the method of least squares so that the transient response of T_{in} calculated from Eq. (2) agrees with the experimental results on T_{in}. Then the dimensionless theoretical curves, calculated from Eq. (1) were transformed into dimensional theoretical curves that express the relation between T_{out} and t with h as parameter. And from the dimensional theoretical curve which fits best with the experimental T_{out}, the heat transfer

coefficient, h, is determined. In this case, h and a are based on the surface area of separate particles.

In order to correlate the experimental results, the j-factor for heat transfer, j, and Reynolds number, Re, are introduced as

$$j = \frac{h}{c_f G}\left(\frac{c_f \mu_f}{\lambda_f}\right)^{2/3}, \quad Re = \frac{G}{a\mu_f}. \tag{9}$$

The relationship between j and Re is shown in Fig. 6. Since the effect of the change of the heat transfer coefficient on the transient response of the outlet temperature of HTF is comparatively small, some scattering of the data points is observed. However, no significant differences are observed for the type and the shape of the PCM. By the method of least squares, the relationship between j and Re is obtained as

$$j = 0.090 Re^{-0.33} \quad (0.2 < Re < 3). \tag{10}$$

For comparison with the present results, the published empirical equations on heat transfer in fixed-bed packed with cylindrical and spherical particles are also shown in Fig. 6. It appears that the present experimental results are considerably lower in values compared to the published empirical equations. This is attributed to the following two factors caused by the melt adhesion of the particles during the melt-freeze cycles. Firstly, there is an increase in the contact surface area between the adjacent particles. Secondly, the generation of enlarged and contracted flow paths causes the flow to deviate mainly along the enlarged paths, resulting in an increase of local dead space of the flow.

5.2 Discharge characteristics of the heat storage column

The transient response of T_{in} and T_{out} is shown in Fig. 7 under typical experimental conditions. T_{in} changes with time due to the characteristics inherent to the experimental apparatus, as described previously. After discharging is started, T_{out} remains constant for a while as HTF at the charging temperature T_0 flows away from the column and entering HTF is also heated up to T_0 by heat transfer from the PCM. After that, as the sensible heat of the molten state of the PCM is removed, T_{out} drops down rapidly near to the temperature at which crystallization of the PCM starts, and during the removal of the latent heat of crystallization, the rate of temperature drop slows down. Finally, as the sensible heat of the crystallized state of the PCM is removed, T_{out} drops down to the same temperature as $T_{in,\infty}$.

In case of R1, nearly constant temperature of T_{out} is achieved during the removal of the latent heat of crystallization, while in case of R2, T_{out} drops gradually because the crystallization of the PCM occurs over a wide temperature range and the latent heat of crystallization is also small compared to R1 (see Fig. 2).

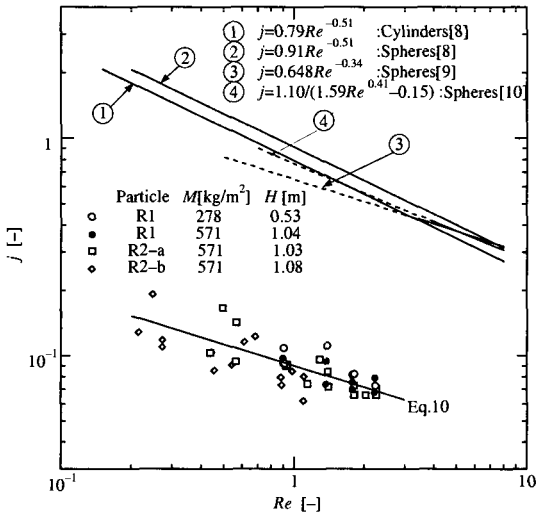

Fig. 6. Relationship between the j-factor for heat transfer and the Reynolds number.

6 Numerical Results

By using the measured T_{in} as the boundary condition, and by evaluating h from Eq. (10), the transient response of T_{out} was calculated. The calculated T_{out} is shown also in Fig. 7 by the solid lines. In all cases, the numerical results are found to be in good agreement with the experimental results.

The typical transient response of the temperature within the heat storage column is shown in Fig. 8. During discharging, the column can be divided into three regions: the first region where the removal of the sensible heat of the crystallized state of the PCM occurs, the second region where the removal of the latent heat of crystallization occurs at nearly constant temperature of the PCM, and the third region where the removal of the sensible heat of the molten state of the PCM proceeds. Each of the regions moves from the bottom ($z = 0$) to the top ($z = H$) of the column with time. In case of R1, each of the regions is clearly distinguishable, while in case of R2-a, the regions are not so clear because the crystallization of the PCM occurs over a wide temperature range and the latent heat of crystallization is also small compared to R1. The value of $(T_p\,|_{r=0} - T_p\,|_{r=D/2})$ is remarkably small compared with $(T_p\,|_{r=D/2} - T_f)$, so the demerits of using the low thermal conductivity material as the PCM is overcome. The thermal resistance in the PCM is always negligible compared with that in HTF when G is changed, because the increase in the value of the heat transfer coefficient between the PCM and HTF as G increases is compensated by the short contact time between the PCM and HTF.

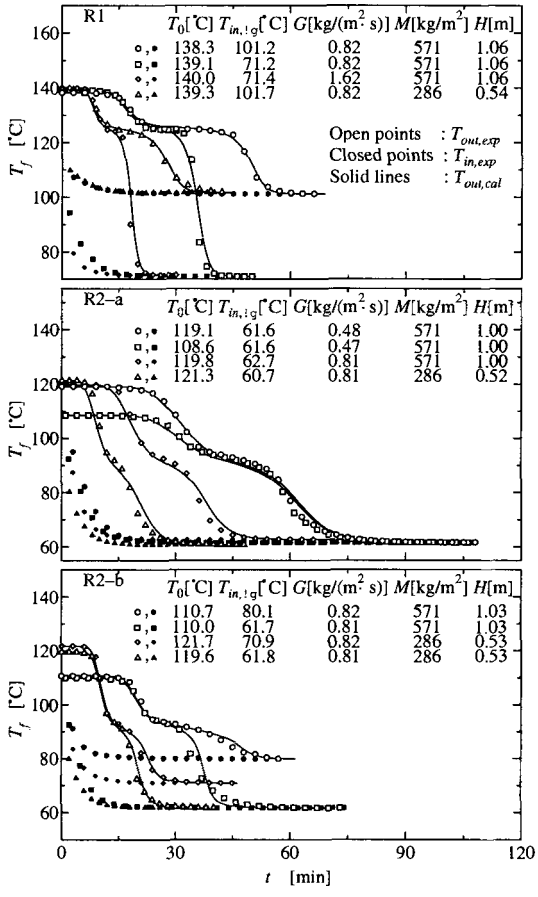

Fig. 7. Transient response of the temperature of HTF.

7 Conclusions

The heat transfer coefficient between the phase change material (PCM) and heat transfer fluid (HTF) in latent heat storage columns packed with the cross-linked cylindrical polymer particles was evaluated experimentally using Schumann's extended theory, and an empirical formula for estimating the heat transfer coefficient was presented. The resulting heat transfer coefficients were found to be definitely lower than those predicted from previously published work.

The transient response of the outlet temperature of HTF were calculated numerically by using the empirical formula for estimating the heat transfer coefficient. Fair agreement between the numerical and the experimental results proved the validity of the present numerical method in analyzing the discharge characteristics of a latent heat storage column.

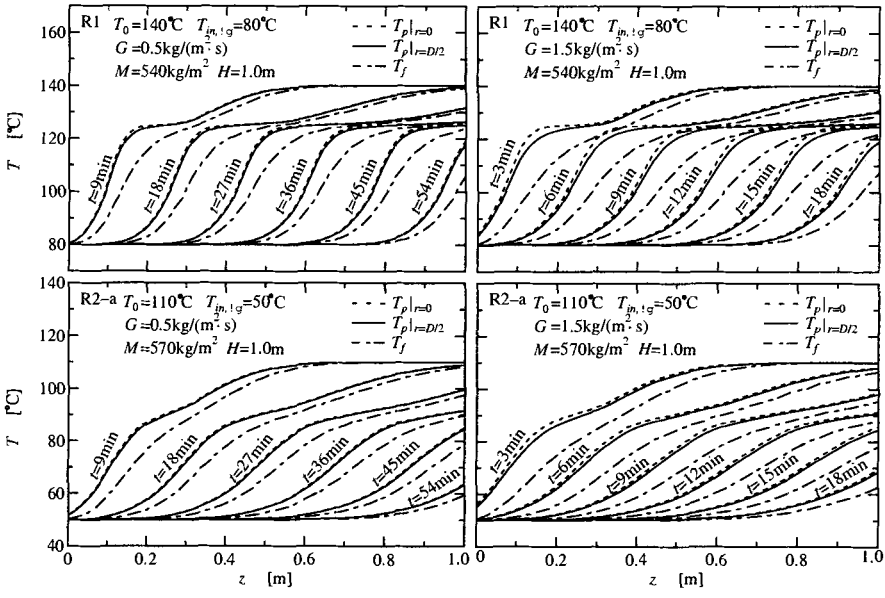

Fig. 8. Transient response of the temperature within the heat storage column.

Nomenclature

a = surface area of the particles unit volume of the heat storage column [m^2m^{-3}]
c = specific heat capacity [$Jkg^{-1}K^{-1}$], [$kJkg^{-1}K^{-1}$]
D = specific surface diameter of the particle [mm], [m]
G = superficial mass velocity of fluid (mass flow rate of fluid per unit cross sectional area)
H = height of the heat storage column [m]
h = heat transfer coefficient [$Wm^{-2}K^{-1}$]
j = j-factor for heat transfer defined by Eq. (9) [-]
k = time constant in Eq. (2) [s^{-1}]
M = mass of particles per unit cross sectional area of the heat storage column [kgm^{-2}]
r = radial coordinate [m]
Re = Reynolds number defined by Eq. (9) [-]
T = temperature [°C]
t = time [s], [min]
v_m = mean interstitial velocity of fluid [ms^{-1}]
z = longitudinal coordinate [m]
ϵ = void fraction in the heat storage column [-]
λ = thermal conductivity [$Wm^{-1}K^{-1}$]
μ = viscosity [$Pa \cdot s$]
ρ = density [kgm^{-3}]

τ = dimensionless time, $\tau = ah(t - z/v_m)/\{\rho_p c_p(1-\epsilon)\}$ [-]
ϕ = dimensionless time constant,$\phi = k\rho_p c_p(1-\epsilon)/(ah)$ [-]
ζ = dimensionless longitudinal coordinate, $\zeta = ahz/(\rho_f c_f \epsilon v_m)$ [-]
θ_f = dimensionless temperature of fluid,
$\theta_f = (T_f - T_{in,\infty})/(T_0 - T_{in,\infty})$ [-]
$0, \infty$ = initial state, final state
cal, exp = numerical, experimental
in, out = inlet, outlet

References

1. Davison, J. E. and Salyer, I. O., "Electron Beam Irradiation of High Density Polyethylene Pellets for Thermal Energy Storage," *Oak Ridge National Lab. Rep.* , ORNL/SUB-7641/1 (1980)
2. Salyer, I. O., and Davison, J. E., "Thermal-Energy Storage in Crosslinked Pellets of High-Density Polyethylene for Home Heating and Cooling via Off-Paek Electric Power Utilization," *J. Appl. Polymer Sci.*, Vol. **28**, pp. 2903–2924 (1983)
3. Boneh, H., Marmur, A., and Narkins, M., "Thermal Energy Storage in Columns Packed with Crosslinked Polyethylene Tube," *Polymer Eng. Sci.*, Vol. **24**, pp 1227–1231 (1984)
4. Kamimoto, M., Abe, Y., Sawata, S., Tani, T., and Ozawa, T., "Latent Thermal Storage Unit Using Form-Stable High Density Polyethylene; PartT: Performance of the Storage Unit.," *ASME Journal of Solar Energy Engineering* , Vol. **108**, pp. 282–289 (1986)
5. Kamimoto, M., Abe, Y., Kanari, K., Takahashi, Y., Tani, T., and Ozawa, T., "Latent Thermal Storage Unit Using Form-Stable High Density Polyethylene; PartU: Numerical Analysis of Heat Transfer," *ASME Journal of Solar Energy Engineering* , Vol. **108**, pp. 290–297 (1986)
6. Schumann, T. E. W., "A Liquid Flowing Through a Porous Prism, " *J. Flanklin Inst.* , Vol. **208**, pp. 405–416 (1929)
7. Cyuma, Y., Murata, S., and Iwamoto, M., "Unsteady State Heat Transfer in Packed Beds of Farm Products," *J. Soc. Agric. Machinery* , Japan, Vol. **31**, pp. 45–51 (1969)
8. Yoshida, F., Ramaswami, D., and Hougen, O. A., "Temperatures and Partial Pressures at the Surface of Catalyst Particles," *A. I. Ch. E. J.* , Vol. **8**, pp. 5–11 (1962)
9. Satterfield, C. N., and Resnick, H., "Simultaneous Heat and Mass Transfer in a Duffusion-Controlled Chemical Reaction; PartU: Studies in a Packed Bed," *Chem. Eng. Prog.* , Vol. **50**, pp. 504–510 (1954)
10. DeAcetis, J. and Thodos, G., "Mass and Heat Transfer in Flow of Gases Through Spherical Packings," *Ind. Eng. Chem.* Vol. **52**, pp. 1003–1006 (1960)

(Received 12 Feb. 1999, accepted 29 April 1999)

Development of an Efficient Static-Type Ice Thermal Energy Storage Vessel Using a Low Concentration Aqueous Solution

Kengo Sasaguchi[1], Tomoaki Yoshiyama[1], Testushi Nozoe[1], and Yoshiyuki Baba[2]

[1] Department of Mechanical Engineering and Materials Science, Kumamoto University 2-39-1, Kurokami, Kumamoto 860-8555, Japan
[2] Kyushu Electric Power Co., Inc. 2-1-82, Watanabe-Dori, Chuo-Ku, Fukuoka 810-8720, Japan

Abstract. If an aqueous solution with low concentration is used for static-type ice-storage-vessels, even when a large amount of solution (aqueous ethylene glycol in this study) is solidified and bridging of ice developed around cold tubes occurs, the pressure increase can be prevented by the existence of a continuous liquid phase in the solid-liquid two-phase layer (mushy layer) which opens to an air gap at the top of a vessel. Therefore, one can continue to solidify an aqueous solution after bridging occurs, achieving a high ice packing factor (IPF) which is defined as the ratio of mass of created ice to initial mass of water in a vessel. In the present study, experiments using small-scale test cells have been conducted with initial concentration, C_0, of aqueous ethylene glycol ranged from 0 mass % to 5.0%. It was seen that the IPF obtained using the solution with $C_0 \leq 1.0\%$ is much greater than the IPF of 65%-70% using pure water for which the solidification must be stopped before bridging, and that a large pressure increase is not observed during solidification of the solution with $C_0 \geq 0.5\%$. Therefore, if we use the solution with $0.5\% \leq C_0 \leq 1.0\%$, we can probably obtain a large IPF without a large pressure increase for real ice-storage-vessels.

1 Introduction

Recently, for the purpose of effective load leveling of electric power at night, much attention has been given to ice thermal energy storage systems, e.g., see Sasaguchi, K., Kusano, K., Viskanta, R., (1997) and Seki, N., (1997). There are two types of ice-storage-vessels, that is, a static-type and a dynamic-type. IPF (ice packing factor), defined as the ratio of the mass of produced ice to the mass of water initially contained in a vessel, is larger for the static-type ice- storage-vessels (STISV) than for the dynamic ones. Among STISV, a type shown in Fig. 1 for which both solidification and melting occur on heat-exchanger tubes has the simplest structure. Hence, this type of ice-storage-vessel is most appropriate for small or medium scale air conditioning systems. However, IPF is still restricted to $65\% - 70\%$ for such vessels because the pressure in confined water is largely increased, resulting in damage of the

tubes when solidification is further developed after bridging of ice developed around cold tubes so that solidification should be stopped before the bridging.

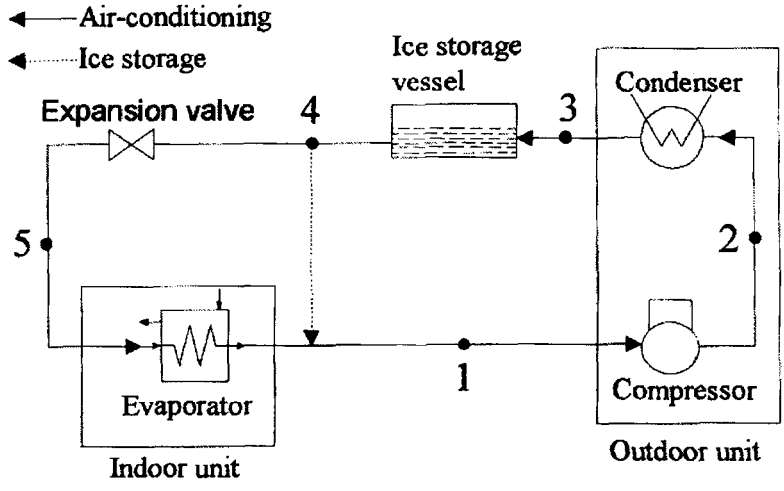

Fig. 1. An air conditioning system including an ice storage vessel

If an aqueous solution with low concentration is used for a static-type ice-storage-vessel, even when a large amount of solution (aqueous ethylene glycol in this study) is solidified and the bridging occurs, the pressure increase can be prevented because of existing of the continuous liquid phase in the solid-liquid two-phase layer or mushy layer, see Sasaguchi, K., Noguchi, T., Moriyama, Y., (1991), which opens to an air gap at the top of the vessel. Furthermore, there is some possibility of augmentation of the melting rate, because hot melt could permeate the mushy region and could melt the mush.

In the present study, experiments using small-scale test cells have been conducted for initial concentration of aqueous ethylene glycol ranged from 0 mass % to 5.0%. We prepared two types of test cells; one was a rectangular cell with a cold (-5°) or a hot (10°) bottom wall (test cell I) on which melting or solidification was developed, and the other was a rectangular cell in which a single or two cold or hot cylinders (test cell II) were placed. We observed the change in the morphology of the solidified layer with the change in the concentration of aqueous ethylene glycol. Timewise variations of the shape of the melt and the temperature distribution in the melt were also observed using a thermo-viewer. The melting and solidification rates were evaluated by measuring a change in the volume of water in burettes connected to the test cells. In addition, pressure measurements were conducted using a specially prepared test cell (test cell III).

2 Experiments Using Test Cells I and II

2.1 Experimental apparatus and procedure

Figs. 2 and 3 show test cells I and II, respectively. The internal width, height and depth of test cell I are 100mm, 40mm and 50mm, and those of test cell II are 112mm, 196mm and 50mm, respectively. The temperatures of the bottom wall for test cell I and the cylinder walls for test cell II are set at -5° or 10° and solidification or melting is initiated. All other walls are well insulated. The initial temperature of the liquid for the solidification is set at 1.5° above the liquidus temperature corresponding to the initial concentration. The melting is started after 4 hours solidification for cell I or 10 hours solidification for cell II. We observed the change in the morphology of the solidified layer with the change in the concentration of aqueous ethylene glycol. Timewise variations of the shape of the melt and the temperature distribution in the melt were also observed using a thermo-viewer. The melting and solidification rates were evaluated by measuring the change in the volume of water in burettes connected to the test cells (not shown in Figs. 1 and 2), assuming that solid created during solidification processes is pure ice.

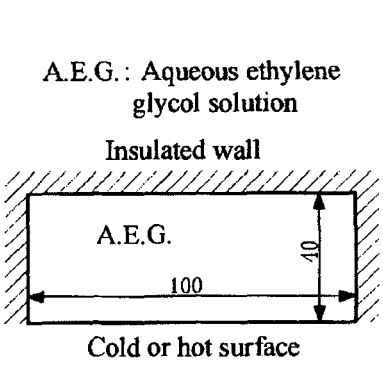

Fig. 2. Test cell I with a cold or hot flat surface

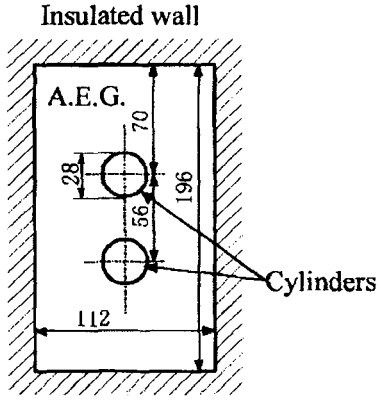

Fig. 3. Test cell II with cylinders

2.2 Results and discussion

Fig. 4 shows timewise variations of created ice volume, V_s, divided by the surface area, A, of the bottom wall of test cell I for initial solution-concentration, C_0, of 0%, 0.25%, 0.5%, 1.0% and 5.0%. The numbers in parentheses indicate the percentage of the volume of ice for the corresponding concentration to that for $C_0 = 0\%$ at time $t = 10800$s. As is seen in the figure, the value of V_s/A decreases with increasing C_0. This is because the amount of rejected solute increases with C_0 and the solute accumulates near the interface

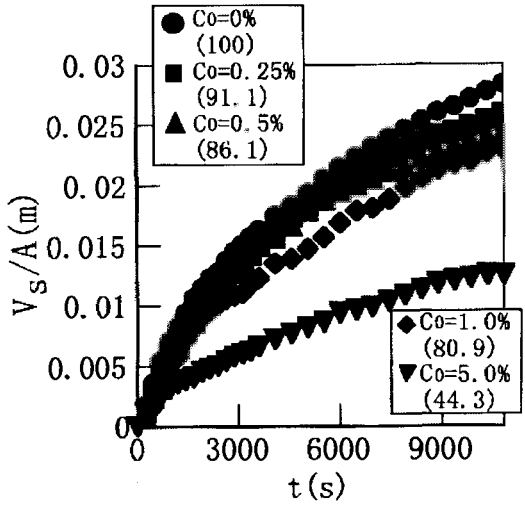

Fig. 4. The effect of initial concentration on solidification for test cell I

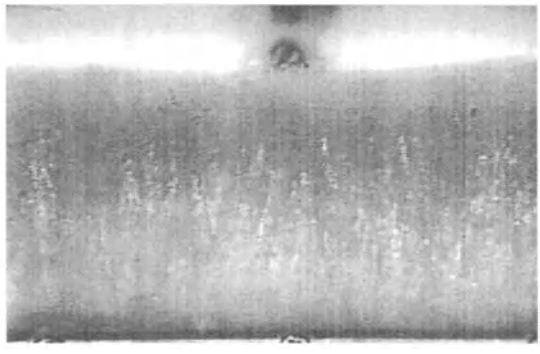

Fig. 5. Morphology of solid at $t = 10800$s for $C_0 = 0.5\%$ (Test cell I)

between the solidified layer and the melt, resulting in a decrease of the freezing temperature. However, the value of V_s/A for $C_0 \leq 0.5\%$ is still close to that for $C_0 = 0\%$, and the solidified layer consists of solid-liquid coexisting phases as shown in Fig. 5 for $C_0 = 0.5\%$. Therefore, it seems that one is able to solidify a large amount of liquid after the ice bridging occurs.

Fig. 6 shows the comparison between the experimentally obtained solidification fraction, R_s, and that calculated with a numerical code proposed by Sasaguchi, K., Moriyama,Y., (1993) in which only thermal and solutal diffusion is considered. The solidification fraction is defined as the ratio of solidified volume to the volume of test cell I. It is seen in the figure that agreement between the values of R_s obtained by the experiments and calculations

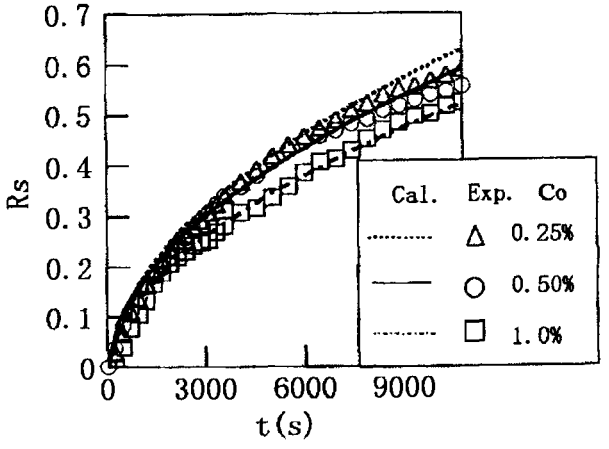

Fig. 6. Comparison of calculated and experimental solidification fraction for test cell I

is very good, meaning that thermal and solutal diffusion mainly dominates the development of solidification for this simple test cell geometry.

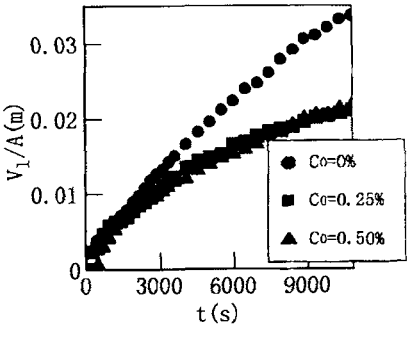

Fig. 7. The effect of initial concentration on melting for test cell I

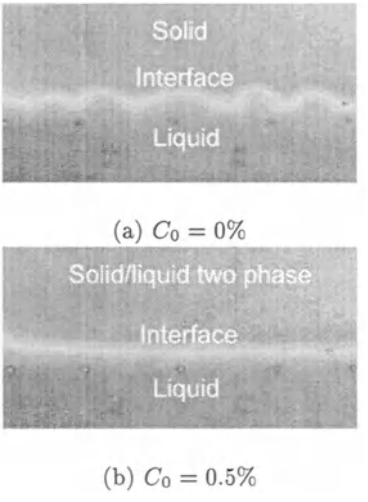

Fig. 8. Comparison of melt for test cell I

Fig. 7 shows the timewise variations of the melt volume, V_l, divided by A obtained by the melting experiments. Unlike the value of V_s/A for the solidification, the value of V_l/A drastically decreases with a slight increase in the initial concentration, C_0. To clarify the physical meaning of this fact,

temperature fields were observed by a thermo-viewer. The results are shown in Fig. 8. For $C_0 = 0\%$ (pure water) in Fig. 8a, Bénard-cell-like convection cells arise so that a wavy interface between the solidified layer and the liquid region observed in Fig. 8a (the interface is shown as a white curve in the figure). Convection enhances melting so that the value of V_l/A for $C_0 = 0\%$ nearly linearly increases with time (compare to Fig. 4 for the solidification). However, for $C_0 = 0.5\%$ in Fig. 8b the interface is almost parallel to the hot wall, and therefore no natural convection is generated in this case. This is probably because nearly pure water produced by melting of the solid in the solid/liquid two phase region accumulates near the interface and a stable concentration gradient is formed in the melt so that thermal convection is depressed.

Next, Fig. 9 shows timewise variations of V_s/A, where A is the total surface area of the two cylinders, for test cell II. Comparing Fig. 9 with Fig. 4 for test cell I, it is seen that the reduction of the value of V_s/A for $C_0 \leq 0.5\%$ from that for $C_0 = 0\%$ is also small for test cell II. As seen in Fig. 10, the solidification for $C_0 = 0.5\%$ develops in almost the same shape around the two cylinders. This indicates almost no effect of rejected solute on the development of solidification.

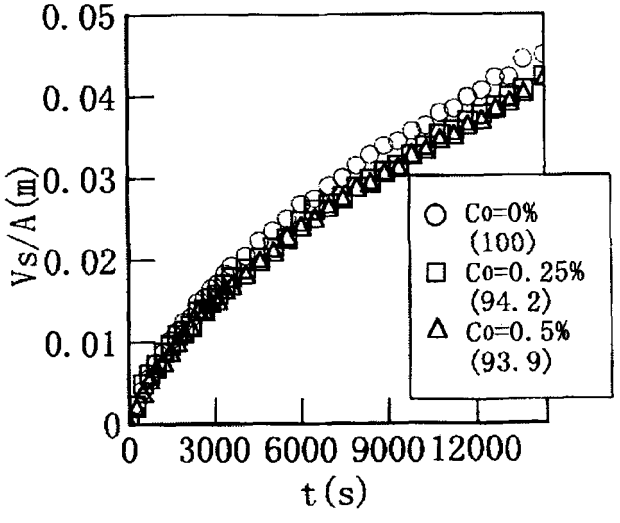

Fig. 9. Effect of initial concentration on solidification for test cell II

Fig. 11 shows the timewise variations of V_l/A for test cell II. Unlike the case for test cell I shown in Fig. 7, the value of V_l/A for test cell II does almost not decrease with the concentration, C_0. Figs. 12 and 13 by a thermo-viewer

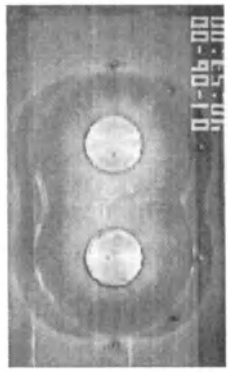

Fig. 10. Shape of solid at $t = 14400$s for $C_0 = 0.5\%$ (Test cell II)

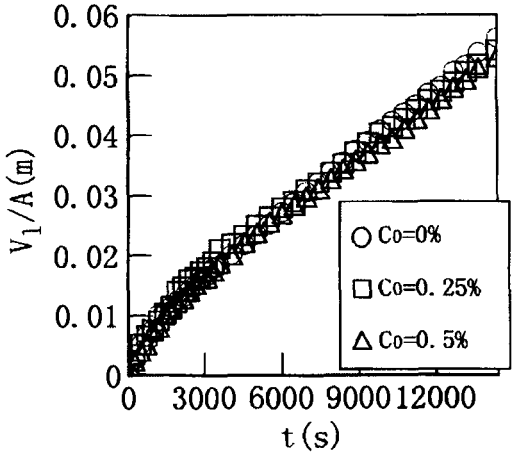

Fig. 11. Effect of initial concentration on melting for test cell II

show the melt shapes (white portions around the cylinders in the figures) for $C_0 = 0\%$ and 0.5%, respectively. For $C_0 = 0\%$ (Fig. 12), the melting above the upper cylinder is enhanced due to natural convection. However, $C_0 = 0.5\%$ (Fig. 13), the melting enhancement above the upper cylinder is depressed, and the melting in the lateral directions of the cylinders is enhanced. For test cell II, liquid with low concentration is accumulated in the upper portion of the melt, but a thermally driven upward flow along the cylinder surfaces can change the direction to the lateral one. Therefore, the melting in the lateral directions of the cylinders is enhanced. A similar phenomenon was observed by Yamada, et. al., (1993). The only slight decrease in V_l/A with $C_0 = 0\%$ and 0.5% for test cell II (Fig. 11) is due to the enhancement of the lateral melting. This is pronounced contrast to the case for test cell I (Fig. 7).

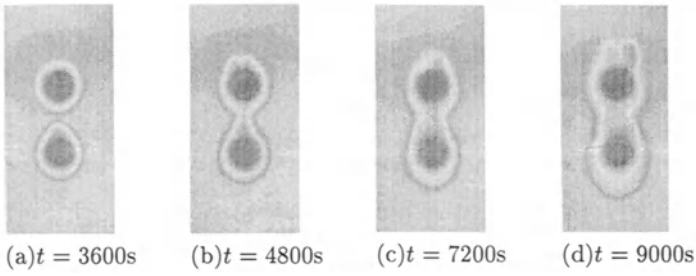

Fig. 12. Development of melt for $C_0 = 0\%$

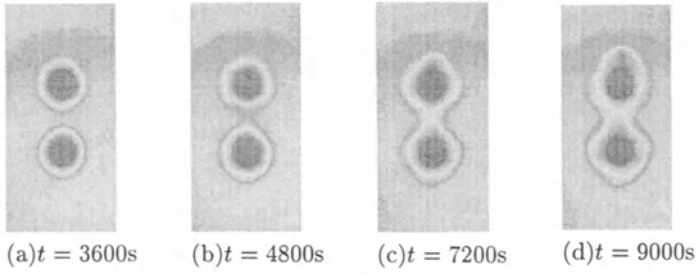

Fig. 13. Development of melt for $C_0 = 0.5\%$

3 Experiments Using Test Cell III

In order to measure the pressure increase during solidification, test cell III (Fig. 14) was prepared. The inner width, height and depth are 180mm, 230mm and 60mm, respectively. Four cylinders with the outer diameter of 28mm are set in the cell, and the vertical and horizontal pitches of the cylinders are both 80mm. A pressure sensor is placed at the center of the area surrounded by the cylinders. The cell is filled with pure water or aqueous ethylene glycol with a prescribed concentration, and the liquid temperature is set at 1°. The temperature of the four cylinders are all set at -5° by circulation of a cold brine from a constant temperature bath, and the solidification is initiated. A burette is installed on the top wall of the test cell, and it is open to the ambient at atmospheric pressure. Since all cell walls are brass plates, they are cooled the same as the cylinders are. Therefore, it seems that the liquid is confined by solid developed around the cylinders and on the front and back cell-walls as solidification progresses, that is, so-called *bridging* occurs. For pure water, the solid is pure rigid ice containing no liquid phase. Hence, it can be imagined that the water pressure is greatly increased if the solidification proceeds after *bridging*.

Fig. 15 shows the pressure variations with time for $C_0 = 0\%$, 0.1%, 0.25% and 0.5% in weight. For pure water ($C_0 = 0\%$), the pressure increase is abrupt, and it becomes over 2.0×10^6 Pa (the experiment was stopped to

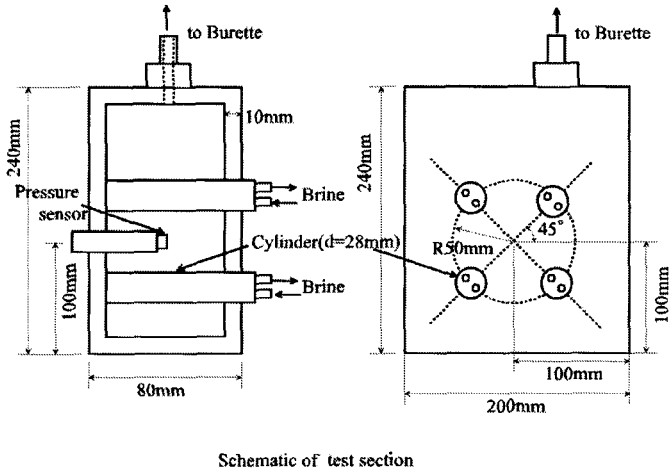

Fig. 14. Test cell III for pressure measurement

protect the test cell from damage when the pressure would be larger). As the concentration becomes larger, the onset of the pressure increase is delayed, its peak becomes smaller, and the pressure is finally reduced to the atmospheric value. In particular, for $C_0 = 0.5\%$ only a very small pressure increase is observed. This means that the liquid phase contained in the solidified layer of the aqueous ethylene glycol makes a continuous passage to the atmosphere through the burette.

From the facts mentioned above, it can be said that we can change the whole amount of aqueous ethylene glycol to a solid/liquid two phase state for $C_0 \leq 1.0\%$ and the amount of solid (nearly pure ice in ingredients) is much larger than that for the conventional vessels with pure water.

4 Conclusion

The quantity of ice is decreased with increasing initial concentration, C_0, of the solution because the quantity of liquid contained in the mushy layer is increased as C_0 is increased. For example, after three hours solidification for test vessel I, the quantity of ice for $C_0 = 0.25\%$, 0.5%, 1.0% and 5% are 91.1%, 86.1%, 80.9% and 44.3% of the quantity of ice for $C_0 = 0\%$ (pure water), respectively. The ice packing factor (IPF) for conventional ice-storage-vessels with pure water is around 70%, meaning that solidification must be stopped after 70% of the initial water-quantity is solidified because of a large pressure increase in confined water due to the bridging of ice. A large pressure increase in liquid surrounded by ice is not observed for $C_0 = 0.5\%$. Therefore, if we use aqueous ethylene glycol with $0.5\% \leq C_0 \leq 1.0\%$, we can change the whole amount of aqueous ethylene glycol to a solid/liquid two phase state without

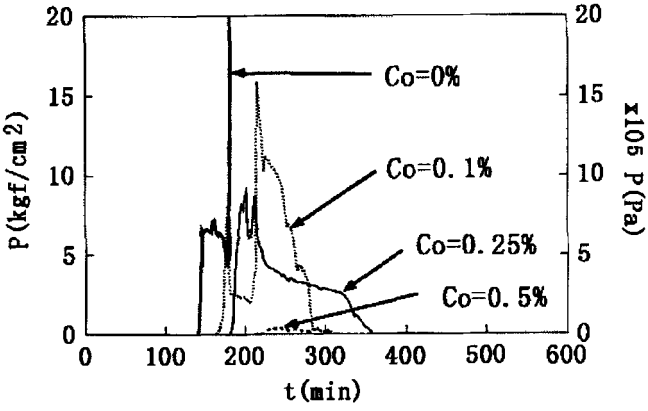

Fig. 15. The effect of initial concentration on pressure increase

a large pressure increase and the IPF becomes much larger than that for the conventional vessels with pure water. The augmentation of the melting rate was not achieved using the solution with $0.5\% \leq C_0 \leq 1.0\%$, because the mushy layer was too dense for melt to permeate it. Therefore, some ways are needed to enhance the melting.

References

1. Sasaguchi, K., Kusano, K., Viskanta, R., (1997) A Numerical Analysis of Solid/Liquid Phase Change Heat Transfer around Two-Horizontal, Vertically Spaces Cylinders in a Rectangular Cavity. *Int. J. Heat Mass Transfer*, **40**, 1343
2. Sasaguchi, K., Moriyama, Y., (1993) The Effect of Initial Superheat on the Solidification of a Binary Mixture, In: Lee, J., S., Chung, S., H., Kim, K., H., (Eds.), *Proc. of the 6th Int. Symposium on Transport Phenomena in Thermal Engineering*, Seoul, Korea, May 9-13, Bell House Inc., **1**, 309-314
3. Sasaguchi, K., Noguchi, T., Moriyama, Y., (1991) An Experimental Study on Solidification of a Binary Mixture, *Proc. of 3rd ASME/JSME Ther. Eng. Joint Conf.*, **1**, 209-216
4. Seki, N., (1997) *Thermal Storage Engineering* (in Japanese), Morikita Suppan, Japan
5. Yamada, M., et. al., (1993) Melting Heat Transfer along a Horizontal Heated Tube Immersed in Liquid Ice, *JSME Int. J.*, Ser.B, **36**, 343

(Received 12 Feb. 1999, accepted 15 May 1999)

Heat Storage for a Bus Petrol Internal-Combustion Engine

Leonard L. Vasiliev, Victor S. Burak, Andry G. Kulakov, Donatas A. Mishkinis, and Pavel V. Bohan

Luikov Heat & Mass Transfer Institute, P.Brovka 15, 220072 Minsk, Belarus

Abstract. The heat storage (HS) system for pre-heating a bus petrol internal combustion engine to starting was mathematically modelled and experimentally investigated. The development of such devices is an extremely urgent problem especially for regions with a cold climate. We discuss how HS works on the effect of absorption and rejection of heat energy at a solid-liquid phase change of a HS substance. In the first part of the paper a numerical method to calculate the HS mass-dimensional parameters and their characteristics are described. In the experimental part of the paper results are given of experiments on the pre-heating device aiding to start a carburettor engine under operational conditions and analysis of data received. Practical confirmation of the theoretical development of HS devices for a bus engine for starting by pre-heating is given.

1 Introduction

Heat storage (HS) devices mounted on automobiles permit elimination of numerous negative factors connected with the 'cold' start of an engine: These are increased charge of a fuel, large concentration of CO and C_nH_n in the exhaust, decrease of engine resources and high load onto accumulator and starter [1, 2]. For example, Schatz Thermo Engineering Company reported that reductions of 40 and 50% in unburnt hydrocarbons and CO, respectively, were achieved during the test of a latent HS with barium hydroxide as a phase change material (PCM) [3]. Bridgegate Ltd. developed and tested a latent HS device for BMW 5-series model vehicles. The HS provides a 30% reduction in unburnt hydrocarbons and CO during the engine starting period. The salt mixture $Mg(NO_3)H_2O$ and $LiNO_3$ are used as a PCM [4].

Presently, different systems for minimizing the energy consumption and pollutant production from automobile engines during cold starting are proposed. There are adsorption based start-preheating devices, electrically heated catalysts systems, latent heat storage, electric engine heaters, etc. A detailed analysis of the advantages and disadvantages of the proposed systems is given in [5].

HS systems should have high heat capacity, minimum thermal storage losses, comparatively small dimensions and mass, vibration resistance design to satisfy the conditions of the bus operation and compatibility with the environment. In the Luikov Heat and Mass Transfer Institute, Porous Media

Laboratory, an experimental sample of HS systems for an urban bus LAZ-695 N was developed, made and tested . This HS works on the basis of rejection and absorption of latent heat of the phase-change material. The main advantages of such types of HS devices are high density of the storage energy and stable exit temperatures of the antifreeze from the HS.

The key part of the HS systems is a heat storage material or phase-change material. For the low-temperature range the following PCM are particularly useful [6]:

$Na_2CO_3 \cdot 12H_2O$, $NaCH_3$, $CaO \cdot 3H_2O$,
$NaOH \cdot H_2O$, $Ba(OH)_2 \cdot 8H_2O$, $LiNO_3 \cdot 3H_2O$.

To select the PCM one needs to obey the following criteria: high latent heat at phase change; relatively high thermal conductivity of the solid state and high specific heat capacity of the liquid state; good chemical stability in the working-temperature range; high density; reasonable costs. Crystal hydrates of salts are compatible with stainless steel with Cr-Ni additives [7, 8]. SS is a material applicable for HS capsules and envelopes. Among polymers, the most suitable as an envelope material is polyethylene.

2 Numerical Model

The technique of the calculation of HS parameters consist of two stages.

At the first stage the mass-dimensional characteristics of the HS are defined. The heat necessary for heating the engine over a temperature difference ΔT is determined as

$$Q = \sum c_i m_i \Delta T, \tag{1}$$

where c_i and m_i denote the specific heat and weight of the engine components. The input data and parameters are (Fig. 1): R radius of the HS envelope, r radius of the capsules, Δr thickness of the capsule wall, d width of the cavities for uniform flow over of the capsules by a circulating liquid, thermal properties of the PCM, material of the capsules and the heat transfer fluid, geometrical dimensions and specific heats of the materials. The next step is then the determination of the number of capsules, n, their length L and the necessary amount of the PCM m. At this stage of the calculation updating of the dimensions R, r, d to define the most reasonable ratio of the envelope radius R and the length of the capsules L is carried out [10].

In the second stage the discharge process rate of the HS is calculated. The following assumptions were made in the physical model:

- The crystallization process of the PCM occurs simultaneously over the whole length of the capsules, the phase boundary is moving in the radial direction. It is caused by a large temperature drop between the PCM and the heat transfer fluid, when the phase boundary in the axial direction has no time to be generated.

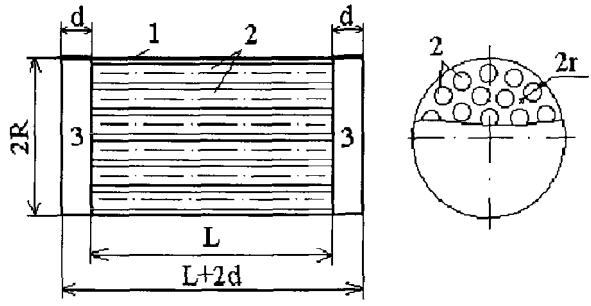

Fig. 1. Design dimensions of the HS, used in calculations. 1 - envelope of the HS, 2 - capsules, 3 - cavities for the creation of a uniform flow around the capsules

- At each instant of time the temperature distribution in the crystalline PCM layer and the temperature of the capsule wall correspond to the temperature distribution in a stationary mode.
- The average heat transfer characteristics for the capsule length were used.
- The specific heat of the HS materials in case of superheating was not taken into account in the calculation of the discharge-process rates.

The specific heat flux transmitted from the PCM to the heat transfer fluid during HS discharge is defined as [11]

$$q = h\Delta T, \tag{2}$$

where ΔT is the average-logarithmic temperature gradient,

$$\Delta T = (T_{out} - T_{in}) / \ln \frac{T_p - T_{in}}{T_p - T_{out}}. \tag{3}$$

T_p denotes the melting temperature of the PCM. The overall heat transfer coefficient h for this case is

$$h = \left[\frac{1}{a} + \frac{r}{\lambda_w} \ln \left(\frac{r}{r - \Delta r} \right) + \frac{r}{\lambda_t} \ln \left(\frac{r - \Delta r}{r - \Delta r - \sigma_t} \right) \right]^{-1}, \tag{4}$$

where a is the heat exchange coefficient between the wall of the capsules and the heat transfer fluid, λ_w, λ_t are the thermal conductivity of the wall material, of the capsules and the PCM, respectively, and σ_t is the time-dependent thickness of the solidified PCM.

Thus, the problem of the discharge process rate calculation, i.e. the determination of the dependence of the heat flux on time, $q(t)$, is to define the time dt of crystallization of an elementary cylindrical layer with the thickness dr. The dependence can be found from the appropriate ratio of the weight

of the crystallizing PCM. On the one hand this weight is proportional to the heat flux from the PCM to the heat transfer fluid,

$$dm = 2\pi r dt q L/H, \tag{5}$$

on the other hand, this weight equals

$$dm = 2\pi r_1 dr P_t L, \tag{6}$$

where P_t, H are the density and latent heat of the PCM, respectively, and r_1 is the radius of the phase-change border at that instant.

For the determination of the heat flux q it is necessary to define input and output temperatures of the HS, T_{out} and T_{in},

$$T_{out} = T_{in} + \frac{2\pi P_t r_1 dr L H + Q_2}{dt c_l g P_l}. \tag{7}$$

Here P_l, c_l, g are the density, specific heat and the volumetric flow rate of the heat transfer fluid, respectively, and

$$Q_2 = 2pL \left[P_t c_t \int_{r_1}^{r-\Delta r} \Delta T_1(r)\, r dr + P_w c_w \int_{r-\Delta r}^{r} \Delta T_1(r)\, r dr \right]. \tag{8}$$

Q_2 takes into account the quantity of rejected heat which was stored in the materials of the capsule by the specific heat. $\Delta T_1(r)$ is the temperature difference of the elementary layers of the capsule while the thickness of the crystallized layer increases by dr. P_t, c_t, P_w, c_w are the density and specific heat of the PCM and the capsule wall, respectively. In case of the temperature distribution for a stationary mode, the sum of the integrals (8) is evaluated analytically and is reduced to the finding of the inner and outer wall temperatures of the capsule.

The temperature T_{in} depends on time and is defined by the amount of heat, $Q = Q(t - t_0)$ (Q is a function of the time), extracted from the HS to the heat transfer fluid at time $t - t_0$, where $t_0 = V/g$ is the time of the heat transfer-fluid replacement in a cooling jacket of the engine with volume V. The dependence of the temperature on an input of the HS as a function of the time is defined by the equations

$$\begin{aligned} T_{in} &= T_{in0}, && \text{for } t<t_0, \\ T_{in} &= T_{in0} + T\frac{Q_3 g}{V_1 \sum c_i m_i}(t - t_0), && \text{for } t_0<t<t_0 + V_1/g, \end{aligned} \tag{9}$$

where T_{in0} denotes the temperature of the engine before the beginning of the HS discharge, and Q_3 is the heat rejected from the heat transfer fluid in the HS volume V_1 during the liquid cooling down from the melting temperature T_p to the temperature

$$T = \frac{T_p V_1 c_1 P_1 + \sum c_i m_i T_{in0}}{V_1 c_1 P_1 + \sum c_i m_i}.$$

For $t > t_0 + V_1/g$,

$$T_{in} = T_{in0} + T + \frac{Q(t - t_0 - V_1/g)}{\sum c_i m_i}. \tag{10}$$

This mathematical model assumes that crystallisation of the PCM is started at time $t = V_1/g$, i.e., after replacement of the heat transfer fluid in HS.

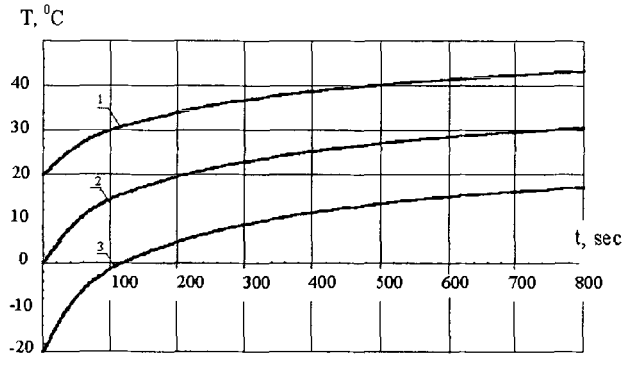

Fig. 2. Temperature evolution as a function of time for different ambient temperatures, 1 - 20 °C, 2 - 0 °C, 3 - -20 °C

The system of equations was solved by a numerical iteration method. The quantity of the evolving heat, Q_i, was defined with the varying thickness of the solidified layer Δx ($r_1 = r - i\Delta x - \Delta r$), i.e., the crystallisation time Δt_i of a layer of thickness x was calculated. The value of the heat-transfer coefficient was specified after each step along r, accounting for the changes of thermal properties of the heat-transfer fluid [10].

Numerical dependence of the engine temperature as a function of time, for different values of the ambient temperature, is presented in Fig. 2 . The lowest ambient temperature corresponds to the highest value of the engine temperature difference before and after the HS discharge process, due to the largest temperature difference between the HS and the engine.

The dynamic behavior of the heating of the engine for different flow rates of the antifreeze is shown in Fig. 3. An increase in the flow rate up to 60 $\mathrm{l\,min^{-1}}$ does not give rise to a substantial rise in the engine-heating rate. The results of the calculation were used for the design of the experimental HS prototype .

3 Heat Storage Design

The experimental HS (Fig. 4) consists of three basic parts: the cylindrical envelope, capsules with PCM and a jacket with a thermal insulation. The

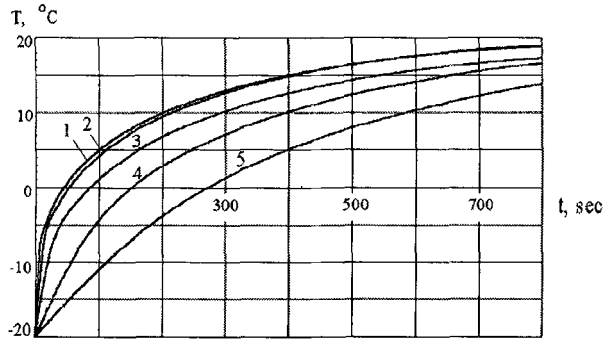

Fig. 3. Dynamics of the heating of the engine for different flow rates of antifreeze, 1 - 120 l min^{-1}, 2 - 60 l min^{-1}, 3 - 30 l min^{-1}, 4 - 10 l min^{-1}, 5 - 5 l min^{-1}

height of the HS without thermal insulation is 470 mm, the diameter 300 mm. The SS steel meshes (6) are required for fixing the PCM capsules and for the creation of entrance and outlet cavities. The cavities are responsible for the uniform passing of the liquid (antifreeze) over the capsules. The SS steel meshes stimulate additional tribulations of the liquid inside the channels, enhancing the heat-transfer coefficient and improving the dynamic characteristics of the heat storage device.

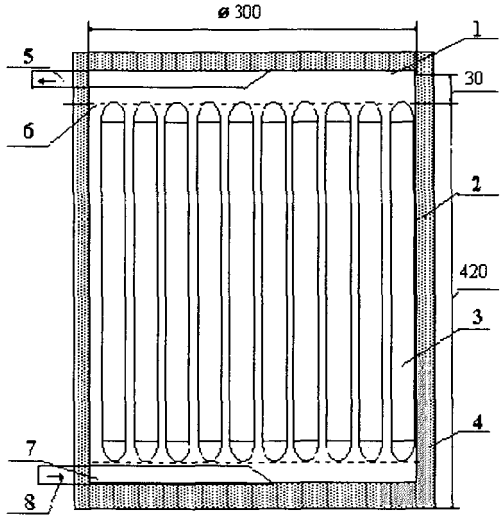

Fig. 4. Scheme of the experimental heat storage device: 1 - cover, 2 - envelope, 3 - capsule containing the PCM, 4 - thermal insulation, 5 - outlet pipe, 6, 7 - SS steel mesh, 8 - entrance pipe

The capsules are made of SS tubes with an external diameter of 25 mm. Crystal-hydrate $NaOH \cdot H_2O$ with an additive to prevent overcooling of the substance during the discharging of the HS is used as PCM. The phase change temperature is 64°C. Vacuum-powder thermal insulation for the HS is used for reducing heat losses during the engine switch-off period.

The arrangement of the PCM capsules inside the envelope is shown in Fig. 5. Table 1 summarises the characteristics of the experimental HS.

Table 1. Characteristics of the experimental HP

Parameter name	Value
Number of capsules	109
HS mass	65 kg
Thermal energy, stored by HS	14 MJ
HS overall dimensions	350×350×500 mm
Flow rate of circulated liquid	15 $l\,min^{-1}$
Heat storage period for heating bus engine (650 kg) up to 30°C	36 hours
HS discharging time	10 min

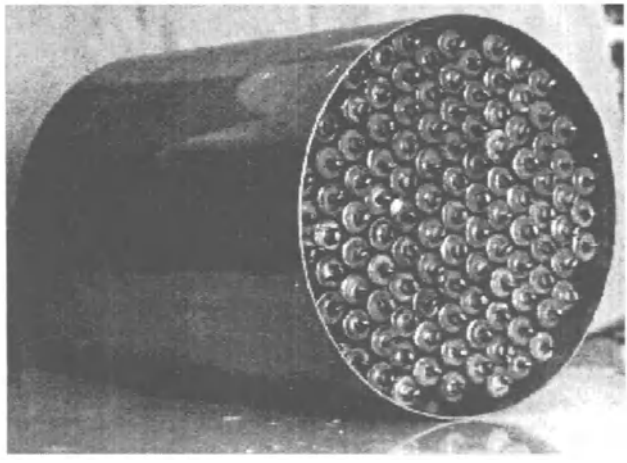

Fig. 5. PCM capsules inside the envelope

4 Operational Tests

4.1 Location of the HS device in the bus

The experimental device to start the pre-heating of the engine (Fig. 6) consists of the heat storage 4, electrical pump 6 with the control block 2, inlet 8 and outlet 3 pipes with valves 5. The outlet pipe of the HS is connected to the outlet of a water jacket before the thermostat 1. The HS is horizontally positioned, and an electrical pump is mounted on a single plate, and is placed at the right side nearer to the bus saloon. The basic scheme of the HS connection to the cooling system of the engine is shown in Fig. 7.

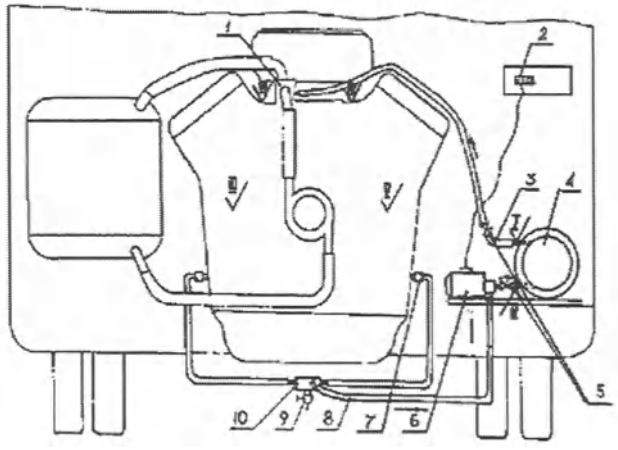

Fig. 6. Sketch of the experimintal HS device location in the bus LAZ-695N.
1 - thermostat, 2 - control block of electrical pump, 3 - outlet pipe of HS, 4 - heat storage (HS), 5 - valves, 6 - electrical pump, 7 - union, 8 - inlet pipe of HS, 9 - draining valve, 10 - T-pipe

The HS is connected in parallel to the engine water jacket. During discharge, the HS cooling liquid moves with the help of the electrical pump through the HS and the water jacket of the engine. A part of the liquid thus passes through a branch pipe of a small cooling loop bypassing the head of the cylinders. This reduces the heating efficiency of the engine a little bit, however, the thermal losses due to the small sizes of a branch pipe are insignificant. During the charge of the HS, when the thermostat is closed, the cooling liquid is simultaneously pumped by the water pump of the engine within a small cooling loop of the engine and the HS. Once the thermostat is open, the heat transfer liquid is pumped through the radiator (big cooling loop). During the storage period the valves 5 (Fig. 6) are closed and prevent a natural convective circulation of the liquid through the cooling system.

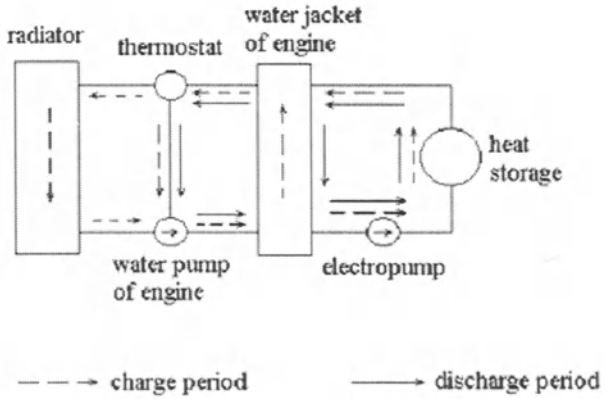

Fig. 7. Sketch of the HS connection to the cooling system of the engine

4.2 Operational test results

Operational tests were carried out for different regimes of the HS operation. These regimes are different in periods of heat storage, discharging and charging. The operation of the experimental HS under full-scale conditions was controlled with the help of six copper-constantan thermocouples (Fig. 6, positions I-VI).

The temperature history of the engine during discharging is shown in Fig. 8. Curve A is the theoretical average temperature of the bus engine. Lines III-VI are assigned to the thermocouples shown on Fig. 6. Experimental data have shown close agreement to the theory. Some overestimation of the theoretical values is caused by the heat losses to the surroundings.

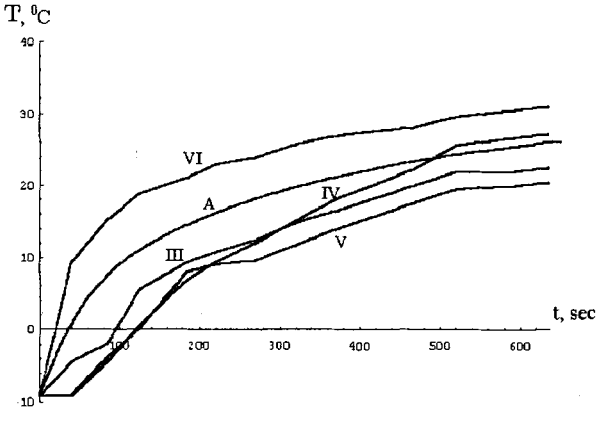

Fig. 8. Dependence of the engine temperature on discharge time. A -theoretical average temperature, III-VI - temperatures in different points of engine (Fig 6.)

Thus, the operational tests have shown the validity of the application of the developed engineering technique for the calculation of the heat storage parameters.

5 Conclusion

The result of this work is a practical confirmation of theoretical developments to facilitate a heat storage device in an internal combustion engine for starting by heating the engine from the energy stored in the heat storage device. The mathematical model allows to determine the design data and operational characteristics of heat storage.

The experimental sample of the HS works on the effect of the rejection and absorption of latent heat of the phase-change material for an urban bus "LAZ-695 N" and was developed in the Luikov Heat and Mass Transfer Institute. The HS was mounted on a bus and operated under real conditions. Experimental data showed close agreement with the mathematical model. Operational tests have corroborated the validity of the application of the developed engineering technique to calculate the heat storage parameters .

References

1. Wentworth J.T. (1968) Piston ring variables affect exhaust hydrocarbon emissions. Paper 680109 *Society of Automotive Engineers (SAE). Warrendale, PA*
2. Boam, D.J. (1986) Energy audit on a two litre saloon car driving an ECE 15 from a cold start. *Proc. Inst. Mech Engrs. Part D. J. Automobile Engng.* **200,** 66-67
3. Schatz O. (1992) Cold-start improvements with latent heat store. *Automotive Engng J.* February, 58-61
4. Bridgegate Ltd (Authorized dealership of BMW (GB)Ltd, Chesterfield) (1996) *Internal technology document.* 1-4
5. Darkwa K. and O'Callaghan P.W. (1997) Green transport technology (GTT): Analytical studies of a thermochemical store for minimising energy consumption and air pollution from automobile engines. *Applied Thermal Engineering* **17**, **7**, 603-614.
6. Nauman R., Emos H.(1986) Salt hydrates as a materials for latent heat storage. *Deutsche Akademie der Wissenschaften. Sitzungsberichte,* **3**
7. Porisini F.S.(1988) Salt hydrates used for latent heat storage: corrosion of metals and reliability it thermal performance. *Solar energy.* **41**, No.2
8. Panasienko T.I., Kudra S.A., Iacenko L.V.(1983) Corrosion behaviour of same heat storage construction materials. *Geliotehnika,* **5** (in Russian)
9. Isachenko V.P., Osipova V.S., Sukomel S.S.(1975) *Heat Transfer Energia,* Moscow (In Russian)
10. Vasiliev L.L., Burak V.S., Kulakov A.G. Mishkinis D.A., Bohan P.V. (1999) Heat storage device for pre-heating internal combustion engines at start-up. *Int. J. Therm. Sci.* **38**, 98-104
11. Iudaev B.N. (1988) Technical thermodynamics. *Heat Transfer.* Visshaia Shkola, Moscow (In Russian)

(Received 2 March 1999, accepted 12 June 1999)

Heat Pumps and Heat Pipes for Applications in Cold Regions

Leonard L. Vasiliev

Luikov Heat & Mass Transfer Institute, P.Brovka 15, 220072 Minsk, Belarus

Abstract. Advanced active carbon fibre/NH_3 heat pumps with dual sources of energy (solar/gas) were developed for providing space heating, cooling and sanitary hot water for buildings. The next heat pump generation will include a combination of chemicals with an active carbon fibre to increase the NH_3 absorption. Combination of heat pipes and heat pumps solves the problem of heating the ground and air in green houses using the heat of the ground, hot ground waters, solar energy and gas flames with heat storage.

1 Introduction

Even in the cold regions of the globe the soil temperature at the 10 – 20 m depth is all year round constant and equal to 10 – 12°C. The thermal energy of the ground water is thus very promising to recover and increase its potential; to this end heat pipes and heat pumps are used. Heat pumps, thermal storage and heat pipes as heat exchangers are used for heating and air-conditioning purposes in many different parts of the globe but in particular in its cold regions.

Environmental protection initiatives of different agencies have led to an intensification of research efforts in the technology of safe heat pumps and heat pipes due to the increased ozone concentration and due to global warming. Solid-gas sorption of heat powered cycles are one of the most attractive alternatives for heat pump applications [1], because they are absolutely benign for the environment: zero ODP (Ozone Depletion Potential), zero GWP (Global Warming Potential), insensitivity to movement and orientation and high performance in avoiding extra primary energy consumption. Actually, two different types of solid sorption are generally used – adsorption and chemical reactions [2,3].

Recently, practical and theoretical interest has concertrated on the combined action of physical adsorption and chemical reactions in the same volume at the same time [4-5]. As a solid-gas complex compound system a combination of an active carbon fiber Busofit and $CaCl_2$ salt were analyzed with a sorption capacity of more than 0.8 kg of ammonium in 1 kg of this complex compound. A cascaded cycle of NaX/ NH_3 (280 °C) and Busofit-$CaCl_2$/NH_3 was suggested [5] to improve the COP (Coefficient of Performance) of a solid sorption machine.

Conversion of solar energy into mechanical or electrical energy, hot or cold, may be achieved by means of various thermodynamic (Carnot, Rankine, Brayton, Stirling, Vuilleumeir, and Ericsson) cycles. The Carnot cycle is the most convenient to compare the COP of different liquid and solid sorption machines. The Rankine cycle is the most convenient for the electrical generation, and it is efficient for small temperature differences between the hot and cold sources of energy.

It is interesting to consider a combined heating, refrigeration and power-generation system with short cycles and capillary pumped evaporators, which would allow operation systems providing the power for valve operation; and a combined system would allow unencumbered operation [6]. Such a system could remain operational when the solar insulation is low, emitting its all-year-round operation and could be used in areas where solar energy alone is impractical. Many solar-powered domestic water-heating systems have a provision for a one-person gas heater as a back-up. Use of a gas system would be more economical, and utilizing gas and solar power simultaneously would reduce the costs and size of solar collectors employed in solar-driven adsorption systems, and it is beneficial to the gas consumption. Long heat pipes are very promising to recover the low potential ground energy with the help of heat pumps. We are interested to design a system with short cycles of operation. The type of implemented adsorbent (Busofit) strongly influences the COP of a cycle. Combination of different sorbent beds provides the possibility to increase the heat output of the heat pump. Among the solid sorption machines which operate as a vacant heat pump we need to consider a liquid/vapor equilibrium (L/V) and a solid/gas equilibrium (S/G) [1]. There are three modifications of such systems: the resorption system (2S/G), the internal heat-recovery system (1L/V and 2S/G) and the resorption-internal-heat-recovery system (3 S/G). Recently, a multisalt-reactor process was suggested, which implements a L/V balance and several S/G equilibria [2]. Following Castaing-Lasvignottes and Neveu [2] for two salt-resorption systems, application of the first and second law of thermodynamic gives

$$\begin{gathered} Q^1_{reg} + Q^1_{abs} + Q^2_{reg} + Q^2_{abs} = 0, \\ \frac{Q^1_{reg}}{T^1_{reg}} + \frac{Q^1_{abs}}{T^1_{abs}} + \frac{Q^2_{reg}}{T^2_{reg}} + \frac{Q^2_{abs}}{T^2_{abs}} + \Delta_i S = 0 \end{gathered} \tag{1}$$

with negligible internal irreversibilities. The external irreversibilities are

$$\Delta_i S^{ext} = \sum \left(\int \frac{\delta q_i}{T} - \frac{1}{T_i} \int \delta q_i \right). \tag{2}$$

Introducing the entropic temperature as

$$\widetilde{T} \equiv \int \delta q_i \Big/ \int \frac{\delta q_i}{T}, \tag{3}$$

eqs. (1) take the form

$$\begin{aligned} &Q^1_{reg} + Q^1_{abs} + Q^2_{reg} + Q^2_{abs} = 0, \\ &\frac{Q^1_{reg}}{\widetilde{T^1_{reg}}} + \frac{Q^1_{abs}}{\widetilde{T^1_{abs}}} + \frac{Q^2_{reg}}{\widetilde{T^2_{reg}}} + \frac{Q^2_{abs}}{\widetilde{T^2_{abs}}} = 0 \end{aligned} \tag{4}$$

with the internal heat recovery

$$R_1 \begin{cases} Q^1_{reg} + Q^1_{abs} = \Delta Q, \\ \dfrac{Q^1_{reg}}{\widetilde{T^1_{reg}}} + \dfrac{Q^1_{abs}}{\widetilde{T^1_{abs}}} = \Delta S, \end{cases} \qquad R_2 \begin{cases} Q^2_{reg} + Q^2_{abs} = \Delta Q, \\ \dfrac{Q^2_{reg}}{\widetilde{T^2_{reg}}} + \dfrac{Q^2_{abs}}{\widetilde{T^2_{abs}}} = -\Delta S, \end{cases} \tag{5}$$

$$COP = \frac{\frac{1}{\widetilde{T^2_{abs}}} - \frac{1}{\widetilde{T^2_{reg}}}}{\frac{1}{\widetilde{T^1_{abs}}} - \frac{1}{\widetilde{T^1_{reg}}}} \left[1 + \frac{\Delta Q}{Q^2_{reg}} \left(\frac{\frac{1}{\widetilde{T^2_{abs}}} - \frac{1}{\widetilde{T^1_{abs}}}}{\frac{1}{\widetilde{T^2_{abs}}} - \frac{1}{\widetilde{T^2_{reg}}}} \right) \right], \tag{6}$$

and

$$COP = \frac{1 - \frac{\widetilde{T^2_{abs}}}{T^2_{reg}}}{\frac{\widetilde{T^1_{abs}}}{T^1_{reg}} - 1} + \frac{\Delta S}{Q^2_{reg}} \frac{\widetilde{T^1_{abs}} - \widetilde{T^2_{abs}}}{\frac{\widetilde{T^1_{abs}}}{T^2_{reg}} - 1} = COP_c^{4\widetilde{T}} + \frac{\Delta S}{Q^2_{reg}} \frac{\widetilde{T^1_{abs}} - \widetilde{T^2_{abs}}}{\frac{\widetilde{T^1_{abs}}}{T^2_{reg}} - 1}. \tag{7}$$

In (1) - (7), p, T, Q and S are, respectively, vapor pressure, temperature, heat and entropy. Furthermore, the supscripts 1, 2 are the reactor numbers and the subscript *abs*, *reg* indicate *absorption* and *regeneration*, respectively.

2 Solar Adsorption Heat Pump

2.1 Solar collector

The solar concentrator (Fig. 1) is made from an aluminum plate as a tray (TV parabolic antenna) with diameter 1.2 – 1.8 m, the inner surface is covered by a metallic polymer film with high degree of reflection 0.68 (mirror). An aluminum-nitride coating increases the absorption coefficient of a solar receiver up to 92%. This system needs to have a solar oriented mechanism to move the solar concentrator.

The second solar concentrator (Fig. 3) is equipped with several vacuum tube collectors[1] 14; it is connected directly with cylindrical evaporators 13 of the two-phase heat-transfer system and subcooled water pipes 12 inside these evaporators. Such types of solar collectors can be installed without difficulty on any kind of roof. About 3 m^2 of the solar collector are sufficient to cover

[1] The numbers refer to the identifiers in Figs. 1-3.

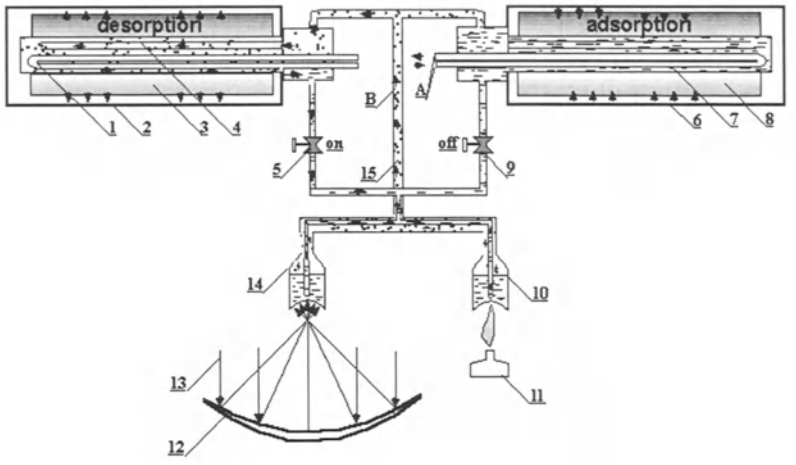

Fig. 1. Solar/gas heat pump for space heating: 1,7 - water heat exchangers; 2,6 - adsorbers; 3,8 - sorbent bed ("BUSOFIT" with chemicals); 4 - vapour channel; 5,9 - valves; 10, 14 - boilers/evaporators; 11 - gas heater; 12 - solar concentrator; 13 - solar radiation; 14 - vaour pipe; 15 - liquid pipe; A - cooling water; B - vapour channel

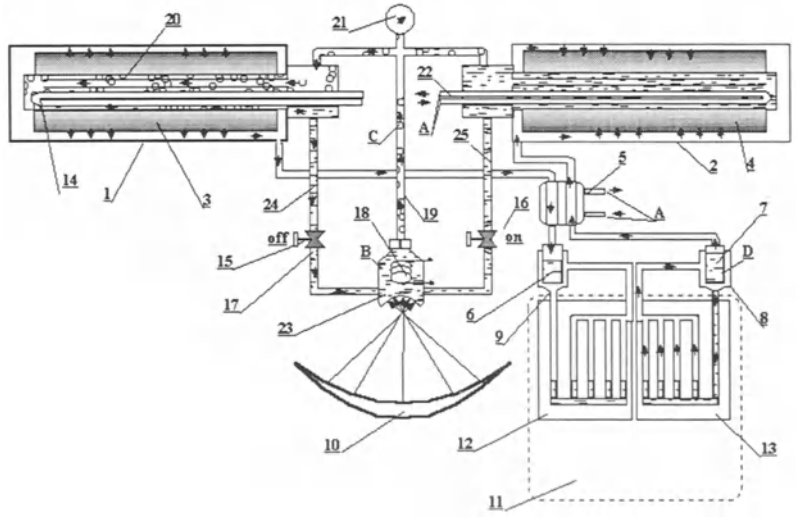

Fig. 2. Solar-gas-electric heat pump: 1,2 - adsorbers; 3,4 - sorbent bed; 5 - condenser; 6,7 - capillary-porous evaporators; 8,9 - condensers (loop heat pipes, or long heat pipes disposed underground); 10 - parabolic solar collector; 11 - cooling chamber (low temperature source of energy); 12,13 - loop heat pipes; 14,22 - condensers; 15,16 - valves; 17, 24, 25 - liquid pipes; 18 - electric heater (or gas heater); 19 - vapour pipe; 20 - vapour channel; 21 - pressure gauge; 23 - boiler/evaporator; A-cooling water; B - boiling water; C - vapour

the necessary heat demand for a 10 m^2 room heating. 12 borosilicate glass tubes with 12 thermosyphon evaporators inside are sufficient for 3 m^2 of the solar collector surface. Such solar collectors do not need to have a sun orientation system. Their efficiency is higher than that of flat collectors.

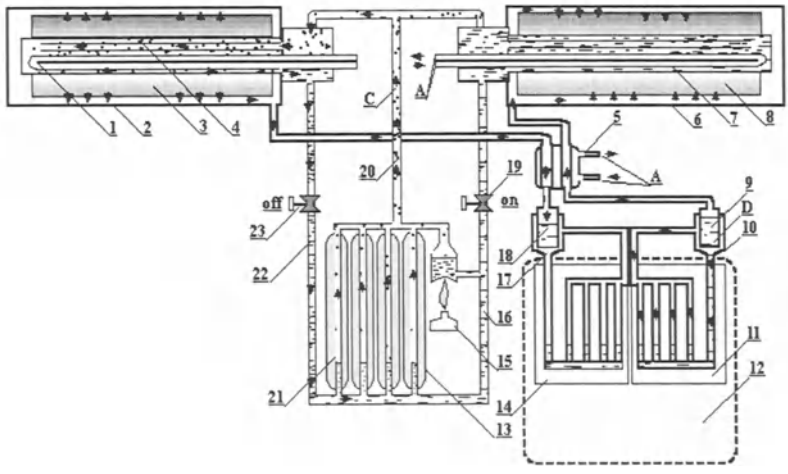

Fig. 3. Solar/gas heat pump for room or ground heating 1,7 - water heat exchangers; 2,6 - adsorbers; 3,8 - sorbent bed; 4 - vapor channel; 5,9 - valves; 10,13 - water boilers (evaporators); 11- gas heater; 12 - liquid channel; 14 - vacuum tube solar collector; A - cooling water; B -vapour

2.2 Two-phase heat transfer device

The two-phase heat-transfer device B (Fig. 1) is designed to heat the adsorbers; it is made as a vapor-dynamic thermosyphon, which has two small boilers 10 and 14, two elongated cylindrically finned condensers 4 inside sorbent canisters, a vapor channel 15 and two flexible liquid pipes with special valves 5 and 9 to regulate the water feeding of the boilers. The basic particularity of this thermosyphon is the periodical switch on and off (by valves) of the condensers with constant rate of the boiler-heat load (Fig. 1, Fig. 3). The first boiler 14 (Fig. 1) is positioned at the focus of a solar concentrator. The second boiler 10 is heated by a gas flame. The experimental data-acquisition system includes temperature sensors, a vapor-pressure gauge and a computer. The gas-flow rate is regulated as a function of the vapor temperature. A capillary pumped evaporator is more flexible with the point of view of its orientation in space, and it is more compact. A cylindrical evaporator was made of Ti sintered powder wick with a central tube for the liquid flow and some vapor channels on the inner surface of the stainless steel tube. The vapour

output and the liquid input are separated by a titanium sintered powder-capillary pump. The length of the evaporator is 280 mm, outer diameter - 38 mm, the wick porosity - 45 %, maximum pore diameter - 10 μm, medium pore diameter - 3-5 μm, capillary pressure head - 0.4 bar, wick thickness - 4 mm. Such a design of the evaporator ensures a minimum pressure loss in the wick and guarantees favorable conditions for vapor generation inside a porous structure.

This evaporator is operating with water, ammonium, methanol, acetone and propane. The maximum heat flux for this evaporator with ammonium is 1000 W. This evaporator is functioning together with the condenser made as a multiple U-turn-capillary tube with common fines. The overall thermal resistance of such a cooler is $R = 0.06\mathrm{K\,W^{-1}}$.

2.3 Solid sorbent canisters

Two solid sorbent canisters 3 and 8 (Figs. 1-3) are filled with an active carbon fiber Busofit wrapped on the surface of the condensers 4 between the aluminum fins. The length of the canister is 1.2 m, the outer diameter of the canister is 50mm. Five different metal salts (NiCl2, MgCl2, MnCl2, CaCl2, BaCl2) were used as sorbent media together with the active carbon fiber Busofit in five reactors. When the Busofit-salt composition was used the full heat output was at least two times more (for the Busofit -CaCl2 combination the full adsorption capacity is more than 0.85 kg of ammonium for 1 kg of the sorbent bed), but the time of reaction increased up to 20-25 min. In our first experiments we used only an active carbon fiber as a sorbent material to realize the cycle in the limit of 12 min.The full adsortion capacity of an active carbon fiber Busofit for different gases is presented in Table 1. The second experiments were performed with the combination of Busofit with chemicals.

Table 1. Adsorption capacities

Full adsorption capacity, kg/kg adsorbent	Busofit TM	Busofit TM $CaCl_2$
Acetone	0,61	-
Ammonia	0,62	0,85
Ethanol	0,60	-
Methanol	0,55	-

2.4 Evaporators

Two special type of porous ammonium evaporators 10, 15 (Fig. 2) were used to ensure its temperature fall during the ammonium adsorption cycle down to

-30°C. These evaporators are thermally connected with the loop-heat pipes 11, 14; the heat-pipe condensers are made as coaxial tubes on the outer surfaces of the evaporators to ensure condensation of the heat-pipe-working fluid (ammonium) on the outer evaporator surface.

The capillary porous wick for the evaporators (Fig. 4) was made by the gas-thermal Al powder sintering method in a water-vapor atmosphere. The metal-oxide $Al_2\ O_3$ powder wick was made with particle diameters $(10 - 40) \times 10^{-6}$m, thermally sintered together with the porosity 40 – 50% and pore diameter $(2 - 10) \times 10^{-6}$m ($Al_2\ O_3$ ceramic). The total pore volume in this ceramic is $(0,4 - 0,5) \times 10^3 mm^3 g^{-1}$. The macro-pore volume is $(0,35 - 0,38) \times 10^3 mm^3 g^{-1}$; the micro-pore volume is $(0,05 - 0,07) \times 10^3 mm^3 g^{-1}$. The permeability of such a system due to the macro pores is equal to $(2 - 3) \times 10^{13} m^2$ with the specific macro-pore surface of $(25 - 35) \times 10^{-6} m^2 g^{-1}$.

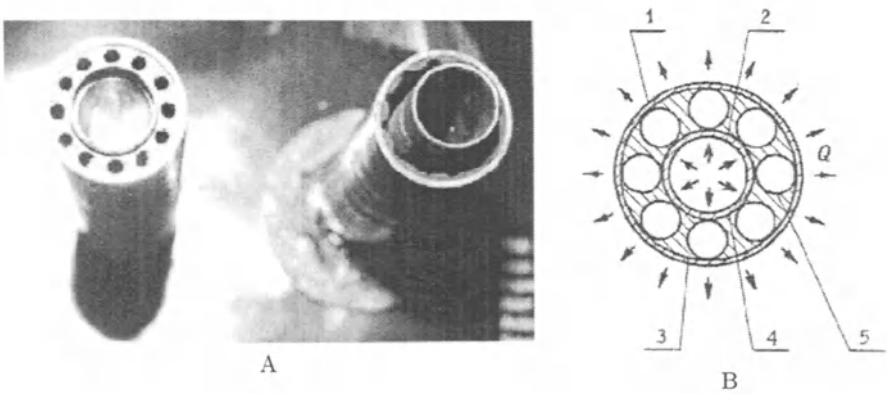

Fig. 4. Inverted meniscus evaporator: A - cross section from both sides; B - schematic of the evaporator cross section with vapor channels: 1, 2 - outer and inner walls of the evaporator; 3, 4 - porous wick with two layers of porous structure; 5 - vapor channels

The mechanical strength of such an $Al_2\ O_3$ ceramic under compression is not less than 30 – 40 mPa. Such a ceramic is a good adsorbent for the ammonium vapor and the capillary pressure Pcap = 2 (Wsg - Wsl)/ R is near 0.5 bar.

2.5 Condenser

The ammonium condenser 5 is made as a stainless steel tube-in-tube heat exchanger cooled by water to ensure complete vapor condensation and liquid ammonium cooling down to the room temperature. It is connected with the evaporators 10 and 15. There is another version of the compact condenser for such an evaporator (Fig. 5) [7]. An aluminum condenser shell with a liquid

cooling channel in the interior and capillary circumferential microgrooves on the inner surface of the condenser envelope is connected with the adsorbers through two bendable capillary tubes. One tube is for the vapor, the other tube for the subcooled liquid.

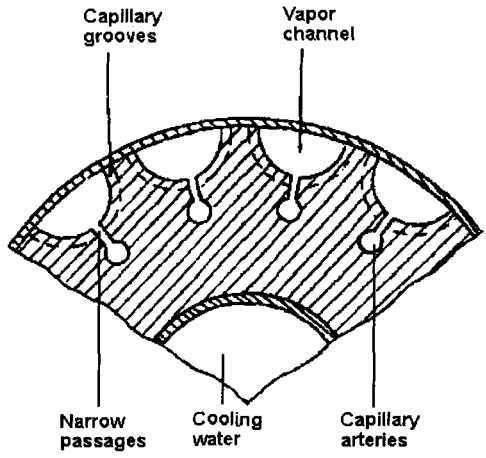

Fig. 5. Compact condenser with capillary microgrooves and arteries to remove liquid

These circumferential microgrooves serve as extended surfaces for the vapor condensation. Capillary forces move the film of liquid to the arteries through the narrow capillary passages (slots). Arteries are connected with the evaporator through the capillary tube.

The condenser is working as follows: the vapor flow from the evaporator is entering the vapor channels and condensing on the microchannels due to the temperature difference. The thin film of the liquid under the capillary forces is transported to the narrow slots and enters the arteries. Liquid enters through these arteries the inner part of the evaporator.

Since the liquid film moves only a short distance and because of the capillary action on this liquid film the heat transfer intensification is very high and exceeds the Nusselt heat transfer with condensation on a smooth surface. The experimental data with ammonium condensation on such a surface are shown in Fig. 6.

2.6 Loop heat pipes as cooling panels

The loop-heat-pipe panels (Fig. 7) are used as uniform temperature sheets inside the cold chamber connected with the ambient air. Two loop-heat-pipe panels, bent as an L-shape, were installed inside the cold chamber, situated outside the building. The evaporators 10 and 15 are positioned on the upper

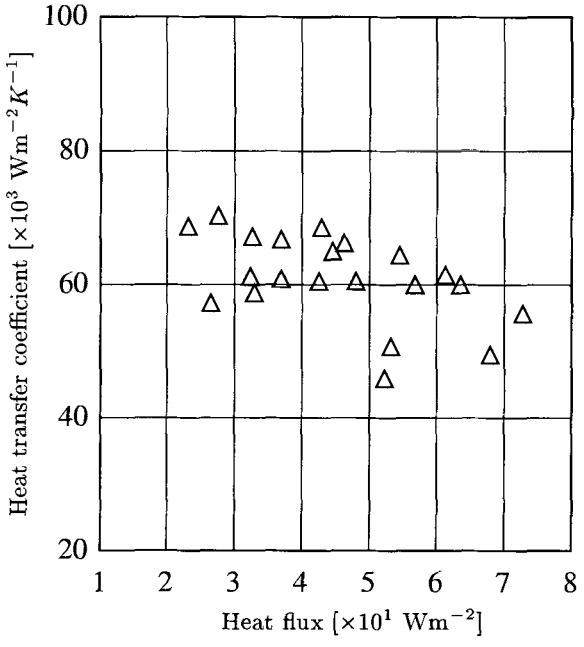

Fig. 6. Experimental data on heat transfer intensity with ammonium condensation

part of the cold chamber. The heat-pipe panels on their upper side (heat pipe condenser) have good thermal contact with the evaporators 10, 15; the extended lower part of the heat-pipe panels is used as a heat-pipe-finned evaporator. Such types of heat pipes with diameter 3 mm and length close to 1 m have no interior capillary structure and are functioning under the oscillating motion of the two-phase ammonium due to a large difference between the liquid and vapor density under the heat load. The driving force of the loop-heat pipes is the pressure force generated by the liquid, boiling at high temperatures (ambient air), with the non-equilibrium state between vapor and liquid and the vapor bubbles collapsing in the upper, cold part of the panel. Vapor plugs (bubbles) push the liquid plugs to the cold part of the unit, where vapor bubbles collapsed with the increase of the pressure difference between the vapor and the liquid. Due to the inter-connections between the two-phase channels the motion of the vapor bubbles and the liquid plugs is influenced by the motion of the fluid in the next sections on the loop-heat-pipe panel.

The total surface of the two-loop-heat-pipe panels was 1.2 m^2; the ammonium mass inside one panel was 50 g. Cold output from the heat-pipe panels was 300 W. Due to the cycling action of the solar refrigerator the time of the panel active cooling of the panel was limited by 12 min for one cycle. The temperature deviation of two-loop-heat-pipe panels for the time interval 0 - 200 min is shown in Fig. 8. The ambient air temperature was 7°C.

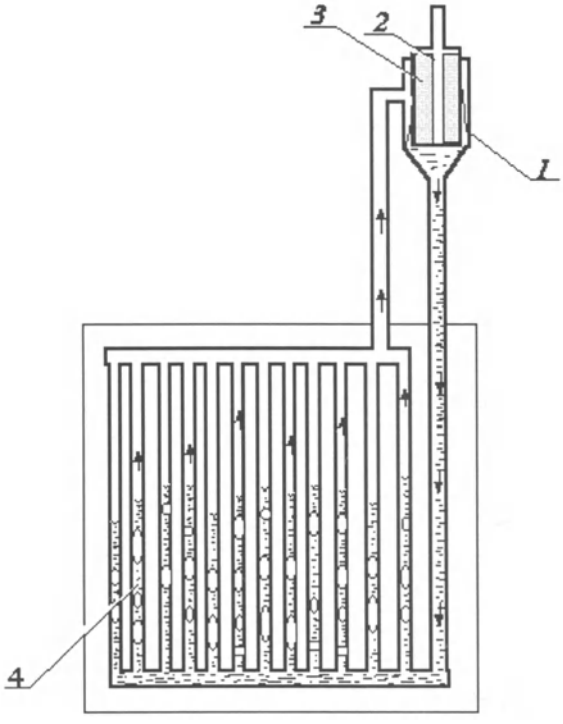

Fig. 7. Scheme of the first kind of loop-heat-pipe panel: 1- condenser of the heat pipe, 2- evaporator of the adsorption refrigerator, 3- porous structure, 4- heat pipe evaporator

3 Description of the Heat Pump Operation

The solar/gas heat pump (Fig. 1) has a solar receiver 12 (mirror with aluminum nitride film), a gas flame system 11 to heat the water boilers 14, 10, two sorbent bed canisters 2, 6, connected by the heat-recovery loop A, two phase-heat-transfer systems B (vapor-dynamic thermosyphon), one condenser 5 (Fig. 2) with two evaporators 10, 15 and two cold panels 11, 14 (loop heat pipes) heated by the air. When there is a forced convection heating, two finned evaporators 10, 15 are used without loop-heat pipes.

The energy required comes mainly from the heat supplied to the solar receiver (high temperature source of energy). The air is considered as a second low temperature source of energy. During cloudy days, or when the solar energy is insufficient the gas flame-heating system is switched on automatically in parallel with the solar heater. However, a small amount of work is required by the valve system to switch on and off the vapor-dynamic thermosyphon 15, to heat or to cool one sorbent bed after another (two step heat machine). This is in contrast to conventional vapor-compression systems, which require shaft work for the compression process. The main parameters of the heat

pump are included in Table 2. Such types of devices can be used as a heater and cooler, the heater and electricity generator, the cooler and desalination system, the cooler and air conditioning.

Table 2. Characteristics of the experimental Heat pump

Parameter name	Value
Solid-gas adsorber dimensions	L = 1.2 m, D = 0.05 m
Carbon fiber Busofit mass in one adsorber	0.75 kg
Ammonium mass in one adsorber	0.35 kg
Water mass in one thermosyphon	1 kg
Ammonium mass inside one loop heat pipe	0.05 kg
Total mass of heat pump	22 kg
Temperature of a hot adsorber	120°C
Condenser heat rejection temperature	50°C
Loop heat pipe temperature	0°C
Finned evaporator temperature (without loop heat pipes)	18°C
Heating capacity (Wkg^{-1} adsorbent)	350

The dynamics of a solar/gas heat pump is as follows: during the heating of the adsorbers by solar radiation or gas flame the heat is supplied to the sorbent bed by the two-phase heat transfer device-thermosyphon guided by the alternative valve operation. Two special valves 5 and 9 (Fig. 1) provide the possibility to switch on and off one, or the other adsorber (2, 6). The temperature of the carbon fiber 3 and 8 inside the adsorber 2 and 6 is increasing up to 110-120 °C and there is a high-pressure ammonium generation in pores, the process being endothermic. The superheated ammonium is entering the condenser 5 (Fig. 2) and cooling and condensing on the cold surface of the water heat exchanger A (Fig. 2). The liquid ammonium enters the porous evaporator 10 or 15 and is stored in the liquid reservoirs 9 or 16 disposed inside the evaporators. By this time the first half of a cycle is complete. During the second half of the cycle the active cooling of the water of the adsorbers 2 or 6 (water heat exchanger A, Fig.1) is starting, the sorbent bed temperature is falling down to 20-30 °C, and the ammonium pressure is falling down to 0.5 bar or less. When this pressure in the adsorber becomes lower than the ammonium pressure in the evaporator, the liquid ammonium inside the porous structure begins to evaporate with intense evaporator-wall cooling down to -30°C (Fig 8).

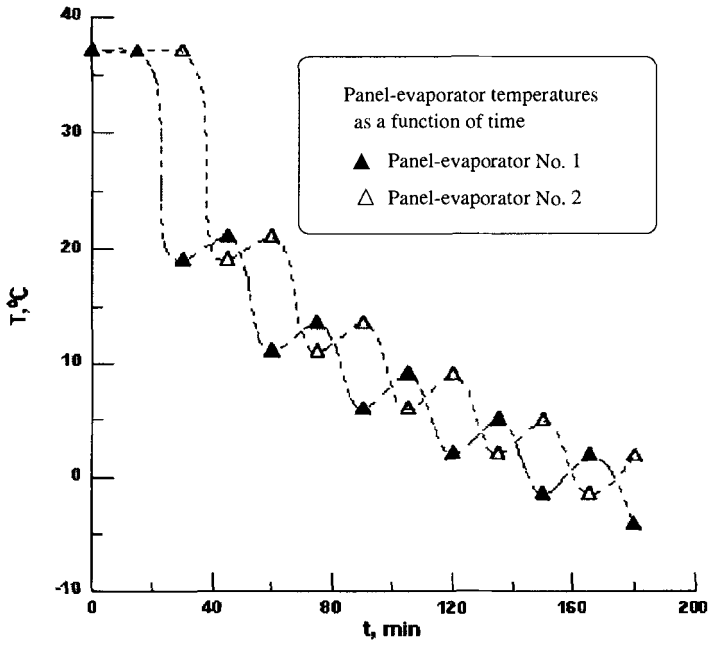

Fig. 8. The temperature deviation of the two-loop-heat-pipe panels

The evaporators 10,15 (Fig. 2) are thermally connected with the surroundings through the loop-heat pipes 11 and 14. Heat-pipe condensers are positioned on the outer surface of the evaporators. The multibent heat-pipe evaporating part is heated by the air. These two heat pipes are used as a second ammonium circuit thermally connected with the first ammonium circuit (evaporators 10,15). When the temperature of the evaporator 10, 15 decreases and becomes smaller than the air temperature, the ammonium in the heat pipes 11,14 starts to evaporate with continuing condensation on the outer surface of the evaporator 10, 15. The heat transfer between the air and the cold heat-pipe panels is realized by natural convection, the temperature of the heat pipe being lower by 3°C. Periodic switching on and off of the loop-heat pipe is realized automatically following the adsorption/desorption cycles of the sorbent bed (12 min). The second alternative is to use finned evaporators 10, 15 and fan to heat these evaporators by the air. Such a device is more compact, but needs to use electric energy for fan action. The third alternative is to use long heat pipes, Fig. 9.

4 Conclusions

A solar and gas-solid-sorption machine with 1.2 m^2 collection surface was designed and studied to build in the future an industrial heat pump. The ratio

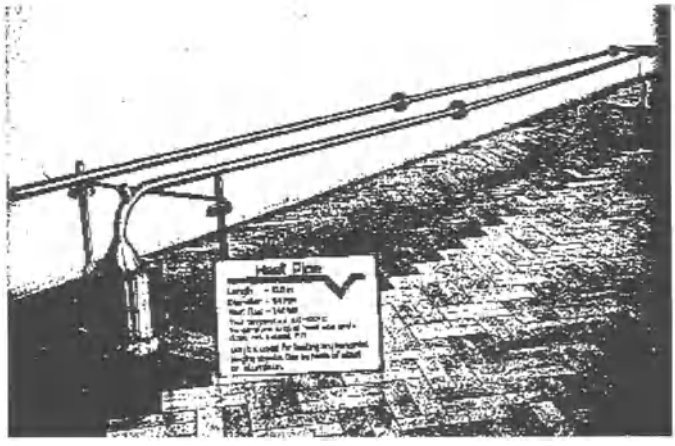

Fig. 9. Long heat pipe for the space or ground heating as a heat pump element

between the solar and gas flame energy supply is automatically maintained on the total level of 1 kW. It is an adsorption machine with very short (12 min) non intermittent cycles that uses the active carbon fiber "Busofit" as a sorbent bed and ammonium as a working fluid. The air is used as a medium to cool (inside the cold chamber) and water as a medium to heat (inside the adsorbers and the condenser). The system management consists only in actuating the special type valves to change the heating circuit and water valves to change the water cooling circuit. With the solar collector efficiency comprised near 0.7 it is possible to obtain a high solar COP value near 0.3. There is considerable scope for the application of such a hybrid electricity solar-adsorption system where intermittent or low solar insulation currently restricts their use. Such working fluids and energy sources are attractive on environmental grounds. Calculations for a combined refrigeration and power-generation system operating on electrical/solar, or gas/solar energy with heat recovery shows that a COP of 0.75 is achievable. Further increases in performance may be realized using multi-effect systems. The research into the economical viability of such systems is required to assess their commercial potentials. Such research should take into account anticipated changes in legislation governing the use and manufacture of conventional heat pumps and refrigerators.

A new SS (Stainless Steel)-water vapor-dynamic thermosyphon with two coaxial condensers was tested as a new thermal control device for the solar sorption refrigerators with heat load 1 kW and thermal resistance $Rts = 0.01\text{kW}^{-1}$.

A new type panel was developed and tested as a vacant alternative to the flat aluminum panel made by the Roll-Bond technology for the refrigerator cabinets. The cold output for such panels was near 300 W.

References

1. Boginsky, L.L., Reut, O.P. Sagaigora, I.G., Petiyshek, E.E., Vasiliev, L.L. Jr. (1997) Capillary Pumped Evaporator. *3rd Int. Seminar Heat Pipes, Heat Pumps, Refrigerators, Minsk, Belarus*, Sept. 15-18, pp.198-202.
2. Meunier, F. (1998) Solid Sorption Heat Powered Cycles for Cooling and Heat Pumping Applications, *Applied Thermal Engineering*, **18**, 715-729.
3. Miles, D.G., Sanburn, D.M., Nowakowski, G.A., Shelton, S.V. (1992) Gas Fired Sorption Heat Pump Development. *Proc. 1992 Solid Sorption Refrigeration Symposium, Paris*, Nov. 18-20, pp.91-96.
4. Neveu, P., Castaing, J., (1993) Solid-Gas Chemical Heat Pumps: Field of Applications and Performance of the Internal Heat of Reaction-Recovery Process. *Heat Recovery System and CHP* **13**(3), pp.233-251.
5. Vasiliev, L.L., Kanonchik, L.E., Antoukh, A.A., Kulakov, A.G. (1996) NaX Zeolite, Carbon Fibre and CaCl2 Ammonia Reactors for Heat Pumps and Refrigerators. *Adsorption* **2**, pp.311-316.
6. Vasiliev, L.L., Kanonchik, L.E., Antoukh, A.A., Kulakov, A.G., Rosin, I. (1994) Waste Heat Driven Solid Sorption Coolers. *SAE Technical Paper* no.941580, *24th Int. Conf. on Environmental Systems and 5th European Symposium on Space Environmental Control Systems, Friedrichshafen*, Germany, June 20-23.
7. Vasiliev, L.L., Khrustalev, D.K., Kulakov, A.G. (1991) High-Efficient Condenser with Porous Element. *SAE Technical Paper* No. 911524, *21st Int. Conf. on Environmental Systems, San Francisco, California*, July 15-18.
8. Critoph R.F. (1988) Performance limitations of adsorption cycles for solar cooling. *Solar Energy*, **41**- 1, 21-31 (1988)
9. Grenier Ph.,Guilleminot J.J., Meunier F., Pons M. (1988), Solar Powered Solid Adsorption Cold Store, *Trans. ASME*, **110**, 192-197
10. Bougard J.,VeronikisG. (1992), Adsorbeur modulaire pour machine frigorique so laire charbon actif-ammoniac, *Le Froid a Sorption Solide Symposium, Paris* 18-20 Novembre, pp. 282-287
11. Passos E.F., Escobedo J. F.,Meunier F. (1989), Simulation of an intermittant adsorptive solar cooling system, *Solar Energy*, **42**, 103-111
12. Mhiri F., Golli S.E. (1996), Etude d'un refrigerateur solaire a adsorption solide avec le couple charbon actif-methanol, *Revue Generale de Thermique*, **35**, N 412, pp.269-277
13. Speidel K., Kleinemeier H.P. (1992), Solar cooling processes using chemical reactions. *Proc. 1992 Solid Sorption Refrigeration Symposium, Paris*, Nov. 18-20, pp.288-293
14. Vasiliev L.L., Mishkinis D.A., Antukh A.A., Vasiliev L.L. Jr. (1999), Solar and electrical solid sorption refrigerator, to be published in *Int. J. Therm. Sci.* / Rev. Gen. Therm.
15. Vasiliev L.L., Nikanpour D., Antukh A., Snelson K., Vasiliev L. Jr., Lebru A., (1999), Multisalt-carbon chemical cooler for space applications, to be published in *ISHPC Proceedings, Munich'99*
16. Vasiliev L.L., Mishkinis D.A.,Vasiliev L.L. Jr., (1996), Multieffect-complex compound/ammonia sorption machines, *AB-Sorption 96, Montreal*, Quebec,Canada, September 17-20,1996, Keynote Papers, v. III, pp

(Received 14 June 1999, accepted 18 June 1999)